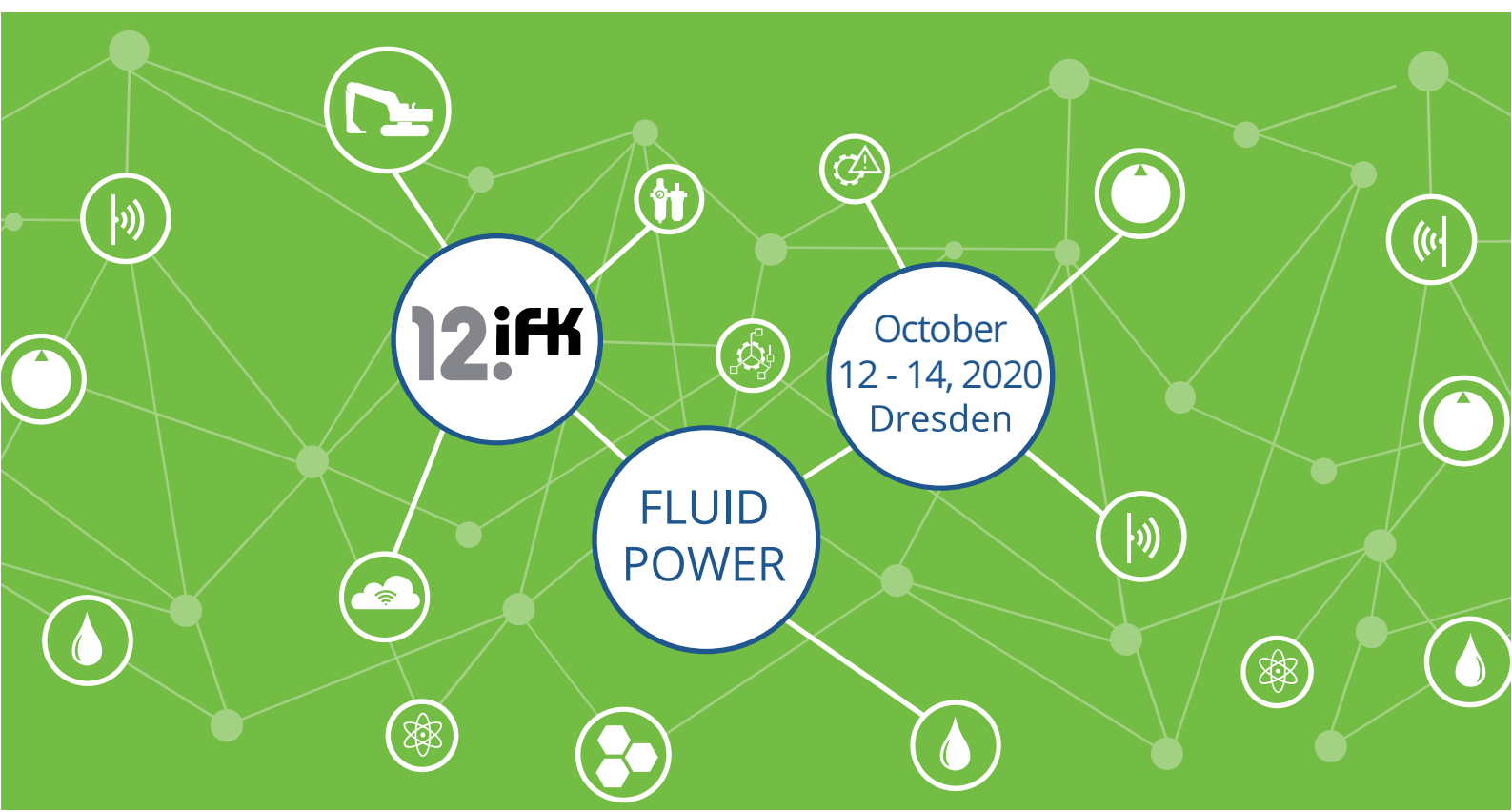


FLUID POWER FUTURE TECHNOLOGY!



CONFERENCE PROCEEDINGS



12th International Fluid Power Conference (12. IFK)

**October 12 – 14, 2020
in Dresden**

Volume 3 – Conference

Group 8:	Pneumatics
Group 9 11:	Mobile applications
Group 10:	Special domains
Group 12:	Novel system architectures
Group 13 15:	Actuators & sensors
Group 14:	Safety & reliability

Publisher:

Dresdner Verein zur Förderung der Fluidtechnik e. V. Dresden
c/o Professur für Fluid-Mechatronische Systemtechnik
Technische Universität Dresden
01062 Dresden

Alle Rechte vorbehalten.

Alle hier veröffentlichten Beiträge sind als Manuskript gedruckt.

Die Autoren sind für ihren Beitrag inhaltlich und redaktionell verantwortlich.

Nachdruck – auch auszugsweise – nur mit Zustimmung des Herausgebers und des Verfassers.

All rights reserved.

All papers are published as manuscript.

The authors are responsible as regards content and edition.

No part of this publication – also in extracts – may be produced without prior permission of the publishers.

Online Publication:

Eine elektronische Version der Tagungsbände wird dauerhaft archiviert und öffentlich zur freien Benutzung bereitgestellt.

Sie finden die Dokumente unter der dauerhaften stabilen URN: urn:nbn:de:bsz:14-qucosa2-386614

An electronic version of these proceedings will be permanently archived and publicly available for free personal use.

It can be found using the persistent identifier URN: urn:nbn:de:bsz:14-qucosa2-386614



<https://nbn-resolving.org/urn:nbn:de:bsz:14-qucosa2-386614>

WELCOME TO THE 12TH IFK

Dear Sir or Madam,

we are pleased to present the conference proceedings for the 12th edition of the International Fluid Power Conference (IFK). The IFK is one of the world's most significant scientific conferences on fluid power control technology and systems. It offers a common platform for the presentation and discussion of trends and innovations to manufacturers, users and scientists.

The Chair of Fluid-Mechatronic Systems at the TU Dresden is organizing and hosting the IFK for the sixth time. Supporting hosts are the Fluid Power Association of the German Engineering Federation (VDMA), Dresdner Verein zur Förderung der Fluidtechnik e. V. (DVF) and GWT-TUD GmbH. The organization and the conference location alternates every two years between the Chair of Fluid-Mechatronic Systems in Dresden and the Institute for Fluid Power Drives and Systems in Aachen.

The symposium on the first day is dedicated to presentations focused on methodology and fundamental research. The two following conference days offer a wide variety of application and technology orientated papers about the latest state of the art in fluid power. It is this combination that makes the IFK a unique and excellent forum for the exchange of academic research and industrial application experience.

A simultaneously ongoing exhibition offers the possibility to get product information and to have individual talks with manufacturers.

The theme of the 12th IFK is “Fluid Power – Future Technology”, covering topics that enable the development of 5G-ready, cost-efficient and demand-driven structures, as well as individual decentralized drives. Another topic is the real-time data exchange that allows the application of numerous predictive maintenance strategies, which will significantly increase the availability of fluid power systems and their elements and ensure their improved lifetime performance.

We create an atmosphere for casual exchange by offering a vast frame and cultural program. This includes a get-together, a conference banquet, laboratory festivities and some physical activities such as jogging in Dresden's old town.

I hope you enjoy reading the conference proceedings.



Prof. Dr.-Ing. Jürgen Weber

PROGRAM COMMITTEE

Achten, P.	Dr. ir., INNAS B.V., Breda NL
Bauer, F.	Dr.-Ing., Hydac Technology GmbH, Sulzbach/Saar
Boes, C.	Dr.-Ing., MOOG GmbH, Böblingen
Fabianek, M.	Dipl.-Ing., Liebherr Machines Bulle S.A., Bulle CH
Faß, U.	Dr.-Ing., Volvo Construction Equipment Germany GmbH, Konz
Fedde, T.	Dr.-Ing., CLAAS Tractor, Paderborn
Fiedler, M.	Dr.-Ing., Norgren GmbH, Fellbach
Fischer, M.	Dr.-Ing., Argo-Hytos Management + Consulting GmbH, Zug CH
Hahmann, W.	Dr.-Ing., Hydac International GmbH, Sulzbach/Saar
Hunger, I.	Lic. oec., Hunger DFE GmbH, Würzburg
Huster, G.	Dipl.-Ing., KraussMaffei Technologies GmbH, München
Igelhorst, W.	Dipl.-Ing., SMS Group, Mülheim an der Ruhr
Jähne, H.	Dr.-Ing., Hydrive Engineering GmbH, Freital
Kempermann, C.	Dr.-Ing., Fluitronics GmbH, Krefeld
Klug, D.	Dr.-Ing., Schuler Pressen GmbH, Waghäusel
Knobloch, M.	Dipl.-Ing., HAWE Hydraulik SE, München
Krallmann, J.	Dr.-Ing., Thomas Magnete GmbH, Herdorf
Krieg, M.	Dr.-Ing., Bosch Rexroth AG, Lohr am Main
Langen, A.	Dr.-Ing., Linde Hydraulics GmbH & Co. KG, Aschaffenburg
Legner, J.	Dipl.-Ing., ZF Friedrichshafen AG, Friedrichshafen
Leonhard, A.	Dr.-Ing., Parker Hannifin Manufacturing Germany GmbH & Co. KG, Chemnitz
Lindemann, L.	Dr., Fuchs Petrolub SE, Mannheim
Luther, R.	Dipl.-Ing., Fuchs Schmierstoffe GmbH, Mannheim
Lüüs, H.	Dipl.-Ing., Bucher Hydraulics GmbH, Klettgau
Martens, O.	Dr.-Ing., KOMATSU Mining Germany GmbH, Düsseldorf
Mundry, S.	Dr.-Ing., Caterpillar Global Mining Europe GmbH, Lünen
Neumeier, R.	Dipl.-Ing., Bürkert Werke GmbH, Ingelfingen
Pfab, H.	Dr.-Ing., Liebherr-Werk Biskhofshofen GmbH, Biskhofshofen AUT
Post, P.	Prof. Dr.-Ing., Festo AG & Co. KG, Esslingen
Rahmfeld, R.	Dr.-Ing., Danfoss Power Solutions GmbH & Co. OHG, Hamburg
Saffe, P.	Dr.-Ing., Aventics GmbH, Laatzen
Schmitz, K.	Prof. Dr.-Ing., RWTH Aachen
Schultz, A.	Dr.-Ing., Magnet-Schultz GmbH & Co. KG, Memmingen
Tappe, P.	Dr.-Ing., Magnet-Schultz GmbH & Co. KG, Memmingen
Sondermann, G.	Dipl.-Ing., Siempelkamp Maschinen- und Anlagenbau GmbH & Co. KG, Krefeld
Synek, P.	Dipl.-Ing., Fachverband Fluidtechnik im VDMA, Frankfurt am Main
Weber, J.	Prof. Dr.-Ing., TU Dresden

INTERNATIONAL ADVISORY COMMITTEE

Professor Eric Bideaux

INSA de Lyon, France

Professor Kalevi Huhtala

Tampere University of Technology, Finland

Professor Petter Krus

Lingköping University, Sweden

Professor Andrew Plummer

University of Bath, United Kingdom

Professor Kazushi Sanada

Yokohama National University, Japan

Professor Rudolf Scheidl

Johannes Kepler University Linz, Austria

Professor Kim Stelson

University of Minnesota, USA

Professor Huayong Yang

Zhejiang University, China

Professor Andrea Vacca

Purdue University, USA

Professor Takao Nishiumi

Shibaura Institute of Technology, Japan

PEER REVIEW AT THE 12TH IFK

peer reviewed

Many public institutions that support research projects require regular publication of the results. To ensure that the results are of scientific value, peer review is often required. Therefore we offer all authors the opportunity to have their work evaluated in order to be able to prove the scientific value.

A paper that has been chosen by the author to be reviewed will be subjected to an independent examination by a total of three specialized experts among the Program Committee as well as the Institute of Mechatronic Engineering at the TU Dresden, or the Institute for Fluid Power Drives and Systems at RWTH Aachen University. After this initial evaluation, the authors have the opportunity to revise their paper as needed and resubmit it with the necessary changes. If the reviewers accept the changes, the paper will be included in the conference proceedings as peer reviewed.

This extensive assessment process serves the purpose of quality assurance in terms of content and form, and would not have been possible without the expert support of the Program Committee. The organizers of the IFK want to thank all reviewers for their support.

The IFK traditionally is a colloquium where both scientists and representatives of industry come together to exchange their knowledge and experience. Accordingly, a peer review is only meaningful for some of the speakers, with the associated additional effort for both sides. Therefore the peer review is not intended to classify the paper but rather to support the need for it.



GROUP 8

Pneumatics

8-0	PNEUMATICS AND INDUSTRIE 4.0 – OPPORTUNITY OR CONTRADICTION? Peter Post, Festo AG, Germany	15
8-1	INCREASE OF ENERGY EFFICIENCY IN VACUUM HANDLING SYSTEMS BASED ON BIOMIMETIC PRINCIPLES Harald Kuolt, J. Schmalz GmbH, Germany	17
8-2	BEHAVIOUR AND IMPACT OF LEAKAGE IN VACUUM GRIPPING SYSTEMS David Straub, Universität Stuttgart, Germany	27
8-3	MUCH DOES NOT HELP MUCH: 3D PARETO FRONT OF SAFETY, COMFORT AND ENERGY CONSUMPTION FOR AN ACTIVE PNEUMATIC SUSPENSION STRUT Peter F. Pelz, Technische Universität Darmstadt, Germany	37
8-4	COMBINATIONS OF ENERGY SAVING MEASURES IN PNEUMATICS Vladimir Boyko, Technische Universität Dresden, Germany	43
8-5	ENERGY EFFICIENCY IN PNEUMATICS WITH THE “AIR SAVING BOX”: THE REVOLUTIONARY PLUG & PLAY SOLUTION FROM SMC Mario Heitmann, SMC Deutschland GmbH, Germany	53
8-6	ENERGY EFFICIENCY AND PERFORMANCE OF SERVOPNEUMATIC DRIVES FOR SPEED GOVERNORS BASED ON OPERATING POINTS Victor Juliano De Negri, Federal University of Santa Catarina, Brazil	59



GROUP 9 | 11

Mobile applications

9-0	ZF VIEW ON FUTURE DRIVETRAINS FOR COMPACT AND MEDIUM SIZE WHEEL LOADERS Jürgen Legner, ZF Friedrichshafen AG, Germany	71
9-1	AGROTHERMIE – DESIGN AND TESTING OF A NOVEL HYDRAULICALLY-ACTUATED, LOCALLY VIBRATING PLOUGH Jianbin Liu, Technische Universität Dresden, Germany	73
9-2	ASSISTANCE SYSTEM FOR AN AUTOMATED LOG-QUALITY AND ASSORTMENT ESTIMATION BASED ON DATA-DRIVEN APPROACHES USING HYDRAULIC SIGNALS OF FORESTRY MACHINES Chris Geiger, Karlsruhe Institut of Technology, Germany	83
9-3	EMISSION REDUCTION BY HYDRAULIC HYBRIDS Seppo Tikkanen, DIMECC Ltd, Finland	93
9-4	DESIGN AND PERFORMANCE EVALUATION OF NEXT GENERATION CLUTCH CONTROL VALVE Michael Erhard, Thomas Magnete GmbH, Germany	103
11-1	ACTIVE AUTOMATIC CHASSIS ACTUATION FOR AN EXCAVATOR Christoph Boes, Moog GmbH, Germany	113
11-2	INTEGRATED SMART HYDRAULIC DISPLACEMENT MACHINE FOR CLOSED SYSTEMS Rocco Kemnitz, RAPA Automotive GmbH & Co. KG, Germany	121
11-3	HYDROPNEUMATIC ALL-WHEEL SUSPENSIONS: APPLICATIONS, CHALLENGES AND SPECIAL SOLUTIONS Wolfgang Bauer, ARGO-HYTOS GmbH, Germany	129
11-4	FLUID DYNAMIC VIBRATION ABSORBER FOR CABIN SUSPENSION Nicolas Brötz, Technische Universität Darmstadt, Germany	139



GROUP 10

Special domains

10-0	THE ROOF WING OPENING SYSTEM OF THE UAE PAVILION AT EXPO 2020 Paolo Leutenegger, Duplomatic Motion Solutions S.p.A., Italy	149
10-1	PRELIMINARY DESIGN AND TESTING OF A SERVO-HYDRAULIC ACTUATION SYSTEM FOR AN AUTONOMOUS ANKLE EXOSKELETON Emmanuel Viennet, School of Engineering and Architecture of Fribourg, Switzerland	165
10-2	MINIATURE HYDRAULICS FOR A MECHATRONIC LOWER LIMB PROSTHESIS Christian Stentzel, Technische Universität Dresden, Germany	173
10-3	FULLY VARIABLE, SIMPLE AND EFFICIENT – ELECTROHYDRAULIC – VALVE TRAIN FOR RECIPROCATING ENGINES Wolfgang Schneider, W. Schneider Ingenieurbüro, Switzerland	181



GROUP 12

Novel system architectures

12-0	MODEL BASED ENGINEERING FOR ELECTRO-HYDRAULIC SOLUTIONS Matthias Wahler, Bosch Rexroth AG, Germany	193
12-1	BOOTSTRAP RESERVOIR CONCEPTS FOR ELECTRO-HYDRAULIC COMPACT CYLINDER DRIVES Søren Ketelsen, Aalborg University, Denmark	201
12-2	EFFICIENCY THAT BORDERS ON THE IMPOSSIBLE Walter List, Weber Hydraulik GmbH, Germany	217
12-3	ELECTRO-HYDRAULIC SWOT-ANALYSIS ON ELECTRO-HYDRAULIC DRIVES IN CONSTRUCTION MACHINERY Martin Inderelst, XCMG European Research Center GmbH, Germany	225
12-4	MODULAR INDEPENDENT METERING SYSTEM FOR MOBILE APPLICATIONS PROVIDING SMOOTH MODE TRANSITION Jan Lübbert, Technische Universität Dresden, Germany	239
12-5	DEVELOPMENT OF A HYDROSTATIC TRANSMISSION WITH INTEGRATED SUPPLY FOR WORKING HYDRAULICS Jihao Guo, Technische Universität Braunschweig, Germany	249



GROUP 13 | 15

Actuators & sensors

13-0	MEMS SENSORS IN HYDRAULICS, AN OPPORTUNITY TO CREATE SMART COMPONENTS Massimiliano Ruggeri, CNR-IMAMOTER, Italy	259
13-1	SELF-SENSING POSITION DETERMINATION ON A SENSOR-DESIGNED PROPORTIONAL SOLENOID Thomas Kramer, Technische Universität Dresden, Germany	269
13-2	ON/OFF SOLENOID WITH SENSORLESS POSITION DETECTION Peter Tappe, Magnet-Schultz GmbH, Germany	281
13-3	ROTOR SWIVEL MOTOR AS ACTUATOR OF AN INNOVATIVE CONTROL VALVE Ingo Dietrich, Technische Universität Darmstadt, Germany	287
13-4	EXPERIMENTAL AND NUMERICAL STUDY OF A NOVEL PIEZO-ELECTRIC PILOT STAGE FOR SERVOVALVES Paolo Tamburrano, Polytechnic University of Bari, Italy	297
15-1	DEVELOPMENT AND CONTROL OF SMART PNEUMATIC MCKIBBEN MUSCLES FOR SOFT ROBOTS Min Pan, University of Bath, UK	307
15-2	MULTISTABLE VALVE TECHNOLOGY WITH MAGNETIC SHAPE MEMORY ALLOY AS PASSIVE ELEMENT ACTIVATED BY A BIDIRECTIONAL SOLENOID ACTUATOR Julius Happel, ETO MAGNETIC GmbH, Germany	315



GROUP 14

Safety & reliability

14-1	LIFETIME IMPACT PREDICTION OF COMPONENT MODIFICATIONS IN AXIAL PISTON UNITS BY THE FAILURE LIKELIHOOD ASSESSMENT Ivan Baus, Danfoss Power Solutions, Germany	323
14-2	SIMULATION-BASED SYSTEM RELIABILITY ANALYSIS OF ELECTROHYDRAULIC ACTUATOR WITH DUAL MODULAR REDUNDANCY Maxim Andreev, ESI ITI GmbH, Germany	333
14-3	ENABLING SIL2 SAFETY CERTIFIED APPLICATIONS FOR MOBILE MACHINE OEMS Peter Lauer, Eaton Corp., USA	343
14-4	SUPPLEMENTARY FAILURE MODE AND EFFECT ANALYSIS (FMEA) FOR SAFETY APPLICATION STANDARDS DIN EN ISO 13849 SAFETY FUNCTION-FMEA Christa Düsing, XCMG, European Research Center GmbH, Germany	349



GROUP 8

Pneumatics

GENERAL LECTURE:

PNEUMATICS AND INDUSTRIE 4.0 – OPPORTUNITY OR CONTRADICTION?

Peter Post

Festo AG, Germany

* Corresponding author: Tel.: +49 351 46333559; E-mail address: fluidtronik@mailbox-tu-dresden.de

Modern industrial production processes are increasingly characterized by digital solutions in order to continuously increase their efficiency while taking sustainability aspects into account. Pneumatic components and systems have been and will continue to be an essential part of modern production plants and must face the special challenges posed by digitalization.

The mission statement of the Industrie 4.0 platform addresses the topics of autonomy, interoperability and sustainability as essential features of digital industrial processes and define special challenges for future pneumatic solutions.

Technological competence is the prerequisite for ensuring long-term stable autonomy. This is the focal point of joint research activities, which are driven forward by the Fluid Power Research Fund, taking up essential challenges of great

importance for integrated components, intelligent systems and services.

The communication ability of intelligent pneumatic systems is important for interoperability. Here the concept of the asset administration shell enables cross-manufacturing networking and simplified data exchange in a uniform format for a usage throughout the entire life cycle.

Against the background of the current sustainability and energy efficiency debate, the comparison of electrical versus pneumatic systems is addressed again and again. However, the preferred drive technology must be selected in an application-specific, holistic approach that is open to results. Nevertheless, it is necessary to rethink digital pneumatics in order to remain competitive in the long term.



INCREASE OF ENERGY EFFICIENCY IN VACUUM HANDLING SYSTEMS BASED ON BIOMIMETIC PRINCIPLES

Harald Kuolt^{1*}, Tim Kampowski^{2,3}, Simon Poppinga^{2,3}, Thomas Speck^{2,4}, Atena Moosavi⁵, Ralf Tautenhahn⁵, Jürgen Weber⁵, Felix Gabriel⁶, Erika Pierri⁶, Klaus Dröder⁶

¹ J. Schmalz GmbH, Johannes-Schmalz-Str. 1, 72293 Glatten, Germany

² Plant Biomechanics Group, Botanic Garden, Universität Freiburg, Schänzlestr. 1, 79104 Freiburg im Breisgau, Germany

³ Freiburg Materials Research Center (FMF), Universität Freiburg, Stefan-Meier-Str. 21, 79104 Freiburg im Breisgau, Germany

⁴ Cluster of Excellence livMatS – Living, Adaptive and Energy-autonomous Materials Systems, Georges-Köhler-Allee 105, 79110 Freiburg im Breisgau, Germany

⁵ Institut für Mechatronischen Maschinenbau, Technische Universität Dresden, Helmholtzstrasse 7a, 01069 Dresden, Germany

⁶ Technische Universität Braunschweig, Institute of Machine Tools and Production Technology (IWF), Langer Kamp 19b, 38106 Braunschweig, Germany

* Corresponding author: Tel.: +49 7443 2403-462; E-mail address: harald.kuolt@schmalz.de

ABSTRACT

Vacuum handling is a widespread technology in automated production systems for gripping of workpieces. Unfortunately, this solution accounts for a considerable share of industrial energy consumption. This consumption is mainly due to the losses in the involved steps like air compression, distribution, vacuum generation and gripper suction. However, the energy efficiency of vacuum handling systems is still relatively unexplored. The consortium partners are working together in the *BiVaS* project, which is funded by the Federal Ministry for Economic Affairs and Energy (BMWi). In this project, the drawback of high energy consumption is approached by the development of an energy-efficient ejector, a biomimetic suction gripper as well as on system integration and the development of energy-efficient operating strategies and their energetic balancing in order to reduce the consumption of compressed air by 20 %. This reduction will be quantified experimentally in a pilot plant benchmark, where a realistic handling process is developed and examined. This paper shows the state of the art focusing on energy consumption of vacuum handling technology and the behaviour of the involved components during different handling operations. Furthermore, first biomimetic concepts and an estimation of the increase of energy efficiency will be presented for the running project.

Keywords: Vacuum Handling, Energy Efficiency, Bioinspiration, Biomimetics, CFD optimization, Level set, adjoint variable

1. INTRODUCTION

Due to the rising cost of energy, worldwide mitigation of carbon footprint and social demand for sustainable and renewable orientation of industrial activities, efficient energy usage is mandatory. Improving the vacuum handling technology can lead to drastic energy saving possibilities in pneumatic systems. In this regard, the selection of appropriate components for production and the correct system design play important roles.

Energy efficiency in the field of vacuum handling technology is still low, due to the

transformation of electrical energy in compressed air and, subsequently, the transformation of compressed air into vacuum. Besides the vacuum generation, also the further infrastructure, the workpiece, the suction cups and of course the process parameters are influencing the energy consumption of a vacuum gripper in general, as mentioned above.

First research projects have already tried to tackle the existing problems (e.g. [1] and [2]), for example regarding pneumatically driven vacuum generators as a key component (e.g. [3-9]). Due to features like air saving function and others for

influencing the handling process, these research results are not significant enough to evaluate entire handling processes under real production conditions in use.

The predominant component to generate vacuum in industrial handling processes is a pneumatically driven vacuum ejector operated with compressed air. **Figure 1** shows typical energy conversion chains with compressed air supply (compressor and distribution), vacuum generation (ejectors) and transformation in holding force (vacuum gripper).

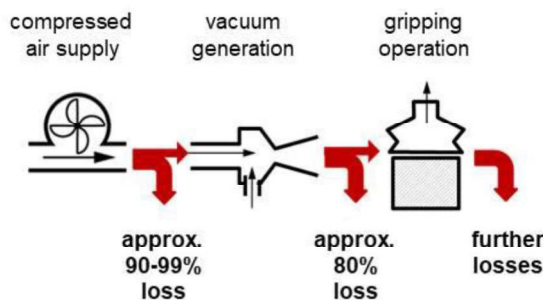


Figure 1: energy transformation and losses in vacuum handling (based on [10], [11])

Focusing on the compressed air supply in medium-sized companies, the efficiency ratio due to losses ranges only between 1 % [10] and 10 % [11], so that the energy supply for the genuine gripping system is one of the most expensive forms of energy [11]. By using pneumatically driven vacuum gripping systems, this already low efficiency ratio is further reduced, because the following energy conversion step with ejectors can not achieve higher efficiency ratios than approx. 20 %, as shown by own investigations. Besides the lossy transformation steps there are even further losses due to leakage and the process itself. At the end of a gripping process, less than 1 % of the used energy is available for the real handling task. If the inherent advantages of vacuum gripping technology should be also used in the future, it is necessary to increase their energy efficiency. For this increase, it is mandatory to optimize the vacuum generation as well as the transformation in a holding force with a gripper and as well as the operating method of the system significantly.

The economic importance of vacuum handling technology is shown by the following estimation: In 2012, the industrial power consumption of the Federal Republic of Germany amounted to 213 TWh, with a share of 7 % (16 TWh) for compressed air supply. An important share of this

air consumption reveals to “vacuum air” – compressed air to generate a vacuum [11]. Own research has shown, that this consumption amounts for approx. 5-20 %, depending on the industry segment. Table 1 shows the resulting economical energy costs and carbon emissions (0.1 €/kWh, 576 g CO₂/kWh [12]).

Table 1: Scenario for the share of “vacuum air” in the energy budget of Germany

Compressed Air [GWh]	Costs [Mio €]	CO ₂ -emissions [Mt]
0.81	81	0.467
1.62	162	0.933
2.43	243	1.400
3.24	324	1.866

Suction cups are the connecting device between handling and workpiece. During the gripping process, a vacuum is generated between suction cup and workpiece. The holding force of the gripper is proportional to the difference of pressure and the effective area impacted by the vacuum. For generating a vacuum between suction cup and workpiece, the system has to be sealed against ambient pressure, because leakage between the suction cup and workpiece will increase the air consumption of the gripping system. Also high amounts of dead volumes in suction cups, vacuum generators or hoses and fittings lead to an increasing energy demand.

Additionally, process safety is very important in handling processes and, therefore, requires a fail-safe gripper-workpiece-connection.

The air consumption of such systems can be reduced by using so-called “compact ejectors”, which allow stopping vacuum generation by their “air saving function” to stop vacuum generation when the predefined vacuum level is reached. As mentioned, these “compact ejectors” can reduce the air consumption up to 90 % [13-14]. Furthermore, there were different approaches for an energy efficient operating method in the past [15-17].

For a holistic approach, all factors influencing the air consumption are being investigated in *BiVaS*, as long as these parameters can be influenced by the distributor of the vacuum technology. E.g., leakage in the infrastructure, like distribution or the compressor itself, is not in focus.

For this holistic approach, new and optimized suction cups, vacuum generators and new ways to operate vacuum handling systems will be developed.

First, a biomimetic approach incorporating the basic investigation and abstraction of adhesion principles in plants and animals and the subsequent transfer of working principles into improved suction cups was started.

2. BIOMIMETIC OPTIMIZATION

Energy-efficient (suction) adhesion not only plays an important role in industrial applications, it as well represents a selective evolutionary advantage in various organisms. Consequently, a wide variety of different taxa have evolved numerous adaptations towards energy-efficient attachment mechanisms on various substrates over time. Since the same physical laws apply to both biological and technical suction devices (if used under comparable surrounding conditions), the analysis of the form-structure-function relationships of such biological adaptations and the transfer into technical adhesive systems by using a biomimetic approach is extremely promising to tackle the challenges described above.

Previous studies of biological suction systems have mainly been carried out on aquatic animals, especially in molluscs (particularly cephalopods like octopi and squids), arthropods (e.g. torrent-living insect larvae or diving beetles), fish (notably remora and clingfish) and lamprey. The adhesive organs of these animals are usually suction discs, which are used in the hunt for prey, in parasitic nutrition, and in copulation. The margins of biological suckers are usually very compliant, oftentimes microstructured and characterised by marginal protuberances (villi), which increase the overall adhesion due to contact splitting and compensate for surface irregularities thereby minimizing leakage currents between the suction chamber and the environment [18]. For instance, the microstructured suction disc rim of *Octopus vulgaris* is characterized by an average roughness of $R_a = 11.3 \mu\text{m}$, which enables a good form fit to the substratum [19]. Additionally, a variety of other animals, such as the Northern clingfish, secretes mucus along the rim of their suction organ to seal the suction chamber efficiently [20]. Last but not least, a good form fit with the

substrate is achieved through a high mechanical adaptability of the sucker margins. In particular, the suction disc rim of the octopus consists of extremely soft tissue (average modulus of elasticity, $E = 7.7 \text{ kPa}$) and can therefore adapt very well to surface asperities [19].

However, energy is not only required for establishing a pressure difference between the inside of a suction device and its surroundings, often energy is also essential for the maintenance of the overall adhesion. Again, some biological role models utilize functional principles which demonstrate that additional energy is not necessarily required to maintain suction adhesion for secured attachment. For example, the octopus does not exert any additional muscle power to stay attached to an object. Here, the deformation of an acetabular protuberance encloses a water torus inside each sucker during the attachment process. Hence, the state of adhesion is solely maintained by the cohesive force of the retained water and by frictional forces between the surfaces of the protuberance and the inner suction cup walls which counterbalance the elastic restoring force of the deformed protuberance [19, 21]. Such locking mechanisms are very promising and could also be implemented into a biomimetic suction device.

While quite a lot of preliminary work has already been done in the field of aquatic suction adhesion, to date very little is known about how (partly) terrestrial animals with suction discs achieve their attachment and which behavior-based, morphological and biomechanical adaptations exist here [18, 22]. Suitable terrestrial role models include, for example, land leeches that comprise several systematic groups (e.g. Haemadipsidae) and slug caterpillars (Limacodidae) [23]. Moreover, a very versatile suction adhesion system on two different suckers (anterior and posterior) that functions both under water and in air is found in medicinal leeches (*Hirudo verbana*) [24]. Here, experiments utilizing light and scanning electron microscopic techniques revealed that both the anterior and the posterior suction disc of *H. verbana* lack pronounced microstructures (e.g. villi), which are otherwise often to be found on the suckers of other organisms. Furthermore, it was possible to accurately resolve the attachment and detachment processes of these suction discs and to analyse corresponding suction cup deformations using high-speed videography. Interestingly, in

addition to other characteristics, a special behaviour was observed, according to which the leech always initiates the attachment process of its suckers by bringing their everted central parts into contact first, thereby preventing the inclusion of fluid inside the suction chambers. Therefore, a reduction of the sucker's dead volume, which is already implemented in the design or takes place before the suction cup is positioned on a given surface or work piece, can again lead to an increase in efficiency, since less or no energy has to be invested for evacuating enclosed fluids ("dead volume").

Comparative attachment force measurements of the two suction cups on differently structured surfaces in air and under water also highlighted that medicinal leeches developed a very versatile and fail-safe (suction) adhesion mechanism. In particular, the enormous adaptivity of the system becomes evident when the leech crawls upside down along a fine metal wire mesh [24]. This observation hints towards the fact that the medicinal leech employs different physical adhesion principles. In this context, the application of multiple physical principles within one adhesive system is not uncommon in nature (as can be seen in the systems of e.g. clingfish, octopi and limpets) and can certainly be regarded as a form of functional resilience which is, however, absent in current technical suction devices.

Another advantage of a biomimetic approach is that the optimization of a technical system does not necessarily have to use form-structure-function relationships that originate from only one role model and correspond to the same field of application as the biological system itself. Even principles of operation of other adhesive mechanisms can be transferred to improve certain aspects of a technical suction device, for example, to accomplish a functionalization of the contact surface. Clingfish, for instance, possess a strong hierarchical structuring at their suction rims, which lead to an increase in friction, which in turn counteracts deformation of the edges and thus failure of the whole system [25]. Furthermore, the toe pads of tree and torrent frogs are micropatterned in a way that enables an oriented drainage of obstructive fluids from the contact zone, thereby improving the adhesion of a system on heavily wetted surfaces [26-29].

To date, the majority of the afore-mentioned biological principles is not implemented in

standard technical suction devices. Conventionally, technical suckers consist of polymers exhibiting material properties that differ from those of potential biological concept generators. In addition, they usually exhibit considerable dead volumes, no microstructuring and generally no additional fluids such as mucus or other liquids that improve their sealing capability. Although there are already a number of biomimetic studies that utilize natural principles in order to optimize technical (suction) adhesion systems [30-32], there is still a lot of innovation potential for the development of biomimetic suction cups.

3. OPTIMIZATION OF EJECTORS

Complementing the research on biomimetic suction process, also the development of an innovative ejector principle that works significantly more efficiently than common ejectors in terms of supply pressure and energy consumption is considered. Research on the achievable performance potentials of low-pressure ejectors, by the use of numerical methods is conducted.

For identifying an optimal design for efficiency enhancement, the parametric shape and topology optimization like shown in **Figure 2** are suggested methods.

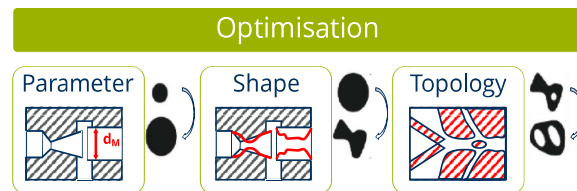


Figure 2: Optimization methods

We suggest applying level set topology optimization to find the optimum topology in order to find the optimal geometry for the desired, more efficient pneumatic ejector.

The level set method (LSM) is a numerical technique for tracking interfaces and shapes, which can travel through the control volumes.

The interface is the outline that separates the solid body and the surrounding fluid. This interface will move with a normal speed that comes from the surface gradient.

As can be seen in **Figure 3**, $\phi(\vec{x}, t)$ the level set function which is defined on the whole domain. $\Gamma(t)$ defines the contour of the geometry where $\phi(\vec{x}, t) = 0$. $\phi(\vec{x}, t) < 0$ and $\phi(\vec{x}, t) > 0$

gives the location of air and the solid body, respectively [33].

$$\begin{cases} \phi(\vec{x}, t) < 0 & \text{when } \vec{x} \in \Omega \\ \phi(\vec{x}, t) = 0 & \text{when } \vec{x} \in \partial\Gamma(t) \\ \phi(\vec{x}, t) > 0 & \text{when } \vec{x} \in R^n \setminus \bar{\Omega} \end{cases} \quad (1)$$

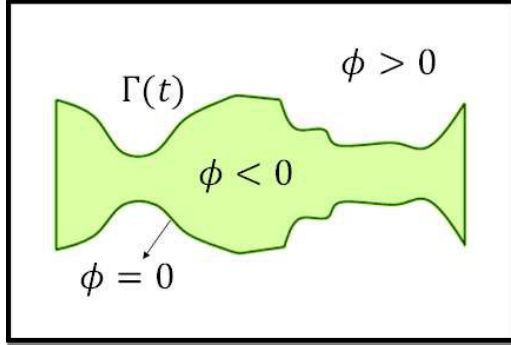


Figure 3: Level set contour of geometry

To follow the change of the contour, the change of the time-dependent zero level set is considered.

$$\frac{d}{dt} \phi(\vec{x}(t), t) = 0 \quad (2)$$

$$\frac{\partial \phi}{\partial t} + \nabla \phi \frac{d\vec{x}}{dt} = 0 \quad (3)$$

Where:

$\frac{\partial \phi}{\partial t}$ is temporal change of the level set function, $\nabla \phi$ is the gradient of the level set function, and $\frac{d\vec{x}}{dt}$ is the speed in the outward normal direction [33], **Figure 4**.

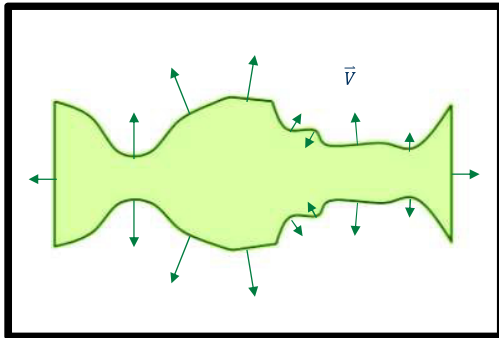


Figure 4: Contour normal velocity

With the combination of the finite element method and efficiency approaches, LSM can be used in topology optimization of an ejector.

However, in LSM the gradient of the target function is used as the normal speed for renewing the level set function. The approximation of the gradient by numerical differentiation is time consuming due to the high number of parameters and requires high computational costs. The direct

derivation of the LSM function can be replaced by a alternative formulation of topology optimization.

For this purpose, a coupling with another numerical method is proposed. The adjoint variable approach, which provides efficient sensitivity information of derivatives, is combined with level set methodology. In gradient-based optimization techniques, the goal is to minimize a suitable cost or objective function with respect to a set of design variables. The adjoint variable method is a very efficient method to compute the cost function gradient, which allows for the solution of general sensitivity analysis problems governed by fluid dynamics models.

Search for $\partial\Gamma = \{\vec{x}(t) | \phi(\vec{x}(t), t) = 0\}$

Minimize f

Subject to $g(\phi, B) = 0$

$$F(\phi, B) = f(\phi, B) + z^T \times g(\phi, B) \quad (4)$$

$$z^T = -\frac{\partial F}{\partial A} \times \left(\frac{\partial g}{\partial A}\right)^{-1} \quad (5)$$

Where z^T is the adjoint variable, f is the objective function, B can parametrize boundary and initial conditions or material properties, and g represents the relation between ϕ and B .

For this purpose, a proper selection of the objective function based upon energy consumption of pneumatic ejector is necessary.

3.1. Objective function

There are many possibilities to be found in the literature on how the efficiency of an ejector can be obtained; some of them are mentioned in the following:

Entrainment ratio

The ejector performance is often measured by the entrainment ratio (λ) defined as:

$$\lambda = \frac{\dot{m}_3}{\dot{m}_1} \quad (6)$$

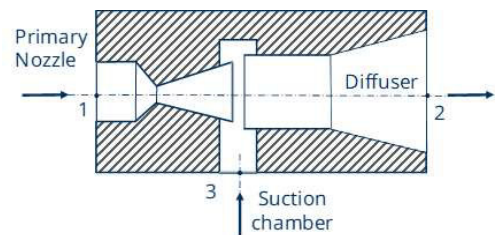


Figure 5: A schematic of an ejector

Where \dot{m}_1 is inlet mass flow rate from primary nozzle and \dot{m}_3 is intake mass flow rate from suction chamber according to **Figure 5**. The entrainment ratio is related to the coefficient of performance of the ejector by the following expression:

$$\eta = \lambda \frac{\Delta h_3}{\Delta h_1} \quad (7)$$

For a given ejector, the entrainment ratio is affected mostly by its geometry [34]. The ejector performance ratio decreases with increasing generator pressure [35]. Another important geometrical issue is the primary nozzle exit position. Eames [36] claimed that the influence of the nozzle exit position on λ could be as high as 40 %.

Components efficiency

In order to include irreversibility associated with the components, friction losses were introduced by applying isentropic efficiencies to the primary nozzle, suction, and diffuser. Therefore, efficiency of different parts of an ejector can be defined as below:

Nozzle [37]:

$$\eta_{nozz} = \frac{h_1 - h_{nozz,ex}}{h_1 - h_{nozz,ex,isn}} \quad (8)$$

Suction chamber [38]:

$$\eta_{suc} = \frac{h_3 - h_{nozz,exit}}{h_3 - h_{nozz,exit,isnt}} \quad (9)$$

Mixing chamber [39, 40]:

$$\eta_{entr,mix} = \frac{(\dot{m}_1 + \dot{m}_3) \cdot v_{mix}}{\dot{m}_1 \cdot v_{nozz,exit} + \dot{m}_3 \cdot v_{sec,nozz,ex}} \quad (10)$$

Energy conversion efficiency

In practice it is not possible to assign the energy consumption of single consumers directly to electrical energy input used for the system of compressed air supply network [3]. Therefore, the first law of thermodynamic is applied with assumption of adiabatic process and considering air as an ideal gas:

$$\eta = \frac{P_{32}}{P_{12}} \quad (11)$$

Where

$$P = \sum_{out} \dot{m}_o \left(c_v T + RT + \frac{1}{2} \left(\frac{\dot{m}_o RT}{p} \right)^2 \right)_o - \sum_{in} \dot{m}_i \left(c_v T + RT + \frac{1}{2} \left(\frac{\dot{m}_i RT}{p} \right)^2 \right)_i \quad (12)$$

Because the ejector has no interface for output of mechanical power, and the kind of the state change within the ejector is unproven and difficult to predicate, direct application of first law, with shown system boundary in **Figure 6**, is not suitable for energy efficiency determination.

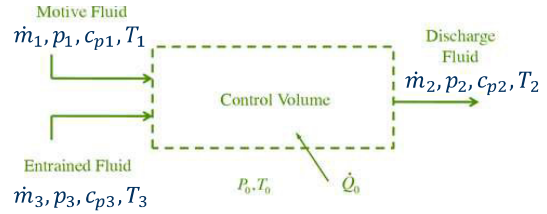


Figure 6: Ejector control volume

Exergy efficiency

With the use of exergy, the non-reasonable assumption of isentropic state change can be avoided. Because the exergy is characterized as the maximum useful work, the surrounding itself has to be in thermodynamic equilibrium [3]. According to ISO 6358 [41] $T_0 = 293.15 \text{ K}$ is a technical exergyless reference condition.

The exergy of a fluid flow can be determined with application of the first and second law of thermodynamics [42] and with consideration air as an ideal gas.

$$\dot{E}(T, p) = \dot{m} \left[(\Delta T \cdot c_p^{ig} - T_0 \cdot c_p^{ig} \cdot \ln \frac{T}{T_0} + T_0 \cdot R \ln \frac{p}{p_0} + \frac{1}{2} v^2) \right] \quad (13)$$

The exergetic conversion efficiency of an ejector can be described as in (14) and (15).

$$\eta_{exergy} = \frac{\dot{E}_{out}}{\dot{E}_{in}} \quad (14)$$

$$\eta_{exergetic} = \frac{\dot{m}_3 \left[(T_3 - T_0) c_p^{ig} - T_0 \cdot c_p^{ig} \cdot \ln \frac{T_3}{T_0} + T_0 R \cdot \ln \frac{p_3}{p_0} + \frac{1}{2} \left(\frac{\dot{m}_3 RT_3}{p_3 A_3} \right)^2 \right]}{\dot{m}_1 \left[(T_1 - T_0) c_p^{ig} - T_0 \cdot c_p^{ig} \cdot \ln \frac{T_1}{T_0} + T_0 R \cdot \ln \frac{p_1}{p_0} + \frac{1}{2} \left(\frac{\dot{m}_1 RT_1}{p_1 A_1} \right)^2 \right]} \quad (15)$$

To develop a novel methodology for boundary design of a pneumatic ejector, an algorithm will be implemented with the use of level set methods to minimize energy losses. It is expected that level set based topology optimizations are capable of handling the ejector optimization and will provide useful tools for design of ejectors.

According to efficiency approaches, the most eligible method to optimize the ejectors is based on exergy which covers almost all the influential parameters. To find the desirable higher-efficient ejector, $f(\phi, B) = 1 - \eta_{exergetic}$ can be

considered as objective function to be minimized during material distribution optimization.

4. OPERATING STRATEGIES FOR ENERGY-EFFICIENT VACUUM HANDLING PROCESSES

The process design can have a huge influence on the resulting energy consumption. In general, vacuum handling processes can be divided into four process phases (**Figure 7 top**) in accordance with [43]. Potential for energy savings can be identified in each of the first three main phases (**Figure 7, bottom**).

In the evacuation phase, a feasible strategy is to evacuate most of the air by pressing the gripper onto the surface of the part to be handled. This enables a reduction of the dead volume that must be actively evacuated by operating an ejector. Also, high consumption of compressed air for a safe blow-off of the grasped object can be avoided by adequate ventilation mechanisms.

However, the highest potential for energy savings is attributed to leakage prevention. In practice, it is technically feasible to compensate for a small leakage air flow by an ejector with an

In order to prevent permanent leakage between gripper and object prior to the operation of the handling process, it is necessary to enable the knowledge-based design of both the gripping system and the handling process. For the efficient acquisition of such knowledge, a method for the comparable characterization of suction grippers has been developed at IWF. In this method, suction grippers are tested in combination with multiple test objects with parametrized primitive geometries (**Figure 8**).

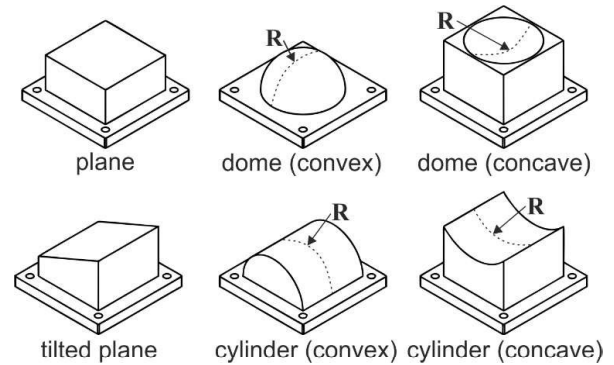


Figure 8: Parametrized primitive objects for standardized gripper tests

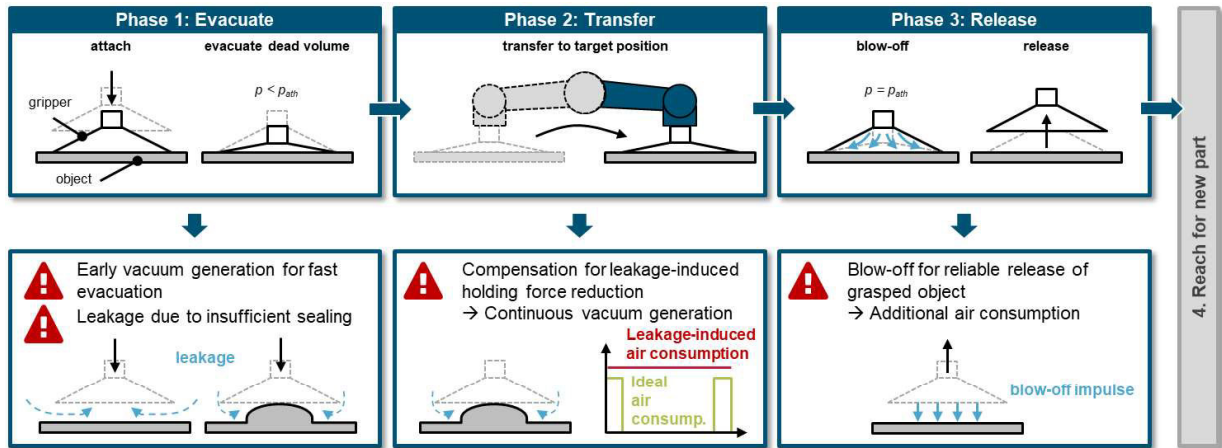


Figure 7: Process phases of vacuum handling processes and corresponding potentials for energy savings

adequate suction capability, as it is highly unlikely to achieve perfect sealing and thus zero leakage. Yet, permanent excessive leakage requires continuous vacuum generation and therefore leads to high energy consumption. Up to now, these uncertainties are encountered with adequate safety factors with which both the gripping system and the process parameters are overdimensioned.

This allows for the evaluation of specifically designed experiments, for example the investigation of the leakage during the evacuation phase.

Although it is intuitive that the sealing in combination with a plane will potentially be significantly better than in the case of a curved surface, through application of these standardized experiments, novel gripper designs could be

designed specifically to offer behavior opposing to standard grippers.

With this gripper-specific knowledge, the gripper system can be designed for an application-specific handling task with regard to the optimal positions of the required suction grippers. Such an optimization problem becomes increasingly complex with a rising amount of required grippers. In addition, the geometry of the part to be handled significantly influences the complexity, as well.

As soon as the gripping system has been designed, the gripper-specific knowledge can be applied for process design. Based on the allowed duration for one entire handling cycle, a certain duration can be attributed to each process phase as depicted in **Figure 7**. This directly influences the required ejector model, since the evacuation must be completed within the defined time interval. Furthermore, the accelerations which occur due to the defined robot trajectory result in loads that act upon the gripper-object interface (GOI).

Therefore, the robot trajectory can be designed to ensure that process-induced forces do not exceed the gripper-specific limitations. Finally, this enables to significantly reduce or even eliminate the currently applied safety factors which results in significant decreases of the energy consumption.

5. CONCLUSION AND OUTLOOK

As mentioned, energy efficiency of vacuum handling systems is still low. But there are several measures to optimize the energy consumption by designing new components and improving the process itself. Due to fact that the *BiVaS* project is still ongoing, there could only be presented approaches and some first results. Based on these results, we anticipate a reduction of the energy consumption in vacuum handling of up to 20 %.

NOMENCLATURE

A	Surface
B	Adjoint parameter
c	Specific heat
e	Exergy
f	Objective function
g	
h	Enthalpy
I_g	Ideal gas

IWF	Institute for machine tools, TU Braunschweig
LSM	Level set method
\dot{m}	Mass flow
p	Pressure
R	Gas constant
R_a	Average roughness
s	Entropy
T	Temperature
t	Time
v	Velocity
x	Coordinate
z^T	Adjoint variable
ϕ	Level set function
λ	Entrainment ratio
η	Efficiency
Γ	Geometry contour

REFERENCES

- [1] Fritz, F. (2017). Ein Modell zur energetischen Analyse und Bewertung von Vakuum-Greifsystemen. Dissertation. Stuttgart University, Shaker, 2017
- [2] Kuolt, H. (2013). Automatisierung in der Produktionstechnik – Herausforderungen und Lösungen zur Steigerung der Energieeffizienz von Handhabungssystemen. Stuttgart, GSaME Jahrestagung, 21.03.2013
- [3] Fritz, F., von Grabe, C., Kuolt, H., Murrenhoff H. (2013). Benchmark of existing energy conversion efficiency definitions for pneumatic vacuum generators. In: Proceedings of the 20th CIRP International Conference on Life Cycle Engineering", Singapore, 2013.
- [4] Kuolt, H., Gauß, J., Schaaf, W., Winter, A. (2016). Optimization of pneumatic vacuum generators – heading for energy-efficient handling processes. In: Proceedings of the IFK2016, Dresden, S. 267-280
- [5] Löser, H. R. (1966). Untersuchungen an ein- und zweistufigen Überschallejektoren mit zylindrischer Mischkammer, Darmstadt, 1966
- [6] Leistner, G. (1966). Experimentelle und theoretische Untersuchungen an einem Hochtemperatur-Überschallejektor mit zylindrischer Mischkammer, Darmstadt, 1966
- [7] Lucas, C., Rusche, H., Kaiser, C. Schröder, J. (2014). Numerical investigation of a two-phase CO₂ ejector. International Journal of Refrigeration, Bd. 43, p. 154–166, 2014.
- [8] Alimohammadi et al. (2013). A Validated Numerical-Experimental Design Methodology for a Movable Supersonic Ejector Compressor

- for Waste-Heat Recovery. *Journal of Thermal Science and Engineering Applications*, 2013
- [9] Opgenorth, M. J., Sederstrom, D., McDermott, W., Lengsfeld, C. S. (2012). Maximizing pressure recovery using lobed nozzles in a supersonic ejector. *Applied Thermal Engineering*, Bd. 37, p. 396–402, 2012
- [10] Schestag, R. (2015). *Betrieblicher Umweltschutz in der Metallbearbeitung*. Ministerium für Umwelt, Klima und Energiewirtschaft Baden-Württemberg, Stuttgart, 2015
- [11] EnEffAH (2012). *Energieeffizienz in der Produktion im Bereich Antriebs- und Handhabungstechnik*, Brochure of BMWi Project EneffAH, 2012.
- [12] Icha, P. (2013). *Entwicklung der spezifischen Kohlendioxid-Emissionen des deutschen Strommix in den Jahren 1990 bis 2012*, Umweltbundesamt, Hrsg., Deassa-Roßlau, 2013
- [13] J. Schmalz GmbH (2017). *Kompaktejektoren X-Pump SXPi* Available: <https://www.schmalz.com/de/vakuumtechnik-fuer-die-automation/vakuum-komponenten/vakuum-erzeuger/kompaktejektoren/kompaktejektoren-x-pump-sxpi-sxmpi-mit-io-link>. Access:14 2 2017].
- [14] Kuolt, H. (2015). *Verfahren zum Betreiben einer Unterdruckhandhabungsvorrichtung, sowie Unterdruckhandhabungsvorrichtung*. 2015.
- [15] Wigren, G. (2015). *Object-sensing valve for a vacuum gripper*, 2015.
- [16] Mayer, M., Anderle, J., Wirtl, H. (2017). *Vakuum-Greifvorrichtung und Verfahren zum Betreiben einer Vakuum-Greifvorrichtung*, 2017.
- [17] Holecek, T., Eisele, T., Kuolt, H, Frey, C (2015). *Method for operating a vacuum generator and a vacuum generator*. 2015
- [18] Ditsche, P. & Summers, A.P. (2014). Aquatic versus terrestrial attachment: water makes a difference. *Beilstein J. Nanotechnol.*, 5: 2424–2439.
- [19] Tramacere, F., Kovalev, A., Kleinteich, T., Gorb, S.N. & Mazzolai, B. (2014). Structure and mechanical properties of *Octopus vulgaris* suckers. *J. R. Soc. Interface*, 11: 20130816.
- [20] Wainwright, D.K., Kleinteich, T., Kleinteich, A., Gorb, S.N. & Summers, A.P. (2013). Stick tight: suction adhesion on irregular surfaces in the northern clingfish. *Biol. Lett.*, 9: 20130234.
- [21] Tramacere, F., Beccai, L., Kuba, M., Gozzi, A., Bifone, A. & Mazzolai, B. (2013). The morphology and adhesion mechanism of *Octopus vulgaris* suckers. *PLoS One*, 8: e65074.
- [22] Wolff, J.O. & Gorb, S.N. (2016). Suction cups. In: Wolff, J.O. & Gorb, S.N. (eds.), *Attachment structures and adhesive secretions in Arachnids. Biologically-inspired systems*. Springer, Cham: 87-93.
- [23] Epstein, M.E. (1995). Evolution of locomotion in slug caterpillars (Lepidoptera: Zygaenoidea: Limacodid group). *J. Res. Lepid.*, 34: 1-13.
- [24] Kampowski, T., Eberhard, L., Gallenmüller, F., Speck, T. & Poppinga, S. (2016). Functional morphology of suction discs and attachment performance of the Mediterranean medicinal leech (*Hirudo verbana* Carena). *J. R. Soc. Interface*, 13: 20160096.
- [25] Ditsche, P. & Summers, A.P. (2019). Learning from Northern clingfish (*Gobiesox maeandricus*): bioinspired suction cups attach to rough surfaces. *Phil. Trans. R. Soc. B*, 374: 20190204.
- [26] Federle, W., Barnes, W.J.P., Baumgartner, W., Drechsler, P. & Smith, J.M. (2006). Wet but not slippery: boundary friction in tree frog adhesive toe pads. *J. R. Soc. Interface*, 3: 689-697.
- [27] Drotlef, D.M., Appel, E., Peisker, H., Dening, K., Del Campo, A., Gorb, S.N. & Barnes, W.J.P. (2015). Morphological studies of the toe pads of the rock frog, *Staurois parvus* (family Ranidae) and their relevance to the development of new biomimetically inspired reversible adhesives. *Interface Focus*, 5: 20140036.
- [28] Iturri, J., Xue, L., Kappl, M., García-Fernández, L., Barnes, W.J.P., Butt, H.-J. & Del Campo, A. (2015). Torrent frog-inspired adhesives: attachment to flooded surfaces. *Adv. Funct. Mater.*, 25: 1499-1505.
- [29] Kim, D.W., Baik, S., Min, H., Chun, S., Lee, H.J., Kim, K.H., Lee, J.Y. & Pang, C. (2019). Highly permeable skin patch with conductive hierarchical architectures inspired by Amphibians and Octopi for omnidirectionally enhanced wet adhesion. *Adv. Funct. Mater.*, 29: 1807614.
- [30] Tramacere, F., Follador, M., Pugno, N.M. & Mazzolai, B. (2015). Octopus-like suction cups: from natural to artificial solutions. *Bioinspiration Biomim.*, 10: 035004.
- [31] Follador, M., Tramacere, F. & Mazzolai, B. (2014). Dielectric elastomer actuators for octopus inspired suction cups. *Bioinspiration Biomim.*, 9: 046002.

- [32] Lee, H., Um, D.-D., Lee, Y., Lim, S., Kim, H. & Ko, H. (2016). Octopus-inspired smart adhesive pads for transfer printing of semiconducting nanomembranes. *Adv. Mater.*, 28: 7457-7465.
- [33] Sethian, J. (1998). *Fast Marching Methods and Level Set Methods for Propagating Interfaces*. Karman Institute Lecture Series, Computational Fluid Mechanics.
- [34] Varga, S., Oliveira, A., Diaconu, B. (2009). Numerical assessment of steam ejector efficiencies using CFD. *International Journal of Refrigeration* Vol. 32, 1203-1211.
- [35] Chunnanond, K., Aphornratana S. (2004). An experimental investigation of a steam ejector refrigerator: the analysis of the pressure profile along the ejector. *Applied Thermal Engineering* Vol. 24, 311–322.
- [36] Eames, I., Ablwaifa, A., Petrenko, V. (2007). Results of an experimental study of an advanced jet-pump refrigerator operating with R245fa. *Applied Thermal Engineering* Vol. 27, 2833–2840
- [37] Rogdakis, E., Alexis, G. (2000). Design and parametric investigation of an ejector in an air-conditioning system. *Applied Thermal Engineering* Vol. 20, 213–226.
- [38] Cizungu, K., Mani, A., Groll, M. (2001). Performance comparison of vapour jet refrigeration system with environment friendly working fluids. *Applied Thermal Engineering* Vol. 21, 585–598.
- [39] Eames, I., Aphornratana, S., Haider, H. (1995). A theoretical and experimental study of a small-scale steam jet refrigerator. *International Journal of Refrigeration* Vol. 18(6), 378–386.
- [40] Huang, B., Chang, J., Wang, C., Petrenko, V. (1999). A 1-D analysis of ejector performance. *International Journal of Refrigeration* Vol. 22, 354–364.
- [41] ISO 6358 (1989). *Pneumatic fluid power; components using compressible fluid; determination of flow-rate characteristics*, Beuth, Berlin.
- [42] Baehr, H., Kabelac, S. (2009). *Thermodynamik: Grundlagen und technische Anwendung*. Springer, Berlin, Heidelberg.
- [43] Monkman, G. J. (2007). *Robot grippers*. Weinheim, Chichester: Wiley-VCH

BEHAVIOUR AND IMPACT OF LEAKAGE IN VACUUM GRIPPING SYSTEMS

David Straub*

Graduate School of Excellence advanced Manufacturing Engineering in Stuttgart (GSaME), Universität Stuttgart, Nobelstraße 12, 70569 Stuttgart, J. Schmalz GmbH, Johannes-Schmalz-Straße 1, 72293 Glatten

* Corresponding author: Tel.: +49 7443 2403470; E-mail address: david.straub@gsame.uni-stuttgart.de

ABSTRACT

Leakage in a vacuum system causes the pressure to rise if it is not compensated like in case the supply energy carriers fail. This leads to the workpiece to be dropped. So in order to design vacuum gripping systems that can withstand a failure of the supply energy carriers over a predefined amount of time, it is crucial to know the influences and effects of leakage. In previous examinations the behavior of leakage has been examined on the basis of a closed fluidic reservoir with a hole in its wall. But the only impacts taken into account here are the volume of the reservoir, the diameter of the hole and the pressure difference. Whereas when it comes to vacuum gripping systems, the leakage has significantly more influencing factors as it is neither a single component nor a closed system. In vacuum gripping systems leakage mostly occurs at the interface between the suction cups and the workpiece. So in this contribution the focus is on the impact of the properties of those components, and how the variation of these properties affects leakage. To achieve this, a theoretical description is done based on the aforementioned research, which is expanded in order to the relevant characteristics of a vacuum gripping system. After that the description is evaluated on a test bench. The goal is to be able to make a statement about the leakage rate for a vacuum gripping system composed of standard components. This can then be used in the design process of such gripping systems, which have to fulfil the requirement of compensating leakage in case the energy supply fails.

Keywords: vacuum gripping systems, leakage

1. INTRODUCTION

Current design methods for vacuum gripping systems mostly focus on load transfer or selection of gripping points (c.f. e.g. [1–5]). They do not take into account a possible failure of the supply energy carriers. Especially in cases where dropping the workpiece can result in severe damage knowledge about leakage is crucial. This occurs for example in special human-robot collaboration applications where extraordinary heavy objects like batteries for vehicles with a hybrid powertrain are handled [6]. Dropping these can harm bystanders on one hand through their mass that can be above 100kg, and on the other hand through an exothermic chemical reaction that is caused by the drop.

In order to avoid that, knowledge about the impacts and effects of leakage is crucial.

2. STATE OF THE ART

Since a vacuum system consists of different components which have to be sealed to each other, so-called leaks can occur. They cause a gas inflow and can have different geometric characteristics [7]. These occur in vacuum gripping systems, when there is no completely closed sealing lip. This incomplete seal can be caused, for example, by uneven and rough workpiece surfaces [8]. The shape of the suction cup can also influence the leakage [9]. In general, the gas inflow I_E into a vacuum system can be divided into several inflow components:

$$I_E = I_L - I_D - I_P - I_V \quad (1)$$

These are described as follows [10]:

- I_L describes the inflow due to geometrical openings between the vacuum system and the environment.

- I_D describes the gas flow that occurs due to induced or thermal desorption, the process by which atoms or molecules on the surface of a solid enter the gas phase.
- I_p describes the gas flow through completely dense parts (so-called permeation), a diffusion process due to a pressure gradient.
- I_v describes the process flow that occurs in the vacuum system due to a vacuum technology process such as sublimation or evaporation of substances under vacuum.

The leakage I_L due to openings between the vacuum system and the environment (in particular at the contact area of workpiece and suction cup) can be divided into three categories (cf. **Figure 1**) [11].

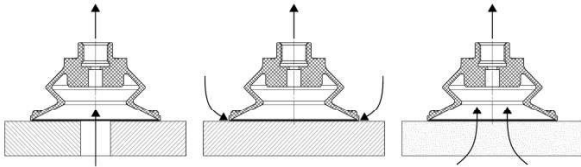


Figure 1: Three categories of leakage in vacuum gripping systems according to [11]

First order leakage (left) occurs within the suction surface at an opening in the workpiece. This is the case, for example, with perforated sheets. The second order leakage (middle) results from leaks between the contact surface of the suction cup and the workpiece. This can occur, for example, with uneven workpieces such as checker plates. Consequently, the surface roughness of the workpiece has an influence on the leakage [12, 13]. Third order leakage (right) is due to air permeability of the workpiece, for example with wood or cardboard. This means that this type of leakage occurs continuously with these materials. The inflow component can be described as [14]:

$$I_L = V \cdot \frac{dp}{dt} + p \cdot \frac{dp}{dt} \quad (2)$$

Assuming that the product of pressure p and volume V changes, this results in [15]:

$$I_L = \frac{\Delta(p \cdot V)}{\Delta t} \quad (3)$$

If the volume is constant it results in:

$$I_L(t) = V \cdot \frac{dp}{dt} \quad (4)$$

With this correlation it is possible to determine the pressure rise Δp at a known volume V . Since the increase in pressure is caused by an opening

between the vacuum system and the environment, and thus a so-called leak is present, the inflow is constant over time [10, 14, 16]:

$$I_L(t) = V \cdot \frac{\Delta p}{\Delta t} = \text{const.} \quad (5)$$

The leakage can be described as follows:

$$L = \frac{I_L}{V} = \frac{\Delta p}{\Delta t} = \text{const.} \quad (6)$$

This allows the leakage to be determined by measuring the pressure increase over time (so called *pressure rise method*) [17, 18]. However, the constancy only applies to a certain pressure range. When the vacuum generator is switched off and the temperature is constant, the following applies according to (5):

$$t = \int_{p_2}^{p_1} \frac{V}{I_L} dp \quad (7)$$

Thereby the pressure p in the system ranges below the critical pressure p_{cr} . Here the gas flow is constant. The critical pressure p_{cr} is described by [19]:

$$\frac{p_{cr}}{p_0} = \left(\frac{2}{\kappa}\right)^{\frac{\kappa}{\kappa-1}} \quad (8)$$

As soon as the critical pressure p_{cr} is exceeded the the inflowing gas flow decreases with increasing pressure. In general, the relationship between time and pressure over the entire vacuum range can be described as follows [19]:

$$t = 6,42 \cdot 10^{-2} \frac{V}{d^2} \cdot \left[\chi \left(\frac{p}{p_0} \right) - \chi \left(\frac{p_{end}}{p_0} \right) \right] \quad (9)$$

Depending on the application, a certain leakage can also be deliberately permitted. The prerequisite for this, however, is that the vacuum generator ensures a sufficiently low pressure despite leakage [21]. Measures to reduce or compensate for leakage are the use of suction cups with a smaller circumference or more powerful vacuum generators [8, 22].

3. ANALYSIS OF THE BOUNDARY CONDITIONS

The following applies to the vapor pressure of water p_w^s [20]:

$$p_w^s(T) = p_d \cdot e^{\frac{17,2799}{T} - \frac{4102,99}{T+237,431}} \quad (10)$$

with $p_d = 6,11657 \text{ mbar}$ and the range of T defined as $0,01^\circ\text{C} \leq T \leq 60^\circ\text{C}$. For the reference temperature of 20°C p_w^s can be determined:

$$p_w^s = 23,4 \text{ mbar} \quad (11)$$

This is below the pressure range of vacuum handling systems which is between 100 and 900mbar [1]. This means the influence of desorption I_D does not have to be considered. The order of magnitude of the inflow component I_P is even smaller [10]. Since no vacuum-technical process takes place in the vacuum gripper, the inflow component I_V does not occur here. From (9) the relationship between the time t and the pressure after completion of the evacuation process p_{end} to the pressure p increasing due to leakage in a closed container with a circular opening having the diameter d is known. The calculation factor χ is determined by:

$$\chi\left(\frac{p}{p_0}\right) = \begin{cases} \frac{p}{p_0} & \text{for } 0 < p \leq p_{cr} \\ \tilde{\chi} & \text{for } p_{cr} < p \leq 1000\text{mbar} \end{cases} \quad (12)$$

For the calculation factor χ over the pressure ratio p/p_0 see **Figure 2**.

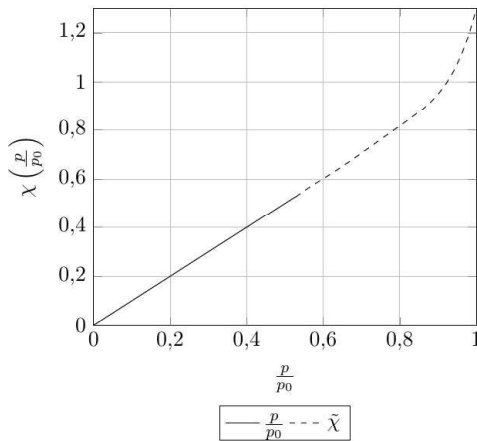


Figure 2: pressure calculation factor over pressure ratio for pressure increase in a closed container with a defined leak

Whereby according to (8) $p_{cr} = 528\text{mbar}$. The linear relationship therefore applies in the range $p < 528\text{mbar}$. If the function $\chi(p/p_0)$ is examined more closely, the area $p \leq 800\text{mbar}$ is approximately linear (c.f. **Figure 3**) with the following correlation:

$$\tilde{\chi}\left(\frac{p}{p_0}\right) = 1,025 \frac{p}{p_0} \quad (14)$$

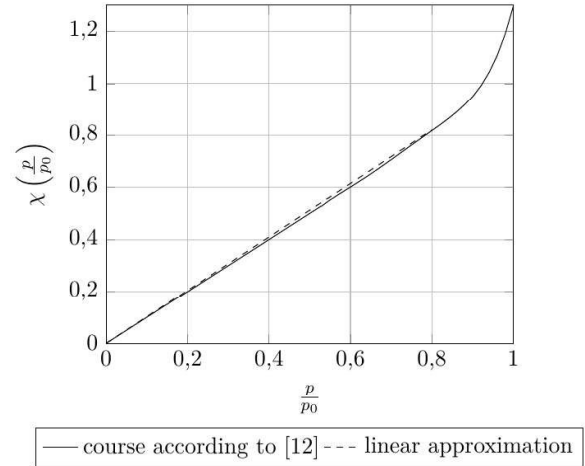


Figure 3: linear approximation of the calculation factor over pressure ratio for pressure increase in a closed container with a defined leak

According to the magnitude of pressure increase over time the leakage can be assigned to different states of the vacuum gripping system. **Table 1** shows the different states of vacuum gripping systems depending on leakage for suction-tight sheets [23].

Table 1: different states of vacuum gripping systems depending on leakage

system state	leakage in $\frac{\text{mbar}}{\text{s}}$	holding time in s
tight	< 67	> 6
low leakage	67..133	3..6
heavy leakage	134..200	2..3
Not tight	> 200	< 2

In addition, the holding time of the workpiece is listed for which the workpiece can no longer be gripped. It is based on a final pressure of 400mbar, a pressure of 800mbar at which the workpiece is dropped, and the assumption that the leakage is not compensated. The ranges of leakage show that the pressure rise method is sufficient, as other methods can measure leakage several orders of magnitude below the values listed in **Table 1** [24].

Furthermore, the handling of flexible workpieces poses a danger as they change their shape significantly during the handling process [25, 26]. If these protrude beyond the suction cups of the gripper system, there is a risk that the deflection of the workpiece will cause marginal gaps to form, which will promote

second order leakage and ultimately lead to the tearing off of the workpiece [22].

Workpieces that allow first and third order leakage to occur are also risky to handle in a HRC application. Here the leakage is so high; the workpiece is almost immediately dropped.

This means the workpieces that can be used here have to be rigid as well as suction-tight.

4. EXAMINATION OF LEAKAGE

Figure 4 shows the different components of the handling process and their parameters that can influence the leakage. Preliminary examinations show that leakage of a closed vacuum gripping system where the suction cups are replaced by sealed plugs is $0,002\text{mbar/s}$. Considering the values in Table 1 leakage of this magnitude is negligible.

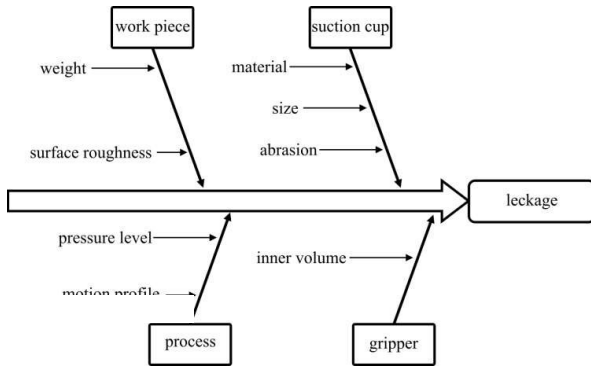


Figure 4: influence factors of leakage

Both the gripping system as a whole and the suction cup as a single component influence the leakage, depending on their characteristics. There are also influences from the workpiece, and characteristics of the handling process. The gripping system influences the leakage by the

size of the internal volume, which is made up of the suction cups, hose lines and any fluidic reservoirs. Due to the variety of applications there are many types of suction cups which differ in properties such as material and the Shore hardness, geometric shape and diameter. It should be noted however, that in most cases a larger diameter is accompanied by a larger volume of the suction cup (see e.g. [27]). It is therefore more appropriate to consider the ratio of volume to circumference. The suction cups are also subject to wear, as they are in direct contact with the (rough) workpiece. This is therefore dependent on the number of load cycles. The workpiece has a surface roughness and a weight that influences the leakage.

If (9) is applied to the vacuum gripper system, the relationship between t and V in the range $p < 800\text{mbar}$ can be described as follows:

$$t \sim V \quad (15)$$

In addition, the following relationship applies to t and d :

$$t \sim \frac{1}{d^2} \quad (16)$$

Or with the quadratic dependence of the area A of the diameter d :

$$t \sim \frac{1}{A} \quad (17)$$

If the quantity d^2 resulting from the opening of the container is transferred to the openings between the suction cup and the workpiece interface, the area A can be described on the basis of the equations for the mean roughness value Ra as follows [28]:

$$A = Ra \cdot s = \int_0^s |y(x)| dx \quad (18)$$

Whereby $y(x)$ describes the course of the surface profile in the direction of the coordinate x over the length s with the maximum expression z . This leads to the conclusion that there is the following relationship between t and Ra :

$$t \sim \frac{1}{Ra} \quad (19)$$

Moreover, it follows from equation (18) that $A \sim s$ which means that:

$$t \sim \frac{V}{s} \quad (20)$$

Where s is the length of the circumference U of the suction cup and the quotient V/U is the ratio between volume and circumference of the suction cup. In addition, equation (9) shows the relationship:

$$t \sim \left[\chi \left(\frac{p}{p_0} \right) - \chi \left(\frac{p_{end}}{p_0} \right) \right] \quad (21)$$

so

$$t \sim \chi \left(\frac{\Delta p}{p_0} \right) \quad (22)$$

where:

$$\chi \left(\frac{\Delta p}{p_0} \right) \sim \frac{p}{p_0} \quad (23)$$

It therefore applies with equation (9):

$$t \sim \Delta p \text{ für } p < 800 \text{ mbar} \quad (24)$$

If the mass m of the workpiece is considered in the form of the weight force F_G with $m \cdot g = F_G$ and the context $p = F_G/A$

$$t \sim m \quad (24)$$

follows.

4.1. Test Design and Setup

First, the changes of the determined influencing

factors of the leakage are examined in a one-factor-at-a-time test design. In the process the proportional correlations derived from the theoretical consideration are to be checked. The factors examined and their levels are shown in **Table 2**. The parameters highlighted in grey form the reference system. The remaining parameters with the expected non-linear or unknown correlation between pressure and time are determined by a completely factorial test design with 3 factors of 3 to 5 levels [29]. The structure of the test bench is shown in **Figure 5**. The workpiece (1) is positioned on a frame (2) in order to enable an approximately reproducible position of the workpiece parallel to the suction cups (3). The gripper consists of four suction cups, and is brought to the desired pressure level by the vacuum generator (4). The pressure is measured by a pressure sensor (5).

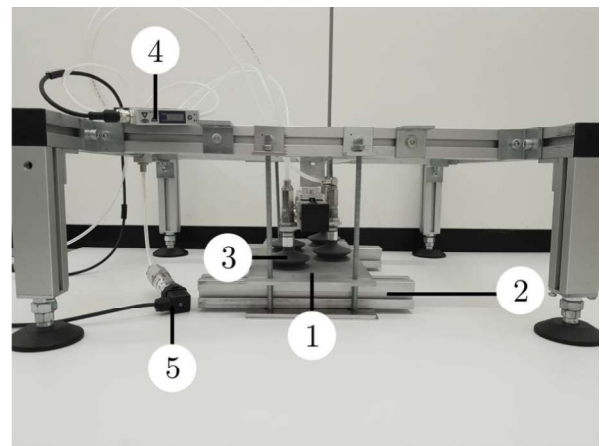


Figure 5: test bench for measuring leakage

4.2. Test results of the one-factor-at-a-time test execution

The test results for the individual parameters

Table 2: factors and levels of the one-factor-at-a-time design for the examination of leakage

factor	unit	level				
		1	2	3	4	5
volume/circumference	mm ³ /mm	53	89	153		
abrasion	-	new	50xP220	100xP220		
material	-	NR	NBR	AU		
weight	kg	1	2	3	4	5
surface roughness	μm	0,3	2,5	5,7		
volume	ml	161	281	409	560	910
pressure level	mbar	300	400	500	600	700

examined are listed below. These are shown in **Figure 6** including the theoretical linear approximation.

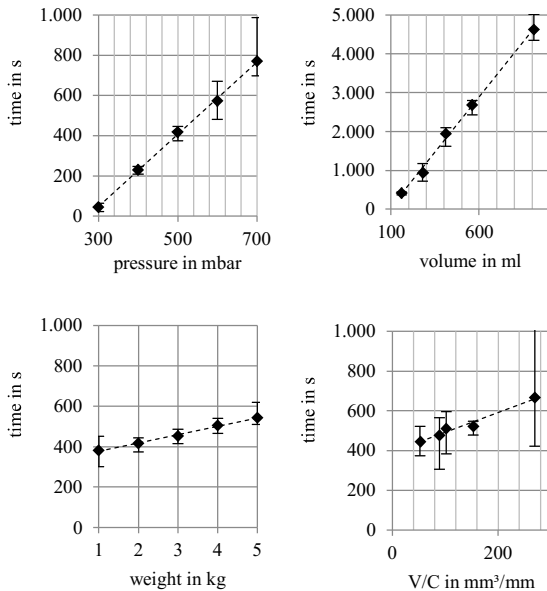


Figure 6: mean values and dispersion of the duration up to 800 mbar are reached as well as linear regression at different initial pressures (top left), different volumes (top right), the workpiece weight (bottom left) as well as the ratio of volume to circumference (bottom right)

Figure 6 (top left) shows the relationship between pressure level and ventilation time up to an absolute pressure of 800 mbar. It can be seen that this is approximately linear. The ventilation times of the system with different internal volumes also show a linear correlation between the ventilation time until 800 mbar is reached and the volume of the system (see top right). The same applies to the variation of the workpiece weight, where there is also an approximately linear correlation (see bottom left). Whereas here the effect is smaller compared to the previous factors. In the static state a change in the workpiece weight corresponds to a change in the differential pressure and therefore too results in a linear correlation. A variation in the ratio of volume to circumference of the suction cup also shows that a linear approximation of the relationship is possible (see bottom right). The effect is also comparatively small here.

The most likely reason for variation in all experiments is that the workpiece has a little

tolerance in its positioning. This means that the suction cups have slightly different contact areas. Due to the marginally uneven surface of the workpiece this affects the leakage. It is noticeable that with increased compressible volume (see bottom right) there is a significant variation. A possible reason for this is the different roughness of the contact area in combination with the compressible volume. If the surface is smooth, leakage slowly increases pressure and volume leading to a ventilation time above average. If the surface is rough, leakage causes a fast increase of the volume to its maximum. After that, leakage causes a speeded pressure increase below average.

In order to be able to make tendentious statements regarding the influence of the roughness of the surface of the workpiece on the leakage, test specimens with surfaces with Ra values of 0,3 μ m (polished), 2,5 μ m (smoothed) and 5,7 μ m (roughened) are examined. The results are shown in **Figure 7** (top left).

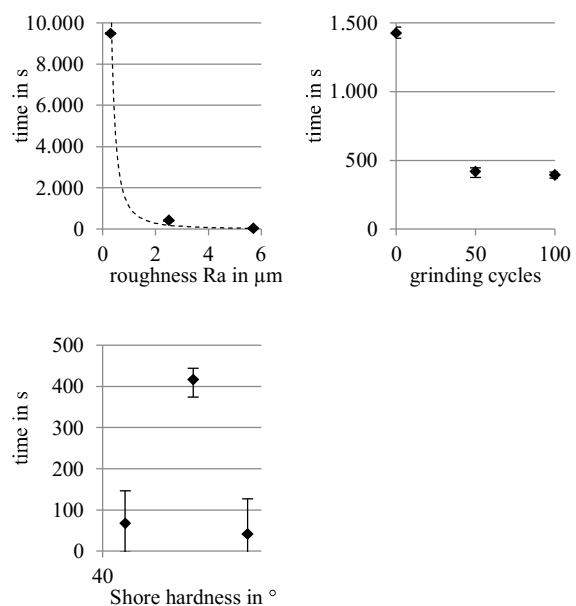


Figure 7: mean values and dispersion of the duration up to 800 mbar is achieved with different surface roughness of the workpiece (top left), wear conditions of the suction cup (top right) as well as suction cup materials (bottom left)

It can be seen that the ventilation times here differ by several orders of magnitude and a hyperbolic approximation (dashed curve) can therefore be suitable. In order to make an initial statement regarding the wear condition it is

simulated using abrasive paper with a grain size of P220. For this purpose 50 sanding strokes per suction cup are performed for the *slightly worn* condition and 100 sanding strokes per suction cup are performed for the *heavily worn* condition. For the condition *as good as new* there is no treatment by the abrasive paper. The measurements in **Figure 7** (top right) show that abrasion significantly reduces the ventilation time.

Suction cup materials that are suitable not only for a specific material, but also universally for suction-tight and rigid workpieces are investigated. The ventilation curves for different suction cup materials are shown in **Figure 7** (bottom left), whereby the suction cup materials have the following Shore hardness: NR 45°, NBR 60° and AU 72°. It can be seen that the material selection has a large influence on the ventilation time.

4.3. Test results of the full factorial test procedure

The previous experiments show that non-linear relationships exist between time and the factors surface roughness, wear condition, and material of the suction cup according to the findings of the experiments in the previous section. These influences are therefore investigated on the basis of a completely factorial test procedure. The test setup is identical to the previous tests. In order to investigate different surface roughness, the test workpieces are sandblasted with different grain sizes. The different Ra values as well as the different amount of load cycles applied on the suction cups and the materials used are shown in **Table 3**. Here the load cycles are applied via compression and decompression of the section cups and therefore show way less abrasion compared to the sanded suction cups from the previous section.

Table 3: factors and levels of the full factorial test design for the examination of leakage

factor	level							
	1	2	3	4	5	6	7	8
load cycles	10^2	10^3	10^4	10^5	10^6			
material	NR	NBR	AU					
roughness in μm	0,3	1,44	1,73	1,94	2,45	3,11	4,8	6,07

In the following the test results are presented separately according to the different suction cup materials. **Figure 8** to **Figure 10** show the time durations up to 800 mbar depending on the surface condition and the load cycles. At least with regard to surface roughness, there is a clear tendency to recognize that the ventilation time decreases with increasing Ra value. The number of load cycles on the other hand influences the molecular structure of the suction cups and is thus also influenced by the material. No clear tendencies can be identified here.

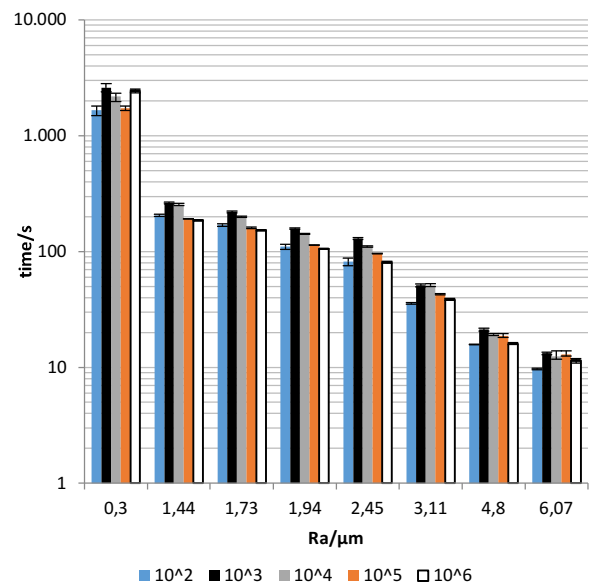


Figure 8: ventilation times for different degrees of surface roughness and load cycles for NR

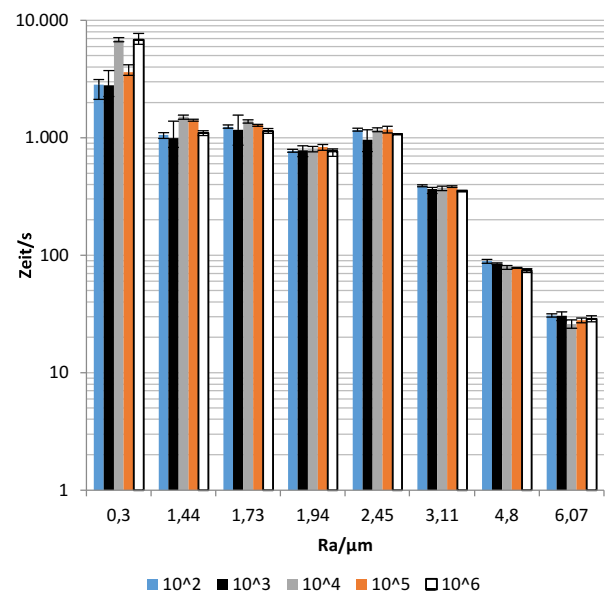


Figure 9: ventilation times for different degrees of surface roughness and load cycles for NBR

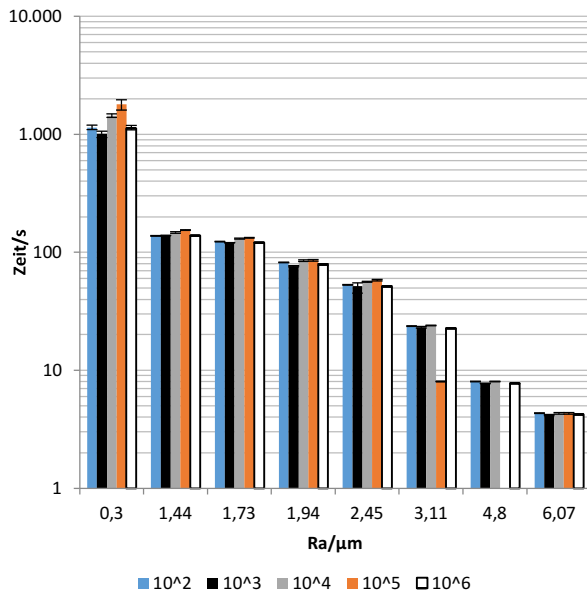


Figure 10: ventilation times for different degrees of surface roughness and load cycles for AU

4.4. Discussion

The measurements show that the theoretically determined linear relationships between individual influencing parameters and the ventilation time up to 800 mbar are appropriate. Consequently, the ventilation time can be regarded as proportional to the internal volume, the ratio of volume and circumference of the suction cup, the pressure difference and the workpiece weight. The completely factorial tests show that the relationships between ventilation duration and surface roughness, number of load cycles and suction cup material cannot be clearly described mathematically and thus have to be measured separately for every single application.

5. SUMMARY AND OUTLOOK

This paper presents new theoretical and experimental examinations of leakage in vacuum gripping systems. They fill the gap between state of the art design methods for such systems and the need for safety in case of an energy failure.

The theoretical and experimental examinations of the impact factors and effects of leakage show that some of the identified factors correlate linear with the ventilation time. Others do not but their effects are also shown in this paper.

These results can be used as a basis to design vacuum gripping systems in order to obtain the lowest leakage possible. Thereby the compensation of leakage can only be temporary, and the duration of this compensation has to be determined long enough to transfer the workpiece to a safe state.

Further examinations can include more factors like different suction cup materials and differently shaped workpieces. This can give an additional understanding of the effect on leakage and makes the design of vacuum gripping systems based on leakage suitable for more applications.

NOMENCLATURE

A	Area
AU	polyester-urethane rubber
C	circumference
d	diameter
L	leakage
m	mass
NBR	Nitrile rubber
NR	natural rubber
p	pressure
p_0	ambient pressure
s	length
t	time
V	Volume

REFERENCES

- [1] Hesse, S., 2011. Greifertechnik: Effektoren für Roboter und Automaten. Hanser, München.
- [2] Grubba, M.-A., 2002. Untersuchungen zum Kraftübertragungsverhalten von Vakuumbreifsystemen für Hohlkörper. Universität Dortmund.
- [3] Schmalz, J., Giering, L., Hölzle, M., Huber, N. et al., 2016. Method for the Automated Dimensioning of Gripper Systems 44, p. 239.
- [4] Schmierer, G., 2001. Ein modulares Baukastensystem für Kletterroboter nach dem Gleitrahmenprinzip. Jost-Jetter, Heimsheim.
- [5] Sdahl, M., 2006. Beitrag zum autonomen Dreipunkt-Sauggreifen.
- [6] Daimler AG, 2017. Mercedes-Benz Cars: Der Rohbau der Zukunft ist flexibel.

- [7] Demtröder, W., 2018. Experimentalphysik 1. Springer Berlin Heidelberg, Berlin, Heidelberg.
- [8] Festo. Grundlagen der Vakuumtechnik, Kurzübersicht - Einführung.
- [9] Jodin, D., 1991. Untersuchungen zur Handhabung von biegeweichen Flächenzuschnitten aus Leder mit pneumatischen Greifern, Dortmund.
- [10] Edelmann, C., 1998. Vakuumphysik: Grundlagen, Vakuumerzeugung und -messung, Anwendungen. Spektrum Akad. Verl., Heidelberg.
- [11] Fritz, F., 2017. Ein Modell zur energetischen Analyse und Bewertung von Vakuum-Greifsystemen, 1st edn. Shaker, Herzogenrath.
- [12] Tiwari, A., Persson, B.N.J., 2019. Physics of suction cups.
- [13] Tiwari, A., Persson, B.N.J., 2019. Theory for diffusive and ballistic air leakage and its application to suction cups.
- [14] Li, L., Li, K., Zhao, Z., Wang, H. et al., 2015. A Novel Test Method of Low Leakage Rate of MEMS Vacuum Packaging, in Proceedings of the 10th IEEE International Conference on Nano/Micro Engineered and Molecular Systems (IEEE-NEMS), IEEE, [Piscataway, New Jersey], p. 175.
- [15] Umrath, W. Grundlagen der Vakuumtechnik, Köln.
- [16] Jousten, K., Editor, 2013. Wutz Handbuch Vakuumtechnik, 11th edn. Springer Vieweg.
- [17] Deutsches Institut für Normung e.V. Zerstörungsfreie Prüfung - Dichtheitsprüfung: Prüfgasverfahren, Berlin. Beuth Verlag 19.100, 2011(13185).
- [18] Deutsches Institut für Normung e.V. Zerstörungsfreie Prüfung - Dichtheitsprüfung - Druckänderungsverfahren, Berlin. Beuth Verlag 19.100, 2001(13184).
- [19] Wutz, M., Adam, H., Walcher, W., 1992. Theorie und Praxis der Vakuumtechnik: Mit 74 Tabellen, 5th edn. Vieweg, Braunschweig u.a.
- [20] Baehr, H.D., Kabelac, S., 2012. Thermodynamik: Grundlagen und technische Anwendungen, 15th edn.
- [21] Seegräber, L., 1993. Greifsysteme für Montage, Handhabung und Industrieroboter: Grundlagen - Erfahrungen - Einsatzbeispiele. Expert-Verl., Ehningen bei Böblingen.
- [22] Götz, R., 1991. Strukturierte Planung flexibel automatisierter Montagesysteme für flächige Bauteile. Springer, Berlin u.a.
- [23] J. Schmalz GmbH, 2016. SXPi/SXMPi: Betriebsanleitung, Glatten.
- [24] Deutsches Institut für Normung e.V. Zerstörungsfreie Prüfung - Dichtheitsprüfung: Kriterien zur Auswahl von Prüfmethoden und -verfahren, Berlin. Beuth Verlag 19.100, 1999(1779).
- [25] Fantoni, G., Santochi, M., Dini, G., Tracht, K. et al., 2014. Grasping devices and methods in automated production processes 63, p. 679.
- [26] Shchekutin, N., Bouzakis, A., Overmeyer, L., Shkodyrev, V., 2014. Handling concept for ultra-thin glass sheets.
- [27] J. Schmalz GmbH, 2017. Vakuum-Komponenten: Katalog 2016/2017, Glatten.
- [28] Grote, K.-H., Feldhusen, J., 2011. Dubbel. Springer Berlin Heidelberg, Berlin, Heidelberg.
- [29] Kleppmann, W., 2013. Versuchsplanung: Produkte und Prozesse optimieren, 8th edn. Hanser, München.

MUCH DOES NOT HELP MUCH: 3D PARETO FRONT OF SAFETY, COMFORT AND ENERGY CONSUMPTION FOR AN ACTIVE PNEUMATIC SUSPENSION STRUT

Manuel Rexer, Nicolas Brötz, Peter F. Pelz*

Institut für Fluidsystemtechnik, Technische Universität Darmstadt, Otto-Berndt-Straße 2, 64287 Darmstadt

* Corresponding author: Tel.: +49 6151 1627100; E-mail address: peter.pelz@fst.tu-darmstadt.de

ABSTRACT

With regard to autonomous driving the demands on comfort are increasing. This makes it attractive to use active suspension systems. The system developed at TU Darmstadt is able to increase driving comfort up to 28 % while maintaining driving safety compared to a passive suspension system.

This paper investigates the influence of available energy and power of the active system. The investigation is based on a simulation of a quarter car model and an uneven country road. This paper shows that the more energy the active system has at its disposition, the greater is the range between a comfortable and a sporty chassis. Furthermore the driving comfort can be increased by 28 % with constant driving safety. The average power required for this is 15 W and the maximum power is 300 W.

Keywords: air spring, active suspension, energy demand, power demand

1. INTRODUCTION

With regard to autonomous driving the demands on comfort are increasing. Passengers may engage in other activities during the ride but may also suffer from kinetosis more frequently [1, 2]. This makes it attractive to use active systems in the suspension system. Previous studies showed that an active air suspension system as in **Figure 1** is well suited to calm the chassis and increase driving comfort [3–5]. The system developed within the Collaborative Research Center 805 “Control of uncertainty in load carrying structures in mechanical engineering”, increases driving comfort by up to 28 % while maintaining driving safety compared to a passive air suspension [6]. These results were found in simulations as well as in hardware-in-the-loop experiments [5, 6].

The average available actuating power is one influencing factor to increase driving safety and comfort. The average available actuating power represents the energy demand of the active system which makes it an important indicator as especially for electrified vehicles energy supply is limited. This is simulatively investigated on the basis of the vertical dynamics of a quarter car model. Therefore, in the following first is the quarter car model as well as the principle of the

active air spring is introduced. Then the performance parameters and the calculation of the actuator power are presented and finally results are discussed.

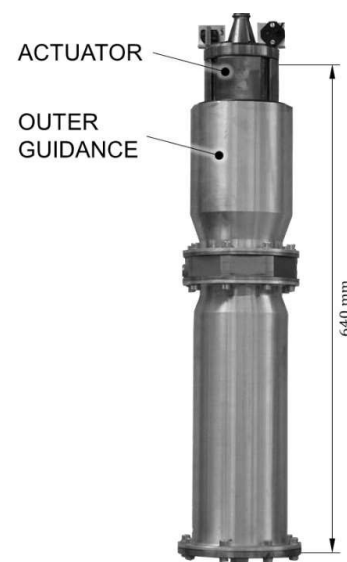


Figure 1: Active air spring.

2. METHOD

2.1. system description

quarter car model

The actuator of the active air spring is considered in the quarter car model as a force connected in parallel both to spring and damper (c.f. **Figure 2**).

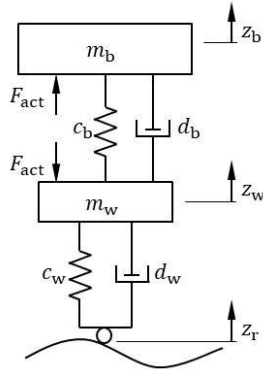


Figure 2: Quarter car model with active suspension system.

The equations of motion of this quarter car are

$$m_b \ddot{z}_b + d_b \dot{z} + c_b z + F_{act} = 0, \quad (1)$$

$$m_w \ddot{z}_w + d_w (\dot{z}_w - \dot{z}_r) + c_w (z_w - z_r) - d_b \dot{z} - c_b z - F_{act} = 0, \quad (2)$$

with the deflection z and the deflection velocity \dot{z}

$$z = z_b - z_w, \quad (3)$$

$$\dot{z} = \dot{z}_b - \dot{z}_w. \quad (4)$$

All results refer to a quarter car model with parameters based on a middle class car as in **Table 1**.

Table 1: Parameters of the quarter car model.

m_b	270 kg	m_w	50 kg
c_b	10 N/mm	c_w	200 N/mm
d_b	1140 Ns/m	d_w	566 Ns/m

active air spring

This paper investigates an active air spring suspension system. The force of an active air spring is given by a static load F_0 , a deflection force cz and the actuator force

$$F = F_0 + cz + F_{act} \quad [6]. \quad (5)$$

In principle the actuator force is changeable either by (i) the air mass, (ii) the load carrying

area or (iii) the volume of the air spring. Hedrich [6] shows that only a change of the load carrying area is useful.

An air spring is usually sealed by rolling bellows which are guided on the inside by a piston and on the outside by an outer guidance. However, the load carrying area of an air spring is approximately

$$A_c \approx \pi \left(\frac{r_o + r_p}{2} \right)^2. \quad (6)$$

The load carrying area at the active air spring varies by changing the piston radius r_p (c.f. **Figure 3**) [3]. For this purpose segments are moved as hydraulically single-acting cylinders. The return takes place through the bellows and the pressure in the air spring.

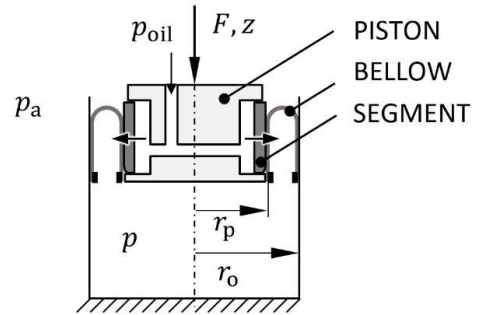


Figure 3: Principle of the active air spring. Single-acting cylinder that changes the load carrying area.

Whenever the actuator force increases, oil must be forced into the actuator. A pump and valve supply the hydraulic power. To reduce the actuator force, the oil is drained.

Measurements show approximately a PT1 transfer characteristic for the actuator with a cut-off frequency of 5 Hz and a maximum actuating force of $F_{act,max} = \pm 1$ kN [7].

performance indicators

In order to evaluate the performance of the actuator, driving safety and driving comfort are taken into account. Mitschke shows the according definitions [8]. The standard deviation of the relative wheel load variation is regarded as driving safety

$$\frac{\sigma(F_w)}{F_{w,0}} = \frac{1}{F_{w,0}} \sqrt{\frac{1}{T} \int_0^T (F_w(t))^2 dt}. \quad (7)$$

The standard deviation of the body acceleration is regarded as driving comfort

$$\sigma(\ddot{z}_b) = \sqrt{\frac{1}{T} \int_0^T (\ddot{z}_b(t))^2 dt}. \quad (8)$$

Both performance indicators are determined without frequency weights. The results depend on

1. the road,
2. the driving speed and
3. the car.

This investigation excites the system applying a stochastically generated road. The road corresponds to an uneven country road at a speed of 70 km/h and can be generated from white noise n by form filters [6]. The parameters of the country road are from Mitschke [8] with a waviness of $w = 2$ and an unevenness dimension of $\Phi_{z_r z_r, \Omega}(1/m) = \pi \cdot 12.2 \cdot 10^{-6} m^3$.

Figure 4 shows the active and passive boundary line next to the passive reference car in a conflict diagram. The reference car results from the simulation of the quarter car with parameters from **Table 2** and no actuator force $F_{act} = 0$.

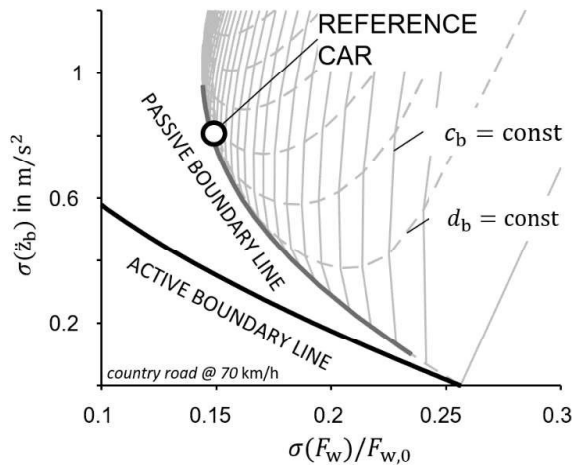


Figure 4: Conflict diagram for driving comfort and safety.

The passive boundary line is reached by varying stiffness and damping. The isolines for $c_b = \text{const}$ or $d_b = \text{const}$ show this as well. The active boundary line assumes an ideal actuator with the transfer function of 1 and a maximum actuating force $F \rightarrow \infty$. Active suspension systems can therefore cross the passive boundary line.

controller design

The controller for the active system is designed with a model-based H2-optimal controller design according to Lenz et al. [7]. For this purpose the objective function considers driving safety and driving comfort. Since they are in conflict with each other, a compromise between the two can be

found by weighting them. A pareto front represents the results in the conflict diagram as in Hedrich [6] (see **Figure 4**).

2.2. power demand

average power demand

The power of the actuator is given by the product of deflection velocity and the actuator force

$$P(t)_{act} = \dot{z}(t)F_{act}(t). \quad (9)$$

Due to the actuator's functionality power at pressure $P(t)_{act,p}$ meaning increasing actuator forces and at tension $P(t)_{act,t}$ meaning decreasing actuator forces need to be distinguished. The pressure power is determined by

$$P(t)_{act,p} = \begin{cases} 0 & \forall \frac{dF_{act}(t)}{dt} \leq 0 \\ |P(t)_{act}| & \forall \frac{dF_{act}(t)}{dt} > 0 \end{cases}, \quad (10)$$

and tension power by

$$P(t)_{act,t} = \begin{cases} |P(t)_{act}| & \forall \frac{dF_{act}(t)}{dt} \leq 0 \\ 0 & \forall \frac{dF_{act}(t)}{dt} > 0 \end{cases}. \quad (11)$$

External energy sources supply the pressure power.

Due to the fact that the resetting forces of the air spring cause the decrease of the actuator force, external power supply does not provide the tension power.

The power demand of an active suspension system is considered as an average power demand, which is equivalent to the required energy. The average power is calculated over a time average of

$$\bar{P} = \frac{1}{T} \int_0^T P(t) dt. \quad (12)$$

The average power demand of the active system can therefore be specified as

$$\bar{P}_{act} = \bar{P}_{act,p} - \gamma \bar{P}_{act,t}. \quad (13)$$

γ is the energy recuperation factor, which varies between 0 (no energy recuperation) and 1 (total energy recuperation). This investigation does not take energy recuperation into account as a conservative estimation ($\gamma = 0$).

The energy required by the active system is obtained from the product of average power \bar{P} and duration T .

consideration of the available power in the controller design

Due to nonlinearity the actuator power is simulated in time domain in contrast to controller design simulated in frequency domain.

Therefore **Figure 5** shows the extended controller design process.

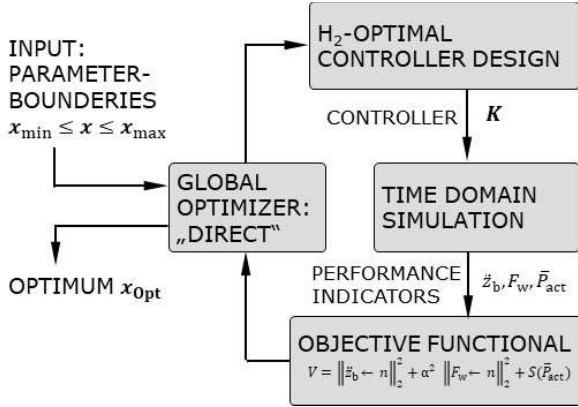


Figure 5: Extended controller design to consider the available actuator power (in accordance to [6]).

The global optimizer "DIRECT" [9] is used in addition to controller optimization. In order to influence the power of the actuator the parameters of the transfer function of the actuator are adjusted. **Table 2** presents the parameter limits.

Table 2: parameter range of global optimization.

parameter	Range
maximum force F_{PT1}	0 ... 1 kN
base frequency f_{PT1}	0 ... 30 Hz

The global optimization specifies a transfer function for the actuator determining the optimal controller. The model is then simulated in time domain to determine the evaluation variables for the objective function

$$\min \left\| \ddot{z}_b \leftarrow n \right\|_2^2 + \alpha^2 \left\| F_w \leftarrow n \right\|_2^2 + S(\bar{P}_{act}). \quad (14)$$

A Big-M method takes compliance with the actuator power into account

$$S(\bar{P}_{act}) = \begin{cases} 0 & \forall \bar{P}_{act} \leq \bar{P}_{act,max} \\ M & \forall \bar{P}_{act} > \bar{P}_{act,max} \end{cases}. \quad (15)$$

The used optimizer "DIRECT" searches for the optimum in both depth and width but cannot guarantee to find the global optimum. This may lead to inaccuracies in the results which is not further examined in this paper.

These basic investigations take no efficiency of the actuator into account. Dietrich et al. [10] considers the efficiency of the example actuator.

3. RESULTS

3.1. 3D pareto front

Figure 6 shows the result in a 3D Pareto front where the driving comfort and driving safety are plotted against the average available actuating power. This corresponds to the energy requirement of the system. Inconsistencies as kinks and discontinuities in the lines occur from the optimizer not reaching the global optimum. These are neglected, as the fundamental trends are nevertheless recognizable and not influenced by them.

Starting from the passive reference car which has no power available the active chassis enables increasing flexibility in the weighting between driving comfort and safety as the available power increases. The driver has the choice between a comfortable and a sporty chassis.

In total the ideally active system requires around 90 W of average power i.e. 360 W for the whole car.

In addition a saturation occurs. With a power of about 50 W the driving safety cannot be increased by further available actuating power. It is only possible to increase maximum comfort. This can be seen from the fact that the upper end of the curves do not drop increasing the power in terms of driving safety, but the lower end of the curve drops further in terms of driving comfort.

3.2. much does not help much: average power demand

Considering driving comfort of the reference car with a constant safety level of $\sigma(F_w)/F_{w,0} = 0.149$, **Figure 7** is obtained.

The driving comfort increases with increasing available average actuating power. However, saturation occurs. For this vehicle driving comfort improves by about 28 %. This value is

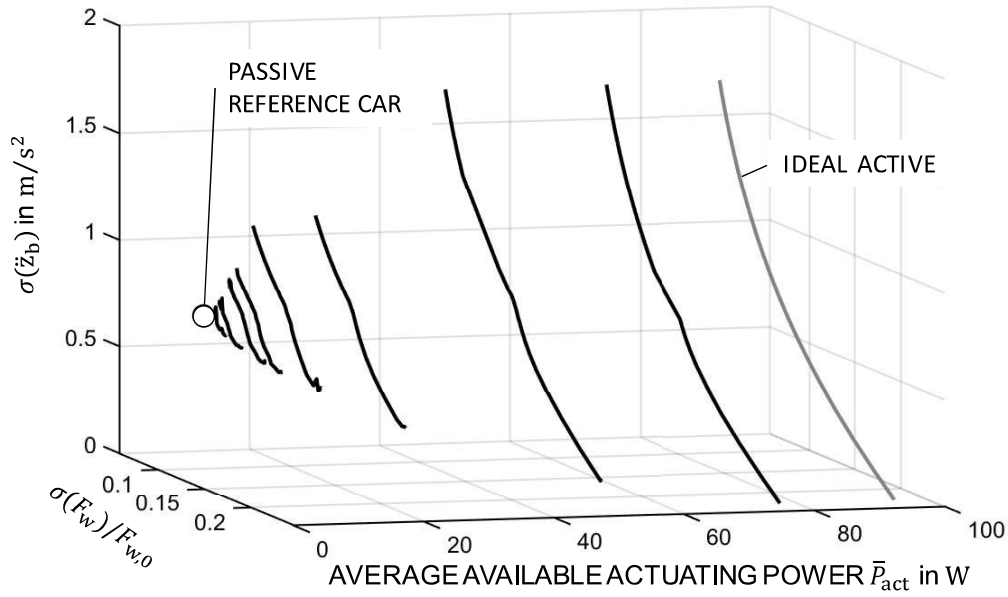


Figure 6: 3D pareto front as a function of the average available actuating power.

already reached for an average available actuating power of 15 W.

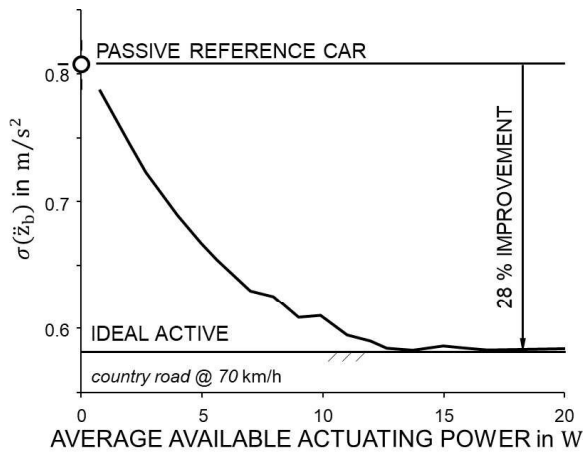


Figure 7: Driving comfort as a function of the average available actuating power with a constant driving safety.

3.3. peak power demand

Finally **Figure 8** investigates the peak power demand of the active suspension system and considers both the maximum occurring power and the 0.9974 quantile. The second value therefore takes 99.74 % of the power occurring in the simulation into account. However the statistical value is more significant since deviations between simulation and reality do not have an effect as significant as the maximum power.

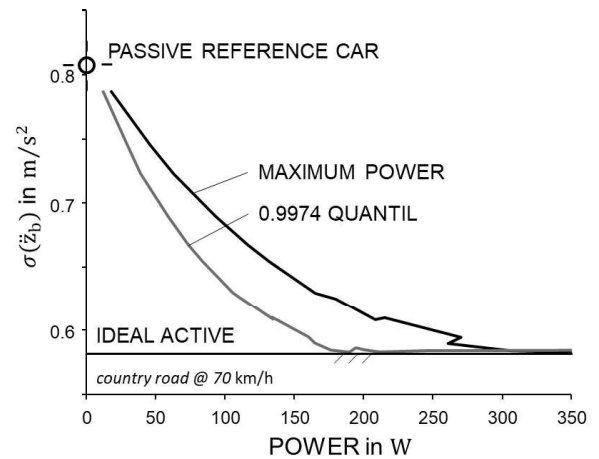


Figure 8: Driving comfort as a function of the maximum power and the 0.9974 Quantil power with a constant driving safety.

For the peak power demand, a similar picture is obtained as for the average available power demand. If starting from the passive reference car the driving safety is kept constant and only the driving comfort is improved. The maximum power requirement is about 300 W, the 0.9974 quantile is saturated at 180 W. The peak powers are therefore at least one order of magnitude greater than the average powers.

4. CONCLUSION

The available power has a considerable influence on the performance of the system. Thus the driver with more available power can choose a larger range between driving safety and driving comfort.

Furthermore to increase driving comfort while maintaining driving safety saturation occurs and only 15 W of average power is required to achieve an improvement of 28 %. This circumstance is advantageous for autonomous driving electrified vehicles as the energy supply is limited there. Also the maximum power saturates at a level of 300W.

ACKNOWLEDGMENT

Funded by the Deutsche Forschungsgemeinschaft (DFG, German Research Foundation) – project number 57157498 – SFB805.

NOMENCLATURE

A_c	load carrying area
c_b	body stiffness
c_w	wheel stiffness
d_b	body damping
d_w	wheel damping
F_{act}	actuator force
F	air spring force
F_w	wheel load
$F_{w,0}$	static wheel load
K	controller
m_b	body mass
m_w	wheel mass
n	white noise
P	power
p	air spring pressure
p_a	ambient pressure
p_{oil}	oil pressure
\bar{P}	average power
P_{act}	actuator power
$P_{act,p}$	actuator pressure power
$P_{act,t}$	actuator tension power
r_o	outer guidance radius
r_p	piston radius
S	penalty
t	time
T	duration
w	waviness
z	deflection
\dot{z}	deflection velocity

z_b	body excitation
\dot{z}_b	body velocity
\ddot{z}_b	body acceleration
z_w	wheel excitation
\dot{z}_w	wheel velocity
\ddot{z}_w	wheel acceleration
z_r	road excitation
α	weighting factor
γ	energy recuperation factor
σ	standard deviation
$\Phi_{z_r, z_r, \Omega}$	unevenness dimension

REFERENCES

- [1] Heinrichs D (2015) Autonomes Fahren und Stadtstruktur. In: Maurer M, Gerdes JC, Lenz B, Winner H (Hrsg) Autonomes Fahren: Technische, rechtliche und gesellschaftliche Aspekte. Springer Berlin Heidelberg, Berlin, Heidelberg, S 219–239
- [2] Sivak M, Schoettle B (2015) Motion Sickness in Self-Driving Vehicles
- [3] Hedrich P, Johe M, Pelz PF (2017) Aktor mit einem linear verlagerbaren Stellglied (DE 102015120011 A1)
- [4] Hedrich P, Lenz E, Brötz N, Pelz PF (Hrsg) (2018) Active Pneumatic Suspension for Future Autonomous Vehicles: Design, Prove of Concept and Hardware-in-the-Loop Simulations, Bd 3
- [5] Hedrich P, Lenz E, Pelz PF (2018) Minimizing of Kinetosis during Autonomous Driving. ATZ Woldwide 120(7-8):68–75
- [6] Hedrich P (2018) Konzeptvalidierung einer aktiven Luftfederung im Kontext autonomer Fahrzeuge, 1. Aufl. Forschungsberichte zur Fluidsystemtechnik, Bd 20. Shaker
- [7] Lenz E, Hedrich P, Pelz PF (2018) Aktive Luftfederung – Modellierung, Regelung und Hardware-in-the-Loop-Experimente. Forschung in Ingenieurwesen:1–15. doi:10.1007/s10010-018-0272-2
- [8] Mitschke M, Wallentowitz H (2014) Dynamik der Kraftfahrzeuge, 5. Aufl, Wiesbaden
- [9] Finkel DE (2003) DIRECT Optimization Algorithm User Guide
- [10] Dietrich I, Hedrich P, Bölling C, Brötz N, Geßner F, Pelz PF (2018) Concept of a Resilient Process Chain to Control Uncertainty of a Hydraulic Actuator. AMM 885:156–169. doi:10.4028/www.scientific.net/AMM.885.156

COMBINATIONS OF ENERGY SAVING MEASURES IN PNEUMATICS

Vladimir Boyko*, Jürgen Weber

Institute of Mechatronic Engineering, Technische Universität Dresden, Helmholtzstrasse 7a, 01069 Dresden

* Corresponding author: Tel.: +49 351 46334109; E-mail address: vladimir.boyko@tu-dresden.de

ABSTRACT

Within a production machine, various electromechanical and pneumatic structures can be used for drive tasks. As these drive technologies can often replace each other, the energy efficiency, performance and TCO of pneumatic drives must be permanently enhanced to remain competitive. There is a large number of known measures for the reducing their energy consumption, e.g. minimizing of filling volumes, energy saving circuits etc. However, these measures are mainly considered separately and the possible overall energy saving effect resulting from their combination is rarely taken into account.

The main goal of this paper is therefore to explore the possible combinations of pneumatic energy saving measures and their cumulative saving effect. Due to the fact that some measures are mutually exclusive (e.g. a general pressure reduction in properly sized drive), each combination should be considered separately. To evaluate their efficiency plausibly, a comprehensive assessment is required that contains both the total cost of ownership analysis (TCO) and a mechanical properties assessment. The presented comprehensive approach of the task analysis can serve as example of how an optimal drive configuration for the specific task can be found, thus creating a basis for solving constructive challenges in designing of pneumatic automation systems.

Keywords: Pneumatics, Energy saving circuit, Efficiency, Exergy, TCO

1. INTRODUCTION

In the design of automation systems, engineers nowadays often have the choice of performing the drive technology pneumatically or electrically. For both drive solutions, a variety of predestined application fields results from their technological properties and the cost-specific situation. Due to the large number of ready-made control concepts for position, speed and force, high rigidity and accuracy of the drive system as well as high availability, electric drives are often preferred in the implementation of positioning tasks. In contrast, pneumatic drives have such advantages as simple realization of point-to-point movement, usage of multiple parallel drives (many actuators on a valve terminal) and a range of possible movement and handling solutions (linear movement, clamping, suction, gripping etc.). Also, much lower investment costs and realization of holding functions without steady energy consumption are clearly beneficial in comparison to the electromechanics.

The higher energy consumption of pneumatic drives is often criticized where both drive technologies compete for their implementation.

To keep up with the competition, manufacturers and users of pneumatic systems are required to increase the energy efficiency of pneumatics at all three levels (compressed air generation, conducting part and consuming actuator part). A reduction of the energy consumption of the drive also contributes to the achievement of climate protection goals, as they stated e.g. in the Europe 2020 initiative [1].

The following article deals exclusively with the energy efficiency at the actuator level for linear movement actuators. There is already a large variety of known energy saving measures, which make it possible to reduce the compressed air consumption of actuators significantly and thus the total operating costs of a pneumatically operated plant. These include primarily the operating pressure reduction of a system and the reducing its filling volumes by shortening the hoses and using micro-valves (e.g. [2]). On the other hand, it is conceivable to use various investigated energy saving circuits such as exhaust air storage [3], [4] or cutting off the supply air to use its expansion energy [5], [6].

However, the application of these measures and their impact on energy consumption were mainly studied individually. It would be therefore reasonable to analyse how energy saving measures can be combined in order to be used simultaneously and whether such a combination can possibly achieve larger cumulative savings effects compared to individual measures.

The study [7] mentions (without making a quantifiable statement) that a combination of measures can be expected to increase savings. According to the results of the study, the measures influence each other, so that an implementation must always be examined in the overall context. Individual measures can even be mutually exclusive (e.g. general pressure reduction and a needs-based design of drives). Because of the mutual influence, no statement of an increase in the overall efficiency of a plant on the basis of the values presented is possible. The percentage efficiency gains cannot be added easily to determine total energy savings and should be determined separately for each case.

The dissertation [8] demonstrates the principle feasibility of the combinatorial approach and shows the possible cumulative savings. However, the results obtained there are valid only for a horizontal movement task with a symmetrical constant loading.

The main goal of the present article is therefore to supplement and investigate the possible combinations of energy saving measures on various drive tasks typical for a pneumatic automation system.

In order to evaluate and contrast the combinations objectively, a complete cost-benefit analysis is required. A statement on the basis of achievable savings alone would be incomplete. For this purpose, a method for the technical-economic evaluation of the combinations is also developed in the present work.

2. COMBINATORIAL APPROACH

2.1. Combinations generation

The energy saving measures to be investigated are based on the classification shown in [4] and [9]. For the generation, the measures and their combinations are divided into the following groups:

Table 1: Combination groups

Group	Description	Code
G1	<u>Separate circuits:</u>	
	Standard circuit	0
	Short circuit	1
	Expansion (cut-off) circuit	2
	Exhaust air storage	3
G2	Pressure-reduced stroke	4
	<u>Combinations of separate circuits,</u> e.g.:	
	Short and expansion circuit	12
G3	Pressure-reduces backstroke with short and expansion circuit	124
	<u>Combinations of groups G1 and G2 with the measure “Filling volumes reduction” (code no. 7),</u> e.g.:	
	Short circuit with reduced filling volume	17
G4	<u>Combinations of groups G1 and G2 with the measure “General pressure reduction” (code no. 6),</u> e.g.:	
	Short circuit with reduced working pressure	16
G5	<u>Combinations of the group G3 with the measure “General pressure reduction” (code no. 6),</u> e.g.:	
	Expansion circuit with exhaust air storage, reduced filling volume and reduced working pressure	2376

Only meter-out throttling circuits are considered, with the exception of exhaust air storage circuits (3), where the forward stroke is realized as a meter-in throttling. Furthermore, each measure/measure combination is examined in three possible versions:

- with 3/2 way control valves (code “a”)
- with 5/2 way control valves (code “b”)
- with 5/3 way control valves (code “c”)

Some examples of generated combinations are shown in **Figure 1**.

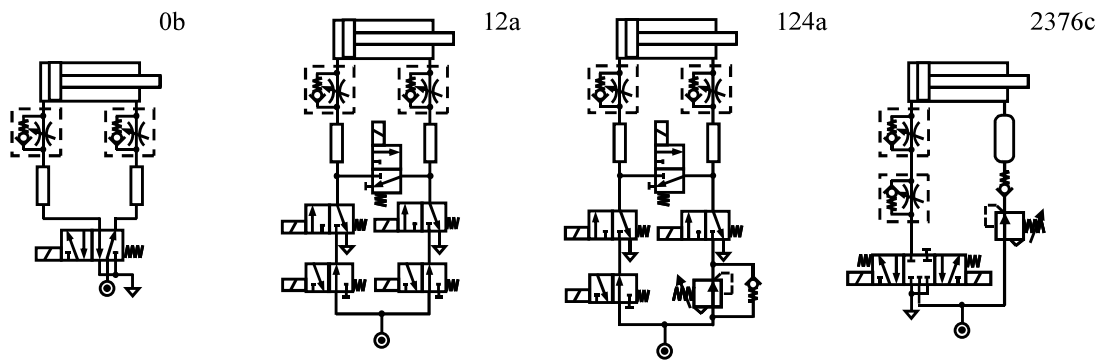


Figure 1: Examples of generated combinations: (0b) Standard circuit with 5/2 way control valve; (12a) Short and expansion circuit with 3/2 way control valves; (124a) Pressure-reduced backstroke with short and expansion circuit with 3/2 way control valves; (2376c) Expansion circuit with exhaust air storage, reduced filling volume and reduced working pressure with 5/3 way control valve.

In this way, 150 theoretically possible combinations were generated.

2.2. Selection of use cases

The generated combinations are to be tested on customary tasks in the drive technology. For this purpose, three common pneumatically operated automation systems are analysed in order to select typical tasks and to test the combinatorial method using their example. As a result of the analysis, the following tasks shown in **Table 2** were chosen. The table also contains such operations conditions as the working pressure of the drive p and its hose length l between the control valve and the cylinder.

Table 2: Use cases

Drive task	Operation conditions
1) Feed drive: movement and ejection of a workpiece Orientation: horizontal	$p = 7 \text{ bar}_{\text{abs.}}$ $l = 1 \text{ m}$ Cylinder dimensions: $\varnothing 10$, stroke 20 mm
2) Force drive: pressing force ($F_{\min} = 180 \text{ N}$) at the end of the stroke Orientation: horizontal	$p = 7 \text{ bar}_{\text{abs.}}$ $l = 1 \text{ m}$ Cylinder dimensions: $\varnothing 25$, stroke 50 mm
3) Feed drive: constant mass ($m = 10 \text{ kg}$) movement on whole stroke and backstroke Orientation: vertical	$p = 5 \text{ bar}_{\text{abs.}}$ $l = 1,2 \text{ m}$ Cylinder dimensions: $\varnothing 40$, stroke 300 mm
4) Feed drive: constant mass ($m = 9,2 \text{ kg}$) movement on whole stroke and backstroke Orientation: horizontal	$p = 5 \text{ bar}_{\text{abs.}}$ $l = 5 \text{ cm}$ Cylinder dimensions: $\varnothing 32$, stroke 100 mm

With this selection, the large range of typical pneumatic drive applications should be covered. The drive size for each task was selected on the basis of the median value of all actuators used for the specific task on the analysed automation systems. The operation conditions are also based on the original manufacturer specifications.

2.3. Cost-benefit analysis

In the next step, each generated combination is examined for its suitability for the specific task and graded on a scale of 0 to 3:

- 3 – circuit usage possible without hesitation
- 2 – circuit usage partially limited (one limitation, e.g. possible in one stroke direction only)
- 1 – circuit usage very limited (two or more limitations, e.g. a pressure reserve required and possible only in one stroke direction)
- 0 – circuit not functional or redundant

For instance, a short circuit (1) could not be applied for the force drive task 2 because of its force loss at the stroke end. Therefore, the variant (1) and all combinations with it are not functional and obtain the grade “0”. Whereas, the short circuit application for the feed drive task 1 is possible, but only for one direction (forward). The grade for the variant (1) in this case is “2”.

After the preliminary grading, there follows the subsequent calculation of each combination that has been graded at least with “2”. The combinations are evaluated from a technical-mechanical and economic point of view. As a final result, the technical benefit value (as a dimensionless score between 0 and 1) and the total cost of ownership balance (as a TCO-value

per year) should be determined for each combination.

Technical benefit

For a technical-mechanical balancing, the following relevant properties of each circuit must be calculated:

- Exergy consumption of a drive Ex [J/cycle]
- Achievable stroke times t_{for} and t_{back} [s]
- Payback time t_p
- For task 2: pressing force safety factor at the stroke end S_{force} [-]
- For tasks 3 and 4: maximum acceleration at the stroke end a_{max} [m/s²]

The exergy consumption of a drive is calculated accordingly to [8]:

$$Ex = \int [\dot{m}_1 \cdot c_p \cdot (T_1 - T_0) + \dot{m}_1 \cdot T_0 \cdot \left(R_s \cdot \ln\left(\frac{p_1}{p_0}\right) - c_p \cdot \ln\left(\frac{T_1}{T_0}\right) \right)] dt \quad (1)$$

The ambient temperature T_0 and atmospheric pressure p_0 represent the calculation reference (environment). The values mass flow \dot{m}_1 , temperature T_1 and pressure p_1 are defined at the circuit inlet before the way control valve(s). Thermodynamic properties of air include specific heat capacity at constant pressure c_p and specific gas constant R_s .

The force safety factor S_{force} is defined as the relationship between the current and the required force. The payback time expresses the reasonableness and suitability of a retrofit with the concrete combination. It is simplified calculated as the ratio between the additional acquisition costs and the energy cost saving per year compared to the reference standard circuit (0).

In the course of the benefit analysis, it is checked to what extent each combination fulfils the predefined mechanical objectives. For this purpose, a utility function is set up for each named technical-mechanical variable, which makes it possible to determine a dimensionless fulfilment degree of a requirement E corresponding to [10]. The designed utility functions are shown in **Figure 2** using the example of the force drive task 2.

The individual requirements for the task are derived from the manufacturer information.

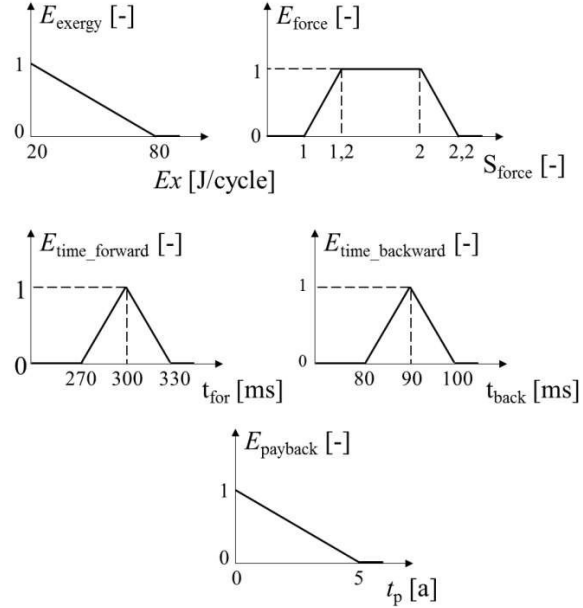


Figure 2: Utility functions of the task 2

To determine the total technical benefit value of a combination N_{total} , it is necessary to set the weights of each goal w_i , which are defined in the present case as follows:

Table 3: Weight factors for task 2

Value	Weight factor w_i , %
Exergy consumption Ex	25
Stroke time forwards t_{for}	10
Stroke time backwards t_{back}	10
Payback time t_p	25
Pressing force F_{press}	30

The stroke times have the smallest weighting due to the fact that the drive settings (e.g. throttle opening, pressure level) were chosen so that the mechanical properties could be kept according to the specification. For instance, by even more reduced operating pressure in a specific case even larger compressed air savings could be achieved, but it would cause a failure to comply with the stroke time requirements. Therefore, all considered combinations meet the set time requirements, although with different quality, and their consideration is not so important for the comparison as the other values. Whereas the capability of the drive to achieve the required pressing force is of the highest importance for the manufacturer, otherwise the task will not be fulfilled. Consequently, the pressing force weight factor has the largest value in this case. The weighting for the remaining two criteria is distributed evenly.

The value N_{total} can now be calculated e.g. by the weighted sum of the individual fulfilment degrees E_i or by their multiplication. According to [10], the additive linkage type is more accurate than multiplicative. Hence, the total technical benefit value is defined as follows:

$$N_{\text{total}} = \sum_i^n w_i \cdot E_i \quad (2)$$

TCO analysis

From the other side, the total cost of ownership should be considered to describe the economic value of a circuit. Following cost parts were calculated:

Table 4: Cost parts of the TCO analysis

Cost object	Calculation
Acquisition	based on market list prices of circuit components;
Shipping	based on delivery costs of the manufacturer and supplier;
Commissioning	medium assembly time of one component (10 min assumed) multiplied by the component number and industrial worker salary;
Energy costs	circuit air consumption multiplied by medium compressed air price (0,0192 €/Nm ³) [11];
Maintenance	assumed as 5% of acquisition costs;
Space	industrial monthly rate for 1 m ² space usage multiplied by the installation area of the drive;

Dismounting medium disassembly time of one component (5 min assumed) multiplied by the component number and industrial worker salary;

Rate of interest	10% assumed [12].
------------------	-------------------

The TCO is accounted for over a period of 5 years.

3. RESULTS OF THE COST-BENEFIT ANALYSIS

For each generated combination of the respective task, a lumped-parameter simulation model was created in order to determine the relevant technical properties of a circuit. Subsequently, based on defined utility functions, the total technical benefit of each combination and, according to **Table 4**, the annual TCO were calculated. The values defined in this way can be graphically represented and compared for each task in the form of a cost-benefit-diagram (see **Figures 3 to 6**).

Each labelled dot corresponds to a calculated energy saving circuit combination. Combinations that are considered to be optimal for the specific task are highlighted in green and bold, the standard circuits (0) in grey. The optimal variants were chosen as a balance between the achievable technical benefit and the TCO value:

- Task 1: (7b) Filling volumes reduction
- Task 2: (47b) Filling volumes reduction and a pressure-reduced back stroke (3 bar_{abs.})
- Task 3: (176c) Short circuit with reduced filling volumes and operating pressure (3 bar_{abs.})

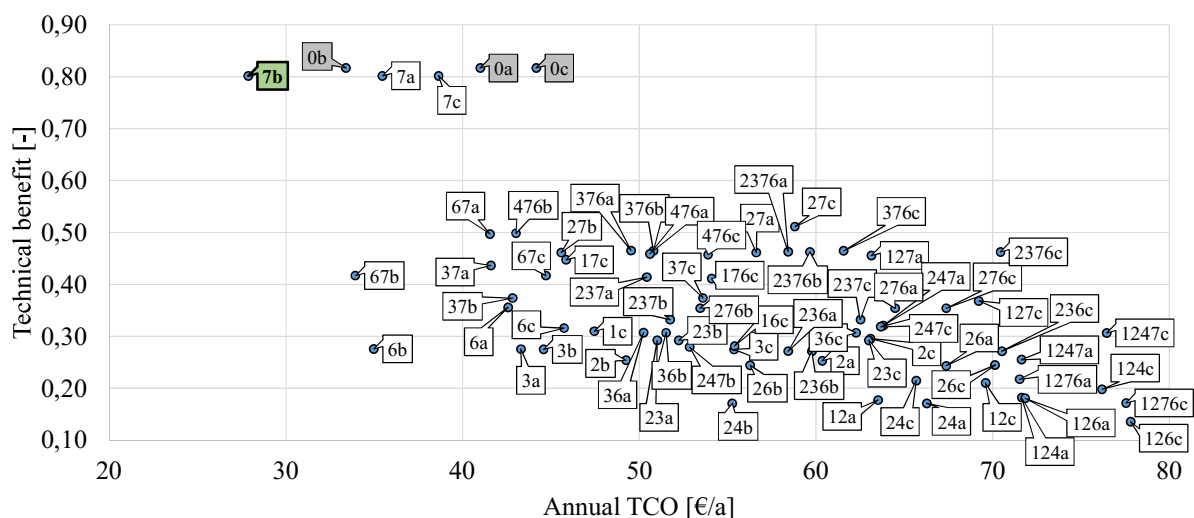


Figure 3: Cost-benefit diagram for the task 1 “Feed drive”



- Task 4: (6b) General operating pressure reduction (2 bar_{abs.})

It can be seen that in the case of smaller and medium-sized handling tasks (up to 25 mm diameter), large cost savings and an improved technical benefit value can be achieved with simple energy saving measures (reduction of operating pressure (6) and/or filling volumes (7)), which involve relatively few acquisition and assembly costs. In case of the task 2, even greater TCO savings can be achieved with help of the exhaust air storage (3) and its combinations, however at the expense of the technical value.

For the task 4 too, a simple reduction of the operating pressure was sufficient to increase the technical value and significantly reduce the annual costs. The measure "Reduction of the filling volume" (7) was not considered here, since the tube length was already low in the present task.

The situation is different for the task 3 with a larger-sized cylinder. There, the combination 176c of a short circuit (1) with other two measures (reduction of filling volumes and operating pressure) has prevailed.

It can be concluded that known energy saving circuits and their combinations are mostly worthwhile for larger cylinders (from a diameter of 32 mm) in the considered cases. Although the combination of different savings circuits makes it possible to reach even greater compressed air savings than with individual circuits, the ever-higher initial acquisition costs and other cost factors compared to the standard circuit exceed this saving in the most cases thus reducing their technical benefit and even increasing the annual TCO in overall terms.

Especially for the task 1 it can be made clear that although many combinations bring significant savings in compressed air compared to individual circuits, but for their achievement a costly acquisition is necessary, which does not pay in 5 years of observation space (Figure 7).

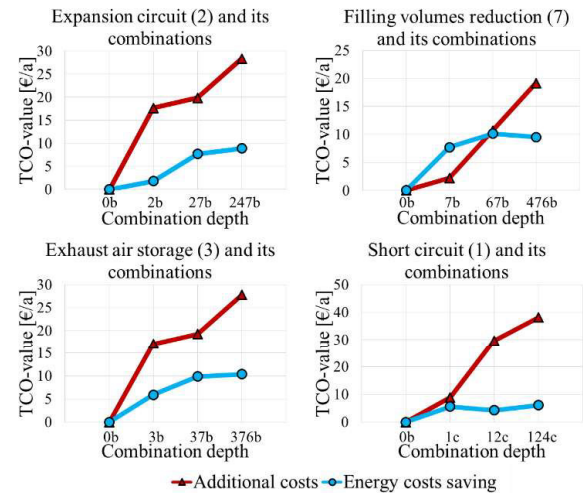


Figure 7: Comparison of energy costs saving and additional costs for each further combination for the task 1

4. VALIDATION

In each task, its optimal combination of energy saving measures and the corresponding standard circuit were reconstructed on test benches and measured to validate the calculated mechanical properties and the compressed air saving:

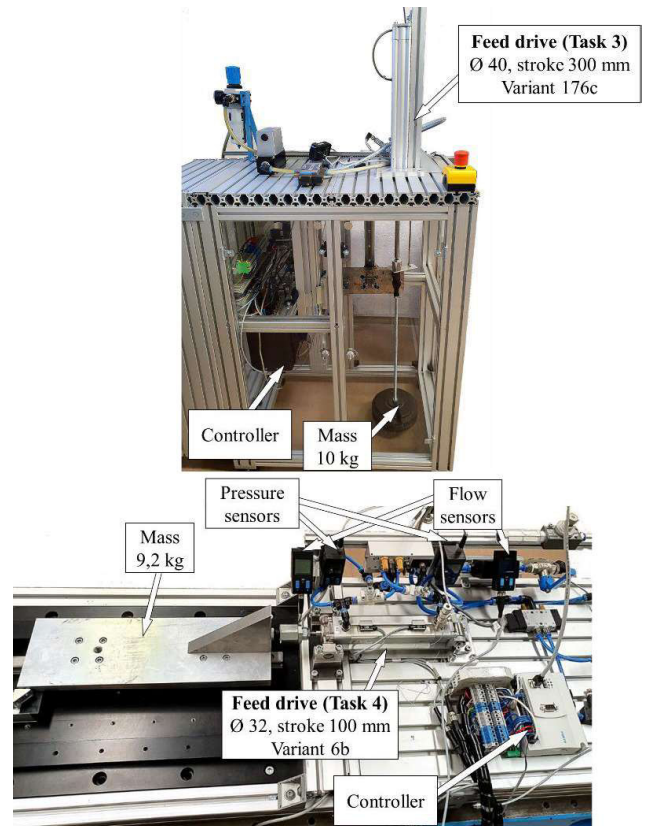


Figure 8: Examples of test benches

Table 5: Standard and optimal circuits

No.	Air consumption		Stroke time forwards		Stroke time forwards		TCO [€/a]	Additional acquisition costs [€]
	[Nl/cycle]		t_{for} [s]		t_{back} [s]			
	simulated	measured	simulated	measured	simulated	measured		
1) Feed drive								
0b	0,0801	0,089	0,015	0,014	0,010	0,010	33,40	0,00
7b	0,0297	0,032	0,015	0,016	0,011	0,012	27,87	10,12
2) Force drive								
0b	0,431	0,445	0,302	0,306	0,092	0,092	89,76	0,00
4b	0,319	0,327	0,301	0,306	0,096	0,094	82,36	30,83
7b	0,336	0,350	0,298	0,301	0,088	0,092	80,37	20,10
47b	0,251	0,267	0,300	0,301	0,090	0,092	77,11	50,93
3) Feed drive								
0c	3,80	3,68	1,85	1,76	3,94	3,92	627,23	0,00
1c	1,946	1,86	1,83	1,72	3,94	3,92	351,16	30,68
7c	3,47	3,27	1,84	1,71	3,90	3,87	580,95	20,10
6c	2,23	2,14	1,87	1,77	4,01	3,96	411,86	109,02
17c	1,79	1,71	1,81	1,72	3,92	3,90	331,60	50,78
16c	1,13	1,10	1,84	1,75	4,01	3,97	251,60	139,70
67c	2,63	2,54	1,86	1,78	3,98	3,93	477,70	129,12
176c	1,05	1,02	1,89	1,91	3,98	3,93	243,71	159,80
4) Feed drive								
0b	0,759	0,736	0,354	0,361	0,351	0,359	144,58	0,00
6b	0,298	0,315	0,349	0,353	0,340	0,344	82,34	30,83

The results of measurements are shown in **Table 5**.

As the exergy consumption of a drive cannot be measured directly, the compressed air consumption was measured instead.

The modelling of the end-cushioning system in the cylinder chambers was neglected in this work to reduce the calculation effort. Instead, the simple elastic end stop model (spring-damper element) was assumed. For this reason, the maximum acceleration at the stroke end a_{max} was determined exclusively simulative.

The pressing force value F at the stroke end for the task 2 was derived from the measured pressure and the cylinder geometry. The force values in this case are:

Table 6: Pressing forces of task 2 combinations

No.	Pressing force F	
	Simulation	Measurement
0b	282	293
4b	279	290
7b	281	294
47b	278	292

The TCO balance cannot be validated because of its long-term observation.

As the measured and calculated values agree well, the calculated savings could be proven. The deviations of the air consumption are due to the

problematic consideration of dead volumes of a real system and inaccuracy of the flow sensors. In particular, the dead volumes of the cylinder and the pressure sensors for the simulation were estimated from their geometry and might not completely correspond to real values.

5. CONCLUSION AND OUTLOOK

In the present article, a range of combinations of energy saving measures and circuits in the pneumatics has been studied using the example of four common automation tasks. Cumulative effects of combining could be demonstrated: in the vast majority of cases, an additional measure increases the compressed air savings. With each further combination, higher savings can be achieved than with the individual circuits. However, the overall balance shows that these savings are often offset by the additional costs and/or deteriorated mechanical properties. Nevertheless, there could be also found combinations that make it not only possible to reduce the TCO drastically, but at least sustain or even improve the mechanical properties in general.

The research results can be transferred to similar tasks in pneumatics. The presented comprehensive approach of the task analysis can serve as example of how an optimal configuration for the specific task can be chosen thus creating a

basis for solving constructive challenges in designing of pneumatic automation systems.

It could also be possible to enhance the presented combinatorial approach e.g. by means of a needs-oriented parameter optimisation (determining its optimum cylinder piston diameter etc.) The article aimed, though, to make recommendations primarily for already given fixed system parameters such as cylinder geometry.

NOMENCLATURE

a_{\max}	Maximum acceleration at the stroke end [m/s^2]
c_p	Specific heat capacity at constant pressure [$\text{J}/(\text{kg}\cdot\text{K})$]
E	Fulfilment degree [-]
Ex	Exergy consumption [J/cycle]
F	Pressing force [N]
l	Hose length [m]
m	Load mass [kg]
\dot{m}_1	Mass flow at the circuit inlet [kg/s]
N_{total}	Total technical benefit value [-]
p	Pressure [Pa]
p_0	Atmospheric pressure [Pa]
p_1	Air pressure at the circuit inlet [Pa]
R_s	Specific gas constant [$\text{J}/(\text{kg}\cdot\text{K})$]
S_{force}	Pressing force safety factor at the stroke end [-]
t_{back}	Stroke time backwards [s]
t_{for}	Stroke time forwards [s]
t_p	Payback time [a]
T_0	Ambient temperature [K]
T_1	Air temperature at the circuit inlet [K]
TCO	Total cost of ownership
w	Weight factor [%]

REFERENCES

- [1] Barroso JM (2010) Communication from the commission - Europe 2020 - A strategy for smart, sustainable and inclusive growth, Brussels, 2010
- [2] NN (2015) Schunk Mikroventile. Installation and operating instructions, SCHUNK GmbH & Co. KG, Lauffen/Neckar
- [3] Gauchel W (2006) Energiesparende Pneumatik. O+P Ölhydraulik & Pneumatik, 1/2006:33-39
- [4] Hepke J, Weber J (2013) Energy saving measures on pneumatic drive systems. Paper presented at the 13th Scandinavian International Conference on Fluid Power, SICFP'13, Linköping, Sweden, 4–9 June 2013
- [5] Doll M, Sawodny O, Neumann R (2012) Energy efficient adaptive control of pneumatic drives with switching valves. Paper presented at the 8th International Fluid Power Conference, SICFP'13, Dresden, Germany, 26–28 March 2012
- [6] Kawakami Y, Terashima Y, Kawai S (1999) Application of energy-saving to pneumatic driving systems. Paper presented at the 4th JHPS international symposium on fluid power, Tokyo, Japan, 15–17 November 1999
- [7] NN (2012) EnEffAH – Energy efficiency in production in the drive and handling technology field. Funding code 0327484A, final report, Esslingen, Germany
- [8] Hepke J (2017) Energetische Untersuchung und Verbesserung der Antriebstechnik pneumatischer Handhabungssysteme. Dissertation, Technical University of Dresden
- [9] Arinaga T et al. (2000). Approach for energy-saving of pneumatic systems. Proceedings of 1st FPNI-PhD Symposium Hamburg 2000, p. 49-56
- [10] Rinza P, Schmitz H (1992) Nutzwert-Kosten-Analyse: eine Entscheidungshilfe. VDI-Verlag, Düsseldorf
- [11] NN (2014) Energiekosten in Druckluftsystemen bis zu 60% senken. White Paper Festo, Festo AG & Co. KG, Esslingen
- [12] Wöltje J (2011) Betriebswirtschaftliche Formelsammlung. Haufe-Lexware, Freiburg

ENERGY EFFICIENCY IN PNEUMATICS WITH THE “AIR SAVING BOX”: THE REVOLUTIONARY PLUG & PLAY SOLUTION FROM SMC

Mario Heitmann*, Ferdinand Rein

SMC Deutschland GmbH, Boschring 13-15, 63329 Egelsbach

* Corresponding author: Tel.: +49 162 2999709; e-mail address: Heitmann.Mario@smc.de

ABSTRACT

For many companies, energy efficiency starts with production. For this reason, special consideration must be given to the production operation as a whole as well as its sub-areas. The strict legal requirements, as well as the companies' green policies which are defined as a result of these, create complex challenges, which SMC meets with expertise and passion as a manufacturer, partner and solution provider in electric and pneumatic automation technology. On the basis of an actual customer requirement, SMC Germany has developed an innovation in the field of pneumatic energy efficiency: “The Air Saving Circuit for double acting pneumatic cylinders”, under the working title of “Air Saving Box”. The underlying idea and focus of the solution was to make good use of the compressed air generated in existing cylinders, instead of simply allowing it to go to waste. The “Air Saving Box” enables significant energy savings in production. Based on this customised solution, SMC has also developed an industry-independent concept that can also be integrated into existing applications.

Keywords: Automation, energy efficiency, pneumatics, air saving, energy saving

1. INTRODUCTION AND PROBLEM DEFINITION

In 2015, a new agreement containing binding climate targets for all 195 member states of the UN Climate Convention was concluded in Paris as the successor to the Kyoto-Protocol. It was decided to limit global warming to less than 2°C in order to keep the effects of climate change within manageable limits. This requires a reduction in net greenhouse gas emissions. The intention therefore is to reduce net greenhouse gas emissions worldwide in the second half of this century [1].

Carbon dioxide (CO₂), the gas produced by the combustion reaction of carbon-containing materials such as wood or oil, makes up 72% of greenhouse gases emitted each year. The global concentration of CO₂ has increased by a good 44% since the beginning of industrialisation. In the 10,000 years before the Industrial Revolution, CO₂ concentration remained almost constant [2]. Despite strong economic growth, CO₂ emissions in Germany remained almost continuous at 800 million tonnes per year in the period from 2014 to 2017.

The German government's goal is to achieve a

reduction to 749 million tons by 2020 to meet the targets it has set itself under the Paris Climate Agreement [3].

In Europe, compressed air supply in the industrial and service sectors accounts for more than 80 TWh of electricity per year – that's around 10% of total industrial electricity consumption. Case studies have shown that possible savings potentials are not fully exploited due to opposing market and decision-making mechanisms [4].

SMC Germany offers energy saving audits as part of its service portfolio. Automation experts from SMC will examine a company's existing systems and offer individual advice on how it can reduce its compressed air consumption.

1.1. Practicability is a must

Experience from these audits has shown that, beyond the existing possibilities for saving compressed air, efficient solutions are needed in which cylinder force and cylinder speed remain unaffected, since the performance of existing machines must be available without any changes.

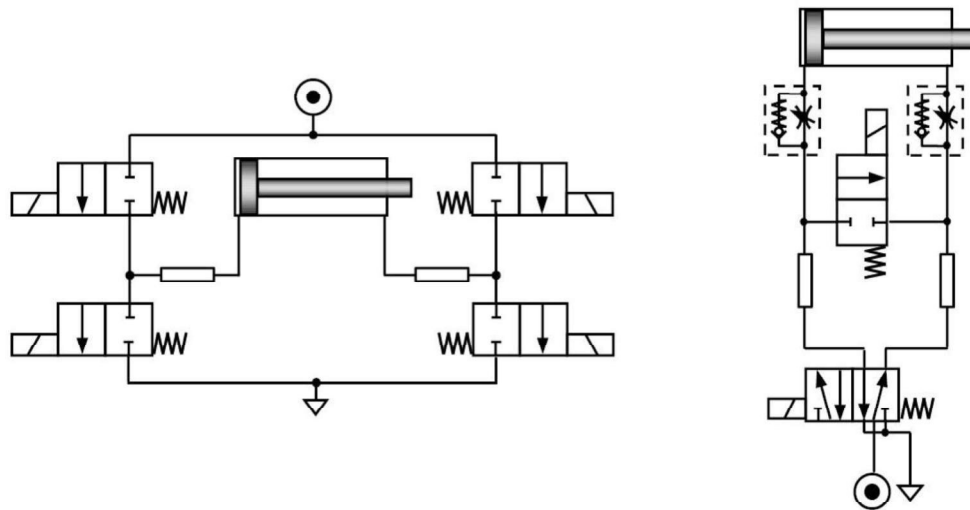


Figure 1: Schematic diagram of a bridge circuit consisting of four 2/2-way switching valves (left) and a short-circuited circuit (right).

SMC was set this objective by a customer who operates complex pneumatic systems in its production.

The initial starting point for the development was a detailed examination of the current state of technology and research.

2. STATE OF THE ART RESEARCH AND TECHNOLOGY

Preliminary investigations have shown that two switching methods are in principle particularly well suited for increasing the energy efficiency of pneumatic systems: a bridge circuit of four 2/2-way switching valves or a short-circuited circuit. These two circuits shown in **Figure 1** display an increased degree of functionality and a high compressed air savings potential in use [5]. Hence these two switching methods were first examined with regard to their practicability for installation in existing plants.

To implement a bridge circuit as shown in **Figure 1** a new control concept for the cylinder would have to be developed. This would require a deep intervention in the machine control system. When it comes to achieving an energy-, time- and cost-efficient compressed air reduction for existing plants, as required at the outset, this circuit is therefore only suitable to a very limited extent. A short-circuited circuit, on the other hand, would be easier and faster to integrate. This switching method was therefore pursued further.

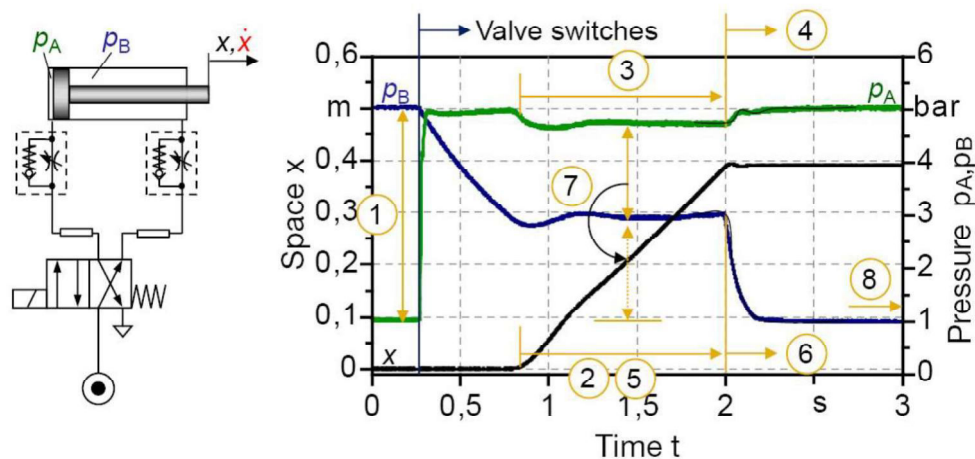
2.1. Different saving potentials

Based on the chamber pressure curves of a double-acting piston rod cylinder with standard circuitry, the following compressed air saving possibilities were identified [5]:

- Chamber short circuit before switching the directional valve
- Chamber short circuit during the stroke
- Closing the compressed air supply during the stroke
- Closing the compressed air supply at the stroke end
- Exhaust air storage during the stroke
- Incomplete venting at stroke end
- Lower pressure level for required differential pressure
- Return stroke with reduced operating pressure

These eight possible operating methods were examined for their theoretical savings effects. At the same time, their practical feasibility for operators of existing plants with pneumatic components and systems was tested. Only practicable solutions that can be easily retrofitted were considered for the development of the individual customer solution.

A bidirectionally acting horizontal drive with a piston diameter of 32 mm, stroke of 100 mm, operating pressure of 7 bar, inner hose diameter of 4 mm and a length of 2 m [5] was considered, see **Figure 2**. Of the eight operating methods tested, six were rejected as unsuitable for the application. Although energy savings of up to 78%



Possible savings potentials		Savings potential
1 Chamber short circuit before switching the directional valve		18%
2 Chamber short circuit during the stroke		40%
3 Close compressed air supply during the stroke (use expansion energy)		78%
4 Close compressed air supply at stroke end		20%
5 Exhaust air storage during the stroke		47%
6 Prevent complete venting at stroke end		12%
7 Required differential pressure at lower pressure level		33%
8 Return stroke with reduced operating pressure		23%

Figure 2: Possible theoretical savings effects with exhaust throttled cylinders.

can be achieved, for example by shutting off the air supply during the stroke (method 3 in the picture), this always has a negative effect on cycle time, cylinder force or both. The same applies to methods 4 to 7, so they are not suitable for developing an energy-efficient and easily integrated solution that does not compromise on performance.

In contrast, methods 1 and 2 offer savings potentials of 18% and 40% with cylinder force and cycle time comparable to the initial state. For this, however, they require a specific control of the short-circuit valve. This represents too much interference with the control system for the specific application. The two methods were therefore considered to be only partially suitable.

2.2. New solution needed

Even if only standard components are used for the short-circuited circuit, a system operator cannot be expected to find the optimum operating point for the cylinder in the respective application. It is also unclear whether operators have the necessary

possibilities and knowledge to intervene in the machine control system in order to subsequently control a short-circuit valve.

Therefore, the two currently available short-circuit machine and plant manufacturers' entirely new designed system solutions. The specific application of a customer method are ultimately reserved for who wants to convert its existing machines in an energy-efficient way requires a completely newly developed technology.

3. OBJECTIVE

The new operating concept requires a solution that can be retrofitted to existing circuits, significantly reduces compressed air consumption and has no negative impact on force and cycle time. The solution should function independently so that it can be used with components from any manufacturer.

In addition, the innovation should be as industry-independent as possible, to ensure that it can be used beyond the individual application and thus help as many operators of pneumatic systems as possible to save energy.

4. PROCEDURE

On the basis of the short-circuited circuit, tests are being carried out to determine whether a pneumatically controlled variant can be implemented that takes account of the pressure conditions on both sides of the cylinder chamber and thus achieves the optimum energy-saving effect with practically no additional control. All basic load cases are considered in addition:

- horizontally operating, double-acting cylinder

- double-acting cylinder working vertically upwards against the load
- double-acting cylinder working vertically downwards with the load

The values for piston diameter, stroke and load are varied during the experiment.

4.1. Real application

A real application with classic circuitry of a double-acting cylinder via 5/2-way valve serves as a reference and starting point for the development. In the reference application, a speed controller is not used to achieve a shorter cycle time and thus higher machine speed, see **Figure 3 left**.

The classic circuit was compared with the newly developed short-circuited circuit by SMC using the “Air Saving Box”, **Figure 3 right**.

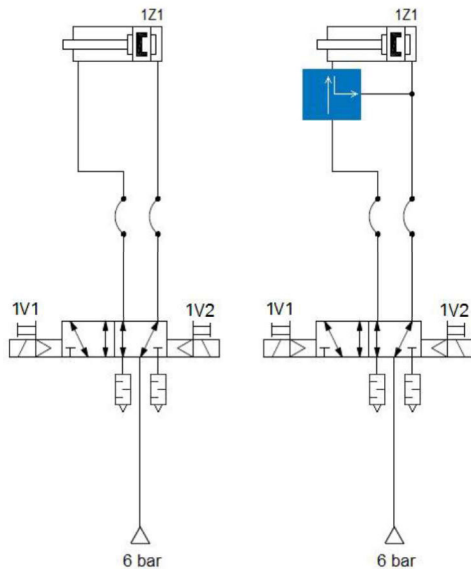


Figure 3: Classic control of a bidirectional cylinder with 5/2-way valve (left) and compressed air-saving control based on the short-circuited circuit with the “Air Saving Box” (right).

The respective pressure curves in the cylinder chambers are measured as well as the compressed air consumption, which was documented before the valves with the help of a flow sensor. The respective results are put in relation to each other according to the following formula:

$$E [\%] = \frac{V_{\text{classic}} - V_{\text{Air Saving Box}}}{V_{\text{classic}}} \quad (1)$$

5. CURRENT STATUS

The performance of cylinders with the “Air Saving Box” must not be less for the customer application than that of a conventionally switched cylinder. SMC therefore measured the energy efficiency, cylinder force and stroke time under various parameters, such as cylinder diameter, cylinder stroke, hose volume and installation direction of the cylinder without and with load. The “Air Saving Box” is mounted on the piston rod side cylinder chamber. It therefore acts in the extension stroke and reduces the compressed air consumption without further control measures, (see **Figure 4**) making it easy to integrate into existing systems.

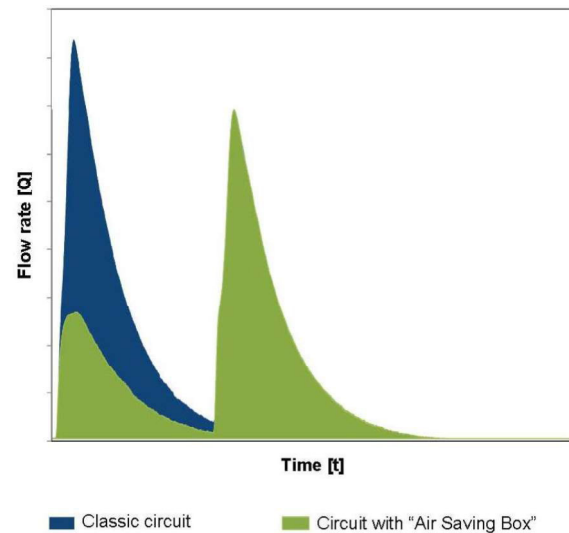


Figure 4: Comparative display of the required compressed air flow rate of a classically controlled bidirectional cylinder (dark) and a cylinder controlled to save compressed air with the “Air Saving Box” (light). Good to see: the significantly reduced flow rate in the extension direction.

As **Figure 4** shows, the short-circuited circuit with the “Air Saving Box” in the extension direction significantly reduces the required compressed air flow. This value and the associated reduction in compressed air consumption as an area under the compressed air flow serves as a measure of the energy saving and energy efficiency of the application. In laboratory tests, savings of up to 50% have been achieved with this formation. In the retraction direction, however, the compressed air flow – and thus the compressed air consumption remains unchanged.

5.1. Positioning and load mounting

Further laboratory tests have confirmed that the compressed air savings depend largely on the installation direction and the mounted load. For example, a vertical set-up in the laboratory showed that the statically applied positioning energy of the moving load can be converted into compressed air savings. Furthermore, the hose length and the hose volume have a significant influence on the cylinder speed.

The next step is to further develop the solution for cross-industry use. For this purpose, the parameter influences are determined in the laboratory under scientific aspects. This allows the characteristic map data for the use of the “Air Saving Box” to be worked out. SMC also focuses on customer applications in order to be able to define the application parameters as realistically as possible.

6. CONCLUSION AND OUTLOOK

On the basis of an actual customer requirement, SMC Germany has developed an innovation in the field of pneumatic energy efficiency: “The Air Saving Circuit for double acting pneumatic cylinders”, or “Air Saving Box” for short. The focus was on making good use of the compressed air generated in existing cylinders, instead of allowing it to go to “waste”, and use “fresh” compressed air.

SMC’s “Air Saving Box” creates significant energy savings in production. Based on the knowledge gained from the development process of this initially individual customer solution in Germany, SMC is now developing a product for worldwide use that is industry-independent and can be integrated into all applications.

Current societal and industrial efforts suggest that plant operators are opening up to energy-efficient solutions that involve the lowest possible investment costs and operating risks.

The “Air Saving Box” optimally meets these requirements and will considerably increase the efficiency of pneumatics in a wide range of applications. SMC is thus contributing to the goals of our federal government to drastically reduce CO₂ emissions and to reduce overall net greenhouse gas emissions to zero in the foreseeable future.

NOMENCLATURE

E	Savings
$V_{classic}$	Compressed air consumption (classic)
$V_{Air\ Saving\ Box}$	Compressed air consumption (with “Air Saving Box”)

REFERENCES

- [1] ZEIT ONLINE (2015) “A new global climate treaty”. <http://www.zeit.de/thema/klimagipfel-2015>. Last accessed 19.12.2019
- [2] German Environment Agency (2019) “Atmospheric greenhouse gas concentrations”. <https://www.umweltbundesamt.de/daten/klima/atmosphaerischetrgaskonzentrationen#textpart-1>. Last accessed 19.12.2019
- [3] German Environment Agency (2016) Position // April 2016 “Climate protection in the German powerplantcomplex” https://www.umweltbundesamt.de/sites/default/files/medien/376/publikationen/klimaschutz_im_deutschen_kraftwerkspark.pdf. Last accessed 19.12.2019
- [4] Peter Radgen, Edgar Blaustein (2001) “Compressed Air Systems in the European Union”. http://air.avexa.se/air/down/eu_compressed_air.pdf. Last accessed 19.12.2019
- [5] Jan Hepke (2016) “Energetic investigation and improvement of the drive technology in pneumatic Handling Systems”, dissertation at the Dresden University of Technology’s Faculty of Mechanical Engineering

ENERGY EFFICIENCY AND PERFORMANCE OF SERVOPNEUMATIC DRIVES FOR SPEED GOVERNORS BASED ON OPERATING POINTS

Vinícius Vigolo¹, Gregori Conterato¹, Talles Spada¹, Leonardo Augusto Weiss², Victor Juliano De Negri^{1*}

¹Mechanical Engineering Department, Federal University of Santa Catarina, Trindade, 88040-900, Florianópolis, Brazil

²Reivax S/A Automation and Control, João Paulo, 88030-904, Florianópolis, Brazil

* Corresponding author Tel.: +55 48 3721 9396; E-mail address: victor.de.negri@ufsc.br

ABSTRACT

In this paper, the energy efficiency and dynamic performance of servopneumatic drivers are studied aiming at the correct sizing of the system components. The study is carried out through a non-linear dynamic model of a servopneumatic system. The simulation data are used along with the operating point method in order to understand the effect of loading conditions in the system performance, which is then used as a tool for component sizing. The results show the effects that the piston area has on the energy efficiency and dynamic behavior of the system. Moreover, the dependency of the servovalve size on the piston area is elucidated. A procedure to design an effective combination of piston area and sonic conductance of the servovalve is presented. A practical case where a servopneumatic system is being designed for the speed governor of a hydraulic turbine is described, evidencing the suitability of the proposed method for servopneumatic systems.

Keywords: Servopneumatic systems, sizing method, operating point, turbine speed governors

1. INTRODUCTION

Pneumatic systems are widely used in the automation industries due to its low acquisition and maintenance costs, high reliability and high power/weight ratio, beyond that they provide speedy actuations. Pneumatic systems are being used for point-to-point automation purposes since the 60's [1] and in the 80's the first commercial servopneumatic system has been made available [2]. Since then, the application of servopneumatic systems has increased widely, being applied in the fields of automation, robots and manufacturing. According to [3], pneumatic servosystems are capable to replace electromechanical and hydraulic actuators, which are less efficient and costly [4] and [5].

In the past few decades, many control strategies have been developed for pneumatic servosystems, including linear and nonlinear controls, fuzzy based techniques and state observers with compensators strategies [3]. In the same way the mathematical modelling also had many improvements, for which models for nonlinearities such as the piston friction, end

stroke cushioning and valve mass flow rate have been developed. These models are combined with equations based on the physical principles that govern the system, resulting in a global model capable to predict the behavior of the state variables of the drive with high accuracy [2].

However, in the sense of pneumatic system sizing, there is still the need of consistent method for the selection of the system components. An optimal system design is proposed by [6], even so the method is based on an optimization algorithm, which limits the applicability of the method for software implementing tools. On its review on recent research trends in servo pneumatic systems, [3] describes the systems parameters that have a significant impact in the system dynamic. Still, no guidelines are given in order to select the main components.

In this context, this paper studies the characteristic behavior of a servopneumatic system in order to propose guidelines to size the systems parameters. The inflection point of the velocity profile and the operating point of system are used as key points in the design process of the servovalve and the cylinder diameter.

2. MATHEMATICAL MODEL

A conventional servopneumatic system is presented in **Figure 1**. It is composed by a cylinder, a servovalve (SV), a position transducer, a set of hoses and a controller, which receives the position error and sends the control signal to the SV.

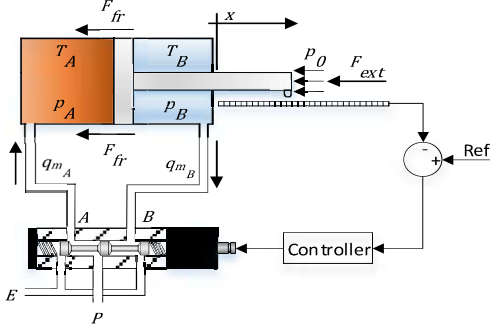


Figure 1: Conventional servopneumatic system

In this study, the components were modelled according to the physical laws that govern the system, including the mass flow rate through the valve, the pressure and temperature inside the cylinder chambers, the motion and friction of the piston. The heat exchange in the actuator is modelled by the Newton's law of cooling and the friction is described by the LuGre Model [7]. These equations result in a non-linear model which is described in [8] and implemented in MATLAB/Simulink® for simulation purposes. The pressure and thermal losses in the hoses were neglected since the PDV is usually connected close to the actuator and their effects on the system dynamics might be included in the dead volume of the cylinder chambers. An experimental validation is performed in order to evaluate the effectiveness of the model and the results are presented in [8].

3. ANALYSIS OF THE SYSTEM DYNAMICS

A servo pneumatic actuator is, in the point of view of control, a system working in closed loop, where the output is the piston position and the input is a reference position of the actuator stroke. As in many control systems, the general response of a servo pneumatic system might be approximate by a second order system, that is

$$\frac{y(s)}{y_{Ref}(s)} = \frac{\omega_n^2}{s^2 + 2\zeta\omega_n s + \omega_n^2}. \quad (1)$$

This approach is convenient since the design requirements are easily converted into a second

order system parameter, such as natural frequency and damping ratio. A similar approach is used in [9] and [10], where a design method for hydraulic positioning system is proposed.

3.1. Inflection point of a step response

The design requirements of a positioning system usually are composed by the maximum displacement, settling time, maximum forces and overshoot. Therefore, the design requirements can be converted into natural frequency and damping ratio by the settling time

$$t_s = \frac{6}{\omega_n} \quad \text{for } \zeta = 1 \quad (2)$$

or

$$t_s = \frac{5.7}{\omega_n} \quad \text{for } \zeta = 0.7. \quad (3)$$

In a second order system, the maximum velocity occurs at the inflection point of the velocity profile. At this point, the acceleration is null and the velocity is given by.

$$v_{max} = 0.4668x_{max}\omega_n \quad \text{for } \zeta = 0.7 \quad (4)$$

or

$$v_{max} = 0.3678x_{max}\omega_n \quad \text{for } \zeta = 1 \quad (5)$$

where x_{max} stands for the expected maximum step response [9].

Figure 2 presents an example of a step response of a servo pneumatic system along with the response of second order system with $\omega_n = 1.772 \text{ rad/s}$ and $\zeta = 1$.

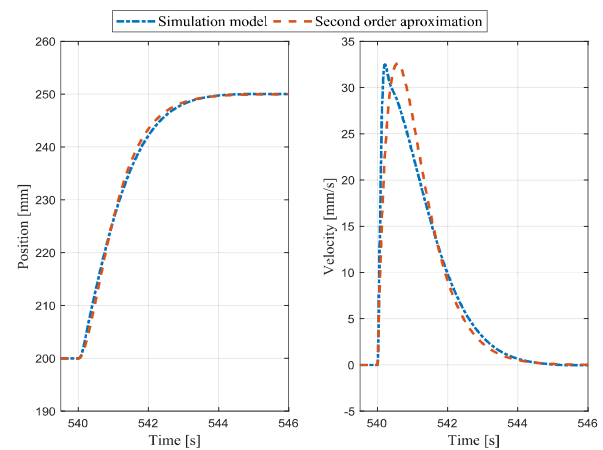


Figure 2: Comparison of a simulation model with a second order system

It can be seen that the characteristic second order model is capable to represent accurately the dynamic of the servopneumatic system, demonstrating the applicability to estimate the

maximum velocity through the design requirements.

3.2. System simulation analysis

The effects of the chamber pressures during the displacement of the piston have an important impact on the system dynamics. Consequently, it is important to understand the characteristic behavior of the system in order to size it accordingly. As an example, a sequence of 10 step inputs, each one of 10% of the actuator stroke, was analyzed.

An important aspect of the study is that the closed loop control has a direct impact in the results. Therefore, the closed loop control is made with a simple proportional controller. The gain is calculated in such a way that the maximum error results in 100% of the valve opening and the sonic conductance was adjusted to have a critical damping behavior. The parameters of the system are presented in **Table 1**.

Table 1: Parameters of the simulation

Parameter	Value
Piston diameter D_p	0.032 m
Rod diameter D_r	0.012 m
Area ratio r_A	0.8594
Cylinder stroke L	0.5 m
System mass M	8.6 kg
Load force F_L	470 N
Viscous friction coefficient B	200 N.s/m
Supply pressure p_s	8 bar
Sonic conductance C	$6 \times 10^{-10} \text{ m}^5/\text{N.s}$
Critical pressure ratio b	0.3

Results from simulation of the pneumatic positioning system are presented in Figures 3 to 5.

It can be seen that the maximum velocity is not constant throughout the piston stroke. This fact is mainly related to the amount of air inside the counter pressure chamber, which is maximum in the beginning of the movement and reduces at each step. However, either the pressures and the maximum velocity tends to be constant as the piston reaches its end stroke. Further analysis related to these simulations are presented in Chapter 4.

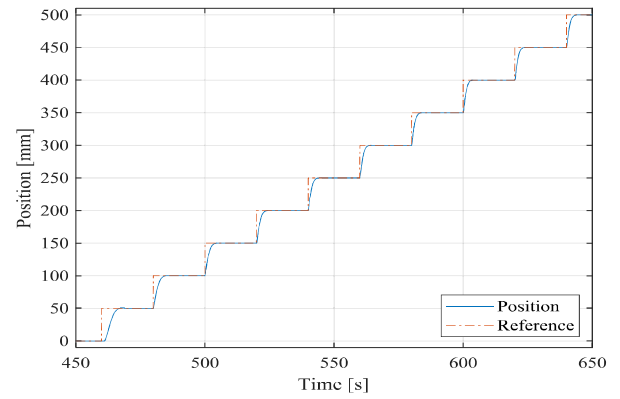


Figure 3: Reference and piston positions

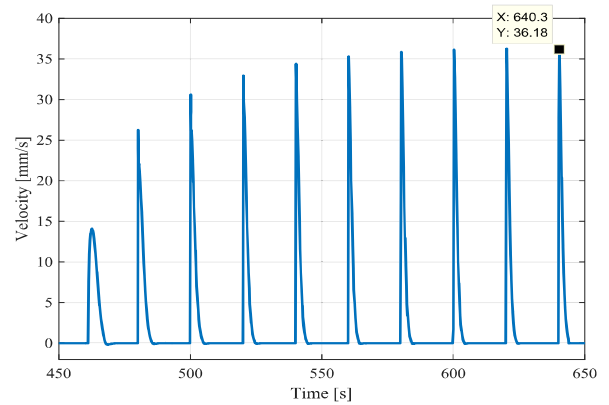


Figure 4: Piston velocity

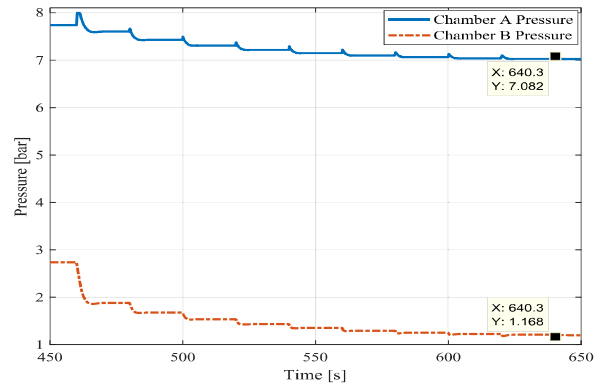


Figure 5: Chamber pressures

4. STEADY STATE ANALYSIS

The inflection point of the velocity has important characteristics that might be used for sizing purposes. For this reason, the pressure of both chambers was recorded at the inflection point in order to obtain the pressure ratios at this condition.

The operating point method was introduced by [11] and [12] and it describes the pressures of the system as a function of pressure ratios, for instance, in the extending movement p_A/p_s is a function of p_0/p_B .

As shown in **Figure 6**, the pressure ratios (p_A/p_S and p_0/p_B) at the maximum velocity points result in ten different operating points (red circles). They are analyzed along with the operating point chart, which is composed of a constant pressure curve (*Op* curve) and a constant velocity curve (*Ldg* curve). The intersection of both curves occurs when both pressure and velocity are constant. The curves are described by

$$\frac{p_0}{p_B} = b + \sqrt{\frac{b^2 - 2b + 1 + r_A^2 + (2br_A^2 - r_A^2)\left(\frac{p_S}{p_A}\right)^2 - 2br_A^2\left(\frac{p_S}{p_A}\right)}{(2br_A^2 - r_A^2)\left(\frac{p_S}{p_A}\right)^2 - 2br_A^2\left(\frac{p_S}{p_A}\right)}} \quad (6)$$

and

$$\frac{p_A}{p_S} = \frac{F_T}{p_S A_A} + \left(\frac{p_B}{p_0}\right) \left(\frac{p_0}{p_S}\right) r_A + \frac{p_0}{p_S} (1 - r_A). \quad (7)$$

where Equation (6) corresponds to the *Op* curve and Equation (7) to the *Ldg* curve. The cylinder area ratio is defined as $r_A = A_B/A_A$. The equation derivations for this forward movement as well as for returning movement are presented in [12].

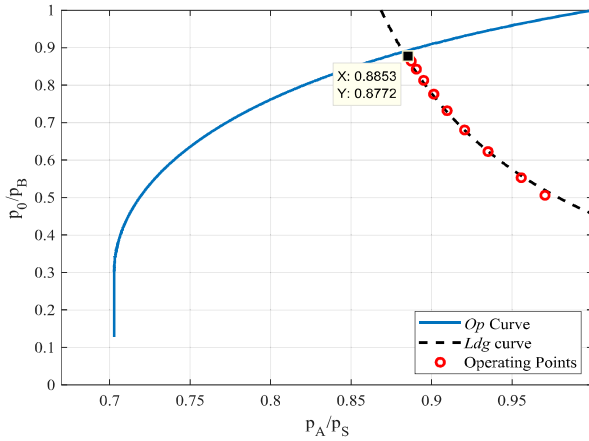


Figure 6: Operating point chart

The highlighted point corresponds to the last maximum velocity peak, whereas the first circle from right to left corresponds to the first maximum velocity peak. It can be seen that during the displacement of the piston along its stroke, the pressure ratios of the maximum velocity points are located exactly on the *Ldg* curve, which is due to the nullity of acceleration at this point. It is also important to notice that the intersection between both curves occurs at the higher value of the maximum velocities and all the remaining points are below to the *Op* curve.

The *Op* curve is dependent of critical pressure ratio (b) and the area ratio (r_A), which are parameters that have a small influence on the dynamic behavior of the system. Usually, even

when these parameters are not known, assuming typical values is enough to obtain the *Op* curve. However, the *Ldg* curve depends on the load force and the piston area, that means, from the different loading ratios ($F_T/p_S A_A$). Therefore, the obtaining of the *Ldg* curve depends on the determination of the chamber A piston area and the supply pressure, which will be discussed in Chapter 5.

5. PISTON DIAMETER DETERMINATION

For the same pneumatic actuation system, the variation of the piston diameter has a significant influence on the dynamic of the system. The main aspects are related to velocity, displacement time and energy efficiency [8].

In order to understand the effects of the piston diameter in the dynamic of a pneumatic servosystem, a sensitivity analysis is performed with 6 different diameters simulated under the same loading conditions, including the viscous friction coefficient and the area ratio. Table 2 presents the parameters of the different cylinder used on the sensitivity analysis. The loading ratio (L_r) is given by:

$$L_r = \frac{F_L + p_S A_A \mu}{p_S A_A} = \frac{F_T}{p_S A_A} \quad (8)$$

where F_L stands for the load force (470 N) and the parcel $p_S A_A \mu$ represents the friction force, where μ is the coefficient that correlates the friction force with the maximum force in the chamber A of the actuator. Due to the low velocities, μ was assumed to be 1%.

Table 2: Cylinder data for the sensitivity analysis

Piston diameter [mm]	Rod diameter [mm]	Loading ratio [1]
30	11.25	0.8411
32	12	0.7405
34	12.75	0.6571
36	13.5	0.5872
38	14.25	0.5280
40	15	0.4775

Figure 7 presents the operating point chart with the results of the 6 simulations from the sensitivity analysis.

It can be seen that each loading ratio resulted in a different *Ldg* curve and the pressure ratios at the maximum velocity points lie on the *Ldg*

curve. Moreover, for lower loading ratios, the pressure ratios no longer reach the Op curve, a similar behavior occurs for point to point applications, as described in [8].

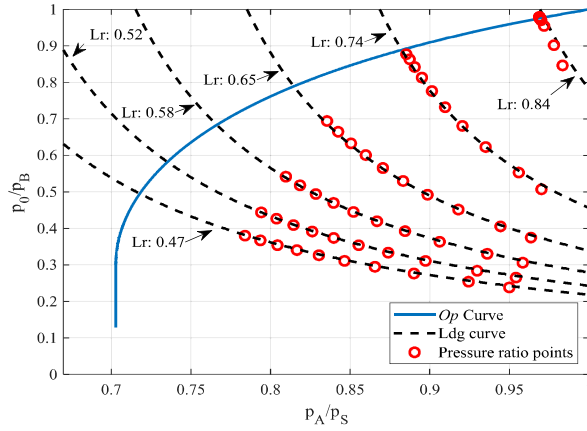


Figure 7: Operating point chart for different loading conditions

The main aspect related to this analysis is the choice of the best loading ratio. To support this decision, **Figure 8** presents the maximum velocity of the last step (Figures 3) and the energy efficiency along with the loading ratio. The energy efficiency is the ratio of the delivered pneumatic energy with the supplied exergy, the calculus procedure is presented in [8].

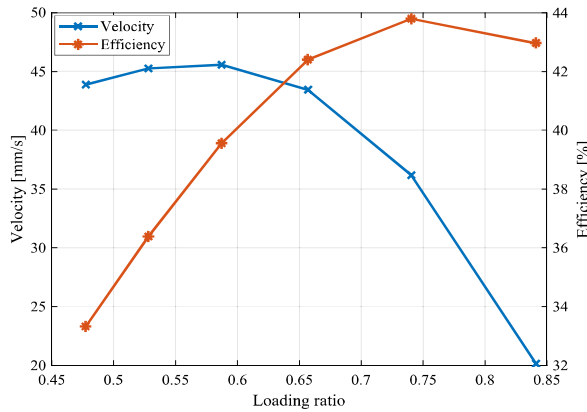


Figure 8: Maximum velocity and energy efficiency for different loading ratios

Figure 8 shows that as the piston diameter increases, the maximum velocity and the energy efficiency increases up to a limit. At a certain

point, both start to decrease, pointing out the importance of a correct sizing of the actuator. In this case, the best configuration occurs with $Lr \cong 0.63$, which is close to the maximum velocity condition.

In order to estimate this optimal condition for a general system, Equation 9 might be used, resulting on an expression of Velocity/Sonic Conductance (C) ratio as a function of the pressure ratio under the hypothesis of constant speed and pressure [8], as exemplified in **Figure 9**.

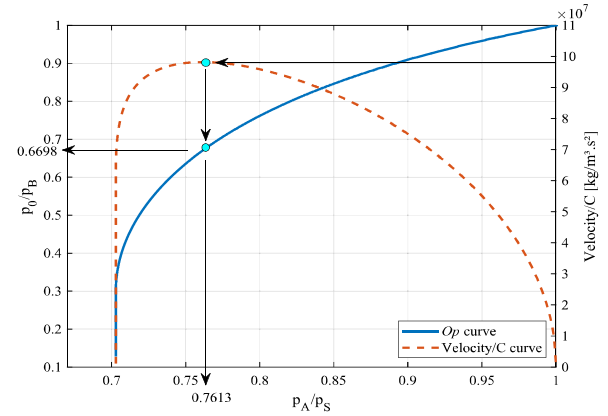


Figure 9: Determination of the maximum velocity point

By the Velocity/ C curve, the p_A/p_S value corresponding to the maximum steady state velocity is obtained. This pressure ratio is then applied in Equation 6 in order to obtain the corresponding p_0/p_B ratio. Both pressure ratios are substituted in Equation 7, yielding a loading ratio corresponding to an optimum condition (Lr_{opt}), which is, in this case, 0.5789. As can be seen, this method results in a loading ratio close to the maximum velocity condition shown in **Figure 8**, which has a loading ratio of 0.5847.

Once the optimum loading ratio is defined, the piston area or the supply pressure can be calculated by

$$A_A = \frac{F_L}{p_S(Lr_{opt} - \mu)}. \quad (10)$$

$$\frac{v_{e ss}}{C} = \frac{p_S p_0 \sqrt{1 - \left(\frac{p_A - b}{p_S} \right)^2} \left(\frac{p_A}{p_S} \frac{p_0}{p_S} (1 - r_A) - \mu - \left(\frac{\left(\frac{p_0}{p_S} \right)}{\frac{b}{r_A} + \sqrt{\frac{b^2 - 2b + 1}{r_A^2} + 1} + \left(\frac{p_S}{p_A} \right) \left(-2b + \left(\frac{p_S}{p_A} \right) (2b - 1) \right)} \right) \right)}{\left(\frac{p_A}{p_S} \right) F_L} \quad (9)$$

6. SERVOVALVE DESIGN

The sizing of the servovalve is an important step to guarantee the system dynamics since it controls the airflow rate to the cylinder [3]. The sizing of the proportional valve (or servovalve) might not be done isolate, since the piston diameter also affects the dynamic behavior of the system [8]. For this reason, the continuity equation for the cylinder chambers must be analyzed along with the mass flow rate equation through the valve.

Applying the continuity equation to the chamber A of the actuator (**Figure 1**), under the hypothesis of isothermal process, results in:

$$\frac{dp_A}{dt} = \frac{1}{V_A} \left(q_{mP-A} T_A R - p_A A_A \frac{dx}{dt} \right). \quad (11)$$

The mass flow rate from the constant pressure source to the chamber A is defined by the ISO 6358-1 (2013) standard [13]. Assuming a subsonic flow and a supply temperature equal to the ambient temperature:

$$q_{mP-A} = p_S C \frac{U}{U_n} \rho_0 \sqrt{1 - \left(\frac{p_A - b}{p_S} \right)^2}. \quad (12)$$

Combining Equations 11 and 12, and assuming the chamber A temperature to be equal to the ambient temperature, the sonic conductance becomes

$$C = \frac{\frac{dp_A}{dt} V_A + p_A A_A \frac{dx}{dt}}{p_S \frac{U}{U_n} \rho_0 \sqrt{1 - \left(\frac{p_A - b}{p_S} \right)^2}}. \quad (13)$$

Equation 13 presents the parameters that should be accounted during the sizing process. Considering that the maximum velocity point is a critical condition for the servovalve, Equation 13 might be used with the parameter values of the inflection point of the step response.

During the design process, the maximum velocity is estimated using Equation 4 or 5. The piston area shall be determined using the Equation 10. The ratio U/U_n might be considered as 1, since the control signal at the maximum velocity usually is close to the maximum opening of the servovalve. The critical pressure ratio (b) has its maximum theoretical value equal to 0.528, however, commercial valves always have a lower value, usually around 0.3.

Through simulation analysis, the parcel relative to the derivative of pressure of Equation

13 has been found to be negative at the point of maximum velocity. Besides that, the product of $V_A dp_A/dt$ represents around 15% of $p_A A_A dx/dt$ parcel. Consequently, neglecting the derivative of pressure parcel it results on a higher sonic conductance, which is favorable for the sizing process.

The remaining parameter to be determined in order to calculate the sonic conductance in Equation 13 is the p_A/p_S ratio. Analyzing the Figures 6 and 7, it can be seen that the pressure ratios are not constant throughout the piston stroke and they lie over the Ldg curve. Since the p_A/p_S for the maximum velocity can be calculated by Equation 9, it is suggested to choose an average value between 1 and the pressure ratio at maximum velocity, as it represents an average working condition along the cylinder stroke. The average pressure ratio is given by

$$(p_A/p_S)_{Av} = \frac{1 + (p_A/p_S)_{v_{max}}}{2}. \quad (14)$$

Under the assumptions presented above, the servovalve can be sized according to

$$C = \frac{(p_A/p_S)_{Av} \cdot A_A \cdot v_{max}}{p_0 \sqrt{1 - \left(\frac{(p_A/p_S)_{Av} - b}{1-b} \right)^2}}. \quad (15)$$

7. CASE STUDY

In this chapter, the method presented above is applied for sizing the actuation system of a speed governor of a Francis hydraulic turbine, which is part of a research and development project that aims the replacement of hydraulic servomotors in small hydropower plants. The applicability of pneumatic servosystem for hydraulic speed governor was previously studied by [14] and [15].

7.1. System description

The speed governor of a hydraulic turbine is the system used to control the rotational velocity of the turbine, which should be held constant in order to maintain a constant frequency of the generated electric energy. The control is made by positioning of the guide vanes, increasing or decreasing the amount of water flowing through the turbine.

In this study, a real hydropower plant with net height of 18.5 meters and a Francis turbine with 438 kW of generation capacity is evaluated. The

main requirements for the actuation system design are the speed governor time constant, the minimum opening time, the load force and the total stroke. Other requirements such as minimum closing time and emergency closing are related to an auxiliary actuation system and will not be discussed in this paper. Additional information about this system is presented in [5].

7.2. Design requirements

According to the standard IEC 61362 (2012) [16] the time constant (τ_y) of the speed governor should range between 0.10 to 0.15 seconds. Assuming a criterion of 1% of error, the settling time is 0.5 to 1.25 seconds ($5\tau_y$).

The load force caused by the water flow through the turbine is not constant. [17] presents a load profile where the maximum load occurs around 80-90% of the actuator stroke and the force is zero around 15% of the stroke.

The load profile proposed by [17] has an hysteresis between the opening and closing movement, which is due the water force in the blades. Due to the uncertainty on determining the transition between the opening and closing forces, [5] proposed an adjusted load profile which includes the maximum load force and the null force, as presented in **Figure 10**. This curve will be used for sizing and simulation purposes.

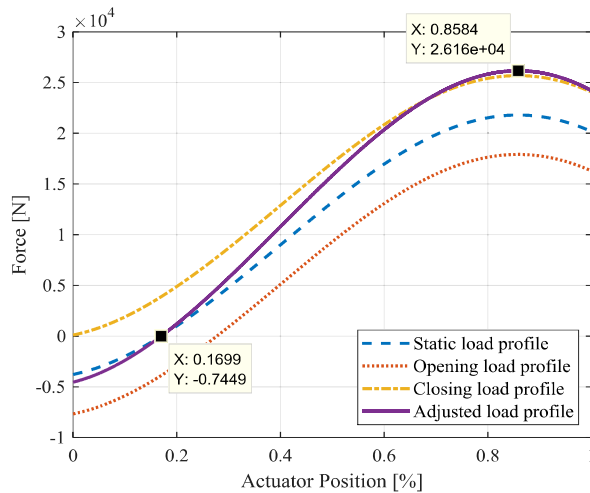


Figure 10: Load profiles in a Francis hydraulic turbine

The mounting of the guide vanes requires a total stroke of 131 mm for the actuation system. A step of 10% of the total stroke can be considered for the dynamic sizing of the actuation system.

7.3. System sizing

The first step to size the actuation system is the definition of the best piston area considering the system loading. In this case, the load is not constant throughout the piston stroke, however, in order to guarantee the dynamic performance required by the IEC 61362 Standard, the system must be sized for the worst-case scenario, which is the maximum load force.

The available pneumatic compressor is capable to work up to 10 bar_{abs}. Due to the high load involved, two actuators working in opposing conditions are used. It is equivalent of a single actuator with the resulting area equal to the sum of area A_A and area A_B of the actuators and the area ratio (r_A) equal to 1. The friction coefficient is estimated to be 1% of the maximum force in chamber A and the maximum load according to **Figure 10** is 26.16 kN. The critical pressure ratio of the servovalve is estimated in 0.3. Based on that, Equation 9 is used to determine the velocity/ C as a function of the p_A/p_S .

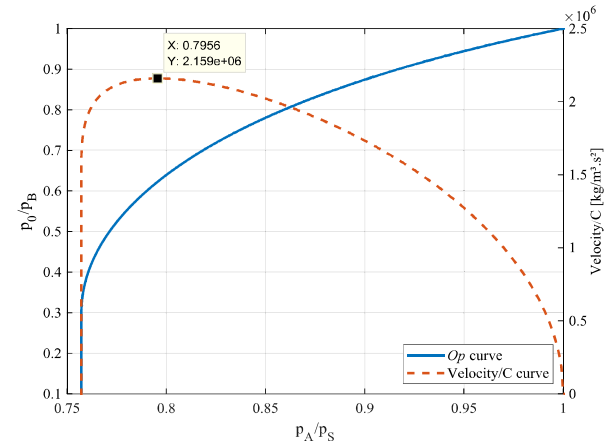


Figure 11: Point of maximum velocity

The pressure ratio p_A/p_S at maximum velocity is 0.7956. The corresponding p_0/p_B ratio is obtained by the Equation 6, which yields 0.6223. The resulting loading ratio ($F_T/p_S A_A$) is 0.6309, which is given by Equation 7.

Using Equation 10, the resulting piston area (A_A) is 0.0421 m², which is equivalent to a cylinder with 231 mm of piston diameter.

The closest commercial area is the combination of two cylinders with 160 mm of piston diameter and 40 mm of rod diameter. The total area is 0.038956 m², resulting in a loading ratio of 0.6815, which is higher than the ratio of the maximum velocity (0.6309). However, as it can be seen in **Figure 8**, loading ratios slightly

higher than the maximum velocity results in higher energy efficiency. An acceptable loading ratio must be chosen carefully in order to avoid an undersized system. **Figure 12** presents the Ldg curve of both loading ratios where it can be seen that the increasing of L_r has a small impact at the velocity curve, which decreased just about 2%.

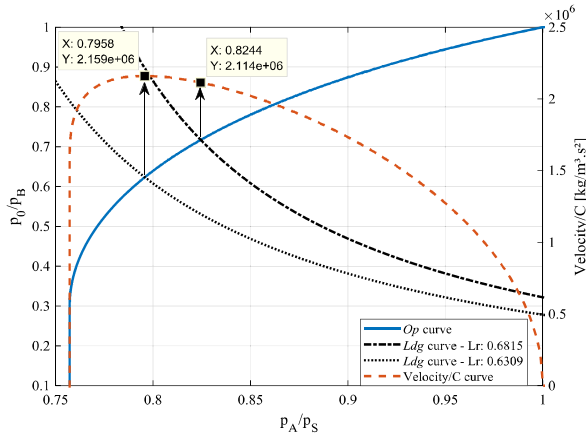


Figure 12: Velocity variation of both loading ratio

The natural frequency of the closed loop positioning system is given by Equation 3, where the settling time is set in 1.25 seconds ($5\tau_y$), in accordance with the IEC 61362 Standard. A small overshoot is acceptable, thus a damping ratio of 0.7 is assumed. Hence, the requested natural frequency is 4.56 rad/s.

The velocity is obtained by Equation 4, where the expected maximum displacement is 10% of the total stroke, which yields 0.0219 m/s.

This velocity is used in Equation 15 to be calculating the sonic conductance of the servovalve. The p_A/p_S of the dashed Ldg curve (**Figure 12**) may be adjusted according to the Equation 14 resulting on 0.8978. Therefore, the result is $C = 14.3629 \times 10^{-9} \text{ m}^5/\text{N.s}$. A commercial model with sonic conductance of $16.5 \times 10^{-9} \text{ m}^5/\text{N.s}$ is chosen for this application. If the same procedure is applied to the dash-dotted line, the resulting sonic conductance is $C = 15.6579 \times 10^{-9} \text{ m}^5/\text{N.s}$.

Simulations were carried out with the designed values of the piston area and the sonic conductance of the servovalve. **Figure 13** presents the results from two different simulations. One is with the exact parameters obtained from the design process and the other is with the commercially available components.

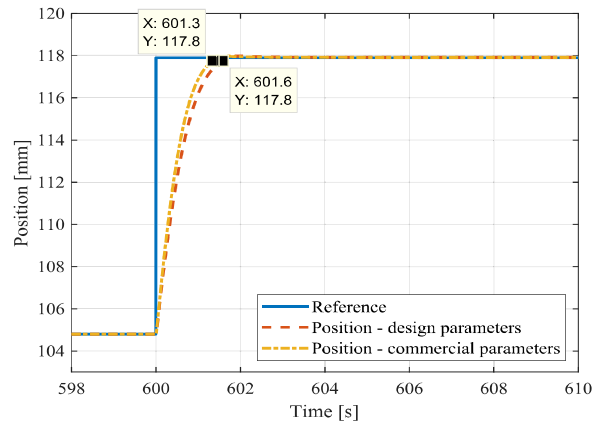


Figure 13: Simulation results of the designed systems.

The simulations are carried out at the most critical point, which is at 85% of the total stroke (maximum load). The proportional controller gain is set to 382, which results in the total opening of the servovalve at the maximum velocity. According to the design process, the system should have a settling time of 1.25 seconds with overshoot. As can be seen, the settling time in both simulations is quite close from the design requirement and no significant overshoot is present in the step response.

It is important to highlight that the control plays an important role in the closed loop results. For this reason, the control gains should be tuned in a more effectively way, and/or an improved controller such as an adaptive PID controller should be used. As an example, the **Figure 14** presents the system using commercial parameter with an increased gain of the proportional controller. The applied control signal to the servovalve is presented in **Figure 15**.

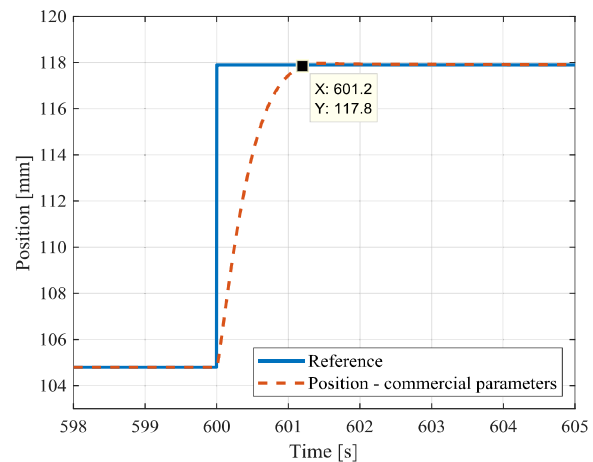


Figure 14: Simulation result with higher proportional gain

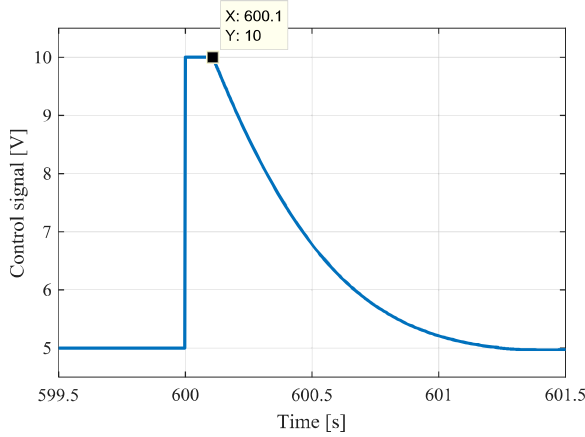


Figure 15: Servovalve control signal

As can be seen in **Figure 15**, with an adjusted controller the design requirements are achieved and the control signal sent to the servovalve shows that its input voltage is saturated during less than 10% of the displacement, evidencing that the sonic conductance of the servovalve is adequate for the positioning task.

8. CONCLUSION

In this paper, the characteristic behavior of servopneumatic systems was studied aiming the correct sizing of the system components. The analysis was carried out by a non-linear dynamic simulation model implemented in MATLAB/Simulink® and the results from the inflection point of the position curve were studied with the operating point chart, which describes the system pressures under the hypothesis of constant speed and pressure.

The study showed that the piston size and the supply pressure affect the dynamic behavior and the energy efficiency of the system. An approach based on the operating point method and the position inflection point was proposed in order to design the system achieving the best dynamic and energetic performance as possible.

A case study was presented where the actuation system of a hydropower plant is being designed. The design requirements were converted into natural frequency, damping ratio and load force. An optimal loading ratio was determined for the piston diameter sizing and the combination of piston area with dynamic requirements were used to size the pneumatic servovalve.

The results presented in this paper evidence that the system sizing method is able to

satisfactorily calculate the system parameters in order to attend the design requirements.

The main advantage of the proposed method is the possibility to design an efficient servopneumatic system, either in terms of energy efficiency and dynamic performance, through an analytical process which is based in the fundamental equations of the system. Since it does not require optimization algorithms, the method can be carried out without the need of software or with simple spreadsheets.

It is important to highlight that the method presented in this paper is not concluded yet, since many aspects of the design process are still object of study, such as the non-linear friction forces and different loading conditions. As a final result, a new methodology for pneumatic system sizing is expected.

NOMENCLATURE

ζ	Damping ratio [1]
μ	Friction coefficient [1]
ρ_0	Density at ambient conditions [kg/m ³]
τ_y	Time constant of speed governor [s]
ω_n	Natural frequency [rad/s]
A_A, A_B, A_r	Chamber A, B and rod area [m ²]
B	Viscous friction coefficient [N.s/m]
b	Critical pressure ratio [1]
C	Sonic conductance [m ⁵ /N.s]
D_p	Piston diameter [m]
D_r	Rod diameter [m]
F_L	Load force [N]
F_{max}	Maximum force [N]
F_T	Total force [N]
L	Actuator stroke [m]
L_r	Loading ratio [1]
M	Load mass [kg]
p_A	Chamber A pressure [N/m ²]
$p_{s,0}$	Supply and ambient pressure [N/m ²]
q_m	Mass flow rate [kg/s]
R	Ideal gas constant [J/kg.K]
r_A	Cylinder area ratio [1]
T	Temperature [K]
t	Time [s]
t_s	Settling time [s]
U	Control signal [V]
U_n	Nominal control signal [V]
V_A	Chamber A volume [m ³]
$v_{e ss}$	Extending steady state velocity [m/s]
v_{max}	Maximum velocity [m/s]
x	Piston displacement [m]
x_{max}	Maximum desired step
y, y_{Ref}	Position and reference position [m]

ACKNOWLEDGEMENTS

This research was funded by China Three Gorgons Corporation of Brazil, Reivax S/A Automation and Control, and CNPq - Brazilian National Council for Scientific and Technological Development.

REFERENCES

- [1] Bollmann A (1997) Fundaments of Pneutronic Industrial Automation - Design of Binary Electro-pneumatic Commands (in Portuguese). ABHP, São Paulo, Brazil
- [2] Beater P (2007) Pneumatic Drives: System Design, Modelling and Control. Springer, Berlin, Germany
- [3] Saravanakumar D, Mohan B, Muthuramalingam T (2017) A review on recent research trends in servo pneumatic positioning systems. Precision Engineering 49:481-492
- [4] Rakova E, Hepke J, Weber J EXonomy analysis for the Inter-domain comparison of electromechanical and pneumatic drives. In: 10th International Fluid Power Conference, Dresden, Germany, 2016. pp 117 - 136
- [5] Conterato GP, Spada TAB, Vigolo V, Weiss LA, Leoncini LL, Araujo Pd, Negri VJD Modeling a pneumatic speed governor using eletronic pressure valves and directional valves. In: 25th International Congress of Mechanical Engineering, Uberlândia, MG, Brazil, 2019.
- [6] Hildebrandt A, Neumann R, Sawodny O (2009) Optimal system design of siso-servopneumatic positioning drives. IEEE transactions on control systems technology 1:35-44
- [7] Canudas-de-Wit C, Olsson H, Astrom KJ, Lischinsky P (1995) A new model for control of systems with friction. IEEE Transactions on Automatic Control 40 3:419-425
- [8] Vigolo V (2018) Theoretical-experimental study to aid the sizing of pneumatic actuation systems (in Portuguese). M.S. thesis, Federal University of Santa Catarina, Florianópolis, Brazil
- [9] De Negri VJ, Ramos Filho JRB, Souza ADC (2008) A design method for hydraulic positioning systems. In: International Power Transmission Exposition, Las Vegas, 2008. Madison: Omnipress, pp 669-679
- [10] Furst FL (2001) Systematization of the preliminary design of hydraulic circuits for position control (in Portuguese). M.S. Thesis, Federal University of Santa Catarina, Florianópolis, Brazil
- [11] Oliveira LG (2009) Determination of the operating points for pneumatic cylinder-valve set (in Portuguese). M.S. thesis, Federal University of Santa Catarina, Florianópolis, Brazil
- [12] Hené MD, Mendonza YEA, Oliveira LGD Determination of the operational point for the penumatic system sizing. In: 7th International Fluid Power Conference, Aachen, Germany, 2010. pp 343-354
- [13] International Organization for Standardization (2013) ISO 6358-1 Pneumatic Fluid Power -- Determination of flow rate characteristics of components using compressible fluids -- Part 1: General rules and test methods for steady-state flow. International Organization for Standardization,
- [14] Mendonza YEA, De Negri VJ, Soares JMC (2014) Pneutronic Speed Governor for Small Hydropower Plants – A New Application for Pneumatics. Journal of the Brazilian Society of Mechanical Sciences and Engineering 8:2661-2633
- [15] Mendoza YEA, de Oliveira LG, De Negri VJ Applicability of Servo-pneumatic Positioning Systems for High Loads. In: ASME Symposium on Fluid Power and Motion Control Bath, United Kingdom, 2008. pp 219-232
- [16] International Electrotechnical Commission (2012) IEC 61362 - Guide to specification of hydraulic turbine governing systems. International Electrotechnical Commission, Switzerland
- [17] Voith (1974) Electro-hydraulic regulator (EHR 74) - Descriptive manual (in Portuguese).



GROUP 9 | 11

Mobile applications

GENERAL LECTURE:

ZF VIEW ON FUTURE DRIVETRAINS FOR COMPACT AND MEDIUM SIZE WHEEL LOADERS

Jürgen Legner^{1*}, Tilo Huber²

¹ZF Friedrichshafen AG, Graf-von-Soden-Platz 1, 88046 Friedrichshafen, Germany

²ZF Friedrichshafen AG, Tittlinger Straße 28, 94034 Passau, Germany

* Corresponding author: E-mail address: juergen.legner@zf.com

1. INTRODUCTION

This paper discusses an investigation on a novel hydraulic pump concept. The idea aims on a pump principle to be directly connected to high-speed electric motors to build compact high-pressure drives. The pump can theoretically work without solid contact and has no kinematic pulsation. The composition of the pump is basically similar to cylindrical journal bearings. A journal bearing is used to support external loads on a rotating shaft. When the shaft rotates with the loads, hydrodynamic fluid force is generated in the fluid film, which compensates the external force and reduces an eccentricity of the shaft. The difference of the introduced pump concept from the bearing is that the eccentricity is fixed and it has an outlet port at the high-pressure area, through which the fluid can be transferred. To examine the functionality of the pump, a test bench is constructed and experiments are performed to investigate the pressure build-up and discharging flow of the pump concept. The experimental results are numerically analysed by using elasto-hydrodynamic lubrication (EHL) simulation, based on the Reynold's equation. From these results, the functionality of the pump concept is confirmed. Moreover, several variables that influence the characteristic curve of the pump are studied. Based on these results, geometric parameters of the pump are redesigned to discharge sufficient flow rate for usage as commercial pumps.

2. ZF STUDY ON FUTURE DRIVE LINES FOR WHEEL LOADERS

ICE will continue to be the primary mover for

small, medium and large construction equipment. Energy portfolio will be enlarged by Gas, eFuels,... Hybrid Topologies do not offer enough additional value. Reduction in fuel consumption by adding hybrid components to highly efficient conventional drivelines like power shift with higher number of gears and lockup converter, or power split transmissions is too small vs. cost (TCO).

With increasing energy density, continuously reduce cost and lower energy generation cost due to renewables, batteries will become an optional primary mover for more and more applications. Vehicle topologies will remain unchanged since conventional and alternative drivelines need to be realized on one platform to manage complexity and maintain scale effects.

For wheel loaders the central drive connected to front and rear axle is the most beneficial solution. Other architectures like axle drives, or individual wheel drives would need to be oversized because during bucket filling max torque is required on the front axle.

3. PRODUCT STRATEGY ON ELECTRIFICATION

So far, no legislative pressure on CO₂ emissions for Off-Highway, corresponding initiatives ongoing with scope and timing still undefined. Focus of municipalities on 0-Emission Zones in urban areas will drive the trend towards "Electrified Urban Construction Sites". Electrification is key to meet local exhaust and noise emission regulations. However, the path to electrification is not disruptive but a diversification - Different driveline solutions will co-exist, which leads to increased complexity of product portfolio. Commercially viable solutions are pre-requisite, technology by itself is not

enough. Lower entry barrier for 48V solutions. Electrification will start on compact applications. Medium applications will follow with a time shift of approx. 5 years.

4. SOLUTION FOR COMPACT WHEEL LOADERS (4 – 8 T EMPTY VEHICLE WEIGHT)

Central drive with single speed with two helical gear sets. Asynchronous E-Motor (ZF design), cost effective, high speed (15,000 rpm), water cooled. Central drive transmission directly mounted to standard compact wheel loader axles. Max. vehicle speed 20 km/h. Goal for tractive effort / weight factor 0,80.

Goal for E-Motor development was max. power out of 48V systems and a cost-effective solution. Permanent power level of 20 kW can be reached.

E-Motor as modular construction kit with constant diameter. Depending on power level only length of E-Motor will change. Same sheet metal cutting for all versions, but different wiring depending on voltage level.

Above 48 V the 96 V is interesting, mainly because of lower cost for power electronics (MOSFET vs. IGBT). For high power solution we see a voltage level of 650 V.

5. SOLUTION FOR MEDIUM WHEEL LOADERS (10 – 20 T EMPTY VEHICLE WEIGHT)

Also, in this weight class the central drive will be the preferred solution for ZF. We work on a system solution with integrated eDrive and ePTO incl. control system. Specification for system solution at lower and upper end of medium wheel loader range is ongoing.



AGROTHERMIE – DESIGN AND TESTING OF A NOVEL HYDRAULICALLY-ACTUATED, LOCALLY VIBRATING PLOUGH

Jianbin Liu^{*1}, Benjamin Beck¹, Jakob Münch², André Grosa², Roman Kahle², Prof. Dr.-Ing. Jürgen Weber¹, Prof. Dr.-Ing. habil. Thomas Herlitzius²

¹*Institute of Mechatronic Engineering – Chair of Fluid-Mechatronic Systems, Technical University of Dresden, Helmholtzstrasse 7a, 01069 Dresden*

²*Institute of Natural Materials Technology – Agricultural Systems and Technology, Technical University of Dresden, Bergstrasse 120, 01069 Dresden*

* Corresponding author: Tel.: +49 351 46338609; E-mail address: jianbin.liu@tu-dresden.de

ABSTRACT

Economic utilization of geothermal networks under agricultural surfaces needs large agricultural areas. In order to exploit the cultivated land more effectively, this paper proposes a novel locally vibrating plough system that employs a hydraulic actuator direct on the plough blade instead of the state of the art external vibration units. Starting with a description of geothermal networks under agricultural surfaces and the construction technology in details, the contribution shows different concepts, the development and test of the most promising solution for imprinting local vibrations at the cutting edge with the goal of traction force reduction. A virtual demonstrator, the test rig set-up and the control concepts are described. Both of the closed-loop simulation and experimental position control of the entire vibration system demonstrate that the novel design has impressive performance improvement. Finally, the integration of the vibration system into a prototype tool is shown and the reduction of the traction force is proven by experiments carried out with a tractor on a testing field.

Keywords: Agrothermie, high frequency, Co-Simulation, OPC UA, traction force

1. INTRODUCTION

Geothermal energy from depth probes in conjunction with heat pumps has been state of the art for several years as an energy efficient heat supply for building heating and hot water production. As a new way of gaining primary energy for the use in heat pumps, underground collector networks have been established in a depth of only about 2 m under agricultural surfaces - an approach called ‘Agrothermie’. As opposed to the geothermal depth probes, those collectors use ambient energy from sources as seepage water or sun radiation onto the ground. Water temperature in these networks typically lies between $T_{\min} = 2\text{ °C}$ and $T_{\max} = 10\text{ °C}$ with a temperature rise between input and output of $\Delta T = 4\text{ °C}$. This temperature level allows for heating via heat pumps and for direct cooling use. As the water in the collector has the temperature of the surrounding soil, heat losses through dissipation don’t occur. More publications about project ‘Agrothermie’ can be found in [1], [2] and [3].

In order to keep the agricultural fields in good condition, the soil structure must not be destroyed during the building of the collector. Thus, a system has been developed in order to erect those networks in a minimally invasive way. A specially designed tractor plows three parallel pipes into the ground at a time, which are connected to form a network at the edges of the field later on. The width of the implement is only 0.1 m at the surface in order to achieve the least possible soil damage.

Even for a highly specialized machine on bulldozer tracks, the traction force of the pipe laying implement 2 m deep in the ground can exceed the pulling capacity depending on soil parameters. In order to significantly reduce the needed traction force, vibration of the implement can be helpful. As part of the research project, a novel locally vibrating plough system that employs a hydraulic actuator direct on the plough blade has been developed.

2. CONCEPTS OF GENERATING LOCAL VIBRATION

Periodic oscillations provide the basis for a wide range of applications in vibration technology. These include sieves, vibrating tables and compressors, vibratory mills, vibratory conveyors, testing machines, vibration pumps, shaking chutes, impact drills and dosing conveyors. Crank drives, unbalance exciters, electromagnetic vibration exciters, hydraulic or pneumatic drives generate the oscillating movements for these. The most commonly used types of drive are also assigned to the application cases [4].

Depending on the process, the vibrations must have different characteristics in order to meet the technological requirements in a process-specific and optimal way. This requires drive systems that can excite and amplify the desired vibrations in the best possible way. Hence, the dynamic behaviour of the excited bodies must be taken into account. At the same time, it is often necessary to decouple the vibrations from the environment or the frame [4].

Due to their high power density, hydraulic drives are always used for vibration excitation when large forces are required. This is the case, for example, in construction machinery, where they are used for demolition hammers and vibratory pile drivers.

Hydraulic vibrators also offer the advantage that the vibration frequency can be continuously varied, allowing the system to be adapted to changing soil conditions. Vibrators with resonance-free starting and stopping can also switch the eccentric weights on and off. If the weight is only switched on when the working frequency is reached, it is easy to pass through the resonance frequency of the soil and resonance peaks are avoided. In addition, the amplitude can be continuously controlled, allowing the frequency and amplitude to be optimally adjusted to the geology.

The requirements for local vibration excitation for the installation tool are shown in extracts in Table 1.

Table 1: Requirements for local vibration unit

Category	Description	Demand d / Wish w
Vibration frequency	Variably adjustable 20 – 50 Hz	d
	Adjustable and operated from the carrier machine	w
Vibration amplitude	Variably adjustable 1 – 10 mm and operated from carrier machine	w
Vibration mass	Max. 50 kg	w
Motion path	Variably adjustable	w
Effective direction	Variably adjustable	w
installation space	Max. width 55 mm, partially extendable to 80 mm	d
Valve technology	Robust and cost-effective	w
components	Available on the market	d
system	Easy to install and maintain	w
Actuator system	Hydraulic	d

The systematic development process according to VDI 2221 was used to find a solution. This procedure was applied on all the identified subsystems (namely: kinematics, valve system and actuators) for the local vibration unit. The combination of subsystem solutions defines the morphological box for new system layouts. Hydraulic motors with eccentrics could be ruled out at an early stage due to the high installation space requirements. The resulting solution space is displayed in **Figure 1**. By means of a weighted point evaluation on the basis of the criteria variability of the vibration parameters, design effort, installation space, complexity of the system, operating modes, process forces that can be applied, number of actuators, requirements on the actuating dynamics and robustness, the grey-shaded preferred variant could be determined. The classical valve-controlled cylinder drive with a 4/3 control valve on a constant pressure system is therefore used in the following for vibration excitation and further investigated.

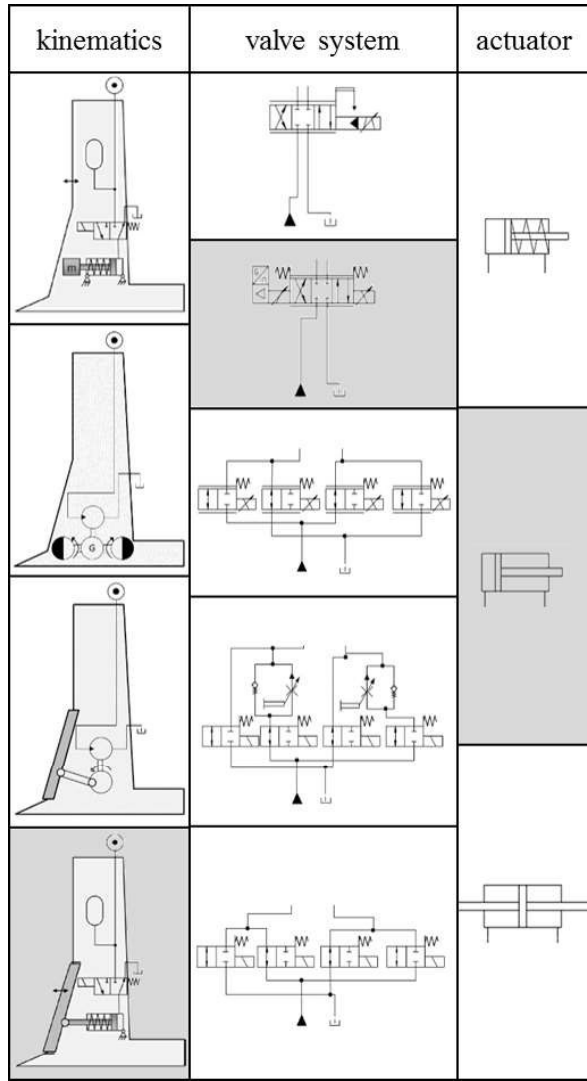


Figure 1: Morphological box and selection of the preliminary concept

3. TEST RIG SETUP AND CONTROL ALGORITHMS

3.1. Mathematical model of hydraulically actuated vibration plough blade

As displayed in **Figure 2**, the hydraulically actuated vibration plough blade system primarily comprises a switching valve, a proportional valve and a hydraulic cylinder with load. The pressure relief valve not only takes charge of system safety, but also holds a constant system pressure of $p_0 = 200$ bar. Because the proportional valve has a small negative overlap in neutral position, it can't hold the position of cylinder without the controller. In order to remedy this defect, a 3/2 switching valve is placed between the proportional valve and pump. For the above reasons, the dynamic property of the system

upstream of the proportional valve can be ignored for control development.

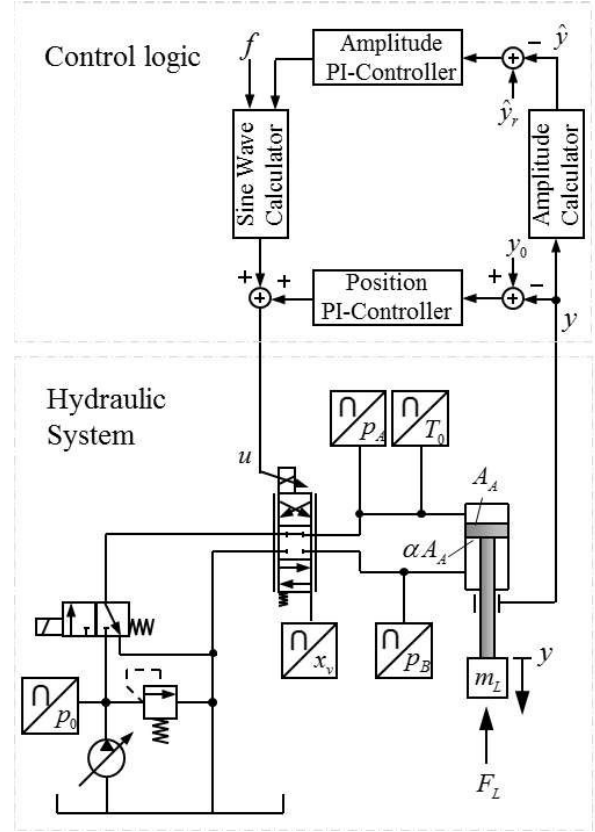


Figure 2: Schematic plan of the hydraulically actuated vibration unit

One of the most important components of the hydraulically actuated vibration unit is the proportional valve, as it must control the volume flow very dynamically and precisely for high frequencies. For the sake of assurance of high dynamics, the characteristic frequency of proportional valve should be at least triple as high as the total system [5]. Therefore, the relationship between input voltage u and displacement for spool valve x_V with electromagnet can be simplified and described as:

$$x_V = K_V \cdot u \quad (1)$$

If the small negative overlap of proportional valve is neglected, according to the operational directions of a hydraulic spool valve and cylinder, the flow rate eq. for valve with zero overlap are obtained as follows:

$$\begin{cases} x_V > 0, & y > 0: \\ Q_A = A \dot{y} = B \cdot x_V \cdot \sqrt{p_0 - p_A} \\ Q_B = \alpha A \dot{y} = B \cdot x_V \cdot \sqrt{p_B - p_T} \end{cases} \quad (2)$$

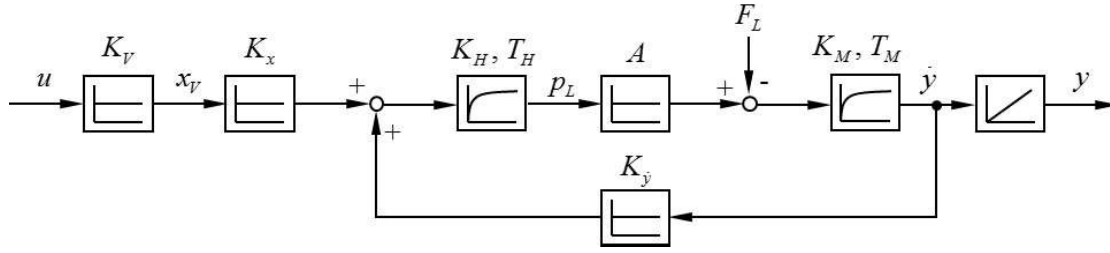


Figure 3: linearized block diagram of the hydraulically actuated vibration plough blade

$$\begin{cases} x_V < 0, & y < 0: \\ Q_A = A\dot{y} = B \cdot x_V \cdot \sqrt{p_A - p_T} \\ Q_B = \alpha A\dot{y} = B \cdot x_V \cdot \sqrt{p_0 - p_B} \end{cases} \quad (3)$$

The load pressure p_L for differential cylinder is defined as:

$$p_L = p_A - \alpha p_B \quad (4)$$

According to eq. (2), (3) and (4), mathematical eq. for cylinder chamber pressure p_A and p_B can be obtained on the premise that the system pressure p_0 is constant and tank pressure p_T is zero ($p_0 = \text{const.}, p_T = 0$):

$$\begin{cases} p_A = \frac{p_L + \alpha^3 p_0}{1 + \alpha^3} \\ p_B = \frac{(p_0 - p_L)\alpha^2}{1 + \alpha^3} \end{cases} \quad (5)$$

Based on the flow rate characteristics of a hydraulic spool valve, the linearized flow rate eq. for hydraulic zero point ($Q_{A0} = Q_{B0} = 0, p_{A0} = p_{B0} = 0$) is given as follows:

$$\begin{cases} Q_A = K_{xA}x_V - K_{pA}p_A \\ Q_B = K_{xB}x_V - K_{pB}p_B \end{cases} \quad (6)$$

If the external leakage is neglected, the leakage can be estimated by:

$$Q_{Le} = K_{Le p}(p_A - p_B) + K_{Le y}\dot{y} \quad (7)$$

According to the flow continuity equation, the expression for the pressure change in cylinder chamber can be derived as:

$$\begin{cases} \dot{p}_A = \frac{1}{C_A}(Q_A - A\dot{y} - Q_{Le}) \\ \dot{p}_B = \frac{1}{C_B}(\alpha A\dot{y} + Q_{Le} - Q_B) \end{cases} \quad (8)$$

The eq. (4) can also be written as:

$$\dot{p}_L = \dot{p}_A - \alpha \dot{p}_B \quad (9)$$

Substituting eq. from (5) to (8) into eq. (9), the first order function for load pressure can be given as:

$$T_H \dot{p}_L + p_L = K_H(K_x x_V + K_y \dot{y}) \quad (10)$$

with coefficient K_x , coefficient K_y , the hydraulic gain K_H and hydraulic time constant T_H :

$$K_x = \frac{K_{xA}}{C_A} + \frac{\alpha K_{xB}}{C_B}$$

$$K_y = -\left[\frac{A + K_{Le y}}{C_A} + \frac{\alpha(\alpha A + K_{Le y})}{C_B} \right]$$

$$K_H = T_H =$$

$$\frac{1}{\frac{1}{C_A} \left[\frac{K_{pA} + K_{Le p}(1 + \alpha^2)}{1 + \alpha^3} \right] + \frac{\alpha}{C_B} \left[\frac{K_{Le p}(1 + \alpha^2) - K_{pB}\alpha^2}{1 + \alpha^3} \right]}$$

According to Newton's second law, the force balance eq. for hydraulic cylinder with load can be described as:

$$m_L \ddot{y} = \Sigma F = A p_L - d_y \dot{y} - F_L \quad (11)$$

The second order function for eq. (11) can be expressed as:

$$T_M \ddot{y} + \dot{y} = K_M(A p_L - F_L) \quad (12)$$

with the mechanical gain K_M and mechanical time constant T_M :

$$K_M = \frac{1}{d_y}, T_M = \frac{m_L}{d_y}$$

With the help of eq.(1), (10) and (12), the linearized block diagram of the hydraulically actuated vibration plough blade can be shown in **Figure 3**.

After simplification, the command response from proportional valve input voltage to the actuator-generated displacement can be written as follows:

$$y = \frac{b_{10} \cdot u}{s^2 + a_1 s + a_0} \cdot \frac{1}{s} \quad (13)$$

The corresponding disturbance response can be expressed as follows:

$$y = -\frac{(b_{21}s + b_{20})F_L}{s^2 + a_1s + a_0} \cdot \frac{1}{s} \quad (14)$$

On the basis of superposition principle, the total system transfer function can be given as follows:

$$y = \frac{b_{10}u - (b_{21}s + b_{20})F_L}{s^2 + a_1s + a_0} \cdot \frac{1}{s} \quad (15)$$

with the coefficients:

$$a_1 = \frac{T_H + T_M}{T_M T_H}, \quad a_0 = \frac{1 - K_H K_M K_{\dot{y}} A}{T_M T_H}$$

$$b_{10} = K_H K_M K_x K_V A, \quad b_{21} = K_M T_H, \quad b_{20} = K_M$$

It can be seen from command response (13) that in order to acquire a higher amplitude of actuator, it is necessary to input stronger excited signal. According to disturbance response (14), it is concluded that the more load force acts on cylinder, the less amplitude is excited. In summary form (15), the amplitude depends mainly on excited input signal and the acting load force.

4. CONTROL ALGORITHMS

Because the PI or PID controller are unsuitable for the electro-hydraulic system with direct position feedback in high frequency area, a novel control logic has been developed, see **Figure 2**. Firstly, in order to realize the high dynamic requirements, a feed-forward control transmits directly a control signal from a sine wave generator to the proportional valve. Thereby, the valves set voltage for retraction and extension is the same. Because of the different acting areas in each cylinder chamber by using a differential cylinder and the internal leakage, the feed-forward control has difficulties to keep the differential cylinder at the desired position. To compensate this drawback, a closed loop position control with a PI-Controller was introduced. A displacement transducer was mounted inside the cylinder to measure its piston displacement y which can serve as a feedback signal. Compared with the set point y_0 , the desired midpoint for the sine wave could be maintained by the controller output. In the meantime, to acquire the actual amplitude of cylinder \hat{y} , an amplitude calculator was implemented. A PI amplitude controller sets the variable \hat{y} so that it corresponds to the setpoint input \hat{y}_r . The output of the amplitude controller and set frequency f act together as

input signals for the sine wave generator. By this way, the amplitude and the frequency of the hydraulically actuated vibrator can be controlled independently. In addition, it is mentioned that the derivative term in the controller was given up for the reason that it amplified process noise from signal which could cause unstable problems in hydraulic system with high frequency.

4.1. Simulation and Test rig results

Simulation Test

With the help of software-in-the-loop testing, the developed algorithms and entire control strategy could be tested within one environment [6, 7], which might reduce risk of integration and improve the reliability of verification in the next phase. Compared with hardware-in-the-loop tests, software-in-the-loop testing is a useful technique at earlier stages of development. It is not necessary to consider the hardware and physical interfaces between controller and plant. Nonetheless, it is inevitable that a coupling layer should be defined. The coupling layer is responsible for exchange of process variables and time synchronisation between controller and simulated model. The coupling layer could be an OPC-UA Server like displayed in **Figure 4**. More specifications about OPC-UA can be found in [8, 9, 10].

The main parameters of simulation model in **Figure 4** are shown in **Table 2**.

Table 2: Main parameters of simulation model

Parameters	Value
Cylinder piston diameter D	40 mm
Cylinder rod diameter d	28 mm
Cylinder max. stroke y_{max}	60 mm
Equivalent load mass m_L	10 kg
Damping coefficient of cylinder $d_{\dot{y}}$	5 Ns/mm
Natural frequency of proportional valve f_V	90 Hz
Damping coefficient of proportional valve d_V	0.75
Hydraulic oil	HLP 46
Cycle time	2 ms

Figure 4 depicts the LabVIEW-SimulationX Co-Simulation with an OPC UA coupling layer. A virtual image of the controller in LabVIEW took

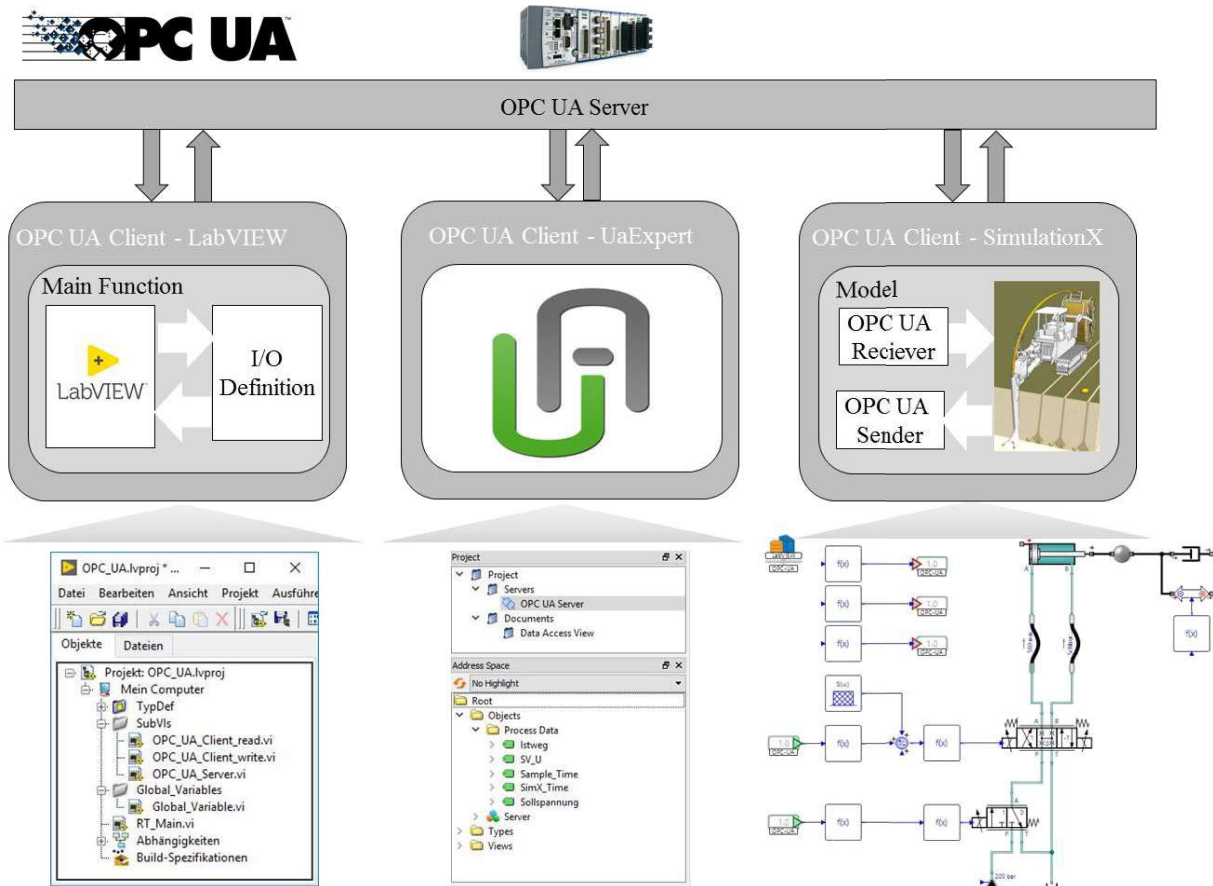


Figure 4: LabVIEW-SimulationX Co-Simulation with OPC UA

over the controlling mission for simulation model in SimulationX. After the definition of the interface, all the relevant input/output signals between virtual controller and simulation model via OPC UA Server were exchanged. The UaExpert was designed as an OPC UA viewer, which supported OPC UA features like browsing OPC UA address space, reading and writing of variable values and UA attributes, monitoring of data changes and events.

Test Rig

To evaluate the theoretical analysis and to validate simulation model, a test rig used to test the hydraulically actuated vibration unit has been set up. According to the schematic plan in **Figure 2**, the experimental set up including pressure relief valve, proportional valve, sensors and load is shown in **Figure 5**. For simplicity, the reactive force from soil was produced by the rubber plates which acted as a load unit. In order to meet the high requirements from control quality, the CompactRIO system with real-time embedded industrial controller was introduced. The developed LabVIEW code from the

software-in-the-loop project was adapted and implemented in the CompactRIO system without much effort. All signals were acquired, delivered, demonstrated and stored with the help of this system. Furthermore, in order to realize the high frequency control and reduce the influence from signal noise at the same time, a compromise for sampling time was made, which was set to 2 ms.

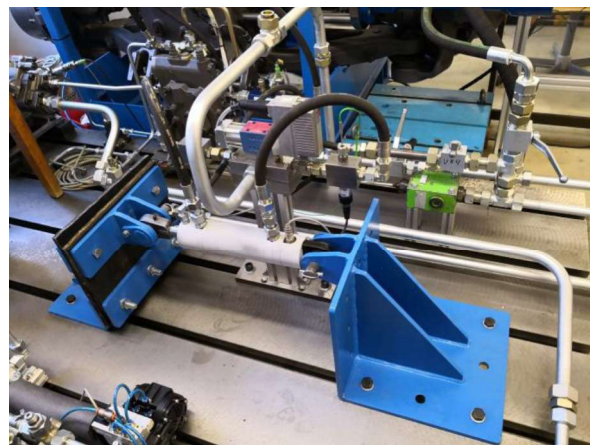


Figure 5: Test rig of hydraulically actuated vibration unit

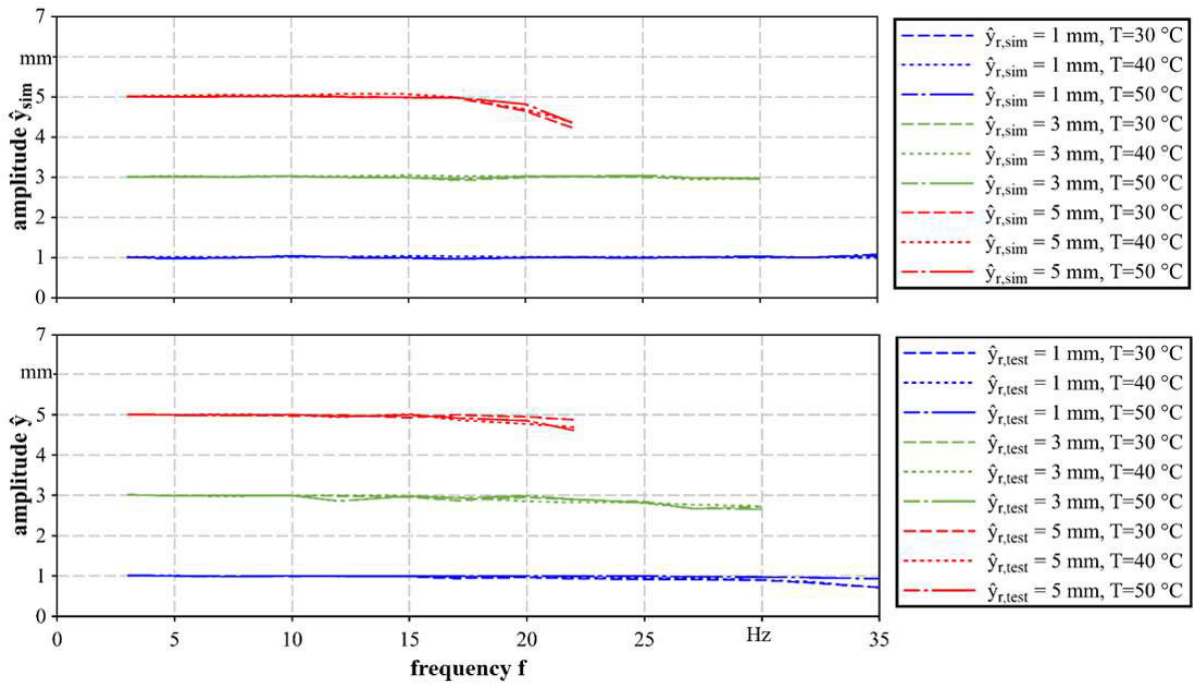


Figure 6: frequency responses between test and simulation at different temperatures

Results and discussion

To test the validity and robustness of the control strategy, a series of tests with the help of the above mentioned Co-Simulation and test rig have been carried out. **Figure 6** presents the experimental results of frequency responses between test and simulation at different temperatures. As a whole, the simulation results are in good agreement with the test results at different temperatures. At the same reference amplitude \hat{y}_r , the control strategy brings about a wide frequency bandwidth. The cylinder amplitude \hat{y} will only attenuate at the high frequency until the input voltage for proportional valve reaches limited value. It can also be seen that the higher reference amplitude \hat{y}_r inputs, the less frequency bandwidth is available. The difference between test results and simulation results at high frequency area could attribute to the uncertainties of various parameters in simulation model, especially the frequency characteristic of the proportional valve from data sheet and other non-linearities in the system like friction. For these reasons, the proportional valve in simulation model reaches the minimal input voltage ($u_{min} = -10 V$) a little earlier. It can also be seen from **Figure 6** how temperatures affect frequency responses under control. As a result, the influence from temperature on frequency response can be almost neglected. In

other words, the control system is robust enough to compensate the effect from temperature. It is easy to draw this consistent conclusion not only from simulation but also from test results.

A deficiency of this control strategy is located at the area of low frequency (0 - 3 Hz). There are two main reasons for that: On the one hand, higher noise compared with the input voltage occurs in this area. On the other hand, the cylinder speed at low set frequencies is also low and the drive tends to stick-slip. In order to solve this problem, it is suggested that direct position control with another PI-Controller for the low frequency area could be implemented in the control strategy. Because the machine in reality would never work in this low frequency area, the control strategy in **Figure 2** could be treated as suitable for the real application.

In the process of high frequencies, it is possible that the hydraulic oil can't exchange with tank, which could give rise to heat accumulation and seal failure in cylinder. In order to observe the heat accumulation in cylinder chamber in the meanwhile, a durability test has been carried out. For this purpose, a classic two point control for tank temperature was adopted and its desired value was set to $40\text{ }^{\circ}\text{C} \pm 2\text{ }^{\circ}\text{C}$ at the central cooling unit of the test rig. If the temperature equaled or exceeded the threshold $42\text{ }^{\circ}\text{C}$, the cooling system turned on until

temperature dropped below the threshold $38\text{ }^{\circ}\text{C}$ and at that point the system turned back off. It is clear from **Figure 7** that the temperature in cylinder chamber remained relative constant and the tank temperature could still exert influence on it. It's no doubt that the heat accumulation could be prevented by the control of tank temperature.

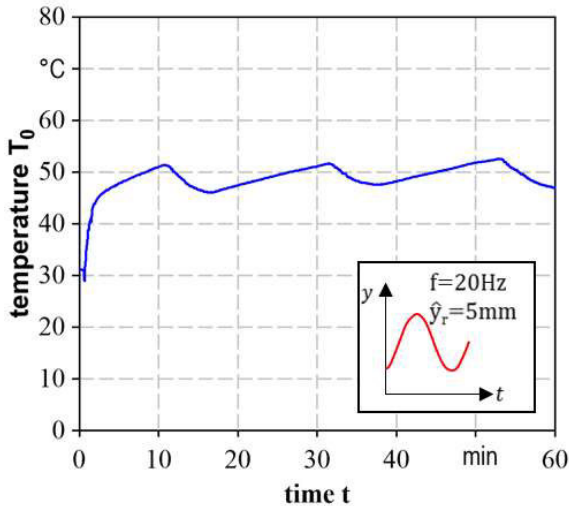


Figure 7: Durability test for temperature in cylinder chamber

5. PLOUGH INTEGRATION AND TRACTOR TEST

In order to analyse influence of the amplitude \hat{y} , frequency f and midpoint y_0 on the traction force, the hydraulically actuated vibration plough blade has been constructed and integrated on a tractor. Because of the ongoing patent application, the corresponding results will be published later.

In order to identify the reduction of traction force, two kind of field tests have been completed. At first, a field test began with constant frequency $f = 15\text{ Hz}$ and an amplitude of $\hat{y}_r = 5\text{ mm}$. During the field test, the excitation would be given up at a certain time ($t = 760\text{ s}$). The corresponding measurement results are shown in **Figure 8**. Compared to the mean traction force of $F_{T,mean,1} = 28.3\text{ kN}$ with excitation in range of $\Delta t(f = 15\text{ Hz})$, the mean traction force without excitation ($\Delta t(f = 0\text{ Hz})$) has increased to $F_{T,mean,2} = 31.6\text{ kN}$. The traction force has been reduced by 11.8 % with the help of the hydraulically actuated vibration plough blade.

The other field test was carried out with variable frequencies up to 20 Hz and a constant amplitude of $\hat{y}_r = 5\text{ mm}$. In **Figure 9**, the relationship between the traction force and frequency is shown. Nevertheless, it is not one

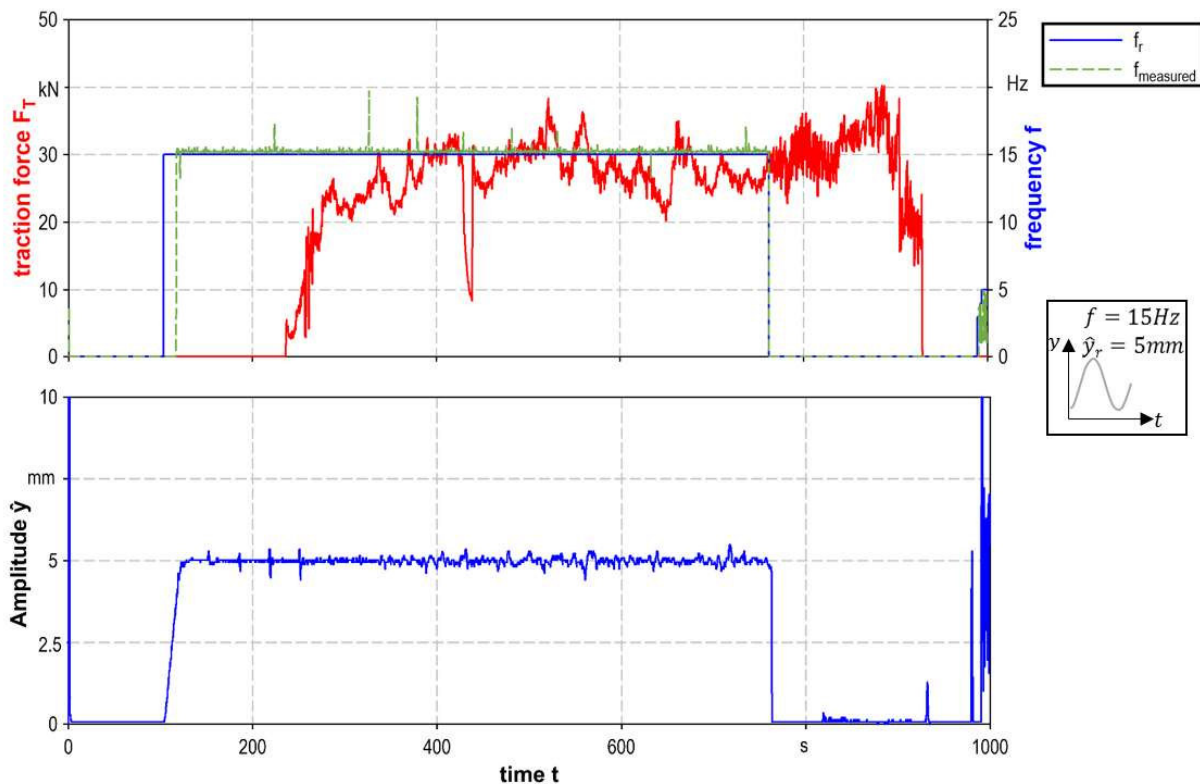


Figure 8: Comparison of traction forces with and without excitation

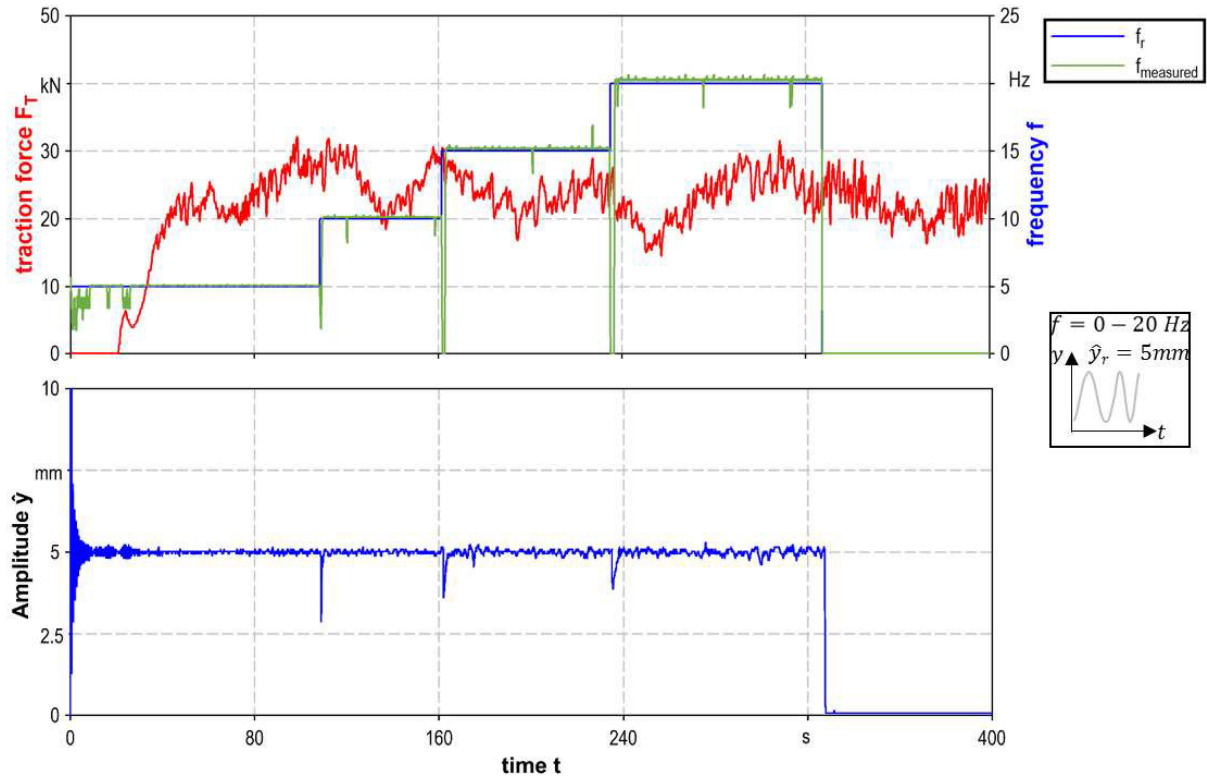


Figure 9: Comparison of traction forces at different frequencies

hundred percent evident that the traction force was reduced by change in frequency. The possible reasons are:

- Inadequate seal for the actuated vibration plough blade
- Unstable soil properties, especially caused by the multiple passes over the same route.
- Unstable driving behaviors, the speed of the tractor could not precisely been controlled for the low set-speed
- Limited vibration amplitude and cylinder force of the proposed system yields to no reaction of the soil yet
- Inappropriate vibration frequency, compared with resonant frequency of soil

6. CONCLUSION AND OUTLOOK

In this study, the linearized mathematical model for the hydraulically actuated vibration plough blade has been presented and used to qualitative analyse. In addition, the novel Co-Simulation with OPC UA aided in tuning the controller and achieving the expected performance before the machine was integrated. The simulation and test results were in good agreement with each other, which demonstrated that the developed control strategy for the hydraulically actuated vibration

plough blade was adequate for the mission. After plough integration and tractor tests, it was shown through comparison experiments that the traction force could potentially be reduced with the help of vibration plough blade.

According to the field tests, there are still a lot of problems to be solved. Firstly, with introduction of road roller, the unstable properties could be partially compensated. Secondly, in order to identify the unstable driving behaviors, it is necessary to acquire the actual driving speed, rotation speed and torque of diesel engine. For future work, it is advised that an intelligent self-tuning PID controller can be developed for the electro-hydraulic system with direct position feedback. Moreover, to reduce the pressure drop for control edge and realize higher frequency and cylinder force, it is considerable to replace the proportional valve with fast switching valves and employ multiple actuators.

NOMENCLATURE

α	Area ratio
a_i	Coefficients in denominator of transfer function
A_A	Piston area (mm^2)
B	Coefficient of flow rate ($1/(\text{min} \cdot \text{mm} \cdot \sqrt{\text{bar}})$)
b_i	Coefficients in numerator of transfer function

C_A	Hydraulic capacity for port A (l/bar)
C_B	Hydraulic capacity for port B (l/bar)
d	Cylinder rod diameter (mm)
d_V	Damping coefficient of proportional valve
d_y	Damping coefficient (N·s/mm)
D	Cylinder piston diameter (mm)
f	Frequency (Hz)
$f_{measured}$	Measured frequency (Hz)
f_r	Reference frequency (Hz)
f_V	Natural frequency of proportional valve (Hz)
m_L	Equivalent load mass (kg)
F	Force (N)
F_L	Load force (N)
F_T	Traction force (N)
K_H	Hydraulic gain coefficient (bar/(l/min))
K_{Lep}	Leakage-pressure-coefficient ((l/min)/bar)
K_{Lev}	Leakage-velocity-coefficient ((l/min)/(mm/s))
K_M	Mechanic gain coefficient (mm/(N·s))
K_{pA}	Flow rate-pressure-coefficient for port A ((l/min)/mm)
K_{pB}	flow rate-pressure-coefficient for port B ((l/min)/mm)
K_V	Coefficient between voltage and displacement of valve spool (mm/V)
K_x	Gain for displacement of valve spool (bar/(min·mm))
K_{xA}	Flow rate - displacement of valve spool - coefficient for port A ((l/min)/mm)
K_{xB}	Flow rate - displacement of valve spool - coefficient for port B ((l/min)/mm)
K_y	Gain for velocity of cylinder (mm ² ·bar/l)
p_0	System pressure (bar)
p_A	Pressure in cylinder chamber A (bar)
p_{A0}	Pressure in cylinder chamber A in hydraulic zero point (bar)
p_B	Pressure in cylinder chamber B (bar)
p_{B0}	Pressure in cylinder chamber B in hydraulic zero point (bar)
p_L	Load pressure (bar)
p_T	Pressure in tank (bar)
Q_A	Flow rate to port A (l/min)
Q_{A0}	Flow rate to port A in hydraulic zero point (l/min)
Q_B	Flow rate to port B (l/min)
Q_{Le}	Leakage (l/min)
T	Tank temperature (°C)
T_H	Hydraulic time constant (s)
T_M	Mechanic time constant (s)
T_0	Temperature (°C)
u	Input voltage (V)
x_V	Displacement of valve spool (mm)
y	Displacement of cylinder (mm)
\dot{y}	Velocity of cylinder (mm/s)
\ddot{y}	Acceleration of cylinder (mm/s ²)
y_0	Mean displacement of cylinder (mm)
y_{max}	Cylinder max. stroke (mm)

\hat{y}	Actual amplitude of cylinder (mm)
\hat{y}_r	Amplitude reference (mm)
$\hat{y}_{r,sim}$	Amplitude reference in simulation (mm)
$\hat{y}_{r,test}$	Amplitude reference in test (mm)

OPC UA Open Platform Communications Unified Architecture

REFERENCES

- [1] Grosa, A (2018) Agrothermie - Minimal invasive Einrichtung von Geothermienetzen unter Landwirtschaftsflächen. 76. Internationale Tagung LAND. TECHNIK, Germany
- [2] Pietruschka, D (2016) Vision 2020 – Die Plusenergiegemeinde Wüstenrot. Stuttgart Fraunhofer IRB Verlag
- [3] Pietruschka, D (2013) Kalte Nahwärme: agrothermische Wärme - Versorgung einer Plusenergiesiedlung. Bauma 2013 TECHNIK
- [4] Dresig, H., Fidlín, A. (2014) Schwingungen mechanischer Antriebssysteme – Modellbildung, Berechnung, Analyse, Synthese. 3rd edition, Berlin, Heidelberg, p. 449 et seq.
- [5] Murrenhoff, H (2008) Servohydraulik – Geregelt hydraulische Antriebe. Shaker Verlag GmbH, p. 235
- [6] Su, S.J, Zhu Y.Y, Li C.J, Tang W.X, Wang H.R (2019) Dual-valve parallel prediction control for an electro-hydraulic servo system. Science Progress 1-21
- [7] Pan, D.L, Gu S.J, Guo G.Y, Kuang H.B, Zhong H, Gao F (2017) Co-simulation design and experimental study on the hydraulic–pneumatic-powered driving system of main steam and feed water isolation valves for CAP1400. Advances in Mechanical Engineering Vol. 9(8) 1-11
- [8] Mahnke W, Leitner S.H, Damm M (2009) OPC Unified Architecture. 2009 Springer-Verlag Berlin Heidelberg
- [9] Rinaldi J (2016) OPC UA Unified Architecture: The Everyman's Guide to the Most Important Information Technology in Industrial Automation. CreateSpace Independent Publishing Platform
- [10] Lange J, Iwanitz F, Burke Th. J (2010) OPC: Von Data Access bis Unified Architecture. VDE Verlag GmbH

ASSISTANCE SYSTEM FOR AN AUTOMATED LOG-QUALITY AND ASSORTMENT ESTIMATION BASED ON DATA-DRIVEN APPROACHES USING HYDRAULIC SIGNALS OF FORESTRY MACHINES

Chris Geiger*, Niklas Maier, Florian Kalinke, Marcus Geimer

Institute of Mobile Machines, Karlsruhe Institut of Technology, Rintheimer Querallee 2, 76131 Karlsruhe

* Corresponding author: Tel.: +49 721 608-48642; E-mail address: chris.geiger@kit.edu

ABSTRACT

The correct classification of a logs assortment is crucial for the economic output within a fully mechanized timber harvest. This task is especially for unexperienced but also for professional machine operators mentally demanding. This paper presents a method towards an assistance system for machine operators for an automated log quality and assortment estimation. Therefore, machine vision methods for object detection are combined with machine learning approaches for estimating the logs weight based on a Convolutional Neural Network (CNN). Based on the dimensions of the object 'log', a first categorisation into a specific assortment is done. By comparing the theoretical weight of a healthy log of such dimensions to the real weight estimated by the CNN-based crane scale, quality reducing properties such as beetle infestation or red rot can be detected. In such cases, the assistance system displays a visual warning to the operator to check the loaded log.

Keywords: Assistance System, Log Assortment, Crane Scale, Machine Learning, Machine Vision, Forwarder, Convolutional Neural Network

1. MOTIVATION

In a fully mechanized timber harvest, a harvester fells the trees and cuts them into logs of specific length according to the log quality. Afterwards, a forwarder loads the logs and moves them from the logging area to a forest road. Here, the operator piles the logs into different assortments regarding their specifications such as length and quality. Loading and piling sums up to 85 % of total working hours. [1–4]

It requires experienced operators with a background in forestry to fulfil these tasks efficiently, economically and sustainably. The main challenges forestry service companies currently face are a high employee fluctuation and a simultaneously increasing average age of the machine operators [5, 6]. Training of a new operator takes 9 months on average [7], resulting in reduced productivity during this time. Hence, this lack of experienced operators results in an economical deficit within the forestry sector.

2. ASSISTANCE SYSTEM FOR ASSORTMENT ESTIMATION

Especially new, young operators show a lack of experience in estimating the log dimension and quality during loading due to an insufficient background in forestry. A wrong assortment assignment leads to a quality reduction of the whole pile where the log was placed and reduces the overall profit of the forest owner and consecutively the forestry contractor. The log quality is based on the log's health and decreases with defects, e.g. red rot or bark beetle infestation at spruces, resulting in reduced weight compared to a healthy log. The aim of this paper is to close this gap in experience by presenting a method for an automated log quality and assortment estimation during a continuous loading cycle, exemplary shown for spruces. **Figure 1** displays the functional principle of the assistance system, which combines two parallel branches, one for measuring the weight and one for measuring the log dimensions, into an assortment estimation for forestry machine operators. The bottom branch receives the weight of the log via a CNN, mainly

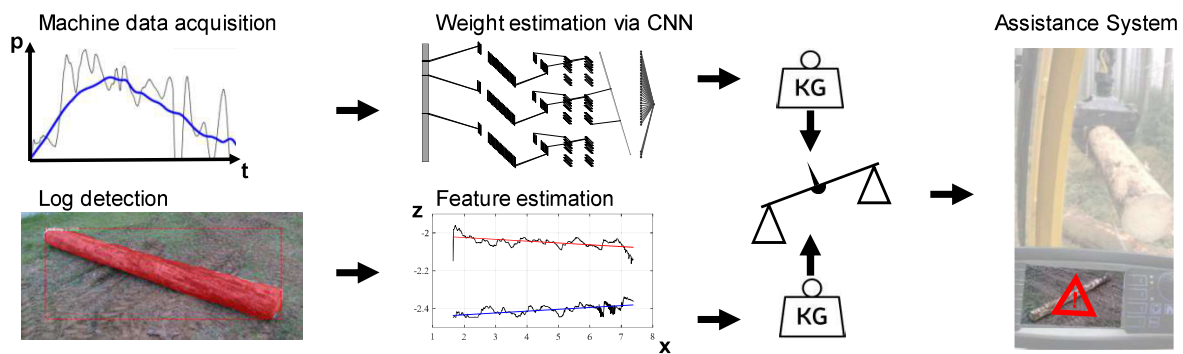


Figure 1: Flow Chart of the Assistance System

based on the input of the hydraulic pressure of the inner boom cylinder and the grapple position. The upper branch estimates the log diameter and length via object detection methods, resulting in the log volume. Assuming the density of a healthy log, the theoretical weight of the log is calculated and compared in the next step to the measured weight. In cases of significant differences, e.g. if the log is lighter due to red rot, a warning appears at the machine operators display, cf. **Figure 1** right. In the following, Chapter 3 shows the state of the art of object detection and crane scales. The two branches for the assistance system are explained in detail in Chapter 4 for the object detection and in Chapter 5 for the databased crane scale.

3. STATE OF THE ART

Currently, a system for forwarders estimating the log assortment automatically is unknown to the authors. Nevertheless, different approaches for the necessary subsystems of such an assistance system, especially measurement systems for the weight and dimensions of a log, are investigated by industry and research.

3.1. Object Detection of Logs

Machine vision is an essential part of many current research projects in the field of automation. However, research focusing on automatic recognition of logs are quite rare. [8] deals with general object recognition in point clouds. The authors discuss a robust method to fit cylinder models in incomplete point cloud data. Based on laser scanning, a method is proposed that combines Principal Component Analysis and RANSAC algorithms [ibid].

A forestry related research topic is the development of an algorithm for recognition and pose estimation of logs using a 3D structured light camera [9]. Herein, a method for analyzing the shape of a log by segmentation and surface patching is described. The focus is on the detection of rotational symmetries in point clouds. With this method, the determination of the volume and location of logs is implementable in automated processes, limited with a success rate under 33 % at a distance of 5 m. [9]

In order to evaluate object recognition algorithms, it is important to deal with the deviation between the determined values and the actual values. In [10] the authors focus on research in the field of volume measurements of logs. The main objective is the experimental determination of the actual log volume according to the Archimedean principle. Comparing the resulting volume data to the harvester measuring system as well as the in forestry common manual method shows an absolute volume error range up to 27 % for the 5 % - 95 % quantiles. [10]

3.2. Crane Scales

Commercial available crane scales for weighing the grapple content are provided by forestry machine manufactures [11, 12]. These scales are mounted between grapple and telescope, resulting in worse maneuverability due to negatively changed crane kinematics. Furthermore, measuring with high accuracy requires a static crane state [13, 14], resulting in reduced overall productivity.

A crane scale based on artificial neural networks was first presented by the authors in [15] and [16]. Based on a Long Short-Term Memory (LSTM) architecture, an Artificial Neural Network (ANN) weighs the grapple

content within a continuous loading process. The focus of this method is on an estimation of the logged mass of a working day in post-processing procedure. During testing, the ANN shows for single loading cycles an average full scale error of 1.5 % per 1000 kg, resulting in an example loading scenario in a total mass error of 1.2 % for a fully loaded forwarder with 10 tons payload [16].

4. LOG DETECTION AND SHAPE ESTIMATION

The aim of the proposed recognition algorithm is the automated determination of log volumes. The approach combines object recognition in 2D images and 3D point clouds. Using the feature of ordered point clouds allows assigning a space point to the corresponding pixel in a two-dimensional image and vice versa.

4.1. Camera technology

An Intel® RealSense™ D415 stereo camera is used for the object recognition method. The camera functions are based on active stereoscopy technology. The manufacturer specifies an application range of 0.45 m to 10 m for depth detection. The D415 generates point clouds via the coupling of two infrared cameras, an active infrared projector and a RGB camera. [17]

A defined number of space points, represented by a location matrix \underline{M} and a corresponding RGB colour matrix \underline{C} , are orderly recorded.

$$\underline{M} = \begin{pmatrix} x_1 & y_1 & z_1 \\ \vdots & \vdots & \vdots \\ x_i & y_i & z_i \end{pmatrix} \quad \underline{C} = \begin{pmatrix} r_1 & g_1 & b_1 \\ \vdots & \vdots & \vdots \\ r_i & g_i & b_i \end{pmatrix}$$

Therefore, the properties of a point with an index i are defined by six scalar quantities:

$$point_i = object(x_i, y_i, z_i, r_i, b_i, g_i)$$

Using the Intel® RealSense™ SDK 2.0, the depth camera is directly coupled to MATLAB®. This enables the integration of recordings into automated processes. Another advantage of the used camera is the comparatively low purchase price, which allows a cost-effective testing of the proposed method.

4.2. Data acquisition

Due to challenging environmental conditions in forestry, the camera was mounted on the

forwarders cabin roof. Therefore, the recorded point clouds lie at a defined angle in space. This setup was considered when recording the validation and verification data. Varying mounting angles and heights improves the robustness of the method due to the independence from the installation setting. The resolution of the camera was set to 1280x720 pixels, which outputs a point cloud with 921.600 points.

4.3. Method of log recognition

Because the elements of point clouds are ordered, an RGB image can be generated from the recorded colour matrix \underline{C} . Each described colour value of a point is assigned to a pixel in the 2D image via the indices of the point cloud.

Using the ordering of the point cloud together with the recorded color matrix \underline{C} as lookup-table, an RGB image $\underline{I} \in \mathbb{R}^{1024 \times 1024 \times 3}$ with pixels I_{jk} can be generated. Next, \underline{I} is processed by a Mask R-CNN [18], which we adapt for log recognition by transfer learning [19]. The network outputs bit-masks for each detected log, which map all I_{jk} to the corresponding object, cf. **Figure 1** left. For the Transfer Learning 100 hand-annotated pictures of single logs were used. The training set consisted of 80 pictures, with the remaining 20 used for validation. An accuracy for log detection of 100% was achieved.

The object pixels, corresponding to the bit-mask, are recalculated into the three-dimensional space. Thus, the 3D points are assigned to the object 'log'. The volume calculation is based on the recognized log length and the local log diameter.

The location matrix of the point cloud is rotated for further processing of the data via matrix transformation. The aim is to rotate the location matrix in a way that the log lies on the X-Y plane parallel to the Y-axis. Thus, the Z-coordinates of the location matrix \underline{M} describe the local log diameters as a height profile, the X-coordinates the log width and the Y-coordinates the log length. As a reference for the necessary rotations, an M-estimator Sample Consensus (MSAC) algorithm is used to fit a plane to the point cloud data [20], which represents the ground. With the normal vector of the plane, the rotation angles around the X- and Y-axis are determined. For the rotation on the Z-axis the direction of the log must be determined.



Figure 2: RGB data with determined log direction

An edge detection of the outline 2D image from the Mask R-CNN is carried out. The outermost points of the log are determined (top, bottom, right and left), cf. **Figure 2** in green. An imaginary box is created around the log based on the four boundary points. The two centres of the front and rear boundary points are calculated. The log direction is determined by connecting these two centres. In order to ensure that the described points are on the logs surface, the points are moved along the direction axis. **Figure 2** shows the RGB image with the generated direction vector in red as a result of the edge detection. The result of the transformation of the location matrix is shown in **Figure 3**, where the log lies parallel to the X-Y-Plane of the original system. After the data has been defined in the original space, the log length is determined. For the further process, the set of points is reduced to the pure log points that the Mask R-CNN generated as output.

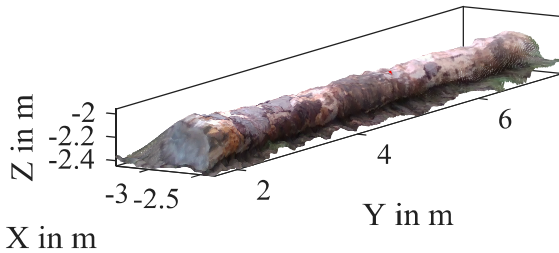


Figure 3: Rotated point cloud with indicated log direction (red)

4.4. Shape estimation

The local minima and maxima of the Z-coordinates along the Y-direction are determined. A profile of the top and bottom points is created as a matrix of Y- and Z-coordinates. To estimate the log length, only the profile of the top side is analysed. By using the MSAC algorithm, the points of the Y-Z-location matrix are fitted as a straight line that approximates the course of the diameter over the log length. We define the end

of the log as the last point of intersection between the Y-Z curve and the approximated diameter curve from the MSAC algorithm. The same algorithm is used for the bottom side of the log. **Figure 4** shows the results of the fitting process.

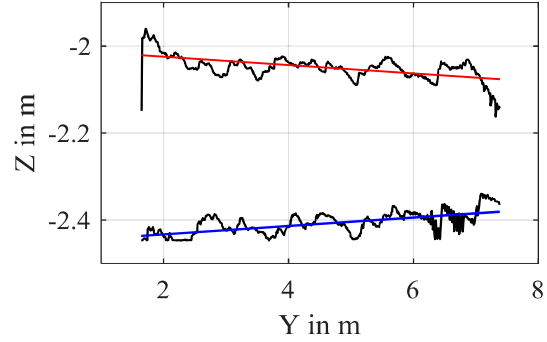


Figure 4: Point data describing log diameter and length with fitted lines

4.5. Error Estimation

Due to technical limitations of the camera, errors occur when measuring the depth. The error is estimated using the manufacturer's formula of the root-mean-square deviation. [21]

$$\text{Depth RMS error} = \frac{\text{Distance}^2 * \text{Subpixel}}{\text{focal length} * \text{Baseline}}$$

With the used camera settings and an estimated maximal working distance of 8 m, a root-mean-square deviation of the depth of 93 mm is calculated. The error increases quadratically with the distance and is influencing the length and diameter determination. Especially the latter leads to an error in the volume calculation.

4.6. Verification Data

To verify and validate the functionality of the log detection and shape estimation, 11 logs with a length about 5.2 m and a diameter range of 0.3 m to 0.5 m were tested. **Figure 5** shows the errors of the diameter and length determination, as well as the error of the calculated volume for these logs. As the absolute error in length is less than 7 % with a median of -0.4 %, the diameter estimation shows an error range between -11 % to 18 % with a median of -5.9 %. Here, the camera error described in Chapter 4.5 leads to a significant deviation of the measurement results. This diameter error influences the volume error significantly as it is included quadratically in the volume calculation.

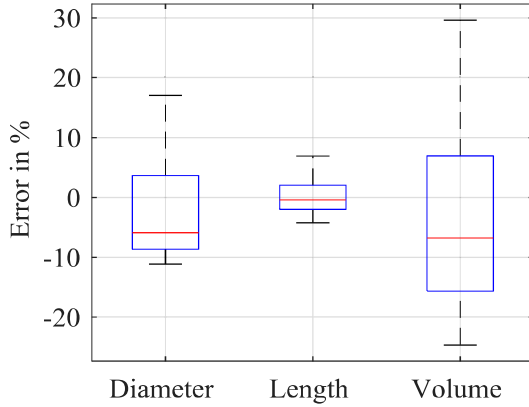


Figure 5: Errors of diameter, length and volume determination

As a basis for the explanation of the assistance system, the best results are presented in the following. With these results, shown in **Table 1**, the coupling possibilities of the crane scale with the log recognition algorithm will be demonstrated exemplarily in chapter 6. The real volume of the log presented in this example is $V = 0.55 \text{ m}^3$, whereby the calculated volume determined by our method is $V = 0.5448 \text{ m}^3$.

Table 1: Results for log with least error

Log parameter	Error [%]
Diameter	2.88
Length	-2.73
Volume	1.26

The results show that the accuracy of the proposed method depends primarily on the camera, cf. Chapter 4.5. In addition, we verified this dependency by using a logs point cloud achieved within the simulation environment GAZEBO, resulting in a volume error of 0.44 %. In future implementations of this system, it will be necessary to use a depth camera with a lower depth resolution error to show the benefit of the presented method for the assistance system.

5. CRANE SCALE BASED ON A CONVOLUTIONAL NEURAL NETWORK (CNN)

Beneath remaining constant crane kinematics, the objective of a data-based crane scale is, that modelling the crane with its non-linearity's and unknown parameters like friction coefficients is not necessary. Therefore, the function drive of the machine is mapped to an artificial neural network [16].

In a static situation, the mass of the grapple content can be calculated, neglecting adhesive friction, on the equilibrium of moments based on the pressure of the inner boom cylinder (IBC) and the grapple distance, cf. **Figure 6**. Avoiding a reduced productivity during loading processes due to stoppage for a weight measurement, the ANN represents a dynamic model of the crane. Therefore, the weighing process can be executed automatically during continuous loading processes.

In contrary to the in [16] presented approach of a crane scale based on a LSTM architecture, a convolution-only architecture is presented in this paper. Hereby, this architecture avoids drawbacks of Recurrent Neural Networks (RNN) with LSTM cells such as higher training and testing time, parallelization issues as well as higher sensitivity concerning overfitting or first examples seen [22]. Based on the idea of [22, 23] and partially conducted by [24], a Convolutional Neural Network was developed to fulfil the task of estimating the mass of the grapple content.

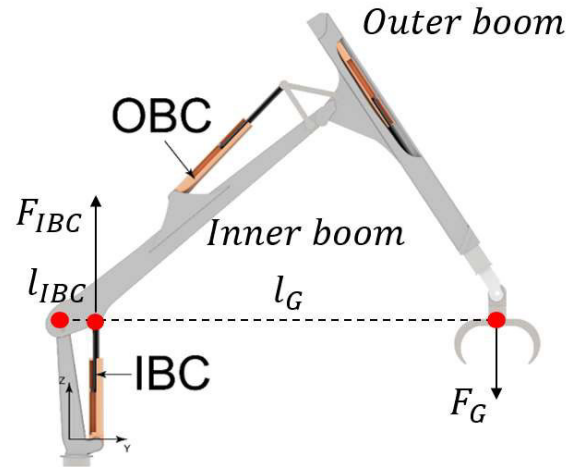


Figure 6: Forestry Crane [16]

5.1. Data Pre-Processing

The challenge of achieving a robust, real-world applicable setup for a crane scale at forestry conditions is using the least sensors possible. In modern in-market forestry cranes, each joint is equipped as standard with a kinematic sensor. With the presented setup, we only added one hydraulic pressure sensor to the system measuring the pressure of the inner boom cylinder (IBC). With this principle, the crane scale is independent regarding the used hydraulic systems for the crane drive [25] as well as the

machine manufacturer. Furthermore, the operator's input in form of the joystick signals, which are just like the other sensors readable from the machine's CAN-Bus, is used as input signals for the CNN [16]. The hydraulic signal of the pressure of the IBC is used as a direct as well as a preprocessed input into the network. Therefore, the pressure signal is filtered by means of a Savitzky-Golay filter. Furthermore, the pressures frequency spectrum calculated by a fast Fourier transform serves as an additional input. Finally, the oil temperature in tank, always available for monitoring and safety purposes on forestry machines, is an input signal. The grapple position as input results from processing the kinematic sensor of each crane joint, the grapple velocity by differentiating the position. [16]

The input consists of time-series data. In a first step, the input signals are standardized. Afterwards, the standardized signals are normalized between values of 0 and 255 and saved as an greyscale image [24]. The resulting image has the size of 18x250 pixels corresponding to the 18 input signals and 250 time steps, meaning that each pixel is equivalent to a specific measurement value.

5.2. Architecture of the CNN

For the CNN architecture, we use three parallel branches, each consisting of Convolutional Layers, Rectified Linear Units (ReLU) Layers and Pooling Layers [22, 24]. **Figure 7** visualizes exemplary the first branch. As input for the CNN serve the converted time series data as an 18 x 250 pixel greyscale image.

The first Convolutional Layer consists of 128 filters with a filter size of 18x1 and stride one. Hence, this filter covers all input signals at each time step. Directly connected to the

Convolutional Layer is the ReLU activation function $f(x) = \{x, x \geq 0; 0, x < 0\}$, which passes only input values greater and equal to zero [26]. Subsequently, the Max Pooling Layer with a size of 5x1 and stride 5 downsamples the input from 250x1 to 50x1. This corresponds to using only the maximum value of the filtered 18 input signals in a time range of five time steps. The second Convolutional Layer consists of 32 filters with a filter size of 1x1 and stride 1. As input serve the 128 channels resulting from the previous layers. Therefore, this recombines the previously divided input signal. The second Max Pooling Layer condense the input to 25x1, whereby the Concatenation Layer receives only 800 inputs for this branch.

The first Convolutional Layer of the second branch consists of 128 filters with a filter size of 18x5 and stride five. Therefore, already with the first layer in the CNN, five time steps are considered. In contrary to the first branch, no max pooling takes place between the first and second Convolutional Layer. The same principle is also applied for the third branch, expect for the fact that the filter size here is 18x51 with stride 4, covering therefore a wider time range. For both second and third branch, the second Convolutional Layer and Max Pooling Layer is the same as in the first branch, resulting to 800 input values for each branch for the Concatenation Layer. The Concatenation Layer combines the outputs of each branch and transfers the values to the Fully Connected Layer. Therefore, only 2400 weights have to be determined during training for this layer. The last layer is a regression output layer, meaning that the output of the 18x250 image is a single integer value representing the mass of the grapple content.

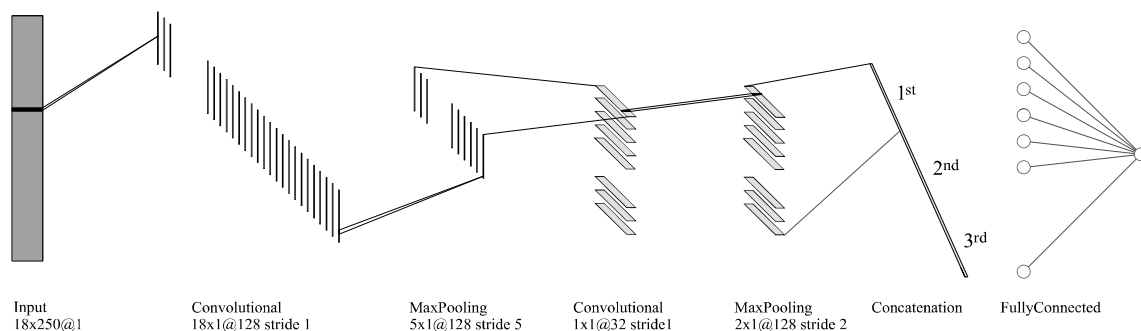


Figure 7: First Branch of used Convolutional Neural Network

5.3. Training of the CNN

We logged training data for the CNN by recording 550 loading cycles under reproducible laboratory conditions between August 2018 and March 2019, while the forwarder as well as the logs were placed on a flat surface. Three different machine operators with, from beginner to professional, varying expert level performed the loading cycles. The real log mass was determined by a scale with 0.5 kg accuracy. The log lengths were about 5.2 m, the log masses were in a range of 100 to 600 kg with a varying diameter up to 50 cm. [16]

31 loading cycles were reserved for testing of the crane scale. The remaining 519 cycles were split during training to 90 % for training and 10 % for validation. Due to the small amount of training data with its resultant issues [27], we used a six-fold cross validation, meaning that all 519 training cycles were randomly separated six times into a training data set and a validation data set [24].

For training, we set the learning rate to 0.01, the mini batch size to 20 and used a maximum of 30 epochs. Each training consists of 20 iterations, resulting overall in 120 networks due to the 6-fold cross validation. After the first training, we successively performed two further training passes with a learning rate of 0.001 using the weights of the pre-trained networks.

5.4. Results of Training and Validation Data Set

We evaluate the performance of the CNN on the trainings and validation data set by the percentage error resulting from difference of the predicted mass to the real mass divided by the real mass. **Figure 8** shows the gauss distribution of the Prediction Error (PE) for the validation set (left) and the training set (right) in a range of -40 % to 40 %. The training data set shows, based on 56,160 values, a mean PE of 0.23 % and a median PE of -0.0263 % with a standard deviation of 4.67 %. The validation data set displays, based on 6,120 values, a mean PE of 0.46 % and a median PE of -0.0095 % with a standard deviation of 7.33 %.

Table 2 lists the Prediction Error for both training and validation data with its 5 %, 25 %, 75 % and 95 % quantiles. Taking the 5 % and 95 % quantiles as well as the mean PE, into

account, the CNN shows a slight tendency of overestimating the mass with its prediction. Consecutively, 50 % of the predicted masses have an absolute PE less than 1.71 % (training data set) respectively less than 3.13 % (validation data set).

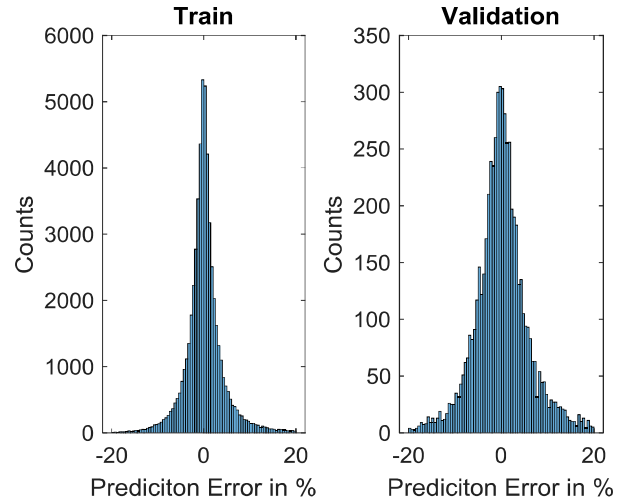


Figure 8: Prediction Error Distribution

Therefore, we observe no significant overfitting of the CNN, resulting in a robust network for detecting the mass based on a minimal amount of sensor data.

Table 2: Statistical analysis of the CNN

Quantile [%]	Prediction Error in Training Data Set [%]	Prediction Error in validation Data Set [%]
5	-6.25	-9.46
25	-1.69	-2.95
75	1.71	3.13
95	7.44	12.18

5.5. Results on Test Data Set

Reducing the variance of the mass prediction, we use bagging for testing [28]. Therefore, we determined the 20 CNNs with the least mean PE on the validation data set. During testing, by using a trimmed mean, the mass of the grapple content is averaged based on these networks without the upper and lower 10 % of the predictions. Embedding this evaluation method into the assistance system increases the robustness of the same against varying machine operators and environmental factors.

The test data set consists of the 11 loading cycles for the in Chapter 4 evaluated logs and 20 randomly chosen loading cycles. None of these

cycles was used during training or testing of the CNN. The loading cycles were performed by two different machine operators with different experience level, one advanced beginner and one professional. In total, these cycles sum up to 6888 kg, tallying nearly to a complete payload of a forwarder. The estimated mass by the CNN for all cycles is in total 6873 kg, resulting in an error of - 0.22 %. **Figure 9** shows the prediction error of the validation set. The Prediction Error of single logs is in a range of -7.73 % to 10.73 % with a mean PE of 1.20 %.

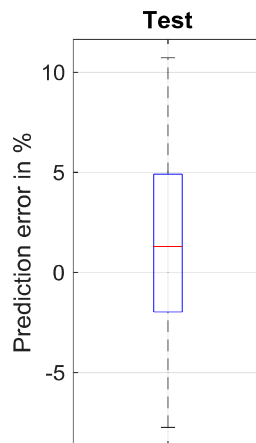


Figure 9: Test Data set

The range of the PE in the validation data set corresponds very well to the error range in the test data set. This underpins the stability and robustness of the Convolutional Neural Network. The fact, that the absolute error can be higher than 10 % is no critical argument against the shown method and network architecture as only a minimum of data was used for training. Increasing training data will reduce the error range significantly.

6. ASSISTANCE SYSTEM

The in **Figure 1** visualized assistance systems for log quality and assortment estimation is the combination of both log detection and mass prediction shown in the previously chapters. By using the log with the best volume estimation, the method and functionality of the assistance system is explained in the following. In this exemplary case, the evaluated log shows a significant bark beetle infestation.

In the first step, the length and diameter of the log specifies its assigned assortment. In the example case, the log is appointed to the

assortment FL (log with standard length) and a diameter class D3b due to a diameter of 0.36 m [29]. In the second step, the mass of the log is calculated based on the log volume and a green wood density of 906 kg/m³, assuming that the log is of healthy state without defects. In our example, this results in a theoretical log weight of 494 kg. Afterwards, this value is compared to the mass predicted by the Convolutional Neural Network, cf. **Figure 1**. As this mass has a predicted value of 404 kg - with a PE of 6.60 % - the log weighs only 81.78 % of the expected value calculated with the green wood density. The deviation is significantly higher than the absolute PE of the Test Data Sets 5 % and 95 % quantiles, resulting in a low certainty of an outlier. The threshold for sending a visual warning to the operator is when the mass difference estimated by the volume information and the CNN output is greater than 15 %. This corresponds directly to the quality classification, as with a red rot percentage over 15 % the log quality decreases [29].

By displaying this warning and the log information on the machine operators monitor, he is able to double-check the log quality. As further information, the theoretical mass for beetle infested logs with 373 kg is displayed, which varies about 7.76 % from the CNN-estimated mass and 1.67 % from the real mass. Therefore, if there is no visual sign of red rot at the front faces of the log, the operator defines the log to quality D due to beetle infestation [29].

7. CONCLUSION

The right assignment of logs to their specific assortment is crucial for an economical harvesting process. The presented method describes an assistance system for machine operators, which supports them in the task of the assortment estimation.

The assistance system combines two parallel branches of object and weight detection to estimate the logs dimension and quality, resulting in its assortment. The functionality of the presented method was verified within this paper.

For object detection, an Intel RealSense D415 depth camera was used. Due to a root mean square error up to 0.1 m within working distance, the logs diameter estimation shows an absolute error range of 17 %, resulting in an error range from -25 % to 30 % regarding the volume

calculation. Therefore, the chosen depth camera limits the potential of the assistant system. The volume error influences directly the theoretical mass calculation based on the green wood density for logs of healthy state. This error could be reduced significantly with an industry-standard depth camera. Nevertheless, the approach for detecting a log via machine learning methods and the consecutive dimension estimation could be verified under laboratory conditions. Of special use is the log length estimation for machine operators, as this parameter defines the assortment of the log in the first place. Distinguishing the common log lengths of 3.6 m, 4.0 and 5.0 is difficult in real forestry conditions and mentally demanding.

For the weight detection system, a databased approach resting on a Convolutional Neural was developed and successfully tested. The chosen CNN shows a prediction error for single loading cycles between -2 % to 5 % for the 25-75 % quantiles of the test data set. This corresponds to a full scale error of 2 % with a maximum absolute error of 20 kg in this range. Due to the results at the validation data set, the CNN shows a high robustness against varying machine operators and changing environmental conditions. Furthermore, the CNN achieves a certain degree of abstraction as in the period of data recording parameter settings and optimizations of the hydraulic system were done. Therefore, it is possible to transfer the crane scale to other machines with the same crane type, accomplishing a universal usage of the presented method.

8. OUTLOOK

In a first step, accuracy of the log dimension estimation will be significantly increased using an industry standard depth camera. The log detection will be extended from the two-dimensional image to an object detection in a 3D dataset. Furthermore, the algorithms for this estimation will be improved towards fitting a three-dimensional truncated cone in the point cloud data which approximates the log. The combination of multiple point clouds recording the same scenery towards one, holistic point cloud with a high accuracy will be investigated.

For the crane scale, additional training cycles under varying conditions will be recorded in forestry environments. Therefore, the accuracy

and robustness of the presented method will improve significantly. After a further optimization of the algorithms, the assistance system will be implemented as a near-time, online system in the forwarder cabin.

REFERENCES

1. Cacot E, Bigot M, Cuchet E (2006) Developing full-mechanized harvesting systems for broadleaved trees: a challenge to face the reduction of the manual workforce and to sustain the supply of hardwood industries. In: 2006 Council on Forest Engineering (COFE) Conference Proceedings: "Working Globally – Sharing Forest Engineering Challenges and Technologies Around"
2. Nurminen T, Korpunen H, Uusitalo J (2006) Time consumption analysis of the mechanized cut-to-length harvesting system. *Silva Fenn.* 40(2). doi: 10.14214/sf.346
3. Kuptz D, Turowski P, Hartmann H et al. (2015) Optimale Bereitstellungsverfahren für Holzhackschnitzel
4. Manner J, Palmroth L, Nordfjell T et al. (2016) Load level forwarding work element analysis based on automatic follow-up data. *Silva Fenn.* 50(3). doi: 10.14214/sf.1546
5. Schulz C (2017) Berufspolitisches Engagement gefragt!: Interview von Christoph Schulz mit Christian Feußner, beide Angestelltenvertreter im Gesamtpersonalrat von Hessen-Forst. *BDF aktuell* 58(1): 20–21
6. Wippel B, Viergutz M (2014) Stärkung der Kooperations-strukturen von Forstunternehmern in Baden-Württemberg. Abschlussbericht
7. Purfürst T (2009) Der Einfluss des Menschen auf die Leistung von Harvestersystemen. Dissertation, Technische Universität Dresden
8. Nurunnabi A, Sadahiro Y, Lindenbergh R (2017) ROBUST CYLINDER FITTING IN THREE-DIMENSIONAL POINT CLOUD DATA. *Int. Arch. Photogramm. Remote Sens. Spatial Inf. Sci.* XLII-1/W1: 63–70. doi: 10.5194/isprs-archives-XLII-1-W1-63-2017
9. Park Y, Shiriaev A, Westerberg S et al. (2011 - 2011) 3D log recognition and pose estimation for robotic forestry machine. In: 2011 IEEE International Conference on Robotics and Automation. IEEE, pp 5323–5328
10. Hohmann F, Ligocki A, Frerichs L (2017) HARVESTER MEASURING SYSTEM FOR

- TRUNK VOLUME DETERMINATION: COMPARISON WITH THE REAL TRUNK VOLUME AND APPLICABILITY IN THE FOREST INDUSTRY. Bulletin of the Transilvania University of Brasov
11. Komatsu Options Forwarders. <https://www.komatsuforest.com/forest-machines/our-forwarders/forwarder-options>. Accessed 13 Apr 2019
 12. Ponsse PONSSE ATTACHMENTS ADD VALUE TO YOUR MACHINE. http://www.toimilgruas.com/pdf/Attachment_ENGL.pdf. Accessed 13 Apr 2019
 13. Korten S, Kaul C (2012) Optimierung der Transportprozesse bei Holzernte und Rundholztransport durch den Einsatz von Wechselbrücken: Schlussbericht
 14. Wide MI (2012) Väg rätt redan i skogen. SKOGFORSK
 15. Geiger C, Starke M, Greff D et al. (2018) THE POTENTIAL OF A WEIGHT DETECTION SYSTEM FOR FORWARDERS USING AN ARTIFICIAL NEURAL NETWORK. In: FORMEC 2018 – Improved Forest Mechanisation: mobilizing natural resources and preventing wildfires
 16. Geiger C, Greff D, Starke M et al. Entwicklung und Evaluation eines Wiegesystems für Forstkräne auf Basis von künstlichen neuronalen Netzen. LANDTECHNIK, Bd. 74 Nr. 5 (2019)
 17. Giancola S, Valenti M, Sala R (2018) A Survey on 3D Cameras: Metrological Comparison of Time-of-Flight, Structured-Light and Active Stereoscopy Technologies. Springer International Publishing, Cham
 18. He K, Gkioxari G, Dollar P et al. (2017) Mask R-CNN. In: The IEEE International Conference on Computer Vision (ICCV)
 19. Waleed A (2017) Mask R-CNN for object detection and instance segmentation on Keras and TensorFlow. https://github.com/matterport/Mask_RCNN. Accessed 25 Nov 2019
 20. Torr PHS, Zisserman A (2000) MLESAC: A New Robust Estimator with Application to Estimating Image Geometry. Computer Vision and Image Understanding 78(1): 138–156. doi: 10.1006/cviu.1999.0832
 21. Grunnet-jepsen A, Sweetser JN, Woodfill J Best-Known-Methods for Tuning Intel® RealSense™ D400 Depth Cameras for Best Performance. <https://dev.intelrealsense.com/docs/tuning-depth-cameras-for-best-performance>. Accessed 21 Nov 2019
 22. Devineau G, Xi W, Moutarde F et al. (2018) Convolutional Neural Networks for Multivariate Time Series Classification using both Inter-& Intra-Channel Parallel Convolutions. https://rfiap2018.ign.fr/sites/default/files/ARTICLES/RFIAP_2018/RFIAP_2018_Devineau_Convolutional.pdf
 23. Groß W, Lange S, Bödecker J et al. Predicting Time Series with Space-Time Convolutional and Recurrent Neural Networks. European Symposium on Artificial Neural Networks, Computational Intelligence and Machine Learning 2017
 24. Greff D (2019) Investigating the development of a dynamic weighing system for forestry machines: -using a data driven approach-. Master's thesis, Karlsruher Institut für Technologie
 25. Hohenlohe, Felix, zu, Geiger C, Geimer M (2019) Hybridantrieb für den Ladekran einer Forstmaschine. In: Hybride und energieeffiziente Antriebe für mobile Arbeitsmaschinen : 7. Fachtagung. KIT Scientific Publishing, Karlsruhe
 26. Nair V, Hinton GE (2010) Rectified linear units improve restricted boltzmann machines. ICML'10 Proceedings of the 27th International Conference on International Conference on Machine Learning: 807–814
 27. Goodfellow I, Bengio Y, Courville A (2016) Deep Learning. MIT Press
 28. Hastie T, Tibshirani R, Friedman JH (eds) (2017) The elements of statistical learning: Data mining, inference, and prediction, Second edition, corrected at 12th printing 2017. Springer series in statistics. Springer, New York, NY
 29. Deutschen Forstwirtschaftsrates e.V., Deutschen Holzwirtschaftsrates e.V. (2015) Rahmenvereinbarung für den Rohholzhandel in Deutschland (RVR)

EMISSION REDUCTION BY HYDRAULIC HYBRIDS

Seppo Tikkanen^{1*}, Mikko Heikkilä², Matti Linjama³, Kalevi Huhtala³

¹ DIMECC Ltd, Korkeakoulunkatu 7, 33720 Tampere, Finland

² Agco Power Ltd, Nokia, Finland

³ Tampere University, Automation Technology and Mechanical Engineering, Korkeakoulunkatu 6, 33720 Tampere, Finland

* Corresponding author: Tel.: +358 40 8402780, E-mail address: seppo.tikkanen@dimecc.com

ABSTRACT

Emissions of non-road machines are reduced by precise control of combustion process inside the engine and by after-treatment systems. One additional measure is the hybridization of the powertrain, which can be used to stabilize the engine load. This reduces harmful emissions because most nitrogen oxide emissions and particle emissions are related to sudden load and speed changes of the engine. In this study, four different hydraulic hybrid systems and their emission reduction potential are tested in one case study of a forwarder. The comparison study was done using a hardware-in-the-loop system (HIL) that consisted of a real-time simulation model, hydraulic secondary controlled loading system, real diesel engine, and emission measurement systems. The most efficient system (i.e., the system with the lowest fuel consumption) was the *Four-pressure* system. However, the difference between this system and the second-best system was negligible, and fuel consumption was about 40% less than with the reference system (a load-sensing system). Results showed that absolute emissions can be reduced by hybridization. Nitrogen oxide emissions were 15–25% lower and particulate matter emissions were 60–75% lower. The *Four-pressure* system had the lowest emissions. All studied hybrid systems resulted in reduction in fuel consumption and harmful emissions in the studied use case.

Keywords: Hydraulic hybrid, emissions

1. INTRODUCTION

The efficiency of mobile machines has been studied widely during the last decade. A lot of effort has been put into reducing fuel consumption and carbon dioxide emissions. At the same time, the exhaust emission regulations of engines in Europe, the USA, and Japan have become more and more strict, leading to reduced emissions from new mobile machines. The regulations limit emission of hydrocarbons (HC), carbon monoxide (CO), nitrogen monoxide (NOx) and particle matter (PM) per produced kilowatt-hour (kWh). However, these regulations only limit the emissions of the engines, not the emissions of the machines directly. The validation tests are made for the engine in laboratory conditions with predefined load cycles. The loading cycle of the emission tests are composed of various measured real cycles, but they are nonetheless laboratory tests without the variation of real conditions and load cycles [1].

The most critical emissions from diesel

engines are nitrogen oxide and particle matter emissions, because they have harmful effects on human health. Both nitrogen oxide and particle emission are limited by regulations, the limiting values of which have been lowered over time (being now over 20 times lower than in the mid-1990s).

Diesel engine produces nitrogen oxide and particle emissions, and the amount varies greatly on engine operation point and engine emissions are reduced by precise control of combustion process and exhaust after-treatment systems. Nitrogen oxides are reduced by exhaust gas recirculation and separate systems like the diesel oxidation catalyst, selective catalyst reduction or NOx storage catalyst, which are part of exhaust systems. Particle emissions are reduced by particulate filters. The size of these systems increases with the cleaning capacity. The size of the after-treatment systems is dependent on the emission reduction performance; if the raw emission can be reduced, the size of the after-treatment systems can be smaller.

Nitrogen oxide emissions and particle emissions are increased when engine load and/or speed is changing rapidly (compared to a constant load situation) [2]. Rapid and continuous changes of engine loading are typical for mobile machines such as excavator, forest harvesters, and wheel loaders. Secondly, the load and speed changes are dependent on the operator's behaviour. Previous studies by Heidari and Marr [3], Ericson, Westerberg, and Egnell [4], Lindgren [5], and Pult [6] have shown that NOx and particulate matter emissions factors are dependent on the engine transients.

The research question is: How much can raw emissions (i.e., emission before after-treatment systems) be reduced by different hydraulic hybrid concepts? To find an answer to the research question, the following experimental research was conducted. The use case was a log loading and unloading with the crane of forest forwarder. The reference system was a typical load-sensing (LS) system with variable pump and proportional valves. The comparison study was done with a hardware-in-the-loop system (HIL) that consisted of a real-time simulation model, hydraulic secondary controlled loading system, real diesel engine, and emission measurement systems. The studied systems were:

- The reference system with proportional valve and one load sensing pump;
- System with independent metering valves and electric load sensing system with one pump;
- Two parallel pumps with accumulator and independent metering valves;
- Accumulator with independent metering valves and on variable pump;
- So called STEAM system with one variable pump and two accumulators
- Four-pressure level system with one constant pump and accumulators

2. STUDIED SYSTEMS

The emission behavior of five different systems and one reference system were studied. The reference system consisted of crane hydraulics for a medium-sized forest forwarder that was used to collect and transport the logs. The maximum reach of the crane was 9.1m and its lifting torque was about 95 kNm, while the slewing torque was 25 kNm. In addition, the slewing mechanics had a turning angle of 360 degrees. The hybrid systems were implemented

in the crane hydraulics; the drive line was not hybridized and test cycle did not contain driving.



Figure 1: Studied reference forwarder crane in action

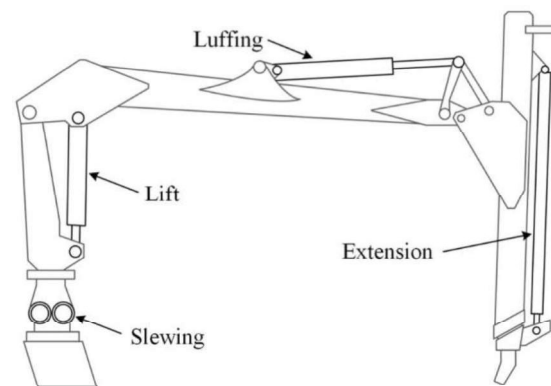


Figure 2: Studied crane of the forwarder

The reference system was a typical load-sensing system equipped with one pressure-controlled variable pump and load-sensing valve. The directional valve was controlled by electronic joysticks manipulated by an operator. The system contained slew, lift, luff, extension, and grapple actuators. The displacement of the pump was 130cm³/rev and the maximum pressure was 27 MPa. The abbreviation *LS-propo* is used for the reference system.

In the first studied system, the original hydraulic load-sensing valve was replaced by an independent metering valves for all actuators and the load-sensing function was realized electronically (the abbreviation *LS-IMV* is used for this). The pump displacement was 130cm³/rev and the maximum pressure was 27 MPa. **Figure 3** shows schematic realisation of the system (only one actuator showed).

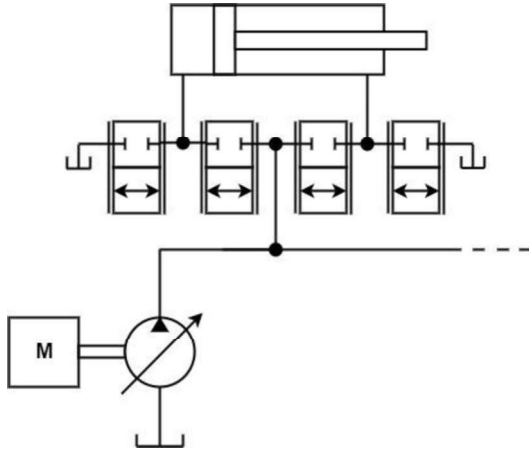


Figure 3: Simplified schematic of the *LS-IMV* system

The second system had two pumps and the additional pump was parallel to the load-sensing pump. The additional pump was a closed-circuit pump and its second port was connected to an accumulator that enabled energy storing (**Figure 4**). References [7] and [8] introduce the system and its operation. This system also had independent metering valves. The system is abbreviated to *Parallel pumps + IMV*. The size of the open circuit pump was $50 \text{ cm}^3/\text{rev}$ and the size of the closed circuit pump was $60 \text{ cm}^3/\text{rev}$, with a maximum system pressure of 27 MPa. The nominal volume of the accumulator was 20 litres and the precharge pressure was 11.5 MPa.

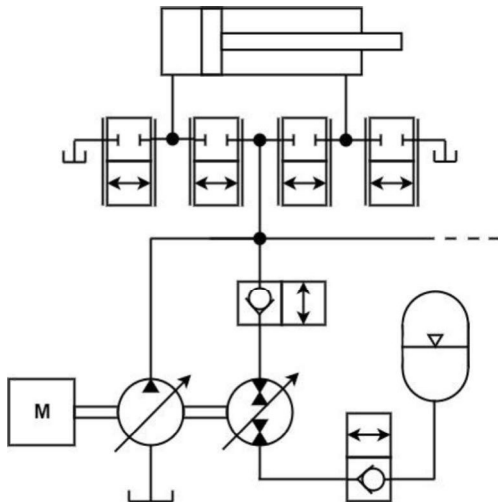


Figure 4: Simplified schematic of the *Parallel pumps+IMV*-system

The third system was similar to the *LS-IMV* system but had an accumulator as energy storage in the supply line. The connection (i.e., the flow in and out to the accumulator) was controlled by a valve with a variable opening. This system is abbreviated *Throttled accu + IMV*. **Figure 5**

shows a schematic realization of the system [9]. The pressure level was 27 MPa, the nominal size of the accumulator was 20 litres, and the precharge pressure was 11.5 MPa.

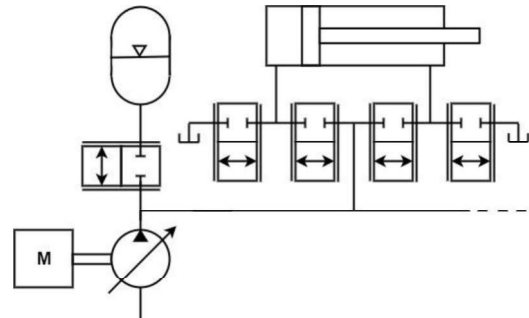


Figure 5: Simplified schematic of the *Throttled accu + IMV*-system

The fourth system was the so-called *STEAM* system which was invented and researched in RWTH Aachen [10]. It is a two-pressure system with low- and high-pressure supply lines with accumulators and is referred to as *STEAM*. **Figure 6** shows a schematic realization of *STEAM* system. The pump for the *STEAM*-system was smaller ($25 \text{ cm}^3/\text{rev}$) and the nominal volumes of the high- and low-pressure accumulators were both 15 litres and the precharge pressures 14 MPa and 7 MPa correspondingly. The maximum system pressure

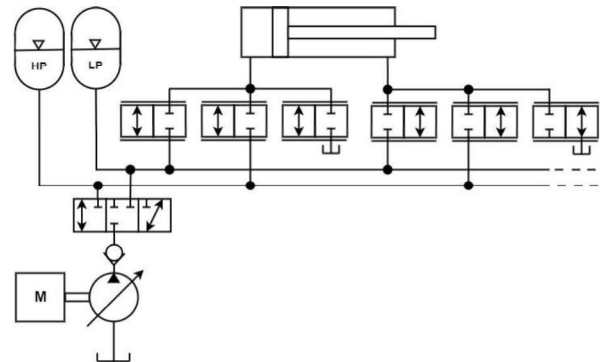
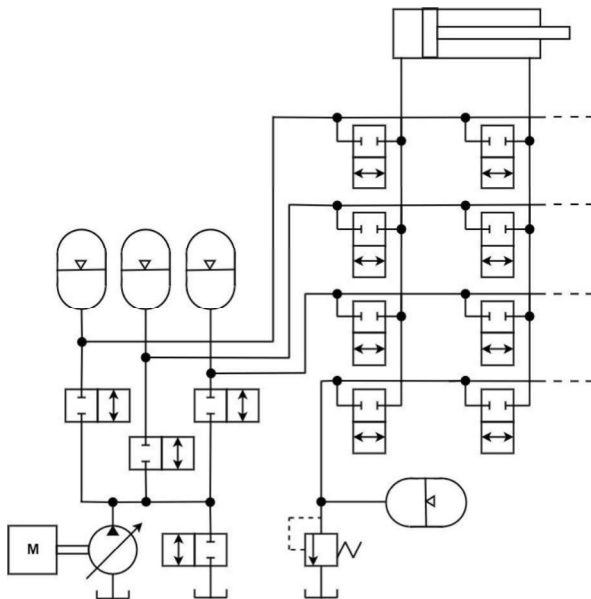


Figure 6: Simplified schematic of the *STEAM*-system

was 28 MPa.

The last studied system was a multi-pressure system with four different pressure levels including return line pressure, called a *Four-pressure* system. Each pressure line had its own accumulator. **Figure 7** shows a schematic realization of the *Four-pressure* system (a similar system is introduced by Huova et al [11]). The constant pump had a displacement of $20 \text{ cm}^3/\text{rev}$. The nominal volumes of all accumulators were 10 litres and the precharge pressures, from high

to low, were 19.6 MPa, 13.1 MPa, 6.5 MPa respectively. The return line pressure was 0.1 MPa. The maximum system pressure was 28



MPa.

Figure 7: Simplified schematic of the *Four-pressure-system*

3. MEASUREMENT SYSTEM

The actual emissions of studied systems and reference were determined with the help of real-time simulation in combination with a real engine. The measurement system consisted of a diesel engine, loading unit that generated load to the engine and real-time control system. The load for the engine was determined by the simulation model of a particular hydraulic system. The inputs for the hydraulic system model were loading of the actuators. The load profiles of the actuators were real and they were measured from the reference crane of the forest forwarder. Emissions were measured by the AVL's PEMS system, which has measurement devices and systems for nitrogen oxides, carbon monoxide, carbon dioxide, hydrocarbons, soot, and particle mass. The post processing calculations of emission measurements were performed with AVL Concerto software. The measurements were performed in a laboratory at a temperature of about 20 degrees Celsius. The used fuel in the tests was regular diesel fuel. The system is shown in **Figure 8**.

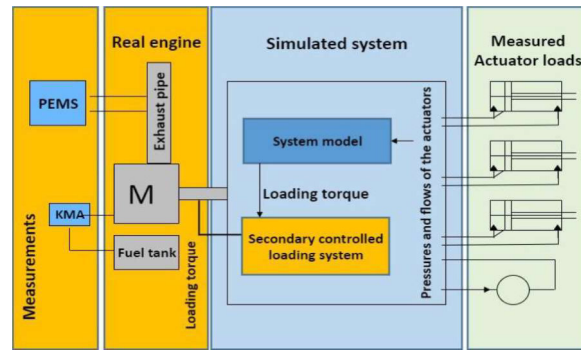


Figure 8: Measurement arrangement

3.1. Load profiles

The load profiles of crane actuators (i.e., slew drive, lift, luffing and extension) were captured during the reference measurements while loading and unloading logs with the crane of the forest forwarder. The power demands of grapple and its rotator were modelled as an average power, being 1 kW. The reference cycle lasted around 20 minutes. The crane was operated during the reference cycle measurement by a professional operator. The torque generated by auxiliary cooling pump and driveline pumps (i.e., the boost pump and main pump) at zero displacement was modelled as a constant average and the torque demand was estimated to be 25 Nm.

3.2. Simulation model

All systems were modelled in Matlab/Simulink. The system models included actuators, main control valves, accumulators and pumps. The inputs for the system models were flows and pressures of the actuators which were captured during reference measurements. The backward simulation of the hydraulic system, including hybrid systems, was used to determine the pressures and flows of the hydraulic pump(s) and torque demand for the diesel engine. Calculations were based on steady-state models that were created based on the power loss models of the system components and control laws defining the use of valves and other subsystems. The analysis starts by calculation of input flow rate and required supply pressure level. A control law designed is used to select pump displacements, which fulfil these requirements. The analysis continues with the calculation of the mechanical input power of the pump. The power losses of the pumps are modelled as well as the pressure drop created by valves. The accumulator pressure level

is modelled using an adiabatic model. Similar method is described in more detail in the reference [12]. The output of the system model is the torque demand for the diesel engine. The torque demand and engine speed set value were the used for set values for the HIL-system that was running in the dSpace DS1103-system.

3.3. Loading unit

A secondary controlled hydraulic system acted as a loading unit and generated the load torque for the diesel engine. The loading unit was capable of operating in four quadrants, but only one was utilized. The load system had the possibility for closed-loop torque or speed control, and in this case closed-loop torque control was used. The set torque was realised by controlling the swivel angle of two 125 cm³/rev axial piston units and the control loop was closed by a torque sensor between the engine and the loading unit. The maximum torque of the loading unit was 800 Nm. The rotational speed was controlled by the diesel engine and the set value was kept constant at either 1250, 1400, or 1600 rpm, respectively.

4. RESULTS

Table 1 shows the operational values of the studied system during the tests. Because of the decreased power demands of the hybrid systems, the engine speed was lowered from 1600 rpm to 1250 rpm. The duration of all cycles was the same (20 minutes and 33 seconds) which means that absolute values are comparable between the systems.

The differences in torque and power demands are clearly seen from the mean torque and mean power values.

The efficiency results, shown in **Table 2**, can be observed from different point of view. The cycle energy value indicates the energy need of the particular system and describes the efficiency of the hydraulic system because, in the all systems, the output work were equal. The *Four-pressure* system clearly had the lowest energy demand, requiring 49% less energy than the reference system for the same work. The second-best system was the *Throttled accu + IMV* system, requiring 43% less energy than the reference system. The third lowest energy need was found in the *STEAM* system, with a saving of about 38%.

Table 1: Operational values

	Mean engine speed [rpm]	Mean engine torque [Nm]	Mean engine power [kW]
<i>LS-propo</i>	1591	133	22.3
<i>LS-IMV</i>	1414	120	17.8
<i>Parallel pumps+IMV</i>	1254	111	14.6
<i>Throttled accu+IMV</i>	1254	97	12.7
<i>STEAM</i>	1254	105	13.8
<i>Four pressure</i>	1254	87	11.4

Table 2: Efficiency values, relative to the reference

	Cycle energy [rel]	Absolute fuel consumption [rel]	Specific fuel consumption [rel]
<i>LS-propo</i>	1	1	1
<i>LS-IMV</i>	0.80	0.74	0.93
<i>Parallel pumps+IMV</i>	0.66	0.64	0.97
<i>Throttled accu+IMV</i>	0.57	0.60	1.06
<i>STEAM</i>	0.62	0.67	1.09
<i>Four pressure</i>	0.51	0.60	1.17

The absolute fuel consumption value indicates the energy needs of the whole system, including the hydraulic system and the diesel engine. Again, the *Four pressure* system had the lowest fuel consumption, with a decrease of 40% compared to the reference, but the difference between this and the second-best *Throttled accu + IMV* system was only 0.6%. The third-best system was the *Parallel pumps + IMV* system, which decreased the fuel consumption by 36%. It is noteworthy that the differences between the systems were smaller in terms of fuel consumption than in terms of the energy needs of the hydraulic system. The reason for the diminishing differences between the systems, is that the low engine efficiency dominates the system efficiency and reduces differences across operation points.

The specific fuel consumption indicates the efficiency of the engine and it was calculated from the cycle energy (diesel engine shaft) and from the energy content of the used fuel. The lowest specific fuel consumption (i.e., the highest engine efficiency) occurred with the *LS-IMV* system, which had 7% lower specific

consumption than the reference case. Interestingly, the most efficient hydraulic system (the *Four-pressure* system) caused the highest specific fuel consumption, with an increased specific consumption of 17% compared to the reference case. The reason for this phenomenon is that hybridization moves the engine operation point towards low torque and low speed region that have low efficiency. This fact illustrates very clear that hybridization requires a smaller engine to exploit all its benefits. The smaller engine would enable the engine to operate on favourable operation area in terms of efficiency resulting lower fuel consumption.

Figure 9 shows power demand of the studied systems for one log loading cycle. The full measurement contained about 20 loading and 20 unloading cycles. The total installed pump capacity is clearly seen on the steady state phase (145 - 146 sec), the system with smallest pumps (*STEAM* and *Four pressure*) have lowest power demand. The log loading phase (lifting, turning, lowering) is in the timeframe 147 – 160 seconds and crane return phase respectively in the time frame 161 – 172 seconds. The reference system (*LS-propo*) has the highest power demand and remarkably many power peaks during the cycle. The shape of the power curves for *LS-IMV*, *Parallel pumps+IMV* and *throttled accu* are quite similar only the level vary. The power curves for

STEAM and *Four pressure*-systems are different. This is a result of different operation principle on hydraulic power generation. In the both systems the pump flow is decoupled from the flow demand of the crane motion. The pressure of accumulators i.e. state of charge of the accumulators controls the pump flow. This feature stabilizes the engine power demand and should reduce emissions as well.

As was mentioned, the engine did not have any exhaust after treatment systems. Therefore, the followed analysis is based on the raw emissions (i.e., emissions that are not processed by any catalysts or filters, such as a diesel oxidation catalyst, selective catalyst reduction, or particle filter). By decreasing the raw emissions it is possible to use smaller catalysts and filters, because decreased raw emissions reduces the required cleaning capacity of catalyst and filters.

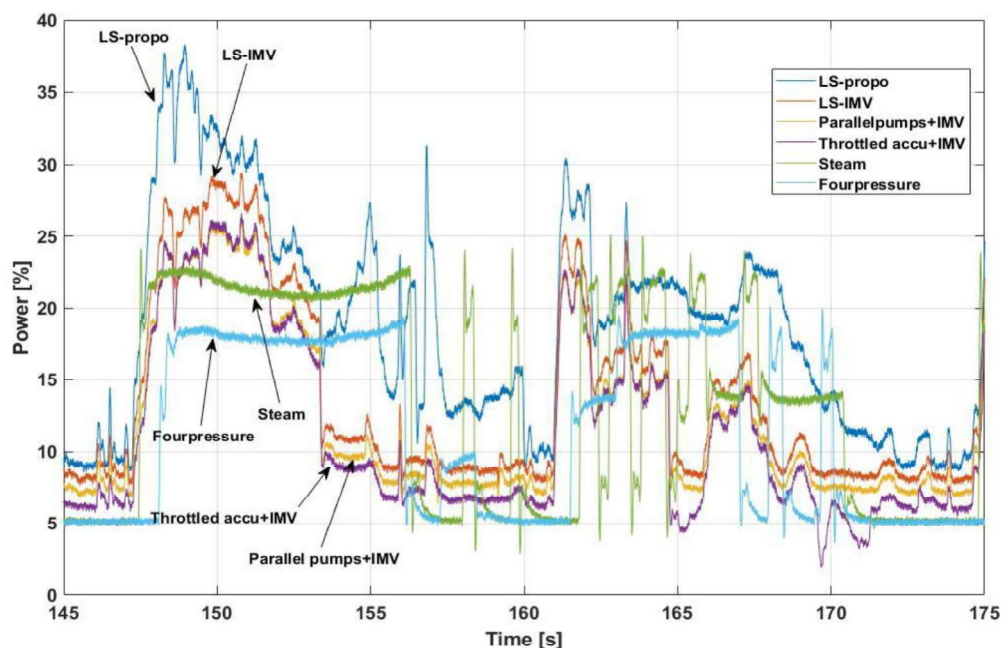


Figure 9: Sample of the engine power for one loading cycle

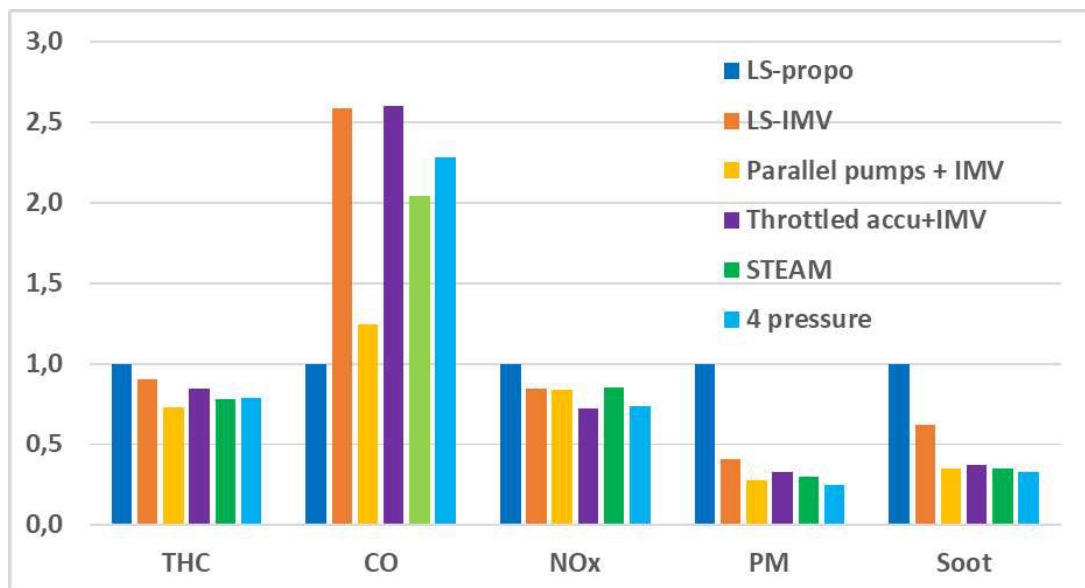


Figure 10: Relative change of absolute emissions; emissions of the LS-Propo system as reference. THC – Total hydrocarbons, CO — Carbon dioxide, NOx – Nitrogen oxide, PM – Particulate matter

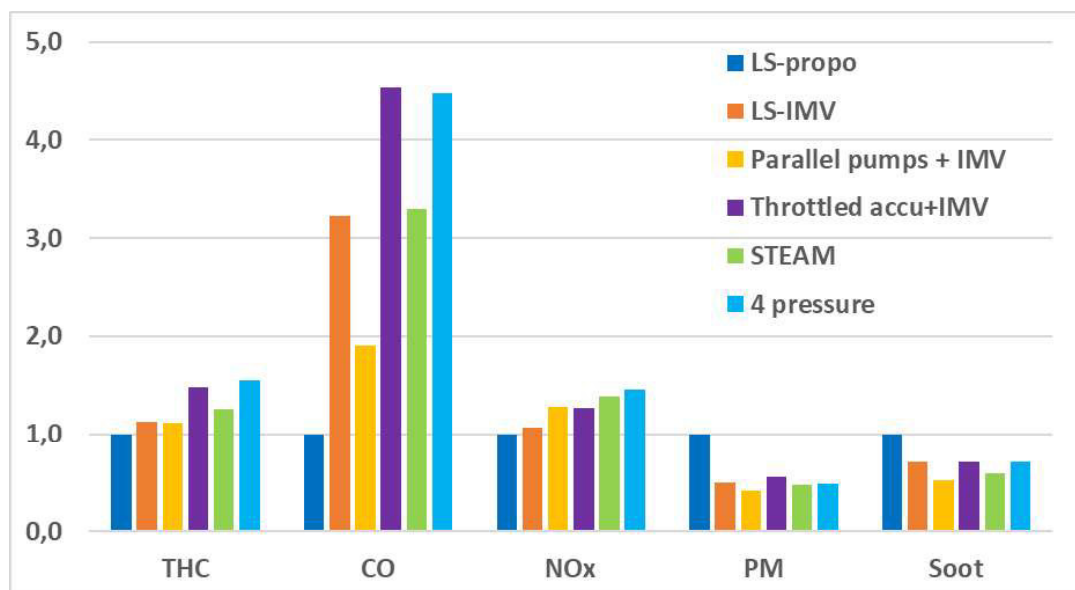


Figure 11: Relative change of specific emissions; emissions of the LS-Propo system as reference. THC – Total hydrocarbons, CO – Carbon monoxide, NOx – Nitrogen oxides, PM – Particulate matter

As an initial assumption, we theorized that emissions should decrease with fuel consumption. In real life, the load dynamics and changes in the engine operation points caused deviation from this assumption. The relative change of the absolute emissions are shown in **Figure 10**. Results show that absolute emissions can be reduced by hybridization. Nitrogen oxide emissions were 15–25% lower and particulate matter emissions were 60–75% lower. Overall, the *Four-pressure* system had the lowest emissions.

The exceptions to the above were carbon monoxide emissions, which showed an increase. The obvious reason for this is the operation points of the engine when hybrid systems are implemented. The new operation points are located in the low load area, load less than 30% of maximum at relative low engine speed. These together mean that the combustion and fuel-air mixture are not perfect. Therefore, in some local points in the combustion chamber, the fuel-air mixture is too rich and combustion lacks oxygen, creating carbon monoxide. For the same reason,

the decrease of hydrocarbons is less than the decrease in fuel consumption because of incomplete combustion resulting in unburned hydrocarbons.

Nitrogen oxide emissions decreased through hybridization but not as much as expected. The reduction was less than the reduction in fuel consumption. Again, the reason for this is the unfavourable engine operation point from an emission formation point of view. The incomplete mixing of fuel and air resulted in very high local combustion temperatures, creating nitrogen oxide.

In terms of particulate matter emissions, the reduction was greater than the reduction in fuel consumption. This is caused by load profile and corresponds the hypothesis that reduction in load changes decreases particulate emission. In the hybrid systems, the load peaks are lower and fewer, which together has a reducing effect on particulate matter emissions and soot. It is known from earlier studies that rapid load changes induce particulate emissions and nitrogen oxide emissions.[2], [4].

The emission limits are defined in the legislation as specific emissions and **Figure 11** shows the results as specific emissions i.e. the emissions are shown in terms of grams per delivered kWh at the engine shaft. Results differed compared to absolute values, and both specific hydrocarbon and specific nitrogen oxide emissions increased when hybridization was applied. This was caused by a non-optimal engine operation point resulting in an incomplete mixture formation and inefficient combustion from an emissions point of view. In contrast to this, specific particulate matter emissions decreased.

It can be deduced that the engine was not optimal sized for this use, because the specific emissions increased through hybridization. Smaller engine, which would operate at a more favourable operating point, would reduce fuel consumption and specific emissions.

The engine did not have any exhaust after-treatment systems and therefore it was expected that the legislation limits (Stage 5, [1]) would not be met. The raw hydrocarbon and particulate matter emission were about 3–4 times higher than the legislation limits, and nitrogen oxide emissions were almost 20 times the limit value. However, the carbon monoxide emissions were only about 10–25 % of the limit value.

5. DISCUSSION

The study was made without any exhaust aftertreatment system and the argument for this choice is: The aftertreatment system would reduce the difference between the studied system, obviously making the differences negligible. The changes in raw emissions give more information on the studied systems and their potential.

The backward simulation method was chosen because it allowed to make the comparison without extensive tuning of control algorithms for each system. Secondly, it made possible that all system made exactly same output work. The drawback of the backward method is that oscillations caused by system dynamics are not taken into account.

The independent metering system is not hybrid system but it was taken with because all studied hybrid systems utilize independent metering principle. This enables to determine the effect of hybridization apart from the independent metering in energy demand of the hydraulic system. The independent metering resulted about 20% reduction in energy need.

Interestingly, the most simplest hybrid system had the second lowest energy need. This is result of electronic load sensing which enables efficient accumulator charging and flow delivery to the actuators.

According the study hybrid systems reduce both fuel consumption and emissions and this study gives one view on this case. The full potential of fuel consumption and especially emission reduction remains unanswered. The main reason to this is engine sizing issue. After hybridization the engine was too big. This very clearly seen from the engine operation points, they located well below 50% of maximum power. However, the engine sizing issue is challenging in applications where the engine supplies many systems with different load demand. In a typical mobile machine the engine serves many systems such as the driveline, crane, and steering. Typically, the maximum power requirement of the driveline and the crane are at same level. Hybrid system with smaller engine and moderate energy storage capacity can fully serve the crane function but the driveline is different because the need of the maximum power lasts longer in time. This would require much bigger energy storage capacity even too big realized by hydraulic accumulator. So, the engine cannot be chosen

according to crane use but according to driveline resulting big engine. From this point of view the results of this study are relevant.

Generalization of the results is always a worth of discussion when a such emission study is made using one application and one engine. The results show the same phenomenon as is observed in the earlier studies; minimizing variations in engine power results reduced emissions. From this point of view, results can be generalized. The absolute values of emission reduction are not applicable directly to other applications, because load profiles vary from one application to other. Also, different engine would give different absolute emission. The hypothesis; the size of the exhaust aftertreatment systems can be reduced by hybridization, cannot be fully guaranteed with these results, the emission reduction is too small. However the *STEAM* and *Four-pressure* systems have highest reduction potential because they decouple pump power demand from actuator power variation and enable engine load stabilization. From cost point of view the *Throttled accumulator* system has low investment costs compared to its benefits. To realize the full emission reduction potential of the hybridization the engine needs to be replaced by smaller one.

6. CONCLUSION

The most efficient system (i.e., the system with the lowest fuel consumption) was the *Four-pressure* system. However, the difference between this system and the *Throttled accu + IMV* system was negligible, and fuel consumption for both was about 40% less than the reference system (*LS-IMV* system).

The initial assumption was that emissions would decrease with fuel consumption. In real life, the load dynamics and changes in the engine operation points caused deviation from this assumption. Overall, the results showed that absolute emissions can be reduced by hybridization. Nitrogen oxide emissions were 15–25% lower and particulate matter emissions were 60–75% lower, with the *Four-pressure* system having the lowest emissions.

Hybridization decreased nitrogen oxide emissions, but not as much as was expected (i.e., the reduction was less than the reduction in fuel consumption). The reason for this was the unfavourable engine operation point from an

emission formation point of view. In terms of particulate matter emissions, the reduction was greater than reduction in the fuel consumption. In the hybrid systems the load peaks were lower and fewer, which had a reducing effect on particulate matter emissions.

As conclusion, it can be stated that all studied hybrid systems reduced remarkably fuel consumption and harmful emissions in the studied use case. The means that the emissions of the diesel engine powered mobile machines can be reduced by hydraulic hybrids.

7. ACKNOWLEDGEMENTS

At the time of the study all authors were employed by Tampere University of Technology. This study was funded by Business Finland.

NOMENCLATURE

<i>AVL</i>	AVL List GmbH
<i>CO</i>	Carbon monoxide
<i>CO₂</i>	Carbon dioxide
<i>HC</i>	Hydrocarbon
<i>HIL</i>	Hardware in Loop
<i>IMV</i>	Independent metering valve
<i>LS</i>	Load Sensing
<i>NO_x</i>	Nitrogen oxides
<i>PEMS</i>	Portable Emission Measurement System
<i>PM</i>	Particulate matter
<i>RWTH</i>	Rheinisch-Westfälische Technische Hochschule
<i>THC</i>	Total Hydrocarbons
<i>g</i>	Gram
<i>kNm</i>	Kilonewton meter
<i>kWh</i>	Kilowatt hour
<i>MPa</i>	Megapascal

REFERENCES

- [1] EU. 2016. Regulation (EU) 2016/1628, 14.9.2016. On requirements relating to gaseous and particulate pollutant emission limits and type-approval for internal combustion engines for non-road mobile machinery, amending Regulations (EU) No 1024/2012 and (EU) No 167/2013, and amending and repealing Directive 97/68/EC
- [2] Hagen, J.R, Filipi, Z.S., and Assanis D.N. (2006) Transient Diesel Emissions: Analysis of Engine Operation during a Tip-In. SAE Paper 2006-01-1151. 2006 SAE World Congress, Detroit (3-6 April 2006).
- [3] Heidari, B. and Marr, L. C. (2015) Real-time emissions from construction equipment

- compared with model predictions. *Journal of the Air & Waste management Association*. Vol. 62, No. 2, 115-125. DOI: 10.1080/10962247.2014.978485
- [4] Ericson, C., Westerberg, B., and Egnell R. (2005) Transient Emission Predictions with Quasi-Stationary Models. SAE Paper 2005-01-3852. Powertrain Fluid Systems Conference and Exhibition, San Antonio, Texas (24-27 October 2005)
- [5] Lindgren, M. (2004) Engine Exhaust Gas Emissions from Non-road Mobile Machinery. Dissertation, Uppsala University, Acta Universitatis Agriculturae Sueciae, Agraria 481. ISBN 91-576-6753-5
- [6] Pult, F. and Geimer, M. (2019) Phlegmatization of a combustion engine for reduction of transient emissions. 16th Scandinavian International Conference on Fluid Power, Tampere, Finland (22-24 May 2019).
- [7] Einola, K. and Kivi, A. (2015) First experimental results of a hydraulic hybrid concept system for a cut-to length forest harvester. The Fourteenth Scandinavian International Conference on Fluid Power, Tampere, Finland (20-22 May 2015), 13 p.
- [8] Erkkilä, M., Bauer, F., and Feld, D. (2013) Universal energy storage and recovery system – a novel approach for hydraulic hybrid. 13th Scandinavian International Conference on Fluid Power, Linköping, Sweden (3-5 June 2013), 8 p
- [9] Linjama, M., Huova, M., Tammisto, J., Heikkilä, M., Tikkanen, S., Kajaste, J., Paloniitty, M., and Pietola, M. (2019) Hydraulic hybrid working machines project – Lessons learned. 16th Scandinavian International Conference on Fluid Power, Tampere, Finland (22-24 May 2019).
- [10] Vukovic, M., Leifeld, R., and Murrenhoff, H. (2016) STEAM – a hydraulic hybrid architecture for excavators. 10th International Fluid Power Conference, Dresden, Germany (8-10 March 2016), 151-162 (Vol. 3).
- [11] Huova, M., Aalto, A., Linjama, M., Huhtala, K., Lantela, T., and Pietola, M. (2017) Digital hydraulic multipressure actuator – the concept, simulation study and first experimental results. *International Journal of Fluid Power*, Vol. 18, No. 3, 141-152. DOI: <http://dx.doi.org/10.1080/14399776.2017.1302775>
- [12] Huova, M., Tammisto, J., Linjama, M., and Tervonen, J. (2018) Fuel efficiency analysis of selected hydraulic hybrids in a wheel loader application. BATH/ASME 2018 Symposium on Fluid Power and Motion Control, University of Bath, UK (12-14 September 2018).

DESIGN AND PERFORMANCE EVALUATION OF NEXT GENERATION CLUTCH CONTROL VALVE

Michael Erhard*, Jörg Schneider, Jan Julius Stein

Thomas Magnete GmbH, Innomotion Park 3, 57562 Herdorf

* Corresponding author: Tel.: +49 2744 929103; E-mail address: michael.erhard@thomas-magnete.com

ABSTRACT

Pressure reducing valves perform various control tasks in mobile machines. In many cases contamination sensitive environments require pilot-operated valves, because of its more robust performance. On the other hand, dynamic valve behavior can be critically in certain applications. Overcoming the restrictions resulting from stand-alone test rig attempts, suitable simulation principles are nowadays the state of art in valve design. Unsuitable model approaches and missing consideration of the application may result in wrong design decisions. This paper discusses two important modeling issues, in particular the solenoid and spool leakage behavior, in combination with the connected system under control, a pressure-actuated clutch. It is shown, that even for standard proportional valves a critical view on customers' excitation strategy and site of installation decides on success or failure of an already used design variant.

Keywords: Pressure Valve, Holistic Simulation, Clutch Control

1. INTRODUCTION

Proportional pressure reducing and relieving valves for pilot applications are together with pilot-operated variants for clutch or fan drive control the main business segments at Thomas Magnete GmbH in the field of mobile machinery. Current developments are aimed among other things at mechatronic subsystems with integrated electronic and possible electro-mechanical actuation. Nevertheless, the continuous development of existing products is a guarantee for further success in the market.

Typical valve variants in use consist of a solenoid mechanical connected to a valve spool, whereas the regulated pressure is directly balanced by the solenoid or a so called pressure pin is inserted as an intermediate element. In contrast to these so-called direct-operated valves, pilot-operated ones uses a hydraulic coupling between the valve spool and the solenoid-controlled pilot stage. This increase in physical complexity may cause problems in some applications, especially under dynamic aspects. Besides step responses, continuous transient input variations as they occur in clutch control applications are also significant. Under unfavorable boundary conditions and fast

transients, inadequate pressure control can sometimes be observed. **Figure 1** illustrates the above mentioned product family with the focused valve at the bottom.

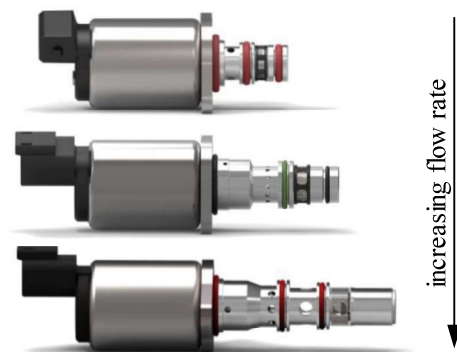


Figure 1: Typical proportional pressure reducing valves with different flow capacity

The article is organized as follows: The 2nd section discusses necessary modeling challenges with special focus on solenoid and spool leakage behavior for a reference valve design. A complete simulation model for typical valve characteristic curves and controller performance, including the pressure-actuated clutch, is mentioned. In the 3rd section modeling basics are used to validate test rig observations from the reference valve design with special focus on pre-developed modeling

approaches. Resulting from this, requirements for a further development avoiding poor dynamic pressure control behavior are identified. The 4th section explains simulation-based design changes and their validation on the test rig. The 5th section summarizes the content of this article.

2. MODELING CHALLENGES

From a control engineering point of view, proportional pressure reducing valves are closed-loop controllers for an output pressure with an electric input specification under a hydraulic disturbance. Otherwise, these electro-hydraulic valves yield from a mathematical perspective an initial value problem arising from a system of stiff nonlinear differential equations as indicated in Equation 1.

$$\dot{\vec{x}} = f(\vec{x}, t) \quad (1)$$

Thus the modeling task is clearly defined. Relevant equations for the different physical domains have to be combined according to the functional structure shown in **Figure 2** resulting in a dynamic model for the entire valve.

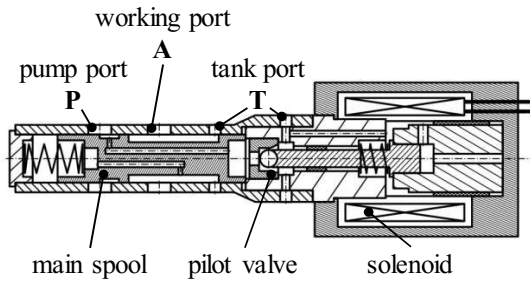


Figure 2: Sketch of investigated valve and its cross-elementary interactions

This model must fulfill the requirements from the controller site meaning besides boundary conditions only time-dependent input and disturbance variations are allowed as “external” model inputs. The controlled pressure results only from the intrinsic closed-loop controller properties.

2.1. Solenoid dynamics

A main component of the entire valve is the electro-magneto-mechanical transducer. A holistic approach should include its position- and current-dependent force characteristic as well as its transient relations between voltage, current and force respectively. Thus the solenoid alone

represents a MIMO system with two inputs and two outputs [1]. Various authors have investigated different approaches to model these system structure based on flux linkage [1], coupled reluctance networks [2] or electric equivalent circuits [3, 4]. Essential differences arise from dealing with eddy currents and moving induction. The parameter for these models are often determined with latest finite-element-methods.

Starting point of the dynamic model development is the electric equivalent circuit approach including eddy currents and moving induction. The necessity results from experimental observations with the reference design shown in the 3rd section whereas different excitation strategies in solenoid current control mode strongly influence accuracy and smoothness of the transient closed-loop pressure control.

Benchmarking several model structures and parameter schemes yield a promising result illustrated in **Figure 3** with governing Equations 2 - 4. This approach models the nonlinear time lag between voltage U_{coil} and current i_{coil} taking into account the additional time lag between current and force F_{arm} because of eddy effects ($i_{eddy_f} + i_{eddy_s}$).

$$\frac{\partial i_{coil}}{\partial t} = \frac{1}{\frac{\partial \Psi}{\partial i_{coil}}} \cdot \left(U_{coil} - R_{coil} \cdot (i_{coil} + i_{eddy_f} + i_{eddy_s}) - \frac{\partial \Psi}{\partial x_{arm}} \cdot \frac{\partial x_{arm}}{\partial t} \right) \quad (2)$$

$$\frac{\partial i_{eddy_f}}{\partial t} = \frac{1}{L_{eddy_f}} \cdot (U_{coil} - R_{coil} \cdot (i_{coil} + i_{eddy_f} + i_{eddy_s}) - R_{eddy_f} \cdot i_{eddy_f}) \quad (3)$$

$$\frac{\partial i_{eddy_s}}{\partial t} = \frac{1}{L_{eddy_s}} \cdot (R_{eddy_f} \cdot i_{eddy_f} - R_{eddy_s} \cdot i_{eddy_s}) \quad (4)$$

Main advantage of this model structure is its range of validity and the straightforward and automated parameter identification procedure easily realized on the basis of static FEM calculations for obtaining the well-known flux linkage $\Psi(i_{coil}, x_{arm})$ and a very small number of dynamic computations for determination of

eddy current parameters $R_{eddy_f,s}$, $L_{eddy_f,s}$.

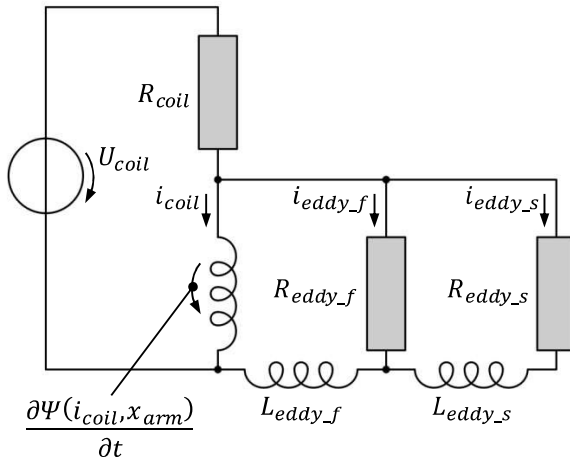


Figure 3: Equivalent electric circuit for proportional solenoid

Using the solenoid illustrated in Figure 2 and above mentioned implementation procedure the content of **Figure 4** shows the obtained results in comparison with FEM calculations. The nonlinear differential inductivity is captured very well, also the saw-tooth-like distortion of the current signal in presence of eddy currents.

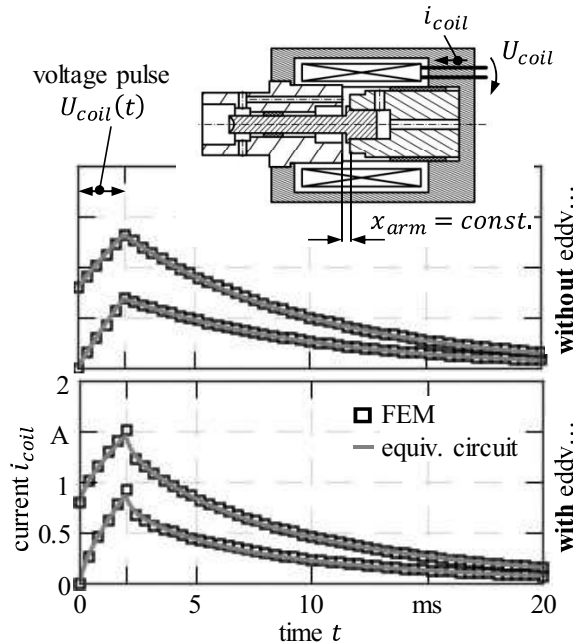


Figure 4: Verification of elaborated model structure

This model extended by a current controller for dither waveforms is well suited for the intended improvement of the reference valve design.

2.2. Spool leakage

In addition to the solenoid model, the leakage

characteristic at the main spool plays an important role in obtaining a generally applicable hydraulic model of the entire system. The reasons are as various as the different test conditions and procedures for this type of valves. While the valve manufacturer typically tests with working port closed, the performance in clutch applications for example can be totally different. Main reason for this is the regularly used positive overlap at the main spool. This leads to miscellaneous operating conditions whereas the traveling range of the main spool either lies completely in the overlap region or partial opening at pressure and tank port happens.

The requirements for such a combined orifice-leakage model arise on one hand from a mathematical point of view ensuring sufficiently smoothness and finiteness. On the other hand, the model approach has to guarantee a physically meaningful behavior. Finally, from the user's point of view, a geometrically based parameter selection should be possible.

The idea behind the utilized model is visualized in **Figure 5**, which is divided into three different stroke ranges for the spool depending on the geometrical overlap. In every spool stroke region parallel flow paths for orifice and leakage flow are present. Fluid flow based on orifice equation through the lateral surface at the bores opened by spool travelling is only existent in the “transition” and “open” state, otherwise it is blocked.

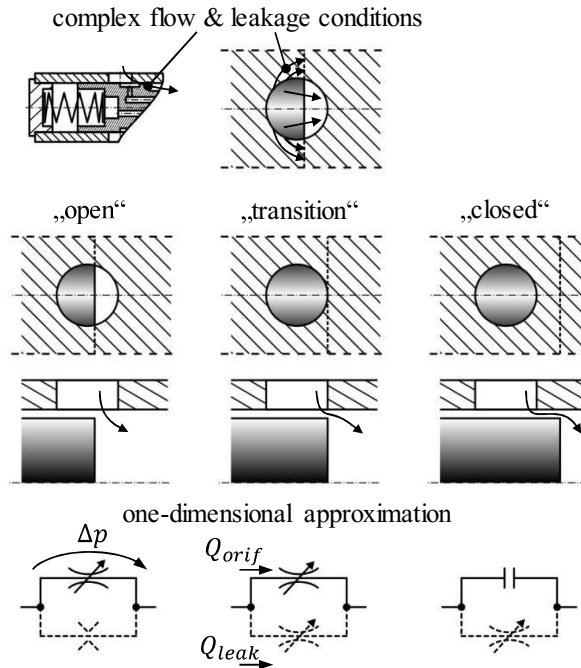


Figure 5: Hydraulic resistance network for fluid flow in different spool travelling regions

Besides the above mentioned regular modeling approach for hydraulic resistances, the parallel leakage path completes the model. This flow path guarantees that in operation situations with closed working port physical meaningful results are obtainable. Therefore, a change in flow rate with varying spool position is absolutely required. The modeling in the “closed” state follows the standard leakage equation whereas geometrical and modeled leakage lengths are shifted relative to each other. Because for zero leakage length fluid flow raises to infinity, some kind of limitation is inevitable. This is done by assuming orifice flow through the cross-sectional area of the leakage gap along the perimeter of the spool as sketched in Figure 5. This raw simplification depends only on geometrical parameters and is easily adjusted by scaling the area of the remaining leakage gap. A smooth crossover in the “transition” region between the “open” and “closed” state is ensured by interpolating the coefficient of resistance in a special manner as shown in Figure 6.

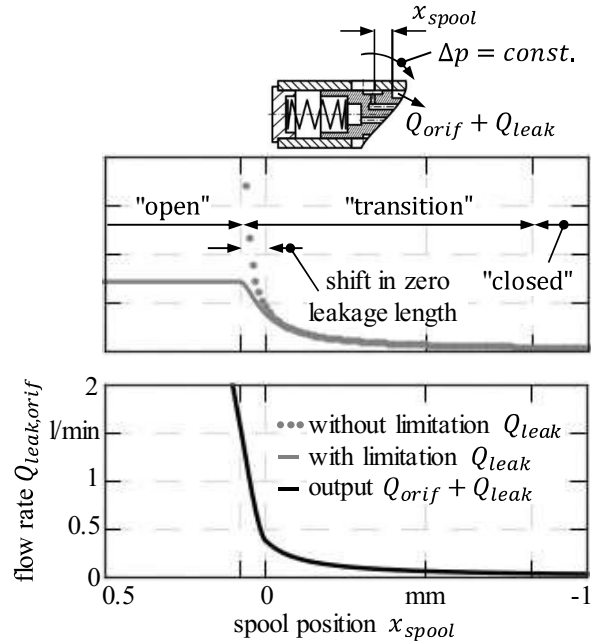


Figure 6: Exemplary simulation results for complete flow rate approximation

Like in the case of solenoid behavior, a better approximation can be achieved by incorporating additional results from numerical field simulation. Even without further effort, this model based on geometric data is more suitable than others for typical computations.

2.3. Pressure-actuated clutch

The final modeling challenge is to consider the customer’s use case. This goes beyond standardized test procedures, but enables an application-oriented evaluation and adaption. A common simplification for a hydraulic clutch actuator is a spring-loaded piston. Here, the filling phase is emulated through the parameters piston area & piston stroke. The load-transmitting behavior of the clutch plates leads to an additional micro-movement, which can be easily implemented via a non-linear spring or a non-linear elastic end stop. Figure 7 illustrates the used model structure with a sketch of two underlying spring characteristics.

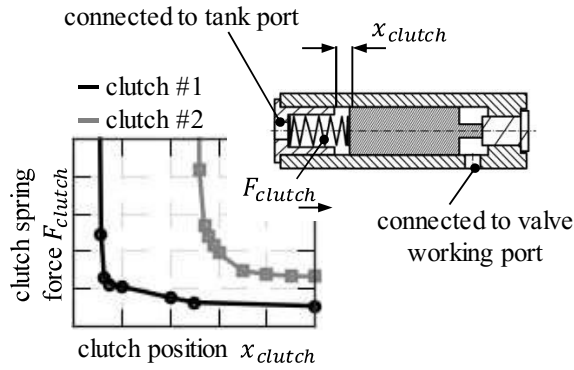


Figure 7: Simplification of pressure-actuated clutch

The parameters of the reduced model place pressure and flow requirements on the connected pressure control valve and have a direct effect on valve design and combined valve-clutch performance.

3. REFERENCE DESIGN

The valve behavior of a reference design is to serve as a starting point for further investigations. Beginning with the explanation of the inherent characteristics of the system, the performance evaluation differentiates between the valve alone and the additionally connected clutch. Measurements on a test bench are compared with the simulation results to confirm the application of the developed model for further simulation-based enhancements of the valve design.

3.1. Quasi-static characterization

Besides the flow capacity of the entire valve, the pressure signal characteristic curve is an important valve feature for reasons of interchangeability. The plotted curves in **Figure 8** show a typical behavior observed in pressure control valves, whereas some main stage and clutch parameters can be read off the measurements. Under both boundary conditions, closed working port or with connected clutch, no functional anomalies occur.

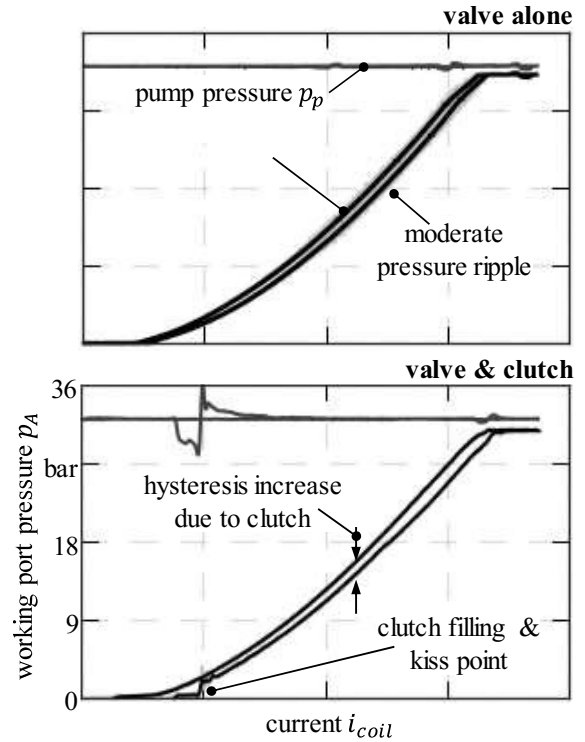


Figure 8: Measured characteristics of valve alone and valve with connected clutch under dither excitation

The static measurements could allow the conclusion that the valve used is suitable for clutch applications and test bench results of the valve alone are sufficient. However, a final evaluation requires at least the inclusion of an additional dynamic characterization.

3.2. Transient input variations

The dynamic investigations are based on typical control profiles for clutch valves as listed in [5]. Here step profiles are used for filling of the clutch and ramp profiles for load transfer. For ease of use, these profiles are separated into different step and ramp profiles and tested sequentially at the test bench. The **Figures 9 - 10** show the obtained results clearly visualizing dynamic anomalies in clutch operation whereas valve alone behavior is completely unremarkable.

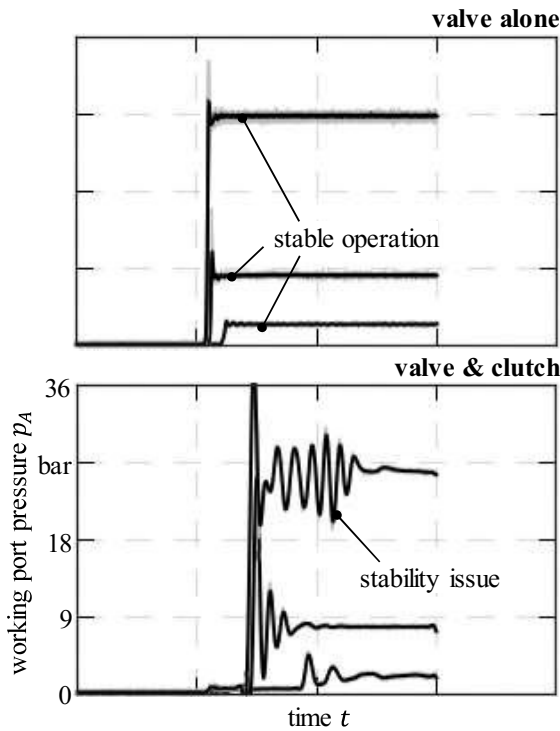


Figure 9: Measured step responses of valve alone and valve with connected clutch under dither excitation

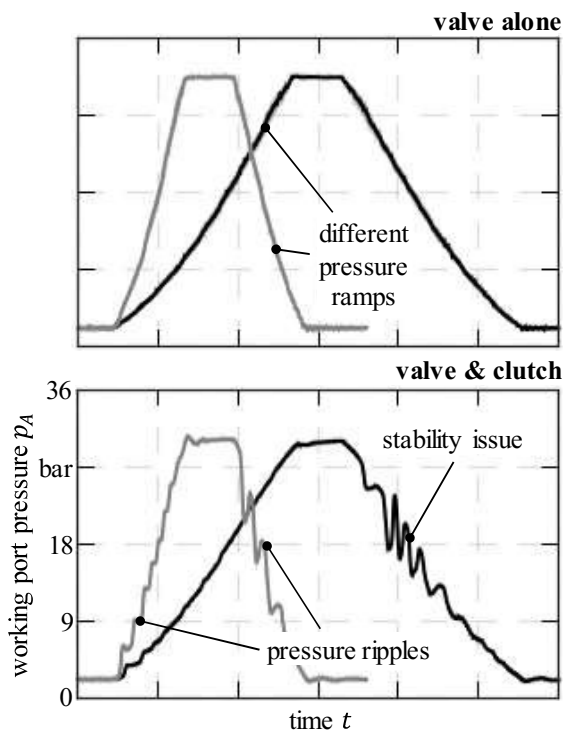


Figure 10: Measured ramp responses of valve alone and valve with connected clutch under dither excitation

Based on these results, valve selection neglecting the field of application can be misleading as well

as designing valves without a detailed consideration of the application case during the development. This is a challenge for the valve manufacturers because the success partially depends on the cooperation with the system or machine supplier.

At this point the metrological characterization ends. The results show a significant difference between the different measurement conditions and motivate the subsequent simulation studies for the reference and next generation design.

3.3. Simulation results

Further development of pressure control valves based on simulation models is state-of-the-art in development departments, which is why the focus of this section is limited to some results of special interest.

Using the results from ramp profiles the necessity of the modified leakage model for an adequate calculation of valve performance is demonstrated. In the valve only case, during the ramp profile the main spool primarily operates in its dead band as illustrated in **Figure 11**.

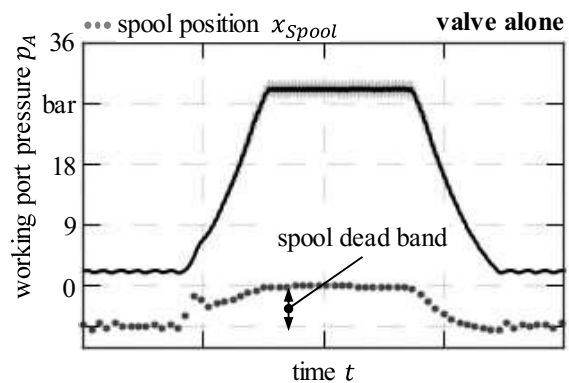


Figure 11: Simulation result for spool position during operation with closed working port

At the same time, Figure 11 also shows that the pressure ripple behavior and overall stability is in equivalence to the measurements for the valve only case.

Although the pressure fluctuations due to dither excitation are plausible, there is an essential point not governed by the simulation model. The lack of a dynamic hysteresis model leads to a disappearing hysteresis in the entire system regardless of the cause of hysteresis. However, since all measurements show a remaining hysteresis, an influence of this inadequacy on simulation accuracy can be

suspected. This becomes particularly clear in the ramp behavior of the valve with connected clutch under dither and dither free current excitation as displayed in **Figure 12**. With dither excitation, the pressure build-up and release behavior of the pilot valve differs from dither free excitation resulting in a noticeably different transient response.

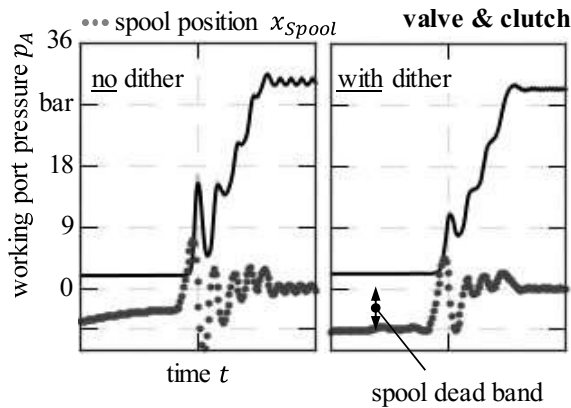


Figure 12: Influence of current control on simulated ramp behavior with connected clutch

As long as the model does not reflect this, deviations in simulated dynamics can be assumed. Another source of uncertainty is the simplified clutch with its not fully known properties.

The two previous examples illustrate the necessity for the modified leakage model to describe the flow rate behavior of the main spool and the solenoid model to map the dynamic force excitation at the pilot valve.

Further validation focusses on the ramp behavior because of its importance for clutch control. **Figure 13** illustrates the final comparison between valve alone and valve with connected clutch. Differences in the simulation results are not as clearly visible as in the measurements in Figure 10. Nevertheless, problem areas can be identified in some regions of the transient response. Compared to measurements, the pressure fluctuations are smoothed out, whereby the cause can be the hysteresis behavior mentioned earlier or different or unknown clutch parameters.

With the present results, a starting point for further improvements of the reference design is given. The focus of the optimization is still the response behavior to transient input signal variations.

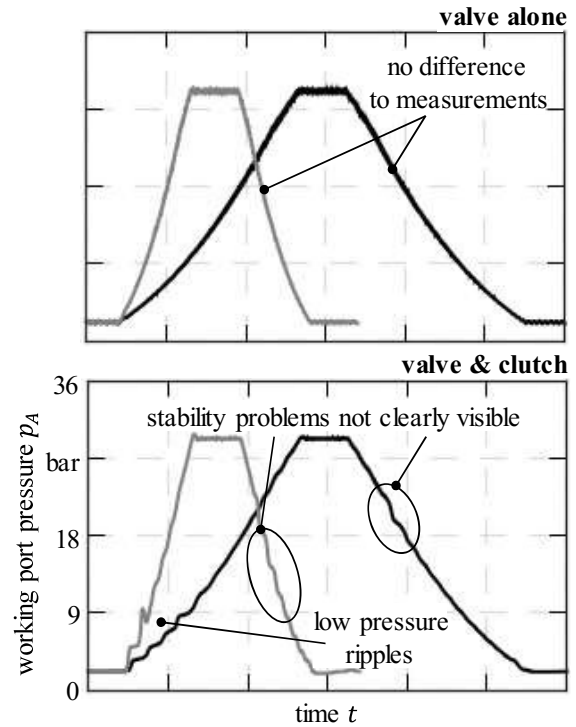


Figure 13: Simulated ramp behavior under dither excitation

4. NEXT GENERATION DESIGN

The aim of this section is to explain and present ideas for improving the dynamic response behavior. As mentioned in the previous section, the spool dead band, the dither excitation of the solenoid and the main spool travel influence the pressure characteristic and the pressure fluctuations. At the end, the suggestions for improvement are validated at the test bench.

Beginning with the pilot part of the clutch control valve from Figure 2, the pressure build-up and release during dither excitation is mainly determined by the amplification factor between opened flow surface and sphere travel. This results from the possible stroke changes due to dynamic solenoid force amplitudes during dither excitation. Another influence factor lies in the armature damping, here a middle way between stability and response time is essential.

At the main spool the situation is much more complex. On the one hand, the dead band of the main spool controls the leakage behavior but slows down the transient response by the time required for the opposite closing or opening of pump and tank port. On the other hand, spool response due to pressurization is influenced by spring forces and hydraulic counterforces from

the opening and closing of the pressure and tank port. Care must be taken during adjustment of the main spool spring, as this will compromise interchangeability due to changes in the pressure signal characteristic curve.

The solution is achieved by targeted scanning of the solution space with plausible combinations of the underlying design variables or parameters. A major problem in the evaluation of every single solution were minor changes observed in the simulation result due to the filtering effect of the dither excitation.

Because the solution with closed working port is totally uncritical, afterwards only the simulation results with connected clutch are shown in **Figure 14**. Despite the only slight change in performance, an improvement is evident. For better visualization, the transient responses are shifted against each other by a small amount. The simulation results motivate the investigation of a hardware prototype to validate the computations and to confirm the interchangeability by means of pressure signal characteristic curve. Therefore, the measurements shown in Figures 8 - 10 are repeated under comparable operating conditions.

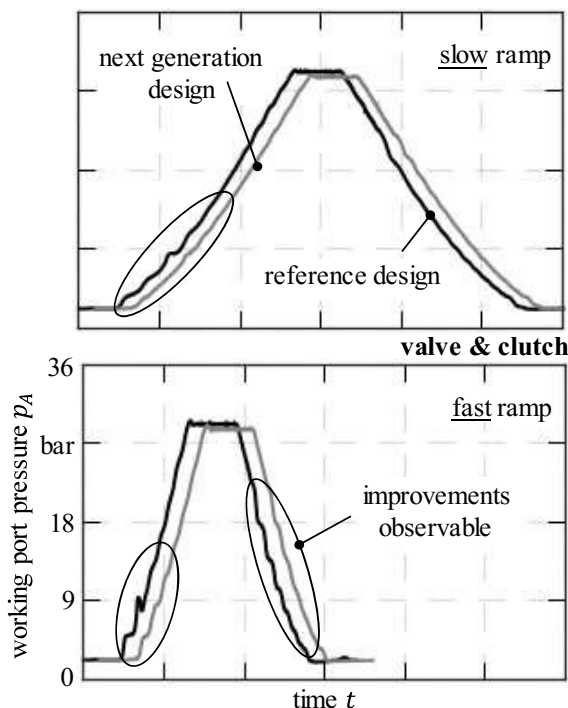


Figure 14: Ramp behavior with connected clutch under dither excitation after simulation-based optimization

The final measurement of the hardware prototype yields very promising results in contrast to the

reference design. The ramp behavior shown in **Figure 15** is completely uncritical and the comparability between valve alone and valve with connected clutch is almost given.

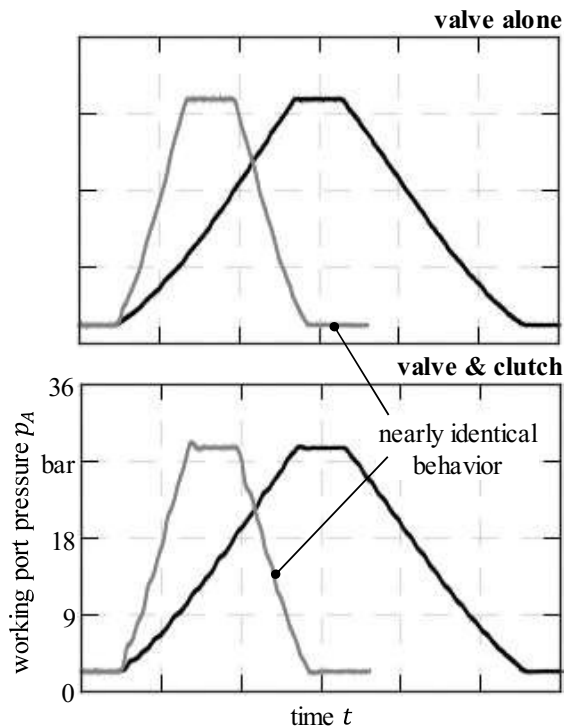


Figure 15: Measured ramp responses of valve alone and valve with connected clutch under dither excitation

A shortened summary of the remaining static and dynamic characterization is shown in **Figure 16**. In the upper part, the interchangeability between the reference and the next generation design is clearly visible. Additionally, an improvement in hysteresis is observable. The lower part visualizes the transient step responses. In comparison to Figure 9 a significant better damping is present and no anomalous vibrations occur.

The received results promise significantly better performance in the customer system by full interchangeability. At the same time the design could be simplified, which has a positive effect on assembly and costs.

5. CONCLUSION

The paper discussed two important modeling challenges for investigated pilot-operated pressure reducing valve used in clutch control applications. It was shown, that spool leakage dominates the static and transient system

behavior in the case of closed working port. The necessity of an accurate solenoid model resulted from the dither excitation used. Without consideration of the clutch, valve optimization was not possible because of missing operating failures as a starting point for improvements.

Despite the slightly difficult comparison of the simulation results an improved solution could be found. Measurements confirmed the predictions and encouraged the approach chosen. Some modeling issues remained unanswered. This applies to the dynamic hysteresis and the clutch modeling and its parameters. These uncertainties provide a basis for further investigations.

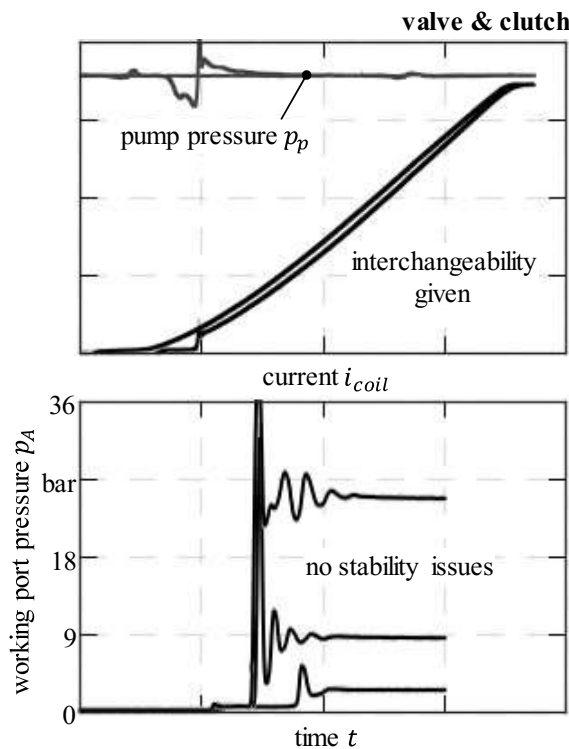


Figure 16: Measured characteristic curve and step responses of valve with connected clutch under dither excitation

NOMENCLATURE

F_{arm}	Armature force [N]
F_{clutch}	Clutch counter force [N]
i_{eddy}	Eddy current [A]
i_{coil}	Coil current [A]
L_{eddy}	Eddy inductance [H]
Δp	Pressure difference [bar]
p_A	Working port pressure [bar]
p_P	Pump pressure [bar]
p_T	Tank pressure [bar]
Q_{leak}	Leakage flow rate [l/min]

Q_{orif}	Orifice flow rate [l/min]
R_{coil}	Coil resistance [Ω]
R_{eddy}	Eddy resistance [Ω]
t	Time [s]
U_{coil}	Coil voltage [V]
\vec{x}	State variable [-]
x_{arm}	Armature position [mm]
x_{clutch}	Clutch position [mm]
x_{spool}	Spool position [mm]
Ψ	Flux linkage [Wb]

REFERENCES

- [1] Cristofori A, Vacca A (2012) The Modeling of Electrohydraulic Proportional Valves. *J Dyn Sys Meas Control*. 134(2):021008
- [2] Kallenbach E, Ströhla T (2002) Dynamic Simulation of Electromagnetic Actuators using Network Models Including Eddy Currents. In: *Proc 8th Int Conf New Actuators (ACTUATOR 2002)*, Bremen, 12-14 June 2002
- [3] Vaughan N D, Gamble J B (1996) The Modeling and Simulation of Proportional Solenoid Valve. *J Dyn Sys Meas Control*. 118(1):120-125
- [4] Biller H (2008) Dynamic Simulation of Electromagnets. In: *Proc. European Comsol Conference*, Hannover, 4-6 November 2008
- [5] Schmidt T et.al. (2005) Verfahren zum Steuern und Regeln eines Automatikgetriebes eines Fahrzeugs. DE102005042933A1, 9 Sept 2005

ACTIVE AUTOMATIC CHASSIS ACTUATION FOR AN EXCAVATOR

Christoph Boes

Moog GmbH, Hanns-Klemm-Str. 28, 71034 Böblingen, Germany

Tel.: +49 7031 622-207; E-mail address: cboes@moog.com

ABSTRACT

This paper shows an electrohydraulic control system to stabilize the chassis of a mobile machine driving across an off-road ground profile. The active hydraulic suspension system is based on new electronics, SW- and control architectures and the use of state of the art industrial components. The paper shows, that the static and dynamic performance of the system is dominated by the servo valve, which represents the central component of the system.

Keywords: Chassis Stabilization, Force Control, Active Suspension, Construction Machines, Forest Machines

1. INTRODUCTION

Mobile machines have been characterized by a limited increase of productivity over the last years compared to the industrial machinery. Now these markets are indicating several efforts to increase the productivity, the connectivity and the grade of automation in parallel with investigations to reduce the energy consumption of these systems. Typical phases of this development from manual operated machines to complete autonomous machines are

- Operator/driver assistance systems
- Teleoperated machines
- Autonomous machines



Figure 1: Spyder Excavator

Spider excavators as shown in **Figure 1** are designed for operation in difficult terrain and areas, which are typically not easy to access. The number of skilled operators for these machines is limited and the biggest challenge is handling of the chassis actuators. This paper shows the

development of a high-performance servo hydraulic actuation system for such mobile machines to allow an “easy drive” and/or teleoperated driving and later on an autonomous driving mode.

The stabilization of the vehicle platform during off road driving requires extreme high loop gains or performance in the force loops of the actuators. Typical mobile solutions based on proportional valves in combination with LS valves cannot fulfil these dynamic requirements. Industrial components, especially industrial direct drive servo valves fit much better to this application. In addition to the high bandwidth of the control valves typical industrial controller structures and elements like electronic pressure compensation, additional feedforward structures and gain scheduling are used to implement the dynamic stabilization of the platform.

2. SYSTEM ARCHITECTURE CHASSIS

The chassis is equipped with 12+2 actuators as shown in **Figure 2**. Each leg consists of 3 actuators for

- Vertical movement
- Horizontal movement
- Steering

The chassis stabilization is done by the vertical actuators. The actual position of the other actuators is used for the kinematics and inverse kinematics calculation.

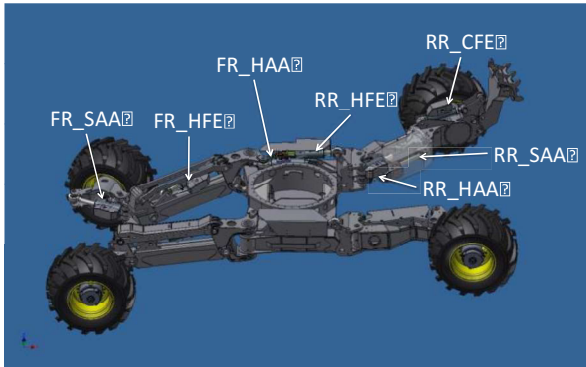


Figure 2: Chassis Actuators

The schematic sketch in **Figure 3** shows the physical principal of used pendulum arm suspension. The kinematics could be linearized by a gear ratio of 3.98, which means 1 mm stroke of the hydraulic actuator effects a lift of the vehicle by 3.98 mm.

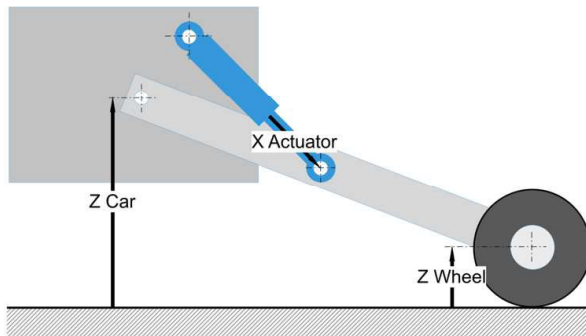


Figure 3: Pendulum Arm Suspension

2.1. Electronic Topology

The architecture of the chassis of the machine is based on a central controller unit, calculating demand values of the four-wheel ground contact forces and decentralized control loop structures integrated into the servo actuators as shown in **Figure 4**.

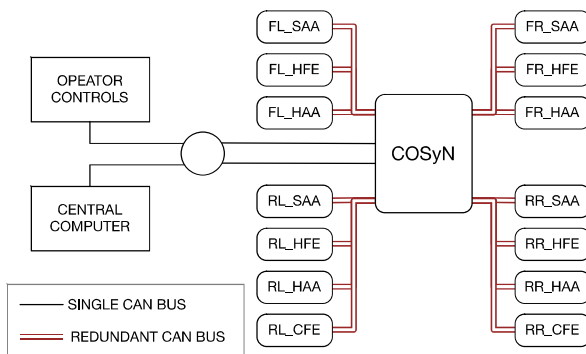


Figure 4: System Layout

The demand values for the high dynamic force loops are calculated by use of IMU / gyros and

the online calculation of the inverse kinematics of the machine. The system is over determined and the solution is online solved numerically.

2.2. Hydraulic Layout

The hydraulic layout of a standard mobile machine in form of a central control manifold with standard proportional valves and LS valves and rubber hoses connecting the manifold and cylinder wouldn't allow the implementation of closed control loops with high dynamic performance. The controlling servo valve has been mounted directly on the hydraulic cylinder to minimize the impact of the hydraulic capacity between servo valve and hydraulic cylinder as shown in **Figure 5**.



Figure 5: Hydraulic Actuator

The servo valve is integrated into a manifold, which contents all additional safety and measurement features.

The check valves CV1 and CV2 in **Figure 6** are used to freeze the actuator in fail safe situations and protect the other hydraulic equipment against extreme pressures in the cylinder chambers, which could be effected by the kinematics of the machine while digging. The check valves and the supply pressure connection SO1 valve are operated by a small solenoid valve SO2, which can be deactivated by the internal SW and the external HW.

The actuator system contents all sensors and transducers to close the loops for

- Force control
- Position control
- Velocity control

in form 3 of pressure transducers, position transducer, IMU and temperature sensor.

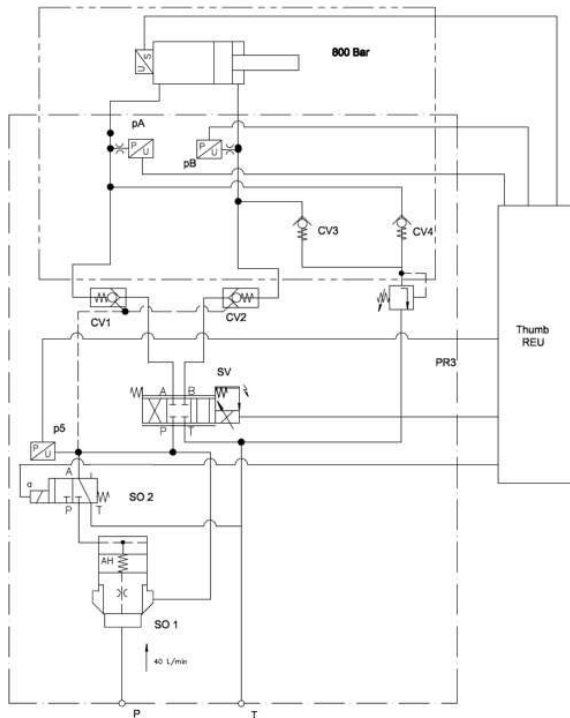


Figure 6: Hydraulic Circuit of the Actuator

Due to the dimensions of the circuit board of 55x25 mm as shown **Figure 7** the complete electronics could be integrated into the manifold of the actuator.



Figure 7: Actuator Electronics

2.3. Controller Structure

The central computer in **Figure 4** and **Figure 8** calculates the demand values for the internal control loops of the actuators. In the automatic chassis stabilization mode this means the demand value for the ground contact force of the wheels. The force-, position- and velocity-loop in **Figure 9** are arranged as alternating loops depending of the commanded Control Mode. These loops command the two internal cascaded

loops of the servo valve in form of spool loop control and current control.

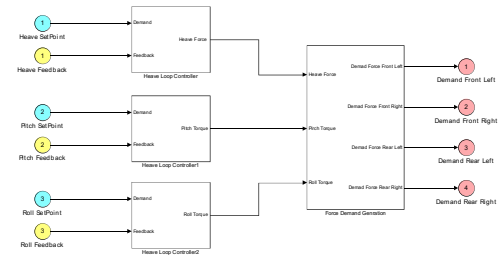


Figure 8: Chassis Controller Structure

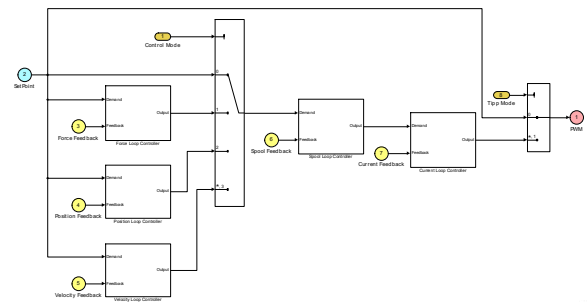


Figure 9: Actuator Controller Structure

The dynamic performance of the complete chassis stabilization system is characterized by the performance or bandwidth of each of the cascaded internal loops and will be discussed in the following.

3. REFERENCE TRACK

For the investigation of the performance of the chassis stabilization system a reference test track is needed. The discussed machine shows similarities or characteristics, which are close to forest machines. The Skogforsk Institute in Upsala/Sweden has designed a test track to test the characteristics of the suspension systems of harvester and forwarder machines [1].

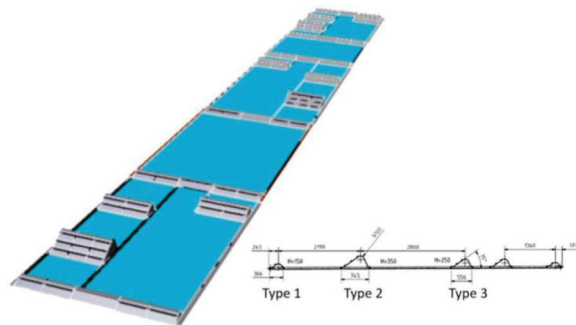


Figure 10: Skogforsk Reference Track

The test track shown in **Figure 10** and **Figure 11** implements a series of defined obstacles for the

left and right wheel track. The obstacles are characterized by a rising slope of 35° and a falling slope of 65° with 3 different altitudes of 150/250/350 mm. The typical driving speed for the forest machines in off road terrain and across this track amounts between 0.2 m/s and 1 m/s.

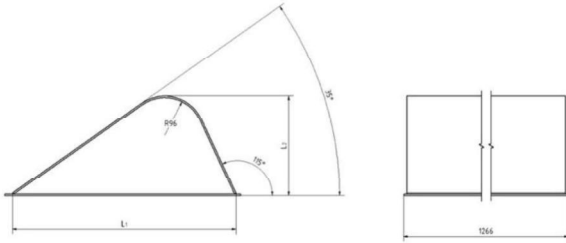


Figure 11: Obstacles of Skogforsk Reference Track

For the discussed excavator a driving speed of $1 \text{ m/s} = 3.6 \text{ km/h}$ has been chosen as a reference.

The shown test track is easy to implement in a simulation model and has been used in the simulation models to design and investigate the chassis control system.

4. SIMULATION MODEL

In parallel to the tests on the real machine simulation models in form of complete car model and quarter model for more detailed and reproducible offline investigations have been developed. The tuned control parameters in the model and real machine deviate 10%, so that the models seem to be precise enough.

4.1. Quarter Car Model

The ridged body model of the complete vehicle is characterized by a certain complexity and has several degrees of freedom. The force control loop could be identified as the dominant element determining the performance of the complete system.

The quarter car model has been established as powerful and effective tool for the study of the suspension system itself in vehicle dynamics. **Figure 12** shows the reduced one-dimensional model of the vehicle as a two-mass-spring-damper-system. The tire is shown as a combination of spring and damper, which effects only pushing forces. The wheel mass is actuated by the tire forces and the force of the hydraulic suspension actuator, considering a linear gear kinematics between vehicle body and the wheel as shown in **Figure 3**.

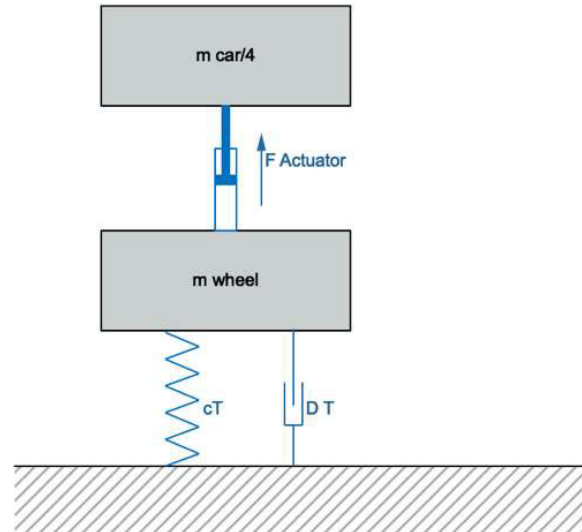


Figure 12: Quarter Car Model

Only a quarter of the mass of complete vehicle has been considered in the reduced one-dimensional model of the vehicle.

The force loop controller is based on a linear core with several non linear compensation features. The step response of the force control loop in **Figure 13** shows an aggressive, but robust tuning. The overshoot will be filtered out by low frequent vehicle dynamics while the focus more on an instant following the change in the demand value.

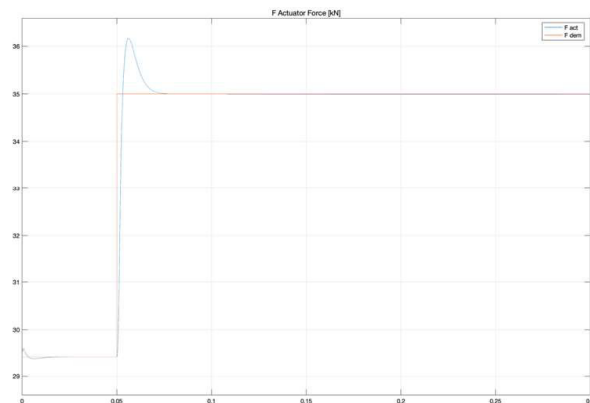


Figure 13: Actuator Force Step Response

The shown force loop tuning is now used to study the characteristics of the suspension system driving across the standardized obstacles. The plots in **Figure 14** indicate 3 critical phases passing the obstacle:

1. Transition from the flat into the rising slope
The gravity force supports the compensation of the suddenly appearing vertical velocity of the

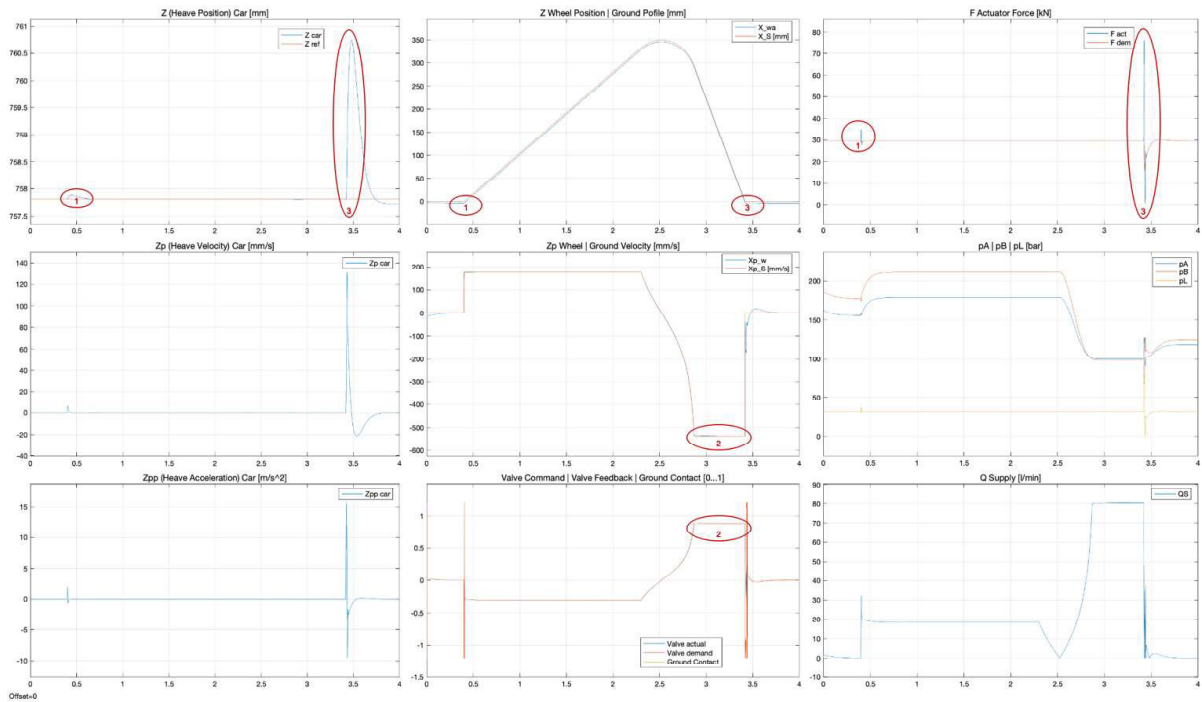


Figure 14: Quarter Car Simulation of one Obstacle, Driving Speed 0.25 m/s

wheel. The high bandwidth of the force loop in combination with inertia of the whole system effects an acceptable lift in the vehicle entering the rising slope of the obstacle.

2. Falling slope with high vertical velocity

This phase of the obstacle is not supported by the gravity force – the actuator has to press the wheel actively down on the ground. The chosen driving

speed of 0.25 m/s indicates also that the system is close to the static flow limits of the servo valve.

3. Transition from falling into flat slope

Entering again the flat slope coming from the falling slope with high velocity represents the most critical phase. During all phases the force controller presses the wheel on the ground with a force, which is equivalent to the gravity force.

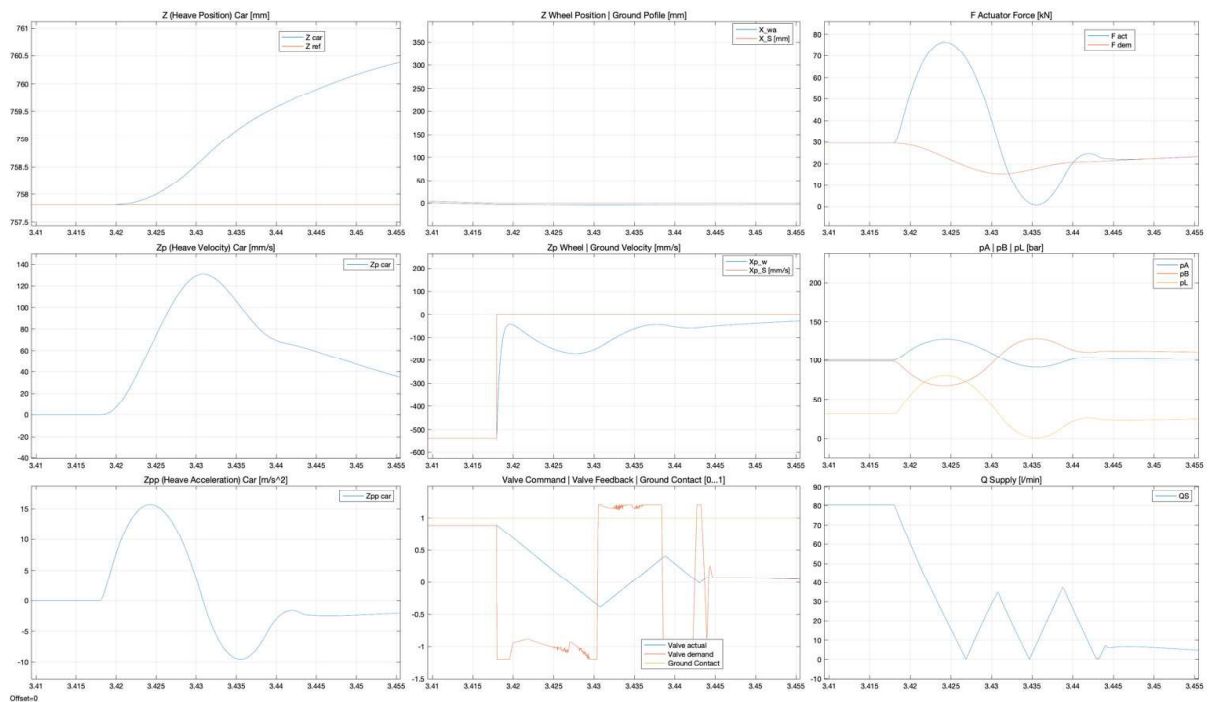


Figure 15: Quarter Car Simulation of one Obstacle, Zoom into Phase 3, Driving Speed 0.25 m/s

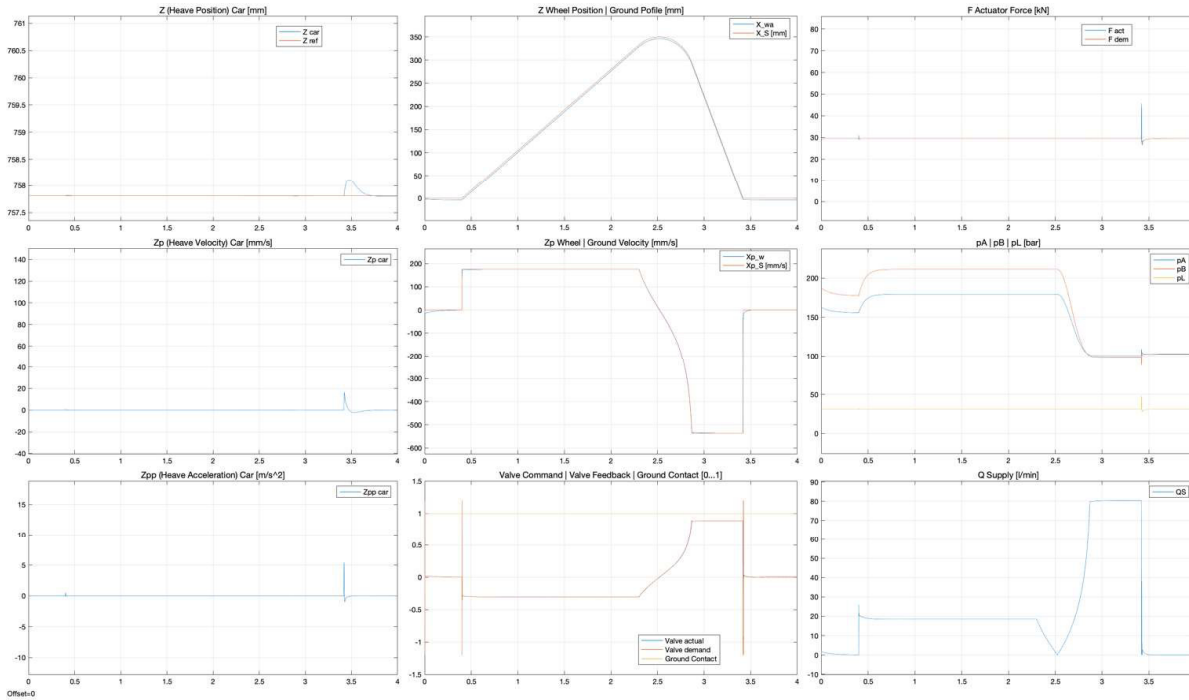


Figure 16: Quarter Car Simulation of one Obstacle, High Response Servo Valve, Driving Speed 0.25 m/s

This force demand level is adjusted by the heave position controller. The challenge of the transition into the flat domain is the high velocity of the wheel system, actively driven by the hydraulic suspension actuator.

Figure 15 shows a zoom into the critical transition phase. The vertical ground speed changes immediately to zero which effects an increase of the ground contact force. The force controller commands the servo valve to maximum negative opening. The spool of the servo valve follows now the command signal with a limited velocity, which means the spool is still on the positive side, while commanded by negative values.

The used servo valve is characterized by a step response time for a 0→100% step of 10 ms. A rework of the valve internal controller structure and the hardware of the valve in form of the linear force motor allows a significant improvement of the dynamic performance of the servo valve. The increase of the bandwidth is one of the well synergy effects, but the focus in this application is on the reduction of the step response time for large magnitudes. The details of this modification of the servo valve are not shown here. All together these changes effect a step response time of 3.5 ms for a 0→100% step and backwards.

Figure 16 shows the impact of the reduced valve response time on the force control loop and therewith on the complete active suspension

system. The scaling of **Figure 14** and **Figure 16** have been chosen equivalent to demonstrate the impact of the dynamic performance of the servo valve.

4.2. Complete Car Model

The focus in the quarter car model was on the tuning of the single control loops and the impact of the component characteristics on the system behaviour. The transition from the one dimensional car model to the complete car model allows the investigation of the complete system.

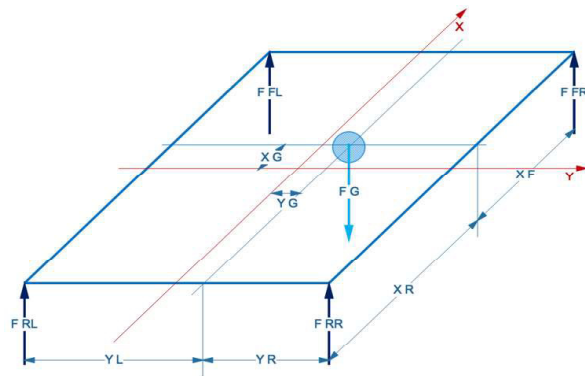


Figure 17: Complete Car Ridged Body Model

The ridged body model for the complete vehicle as shown in **Figure 17** calculates the vehicle dynamics as an impact of 5 forces and their actual locations:

- The 4 ground contact forces of the wheels

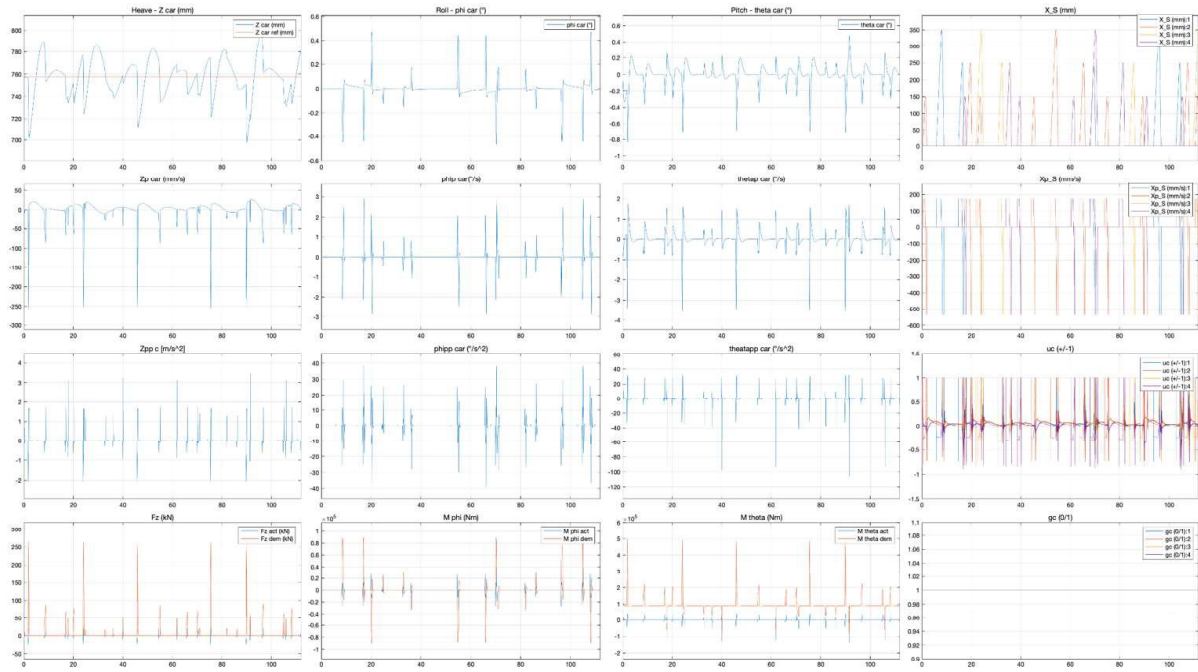


Figure 18: Complete Machine across complete the Test Track, Driving Speed 0.25 m/s

- The gravity force of the complete system

Figure 18 shows the machine driving across the complete test track at a speed of 0.25 m/s. All control loops on machine stabilization and actuator level are working properly at this driving speed without exceeding the limitations of the loops. The maximum values of heave, pitch and roll movements and accelerations allow comfortable drive of the vehicle across the test

track.

Figure 19 shows the same track and driving speed (0.25 m/s) on actuator level. The force plots in the second row of the plots indicate the unbalanced position of the centre of gravity biased to the front axle.

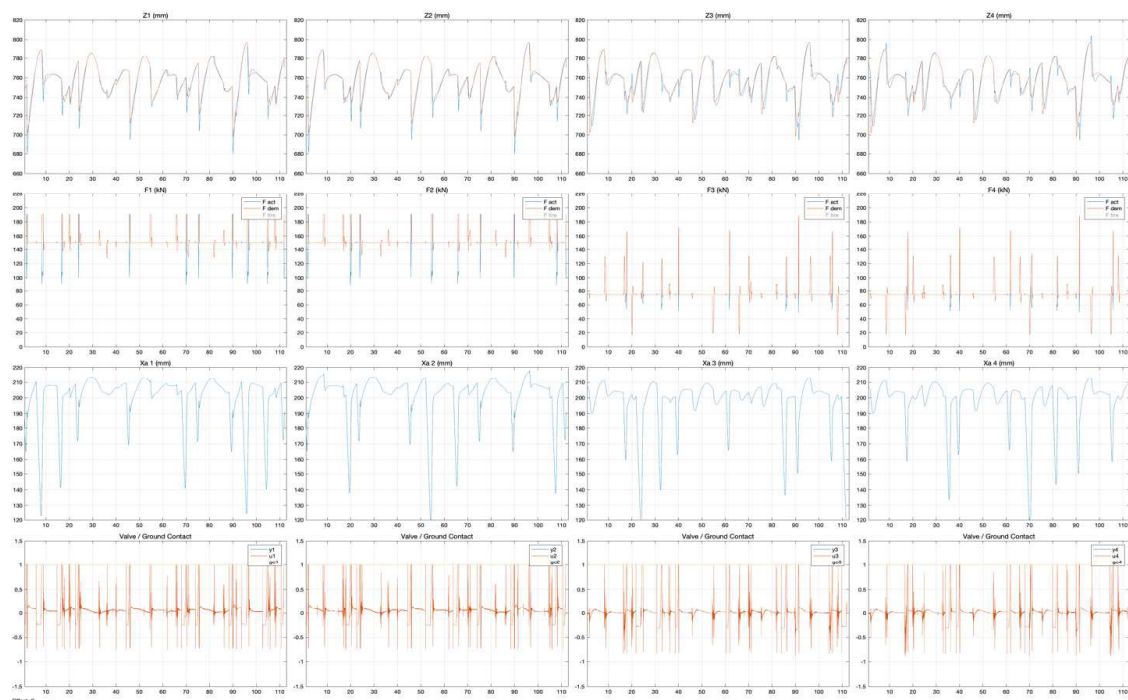


Figure 19: Suspension Actuators versus the complete Test Track, Driving Speed 0.25 m/s

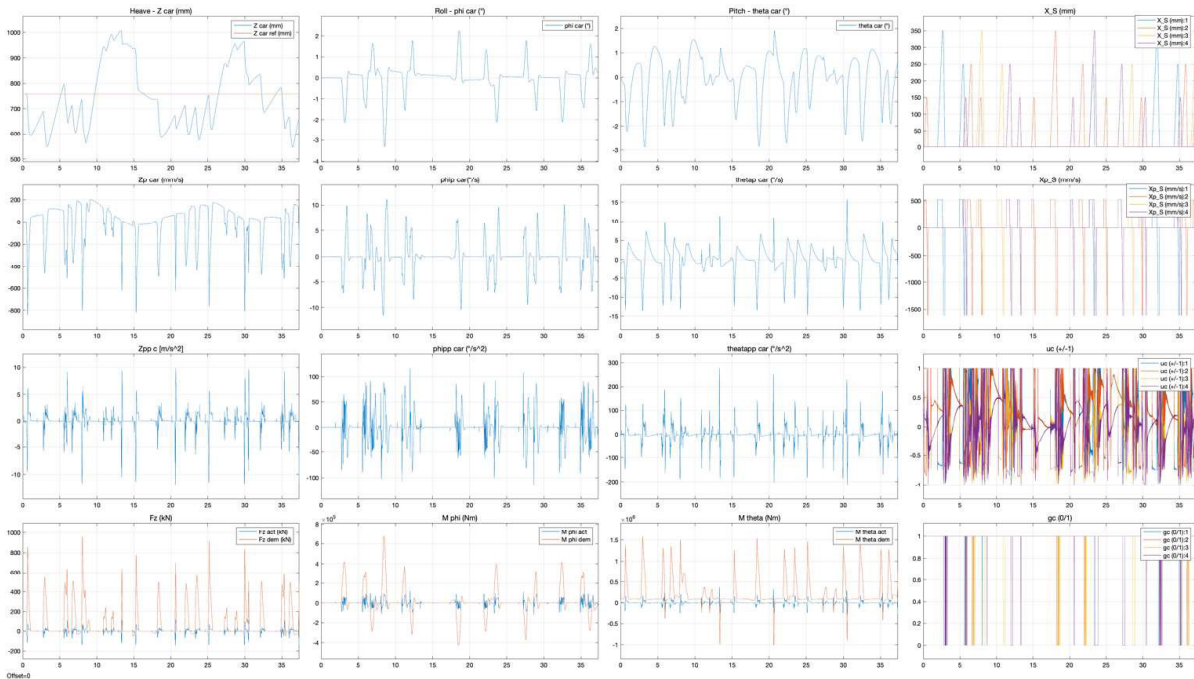


Figure 20: Complete Machine across complete Test Track, Driving Speed 0.75 m/s

4.3. Limitations

An increase of the driving speed up to 0.75 m/s as shown in **Figure 20** has the effect that the control loops on actuator level are running into limitations, which means the wheels lose ground contact and cannot build up the commanded force to stabilize the vehicle chassis.

The consequence of a further increase of the driving speed would be a bigger sizing of the servo valves and therewith a bigger sizing of the complete hydraulic system. On the other hand, bigger valves would implicit smaller bandwidth and dynamic performance.

4.4. Real Machine



Figure 21: Video Clip (only in presentation)

The behaviour of the real machine with the presented active suspension system will be demonstrated in the conference presentation by a video clip.

5. CONCLUSION AND OUTLOOK

The presented active pendulum arm suspension system for mobile machines represents a new performance level of chassis stabilization by use of industrial components.

The critical elements and limitations of these systems have been shown and discussed.

The energy consumption and solutions for the reduction of the energy intake have been developed, but not been presented here due to the limited time for the presentation.

The discussed system represents a high end solution for mobile hydraulic machines like construction or forest machines in the transition from standard machines into automated or at least autonomous machines.

REFERENCES

- [1] Rutting and vibration levels of the On Track concept forwarder on standardized test tracks, Report, [Skogforsk](#)

INTEGRATED SMART HYDRAULIC DISPLACEMENT MACHINE FOR CLOSED SYSTEMS

Werner Döhla¹, Jörg Bauer¹, Rocco Kemnitz¹

¹*RAPA Automotive GmbH&Co. KG*

ABSTRACT

The following article describes the development, validation and series introduction of a novel highly integrated smart electrohydraulic 4-quadrant displacement machine. Starting in 2012, an unique unit consisting of a hydraulic internal gear machine combined with a newly developed electric machine with integrated electronic unit was created. The developed unit aims at the application in fully active automotive chassis in combination with hydraulic shock absorbers. The very special requirements of this application resulted in a new development with numerous detailed solutions which are described below. Parallel and interacting with the product development, all new series assembly and testing devices tailored to this product was developed.

Keywords: Fully active chassis, smart hydraulics, integrated electronics, Motor-Pump-Unit

1. OBJECTIVE

The task of the project was to develop an electrohydraulic displacement machine for fully active chassis systems. The focus was on fully active chassis systems which combine the hydraulic shock absorber with an associated hydraulic displacement machine in the basic conceptual approach. In order to be independent of the drive concept of the vehicle, an electro-hydraulic unit had to be implemented. Through the combination with a hydraulic shock absorber, the electrohydraulic displacement machine becomes part of a closed and permanently pre-pressurized system. This resulted in system-related special functional requirements for the unit which had to be taken into account in the development. In addition to dynamic aspects, the machine have to be also have sufficient compressive strength.

2. TECHNICAL CONCEPT

The result of the detailed concept considerations for the given task was the use of an integrated design consisting of hydraulic displacer and electric machine in the form of an integrated design. Specifically in the form of an under oil running electric machine with direct hydraulic connection to the displacer. With this design, no sealing of the drive shaft to the atmosphere is necessary, an aspect which was given high priority, since such a seal has various

disadvantages. In addition to the entry of mechanical friction as a result of the sealing and risks to the compliance with the sealing requirements over the entire operating range and the service life, the sealing, due to the permanent pressurization of the closed system, also poses requirements that can hardly be met with currently known sealing systems. On the other hand, the electrical machine have to have the appropriate pressure resistance, a challenge whose solution is described in more detail in section 3.1.

3. COMPONENTS

3.1. Electrical motor

A comparison of different types and designs of electric motors showed the use of a permanently excited synchronous machine as the most appropriate solution. In addition to its basic suitability for a wet-running machine, the very compact design is an argument in favour of using such a design due to the high power density of the machine. To define the basic design of the permanently excited synchronous machine, numerous designs were compared with each other by means of simulation analyses. Basically, the use of a so-called 12/10 design was identified as a very suitable topology. This involves 12 stator teeth which are combined with a 10-pole rotor. For the rotor, a star-shaped arrangement of

the 10 permanent magnet stacks within the lamination stack has proven to be the most advantageous solution. The selected rotor design is shown in figure 1.

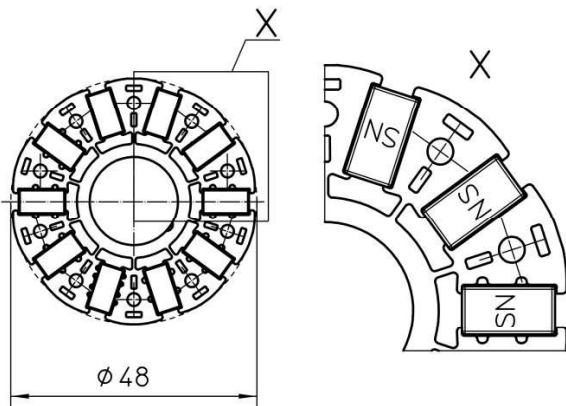


Figure 1: Rotor design

The cuboid permanent magnets are inserted into the correspondingly shaped openings in the sheet metal packet. Radially, the permanent magnets are held positively by the laminated core. In order to fix the magnets axially, the laminated core equipped with the permanent magnets is overmoulded with a thermoplastic material. The plastic overmoulding is also used to make the rotor easy to balance. For this purpose, a type of plastic disc with numerous mounting holes evenly distributed around the circumference is injection moulded onto both axial ends of the laminated core. Balancing elements in the form of metal balls are pressed into the cylindrical openings during the balancing process. This method of additive balancing is, in addition to the simple design, also ideally suited to ensure that, in contrast to negative balancing forms, no contamination is left behind in the production process. The greatest challenge in the development of the electrical machine was to find a suitable design form that combines the necessary compressive strength on the one hand with the requirement for a compact design and high efficiency on the other. Concepts with a completely hydraulically flooded motor, i.e. flooding of the stator space as well, were rejected because the surrounding housing was too large and heavy for this case. Since this variant was not the solution, an other solution had to be developed which would provide a hydraulically pressure-resistant seal between stator and rotor. There are known solutions for this task in the form of so-called can which are arranged in the magnetic working air gap between stator and

rotor. For the pressures occurring in the specific application, the market provides metallic cans. However, the electrical eddy currents occurring in the metallic can reduce the efficiency of the electric machine. Such a decrease was not acceptable under the given objectives regarding the efficiency. The only way out is to use a canned tube made of an electrically non-conductive material. With regard to an automotive series application and the associated restrictive cost structure of the individual parts, a solution made of glass fibre reinforced thermoplastic material is aimed for.

Despite the prevention of eddy currents, the wall thickness of the plastic can must be within a few tenths of a millimeter. A larger magnetic working air gap would also unacceptably damage the efficiency of the machine. Accordingly, a constructive design of the plastic can is found in numerous simulation loops, which on the one hand is supported on the inner diameter of the stator teeth with a wall thickness of approx. 0.5 mm only and on the other hand is thickened in the stator tooth gaps. The thickened area is trapezoidal in shape. Together with the correspondingly shaped counter contour on the stator teeth, this results in a supporting effect which can ultimately fulfil the required compressive strength. Due to the supporting effect of the trapezoidal thickening, the radial build-up is so low that it does not protrude into the winding space and thus does not reduce it. Figure 2 shows a cross-section of the developed can geometry.

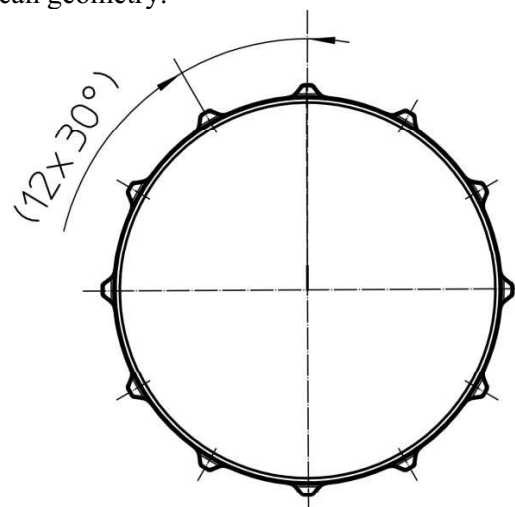


Figure 2: Plastic can design

In this version it is finally possible to use a can made of 40% glass fibre reinforced PPA which

can withstand operating pressures up to 150 bar and 120°C temperature load. The stator is made of two several parts and consists of a stator yoke in which the stator teeth with the single tooth coils on them are inserted in the form of a stator star. Figure 3 shows the design of the stator yoke and stator star.

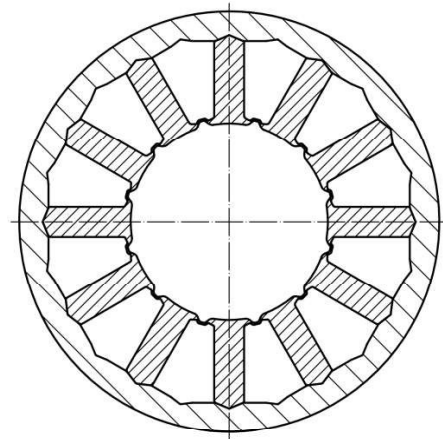


Figure 3: Stator assembly consisting of stator yoke and stator star

For better heat dissipation of the coils, the stator space is filled with a 2-component potting compound. In addition to heat dissipation, the potting compound fixes the motor coils and also provides additional mechanical support for the can. Figure 4 shows a typical torque vs. speed limit characteristic of the developed electrical machine.

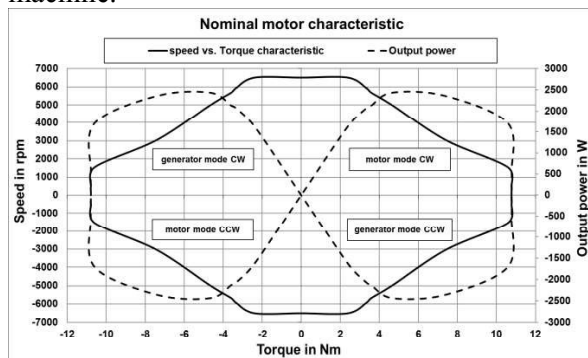


Figure 4: Speed vs. torque limit characteristic

Maximum speeds of approx. 6,500 rpm on the one hand are opposed by a maximum torque of approx. 11 Nm on the other. To achieve high speeds on the motor, the permanent magnetic field of the rotor magnets must be counteracted electromagnetically by means of field weakening in order to be able to increase the speed further.

3.2. Displacer

An internal gear machine with a nominal positive displacement volume of 4.3 cm³ per revolution is used as the displacement principle. This principle represents the ideal solution for the application at hand. The internal gear machine is geometrically compact, is capable of delivering high hydraulic pressures, in this case up to approx. 130 bar, and allows operation in all four quadrants. As a specific design of the internal gear machine, an axial and radial leakage compensated 15/20 version is used. An internal gear with 20 teeth interacts with a 15-tooth pinion. The pinion is driven by the one-piece shaft of the electric machine. The ring gear is supported by a plain bearing in the housing of the displacer. Axially on both sides, so-called axial washers nestle against the gear set. The axial discs are pressed hydrostatically against the gear set and take over the hydraulic control of the machine. Moulded elastomer seals arranged on the rear side give the axial discs axial freedom of movement as tolerance compensation on the one hand and prevent hydraulic short circuits and thus internal pump leakage on the other. Leakage compensation in the machine is carried out radially by means of a split, hydrostatically activated filling piece. The inner segment of the filling piece contacts the pinion, the outer part of the filling piece contacts the ring gear. A sealing element is located between the filler halves. The leakage path between the pressure and suction side is thus closed. Figure 5 shows a top view of the gear unit with the intermediate filler assembly.

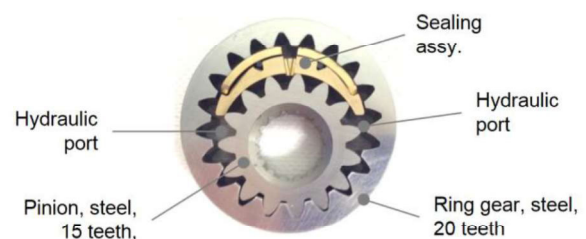


Figure 5: Leakage compensated internal gear machine

The leakage-compensating measures enable an almost ideal volumetric behaviour. At low pressures the volumetric efficiency is almost 100%. The volumetric efficiency versus pressure characteristic is shown in Fig. 6.

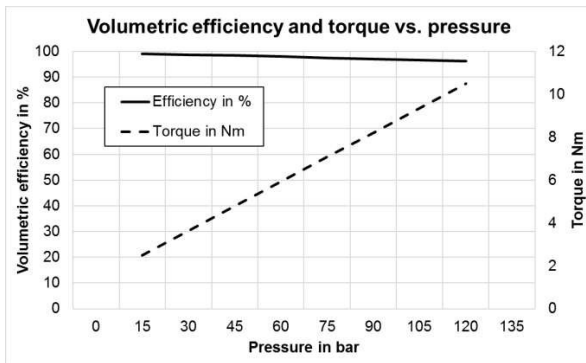


Figure 6: Typical volumetric efficiency vs. pressure and torque vs. pressure curve

The high volumetric efficiency allows a very good response of the machine in reverse operation, an important function in the present application where the machine constantly changes its operating point across all four quadrants. The internal gear machine described here is based on a solution that already exists on the market. The challenge with this component was, on the one hand, the automotive industrialization of the machine originating from the industrial sector and, on the other hand, the necessary optimization of the noise behavior. Although the principle used in industrial applications appeared inconspicuous, considerable detail optimizations were necessary to reduce the pressure pulsation introduced into the downstream system and to reduce the radiated airborne noise. No less challenging is setting up and validation of the series supply chain for the demanding individual parts of the displacer unit.

3.3. Electronics

The electronics unit to drive the electric machine is flanged directly and radially to the bottom of the motor housing on the side facing away from the displacer machine. The motor housing is used as a thermal sink for cooling the power semiconductors. A permanent magnet located at the end of the motor shaft facing the electronics serves as a position sensor for a Hall sensor on the electronics to detect the actual position of the rotor. The housing is thin-walled between the permanent magnet as rotor position sensor and the Hall sensor. The thin wall seals off the hydraulic area from the electronics on the one hand and still allows the Hall sensor to detect the permanent magnetic field sufficiently. The integrated electronics have all the contents for controlling the electric machine and thus make

the machine a smart unit. Besides the power supply, which is designed for 48V, the default signals and status variables are exchanged via a CAN bus connection. Speed or torque can be selected as target values for the motor controller. Various actual values of the machine are available as status information on the CAN connection. It is especially worth mentioning that measured actual pressures are also made available at the two hydraulic connections of the machine. The measured pressure values are determined via two miniature pressure sensors integrated in the hydraulic machine. The two sensors are integrated in the housing of the hydraulic machine, not visible from the outside, and are electrically connected to the electronic unit via a contact assembly through the motor. In addition to measuring pressure, the two sensors also record the temperature at the installation location. In addition to the functional concerns, the electronic unit fulfils an ASIL classification according to Level C for selected features that have been agreed with the customer. Mechanically, the electronic unit consists of two printed circuit boards, the power board attached directly to the motor housing and a signal board. Both printed circuit boards are mechanically and electrically connected to each other via an intermediate assembly. The intermediate assembly is a plastic carrier part in which the geometrically large and heavy electronic components of the electrical intermediate circuit and the input filter are mechanically fixed. In addition, contact bridges are arranged in the part for the electrical connection of the two boards adjacent to the front sides of the intermediate assembly. The intermediate assembly and the two circuit boards form a stacked structure which is screwed to the bottom of the motor housing. The three electrical motor phase connections pass through the bottom of the motor housing and the power board and are screwed to the power board with contact elements. The developed electronic unit can provide electrical string currents of up to 120 Arms. Figure 7 shows the developed machine without electronics housing.

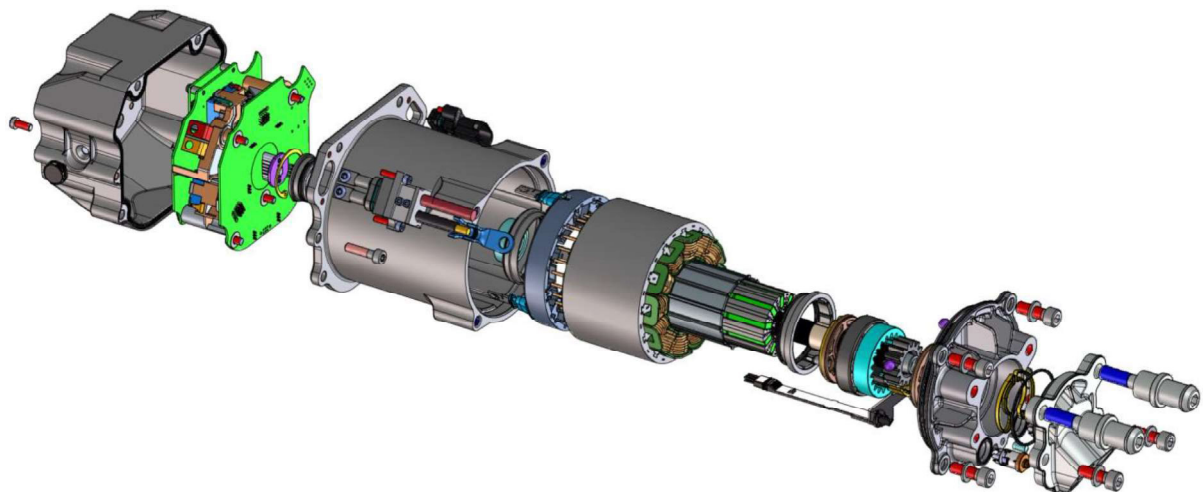


Figure 7: Explosion view

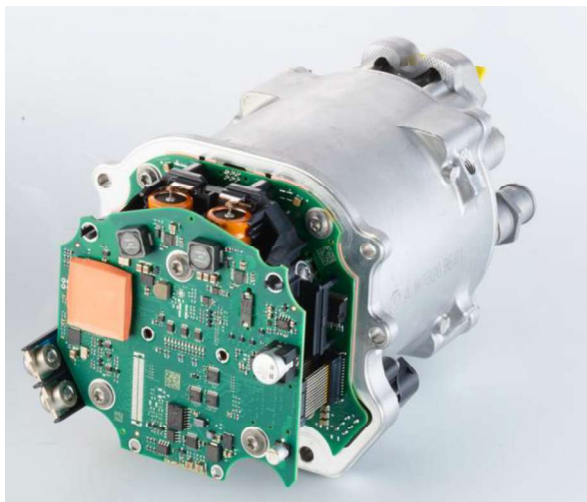


Figure 8: View on the on board electronics unit

3.4. Housing and interfaces

For a compact design, the hydraulic and electric machine are integrated into each other. For this, the two components can no longer be operated as individual components. Thus the unit works with a common shaft coming from the electric machine and projecting into the hydraulic machine. As a consequence, there is only one common bearing point for the shaft between the electric and hydraulic machine. Thus the hydraulic machine forms the A-bearing of the electric machine. The two bearings near the gear set are designed as plain bearings. Opposite this, at the other axial end of the shaft, a fixed bearing in the form of a roller bearing is arranged. Aluminium die-cast parts are used as the surrounding housing for the hydraulic machine, the electric machine and the electronic unit. In

addition to accommodating the components, the housing also serves to provide or accommodate the various interfaces. Figure 8 shows an exploded view of the entire unit. Although the electrical machine is designed to be pressure-resistant, as described above, the pressure in the rotor chamber is additionally controlled by two mechanical check valves. There is one check valve each between the rotor compartment and the two hydraulic connections of the unit. With the help of this hydraulic circuitry, the leakage oil from the pump, which is fed into the rotor chamber via the hollow shaft, is drained off and can only build up pressure in the rotor chamber at the level of the lower pressure of the two connections.

4. TESTING AND VALIDATION

4.1. Functional testing

Figure 9 shows a typical pressure vs. flow limit curve of the developed machine.

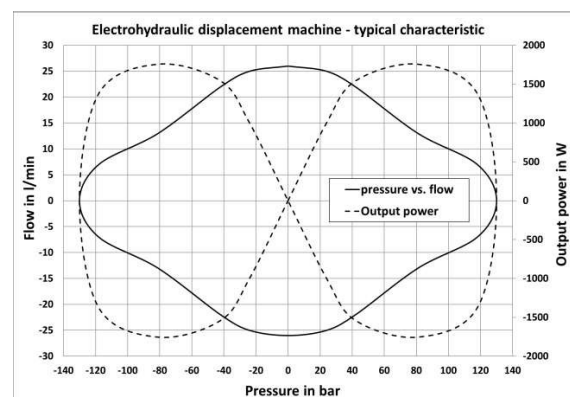


Figure 9: Pressure vs. flow limit characteristic

The unit is capable of delivering volume flows of up to approx. 26 l/min on the one hand and pressures of up to approx. 130 bar on the other. The response times of the unit are particularly relevant for the intended application. It is important to influence the hydraulically coupled shock absorber of the vehicle depending on the current driving situation. **Figure 10** shows a characteristic hydraulic step response measurement.

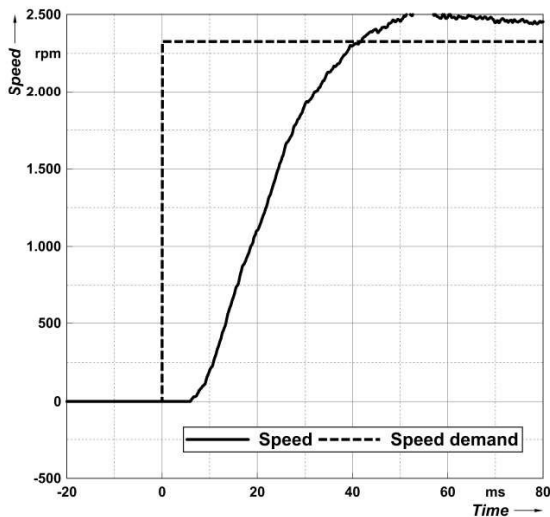


Figure 10: Flow step response

After less than 10ms from the time the setpoint is applied to the CAN connection, a volume flow is available to build up pressure in the downstream system. The pressure response depends on the hydraulic stiffness of the downstream system. Numerous new product-specific test possibilities have been created for the developed displacement machine. At the very beginning of the project, still in the concept phase, a function test bench was put into operation in order to be able to carry out benchmark tests and concept comparisons. In addition to an overall function test bench, a further test bench for measuring the electric motor was created. The characteristic values of the electric motor are determined on the engine test bench. Numerous small test benches for measuring the unit via temperature and especially in the noise measuring chamber round off the testing possibilities.

4.2. Endurance testing

The unit fulfils all requirements which are placed on components installed in the underbody area of motor vehicles. The housing and interfaces are

designed according to protection class IP69. In the lifetime validation, the units were subjected to a load which corresponds to an operating time of 8000h operation. To apply these test loads, specially designed test benches were put into operation. In the endurance tests the extreme robustness of the developed design is demonstrated. Since the motor is designed to be virtually wear-free, the evaluation of the internal gear machine after the endurance tests is of particular importance. Endurance tests in early prototypes have already shown that the selected internal gear machine is excellently suited to the service life requirements. Here, the use of a robust component from the industrial sector pays off particularly well. As a result of the endurance tests, a slight improvement in the overall efficiency of the unit over the test period is characteristic. Such an evaluation is shown in **Figure 11**.

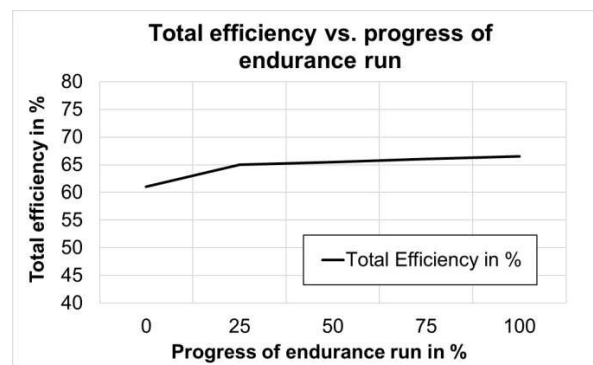


Figure 11: Typical total efficiency characteristic vs. life time testing

5. LAUNCH AND START OF PRODUCTION

The developed unit is completely produced at RAPA Automotive GmbH&Co. KG in Selb. The focus is on the assembly and testing processes. Primary parts as well as the circuit board set of the electronic unit are purchased from external specialists. In the course of the project, a completely new production hall with an impressive production line was built for this product. The assembly sequence is serial with buffer possibilities. Special processes such as the injection moulding of the rotor or the winding of the stator coils are arranged in the assembly flow. Product design and assembly are coordinated. For example, in a winding process two coils are wound simultaneously, a so-called coil pair. On the one hand, this shortens the cycle time in

production for the winding process and the electrical connection of the coils and, on the other hand, enables a simplified design of the connection assembly which electrically connects the coils of the stator to the three phases U, V and W as interface to the electronics unit. A vacuum potting process is used to reliably fill the stator space with the narrow gaps with the 2-component potting compound. Here, the volume to be filled is subjected to vacuum before the filling process. The End of Line function test bench was designed and built in parallel to the development of the product and was already put into operation during sample production and further optimised until the start of series production. The basis for this was the laboratory test bench, which was designed and installed at the beginning of the project. A similar approach was taken in the design of a test step for the electric motor, which was temporarily stored in the assembly line. Here, various measuring methods were first examined and evaluated on the motor laboratory test bench with regard to their suitability for integration into the assembly process before a suitable test method for series assembly was defined.

6. FURTHER DEVELOPMENT

There are already numerous approaches for the development of a further generation of the presented electro-hydraulic displacement machine. One goal is to provide units for use in HV power supplies of motor vehicles in addition to the currently operated supply voltage of 48V. In addition, there are also efforts to further reduce the size of the units by increasing the power density of the electric machine.

7. SUMMARY AND CONCLUSION

In the project presented here, a highly integrated electro-hydraulic displacement machine has been developed since 2012, especially for use in fully active chassis systems of motor vehicles. In addition to the automotive industrialization and optimization of an internal gear machine, the electric machine including an integrated electronic unit was completely developed and could thus be tailored to the very special requirements of the intended application. The first series application in a customer's vehicle started in the fall of 2018. The OEM is a German premium manufacturer that will also offer the

fully active chassis system in which the unit is installed in another model series from 2020. RAPA Automotive GmbH&Co. KG is thus supplying the pressure supply unit for the world's first series active chassis based on fully active shock absorbers. The technology is currently being used in the first premium vehicles. A further distribution in the upscale vehicle segment is possible. Completely new topics, such as measures against motion sickness, will open up further fields of application for active chassis systems in the future and thus also further potential areas of application for the presented technology.



Figure 12: Developed smart device

HYDROPNEUMATIC ALL-WHEEL SUSPENSIONS: APPLICATIONS, CHALLENGES AND SPECIAL SOLUTIONS

Wolfgang Bauer

ARGO-HYTOS GmbH, Industriestrasse 9, 76703 Kraichtal-Menzingen

Tel.: +49 7250 76541; E-mail address: w.bauer@argo-hytos.com

ABSTRACT

All-wheel suspensions are generally challenging, particularly if they are equipped with an automatic level control. In mobile machines, the special application conditions make their use even more demanding regarding layout and control. A high center of gravity, load variations, off-road-conditions etc. require special measures to reduce roll and pitch movements. Additionally the uneven ground along with the mechanical suspension setup often create a need to measure and optimize tyre-to-ground forces in order to provide best traction and suspension properties. Hydropneumatic suspensions have all the potential to meet all these requirements and provide a comfortable, safe and efficient suspension setup.

Keywords: hydropneumatic, all-wheel, suspension, control

1. INTRODUCTION

Hydropneumatic suspensions are well known for their superior qualities in mobile machines: high load capacity, easy and fast level control, adaptable suspension properties, robustness and many more. They provide comfort, safe ride behaviour and efficiency to the machines they are applied to. In many mobile machines, only parts of the under-carriage are actually suspended while others are still rigid or only maybe pivoting. In these cases, normally the front axle is suspended like for example on tractors, dumpers, road sweepers etc.

It is obvious that this partial solution is only a compromise between function, complexity and cost. It comes also with a separation of functions: typically, the rigid axle(s) take(s) over the task to avoid roll movement (=roll stabilization e.g. during cornering) while the suspended axle is responsible for comfort and good traction (=efficiency). In an all-wheel suspension, all these functions are evenly distributed to each of the wheels, which adds complexity to the setup.

2. WORKING CONDITIONS AND REQUIREMENTS IN MOBILE MACHINES

Usually, mobile machines are used as working machines, while the work consists of transportation of heavy loads or working with (heavy) tools. Therefore it is only natural that the

weight on the axles/wheels varies very strongly depending on the working/loading condition - sometimes up to ratios above 5:1 (max:min).

With the load or the tool (and their vertical position) comes a change of the height of the center of gravity. However, with increasing load, the COG will also move to a higher position. It is easy to see that this double influence causes a massive change of roll torque during cornering or whilst driving alongside a hill (depending on the working or loading condition). This is a major challenge in the layout of an all-wheel suspension and can best be mastered with a hydropneumatic suspension (see next chapter).

To make the conditions even worse, in many applications the machine needs to have a narrow track width to make it fit to the specific working conditions, for example driving in narrow streets (sweeper) or driving in predefined crop rows (sprayer). The narrow track width worsens the ratio of COG-height to track width and therefore complicates the setting of the suspension parameters and even includes the danger of tipping over sideways.

Mobile machines are frequently used off roads, which is generally quite demanding for suspension systems. Typically the ground is not paved but raw, therefore the surface is rather slippery, particularly when wet. Additionally, off-road surfaces are very uneven, with many random bumps and potholes of different size and

depth. It also needs to be considered, that off-road machines work in naturally shaped areas with particularly steep surfaces being driven up- and downhill but also alongside hills.

From these above-mentioned adverse working conditions, functional requirements can be deduced for appropriate suspensions (**Fig. 1**). These requirements are sometimes contradictory, therefore often a suitable compromise needs to be found for the suspension setup.

Slippery conditions require the best possible traction. While traction partly depends on the choice of tyres, inflation pressure, etc., the other important factor for traction is the tyre-to-ground (short: ttg) force. Therefore, it is an absolute must, to distribute the ttg forces of all the wheels as evenly as possible – however limited by the laws of physics, as will be shown later.

In order to cope with the undulations of the ground, a certain minimum suspension travel must be provided. If that's not the case, in extreme conditions at least one of the wheels will lift off the ground (\rightarrow ttg force = 0) and will therefore lose traction completely. It is recommended to have at least 20% (better 50%) more suspension stroke than the highest expected difference of wheel position due to ground unevenness.

The suspension stroke is also connected to the level of comfort offered by the suspension. The more suspension stroke, the softer the suspension can be tuned – however limited by unpleasant drivers sensations like sponginess, loss of controllability or even seasickness. It is

recommended for example for a wheel/axle suspension to choose the vertical natural frequency (assumed single mass oscillator) not lower than 1Hz, maybe only depending on certain conditions (damping, the type of vehicle, actual operation conditions etc.) it is possible to go somewhat below that.

Along with strong load changes (be it due to actual change of payload or due to shifting of weight during cornering/braking/accelerating or hilly driving conditions) and a soft suspension setup come strong position changes. These changes in suspension cylinder length must be compensated quickly and accurately by bringing each cylinder back into its default position. ARGO-HYTOS chose to design a dedicated proportional valve for this purpose, as described in a contribution to the IFK in 2014 [1].

Particularly a high COG and a relatively small track width would allow an undesirable amount of roll movement during cornering – therefore countermeasures need to be taken. A roll compensation can help in such cases if the roll movement is normally rather slow. Roll compensation is basically a quick readjustment of the suspension cylinder length to avoid roll movement. It is used for example in the Mercedes-Benz ABC-suspension setup, which was/is available for example on Mercedes S-class models.

If a roll compensation cannot react quickly enough, for example because of a too quick roll movement or a limited amount of „levelling power“, then also an additional roll stabilization

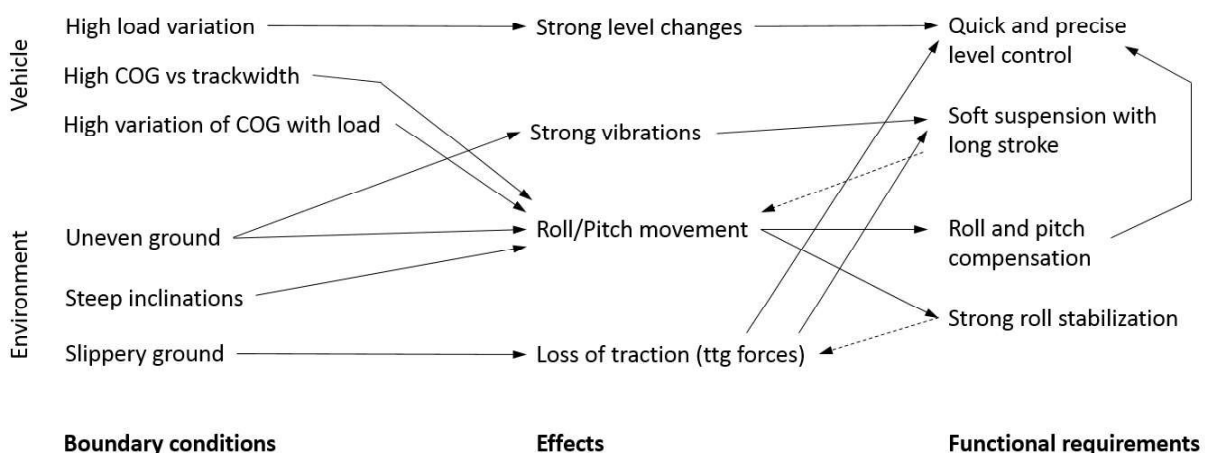


Figure 1: Boundary conditions, their effects and deduced functional requirements for all-wheel suspensions

is needed. Roll stabilization comes from an additional spring that connects both wheels of an axle and only creates counterforce, if these two wheels have a different displacement, so when the left wheel is in another position than the right wheel. On passenger cars this is typically done with a stabilizer bar (also referred to as e.g. sway bar or anti-roll bar), which is a torsion bar between both wheels. This can also be found on mobile machines, however if a hydropneumatic suspension is used, the stabilization can also be done purely hydraulically (see next chapter).

Despite of its undeniable positive effect for corner leaning, the roll stabilization also has negative effects on the ride behaviour on uneven surfaces, where the two wheels of an axle ride over different surface profiles. Then the so-called „copy-effect“ can spoil the ride behaviour since every acceleration of one wheel is (partly) copied to the other wheel and creates an acceleration there as well. This will create an uncomfortable and harsh ride behaviour with additional accelerations easily visible in the time-position-curves (also depending on the strength of roll damping). So the amount of roll stabilization must be wisely chosen in order to find the best compromise between reduced roll and acceptable comfort.

3. SUSPENSION HYDRAULICS: CHALLENGES AND SOLUTIONS

Hydropneumatic suspensions offer significant advantages for the application in all wheel suspensions in mobile machines. With their additional possibilities however also come certain challenges for the design engineer during the layout of the system. Here are the four most important ones.

3.1. Accumulator setup

The accumulator is the component, which determines the spring rate of the suspension. It is the gas inside the accumulator that creates the cushioning effect. So the size and the prefill of the accumulator determine how soft the suspension will feel (the more gas, the softer). As already mentioned before, suspension softness and minimum needed stroke are directly connected to each other. If you allow a stroke of $\pm 100\text{mm}$ or more (at the wheel), you can go for a natural frequency of the suspension of 1 to 1,5Hz (assumed single mass oscillator). If you only want to only

allow $\pm 50\text{mm}$ or maybe even less, the natural frequency should be tuned to 2 to 2,5Hz (single mass osc.). The aforementioned values of course also depend, among others, upon the chosen damping and the rotational inertia of the chassis. Very generally spoken, significantly below 1Hz the suspension will feel too spongy, even uncontrollable, while above 2,5 to 3Hz it will not feel comfortable enough.

Typically, diaphragm accumulators are used in hydropneumatic suspensions, sometimes also piston accumulators. The accumulators must withstand all possible pressures that arise from load variations (payload and curve/hillside weight shift) and dynamic pressure changes when riding over uneven terrain. The typical max. pressure ratio of 8:1 for a diaphragm accumulator must cope with all these mentioned conditions.

Normally for systems with a load ratio above 2:1 (max:min) a preloaded hydropneumatic suspension is recommended in order to not overstrain the accumulator and to have similar suspension behaviour independent from loading conditions. However, in all-wheel suspensions, oftentimes the roll stabilization is done in a certain way by using the rod chamber of the suspension cylinders, too (shown later in this chapter). Therefore, it is not available to be used for preloading the cylinder hydraulically. Of course, there would be other possibilities of preloading (special cylinder with third chamber or external mechanical preload) but they are complex and costly, therefore a simpler hydraulic solution is preferred.

The rather simple solution consists of an arrangement of two accumulators per cylinder [2]. In such a system, both accumulators are only used with heavy loads while with lower loads, only one accumulator is active. A valve is responsible for switching the second accumulator on and off. The transition point at a medium load is calculated during the layout. During operation, the loading condition is permanently monitored by a measurement of the cylinder pressure (low-pass filtered to neglect pressure variations coming from ground unevenness). If the pressure is above a certain value, the valve is opened, if it drops below another, lower value (some hysteresis should be integrated) the valve is closed again. If a proportional valve is used, it is recommended to rather have a transition range than a transition point to make the change smoother and therefore possibly unperceivable.

3.2. Roll compensation and stabilization

Not all mobile working machines have fully individually suspended and level controlled wheels. In fact, many machines come with no suspension at all or just a preset mechanical suspension (with leaf or coil springs). Some machines have mixed mechanical and hydropneumatic suspensions (front different to rear), some machines have a level controlled (normally hydropneumatic) suspension but only one degree of freedom (vertical) for the whole axle, while the roll is completely fixed – this means its 100% roll stabilized this way. Some examples of possible setups are shown in **Fig. 2**.

Those machines with individually level-controlled wheels can be equipped with the possibility for roll compensation and roll stabilization. This is particularly suitable when strong roll motions can be expected for example due to high COG and / or narrow track width.

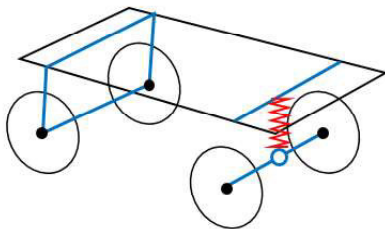
Roll compensation is basically the counteraction of the roll movement with the means of the already available valve that also is responsible for the level control / cylinder position control. The valves need to be operated in a way that, for example during cornering, the valve(s) for the outside wheels direct oil into the

cylinders, while the valve(s) for the inside wheels release oil from the cylinders.

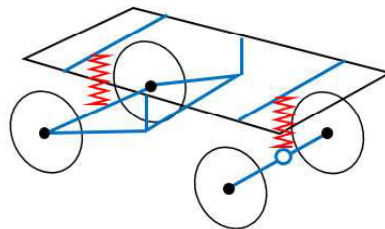
It is easy to see that, the quicker the changes in roll motion, the more flow must be available to compensate the cylinder position. Therefore, the core of the roll compensation is a very quickly reacting cylinder position adjustment. The quick reaction must be covered both from the hydraulic and from the electronic side and sufficient hydraulic power must be available. The simplest way to achieve this is to have a dedicated, quickened control-loop for the cylinder position, which also uses only the position sensor signal for the respective cylinder. This control loop could then be activated (in addition to the regular position control loop) if certain criteria are fulfilled, for example if steering angle and vehicle speed both exceed certain values.

In a more advanced approach, the activation of the valve is combined with special previewing algorithms, which could for example also use steering angle and speed or the signal from a lateral acceleration sensor. From steering angle and vehicle speed the expected lateral acceleration can be calculated and from this the expected roll angle. With this info, the cylinder can be already filled with oil / released from oil

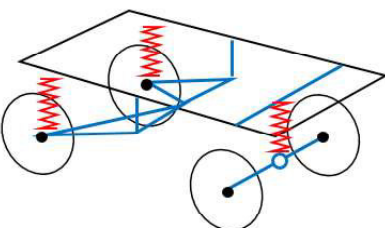
Front: both wheels suspended together, free oscillation
Rear: unsuspended axle, 100% mech. roll stabilized



Front: both wheels suspended together, free oscillation
Rear: suspended axle, 100% mech. roll stabilized



Front: both wheels suspended together, evtl. partially mech. roll stabilized
Rear: wheels suspended individually, hydraulically roll stabilized



Front: wheels suspended individually, hydraulically roll stabilized
Rear: wheels suspended individually, hydraulically roll stabilized

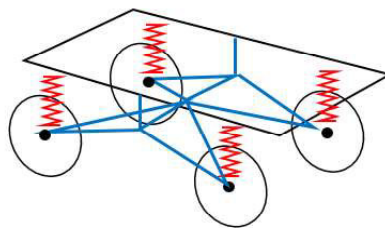


Figure 1: Possible suspension setups for mobile machines

before this expected roll angle actually is reached. So instead of only reacting (as in the example with the quickened control-loop above) the system can „pre-act“ and thus avoid excessive roll motion.

The abovementioned can also be done, if a sensor is used to directly measure the (lateral) acceleration. Such a sensor offers the additional possibility to do an over-compensation of the expected roll-movement. So during cornering the machine could even lean into the corner (like a motorbike) or, when driving alongside a hill, the machine could be brought upright independent from the slope of the hill.

Compared to roll compensation, which acts rather slowly, a roll stabilization will provide instantaneous counterforces against roll movement right at the moment when the chassis is going to an inclined position. This is achieved by spring forces that act in a direction which try to bring the chassis perpendicular to the ground contact plane. As already mentioned, this can be done with mechanical means (stabilizer bar) or, in case of hydropneumatic suspensions, also with a special hydraulic setup.

This hydraulic setup is using two double-acting cylinders of a suspended axle that are „cross-connected“ to each other. This means the pistonside of the left cylinder is connected to the rodsides of the right cylinder and vice versa. In a hydraulic schematic, this is easily visible as a cross-shaped arrangement of hydraulic lines. While, in this setup, the actual load carrying area of the cylinder is the rod diameter, the vertical natural frequency is determined by the accumulator size and precharge. If these parameters are chosen according to the needs of the application, in a next step the roll stiffness can be chosen by a suitable ratio of piston area to rod area. The higher this ratio, the stronger will be the roll stabilization effect.

The very positive effect of hydropneumatic roll stabilization is its inherent adaptation of roll stabilization to the load: the higher the load the higher is also the roll spring rate. This comes from the higher pressure in the cylinders and therefore the compression of the gas volume inside the accumulators. The vertical spring rate rises and with it also the roll spring rate increases. Indeed the latter increases by the power of 2 to the load. For many machines, this has a very positive effect: a linear increase of the roll spring rate with load would be not sufficient, since with

increased load, also the COG rises. Both effects, increased load and increased COG, multiply and dramatically change the roll torque during cornering (like with a heavy load on the roof of a car). So the increase with the power of 2 is quite exactly what such machines need for the (ideally) constant roll behaviour independent from the load.

The described roll stabilization is purely based on the hydraulic and mechanical layout of the system with no need for electronic control. However, roll stability is (just as the vertical spring stiffness) also influenced by the switching of accumulators as mentioned above. The tuning of the switching point and the relative size of the switchable accumulator must therefore consider both the vertical and the roll behaviour of the suspension. This means the test procedure must include pure straight driving on uneven terrain and also fast cornering in different loading conditions as well as the transition from a straight into a curve (needed to tune roll damping).

3.3. Pitch compensation and stabilization

The same principles apply as for the roll motion. Some machines even use the same „cross-connected“ setup for pitch stabilization as described above for roll stabilization. Fortunately, the wheelbase of a machine is typically significantly higher than its track width, so usually the need for additional pitch stabilization is not very urgent. Normally the already available control for cylinder position is sufficient to compensate long-term pitch movements caused for example by weight shifts by driving steep uphill or downhill for a longer time.

For short-term pitch movements, coming for example from heavy braking, it is also possible to quickly increase the damping or quickly increase the spring rate by switching a second accumulator off during the period of deceleration (as described above). By designing a suitable mechanical setup of the suspension, for example a leading link design, the pitch movements can already be significantly reduced just based on mechanics. However, certain boundary conditions (for example design space) do not always allow such a setup.

3.4. Equalization of tyre-to-ground forces

Ensuring optimal ttg forces has several advantages. First of all, it enables best possible traction and therefore driving safety as well as efficiency. Secondly, an unsuitable distribution of ttg forces also spoils comfort, since the stronger loaded wheels will create higher vertical natural frequencies, while the less loaded wheels are suspended too soft and therefore feel spongy. This way, the ride behaviour becomes less comfortable and less predictable. In extreme cases, it could even lead to tipping over of the vehicle.

In a four-wheel / four-corner suspension, an unsuitable distribution of ttg forces typically comes from the hyperstatic character of this setup. Normally three wheels / contact points to the ground would make the system isostatic and thus only one distribution of ttg forces is possible. However, with the fourth wheel, there is one contact point too much so it is unclear how the vehicle weight will be transferred to the ground. Everybody knows the table (or chair) with four legs that rocks in a certain way only because one leg is slightly too short/long or because the ground is not completely even. The table rocks along the axis of the two legs that are slightly longer and therefore need to take most of the load. Indeed sometimes these two legs take all the weight from the table while the other two legs are almost unloaded.

The same applies to a vehicle with four wheels, one in each corner. If the suspension position of each of these wheels is not in exactly the right position, the weight distribution will be unsuitable. Unsuitable in this case means that the weight distribution is not as it would be expected to be ideally due to the COG, the mechanics and the geometry. This is something very important to consider, since in a 4-wheeled vehicle, in almost no condition will the ttg forces at each wheel be a quarter of the weight. For this case the COG would have to be in the center of the vehicle, it would have to be driving on perfectly horizontal ground and with no lateral and no for-aft accelerations. That is nearly never the case and that's why ttg forces of all the wheels can almost never be exactly equal.

The topic of ttg force equalization is important for the design of suspensions already for many decades. In the beginning, it was only considered for sports cars, who had to have, for best traction,

optimal ttg force distribution. The ttg force distribution was manually set using a wheel force scale. Only once the automatic level-readjusting suspensions started to become more important, the ttg forces moved into the foreground of general development. Most work has been done in the area of passenger cars, which typically use pneumatic suspensions. Some work was also based on hydraulics, however often focused on active suspension systems. While in the beginning, the ttg force calculation could be done only during standstill or stationary straight driving [3], later these conditions were not necessary anymore ([4] and [5]) and the readjustment of ttg forces could be done at any driving condition.

Normally, the first step in such an approach is, to calculate the ideal distribution of ttg forces under the given circumstances. To do that, it is necessary to find the (virtual) point of intersection of the vehicle's COG gravity vector with the contact plane of the four wheels. The position of this point then allows to calculate for each wheel the ideal load under these circumstances.

The next step then is, to measure the actual load on each wheel. The deviation of the actual load from the ideal load then allows to calculate corrective actions. Fortunately, in hydropneumatic suspensions, there is an easy source of information for the calculation. A pressure sensor in each suspension cylinder (at each wheel) gives the information about the current situation, from which also the ideal load distribution can be deduced. Indeed the cylinder pressures do not perfectly represent the ttg load (weight of the unsprung masses is not considered, friction inside the cylinders) but in tests they proven to provide a sufficiently accurate information representative for the ttg load.

The corrective actions can be taken for each wheel individually, however for simplification, ARGO-HYTOS chose to group the wheels in diagonals [6]. Diagonal 1 is the front left wheel and the rear right wheel, while diagonal 2 is the front right wheel and the rear left wheel. If a corrective action is done, it is always applied to both wheels of a diagonal. For safety reasons, only the diagonal, where the load is higher than ideally calculated, is corrected by relieving oil from these cylinders. This way the pressure in these cylinders drops, these cylinders contract slightly and thus transfer more weight to the other

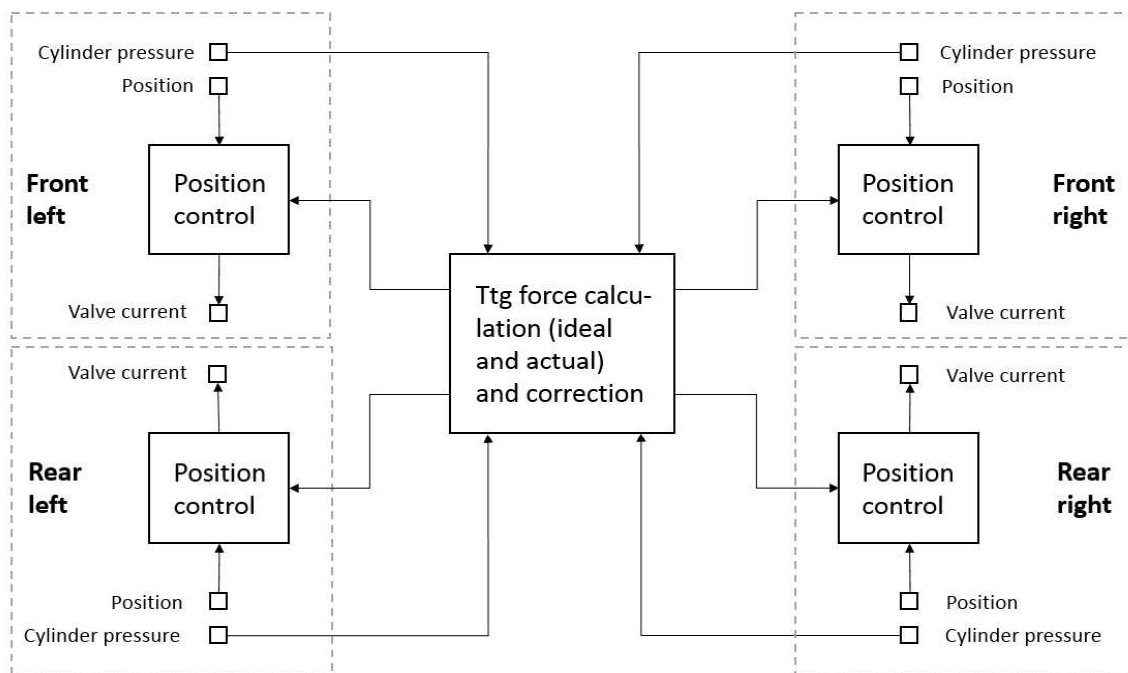


Figure 3: Control schematic for tyre-to-ground force optimization

diagonal. Once the load deviation of the higher loaded diagonal is again inside a tolerance band, the corrective action is ended. By lowering the higher loaded diagonal, it is ensured that at no time the cylinders are extended by the diagonal control loop, which would cause a lifting of the COG and therefore could bring the machine in a critical tip-over condition.

It is obvious, that this control loop interferes with the position control loop of each wheel, which is supposed to keep the vehicle in a defined position. ARGO-HYTOS decided to melt the diagonal control into the position control loop and in the end only get one output signal for the proportional valve that controls the position (Fig. 3). To enable this, the diagonal control loop weight deviation is converted into a „virtual“ position deviation. The latter is then added to the actual position deviation of each of the wheels of the respective diagonal (actual position – set position). This signal is then fed into the regular position control loop, where the normal, state-of-the-art position control procedures are applied. The advantage of melting both loops into one control is firstly simplification and secondly also the right compromise between correct cylinder position and best ttg force distribution. For customization, this compromise can be shifted

towards either one or the other goal by changing the parameterization of the algorithm.

A useful by-product of the aforementioned calculations is the information about the available traction on each wheel as well as the information about how close the machine is to tipping over. These informations are sent to the main machine controller so the OEM can decide himself how to consider this info in his own algorithms.

The described algorithms have proven their efficacy on several all-wheel suspended machines already, among them self-propelled sprayers, a self-propelled feed-mixer and a road sweeper.

4. APPLICATION EXAMPLE

The realization of the above-mentioned methods is shown in the application on a self-propelled sprayer. All wheels are individually suspended while the wheels of an axle are cross-connected for roll stabilization. The schematic for front and rear axle are identical, that's why only the schematic for the front axle is shown in Fig. 4.

Due to the high tank capacity of 5000l and a 36m boom, the load ratio on the hydraulic suspension cylinders is about 3:1 (max:min). For example, the highest load on the front axle appears with full tank and folded boom, while the

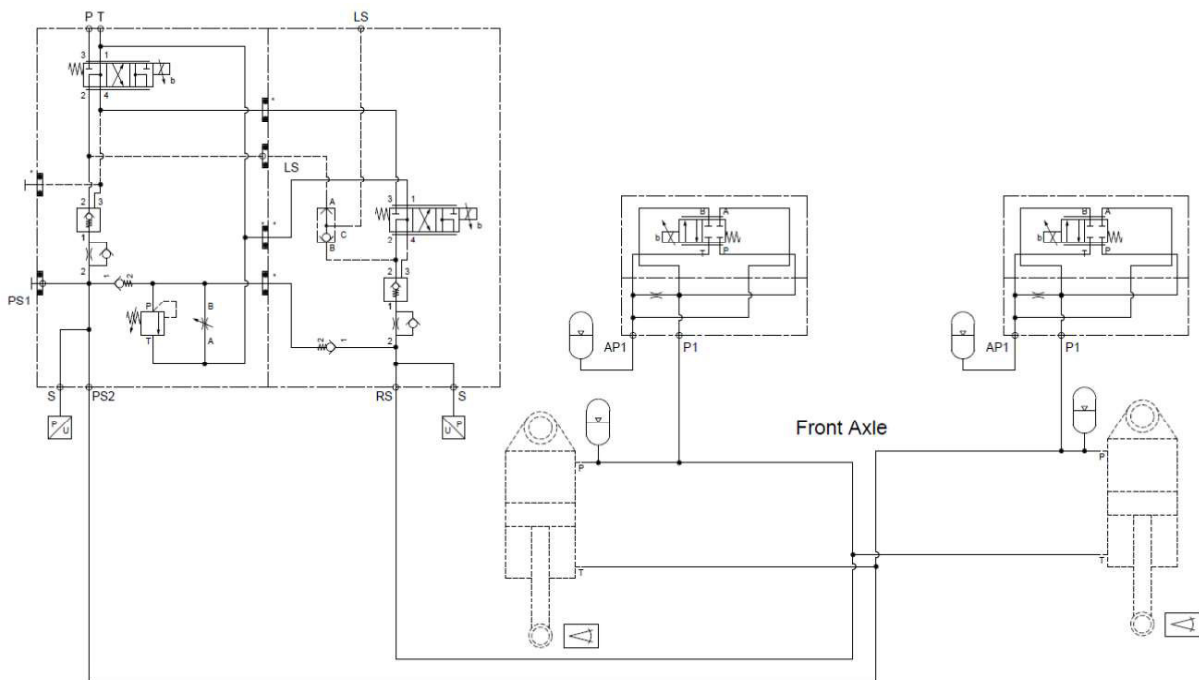


Figure 4: Hydraulic schematic for the front axle of an all-wheel suspended self-propelled sprayer

lowest results from empty tank and boom deployed. Due to the high load ratio, a simple unpreloaded cylinder+accumulator-setup was not possible. Instead, the switching of a second accumulator was implemented as already described in section 3. For this purpose, a standard 4/2-proportional Cetop valve is integrated in „double-flow“ condition, so both metering edges are used for the connection between cylinder and accumulator, which offers very low pressure drop when fully opened. A bypass orifice between accumulator 1 and accumulator 2 ensures permanent pressure equalization of accumulator 2 even if the proportional valve is fully closed.

The hydraulic level control is done based on ARGO-HYTOS special 4/3-prop-levelling valve (25 lpm-version). For each suspension cylinder, one valve is needed. Each of these valves uses only one solenoid, which keeps the number of required PWM-outputs of the control unit low. The input signal for the level control comes from a position sensor (angle sensor). As mentioned in section 3, pressure sensors are attached to each level control circuit to allow to calculate and adjust the right ttg forces for each wheel.

The control is done by one control unit each for the front and the rear axle. With a CAN-connection in between, the front control unit is

the master and also contains the central logics. Both control units read four sensor signals and operate four PWM outputs.

5. CONCLUSION AND OUTLOOK

For maximum comfort, driving safety and best working results, a hydropneumatic all-wheel-suspension offers many advantages over other types of systems. It automatically adapts its roll- and pitch-stiffness to the loading conditions and also allows, based on a dedicated control loop, to permanently measure, calculate and readjust the tyre-to-ground forces to the current operating conditions. Quick level adjustment, with high hydraulic power, can help to quickly adapt to load changes or to compensate roll and pitch movement when driving in hilly terrain. Hydropneumatic all-wheel suspensions are a well-proven technology in many different applications already. Since they fulfil the growing demand for comfort, working performance and efficiency, they are likely to be used in even more machine types in the future.

REFERENCES

- [1] Bauer, W.; Mejsnar, P.; Englberth, E.; Fischer, M.: 4/3 proportional valve with only one solenoid: A new technology for position control in suspension systems, 9th IFK, March 24-26, 2014, Aachen, Germany
- [2] Bauer, W.: Hydropneumatic suspension systems, Springer Verlag, Berlin, Heidelberg, 2011
- [3] DE4003188, Verfahren zur Steuerung der Höhe eines Fahrzeuges, Fuji Jukogyo K.K., Tokyo, JP
- [4] DE4323544, Aufhängungssystem für Kraftfahrzeuge, Mazda Motor Corp and Naldec Corp, both of Hiroshima, JP
- [5] DE10244363, Verfahren zur Regelung und/oder Steuerung eines aktiven und/oder steuerbaren Fahrwerks, DaimlerChrysler AG, Stuttgart, DE
- [6] DE102018118062, Verfahren und System zur Lageregelung eines Fahrzeuges, FSP Fluid Systems Partners Holding AG, Baar, CH

FLUID DYNAMIC VIBRATION ABSORBER FOR CABIN SUSPENSION

Nicolas Brötz*, Manuel Rexer, Peter F. Pelz

Institut für Fluidsystemtechnik, Technische Universität Darmstadt, Otto-Berndt-Straße 2, 64287 Darmstadt

* Corresponding author: Tel.: +49 6151 1627126; E-mail address: nicolas.broetz@fst.tu-darmstadt.de

ABSTRACT

Truck drivers spend all day moving goods. They are exposed to vibrations every time they drive. Modern cabin suspension and an air-suspended seat already offer a high level of comfort. This, however, is designed for vertical dynamics and you can observe the cab of a truck performs large pitching vibrations during acceleration. These are examined here. A pitch model of the cabin is set up for this purpose. On the basis of this model it is examined which reduction of the vibration can be achieved by the use of a hydraulically translated vibration absorber. The advantage of this absorber is the use of the hydraulic transmission to reduce the heavy mass at high absorber inertia. 4 kg of fluid mass act as 131 kg absorber mass reducing vibrations by more than 10%. The conventional vibration absorber is unacceptable due to the additional load. The investigation based on VDI 2057 Part 1 shows that driving comfort can be increased.

Keywords: fluid dynamic vibration absorber, cabin suspension, vibration, health protection, lightweight design

1. INTRODUCTION

Half a million professional drivers are transporting goods in Germany. Driving comfort is essential for health protection. Hence, air-suspended seats [1] are already part of everyday life. Vertical dynamics of the truck cabin are mastered by isolation [2, 3]. Also active systems for the improvement of vertical dynamics are investigated by several studies [4, 5].

The situation is less satisfying with pitch dynamics. Due to the soft suspension of the cabin and its high inertia, pitch oscillations are dominant during acceleration and braking.

The Fluid Dynamic Vibration Absorber developed within the DFG (Deutsche Forschungsgemeinschaft) Collaborative Research Centre 805 “Control of uncertainty in load carrying structures in mechanical engineering”, reduces pitch oscillations. By reducing the pitch oscillations, the exposure to the driver is reduced. In this paper, the exposure reduction achieved by the use of the Fluid Dynamic Vibration Absorber (FDVA) is evaluated with the aid of VDI 2057 Part 1 [6].

2. FLUID DYNAMIC VIBRATION ABSORBER

An absorber is used to reduce vibrations from an oscillating system. A conventional dynamic vibration absorber consists of a heavy mass and a capacity. In comparison to a conventional dynamic vibration absorber, that is not in the sense of lightweight construction due to the additional mass, the Fluid Dynamic Vibration Absorber (FDVA) reduces the dynamic mass by the use of hydrostatic transmission [7]. The movement of the cabin's suspension z_s directs the force via the absorber spring to the piston of the FDVA. The piston with area A pumps oil from one chamber through a duct to the other chamber. **Figure 1** shows the functional demonstrator. A first validation of the model [8] could already be shown with the functional demonstrator [9, 10]. The ratio $\alpha = A/a$ describes the ratio between piston A and channel cross section a . Due to the piston movement the fluid mass inside the ducts is accelerated α -times the piston acceleration caused by the hydraulic transmission. This translation produces the virtual tilting mass.

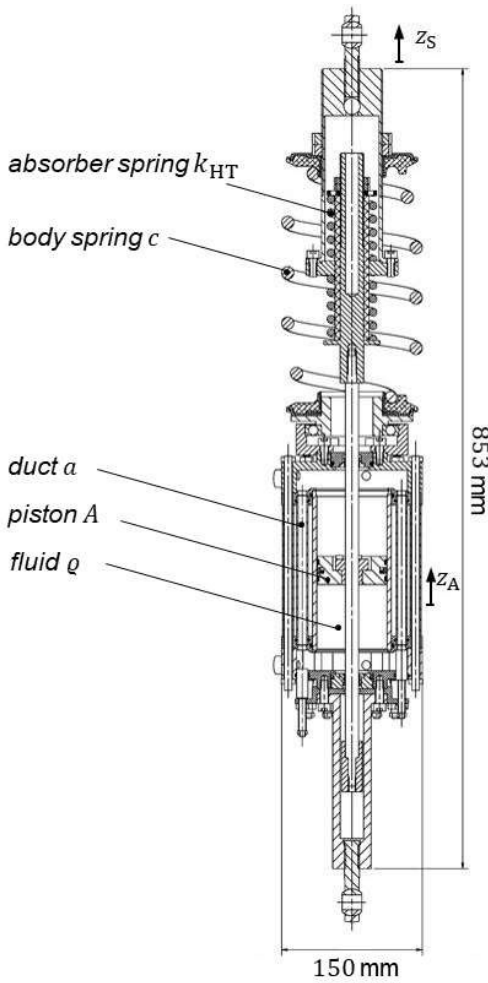


Figure 1: Functional demonstrator of FDVA [9]

The FDVA force $F_{HT} = k_{HT}(z_S - z_A)$ is described by the equation of motion

$$[m_P + (2\alpha\beta + \alpha^2)m_F]\ddot{z}_A = k_{HT}(z_S - z_A) + p_L A \quad (1)$$

with the piston mass m_P , the ratio between cylinder length and duct length β , the absorber stiffness k_{HT} and the pressure loss p_L . The fluid mass m_F is equal to the fluid in the duct. It becomes obvious from the equation of motion that this mass is translated. When we compare the measurement results for transmissibility $V = \dot{z}_A / \dot{z}_S$, phase $\psi = -\arg(\dot{z}_A / \dot{z}_S)$ and FDVA force F_{HT} (Figure 2) with the simulation model they are in good agreement. Small differences in the absorber force F_{HT} appear because friction is linearized.

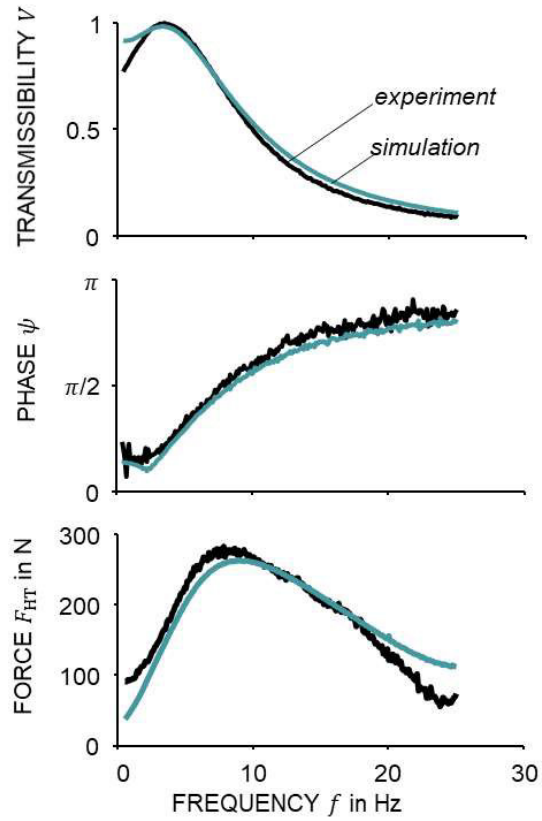


Figure 2: Measurement and simulation of FDVA with spring stiffness 57.4 N/mm and 2 opened ducts at 4 mm excitation

We use the validated FDVA model for the following calculations and optimize the parameters for an adoption to a cabin suspension.

3. CABIN SUSPENSION

The cabin of a truck (Figure 3) is mounted on the front and rear with spring dampers on the chassis. The front suspension is designed to turn the entire cab for access to the engine.

There are many eigenfrequencies of the truck due to the flexibly mounted motor, the wheel suspension and the trailer vibrations [11]. A model is used to analyse the systems vibration reduction (Figure 4).

The rotating behaviour around the front suspension point can be assumed as an approximation.

The rotatory vibration behaviour around the front suspension is described by the equation of motion.



Figure 3: Truck cabin [12]

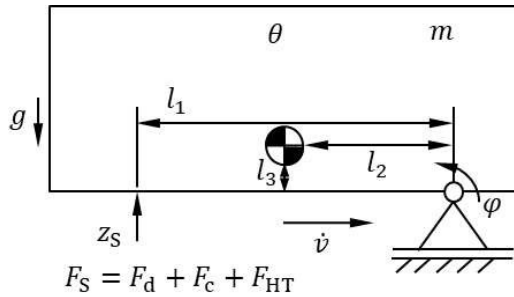


Figure 4: Simplified cabin model

The equation of motion for the simplified cabin model is given by:

$$\theta\ddot{\varphi} = -\sqrt{l_2^2 + l_3^2}m\dot{v}\sin(\varphi + \varphi_0) - \sqrt{l_2^2 + l_3^2}mg\cos(\varphi + \varphi_0) - l_1^2(\varphi k + \dot{\varphi}d) - l_1F_{HT}. \quad (2)$$

The dimensions of the cabin were taken from the manufacturer's data sheet [12]. The other characteristic values were taken from [13] and largely correspond to the values of a ZF test vehicle. Since the model of the cabin is kept very simple, the demand on the accuracy of the parameters is also not very high. **Table 1** shows the parameters used.

Table 1: Parameters of truck cabin [12, 13]

Cabin parameter	Value
Half cabin mass m	650 kg
Length l_1	2 m
Length l_2	1 m
Length l_3	1 m
Suspension stiffness c	40000 N/m
Damping constant d	13300 Ns/m
Gravitation constant g	9.81 m/s

The measured velocity profile shown in **Figure 5** is used for the investigation.

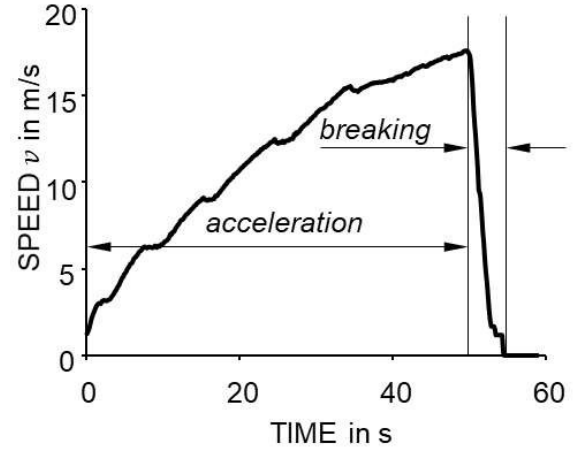


Figure 5: Speed profile

This profile originates from a test run by ZF Friedrichshafen to investigate lightweight components [14]. It represents an acceleration with gearshifts and a braking action. By changing the speed, the cabin is set in rotation.

If one compares the deflection of the rear damper between the simplified model and the evaluation of the measurement run in **Figure 6**, a good agreement can be seen, although the vertical dynamics were disregarded in the model. The maximum deflection of the real system was not taken into account in the model and shows a difference in the braking process.

The model will be used for further investigations to estimate the potential of the FDVA application.

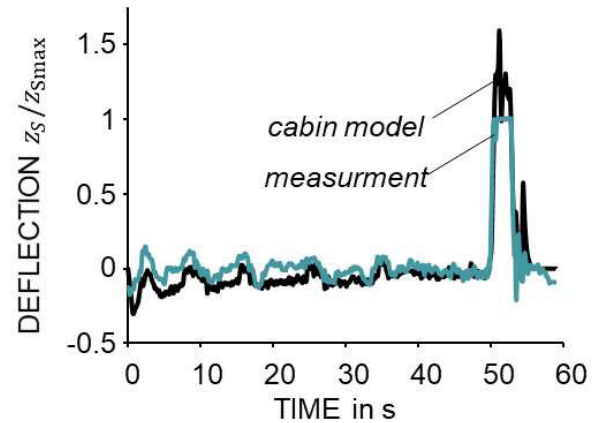


Figure 6: Comparison between simplified model and measurement

4. FDVA DESIGN

A vibration absorber absorbs the vibration energy of a vibrating system. Therefore, the energy is transferred from the vibrating system to the vibration absorber. For this purpose, a capacity with an inertia is added to the system [15]. The inertia is usually at least an order of magnitude smaller than the inertia of the system in order not to unnecessarily increase the total weight. It shows the advantage of the FDVA. The FDVA achieves a much higher inertia with a small additional mass. The optimal design of the FDVA is given by the tuning of the absorber frequency. The optimal eigenfrequency of the FDVA

$$f_A = f_S \frac{1}{\sqrt{1-\mu}} \quad (3)$$

is close to the systems eigenfrequency f_S , but is still dependent on the ratio $\mu = m_A/m_S$ between the tilting mass m_A and the system mass m_S . The frequency response always cuts two points for a variation of damping. We get the optimum eigenfrequency if these two points have the same ordinate value [15]. The damping depends on the transmission ratio. Taking these considerations into account, the tuning parameters of the FDVA can be given in **Table 2**.

Table 2: Parameters of FDVA design

Cabin parameter	Value
Oil mass m_{oil}	3.71 kg
Tilting mass m_A	131.04 kg
Eigenfrequency f_A	1.8 Hz
Ratio α	48

5. SIMULATION RESULT

The equations of motion are transformed into a first order form and solved using the Runge-Kutta method. The input is defined as the speed of the truck. The angular acceleration of the cabin represents the result (**Figure 7**).

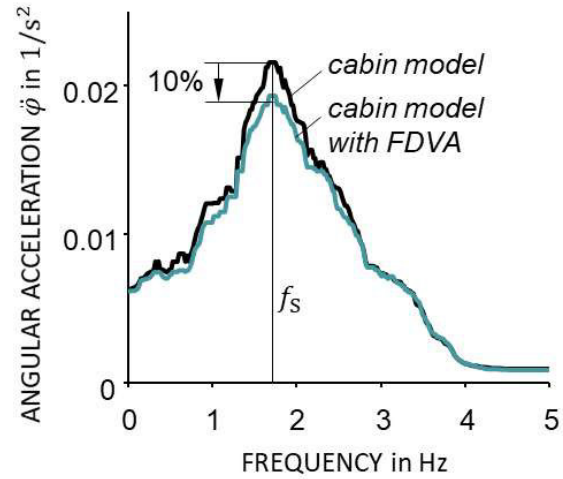


Figure 7: Comparison of angular acceleration between cabin model with and without FDVA

The frequency range of angular acceleration from 0 to 5 Hz is plotted. At higher frequencies the amplitude of angular acceleration is very small and has hardly any influence on the driver. It can be seen that using the FDVA reduces the amplitude by about 10% in the range around the eigenfrequency.

6. EVALUATION OF THE IMPACT ON THE DRIVER

In the following, the effects of angular acceleration on well-being and physical health risk will be investigated. There are regulations that limit the time exposure of humans to vibration through the Ordinance on the Protection of Employees from Noise and Vibration Hazards [16].

The type, extent and duration of exposure shall be assessed. In the case examined here it concerns rotatory oscillations on a seated person which are evaluated in accordance to VDI 2057 Part 1 [6]. Accordingly, the rotation on the seat is weighted with the frequency weighting W_e (**Figure 8**).

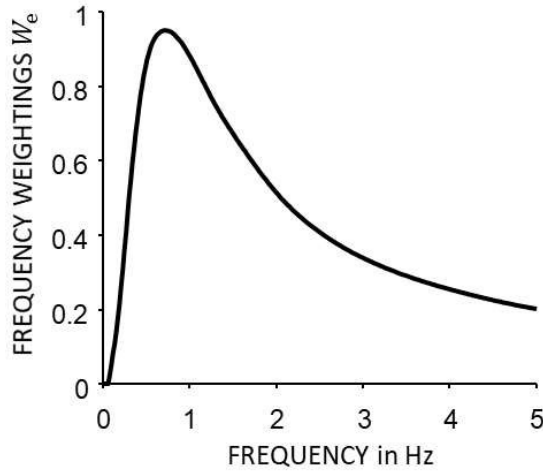


Figure 8: Frequency weightings W_e for a rotation on the seat according to VDI 2057 part 1

The acceleration evaluation of the nodding cabin on the driver in sitting position reflects the well-being. The driver therefore feels the worst at a frequency of 0.8 Hz.

From the determined partial frequency weightings

$$a_{wl,n} = W_e a_n \quad (4)$$

the effective value of the frequency-weighted acceleration of the entire spectrum

$$a_{wl} = \sqrt{\sum_{n=1}^m a_{wl,n}^2} \quad (5)$$

is calculated.

For the cabin model with FDVA a value of 0.059 rad/s^2 is obtained compared to the result without FDVA with 0.064 rad/s^2 . This value is multiplied by the weighting factor $k_1 = 0.4 \text{ m/rad}$ from ISO 2631 Part 1 [17] to convert the value into a linear comparison value. For the assessment acceleration, which is compared with the limit value, the effective value a_{wl} must still be scaled with the action duration T as follows:

$$a_{w8t} = k_1 \cdot a_{wl} \cdot \sqrt{\frac{T}{T_0}} \quad (6)$$

The exposure time T is set in relation to the assessment duration of the working day $T_0 = 8 \text{ h}$. Assuming a 2 h ride in stop and go, $T = 2 \text{ h}$ can be set, as there is constant acceleration and braking during stop and go. This approximately corresponds to the speed profile shown in figure 4. These two hours do not come close to a potential health risk. With a value of $a_{w8t} = 0.0126$ for the cabin model without FDVA, the

assessment acceleration is still an order of magnitude below a potential health risk for which the limit values are shown in **Figure 9**. So even with a full 8 hours of traffic jam no health risk is to be expected here.

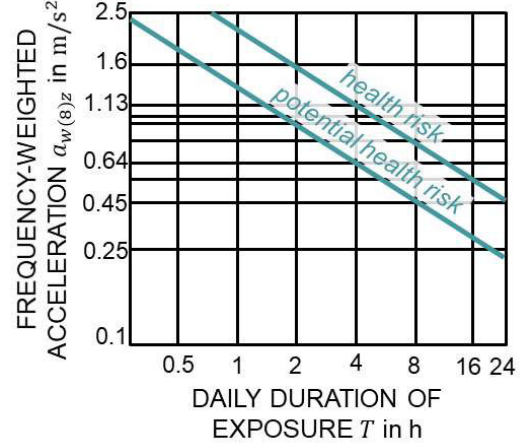


Figure 9: Area of increased health risk by stimulation [6]

However, this result is not surprising for an existing truck. The truck is designed to not expose the driver to any health risk during the journey. Even if there is no health risk, a good driving comfort is a sales argument. In addition to the health risk, the driver's perception can also be evaluated. The effective value with the weighting factor k_1 is used for this evaluation. The perception is perceived as described in **Table 3**. The greater the acceleration value, the stronger the perception. The perception of angular acceleration with an acceleration value $a_{wl} = 0.0256 \text{ m/s}^2$ related to linear movements in cabin suspension without FDVA is evaluated as easily perceptible according to Table 3. With FDVA $a_{wl} = 0.0236 \text{ m/s}^2$ and moves towards barely perceptible, which improves comfort.

Table 3: Scale of subjective perception [6]

Root-mean-square values a_{wl} of the frequency weighted acceleration in m/s^2	Description of perception
<0.01	not perceptible
0.015	threshold of perception
0.015-0.02	barely perceptible
0.02-0.08	easily perceptible
0.08-0.315	strongly perceptible
>0.315	extremely perceptible

A reduction of the pitch oscillation to a barely perceptible sensation is therefore desirable.

7. CONCLUSION

We investigated the effect of pitch vibrations on the driver of a truck and how they can be reduced with a new type of vibration absorber. For this purpose, a simple cabin model for pitch oscillation was set up, which is excited by the acceleration of the truck in longitudinal direction. The comparison of the deflection of the rear suspension between model and measurement shows a good approximation. With this the effects of the pitch vibrations on the driver are investigated and compared between a model with and without integrated hydraulically translated vibration absorber. The simulation model of the Fluid Dynamic Vibration Absorber was validated and adopted to the cabin suspension. In the eigenfrequency of the cabin, about 1.8 Hz, the amplitude can be reduced by 10% with only 4 kg additional mass. This is possible by the hydraulic transmission of the vibration absorber.

Driving comfort rated by the oscillation sensation is classified as easily perceptible. This easy perceptibility reduces the comfort and it is desirable to reduce the oscillations. Thus, a cabin suspension is a possible application for the FDVA. With this knowledge, the next step is to use the model of the FDVA in the half-vehicle truck model. This will show the FDVA's influence on the other eigenfrequencies of the truck.

ACKNOWLEDGMENT

Funded by the Deutsche Forschungsgemeinschaft (DFG, German Research Foundation) – Projektnummer 57157498 – SFB 805. The authors especially would like to thank the project cooperation partner ZF Friedrichshafen AG for supporting this project.

NOMENCLATURE

a	Duct surface
a_n	Partial acceleration amplitudes
A	Piston surface
a_{w8l}	Evaluation acceleration
a_{wl}	Root-mean-square value of the frequency-weighted acceleration
$a_{wl,n}$	Partial
c	Suspension stiffness
d	Damping constant
f_A	Eigenfrequency of the FDVA
f_S	Eigenfrequency of the truck cabin

F_{HT}	Force of FDVA
$FDVA$	Fluid Dynamic Vibration Absorber
g	Gravitation constant
IFK	International Conference of Fluid Power
k_1	Correction factor for assessment quantities
k_{HT}	Absorber stiffness
l_1	Distance between front and rear suspension
l_2	Distance between front suspension and centre of mass in longitudinal direction
l_3	Distance between front suspension and centre of mass in vertical direction
m	Half cabin mass
m_A	Tilting mass
m_F	Fluid mass in duct of FDVA
m_{oil}	Oil mass of FDVA
m_P	Piston mass
m_S	Mass of oscillating System
p_L	Pressure loss
T	Exposure duration
T_0	Assessment duration
v	Truck speed
V	Transmissibility
W_e	Frequency weightings
z_A	Absorber motion
z_S	System motion
α	Ratio between piston surface and duct surface
β	Ratio between cylinder length and duct length
θ	Rotational inertia of truck cabin
θ_A	Inertia of FDVA
μ	Ratio between tilting and system mass
ρ	Oil density
φ	Pitch angle
$\dot{\varphi}$	Angular velocity
$\ddot{\varphi}$	Angular acceleration
φ_0	Starting pitch angle
ψ	Phase shift

REFERENCES

- [1] Choi SB, Choi JH, Lee YS, Han MS (2003) Vibration Control of an ER Seat Suspension for a Commercial Vehicle. *J. Dyn. Sys., Meas., Control* 125(1):60–68.
- [2] Tong RT, Amirouche F (1998) Truck cab suspension design: optimisation and vibration control *International Journal of Heavy Vehicle Systems*, Bd 5. Inderscience, S 236–260
- [3] Appel W, Hoepke E, Breuer S (2013) *Nutzfahrzeugtechnik. Grundlagen, Systeme, Komponenten*, 7. Aufl. Praxis: Kraftfahrzeugtechnik. Vieweg + Teubner, Wiesbaden
- [4] Evers W-J, Besselink I, Teerhuis A, Nijmeijer H (2011) On the achievable performance using

- variable geometry active secondary suspension systems in commercial vehicles. *Vehicle System Dynamics* 49(10):1553–1573.
- [5] Evers WJE (2010) Improving driver comfort in commercial vehicles. Modeling and control of a low-power active cabin suspension system
- [6] Verein Deutscher Ingenieure (2017) Einwirkung mechanischer Schwingungen auf den Menschen. *Ganzkörperschwingungen*, 3. Aufl 13.160(VDI 2057 Blatt 1)
- [7] Pelz PF, Cloos FJ, Corneli T., Hedrich P, Nakhjiri M. (2015) Leichtbautilger für Fahrwerke 3. VDI-Fachtagung Schwingungsdämpfung, Bd 2261. VDI-Verlag, Leonberg, S 121–129
- [8] Corneli T, Pelz PF (2014) Employing Hydraulic Transmission for Light Weight Dynamic Absorber. In: Murrenhoff H (Hrsg) 9th International Fluid Power Conference (9th IFK), Vol. 3. HP - Fördervereinigung Fluidtechnik, Aachen, S 198–209
- [9] Brötz N, Hedrich P, Pelz PF (2018) Integrated Fluid Dynamic Vibration Absorber for Mobile Applications. In: Murrenhoff H (Hrsg) 11th International Fluid Power Conference (11th IFK), 11. Aufl, Vol. 1. RWTH Aachen University, Aachen, S 14–25
- [10] Brötz N, Pelz PF (2020) Bayesian Uncertainty Quantification in the Development of a New Vibration Absorber Technology. *Proceedings of IMAC 2020*: submitted
- [11] Zhang J, Guo P, Lin J, Wang K (2016) A mathematical model for coupled vibration system of road vehicle and coupling effect analysis. *Applied Mathematical Modelling* 40(2):1199–1217.
- [12] MAN MAN TGX - Fahrerhaus für den Fernverkehr.
<http://man.etpl.ch/truck/global/de/fernverkehr/tgx/fahrerhaus/fahrerhaus-xxl/Fahrerhaus-XXL.html>. Zugegriffen: 11. November 2019
- [13] Evers WJE, Besselink IJM, Teerhuis AP, Oomen TAE, Nijmeijer H Experimental Validation of a Quarter Truck Model Using Asynchronous Measurements with Low Signal-to-Noise Ratios
- [14] Heimann J, Müller I, Neu A, Stieglitz A (2019) CLFT - Leichtbau für den schweren Lkw. *Lightweight Des* 12(1):46–51
- [15] Den Hartog JP (1985) *Mechanical vibrations. Dover books on engineering.* Dover Publications, New York
- [16] Bundesministerium der Justiz und für Verbraucherschutz (2007) Verordnung zum Schutz der Beschäftigten vor Gefährdungen durch Lärm und Vibrationen. *Lärm- und Vibrations-Arbeitsschutzverordnung - LärmVibrationsArbSchV*
- [17] International Organization for Standardization (1997) *Mechanical vibration and shock. Evaluation of human exposure to whole-body vibration.* ISO 2631-1:1997, Switzerland



GROUP 10

Special domains

GENERAL LECTURE:

THE ROOF WING OPENING SYSTEM OF THE UAE PAVILION AT EXPO 2020

Paolo Leutenegger^{1,2*}, Carlo Vergano^{1,2}, Rainer Herzinger³, Jürgen Weber⁴, Nicola Bassetto¹, Fabio Belluschi¹, Riccardo Cardani¹, Ina Costin¹, Costanzo Codari¹, Stefano Ferla¹, Giovanni Forti¹, Simon Köhler⁴, Roberto Maddalon¹, Gino Pari², Daniel Panev², Michele Pavanetto¹, Cristian Poli¹, Massimo Ripamonti¹, Alessandro Rossignoli¹, Matteo Traù², Jonas Uhlmann⁴, Renzo Zaltieri¹

¹Diplomatic Motion Solutions S.p.A., Via Mario Re Depaolini 24, 20015 Parabiago (MI), Italy

²Diplomatic Middle East LLC, Office 3 Rooftop, MSM 2 Bldg. Al Safa 1st, Sheikh Zayed Rd - Dubai

³Santiago Calatrava LLC, Parkring 11, CH-8002 Zürich, Switzerland

⁴Technical University Dresden, Chair of Fluid-Mechatronic Systems, Helmholtzstr. 7a, 01069 Dresden, Germany

* Corresponding author: Tel.: +39 329 1010322; E-mail address: p.leutenegger@duplomatic.com

ABSTRACT

The UAE Pavilion will be a major attraction at Expo 2020 in Dubai. The roof of the building consists of 28 operable wings made of carbon and glass fiber, having masses ranging from 5 to 18 tons and total lengths in the range of 30 to 65 m that have to be actuated by a dedicated mechanism.

In this paper we present the turn-key project for the design, manufacturing, installation, test and commissioning of the Roof Wing Opening System, which represents a unique system world-wide for operating the wings. It consists of one Hydraulic Power Unit with approximately 1 MW of installed power, 2 km of piping working at the nominal pressure of 210 bar, 46 hydraulic cylinders with 1.5 tons of mass each and the complete automation and control subsystem that includes 9 separate PLCs, dedicated software, 2.000 sensors and control points, and over 20 km of harness.

One major challenge is the control of the wings. Part of them, due to their huge dimensions and masses, are actuated using two or three hydraulic cylinders that have to be properly synchronized during the movement, preventing unwanted displacements in order to avoid stresses on the wing mechanical structure and ultimately permanent damages. Due to the nature of the project, a final validation of the control algorithms can be done only at system level during the commissioning phase. Therefore, particular care has to be devoted to the verification strategy, anticipating the behavior of the system in the early validation stages and following a V-model approach, in order to identify critical situations and reduce the overall risk.

After a brief system description, we will explain how the verification has been approached by using system level simulations and dedicated testing activities on specific subsystems. In particular, we will detail the verification of the control algorithms that has been performed on a dedicated Hardware-In-the-Loop system first, followed then by dedicated tests on a reduced wing mock-up, allowing the study of the system behavior under the most critical conditions. These include the application of external forces with specified profiles. Finally, we will provide the actual status of the system installation, testing and commissioning activities that have been running in Dubai since January 2019.

Keywords: Hydraulic System, Piping, Valves, Hydraulic Actuators, Motion Control, Synchronization

1. THE UAE PAVILION AT EXPO 2020

The UAE Pavilion at Expo 2020 is designed by the Architect Santiago Calatrava in the shape of a falcon in flight, the official symbol of the UAE, and will be a major attraction at Expo 2020. The roof of the building consists of 28 carbon and

glass-fiber shaped movable wings, having masses ranging from 5 to 18 tons and total lengths in the range of 30 to 65 m. They are actuated by a hydraulic system called Roof Wing Opening System (RWOS) that is going to be discussed in the following paragraphs.

This special application generated a quite unusual list of requirements to be compliant with, a step ahead of the common requests typical of industrial applications. Since the beginning of the project, we became aware that it was mandatory to have a different approach and an open mindset to provide a technical solution fulfilling the requirements that are beyond usual expectations.

Functionality and good performance were not



Figure 1: Pictorial view of the UAE Pavilion at Expo 2020, Dubai.

enough, the final aim of the project was to realize something to let people astonish, a glimpse of perfection which is the expected target for this event and a special town like Dubai. The final Customer was not just looking for something simply working, but to be delighted with. This awareness accompanied us throughout the development of the whole project.

Our purpose has been at highest level to provide a system giving the impression of absolute precision and solemnity during the movement, being compliant with the environment, the Expo 2020 sustainability idea and the expectations of the Client in terms of performance, reliability and aesthetics. Translating it into requirements it means: All wings shall be opened and closed in a synchronized harmonic simultaneous fashion, absolutely silently, with the lowest possible visual impact, having the highest reliability, high power efficiency, implementing a technical solution devoted to solidity and stability.

Based on the above a technical solution was developed from a reference design and a set of performance specifications. The design development was supported by continuous collaborations with the CI Team, giving us the possibility to develop and optimize the system architecture.

The hydraulic system structure has been defined trading-off the system characteristics, the

limited available space inside the building and the aggressive time schedule of the construction. All equipment, including the piping network have been prefabricated in Europe and delivered to Site for installation. As an example, the detailed design allowed the installation of approx. 1,3 km of system piping fully prefabricated without realizing any welding on site.

2. THE ROOF WING OPENING SYSTEM

2.1. Hydraulic Concept

The hydraulic system architecture includes:

- One Hydraulic Power Unit (HPU) with approx. 1 MW of capacity located in the basement of building.
- One piping network implementing the hydraulic backbone of the system. The piping system is composed by two lines: Pressure supply line and Return line. Both start from the HPU and connect to the roof area.
- 46 Valve Stands to independently control the movement of each hydraulic actuator including pressure sensors.
- 46 Hydraulic Actuators equipped with stroke and proximity sensors.
- One Automation and Control Subsystem (AUT) that includes 17 electronic cabinets and more than 20 km of cables.

The basic design idea is to control flow rate and system pressure independently, adjusting them

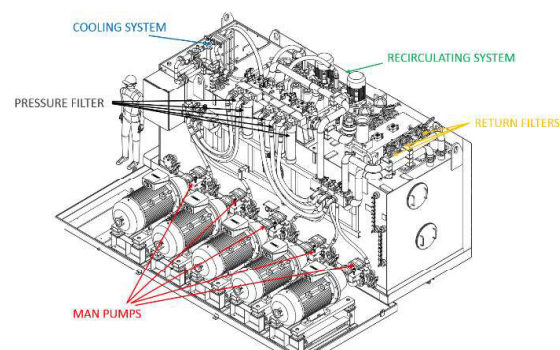


Figure 2: RWOS Hydraulic Power Unit.

according to every specific working condition. For this reason, fixed displacement pumps controlled by electrical motors driven by inverters have been used. This allows an almost instantaneous setting of the system pressure according to the specific load request.

The max oil flow rate has been calculated based on the time requirements specified for wing opening and fast closing sequences. Flow rates have been calculated individually for every actuator taking into consideration their cinematic characteristics and acceleration and deceleration profiles. Since the main architectural project requirement considers the synchronous opening and closing of all wings simultaneously, they have been finally combined in order to obtain the total flow rate required by the working cycle, as shown by the blue curve of **Figure 3**, where the worst-case opening cycle is considered.

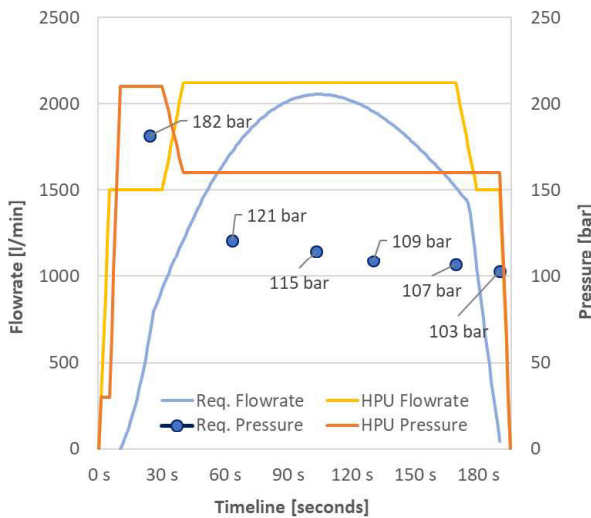


Figure 3: System level requirements and HPU parameters for the opening cycle (180 seconds) under worst-case load conditions.

The system design pressure has been defined in accordance to the dynamic load requirements calculated for every actuator. The envelope of the pressure required for the movement for given angular positions of the wing has been calculated considering the worst-case load condition having both the effect of gravity and the load generated by the wind. Relevant wind load data have been derived from a dedicated test campaign with a representative UAE Pavilion model in the wind tunnel, in which a complete pavilion model including all surrounding buildings has been used to measure wing loads using approximately 900 pressure sensors.

The resulting pressure requirement for allowing the movement of the system is shown by the blue dots in **Figure 3**.

In order to minimize the power consumption, flow rate and system pressure are regulated according to the working cycle. Due to the

cinematic law, the acceleration and deceleration phases and the dependence of the loads from the wing angular position, the pressure request is maximum at the beginning of the opening movement, where the flow rate request is at minimum. After acceleration, the pressure request decreases while flow rate demand increases. This defines a trade-off between pressure and flow rate, giving the possibility to optimize the power consumption.

The HPU generated flow rate and output pressure applied on the P-line are shown by the orange and yellow curves respectively.

The request of having a silent movement drives the choice to use internal gear pump, to introduce bumper elements on all piping system and to define the start-up sequence in order to minimize the possibility of vibration.

Among high-pressure pumps, internal gear pumps are in fact those with lowest noise emission. Additionally, two pumps on each pump unit have been foreseen. Twin pumps have been installed in such a way to have pulsation in counter-phase, thus reducing pressure ripple on the pressure line and consequently the noise emission.

2.2. System Piping

System Piping has been designed taking into consideration different constrains. The main requirement is to guarantee high-pressure hydraulic fluid flowrate at big distance from the HPU (Hydraulic Power Unit), where pressure is generated. This has to be achieved considering the structure deformation of the building, desertic climate that includes extreme temperature excursions, sand storms and heavy rains, different elevations of actuators and power generation.

Non-painted stainless steel 316L has been selected as piping material. This is considered as the most reliable measure to guarantee functionality throughout the pavilion's lifetime, limiting the maintenance demand.

The HPU is designed in order to provide a maximum constant 210bar working pressure with more than 2000l/min flow rate. A schematic picture showing the location of the HPU and the routing of the system piping inside the Pavilion is shown in **Figure 4**.

The HPU is located in Basement 2 (B2) level, 5 meters below the Ground level, and 45m far

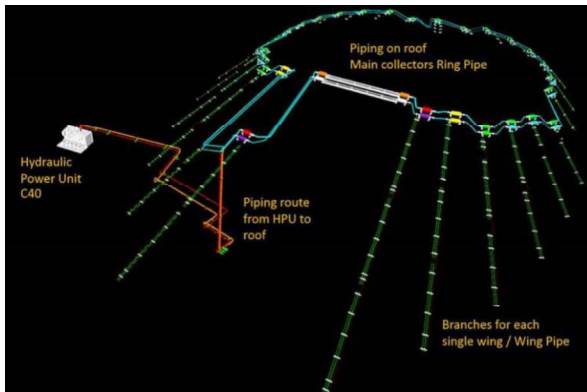


Figure 4: Pictorial view of the piping routed through the pavilion.

from the point where pipes can raise to the roof and approx. 100m from the farthest wing actuator: the design goal is the minimization of pressure losses along the distributions, in order to maintain a good system efficiency. This requirement, in conjunction with the design and test pressure set to 1.5 times the working pressure, leads to have a 5" size main pipe for the high-pressure line to the roof and an 8" size low pressure pipe for the fluid flow return from the roof to the power unit.

These two pipes are routed inside the pavilion B2 level to the designed *Riser* chimney, crossing parking, rooms, walls. This represents a real challenge considering that the weight is as high as 50 kg/m for bare steel without fluid inside for the 5" pressure line. Special supports, dedicated for each area, have been designed, taking into consideration the specific routing for both pressure and return line inside the pavilion area. Each support sustains more than half of a metric ton in such cases.

The vertical part of the pipes reaching the roof, called *Riser*, is a 15m long line ending at the interface between the concrete part of the pavilion and the steel roof. In this area the main design requirement is related to the ability to allow different deformation coefficients between the steel roof and the concrete part of the building. In fact, the steel roof is supported by the concrete structure in such a way, that it is free to move (breathe) when contracting or expanding under thermal changes, in order to minimize the loads transferred from the roof into the concrete base.

On the roof, two pipes are formed in loop, passing through the steel roof ribs. These pipes, called *Ring Pipes*, ensure fluid distribution to

each wing. Their size ranges between 4" and 3" for the pressure line and between 6" and 4" for the return line pipe. The diameter is at maximum near to the *Riser* and is reduced towards the ring termination. The ring topology has been chosen in order to let the fluid take the easiest, therefore less dissipative, way to reach the actuators according to each actuation phase. The ring is made with spool pieces connected by means of flanges, forming a segmented loop with many curves that allow deformation induced by thermal loads. The overall length of each loop is approx. 550m for the pressure pipe loop and 590m for the return pipe.

Flexible hoses have been used to connect *Riser* and Ring Piping. A system based on flexible seals and gutters is used for guaranteeing waterproofing of the roof where flexible hoses are installed.

Particular attention has been devoted to the design of the pipe supports. In fact, the pipe network has to be able to expand due to thermal effects induced by the oil temperature. Moreover, as the roof steel structure can be deformed by thermal effects and wind loads, the opposite condition has to be considered, allowing a roof deformation without impacting on the pipe integrity. Special supports have been designed for this purpose. Pipes are allowed to slide on them, being able to compensate thermal deformations. The fixation points have been designed allowing all degree of freedoms required to accommodate different thermal expansion coefficients. On the roof, the whole ring pipe is "floating" on these supports, allowing any deformation of the roof structure, without impacting the pipes.

An additional issue is represented by system vibrations that could be amplified by the steel structure of the roof generating noise inside the pavilion. For this reason, elastic elements have been introduced in correspondence of any connection point between the hydraulic system and the supporting structure. The complete piping network is sustained by adequate rubber pads.

Each wing is equipped with one to three actuators, according to the wing length, that needs to be fed with high pressure hydraulic fluid. For each wing smaller pipes are sufficient to provide the required flow. One high-pressure line and one return line run along the steel wing rib passing through valves manifolds used for feeding the system: these are called *Wing Pipes*. In order to reduce weight and volume and pipes

waste, pipe dimensions are different according to the amount of flow they have to manage.

Connection between the ring and wing pipes are made with flex hoses in order to leave the ring pipes free to move and expand radially independently with respect to *Wing Pipes'* radial expansion.

2.3. Hydraulic Actuators and Motion Control

The movement of each hydraulic actuator is independently controlled by one dedicated proportional control valve. Additional valves are provided to manage lock-in position, emergency closing and direction of movement. Valves are installed on a block located on the back of each actuator, thus reducing the distance and increasing the control response time. Relief and lock valves are installed directly on the cylinder for safety purposes.

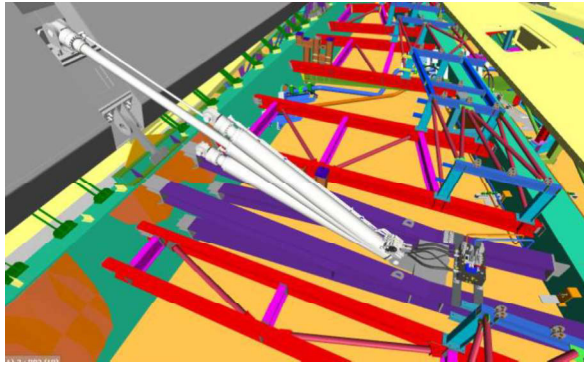


Figure 5: Valve Stand connected with hydraulic actuator.

The motion control solution has been designed in accordance to the specific hydraulic architecture and components. We have followed our standard philosophy in controlling the speed of a hydraulic axis piloting a compensated proportional flow valve and using the signal of a position transducer as feedback.

Two different hardware solutions have been adopted for controlling wings with single and multiple axes.

The system is modular. Each axis has a dedicated motion control card (CAC). In case of a multi-axis wing one additional control card acts as synchronism supervisor (SSC). All cards communicate internally via a dedicated CAN bus. The connection to the automation and control subsystem (AUT) is performed through a PROFINET interface.

Two different functions, discussed hereafter, are implemented in the motion controller: wing and synchronism control.

Wing control

It executes the opening/closing command, operating the wing. The angular speed profile according to [1] is defined by the distance, travel, acceleration and deceleration times with the following equation:

$$\omega_{MAX} = \frac{\alpha_{Tot}}{T_{TOT} - \frac{1}{2}(T_a + T_d)} \quad (1)$$

T_a and T_d have been chosen according to the hydraulic circuit characteristics and power management requirements.

The standard profile consists of a full-stroke opening/closing movement to be performed in 180s +/-2s. Fast closing with max. speed shall be allowed in 120s in case of critical weather conditions. Although it does not represent a nominal working condition, a profile generator allows a recovery movement starting from an intermediate position.

Due to the specific characteristics of the project and the difficulty in predicting the dynamic behaviour of the wing, a special open-loop algorithm has been implemented for controlling the angular speed of the wing using the stroke information of the cylinder as feedback.

The kinematic law of each actuator is defined by equation (2), that has a set of parameters that depend on the geometry and the position of the wing on the roof. Consequently, each cylinder has a unique parameters' set, that is stored in the firmware.

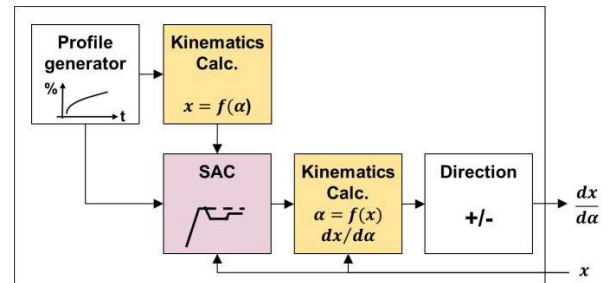


Figure 6: Block diagram of the motion control card algorithm for single axes wings.

$$\alpha[^{\circ}] = \cos^{-1} \left(\frac{R^2 + B^2 - (A_{CYL} + x[mm])^2}{2BR} \right) \times \frac{180}{\pi} \quad (2)$$

Based on the actual position x , the kinematic law is used to calculate the angle, and through the inverted relationship (3), to generate a linear position profile starting from the angular profile required by the travel time-direction relationship.

$$x[\text{mm}] = \sqrt{R^2 + B^2 - 2BR \cos \alpha - A_{CYL}} \quad (3)$$

A derivative function of the kinematic law is used to calculate the output to the proportional flow valve from the angular speed and to scale the control deviation due to the synchronism error in case of a multi-axis subsystem.

$$\frac{dx}{d\alpha} = \frac{2RB \sin \alpha}{2(x + A_{CYL})} \quad (4)$$

Due to the open loop control solution adopted, the tracking quality of the cinematic profile is strictly linked to the behaviour of the proportional flow valve, which has been designed "ad hoc" for this project. In order to compensate for deviations from the theoretical behaviour induced by external influences and tolerances in mechanical and hydraulic components, a Speed Adaptive Control (SAC) algorithm has been used. SAC is a modified version of the MR-Controls concept according to [2], with three main differences:

- SAC doesn't act at the same frequency of the control loop (i.e. 1 kHz), but in a defined number of checkpoints as a supervisor of the followed profile.
- SAC forces a direct correction to the speed at each checkpoint and compensates the cumulated positioning error in the remaining part of the stroke.
- Checkpoints are equally spaced in the angular range.

b. Synchronism control

Synchronization is required for wings with two or three axes. In this case the management of the Open Loop Profile and SAC are moved to SSC. This is required as the cinematics of the axes belonging to the same wing are different so that a normalized profile is required.

A closed-loop PI control ($f_c = 1\text{kHz}$) based on a Master-Slave concept is implemented in CAC, using the synchronization set point passed by the SSC and it's active only for slave axes. The aim is to minimize the synchronism error under the maximum acceptable limit of $\pm 10\text{mm}$ around the normalized linear position.

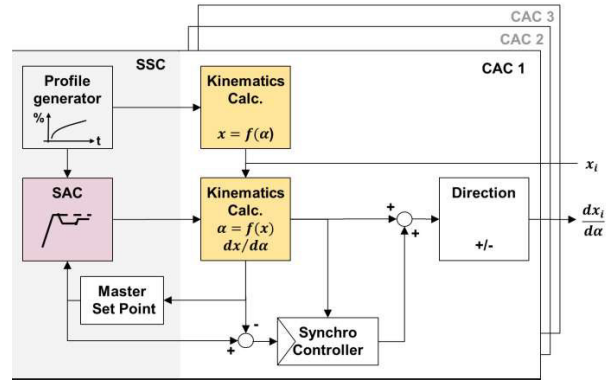


Figure 7: Block diagram of the motion control card algorithm for multiple axes wings.

The main advantages of this choice are:

- With a Master-Slave concept disturbances and oscillations on a slave axis do not influence the whole controller.
- The Master is controlled in open-loop avoiding the complexity arising from the low natural frequency of the system and granting the independence of the tuning of the synchro controller from the wing control.
- SSC, being the fastest observer of the synchronism, is also in charge for the execution of any immediate stop of the wing movement, in case that the synchronization error exceeds an acceptable threshold limit.

2.4. The Control and Automation Subsystem

The AUT subsystem manages the control of all RWOS parts and includes the following main items:

- One HPU Power Supply Cabinet including main PLC (HPU0-Q001)
- Two Wing Power Distribution Cabinets incl. remote PLCs for remote Wing Automation (HPU0-Q003 and -Q004)
- Four Wing Power Supply Cabinets delivering +24V power supply for all actuator subsystems (OCL0-Q001 through -Q004)
- Ten Wing Automation Cabinets including the control electronics for the actuator control and synchronization (OCL0-Q101 through -Q110).
- Several IP67 compliant remote I/O modules

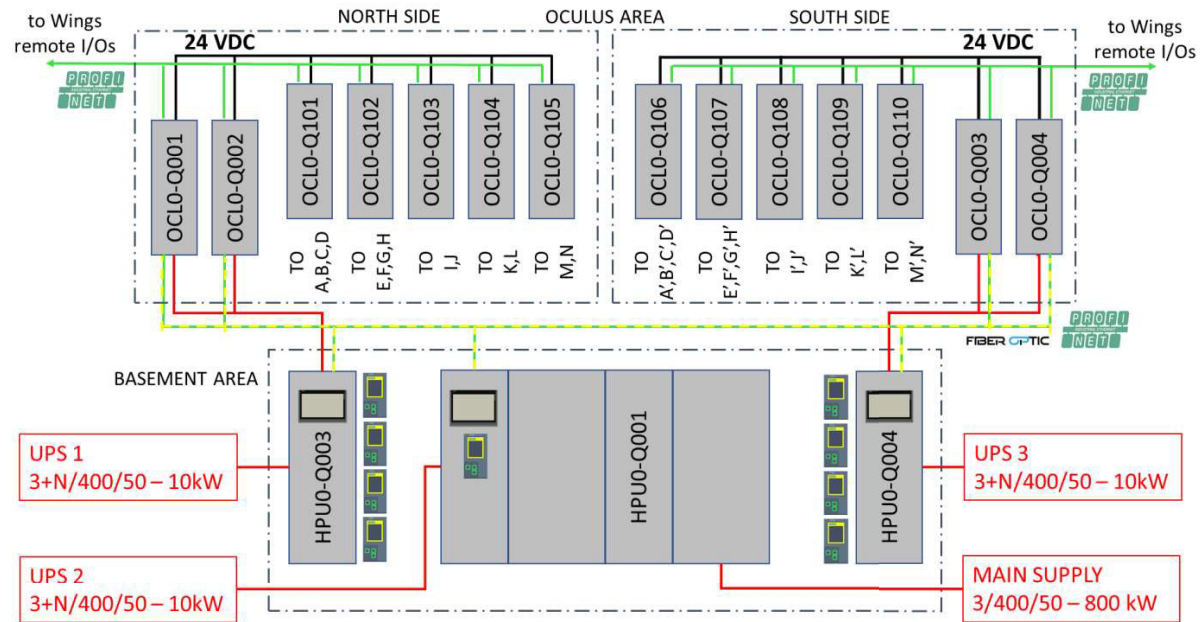


Figure 8: Block diagram of the RWOS AUT architecture including the network communication.

- Temperature sensors, pressure and stroke transducers
- Interconnecting harness including power cables, fiber optic lines, signal lines, sockets and sensors.

All PLCs are physically located in B2. Wing Power Supply and Automation Cabinets are located in the upper part of the roof, called Oculus. No direct roof access is required, since parametrization of any device can be performed remotely, thus simplifying the maintenance.

The roof opening and closing functionality is available from a central Building Management

System (BMS) located in a dedicated area of the building through a dedicated network connection to the main PLC. A scheduler allows the execution of automated sequences based on daily or weekly wing actuation plans. Actuation sequences are limited to the maximum allowed cycles per day and maximum delay time between two consecutive cycles, in order not to overheat the hydraulic fluid.

The top-level block diagram of the RWOS is shown in **Figure 8**. The primary power to the HPU inverters and motors is delivered through the main cabinet HPU0-Q001 that is connected

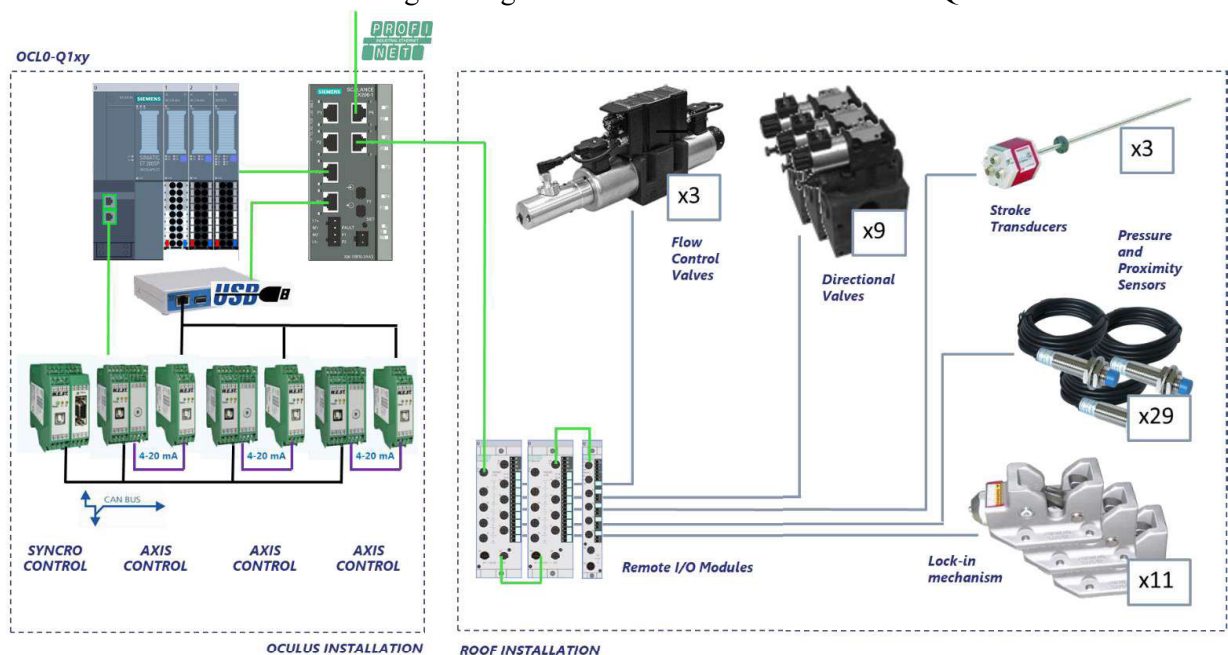


Figure 9: Subsystems connected to one multi-axes wing.

directly to the main transformer and is capable to provide up to 935kW of power.

All control subsystems of all electric panels including the main PLCs are supplied by three UPS subsystems, which allow 10 minutes of operation also in case of main power loss, thus ensuring the possibility to drive the RWOS in a secure condition before switch-off.

For each actuator the wing control electronics has to manage the following subsystems:

- Directional and proportional flow control valves for cylinder actuation
- Pressure transducers
- Stroke transducers
- Temperature sensors

In addition to the above, each wing has a certain number of additional valves for controlling the lock-in mechanism of the wings and for maintenance purposes.

Remote input/output modules are used at each actuator position, complying with the high-temperature requirements applicable to the roof area and IP67 protection class. Each socket is connected to the PROFINET communication network and receives the +24V power supply from the power supply cabinets installed in the Oculus area, as shown in **Figure 9**.

3. EARLY-STAGE SYSTEM VERIFICATION

3.1. Overall Approach

The main verification challenge is related to the system dimensions and to the difficulty of performing representative tests before final testing and commissioning at site. We have overcome this limitation following a V-model verification approach combining system modelling, simulations and tests at subsystem level. In particular, three levels of verification have been addressed, involving:

- The firmware of both CAC and SSC;
- The wing control subsystem including hydraulics, electronics and software;
- The system behavior, that depends from the hydraulics architecture, the operation of the wings and disturbances generated by both internal and external factors (i.e. pressure fluctuations, wind effects, etc.).

The testing activity has been aimed to anticipate the behavior of the components involved in the system and to identify the risks during the development phase prior to the testing

at site. In the following paragraphs we provide an overview of each verification steps, starting from the system modelling, which represents the base of our verification strategy.

3.2. System Modelling and Simulations

System simulations have the objective of identifying critical working conditions during test, commissioning or operational phases. The criterion is the verification of the available system design margin. Two main aspects have been analyzed:

- System pressure losses throughout the various operating conditions, that depend from the power demanded by the actuators during the movement. They answer to the basic question if the cylinders are able to move in any possible load condition.
- Pressure reserve available under worst case operating conditions.

Different simulation models have been developed for this purpose.

Evaluation of pressure losses

The first model includes HPU, pressure relief valves (PRV) used for setting the system pressure and piping network. The pump model is signal-based. The hydro-mechanical and volumetric efficiencies are stored in a map. Both are dependent from the applied system pressure and engine speed, according to . This allows the calculation of the effective torque of the motor shaft and the loss of the volume flow to along its characteristic curve, from the start up to the operating point. The parameterisation and validation are executed with data sheets and pump characterization measurements. The model does not consider the dynamic behaviour and pulsation of the pump, as well as the starting behaviour of the electrical motors.

The manifold includes different valves and filters that have been described exclusively by their flow characteristics. A functional mapping is not necessary, as these are normally only actuated when the system is not moving. The PRV model is based on the functional description of the valve based on pressure-time profiles, dynamic behaviour and volume-flow characteristics.

Design data including lengths, diameters and height differences have been used for the pipe

system model, which is composed by individual pipe elements. Every element considers:

- hydraulic capacity and inductance

$$L_h = \rho \cdot \frac{l}{h} \quad (5)$$

$$p_{acceleration} = L_h \cdot \frac{dQ}{dt} \quad (6)$$

$$C_h = \frac{A}{\rho \cdot g} \quad (7)$$

$$\dot{p} = \frac{1}{C_h} (Q_{in} - Q_{out}) \quad (8)$$

- hydrostatic losses

$$p_{hydrostat} = g \cdot \rho \cdot h \quad (9)$$

- hydrodynamic losses

$$p_{hydrodym} = \zeta \cdot \frac{\rho}{2} \cdot v^2 \quad (10)$$

$$\zeta = \zeta_{pipe} + n_{bend} \cdot \zeta_{bend} + \zeta_{res} \quad (11)$$

- pipe friction according to Haaland

$$\zeta_{pipe} = \lambda(Re) \cdot \frac{l}{d_i} \quad (12)$$

- flow resistance

$$\zeta_{res} = \frac{K_{Lam}}{Re} + \zeta_T \quad (13)$$

Pipe wall expansion effects and fixation interfaces to the building structure were neglected as their real effect on the system was unknown at the time.

Pipe model validation has been limited to a first-order validation based on literature [3], due to the non-availability of measurements and the large scale of the system.

All cylinders have been mapped with their required volume flow through 46 take-over points directly connected to the main piping circuit.

Every sub-model including the related physical behavior has been verified individually before final model assembly.

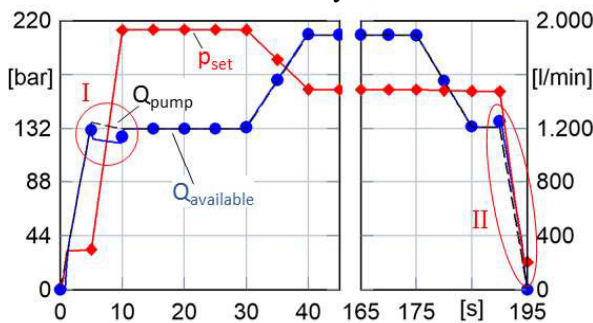


Figure 10: Influence of the hydraulic capacity - pressure build-up and down phase

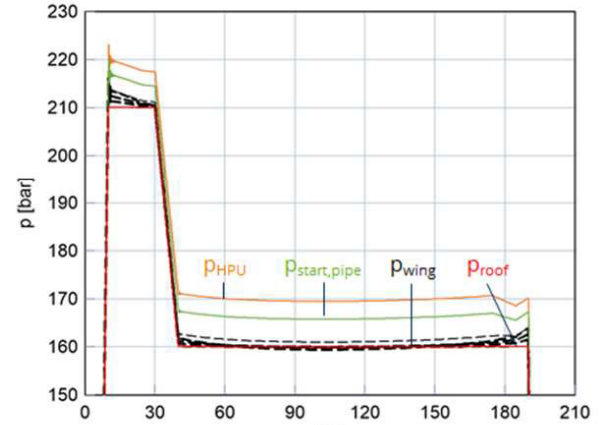
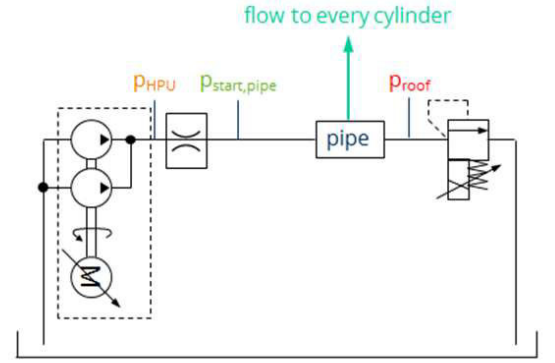


Figure 11: Pressure losses simulation for opening cycle (180 sec, PRV on the roof).

Figure 10 shows an example of the intermediate verification: The influence of the hydraulic capacity on the pressure build-up (I) and drop-down (II) phases for the opening cycle without cylinder flow and other losses is illustrated. In area I, the difference between pump flow and available flow over the PRV is the necessary volume flow for the system pressure build-up. Area II shows an additional volume flow in the pressure drop-down phase.

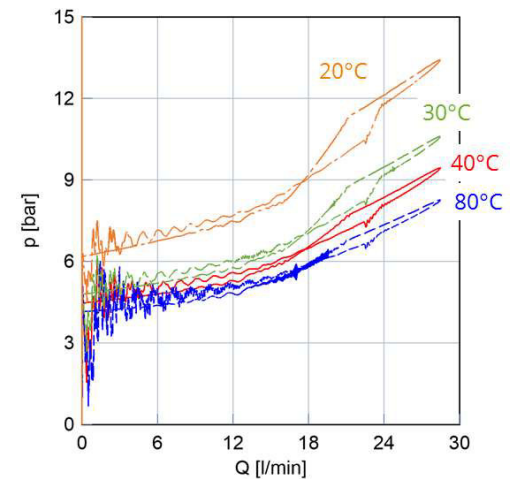


Figure 12: Pressure losses vs. volume flow on cylinder A2 at different temperatures (HLP 46).

Figure 11 presents the results of the pressure loss analysis for the 180 sec opening cycle. The pressure at different locations is shown for HLP46 oil at 40°C. Losses are approximately 10 bar, as expected.

Four temperatures and two oil types have been analyzed, as shown in **Figure 12**, where pressure losses at the cylinder connection joint are shown as a function of the volume flow. Worst-case pressure losses are 13bar at 20°C oil temperature. 15bar have been considered through all simulation work, in order to compensate for model uncertainties and measuring errors from the preliminary investigations.

Evaluation of the pressure reserve

The evaluation of the system pressure reserve requires the modelling of the cylinder hydraulic control, that includes the flow control valve (FCV), as well as additional components. The system behaviour is defined by the FCV characteristics. Depending on the cylinder size, two valve types with nominal volume flows of 60 l/min or 110 l/min respectively have been used. All other components have been modelled exclusively by their flow characteristics.

The FCV includes proportional valve spool, pressure compensator, and pilot valve. The volume flow is kept constant with changing load conditions for a constant set current. This is achieved through the pressure compensator, that ensures a constant pressure drop across a throttle, according to the following throttle equation:

$$Q_{Valve} = \alpha \cdot \sqrt{\frac{2}{\rho}} \cdot A_{Throttle} \sqrt{\Delta p} \quad (14)$$

The FCV has typically non-ideal behaviour, that includes current and pressure dependent flow characteristics and hysteresis. The valve control range begins at a pressure drop of eight bar. The model includes the following components:

- a characteristic valve map;
- a set current dependent hysteresis;
- the valve behavior outside the pressure control range.

Signal-based mapping has been used for the determination of the characteristic FCV map. For this purpose, measurements of the valve recorded in four different set-up configurations have been used and analysed, in order to derive the basic characteristics of the components involved. **Figure 13** shows the valve measurement setup. During the test a pump is providing a constant

volume flow. Two different PRV can set a nearly constant pressure difference across the flow control valve. The following test scenarios have been used:

1. ramp-shaped current build-up without counter pressure
2. ramp-shaped current build-up with constant counter pressure at 180 bar
3. ramp-shaped counter pressure build-up with constant opening current at 1900 mA
4. ramp-shaped counter pressure build-up with constant opening current at 1260 mA

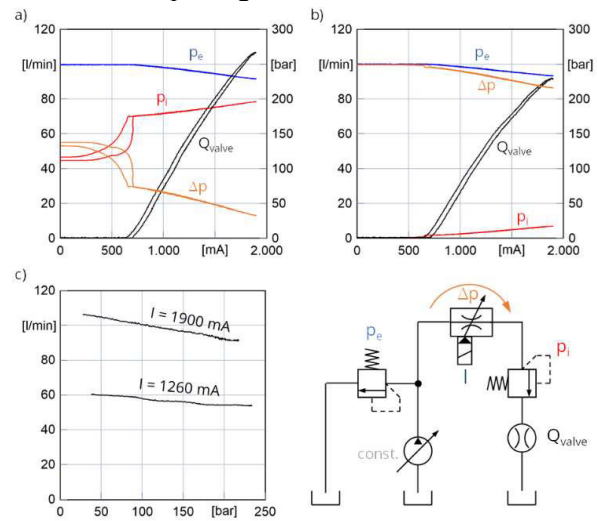


Figure 13: Sketch of the measurement test bench and results – a) with counter pressure; b) without counter pressure; c) two measurement with constant current by changing pressure difference.

The characteristic valve map is derived by fitting the known measured points with polynomial functions using a least squares approximation. The maps generated so far are further reduced to final characteristic maps with significantly less points through a second least squares approximation. The result are characteristic maps that are transferred into the model. Out of the valve pressure control range – i.e. between 0 to 8 bar – the valve behaviour is approximated with an ideal throttle equation, according to (14).

The theoretical derived pressure dependence is evident in the characteristic diagram. Considering a constant set current of 1900 mA, approx. 21 l/min total flowrate variation are generated at the maximum pressure difference. Furthermore, it can be seen that there is no clear linearity between volume flow and control current. Both aspects have to be taken into account when reflecting the control algorithm.

Based on the analysis of the measurement data, the following model components have been generated with an acceptable level of accuracy (**Figure 14**).

- Characteristic valve map

$$Q_{map} = f(\Delta p, I_{solenoid})$$

- Hysteresis dependent on set current change

$$Q_{hyst} = f(I_{solenoid}, dI_{solenoid})$$

- Ideal throttle behavior beyond control range

$$Q_{ctrl} = f(\Delta p)$$

Pressure dependent hysteresis has been neglected.

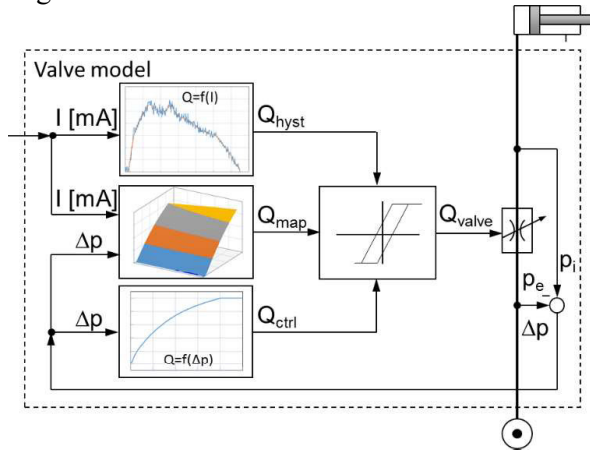


Figure 14: FCV Model.

The model considers the time response of the FCV. Two approaches have been investigated. In the first option, the reaction time of the pressure compensator to changing pressure conditions can be simulated by a delay in the pressure difference signal. In the second approach the signal of the solenoid control current is delayed. Considering the dynamic behaviour of the valve that depends mainly on inertia and friction, a time-dependent solenoid current has been preferred.

The evaluation of the pressure reserve has been carried out with the above model. We have selected the most critical cylinders in terms of loads generated by the wing mass and external forces in worst-case wind conditions. The highest force on each wing angle position under all wings was used to create a synthetic force load profile for the simulation.

Both the opening and closing sequence have been separately investigated. Reaction forces on the cylinder and the pressure on the cylinder valve block have been considered as model

boundaries. The applied system pressure has been reduced by 15 bar in order to account for pressure losses. A simplified version of the cylinder control algorithm has been used for this purpose.

First results evidenced the necessity for modifying the system pressure profile extending the duration of the high-pressure condition at the beginning of the opening cycle, in order to overcome the high loads acting on the actuators. Also, during the closing process pressures were insufficient in some cases.

New profiles have been generated increasing the system pressure from 140 to 160 bar showing that sufficient design margin is present during all operating conditions. An example is given in **Figure 15**, where the results for the most heavily loaded cylinder in the closing phase are shown for the above-mentioned pressure conditions. The pressure difference between piston and return line shall exceed the minimum difference required by the pressure compensator of the FCV, that is 8 bar, in all operating conditions providing an adequate margin. Increasing the system pressure ensures an increase of this value from 0.5 bar to 25.5 bar.

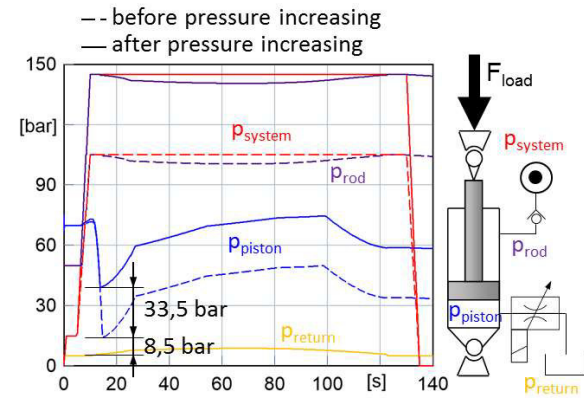


Figure 15: Pressure difference across the FCV throughout the closing cycle.

3.3. Verification of the actuator control algorithms

Hardware-in-the-Loop Test Bench

The tests performed on the software code to verify the behaviour of the control are usually not sufficient to identify all critical working conditions, since with a simple software testing environment it is not possible to reproduce the changing environmental conditions in which the algorithms are supposed to work. For this purpose, a Hardware-in-the-Loop (HiL) system

has been designed and implemented. Hardware-in-the-Loop (HiL) simulation is a common technique used for system-level testing of embedded systems. The HiL test bench contains a virtual simulation environment that includes the cylinder subsystem and different hardware components, as shown in **Figure 16**.

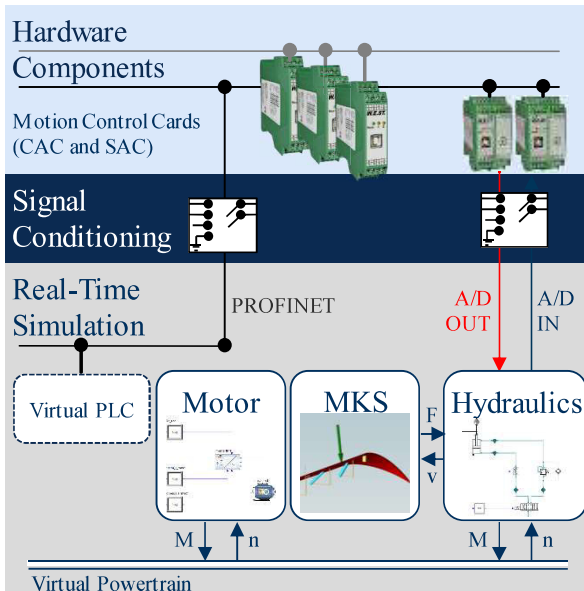


Figure 16: Hardware-in-the-Loop test bench

The test bench can simulate virtual movements of the wings, which are controlled by the motion control cards (CAC and SAC) incl. the corresponding hydraulic valves. Signal conditioning is managed by a dedicated Field Programmable Gate Array (FPGA) and communication occurs through PROFINET fieldbus. The main objective has been the test of the motion control algorithms, answering to the following questions:

1. Has the general functionality been achieved? Have all software bugs been identified?
2. Are the requirements fulfilled? In particular, can the opening/closing time requirements be achieved with the given maximum position error under all circumstances?
3. How sensitive is the influence of different controller parameter on the performance?

Two groups of test cases have been generated for this purpose, in order to study the performance of synchronized actuator movement under safety critical conditions and for specific failure simulations.

Three main results have been obtained by Hardware-in-the-Loop simulation:

- The specific designed Speed Adaptive Control algorithm is able to control the

position error within the specified limit of $\pm 10\text{mm}$ during both opening and closing movements for all wings under worst-case load conditions. The opening/closing time requirements ($180\text{s}/120\text{s} \pm 2\text{s}$) can be met for all test cases. The compliance in terms of time tolerances is a precondition in order to ensure the synchronous movement of all wings on the roof.

- The SSC controller for the movement of wings with more than one axis complies the demanded tolerances for angular deviation during all test cases. The compliance of these tolerances is absolutely necessary for guarantying low bending moments of the wings and therefore a damage-free wing movement.
- The influence of component specific tolerances, as for instance stroke-sensor offset fluctuations, are not affecting the system performance. The wing opening and closing movement can be guaranteed under all conditions.

Figure 17 shows the results for the opening cycle on multi-axes wing L. The three curves represent the angular cylinder deviations α for the three axes.

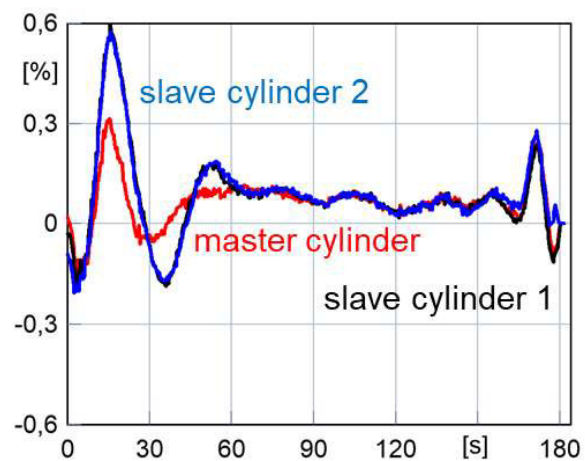


Figure 17: Position error [%] - Testcase 5b), opening 180s cycle with wing L2 as master cylinder und dead-load condition and offset

After the initial 20s acceleration ramp at the beginning of the movement, the error on all three cylinders is decreasing to zero. This condition is maintained throughout the linear movement until the deceleration ramp is started. The speed adaption algorithm is compensating the stroke error correctly, by adapting the speed of the movement. Slave cylinders are behaving in

agreement with the master cylinder (one), showing that the PI controller responsible for axes synchronization is working properly. Throughout the movement all specified tolerances are within the requirements.

Wing Test Bench

The wing test bench is a versatile hardware replica of a wing subsystem, built and stored at DMS premises. Although downscaled to limit occupied space and energy consumption, it accurately replicates the properties of both a single and a multiple axes wing installed on the pavilion.

The wing test bench is composed by the following equipment:

- 3 hydraulics cylinders (stroke 1000mm, bore 50mm, rod 28mm) including SSI linear transducers, the related control axes boards and valve blocks.
- Hydraulic Power Unit (HPU) working at 120bar and fixed flow rate.
- Control PLC, acting as the wing controller;
- Ancillary equipment (sensors, remote I/O-modules, HMI).

The main objectives of the replicated wing system are:

- Validation of the firmware implementation in the motion control boards;
- Debugging and early-validation of the automation software.

In order to thoroughly test the motion algorithms, the hydraulic circuit is equipped with additional proportional pressure valves that are used to inject external disturbances to simulate wind loads and test the algorithms robustness.

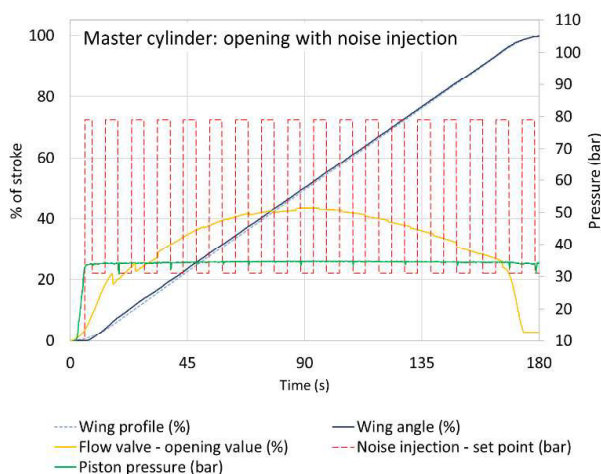


Figure 18: Opening movement with noise injection. Master cylinder.

Figure 18 and **Figure 19** show the results for master and slave axes for an opening movement performed in 180s, where the influence of external disturbances (e.g. wind forces) has been simulated by the injection of a noise pressure square wave.

As in Master-Slave controlled mode, the synchronism control loop that acts on each Slave is not affected by the behavior of other slave axes, a simplified sub-system with 2 axes only has been here represented. The master has been controlled in open loop with speed adaption acting approx. each 9s. Only low-frequency noise effects have been considered. Slave axes have been disturbed with a square waveform performing a frequency sweep (from 0.2 up to 5Hz).

The results confirm that the overall opening time is not affected by the influence of external forces, although the square wave profile creates alternating pushing and pulling forces. The robustness of the synchronization algorithm is demonstrated by the synchronization error on the slave axes, that is well below the max. acceptable threshold of ± 10 mm. It has to be considered, that noise injections for master and slave were not in phase.

This can be observed in the slave behavior, where a “Delta noise injection” representing the normalized difference between Master and Slave noise injections is shown. The relationship between the proportional valve correction and the noise applied on both axes can be appreciated.

Overall Results

Simulations, HiL and WTB have generated results that confirm the feasibility and reliability

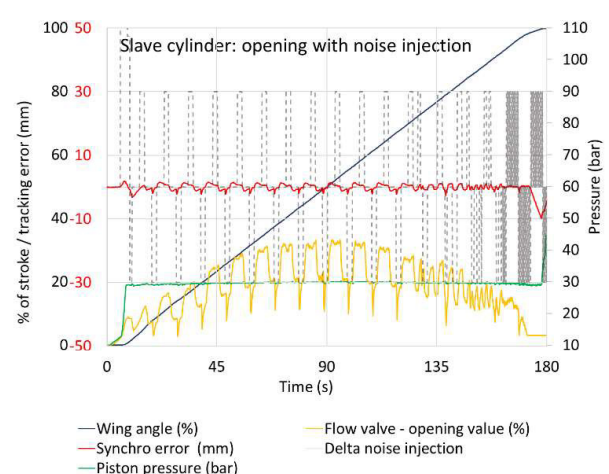


Figure 19: Opening movement with noise injection. Slave cylinder.

of the technical solution proposed, demonstrating in particular the robustness of the synchronism algorithm, but highlighting critical aspects, too.

The necessity of a non-linear characteristic curve for the proportional flow valves, the choice of the proper cylinder as a master in a multi-axis system, the modified ramp-times and pressure levels in the flow-pressure timeline for opening/closing movements are examples of corrective actions implemented during the development that will reduce effort and unexpected events during commissioning.

On the other side, some simplifications on the model and not fully validated behaviors in the simulations will require a deep analysis of the real system at site. Particular care shall be devoted to the choice of wing-level cinematic parameters that shall consider the actual manufacturing tolerances, as well the fine tuning of the synchronism controller.

4. ERECTION & COMMISSIONING

4.1. Activities at Site

Installation of the equipment on site has been running since January 2019. One major difficulty we encountered is related to the coordination with the other activities involving the building. Usually, complex equipment is installed after the completion of civil works. In our case this has not been possible, due to the very aggressive time schedule, the complexity of the building and the technical difficulties encountered in the coordination among different Subcontractors. At the time where this paper is being prepared, the complete piping system only has been fully installed and commissioned, including 10 single axes wings and the first four three-axes wing. Electric installations are still on-going preventing the operation of the wings with the main HPU. Therefore, additional auxiliary equipment has been designed and build in order to allow pre-commissioning and anticipate critical tests.

4.2. Single-axis wings

Ten single axes wings have already been installed and fully tested. The pressure flow for the movement is provided by an auxiliary HPU that is connected to the system piping through by-pass flanges in Basement 2. For the movement the wing angle has been monitored through dedicated transducers and the values compared with the

stroke transducer position information of the cylinder. The calculated wing cinematic parameters based on as-built conditions are very close to the original as-designed parameter, although installation tolerances are in general significantly higher than as-designed ones.

The wing behavior during one opening cycle is shown in **Figure 20**.



Figure 20: Pre-commissioning results on wing A South.

The blue curve represents the stroke of the opening movement. The total travel time is 180,3 seconds, within the specified limit of 180s \pm 2s. The function of the SAC can be observed on the yellow curve. After the first two checkpoints stroke errors are compensated adjusting the speed profile. This is confirmed by the stroke error that reaches its maximum at the first checkpoint, after which compensation occurs.

5. CONCLUSIONS

The Roof Wing Opening System for the UAE Pavilion at Expo 2020 has been presented, showing both the very special requirements related to this particular application and the boundary conditions of the project, that require a different approach compared to conventional

industrial applications. The early-stage verification approach based on the joint use of system simulations, tests at component and subsystem level, as well as pre-commissioning activities at site has been discussed. All results show the validity of our approach and represent a good base for the commissioning activities on the pavilion, that will run on a limited time-frame in spring 2020.

The authors would like to thank Mr. Ulrich and Mr. Winkes of W.E.ST. Elektronik GmbH, Ms. Hina Farooqi and the whole Calatrava International Team for the continuous support and fruitful discussions throughout the whole project. A special thanks to Arabtec Construction Team for its logistic support on site.

- [3] I.E. Idel'chik, [*Handbook of hydraulic Resistance – Coefficients of Local Resistance and of Friction*, 1960, Moscow]

NOMENCLATURE

A	Area
A_{CYL}	Cylinder Length in the fully retracted position
AUT	Automation and Control Subsystem
$B2$	Basement 2
CAC	Single-Axis Control Card
DME	Diplomatic Middle East LLC
DMS	Diplomatic Motion Solutions S.p.A.
FCV	Flow Control Valve
FW	Firmware
HiL	Hardware-In-the-Loop
HMI	Human-Machine Interface
HPU	Hydraulic Power Unit
I/O	Input/Output
IFK	International Conference of Fluid Power
MR	Multi-Recursive
PLC	Programmable Logic Controller
PRV	Pressure Relief Valve
$RWOS$	Roof Wing Opening System
SAC	Speed Adaptive Control
SSC	Synchronism Supervisor Card
SW	Software
ω_{MAX}	Maximum Angular Speed
α_{Tot}	Angular Range
T_{Tot}	Total Time
T_a	Acceleration Time
T_d	Deceleration Time

REFERENCES

- [1] Jack L Johnson - Designer's handbook for electro hydraulic servo and proportional systems
- [2] Ulrich Walter (W.E.St.) - A multiplicative-recursive filter and linearization scheme

PRELIMINARY DESIGN AND TESTING OF A SERVO-HYDRAULIC ACTUATION SYSTEM FOR AN AUTONOMOUS ANKLE EXOSKELETON

Emmanuel Viennet*, Loïc Bouchardy

HES-SO University of Applied Sciences and Arts Western Switzerland, Boulevard de Pérolles 80, 1700 Fribourg

* Corresponding author: Tel.: +41 26 4296670; E-mail address: Emmanuel.Viennet@hefr.ch

ABSTRACT

The work presented in this paper aims at developing a hydraulic actuation system for an ankle exoskeleton that is able to deliver a peak power of 250 W, with a maximum torque of 90 N.m and maximum speed of 320 deg/s. After justifying the choice of a servo hydraulic actuator (SHA) over an electro hydrostatic actuator (EHA) for the targeted application, some test results of a first functional prototype are presented. The closed-loop unloaded displacement frequency response of the prototype shows a bandwidth ranging from 5 Hz to 8 Hz for displacement amplitudes between ± 5 mm and ± 20 mm, thus demonstrating adequate dynamic performance for normal walking speed. Then, a detailed design is proposed as a combination of commercially available components (in particular a miniature servo valve and a membrane accumulator) and a custom aluminium manifold that incorporates the hydraulic cylinder. The actuator design achieves a total weight of 1.0 kg worn at the ankle.

Keywords: Exoskeleton; Ankle-foot orthosis; Hydraulic actuator; Wearable robotics; Rehabilitation

1. INTRODUCTION

Lower limb powered exoskeletons are an emerging technology that shows potential in rehabilitation therapy, for instance by improving functional recovery and psychological well-being after a stroke [1]. In a recent clinical study [2], powered ankle-foot exoskeletons have shown biomedical benefits compared to classical passive ankle-foot orthosis. However, despite the positive results, all participants of the study indicated that

mass and size were concerns with using the powered exoskeleton on a daily basis. With high power-to-weight and force-to-weight ratios, hydraulic actuators are an interesting alternative to electric motors today in use in the vast majority of exoskeleton projects.

2. GAIT CYCLE

The gait cycle, shown in **Figure 1**, is divided into the stance and swing phases. During the stance

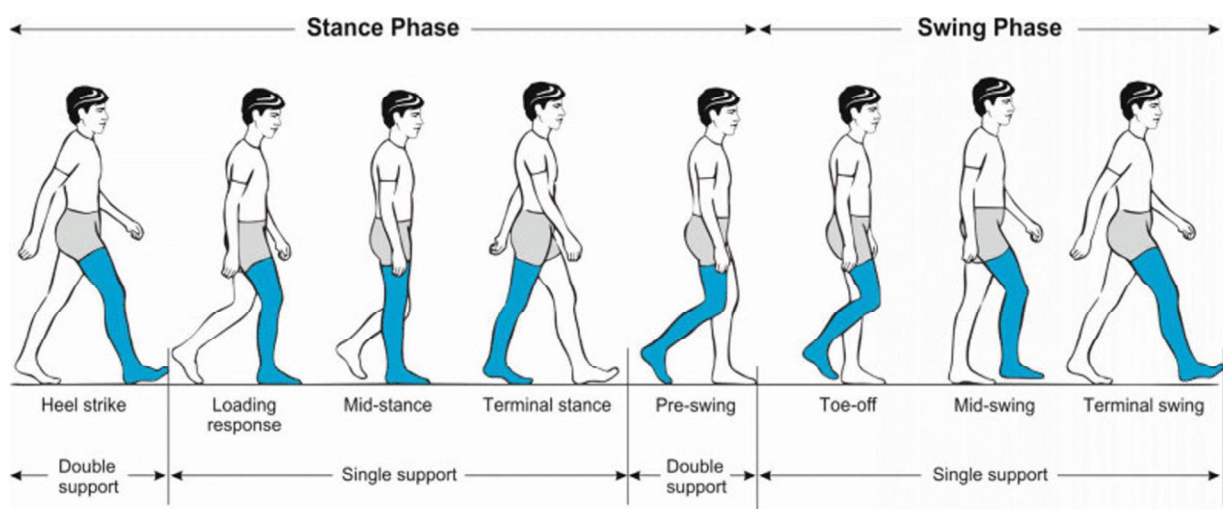


Figure 1: Phases of the normal gait cycle, reproduced from [3]

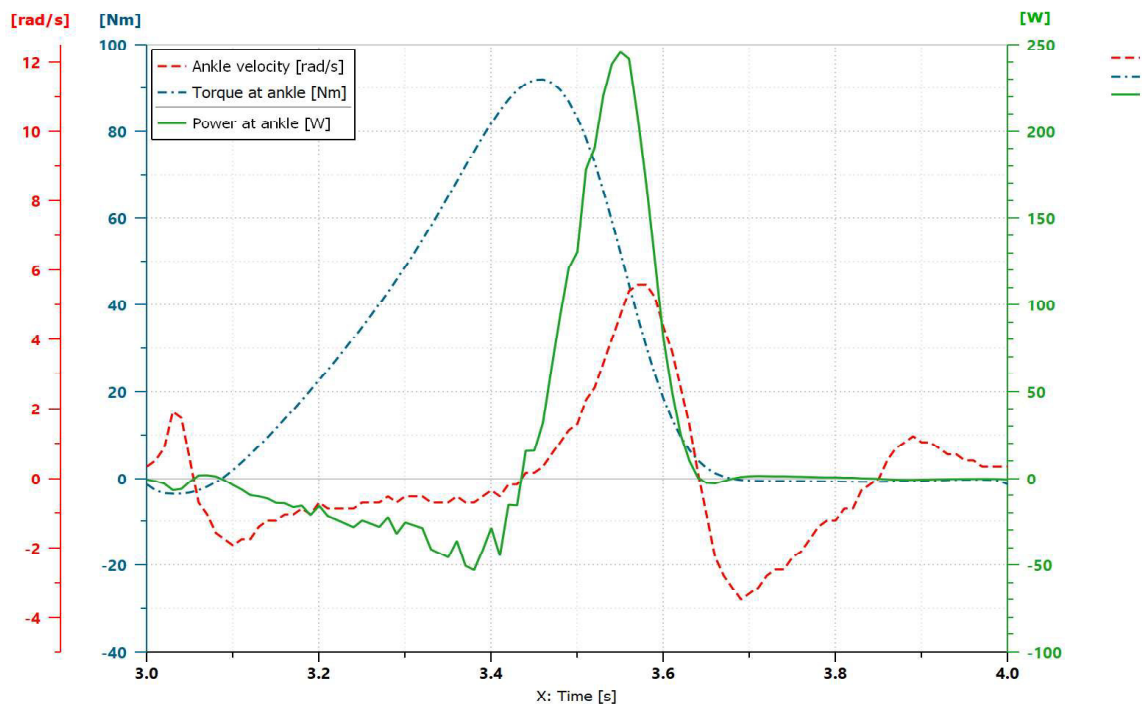


Figure 2: Angle velocity, torque and power at the ankle for 68kg individual, reproduced from [4]

phase, the foot is in contact with the floor and the ankle is loaded. It actually receives power from the body during in the first half of the stance phase and provides power during the second half. During the following swing phase the ankle moves unloaded.

The working cycle of the ankle-foot joint depends on the walking conditions and the subject weight. The design presented in this paper is based on flat-floor normal-speed walking for a 68 kg individual as provided in [4] and reproduced in **Figure 2**.

The analysis of this working cycle provides key information for the design of the actuator:

- The power demand at the ankle is highly variable over the gait cycle. The positive part of this power has the form of a peak that lasts less than 20% of the total cycle and reaches a maximum value of 250W for a 68kg individual.
- There is a potential for recovering energy during the negative power phase. Besides, it occurs naturally for healthy subjects because mechanical energy is stored in the muscle-tendon system during this phase.
- A maximum velocity of 320 deg/s is reached during plantarflexion (foot down) and of 200 deg/s during dorsiflexion (foot up)

- A maximum plantarflexion torque of 90 N.m is necessary (for 100% assistance) during the terminal stance phase (push-off) and a very limited dorsiflexion torque of less than 5 N.m is sufficient during heel strike.

With the help of the FFT shown in **Figure 3**, it appears clearly that, in addition to the maximum speed request, it is necessary to specify that the actuation system shall be able to track frequencies at least up to 4 or 5 Hz without major attenuation.

3. ENVISAGED HYDRAULIC CONCEPTS

While pioneering projects of hydraulic actuated exoskeletons like [5] used servo hydraulic actuation (SHA), two recent researches dealing with ankle-foot orthosis [6] and prosthesis [7] focussed on electro hydrostatic actuation (EHA). In this paper, we compare these two concepts by combining information provided on the datasheets of relevant components and results of numerical simulations.

For virtually assessing its performance, we propose a preliminary design of an EHA concept consisting of:

- E-motor EC 90 flat, 360 Watt, 24V, from Maxon Motors, Switzerland

- Motor controller ESCON Mod. 50/5, from Maxon Motors, Switzerland
- Reversible axial piston pump with fixed displacement TFH-040 (414 mm³) from Takako, Japan
- Hydraulic hoses 1.5 m long, internal diameter 4 mm between pump and cylinder

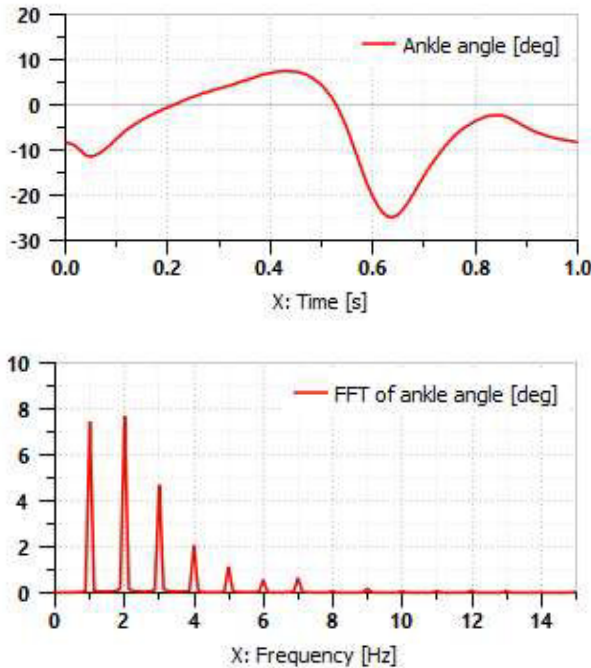


Figure 3: FFT of ankle angle during a gait cycle

We propose a corresponding preliminary design for a SHA concept as follows:

- E-motor EC frameless 60 flat, 100 Watt, 24V, from Maxon Motors, Switzerland
- Motor controller ESCON Mod. 50/5, from Maxon Motors, Switzerland
- Axial piston pump with fixed displacement PB-33.6 (76 mm³) from Hydroeduc, France
- Hydraulic hoses 1.5 m long, internal diameter 4 mm between pump and valve block
- Membrane accumulator AC13-1/4 (13 cm³, 250 bar operating pressure) from HAWE, Germany
- Servovalve E024 Super low leakage from Moog, England
- No hose between valve block and cylinder

The hydraulic schematics of the two concepts are given in **Figure 4** and **Figure 5**. In both cases, a 10/8 hydraulic cylinder with 40 mm stroke and 250 bar operating pressure is considered even if such a cylinder is not found on the market.

We modelled and simulated the two concepts in order to compare their ability in tracking a prescribed sinusoidal displacement of the cylinder rod with an amplitude of ± 5 mm at different frequencies. The results are presented in form of a Bode diagram in **Figure 6**.

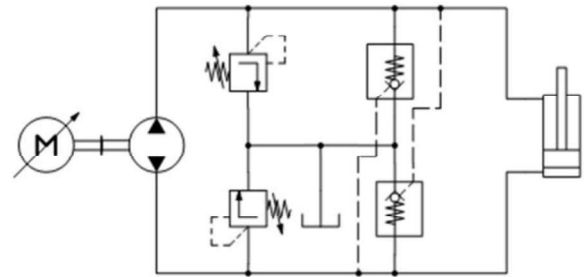


Figure 4: EHA

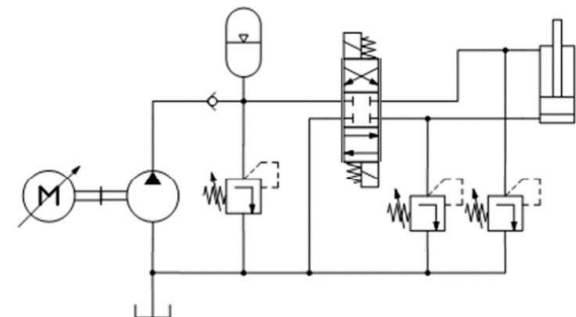


Figure 5: SHA

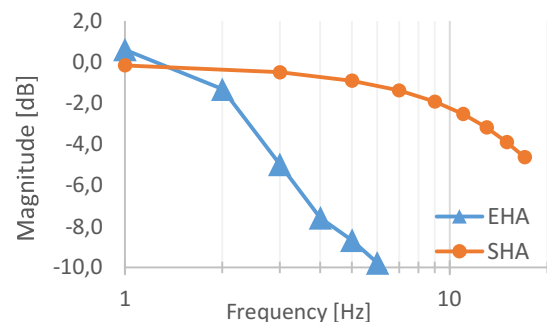


Figure 6: Simulated closed-loop unloaded frequency response for ± 5 mm position

The -3 dB cut-off frequencies are simulated respectively below 3 Hz for the EHA system and above 12 Hz with the SHA system. This makes a big advantage for the SHA system in terms of dynamics, especially when recalling that the typical angle profile during walking involves significant frequency contents up to 5 Hz.

One important reason for EHA to show lower dynamic performance than SHA is due to the time needed to build up the pressure in the hydraulic hoses. In the performed simulations, the oil bulk modulus was that of a mineral oil with 1% entrained air.

Another criterion for comparison is the weight worn at the ankle that we evaluated and summarized in Figure 7 (weight of the actuator only, excluding the structure of the exoskeleton). The values with the mention “estimated” are based on the preliminary design presented previously and shall be considered as ambitious yet realistic targets. The value with the mention “actual” is the result of a first-iteration detailed design presented in section 6 of this paper.

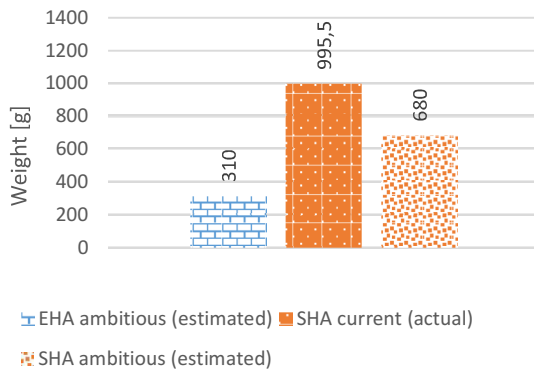


Figure 7: Comparison of weight worn at the ankle for EHA and SHA, mix of actual and estimated values

Finally, choosing between EHA and SHA is a choice between two conflicting objectives – namely dynamics versus light weight – that is inevitably frustrating in applications like exoskeletons where both are equally important.

4. FIRST FUNCTIONAL PROTOTYPE

In the presented project, we decided to develop a SHA concept, thus ensuring sufficient dynamic performance at the price of more effort to be put into weight reduction.

We built a first functional prototype with the goal of better specifying the further development. This functional prototype is based on the Moog servo valve E024 and the Hawe accumulator AC13 already mentioned and illustrated in the **Figure 8** next to a coin of five Swiss francs. A tailored steel manifold was machined to accommodate a miniature check valve

CHFA1566501A from The Lee Company, USA and a high pressure filter QG0127 from Pall Corporation, USA. The manifold also interfaces pressure sensors 3100 from Gems, USA, and standard pressure relief valves.

Due to the lack of hydraulic cylinders commercially available in the needed power range, we used a LB6 0805 0050 4 M differential cylinder from Hawe-Hoerbiger, Germany, that was smaller than initially designed (diameters 8 mm / 5 mm) and limited to 160 bar. For practical reasons, short hoses of diameter 4 mm were used to connect the cylinder to the manifold.



Figure 8: Moog E024 servo valve and Hawe 13cc accumulator used for functional prototype

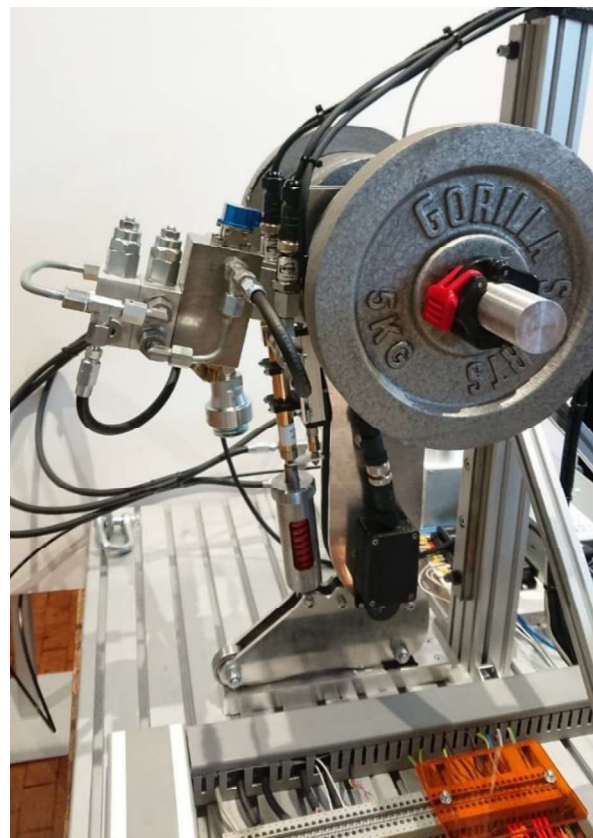


Figure 9: Functional prototype mounted on a test bench aiming at reproducing ankle motion under load (max. 35 kg load)

The functional prototype was supplied with a constant pressure of 160 bar generated by a hydraulic power unit of 750 W. It was mounted on a test bench illustrated in the **Figure 9** whose goal is to allow the realisation of the ankle motion under load. The hydraulic cylinder is placed in front of the leg in order to use the higher force available during cylinder extension for the plantar flexion. The cylinder force is converted into a torque through a 50 mm long lever arm. It should be noted that both cylinder extension and retraction occur under load on the test bench, whereas during a real gait cycle, only cylinder extension would occur under load. For investigating the advantage of a series elastic actuation (not presented here) an encapsulated spring can be mounted in series between the cylinder rod and the “foot” of the test bench (visible in **Figure 9**).

5. PRELIMINARY TEST RESULTS

A position control loop is implemented with the help of a portable controller ChipKit uC32 from National Instruments / Digilent, USA. The control loop can be realised either on the hydraulic cylinder displacement or on the foot angle. We used a PI controller with different gains depending on the sign of the error, accounting for the inherent non-symmetrical behaviour of the differential cylinder and we implemented a Butterworth low-pass filter of 2nd order with a cut-off frequency of 50 Hz on the sensor inputs (linear displacement and angle). During the performed tests, the frequency rate of the controller settled at approx. 1 kHz.

The magnitude of the closed-loop unloaded displacement frequency response of the prototype servo hydraulic actuator is shown in **Figure 10**. The measured -3 dB cut-off frequency ranges from about 5 Hz for large displacement amplitudes (+/- 20 mm) up to 8 Hz for small displacements (+/- 2.5 mm). The measured cut-off frequency is lower than the simulated one (see **Figure 6** for comparison). It is attributed to friction effects in cylinder at high speed and to compressibility effects, especially in the additional hoses used between the servo valve and the hydraulic cylinder.

The closed-loop position step responses given in **Figure 11** were obtained with the gains of the controller being tuned for an overshoot below 10%. It resulted in a maximum angular speed of

about 400 deg/s. With controller gains tuned for critical damping (results not presented here), a settling time of about 0.15 s was achieved for a 40 deg step, i.e. a three times faster response than the one obtained with an EHA in [6].

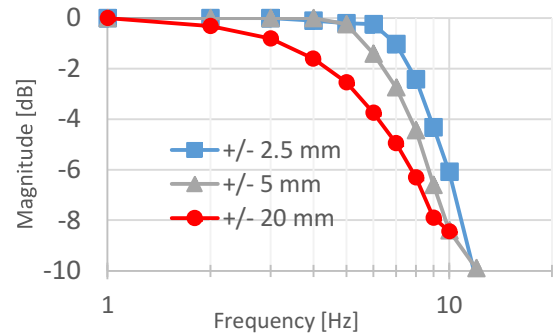


Figure 10: Measured SHA closed-loop unloaded displacement frequency response

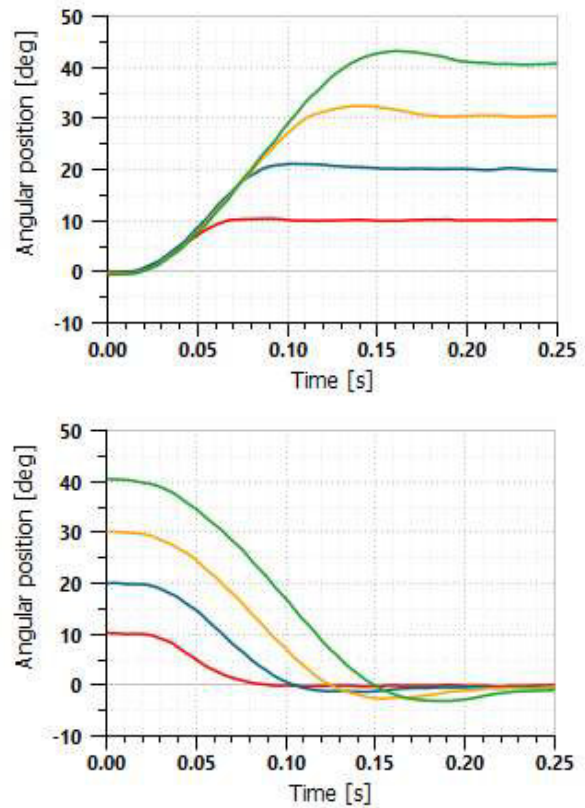


Figure 11: Measured SHA closed-loop PI control unloaded position step responses

6. NEXT STEPS

The test results obtained with the first functional prototype confirmed the adequate dynamic characteristics of the SHA for the application. As an answer to the lack of available hydraulic cylinders suited for our application and to the

need for weight optimization, a tailored aluminium hydraulic manifold was designed to integrate all necessary components of the SHA, including the hydraulic cylinder. An exploded view of the design is given in **Figure 12**.

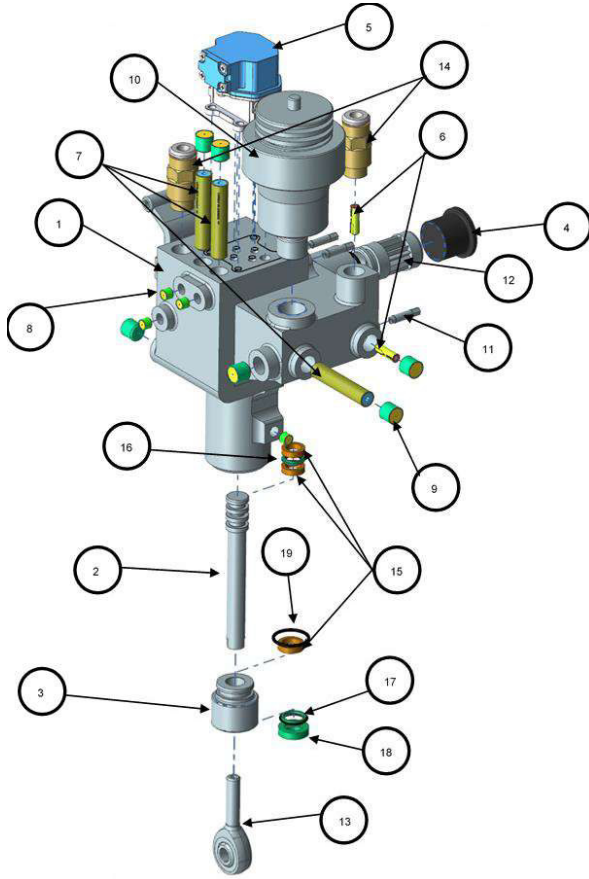


Figure 12: Exploded view of the integrated SHA under development

The overall weight of the actuator is just below 1.0 kg and the detailed weights of the components are listed in Table 1. The heaviest parts are the hydraulic manifold and the accumulator weighting respectively 480 g and 300 g. In the course of this project, only conventional machining techniques were considered for the manifold and not every materials were regarded. However, with the use of 3D metallic printing techniques and advanced materials, we assess that the weight of the hydraulic manifold can be still reduced by 35%. In addition to that, by a better integration of the accumulator in the hydraulic manifold (only possible with the support of the supplier or by developing in-house a specific accumulator) a further reduction of approx. 150 g would be possible. Combining all these efforts, an optimized weight of 680 g can be

achieved, as indicated in **Figure 7**.

Table 1: Weight of SHA components

#	Component	Amount	Mass [g]
1	Hydraulic manifold	1	477
2	Cylinder rod	1	20.3
3	Cylinder cap	1	9.9
4	Plug for filter	1	7.7
5	Servo valve	1	95
6	Checkvalve	2	0.7
7	Pressure limiter	3	6.0
8	Plug 0.187	5	0.51
9	Plug 0.312	6	2.5
10	Accumulator	1	300
11	Pressure sensor	3	3.1
12	Filter	1	9.0
13	Ball-head	1	18
14	Connectors	2	5.0
15	Guide band	3	0.2
16	Piston seal	1	0.2
17	Rod seal	1	0.3
18	Wiper ring	1	1.0
19	O-ring	1	0.1
Total mass			995.5

7. CONCLUSION AND OUTLOOK

The main contribution of this paper is that we have designed a hydraulic actuator for an autonomous ankle exoskeleton that is able to provide full assistance during the gait cycle of a 68 kg individual at normal walking speed (max torque of 90 N.m and max. speed of 320 deg/s at the ankle). By combining results of both numerical simulations and preliminary tests, we have oriented ourselves toward a servo hydraulic actuation (SHA) rather than an electro hydrostatic actuation (EHA) because of its higher dynamic performance. A first design iteration has led to a weight just below 1.0 kg for the whole actuator and a potential for reducing this weight further down to 680 g has been identified. With a total target weight of less than 1.0 kg worn at the ankle, this would give us 320 g for the exoskeleton structure for which a very first concept is illustrated in **Figure 13**.



Figure 13: First concept for the integration of the actuator on an exoskeleton structure

REFERENCES

- [1] Calabrò RS, Reitano S, Leo A, De Luca R, Melegari C, Bramanti P (2014) Can robot-assisted movement training (Lokomat) improve functional recovery and psychological well-being in chronic stroke? Promising findings from a case study. *Functional neurology*, 29(2), 139–141.
- [2] Russell Esposito E, Schmidtbauer KA, Wilken JM (2018) Experimental comparisons of passive and powered ankle-foot orthoses in individuals with limb reconstruction. *J Neuroeng Rehabil*. 2018 Nov 21;15(1):111
- [3] Pirker W, Katzenschlager R (2017) Gait disorders in adults and the elderly: A clinical guide. *Wien Klin Wochenschr*. 2017 129(3-4):81–95
- [4] Bovi G, Rabuffetti M, Mazzoleni P, Ferrarin M. (2010). A multiple-task gait analysis approach: Kinematic, kinetic and EMG reference data for healthy young and adult subjects. *Gait Posture* jan 2011 ; 33(1):6-13
- [5] Zoss A, Kazerooni H, Chu A (2005) On the mechanical design of the Berkeley Lower Extremity Exoskeleton (BLEEX). *IEEE/RSJ International Conference on Intelligent Robots and Systems*, 2005, pp. 3465–3472
- [6] Neubauer BC (2017) Principles of Small-Scale Hydraulic Systems for Human Assistive Machines. PhD thesis, University of Minnesota
- [7] Yu T (2017) Actuation and Control of Lower Limb Prostheses. PhD thesis, University of Bath

MINIATURE HYDRAULICS FOR A MECHATRONIC LOWER LIMB PROSTHESIS

Christian Stentzel*, Volker Waurich, Frank Will

Institute of Mechatronic Engineering, Endowed Chair of Construction Machinery, Technische Universität Dresden, Münchner Platz 3, 01069 Dresden

* Corresponding author: Tel.: +49 351 463 34689; E-mail address: christian.stentzel@tu-dresden.de

ABSTRACT

In Germany alone, 10,000 to 12,000 transfemoral amputations occur every year. Persistent rehabilitation efforts and advanced medical devices like prosthetic knee joints are crucial to reintegrating amputees into daily life successfully. Modern knee joints represent a highly integrated mechatronic system including special kinematics, a lightweight design, various sensors, microprocessors and complex algorithms to control a damping system in the context of the given situation. A knee joint is a passive system and normally has no actuator for an active movement. To enable a natural gait pattern, dampers decelerate the swinging speed of the prosthesis depending on the walking speed and situation. The invention of a novel knee joint called *VarioKnie* provides two kinematics - a monocentric and a polycentric one. Both kinematics have diametrical advantages and the user can choose the preferred setting through an electromechanical switching unit. With this knee joint in mind, a special hydraulic damper is developed to support both kinematics. Requirements and technical data are provided in the present paper. State of art are microprocessor-controlled knee joints with only one kinematic and either a hydraulic, a pneumatic, or a rheological damper.

Keywords: amputee, exoprosthetic, knee joint, artificial knee prostheses, miniature hydraulic

1. INTRODUCTION

Artificial knee prostheses enable amputees to live a self-determined life and allow many daily movements, such as climbing stairs, kneeling, or navigating down inclinations. Even more demanding activities like running or cycling are supported by modern prosthetic knee joints. Everyday activities can constitute a challenge for the patient, as the whole body weight must be carried by the prosthesis reliably without active control of the knee joint. A high confidence in the technology and a long learning process are necessary requisites to utilizing a lower limb prosthesis. To obtain a natural gait pattern, the artificial knee prosthesis (passive system) has to control and damp the swing and stance phase within the gait cycle. For instance, miniature hydraulic cylinders are used to control the flexion and extension of the prosthetic knee joint. Thereby the damping in the swing and stance phase is adapted to different walking speeds. In addition, requirements like low weight and small

package dimensions necessitate the development of a highly integrated mechatronic system.

2. STATE OF THE ART

A typical gait cycle is shown in **Figure 1**. It is subdivided into eight gait phases which are classified into two main phases – stance and swing phase. The stance phase includes every situation with ground contact, while the swing phase represents all situations without.

Modern prostheses are microprocessor-controlled knee joints based on either a monocentric or polycentric kinematic (**Figure 2**). Both kinematics have diametrical advantages. Artificial knee prostheses are usually passive systems (customers reject active knee joints because of noise emissions and higher weight). The only possibility to control pendulum movements is to decelerate, i.e. to damp or to lock, the system. Polycentric and monocentric knee joints are usable in daily life (indoor, outdoor), are splash proofed, support users up to 150 kg, weigh between 0.69 kg to 1.2 kg (2.7 kg

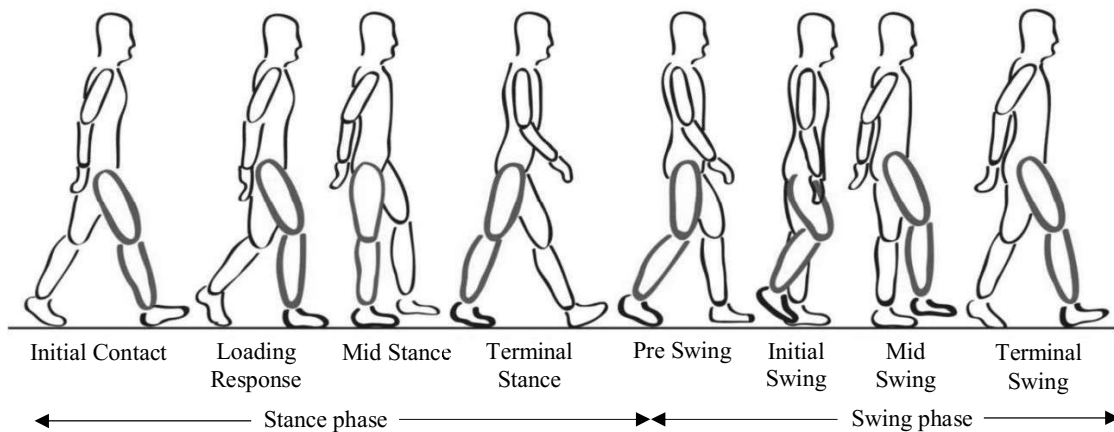


Figure 1: Gait cycle of a human being with eight gait phases cf. [3]

actuated), have a maximum flexion angle of up to 150° and one battery charge can power an operating time of up to five days.

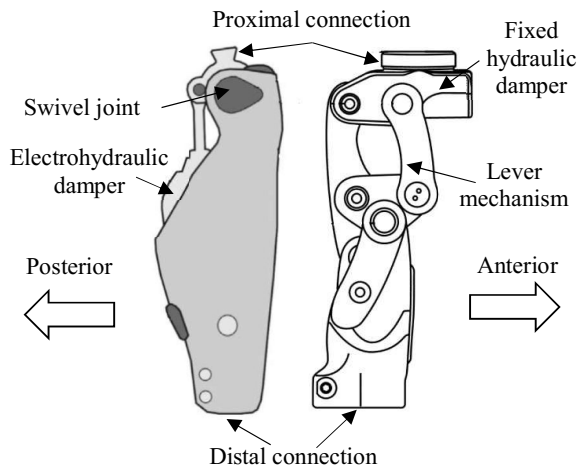


Figure 2: Typical structure of a monocentric (left) and polycentric kinematic (right) with an electrohydraulic and fixed damper cf. [4]. A monocentric kinematic represents a simple revolute joint. This allows a simple and lightweight design. Furthermore, the user benefits from high stability within the stance phase because a weight shifting backwards (posterior) causes no sudden flexion. Another advantage is the possibility to go stairs both upwards and downwards in an alternating way. To control the swing and stance phase, hydraulic, pneumatic or rheological damper systems are mainly used. This allows for a deceleration of the flexion and extension in every situation in order to achieve a natural gait pattern, to include safety functions or to optimise the damping value for different walking speeds. A decisive disadvantage is the distance between knee and ground during the swing phase because of the rigid prosthetic foot (**Figure 3**). The user is

forced to lift the prosthesis to prevent a fall caused by the prosthetic foot sticking to the ground. To lift up the prosthesis it is necessary to lift the hip or to stretch the healthy foot. Both compensations are an unnatural movement and cause overstraining.

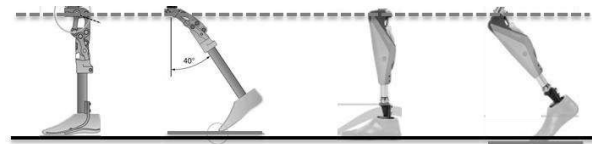


Figure 3: Comparison of a polycentric (left) and monocentric kinematic (right) during the swing phase

A polycentric kinematic consists of a kinematic, usually including a lever mechanism with four or up to seven joints. During the swing phase, a polycentric kinematic shortens the distance between knee and toe (**Figure 3**). The benefit is a more natural gait cycle without unnatural compensation movement and consequently lower loads for the skeleton. Therefore, a reduction of distance between knee and toe of 10 to 20 mm is sufficient. In general, a polycentric knee joint is not microprocessor-controlled. This means that the installed damper is not able to adapt to the specific situations. Only one damping value is adjustable for flexion and extension. The result is an optimised gait pattern for only one walking speed. Besides this, a polycentric kinematic has disadvantages concerning its stability behaviour (uncontrolled flexion due to posterior and unintentional weight shift) and functionality in specific situations, such as no alternating climbing of stairs, no cycling, no short sprints or no safety functions (e.g. no stumbling protection, no stop when falling back in the seat). The main

reason for these disadvantages is the missing microprocessor-controlled damper as a result of the difficult design space of the lever mechanism while simultaneously requiring a large flexion angle. However, it is possible to design a four-bar linkage that allows the use of a mechatronic damper. Therefore, the instantaneous centre of rotation (ICR) has to be positioned in a specific point relative to the Trochanter-Knee-Ankle line (TKA line) (**Figure 4**). Lever mechanism with significant and different behaviours can be designed [1].

In general, amputees with artificial knee prostheses require anywhere from 30% to 70% higher energy input to walk in comparison to a healthy person [2]. Reasons are unnatural gait patterns, less recuperation (no tendons) and the passive system that only decelerates the pendulum movement.

3. MOTIVATION AND GOALS

The research project “*VarioKnie*” involves two universities and four companies from the fields of mechanical engineering, hydraulics, medicine, orthopaedic technology and electronics. The main goal is a microprocessor-controlled knee joint which includes a monocentric and polycentric kinematic. An electromechanical switching unit enables a choice between both options. Advantages of both kinematics are combined and can be used in various situations. The switching operation is initialised via a motion routine or via an app on their smartphone. An electrohydraulic damper is implemented to control the swing and stance phase. Requirements like lightweight and small design space lead to the development of a highly integrated and miniature hydraulic cylinder that damps both kinematics.

As with modern knee joints, many sensors have to be combined (sensor fusion) to create more intuitive behaviour of the system. Sensor data have to be interpreted to identify each specific situation correctly and to determine the required behaviour of the prosthesis in real time. An incorrect interpretation and reaction would lead to a stumble or fall. The following data are available for the interpretation of the current situation of the user and of the knee joint: piston position via ultrasonic sensor (piston position; ~speed; ~acceleration; flexion angle), strain gauges (qualitative force curve; forefoot; heel),

and inertial measurement unit (IMU) (acceleration vector, gyroscopes).

Additional goals are the detection of vital data like blood circulation or temperature of the stump inside the prosthesis stem in order to protect the user from overstressing. Furthermore, environmental detection will be able to predict the behaviour of the knee joint for imminent situations, such as climbing stairs or obstacles. Nowadays, the user has to actively switch to a new mode using a motion routine or an app when faced with new circumstances, e.g. climbing stairs. These aspects increase the comfort for the user but are not explained in detail in this paper.

4. DEVELOPEMENTS

A constructive development process was used to design the *VarioKnie*. Therefore, the *VarioKnie* is divided into three main assemblies: the chassis, switching unit and miniature hydraulic. Three stepper motors are implemented within the design to serve as an electromechanical switching unit and an electrohydraulic damper system.

4.1. Kinematics

The geometric relationships of the kinematics influence the required design space and the behaviour of a knee joint (flexion resistance, inner forces or maximum flexion angle) or hydraulic parameters (pressure, stroke and reversal point of piston). In addition, the geometry of a polycentric kinematic influences the mechanical lock of the lever mechanism, which depends on the position of the ICR and TKA line (**Figure 4**). The reduction of the

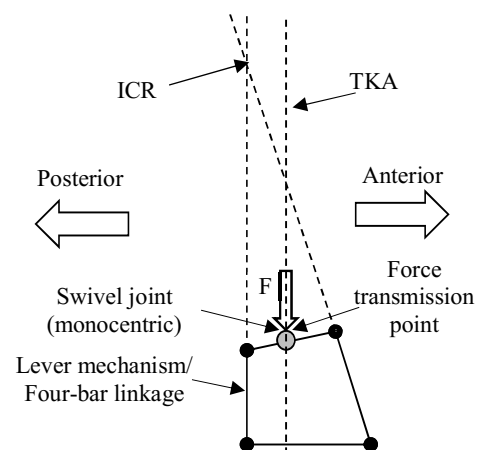


Figure 4: Schematic design of the combined monocentric and polycentric kinematic

distance between knee and toe during the swing phase is based on this geometry as well.

A monocentric kinematic requires a TKA line that passes the revolute joint directly through the axis of rotation or little posterior to achieve an easy swing initialisation (**Figure 4**). In contrast, the polycentric mechanism can be designed in three main configurations [1]. The first results in a stable behaviour of the knee joint by designing a TKA line anterior to the ICR of the four-bar linkage (hyper stabilised). The characteristics here include a high flexion resistance and a high stability (wide range of the mechanical lock). This is useful for users with low demands concerning dynamics and a high desire for safety or stability. The second represents the opposite and the TKA line is located posterior to the ICR (elevated instant centre). The results are a low flexion resistance and no mechanical lock while standing. The third configuration is a compromise between the first and second (both illustrate extreme positions), whereby the TKA line is slightly anterior to the ICR (voluntary control). A low flexion resistance and middle stability/mechanical lock are achieved by this design and the hydraulic cylinder does not have to hold the weight of the user while standing.

The combination of both kinematics has to fulfil all mentioned constraints in order to have two kinematics with full functionality. The geometric link for the monocentric and polycentric combination is the position of the TKA line (**Figure 4**). This prerequisite allows for a deduction of all further geometric parameters while following the requirements of an artificial knee prosthesis.

4.2. Switching unit

The switching unit represents a new assembly in the field of artificial knee prostheses and implements the option to choose between a monocentric and polycentric kinematic. An electromechanical system enables easy handling by the user and locks one of the kinematics. The switching unit consists of a stepper motor, gear stages and four spindle drives which actuate the locking bolts. Because of the limited design space and lightweight restrictions, the switching unit is located in the proximal connection (**Figure 5**).

Based on DIN EN ISO 10328, parts have to be dimensioned to specific load cases. High strength materials like aluminium, steel and titanium are

used to find a compromise between design space, weight and mechanical stress. Especially the switching unit and the lever mechanism are subject to these conditions.

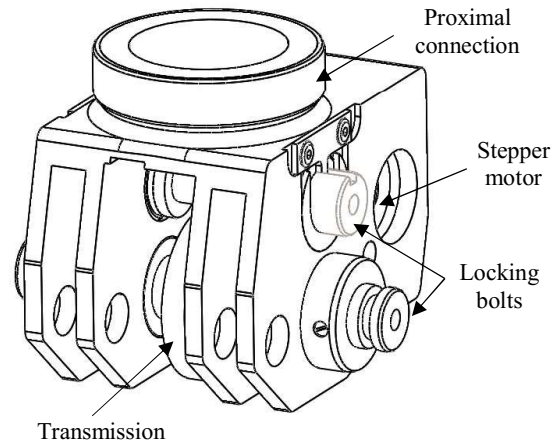


Figure 5: Switching unit as electromechanical system

4.3. Miniature-Hydraulic / damping unit

The damping system is the decisive component to make an artificial knee prosthesis smart. It is the only option to influence the gait pattern by decelerating or locking the flexion or extension. The *VarioKnie* uses a hydraulic differential cylinder with two proportional valves to control the extension and extracting of the piston separately (separate control edges). This configuration represents the state of the art in the industry of knee prostheses.

Requirements

The main goals of a knee prosthesis are a natural and intuitive gait pattern preferably with a low effort of energy. Therefore, four operational modes are necessary to ensure sufficient system behaviour and to implement all required functions. The first one allows for a controlled extracting of the piston with a proportional valve and storing of the displaced volume. The opposite is found in the second mode, which enables a controlled extension of the piston while using the stored energy of the piston accumulator. At this point, a conflict of objectives arises. On the one hand, a low flexion resistance is required to reduce energy efforts needed for walking. On the other hand, the stored energy should be reused to support the extension, a so-called ‘assist spring’. The crucial component is the spring and the preloading of the piston accumulator, which has significant influence on the flexion resistance and

the assist spring. A compromise has to be found. The third and fourth operating modes represent emergency modes guaranteeing aggravated and safe walking if the electrical accumulator is empty. In both modes, the proportional valves are closed and the volume flow between rod side and bore side has to flow through a small and permanently opened bypass, which has negligible influence in modes I and II. The results are a high flexion resistance and a moderate extension resistance. Modes III and IV allow the amputee to flex the knee joint while sitting and to walk safely, among other benefits.

The proportional valves have to operate exactly and fast to set the required damping value. Highly dynamic stepper motors are used to meet these requirements. In consequence, a low flexion resistance (fully open) is quickly adjustable without any noticeable delay for the user and precise control of the damping value is available. Beyond that, an end position damping is required to achieve a smooth extension stop.

As mentioned, a piston accumulator stores the displaced volume of the differential cylinder. Due to high requirements on design space and weight, the storage is positioned in the cylinder wall parallel to the piston axis. In addition, check valves enable a defined volume flow between rod and bore side through the intended proportional valve (**Figure 6**).

A typical gait cycle includes load peaks and impact loads that, for example, occur during heel contact, push off or fall. A pressure relief valve protects the hydraulic system against overloads while connecting the rod and bore side directly with a pre-set pressure difference. Another option to reduce the system pressure is to enlarge the piston diameter or to adapt the lever mechanism. This conflicts with goals regarding design space, volume flow, piston stroke and thermal aspects. Another compromise has to be found.

The requirements necessitate the design of a highly integrated hydraulic cylinder including all mentioned components and functions. It represents a closed hydraulic system and is limited to the most important parts (no filter, no fittings, no tank, passive cooling via cylinder wall).

Design and technical data

The development of the hydraulic cylinder focusses on maintaining a short length, keeping

the device lightweight and limiting the design to a small space overall. Therefore, all parts are made of high strength aluminium alloys, except the piston rod and proportional valve, which are hard chrome-plated steel and steel, respectively. A hard-anodised layer generates a wear protection to protect the cylinder against the sealing elements.

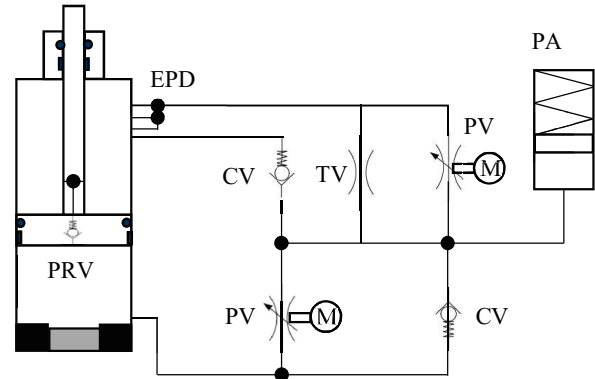


Figure 6: Hydraulic circuit diagram

In **Figure 6** the hydraulic circuit diagram is shown. The miniature hydraulic cylinder includes two proportional valves (each actuated by a stepper motor), two check valves, a pressure relief valve, an end position damping and a piston accumulator to store the displaced volume of the differential cylinder. In addition, an ultrasonic-sensor and a temperature sensor are implemented in the cylinder base to detect the position, velocity and acceleration of the piston. The measurement data are used to deduce the angle of flexion for both kinematics and are processed in the control unit. The temperature monitoring represents a safety function and is used to determine the sonic speed for the ultrasonic waves. Technical data of the hydraulic cylinder are listed in **Table 1**.

Table 1: Technical data of the miniature hydraulic cylinder

Cylinder parameter	Value	Unit
Mass m	540,2	g
Stroke z_{str}	33	mm
Piston diameter $\varnothing d$	26	mm
Max. pressure p_{max}	120	bar

Good controllability of the hydraulic system and of the damping effect is guaranteed if the main pressure difference is generated in the proportional valves. Therefore, the cross-section areas of the check valves are designed to be six times larger than that of the proportional valve.

This approach supports the efforts to create a hydraulic system with low hydraulic losses. It provides benefits regarding thermal aspects, as well. A sectional view of the hydraulic cylinder is given in **Figure 7**.

A prediction of system behaviour is analysed with numerical methods like CFD and a cross-domain simulation including a mechanical and hydraulic system. Components of the hydraulic circuit are simulated by using CFD to estimate pressure losses with different input parameters. In addition, a test arrangement was used to measure the characteristics of the proportional valve at different volume flows and valve openings.

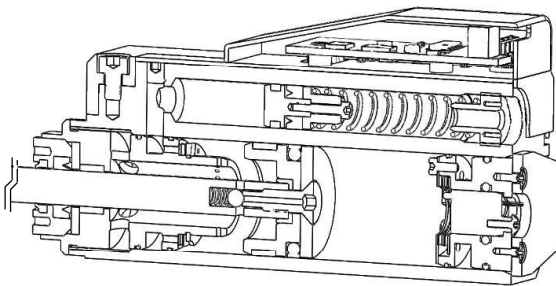


Figure 7: Sectional view of the hydraulic cylinder

5. VARIOKNEE

In **Figure 8**, the *VarioKnee* is shown including a switchable kinematic (monocentric or polycentric) and the miniature hydraulic cylinder. It represents a mechatronic system with several sensors and actors. The housing is made of an aluminium alloy to ensure a lightweight design. The 3D printing manufacturing process (SLM) enables an esthetical and functional design.

The *VarioKnee* project is now in the final year of its three-year development phase and the design, production and assembly have been completed. Preliminary tests on the actors and sensors have been carried out. In the next step, the software development will be finalised in order to allow for the detection of the current situation and to determine the requested system behaviour. Different walking modes, functions and motion routines have to be implemented. Several amputees will test the *VarioKnee* in the last project phase under laboratory and real conditions.

6. SUMMARY AND OUTLOOK

The main innovation of the project is the combination of two kinematics in one artificial

knee joint that are supported by a newly developed damper in the form of a miniature hydraulic cylinder. Two stepper motors allow for separate controlling of the extracting and extension of the piston, thereby enabling a specific damper value for flexion or extension. Adaptability of the system behaviour facilitates a natural gait pattern and supports different functions based on the electrohydraulic damper system. A highly integrated design fulfils the requirements of a lightweight design.



Figure 8: Design of the *VarioKnee*

An electromechanical system allows a smart control of the switching unit, initialised by a motion routine or an app on a smartphone. In the next step, the software of the *VarioKnee* has to be developed to allow for intuitive operability for amputees. Therefore, amputees are involved in the project for testing under laboratory and real conditions. The *VarioKnee* will be usable for the initial temporary application to gain experience with different kinematics, for rehabilitation and for daily life.

NOMENCLATURE

<i>CFD</i>	Computational Fluid Dynamics
<i>CV</i>	Check Valve
<i>EPD</i>	End Position Damping
<i>ICR</i>	Instantaneous Centre of Rotation
<i>M</i>	Motor
<i>PA</i>	Piston Accumulator
<i>PV</i>	Proportional Valve
<i>PRV</i>	Pressure Relief Valve
<i>SLM</i>	Selective Laser Melting
<i>TKA</i>	Trochanter-Knee-Ankle
<i>TV</i>	Throttle Valve

ACKNOWLEDGEMENTS

SPONSORED BY THE



Federal Ministry
of Education
and Research



Technologiezentrum

(BMBF: KMUinnovativ: Medizintechnik; FKZ: 13GW0197E)

REFERENCES

- [1] Radcliffe C. W. (1994) Four-bar linkage prosthetic knee mechanisms: kinematics, alignment und prescription criteria, Prosthetics and Orthotics International, p. 159-173, Mechanical Engineering Department, University of California, Berkeley, USA
- [2] Oehler S. (2014) Mobilitätsuntersuchungen und Belastungsmessungen an Oberschenkel-amputierten, Dissertation TU Berlin, Germany
- [3] Pasurka M. (2012) Videogestützte Ganganalyse - auch für Prothesenträger, eurocom e.V. Orthopädie aktuell, Düren, Germany
- [4] Seifert D., Kampas Ph. (2015) Das neue C-Leg: neue Funktionen und neue Technologie, Orthopädie-Technik;Orthopädietechnik 10/2015, Dortmund, Germany
- [5] Össur Total Knee®2000, Geometrc Locking System

FULLY VARIABLE, SIMPLE AND EFFICIENT – ELECTROHYDRAULIC – VALVE TRAIN FOR RECIPROCATING ENGINES

Wolfgang Schneider*

W. Schneider Ingenieurbüro, Dufourstrasse 3, 3600 Thun, Switzerland

Bieri Hydraulik AG, Könizstrasse 274, 3097 Liebefeld, Switzerland

* Corresponding author: Tel.: +41 79 392 59 71; E-mail address: wolfgang.schneider@bluewin.ch

ABSTRACT

A new camless electrohydraulic valve train concept for combustion engines was developed at Empa (Swiss Federal Laboratories for Materials Science and Technology, Dübendorf, Switzerland) and tested on a spark ignition passenger car engine. Besides full flexibility with regard to lift and timing of the engine gas exchange valves it features robustness, simplicity and in particular a low own drive power need due to a maximum of hydraulic energy recuperation. The engine test results confirm substantial efficiency gains in classical as well as in hybrid power trains while also maintaining additional advantages. The system also has the potential to become a key element for load control of piston based compressors and expanders, reciprocating Joule Cycle engines and derivable future electricity storage systems.

Keywords: Variable Valve Actuation (VVA), Electro-Hydraulic Valvetrain System (EHVS)

1. INTRODUCTION

Besides defossilization with low carbon or synthetic fuels, a continuous improvement of internal combustion engines is one way to reduce the CO₂ emissions of vehicles and for this a fully flexible valve train is essential. Today's series production solutions all are cam-based meaning valve lift and timing not being controllable independently, cylinder deactivation may not be integrated and still the effort for these approaches is not negligible. Despite numerous attempts no full camless systems – neither electric [2] nor electrohydraulic system [3-8] – have reached series-production [1]. Only one mass-produced electrohydraulic system uses a cam shaft with a hydraulic link [9] and finally one system is supposed to be near series production [10].

Empa – in close cooperation with the W. Schneider Ingenieurbüro – undertook a fresh approach for an electrohydraulic valve train. It was named "Flexwork" and actually serves as a development tool but also offers potential for industrial scale-up.

2. IMPORTANT REQUIREMENTS AND DESIGN CONSIDERATIONS

Lifting the engine torque curve throughout the

whole speed range by optimizing inlet valve closing timing and valve overlap always is of interest. The first impact on the efficiency of an Otto engine however is load control by "dethrottling", meaning the air metering is controlled by – ideally fast and near digital – early or late valve closing instead of the throttle device. Internal exhaust gas recirculation (EGR) can be optimized by controlling the valve overlap during gas exchange. So the outlet valves flexibility is of interest as well. Finally complete cylinder deactivation asks for cylinder individual valve control. Last but not least the own drive power need must be as low as possible.

In the past some electrohydraulic solutions had not been far from series realization. Breaking technologies always have difficulty in pushing out existing ones which are supported by their well implemented production processes. A new system has to make a considerable improvement step - preferably based on a low sophistication level and reasonable cost.

Control may have been too sophisticated in existing attempts. For a new approach the fast movement of the gas exchange valves – although disturbed by e.g. varying gas pressures – should not need fast sensor based control which in return would ask for highly responsive and expensive

actuators.

As in cam drives quite a portion of energy is given back to the camshaft by the valve springs a low energy demand for the hydraulic drive is a real challenge. It could be attained by

- minimizing throttling in valves and fluid passages
- minimizing capacitive losses (small dead volumes, high fluid bulk modulus)
- adapting to demand (gas exchange lift)
- recuperating hydraulic energy

Last but not least an easy and universal applicability, also on existing engines, without the need of severely modifying the cylinder heads, is mandatory.

3. THE DEVELOPED SYSTEM

3.1. Hydraulic Layout

The developed system puts the challenges into practice by making use of an “asymmetric hydraulic pendulum” (**Figure 1**).

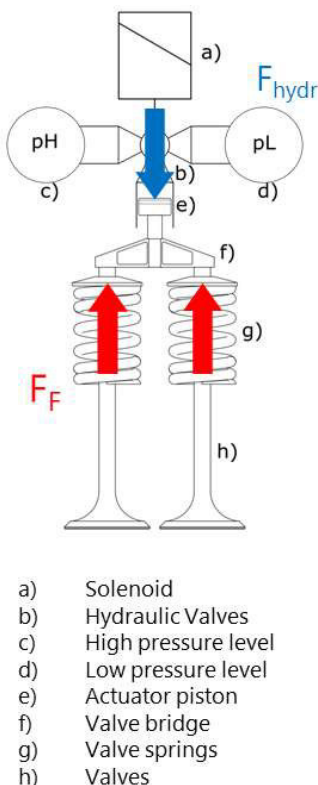


Figure 1: general layout

One advantage of this layout is that the pushing piston allows a clear separation between the valve deck and the actuation deck.

This system does nothing but push a hydraulic piston with a given pressure to accelerate the gas exchange valves against its valve springs. The valves will “fly” in best case to the double of the static force balance point **Figure 2**.

The system is similar as described in [8] but uses a simple check valve as a hydraulic latch (see **Figure 5a**), thus keeping the valve – inavoidably – in the attained position and conserving the stored kinetic energy to the maximum extend (pressure will jump up at the end of the stroke).

To achieve a desired lift nothing but a pressure control (see curve in **Figure 3**) is needed, not e.g. a fast hydraulic control valve to stop in the right moment. On the contrary, the initiating solenoid valve only needs to have opened to its maximum flow area by the time the “flying” mass is in the middle of its stroke when flow is highest. Furthermore, due to the latching check valve, this hydraulic valve is allowed to stay open until some time later it is deenergized for initiating the closing of the gas exchange valve.

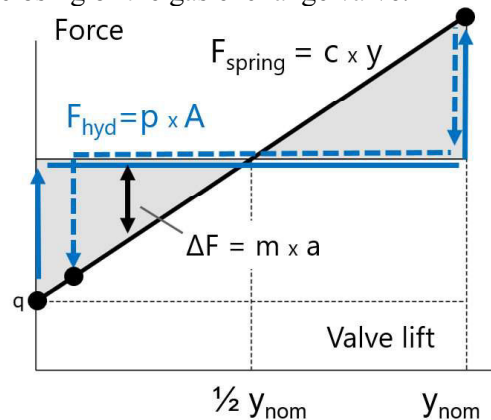


Figure 2: Force-stroke-diagram of an asymmetric hydraulic pendulum

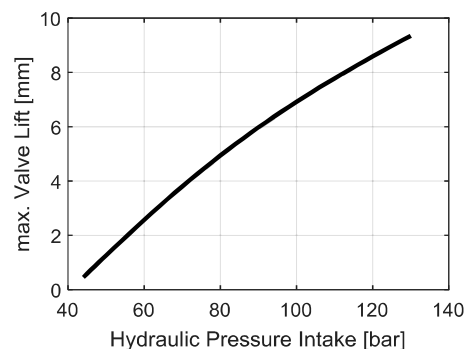


Figure 3: lift-pressure-assignment inlet valves

During closing it is not the pressure but the stored potential energy in the spring that accelerates the mass. The actuator piston works like a pump and

recuperates. As no pendulum is ideal the gas exchange valve will not reach its closed position. At the end of recuperation (see **Figure 4**) a latching check valve keeps the mass safely in position (**Figure 5b**) before pressure deloading actuator cylinder brings the gas exchange valve back to the seat.

To find the right moment for deloading we can profit from the simple fact that the pendulum always needs about half period duration $T/2$ for a single stroke – independently of direction, stroke length or dampening as is perfectly illustrated in **Figure 4**. A 2/2-deloding spool valve integrated in the main valve makes use of this predictable behaviour. and moves on its given pathway with constant speed (see **Figure 5b**) for opening the deloading channel to the low pressure accumulator precisely at the end of recuperation. The constant speed of the 2/2-valve is generated by a typical hydraulic means: a spring acting on the spool surface to pump fluid through a fixed turbulent throttle orifice.

Landing on the valve seat (c in **Figure 4** and **Figure 5c**) has to take place with a speed lower than 0.5 m/s. This happens stroke controlled: when the gas exchange valves come near the seat the actuator piston closes the main flow path by itself and the gas exchange valve spring generates a constant landing speed by pressing fluid through a resting throttling orifice.

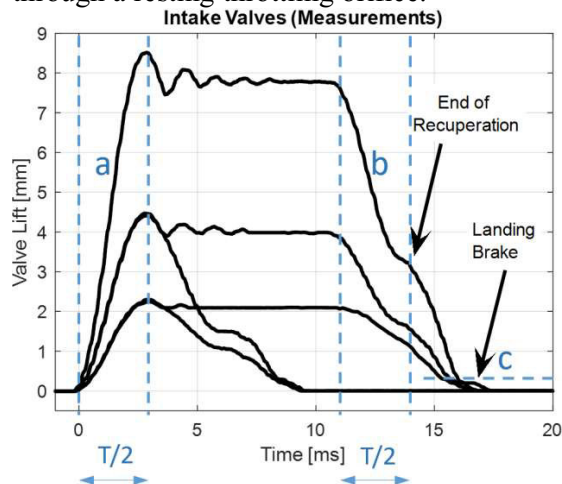


Figure 4: Lift curve sequences of intake valves at various lift heights and durations

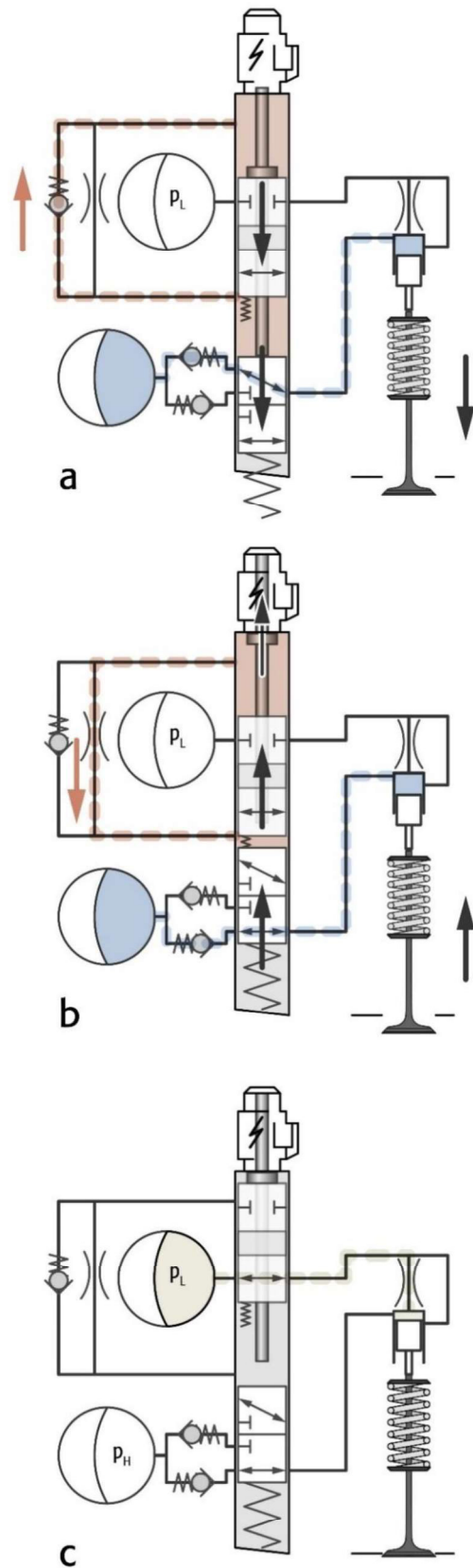


Figure 5: Hydraulic sequence control intake valve (source AUTO&Technik, A. Lerch.)

3.2. Dimensioning

Main parameter for the valve train is the periodic duration T which defines the minimum open time.

$$T = 2\pi \times \sqrt{\frac{m}{c}} \quad (1)$$

m is the total effective mass of two valves, two springs and spring disks, the valve bridge and the actuator piston. c is the spring constant of the combined spring.

T was chosen to about 3 ms according to the open time of the cam at top speed of the engine. The valve lift curve vs. crank angle at full speed would be quite similar to a cam based valve lift curve. In the most frequent low speed range this choice is sufficient for nicely sharp, near digital valve openings. The valve springs were chosen stiffer than the series springs. They still fit into the spring chamber, and have an enduring layout.

3.3. Exhaust Valve Actuation

Exhaust valves of combustion engines typically have to be opened against in-cylinder pressures of 5-15 bar (depending on engine type). The necessary energy input for operating the valves therefore is higher than for the inlet valves and cannot be recuperated completely.

With lift control by pressure as on the inlet valves an overshooting of the valves could happen in case of a combustion failure.

For this reason the exhaust valves are directly lift controlled by turnable actuator pistons with helical grooves for port control of the supply pressure. The fast moving actuator pistons cut off their own pressure supply according to their angular position which is controlled by a worm drive (**Figure 6**). On bottom of **Figure 7** the stepper motor of the worm drive can be seen. Beginning of opening and closing still is controlled by the solenoid valves making cylinder deactivation possible also on the exhaust valves.

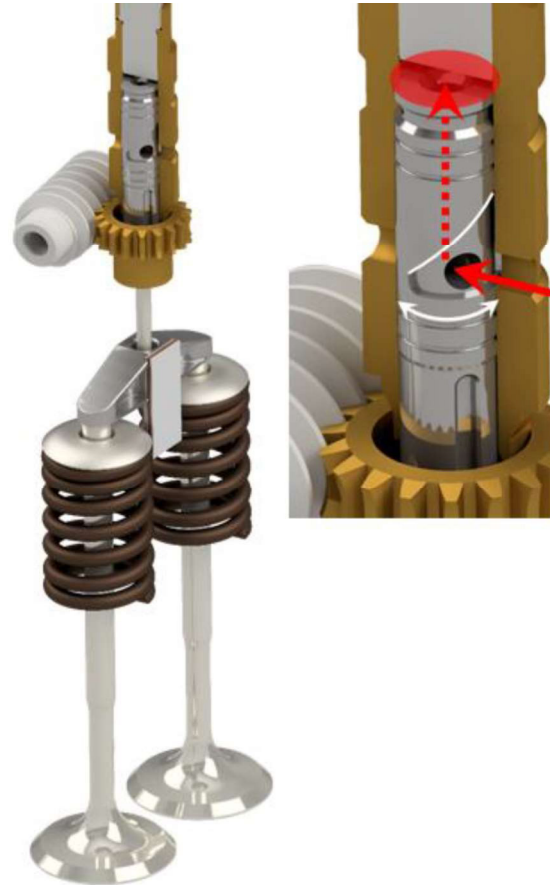


Figure 6: direct lift control mechanism of exhaust valves

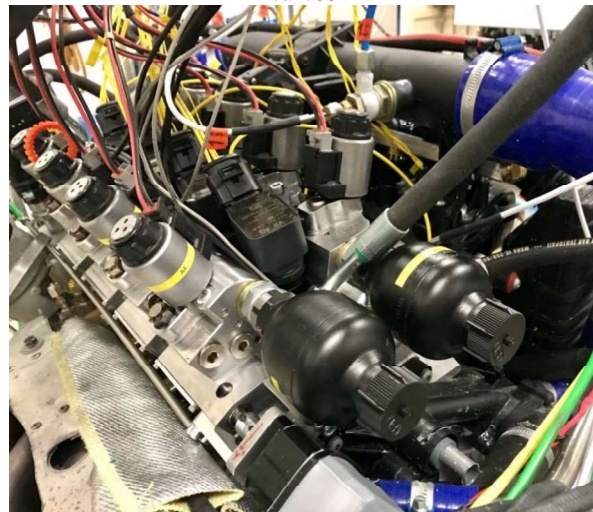


Figure 7: View on readily equipped cylinder head of the 1.4l SI passenger car engine (view along exhaust side)

3.4. Fluid Choice

Already pressurizing and depressurizing cylinder and channel volumes – yet without doing any work – is an inavoidable part of hydraulic cycles but always causes capacitive losses. These can

only be minimized by either small (dead) volumes or by use of a low compressible fluid. As water-glycol features a high isentropic bulk modulus and is the standard cooling fluid of combustion engines, it was worth to try.

There are further advantages associated with this fluid like an oil free cylinder head. (Independently from that there is no need for cam drive lubricating additives which may shorten catalyst life.).

Two 6 m long spiral pipes were installed at the entrance and the exit of a first valve testing apparatus (**Figure 8**).

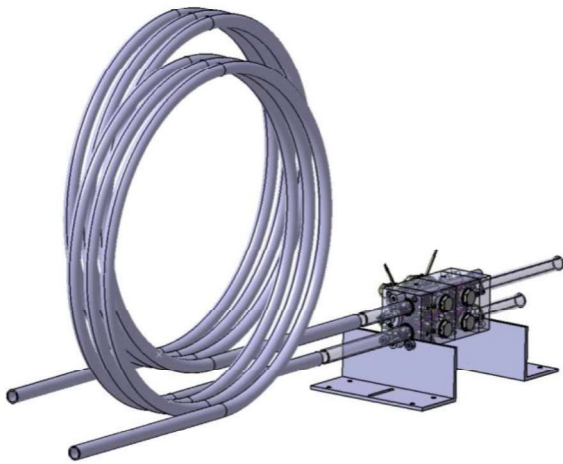


Figure 8: Pipe spirals for measuring fluid sound speed and dynamic flow

Detecting the pressure wave amplitude with a piezoelectric sensor allowed to measure directly the highly dynamic flow into the driving cylinder according (2):

$$\frac{dQ}{dt} = \frac{A_{pipe}}{\rho a} \times \frac{dp}{dt} \quad (2)$$

A BASF 50:50 water glycol cooling liquid was used. The wave speed was determined from the reflected wave travel time to 1620 m/s (@ 30°C, 140 bar). With the fluid density of 1075 the isentropic bulk modulus $E = \rho a^2$ was calculated to 28'200 bar.

To maintain this high bulk modulus during operation it is mandatory to have a good deaeration. A low pressure level of 15 to 20 bar keeps deaeration as well as cavitation on a non harming level.

3.5. Hydraulic Component Choice

Solenoid Valves

The solenoid valves have been constituted by seat valve elements of Bieri Hydraulik AG and pole tubes and slip-on coils from Hydac. The valve parts were press fitted to the housing in order to keep dead volumes small. However other ways of fitting seem possible. The pole tubes so far are not made from eddy-current suppressing steels.

Figure 9 gives a rough impression on the construction. The single valve actuations are assembled into in blocs which are connected to each other by hydraulic pipe pieces.

Check Valves

Market available standard screw-in check valves size 1/8" and 1/4" with slightly elevated cracking pressures were used.

Pressure supply

Pressure supply and control on both high pressure levels should finally be done by a variable flow pump, e.g. a two-circle piston pump with two suction controls. For todays setup the exhaust side of the hydraulic system is being pressurized (up to 200 bar) by a Diesel common rail pump and the inlet side by a conventional pure water pump, both high pressure levels are being controlled by Bieri proportional pressure relief valves. The low level pressure is retained by a mechanical pressure relief.

Accumulators

Hydac Accumulators of the smallest standard size (75 cm³) were used. They look big on **Figure 7** but as will be explained below the size has no relevant impact on the engine dynamics as will be explained below. Nevertheless smaller accumulators would do as the maximum instantaneous fluid need of one cylinder only is half a cm³.

Sensors

Apart from the typical engine and hydraulic testing sensors for monitoring and control of the valve train were needed. ELGO inkremental magnetic strips were glued to the valve bridges. These sensors serve for lift measurement and - only - slow adaptive control.

3.6. Power Electronics and Control

The solenoids are controlled by a dspace microautobox. The rapid prototyping unit contains injection drivers with boost current capabilities as needed for the solenoid valves. The own programming at Empa – low and hi-level control for all kinds of controls in Matlab/Simulink – was helpful for a fast realization without restrictions.

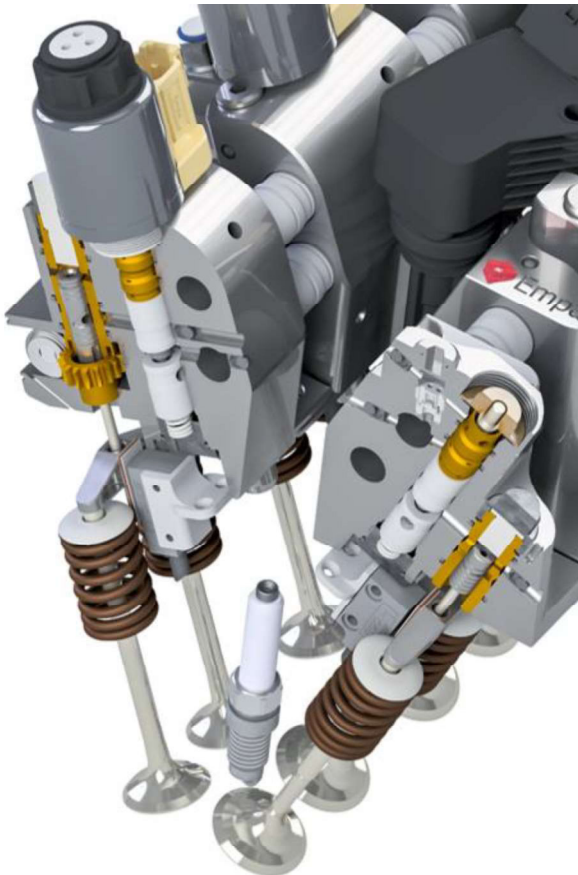


Figure 9: Valve train installation

4. RESULTS AND EXPERIENCE

The engine, a 1.4l VW spark ignited engine, running on methane, has run 100h in the new configuration. Due to the problemless functioning of the valve train Empa already has been able to do a lot of various measurements.

4.1. Power demand of the Valve Train

The hydraulic power need of the new valve train was measured (on the fired engine!) by measuring pressures and flows at taking into account an efficiency of 85% of variable

displacement pressure supplies. As this engine has not been tested in the cam-version a typical value of 0.25 bar mean friction pressure is assumed. Published data on fired cam engines are extremely rare [11].

The low hydraulic energy effort is owed to the high recuperation rate. This was measured to be up to 60%.

The electric power need has not yet been optimized for its task.

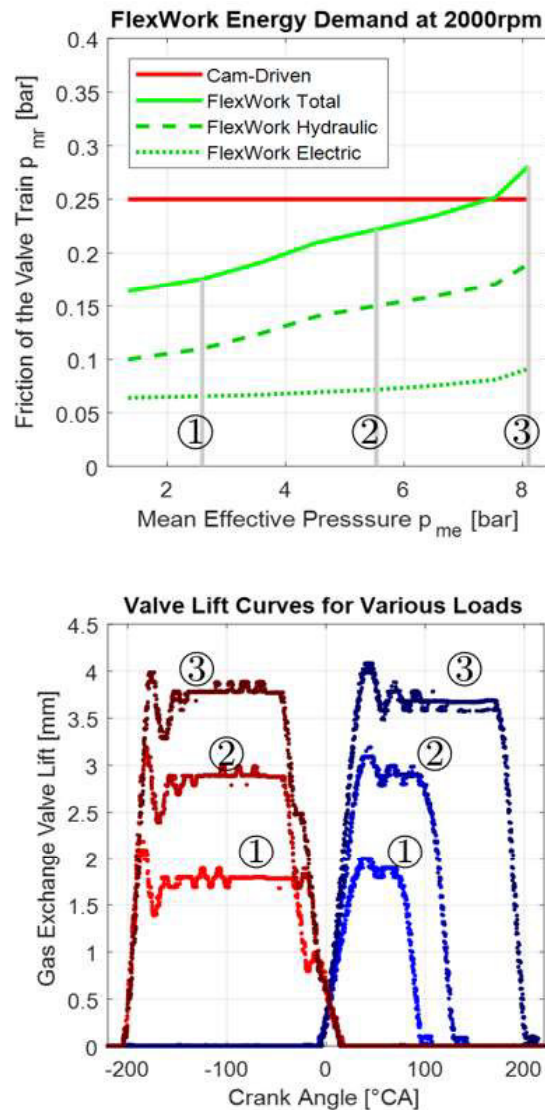


Figure 10: Valve Train energy demand and corresponding valve lift curves

4.2. Experience with the Hydraulic Fluid

Good results have been obtained with water-glycol as a low compressible hydraulic fluid. White-green coloured residues appear where the water evaporates on an open surface.. The choice

of the kind of fluid however (cooling liquid, engine oil, diesel fuel, braking fluid) does not seem to be decisive for the total energy need, as in particular the electric energy need has not been optimized yet, see below.

As the system mostly is running at lower engine speeds the number of switchings of the valve train is about 4'000'000 cycles.



Figure 11: “Like new” helical groove actuator piston after first disassembling after 1 Mill. Cycles

Even the stems of the gas exchange valves – which are not lubricated by engine oil anymore – show no influence of the cooling liquid. This may be owed to the fact, that special attention was given to avoid side forces on the stem

4.3. Test engine results

Figure 12 significantly shows for a typical part load operating point how strongly the size of the negative gas exchange work loop can be minimized by unthrottled early intake closing. For the throttled case the still mounted engine throttle plate was closed to the necessary extent.

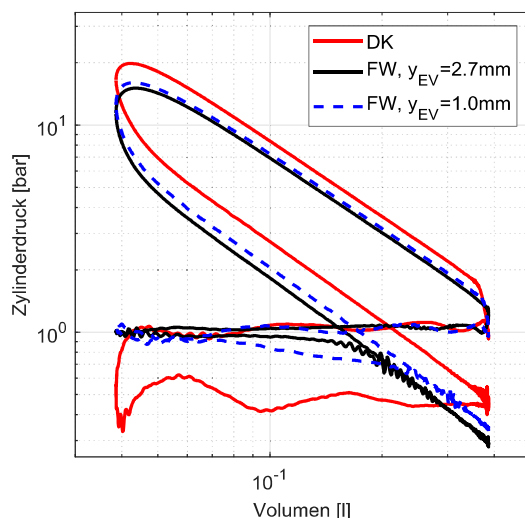


Figure 12: Measured logarithmic pV-diagram on test engine: load control with early intake closing (FW, two valve lifts) versus throttle (DK) @ 2000 rpm/ 2 bar mean eff. pressure, efficiency gain 13.1%

The diagram also shows there is little effect in opening the gas exchange valves more than adequate (3 mm) at this engine speed and that even at full load at this speed a much higher lift is not mandatory, as the suction losses cannot be reduced much more. So the time needed for pressure build up in the hydraulic accumulator will not in the least restrict the engine dynamics. On the contrary valve timings and therewith load changes can be switched not only within engine cycle time but in firing frequency [12], suprisingly faster than the engine reaction one is used to.

4.4. Simulated driving cycles

The stationary engine test results were transponed into a CO₂ driving cycle effect by simulation [12]:

Table 1: Efficiency potential in new WLTP driving cycle of Flexwork (FW) engine in 1400 kg

Engine	Efficiency gain [%]
Base line engine (throttled)	0
Flexwork engine	6
FW engine incl. cyl. deactivation	8
FW engine in hybrid car	3
FW engine in hybrid car incl. cyl. deactivation	4

The results are in so far conservative as the new World Light Vehicle Test Procedure (WLTP) has much less low load conditions as the older NEFZ. The results will improve with the weight of the cars. Also the geometric compression ratio of the test engine is not state of the art

5. CONCLUSION AND OUTLOOK

The newly developed flexible valve train showed impressing performance and efficiency improvements on the 1.4 l Otto test engine and in subsequent driving cycle simulations. It has proven a reliable research tool and - thanks to its excellent and broad controllability - it will further support research work in the field of part load optimization of combustion engines and hybrid power train integration. It can also be used for optimising turbo charger integration, exhaust braking or for control of new low emission combustion concepts like Homogenous Charge Compression Ignition (HCCI) [12].

Due to its simplicity and robustness the question

of chances to become a series product may be put.

The high achievable valve speeds make this valve train also suitable for load control of reciprocating gas compressors and expanders.

Figure 13 shows simulated load variations on a reciprocating compressor and a reciprocating expander. At highest piston speed (half stroke) a fast – near digital – opening respective closing is specially important to keep throttle losses of the gas exchange to a minimum.

In continuation of these thoughts the fast electrohydraulic valve train may also help piston based Joule cycle engines and future Joule cycle based heat pumps (**Figure 14**) to become feasible.

The electrohydraulic system recuperates substantial drive energy, up to 60%, at closing of the gas exchange valves. The energy can be captured on the original supply pressure level and can directly be used for the next actuations. Next step towards a convincing system could be the integration of the power supply which today still is external. May this system idea inspire other hydraulic applications in utilizing moving masses for energy recuperation.

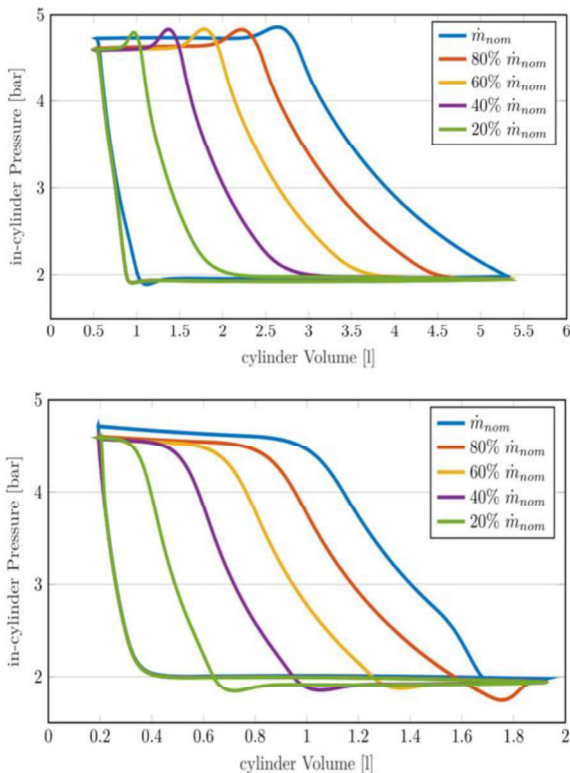


Figure 13: Simulated p-V-diagrams of load control on reciprocating gas compressor (top) and expander (bottom) by fast flexible valve train [13]

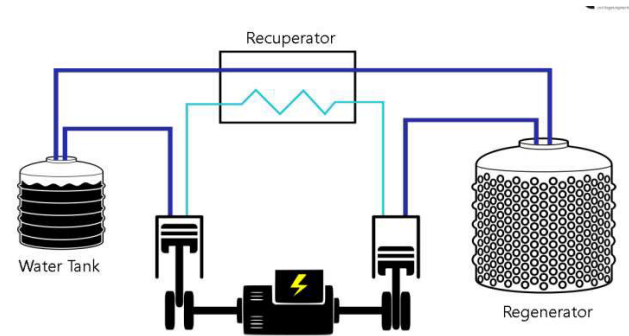


Figure 14: Electricity Storage System by Pumped Heat (ESSPH) [13]

ACKNOWLEDGEMENTS

The project “Flexwork” was made possible by the Swiss Federal office of energy. Preliminary work was supported by VSS-Lubes.

Bernhard Rüst pushed forward the developments with inspiring inputs on variable valve technologies.

Gratitude is also owed to the technology partners BASF, Bieri Hydraulics, Elgo Electronics, Mubea and Hydac with their straightforward help.

Warm thanks go to the whole Empa-team, particularly to name Andyn Omanovic, Norbert Zsiga, Patrik Soltic, Hugo Ehrensperger and Christian Bach who always made forget the work to be work.

NOMENCLATURE

ρ	density
ω	angular frequency
a	sound speed
a	acceleration
c	spring constant
A	Area
E	Isentropic Bulk Modulus
F	Force
m	mass
n	engine speed
p	pressure
t	time
Q	flow
T	period duration
V	engine cylinder volume
w	fluid flow speed
y	Gas exchange valve lift

REFERENCES

- [1] Kirsten, K. (2011) Variabler Ventiltrieb im Spannungs-feld von Downsizing und Hybridantrieb. 32. Intern. Wiener Motorensymposium 2011
- [2] Kreuter, P., Heuser, P., Schebitz, M. (1992) Strategies to Improve SI-Engine Performance by Means of Variable Intake Lift, Timing and Duration. SAE 920449
- [3] Schechter, M.M., Levin, M.B. (1996) Camless Engine. SAE 960581
- [4] Allen, J., Law, D. (2002) Production Electro-Hydraulic Variable Valve-Train for a New Generation of I.C. Engines. SAE 2002-01-1109
- [5] Turner, C. W., Babbitt, G.R., Balton, C. S., Raimao, M. A., Giordano, D. D. (2004) Design and Control of a Two-stage Electro-hydraulic Valve Actuation System. SAE 2004-01-1265
- [6] Denger, D., Mischker, K. (2005) The Electro-Hydraulic Valvetrain System EHVS – System and Potential. SAE 2005-01-0774
- [7] Lou, Z. D. (2007) Camless Variable Valve Actuation Designs with Two-Spring Pendulum and Electrohydraulic Latching. SAE 2007-01-1295
- [8] Battistoni, M., Foschini, L., Postriotti, L., Cristiani, M. (2007) Development of an Electro-Hydraulic Camless VVA System. SAE 2007-24-0088
- [9] Bernard, L., Ferrari, A., Micelli, D., Perotto, A., Rinolfi, R., Vattaneo, F. (2009) Elektrohydraulische Ventilsteuerung mit dem «Multi-Air»-Verfahren. MTZ 70 (2009) 12, S. 892-899
- [10] Möller Andreas (2019) Cam-Less Valve Train Opportunities – Implementing a Freevalve Valve Train in an automotive Application, 8. VDI-Tagung Ventiltrieb und Zylinderkopf, Würzburg 2019
- [11] Mufti, R.A., Priest, M.: Effect of cylinder pressure on engine valve-train friction under motored and fired conditions Proceedings of the Institution of Mechanical Engineers 2012 Part J: Journal of Engineering Tribology 226 (4), p. 306-314
- [12] Zsiga, N., Omanovic, A., Soltic, P., Schneider, W. (2019) Funktionsweise und Potenziale eines neuartigen elektrohydraulischen Ventiltrieb, MTZ 9 (2019) S. 18-26
- [13] Omanovic, A. (2018) Analysis and Optimization of an Electric Energy Storage System, Master Thesis ETH Zuerich



GROUP 12

**Novel system
architectures**

GENERAL LECTURE:

MODEL BASED ENGINEERING FOR ELECTRO-HYDRAULIC SOLUTIONS

Matthias Wahler*, Thomas Sendelbach

Bosch Rexroth AG, 97816 Lohr am Main, Germany

*Corresponding author: E-mail address: matthias.wahler@boschrexroth.de

ABSTRACT

This paper will give an overview about the technological change in Industrial Hydraulics and the impact of the Digital Twin on the related new engineering processes and methods in order to overcome the challenges coming out of that technology change. Simulation models will more and more become a decisive factor for the engineering process. The Digital Twin will be a window of opportunity for innovations and a technology push for the engineering process and the products in the Industrial Hydraulics.

Keywords: Model based engineering, Digital Twin, Simulation model

1. INTRODUCTION

This change is driven by the two major technology trends in the Industry sector:

Electrification: Due to the increasing awareness of energy efficiency, the classical hydraulic solutions will be replaced or transformed into electro-hydraulic solutions. That means that hydraulics will be driven by speed variable electric motors (e.g. SYTRONIX). That will lead to interdisciplinary solutions which must be handled in an interdisciplinary way in the

development process which begins with a first design and ends up with the commissioning & service.

Digitalization: Electronics and software will be added to the hydraulic products and standard hydraulics will lead to more and more software related products. Therefore, the complexity of the products and the technical solutions will increase as well as set-ups and special skills will be required in the development process. Besides the technology trends above, an increasing demand for higher productivity, dynamic and precision of

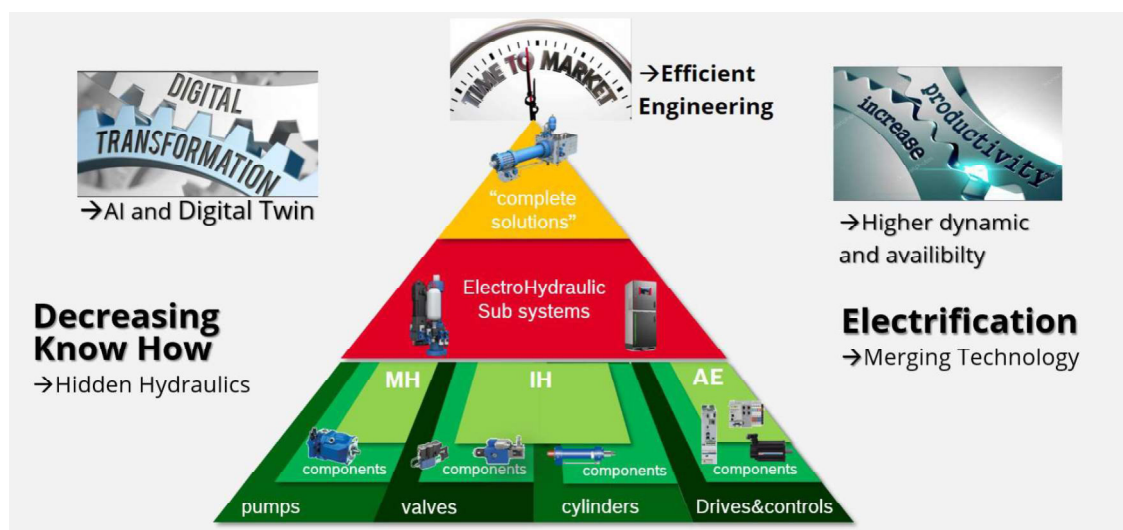


Figure 1: motivation and challenges for Model Based Engineering

production machines within parallel reduced life cycle costs and a general need for short time to market will require a new development approach. From the first concept at the beginning, the design phase up to the engineering and commissioning process the Digital Twin (product data and models) becomes more important and models are needed to achieve the targets.

2. DIGITAL TWIN AND MODELLING

These models are not only domain specific due to the merging technologies. Therefore, a FLUID mechatronic model approach is needed:

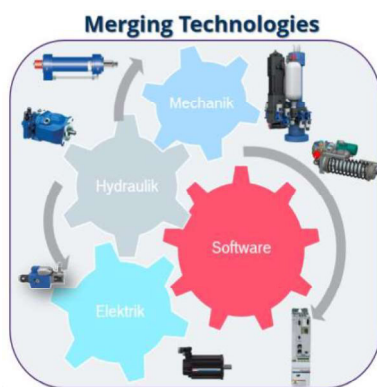


Figure 2: multi technology modelling

Today the first design concepts are typically made by an early multi-technology simulation based on approved component and system models. Afterwards, the functionality is proven by a system simulation with a “Virtual Prototype” (Digital Twin) of the machine. This will help to shorten the development time significantly and to

assure the proper functionality with less efforts than building up a real prototype with iron and oil. Even the software programming process will be shortened by the model based approach of automatically generated software code for the related target system out of the simulation tool chain. But for these purposes we have to get a clear understanding what is the content of the Digital Twin. The author’s definition is shown in **Figure 3**.

However, different models for the various purposes will be needed as shown in **Figure 4**.

For the simple sizing and configuration process, the so called static models (level 1), like CAD-files, EPLAN-Macros and characteristic curves (e.g., Speed-torque curve or pressure-oil flow) are sufficient.

For system design and validation issues you also need dynamic models (level2), where all relevant limitations and dynamics are covered. In most cases it is sufficient, if the system dynamic is approximated by PTn-models with limitations in order to keep it simple. Although, for a machine and program simulation or a virtual commissioning you need models (level 3) for the software and the digital control function, too. Because then you are able to adjust the parameters of the Digital Twin, which is needed for the virtual commissioning and programming of a machine or system.

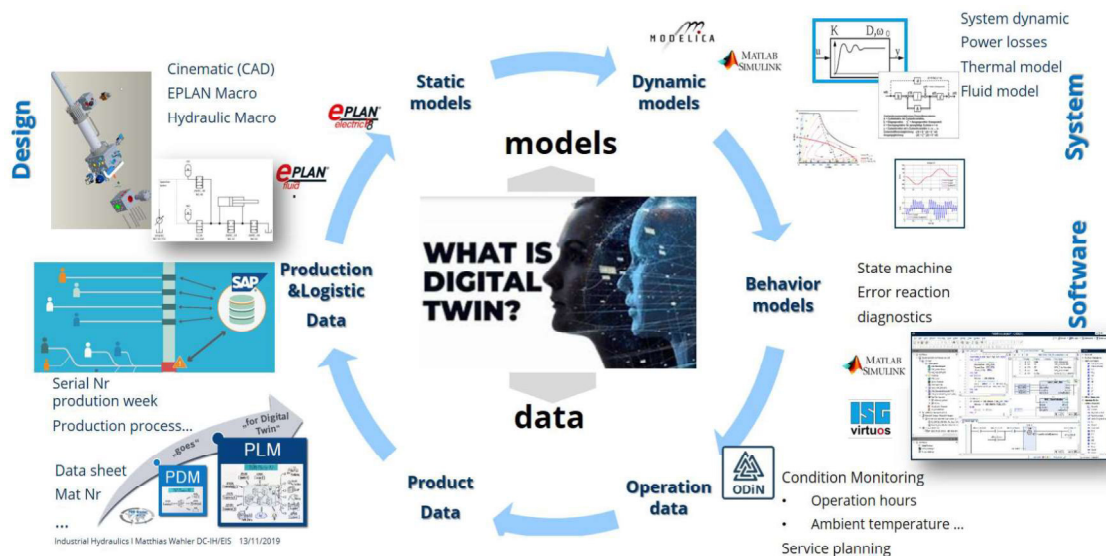


Figure 3: Definition of a Digital Twin

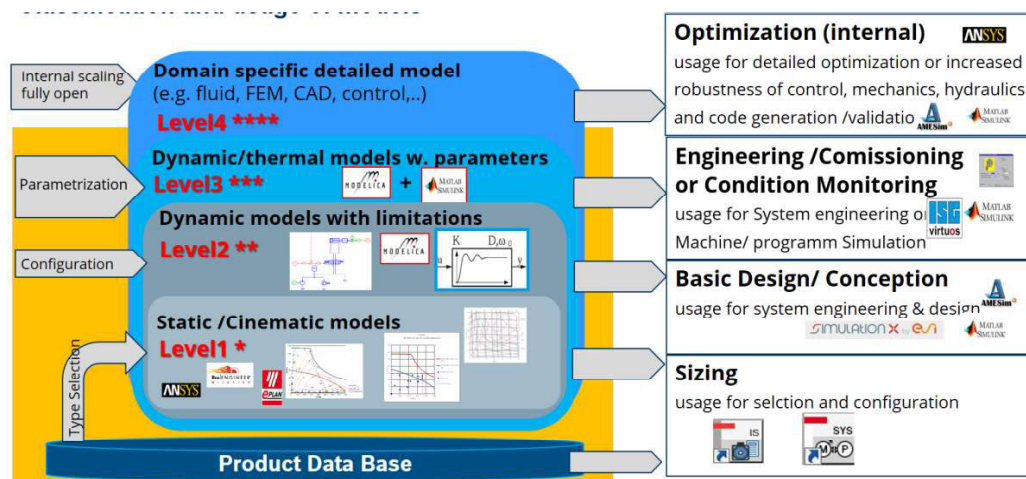


Figure 4: Different model levels for the specific purposes

3. MODEL BASED ENGINEERING

Before showing concrete examples the pre-conditions for a successful Model Based Engineering approach shall be listed:

1. **Product data base** for all data related to the product from the design, production and operation
2. **Simulation models** for the different purposes and use cases with a modular model architecture
3. **Standardized interfaces** between the different simulations tools (FMU, FMI) for data exchange and Co-simulation
4. **Open software architecture** with an option for code generation and software modelling.

For internal design and development issues more detailed and domain specific models are needed in order to make a deep system analysis or optimization (e.g. CFD for fluid). The software itself is also tested in advance by simulations on a PC, which helps to reduce the test efforts by automatically test routines with virtual load and

process models on a virtual test bench.

In summary, the mechatronic engineering process for electro-hydraulic solutions will be assured and improved with models (see **Figure 5**).

In this paper the new tools and processes such as

- an early system simulation (multi-technology models) for the design and concept phase in order to proof the concept
- and a new software development and test process with automatically code generation and validation with a virtual prototype will be described.

In addition to that, it will also be shown how such models will help to improve both operations and service with new methods and solutions for e.g.

- AutoTuning & Adaptive Control: new control algorithms for optimized performance and productivity with system identification and model based control, and
- ModelBased Condition-Monitoring with wear and tear model and virtual sensors during operation.

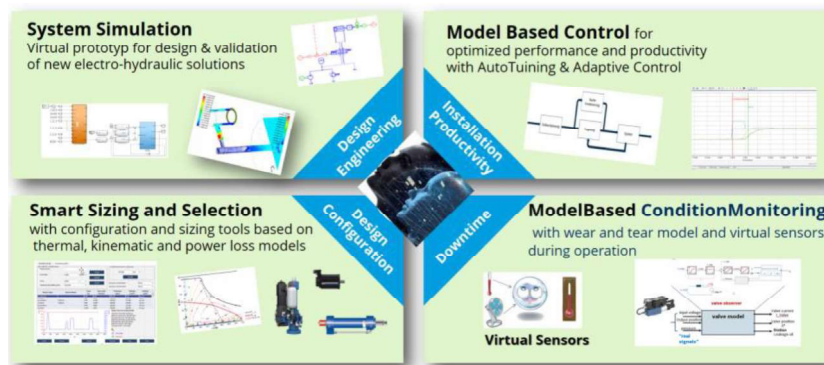


Figure 5: Model Based Engineering - Overview

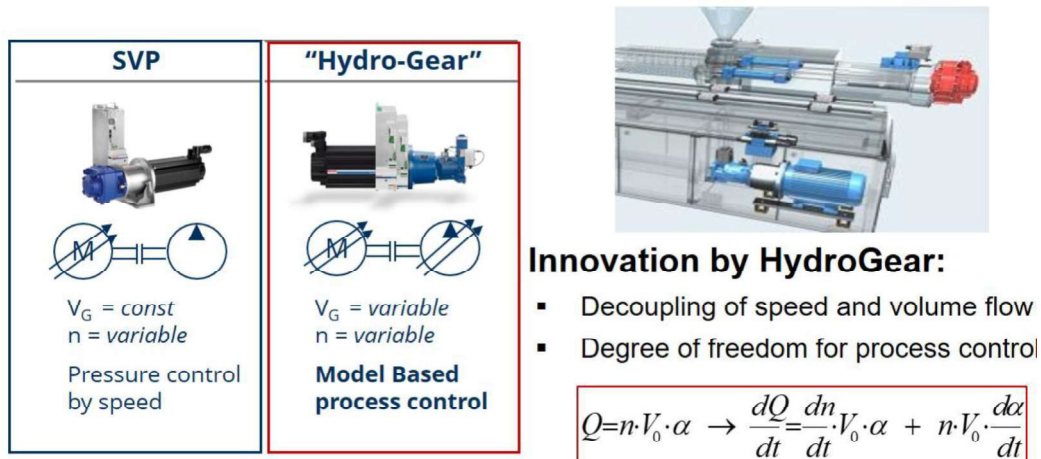


Figure 10: speed variable displacement pump (Hydro Gear)

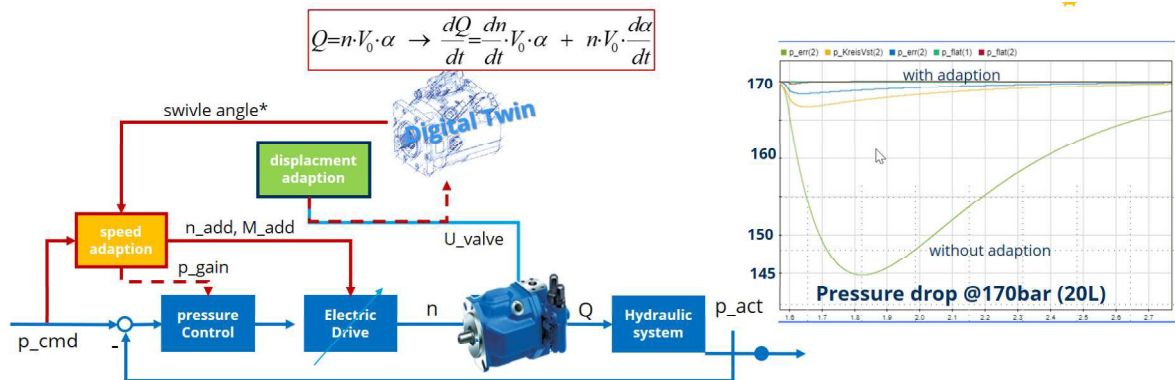


Figure 11: model predictive feed forward for speed variable pump

Therefore, the pump displacement and speed will be adapted to the load condition due to different optimization criteria: dynamic, energy efficiency or noise. The challenge is then that the variation of pump displacement V_G has an influence on the pressure control and stability.

If the pressure control is running, then the variation of the pump displacement in pressure control will have an impact on the

- Oil flow Q
- Motor torque caused by the system pressure
- And the control gain for the closed loop

The result of the pressure drop due to the swifl angle adjust can be seen in **Figure 11** (green curve).

Therefore, a new model based feed forward control based on a system model for the swifl angle pump, was designed which helps to overcome these negative effects. In the model, the system dynamic of the swifl angle adjustment was realized by the modelling of the most important parts in the pump:

- electro magnet of the switch valve

- switch valve mechanic
- adjustment cylinder for the swifl angle
- pump mechanics

With the knowledge of the system dynamic a model based feed forward for torque and speed was designed.

As you can see in **Figure 11** the pressure drop caused by a reduction of V_G (swifl angle adjust 100% \rightarrow 10%) during pressure control can be dramatically reduced if the new model predictive control is used. The graphic shows the result with the different measures:

1. yellow: with adaption of p-gain
2. blue: with adaption of p-gain and speed feed forward
3. red: with adaption of p-gain and speed & torque feed forward.

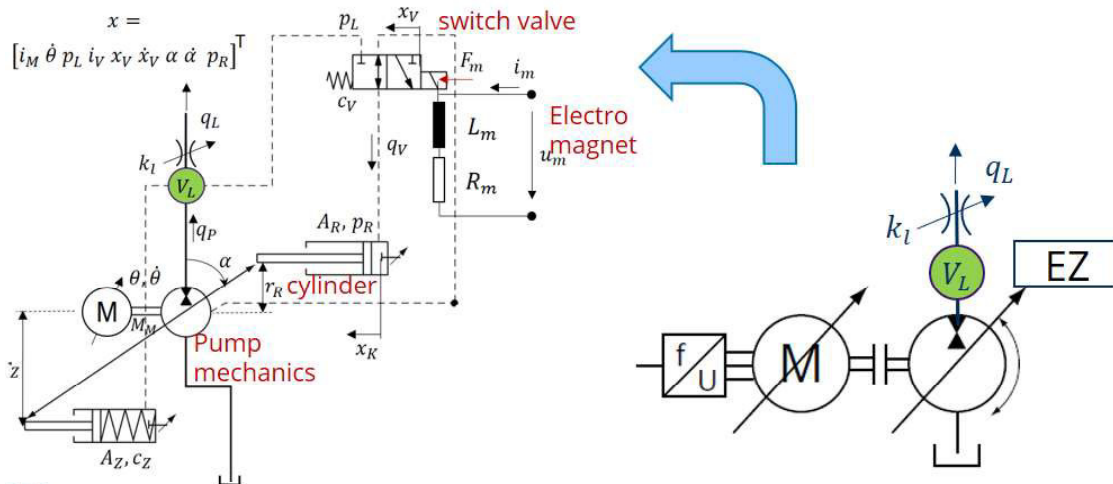


Figure 12: system model of variable pump (EZ)

5. CONDITION MONITORING WITH VIRTUAL SENSORS

In the last chapter the area of condition monitoring will be discussed and the benefits which can be achieved by system models that are used in order to generate virtual sensor signals. But first, some basic definitions and explanations are given in order to have a clearer understanding about condition monitoring.

In **Figure 13** an explanation of condition monitoring and its target are given. Regarding the methods for condition monitoring the following three analytics have to be differentiated

- **Descriptive Analytics**
Trend analysis and monitoring of operation conditions (sensor signals)
- **Diagnostic Analytics**
Generation of representative virtual sensor data (e.g. friction) with a specific test cycle

or online by system-/ component model (Digital Twin)!

- **Predictive Analytics**

Health Index with DataAnalytics based on sensor data. With a life time estimation based on stochastic methods

The system models will help in that area to get a better system understanding and also it is a opportunity to get valuable information about the system condition. Based on a deep product knowledge (domain know how) specific test cycles or system models will help to generate non measurable signals (e.g. like friction, leakage or oil condition see pump model in figure 14). These operation conditions can then be used to monitor the condition of the electro hydraulic system and together with wear and tear models or AI-algorithms it is possible to generate a health index of the system, which is needed for predictive maintenance solutions.

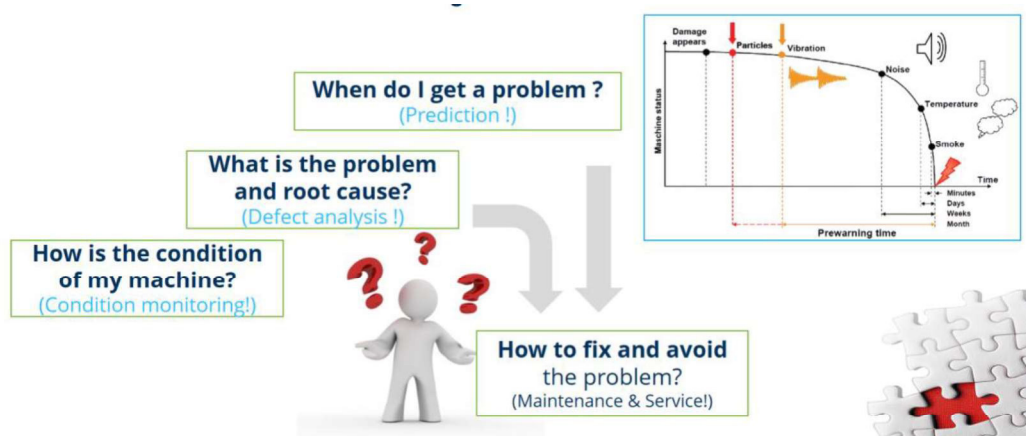


Figure 13: Definition of Condition Monitoring

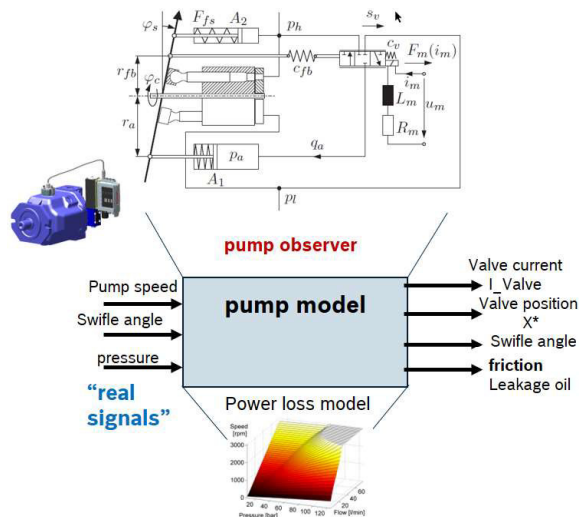


Figure 14: Virtual sensor (example pump model)

6. CONCLUSION AND OUTLOOK

As shown in this paper the Digital Twin will change the development and engineering process fundamentally and which advantages can be taken out of that. For the product quality and productivity, but also for the engineering process due to efficiency increase. But in order to establish the Model Based Engineering process in a company, a fundamental change in mind and the engineering process is needed. And the Digital Twin needs to be filled with content, which means a lot of product data and the corresponding system models are needed first. Therefore a lot of initial effort has to be accepted before on the long term the harvest can be taken out of the new MBE-approach. But in the end it will be worth while to change, because the innovation potential is huge and the Digital Twin will define the future. And the future begins already now.

BOOTSTRAP RESERVOIR CONCEPTS FOR ELECTRO-HYDRAULIC COMPACT CYLINDER DRIVES

Søren Ketelsen^{1*}, Giacomo Kolks², Torben Ole Andersen¹, Lasse Schmidt¹ and Jürgen Weber²

¹Department of Energy Technology, Aalborg University, Pontoppidanstræde 111, 9220 Aalborg East, Denmark

²Institut für Mechatronischen Maschinenbau, Technische Universität Dresden, Helmholtzstrasse 7a, 01069 Dresden

* Corresponding author: Tel.: + 45 28253258; E-mail address: sok@et.aau.dk

ABSTRACT

This paper presents a conceptual study aiming to improve the compactness of electro-hydraulic compact drives (ECD's). In most current ECD architectures, gas accumulators are used as volume compensators for the flow imbalance emerging whenever asymmetric single rod cylinders are used. To stay within a required reservoir pressure range typically from two to four bar, a large gas volume is required, compromising system compactness. Combining conventional ECD architectures with a bootstrap reservoir offers a greater degree of freedom in system design, which enables downsizing or avoidance of the gas volume. Another potential benefit by including a bootstrap reservoir is the possibility of elevating the backpressure of the ECD thus enhancing drive stiffness, expanding the application range and market acceptance. Based on an open analysis of the solution space occurring when introducing a bootstrap reservoir, three system architectures are selected for a conceptual study. The results show that the downsizing potential is strongly dependent on the maximum friction force and the area ratio of the bootstrap reservoir pistons, while a linear analysis reveals that for some system architectures the bootstrap reservoir may severely influence the system dynamics. Simulation results confirm the functionality of the proposed system architectures, and show that a potential for downsizing/avoiding the gas volume, as well as increasing the ECD stiffness is present.

Keywords: Electro-hydraulic, compact cylinder drive, self-contained cylinder, bootstrap reservoir

1. INTRODUCTION

Electro-hydraulic compact drives (ECD's) are an emerging technology in a range of industrially available linear drive solutions. ECD's can generally be characterised as pump-controlled cylinder drives based on variable-speed electric motors and fixed-displacement pumps combined in a compact unit including a fully enclosed oil circuit. A feasible ECD circuit must be able to compensate the flow imbalance emerging whenever asymmetric single rod cylinders are used. Numerous solutions to achieve this have been proposed and an extensive overview is given in [1]. Generally the compensation methods may be divided in two groups: valve-compensation and pump-compensation [2]. Examples of each approach are found in **Figure 1**, wherein (a) an inverse shuttle valve connects the low pressure chamber with the gas accumulator to compensate

the flow asymmetry, while in (b) a pump-compensated architecture is shown. Here the pump displacements are matched, such that the two-quadrant pump is providing the cylinder rod flow. The two examples shown are well-known in research literature and detailed investigations and experimental validations may be found in [2]–[5] for valve-compensated systems, and in [6]–[10] for pump-compensated systems.

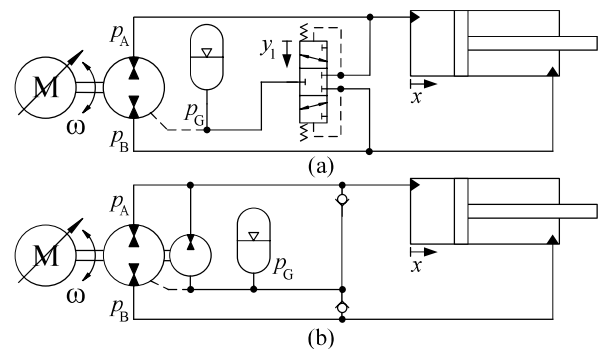


Figure 1: Examples of (a) valve-compensated and (b) pump-compensated ECD.

In current ECD architectures, gas accumulators are used to store the rod volume as well as compression and thermal expansion volumes. The accumulator defines the baseline pressure of the system, which has conflicting optimization targets: On the one hand, it is supposed to be high in order to avoid pump cavitation and to increase the bulk modulus of the oil/air mixture and hence yield stiffer cylinder drives. On the other hand, pump housings and especially their shaft sealing offer longer lifetime at lower pressures and may even malfunction if a low-pressure leakage line is unavailable. For this reason, accumulator pressures usually do not exceed four bar. In order to stay within this narrow pressure range under all operating conditions, the gas volume needs to be significantly larger than the rod volume of the cylinder, rendering the accumulator bulky in comparison to the cylinder. Especially for long stroke cylinders, this compromises the desired compactness of the entire system. One approach for reducing the accumulator volume and increase system stiffness is given by combining the conventional ECD architectures in **Figure 1** with a so-called bootstrap reservoir.

1.1. Bootstrap Reservoirs

Bootstrap reservoirs can essentially be regarded as two interconnected differential cylinders, which may be arranged in different configurations as seen in **Figure 2**. Common for the three configurations is that one or more chambers are vented to the atmosphere, while the effective area between in the bootstrap chamber (A_C) and the reservoir chamber (A_R) differs significantly. In commercially available bootstrap reservoirs the reservoir piston area may be as much as ~ 85 times larger than the bootstrap area [11].

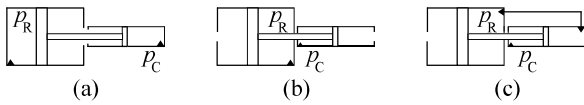


Figure 2: (a)-(c) Bootstrap reservoirs shown as two interconnected differential cylinders.

By the pressure p_C the reservoir pressure p_R is elevated above atmospheric pressure to avoid pump cavitation and to ensure that the reservoir may function in arbitrary orientations. Bootstrap reservoirs are vital in aircraft hydraulic systems ([11], [12]), where either the hydraulic pump pressure or compressed air, pressurises the bootstrap chamber. In this paper, the configuration

shown in **Figure 2 (a)** is utilized for analysis. For relative pressures, in static conditions neglecting friction and gravitational loads it is evident that $p_R A_R = p_C A_C$, leading to $p_R = \alpha_B p_C$ for $\alpha_B = A_C/A_R$, meaning that the bootstrap reservoir may be regarded as a volume-to-pressure transmission [13].

1.2. Paper Outline

In Sec. 2 the solution space occurring when combining a bootstrap reservoir with the two different ECD's from **Figure 1** is derived. From the feasible subspace three different systems have been selected, to each investigate the following three potentials originating from the combination of bootstrap reservoirs and ECD's:

1. Downsizing (Sec. 3)

The volume-to-pressure transmission property of the bootstrap reservoir may be utilised to downsize the gas volume while increasing the gas pressure.

2. Gasless (Sec. 4)

The gas accumulator can be avoided by replacing it directly with the bootstrap reservoir. If no gas volume is present, the baseline pressure of the system must be defined by the bootstrap chamber, which has to be charged by means of additional circuitry in order to define a reservoir pressure above atmosphere.

3. Stiffness (Sec. 5)

If the high pressure bootstrap chamber is connected with the low pressure side of the cylinder, it may be possible to elevate the back-pressure of the cylinder and as such improve the stiffness of the ECD.

2. COMBINING COMPACT DRIVES AND BOOTSTRAP RESERVOIRS

Based on **Figure 3**, it is investigated how a bootstrap reservoir may be included in the design of the two ECD architectures from **Figure 1**.

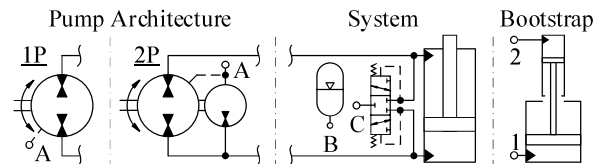


Figure 3: To investigate the solution space, the possible configurations when combining ports A, B and C with ports 1 and 2 are considered.

The valve-compensated ECD emerges when combining the single pump architecture 1P with the system (cylinder, inverse shuttle valve, and accumulator), whereas the pump-compensated ECD emerges if considering pump architecture 2P. Note, that the inverse shuttle valve is usually not included when considering pump architecture 2P, but is inserted here to extend the possible ways of introducing the bootstrap reservoir, thus gaining benefits.

The feasible solution space is initially constrained because port A must be connected to the low pressure port 1. System ports B and C may generally be connected to bootstrap port 1, 2 or stay unconnected. However, for the valve-compensated architecture (1P) system port C cannot stay unconnected. Altogether, this leaves six system architectures for the valve-compensated architecture (1P) and nine for the pump-compensated architecture (2P), which are listed in **Table 1**. In this table, the improvement potentials are indicated, as well as system architectures that are obviously infeasible or that require additional circuitry to obtain the indicated potential. Please note, that only obviously infeasible architectures are indicated, meaning that other architectures may turn out infeasible or needing additional circuitry when analysed thoroughly.

The circuit configurations with ID 2, 4, 6 are obviously infeasible, as the pump leakage oil is

Table 1: Circuit configurations

	ID	X to #		Potential	Comment
		B	C		
Architecture P1	1	1	1	-	
	2	1	2	-	Infeasible
	3	2	1	Downsizing	
	4	2	2	-	Infeasible
	5	-	1	Gasless	Circuitry required
	6	-	2	Gasless	Infeasible
Pump Architecture P2	7	1	1	-	
	8	1	2	Stiffness	
	9	1	-	-	
	10	2	1	Downsizing	
	11	2	2	Stiffness	
	12	2	-	Downsizing	
	13	-	1	Gasless	Circuitry required
	14	-	2	Gasless & stiffness	Further investigation needed
	15	-	-	Gasless	Circuitry required

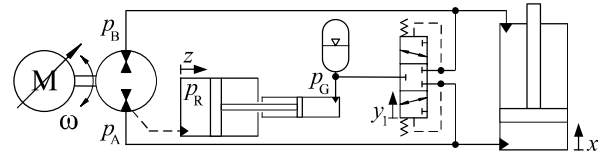


Figure 4: Infeasible system architecture (ID 4).

not able to re-enter the closed oil circuit. For ID 4, this is illustrated in **Figure 4**.

Pump leakage causes oil from the high pressure side (p_G) leaking towards the low pressure side (p_R), thus causing the bootstrap reservoir piston to drift until the end-stop is reached, rendering the device non-functional. To compensate piston drift, leakage oil must be able to re-enter the closed system from the low pressure side of the bootstrap reservoir. Since there is no part of the system with lower pressure available, this is clearly not possible by means of valves.

For the considered architecture this example shows that it is not possible to elevate the back-pressure of the cylinder, without including an active component to displace fluid from the low pressure to the high pressure side of the bootstrap reservoir.

To investigate each of the potentials arising when introducing a bootstrap reservoir in ECD design, three of the circuit configurations from **Table 1** are selected. To investigate the downsizing potential, gasless potential and increased stiffness potential, system ID 3, 5 (valve-compensated) and 8 (pump-compensated) are chosen as a starting point, respectively. The selected architectures are shown in **Figure 5**.

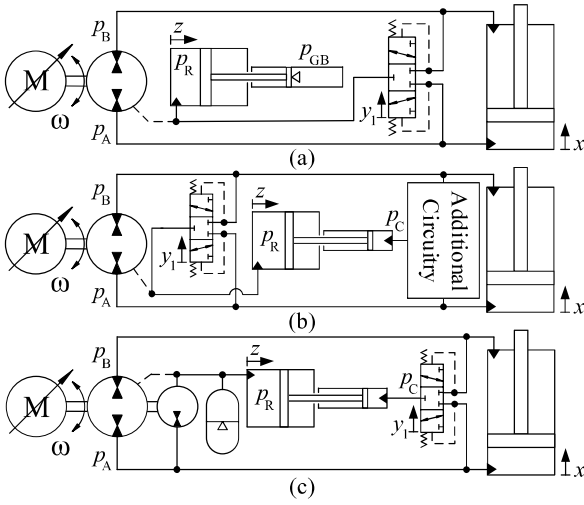


Figure 5: Three system configurations chosen for further investigation. (a) ID 3: Downsizing of gas volume. (b) ID 5: Gasless system architecture. (c) ID 8: Architecture for increased stiffness.

3. DOWNSIZING OF GAS VOLUME

The downsizing potential of the gas volume is investigated using the system architecture shown in **Figure 5 (a)**. In this configuration, the bootstrap reservoir contains a low-pressure oil chamber and a high-pressure gas chamber, and may as such be regarded as a piston accumulator with uneven piston areas. This enables replacing the low pressure/high volume accumulator in **Figure 1** with a gas working under high pressure / low volume. The gas is considered ideal and the compression/expansion process as polytropic obeying:

$$p_{aG0}V_{G0}^{\kappa} = p_{aG1}V_{G1}^{\kappa} = p_{aG2}V_{G2}^{\kappa} \quad (1)$$

$p_{aG0} < p_{aG1} < p_{aG2}$, is the pre-charge, minimum and maximum gas working pressure respectively. The subscripted “a” indicates that absolute pressures are utilised.

The minimum gas volume (V_{G2}) may be found as:

$$V_{G2} = V_{G1} \left(\frac{p_{aG1}}{p_{aG2}} \right)^{\frac{1}{\kappa}} \quad (2)$$

By defining the compensation volume or active volume as $\Delta V = (V_{G1} - V_{G2})$, the ratio of initial gas volume V_{G1} to ΔV for the conventional configuration in **Figure 1 (a)** is from Eq. (2) found as:

$$R_{Acc} = \frac{V_{G1}}{\Delta V} = \left(1 - \left(\frac{p_{aG1}}{p_{aG2}} \right)^{\frac{1}{\kappa}} \right)^{-1} \quad (3)$$

Please note that to utilise ΔV in Eq. (3), no oil is present in the accumulator at p_{aG1} , meaning that the initial gas volume (V_{G1}) is here regarded as the total accumulator size. To achieve proper utilisation and lifetime of the accumulator the pre-charge pressure p_{aG0} is customary chosen to 90% of p_{aG1} yielding a larger accumulator ($V_{G0} > V_{G1}$) than given by Eq. (3). To achieve a fair comparison between the volume of the accumulator and the gas-loaded bootstrap reservoir only the active oil volume ΔV is included in this comparison.

For the configuration in **Figure 5 (a)**, the reservoir piston friction (F_{Fz}) needs to be included when estimating the gas volume. The force equilibrium given in relative pressures for the reservoir piston, neglecting gravitational load is:

$$\dot{z}M_B = A_R p_R - A_C p_{GB} - F_{Fz} \quad (4)$$

Assuming that the mass M_B is small, the acceleration force may be neglected and by expressing F_{Fz} as an equivalent pressure working on A_R ($F_{Fz} = p_F A_R$), yields:

$$A_R(p_R - \alpha_B p_{GB} - p_F) = 0 \quad (5)$$

The force equilibrium is transformed to absolute pressures, by also including the forces working on the system from the surroundings. The reservoir pressure is found as:

$$p_{aR} = \alpha_B p_{aGB} + p_{atm}(1 - \alpha_B) + p_F \quad (6)$$

The minimum and maximum reservoir pressures in the presence of the maximum piston friction p_{Fm} are given by:

$$\begin{aligned} p_{aR1} &= \alpha_B p_{aGB1} + p_{atm}(1 - \alpha_B) - |p_{Fm}| \\ p_{aR2} &= \alpha_B p_{aGB2} + p_{atm}(1 - \alpha_B) + |p_{Fm}| \end{aligned} \quad (7)$$

From Eq. (7) the required limits for the gas pressure in the bootstrap chamber is found as:

$$\begin{aligned} p_{aGB1} &= \alpha_B^{-1}(p_{aR1} - p_{atm}(1 - \alpha_B) + |p_{Fm}|) \\ p_{aGB2} &= \alpha_B^{-1}(p_{aR2} - p_{atm}(1 - \alpha_B) - |p_{Fm}|) \end{aligned} \quad (8)$$

From Eq. (8) it may be observed that piston friction narrows the allowable range of gas pressures, requiring a larger gas volume. It is required that $p_{aGB1} < p_{aGB2}$, from which it follows that $|p_{Fm}| < 0.5(p_{aR2} - p_{aR1})$. The initial gas-volume of the bootstrap chamber, V_{GB1} , may be found from Eq. (3), as:

$$V_{GB1} = \Delta V \alpha_B \left(1 - \left(\frac{p_{aGB1}}{p_{aGB2}} \right)^{\frac{1}{\kappa}} \right)^{-1} \quad (9)$$

The volume of the bootstrap reservoir is calculated as $V_{Boot} = \Delta V + V_{GB1}$, such that the ratio of

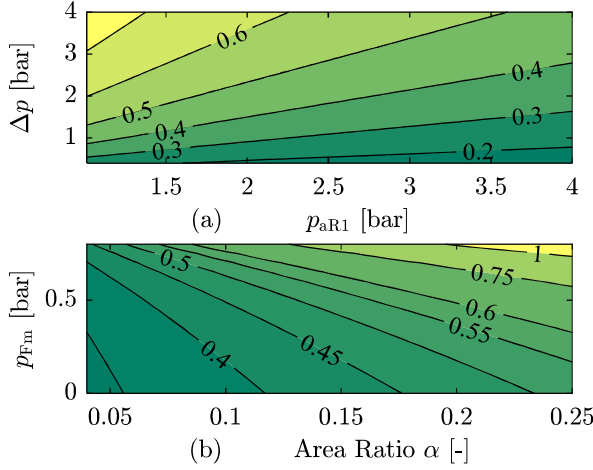


Figure 6: Contour of the bootstrap reservoir size relative to a gas accumulator. (a) Frictionless and $\alpha_B = 0.1$ (b) $p_{aR1} = 3$ bar, $\Delta p = 2$ bar.

bootstrap reservoir volume to ΔV can be established as:

$$R_{Boot} = \frac{V_{Boot}}{\Delta V} = 1 + \alpha_B \left(1 - \left(\frac{p_{aGB1}}{p_{aGB2}} \right)^{\frac{1}{\kappa}} \right)^{-1} \quad (10)$$

By defining $R = R_{Boot}/R_{Acc} = V_{Boot}/V_{G1}$, the relative size of the gas-loaded bootstrap reservoir to the conventional low pressure gas accumulator may be estimated. Note that the potential for downsizing the gas volume only considers the active volumes, such that volume differences caused from different material wall thickness or other inactive volumes are not included. In **Figure 6 (a)**, R is plotted as a function of the required reservoir pressures, while in **(b)** it is plotted as a function of the bootstrap area ratio and the maximum friction force. Adiabatic conditions have been assumed by defining $\kappa = 1.4$.

It is evident that the volume ratio decreases as area ratio and friction force decreases. For a bootstrap area ratio of $1/25$, and low friction the bootstrap reservoir may be up to 65% smaller than a gas accumulator for the considered pressure limits. On the other hand, for a bootstrap reservoir with a large area ratio ($\alpha_B > 0.25$) and large friction forces the gas-loaded bootstrap reservoir is actually larger than using a conventional gas ac-

cumulator. In the current investigation, the reservoir pressure is allowed to span from two bar to four bar (relative pressures).

Table 2 shows examples of bootstrap reservoir and gas accumulator sizes for different parameters.

Table 2: Estimated bootstrap and accumulator sizes. $p_{aR1} = 3$ bar, $p_{aR2} = 5$ bar.

α_B	1/10	1/10	1/20	1/20
$ p_{Fm} $	0 bar	0.75 bar	0 bar	0.75 bar
p_{aGB1}	20.9 bar	28.4 bar	40.7 bar	55.7 bar
p_{aGB2}	40.9 bar	33.4 bar	80.7 bar	65.7 bar
$V_{GB1}/\Delta V$	0.26	0.91	0.13	0.45
R_{Boot}	1.26	1.91	1.13	1.45
R_{Acc}	3.27			
R	0.39	0.59	0.35	0.44

3.1. Selection of reservoir diameter

To reduce throttling losses the inverse shuttle valve connecting the low pressure chamber and the reservoir volume is typically not particularly restrictive. This means that the pressure dynamics of the connected chambers are almost similar, in turn causing volume changes of one chamber to directly influence the adjoining chamber dynamics. As such the two movable masses (cylinder and reservoir rods/pistons) may interact with each other, causing the cylinder motion dynamics to be changed when introducing the bootstrap reservoir. This may cause difficulties designing a position/velocity controller, meaning that these interactions should be reduced if possible.

To investigate how these interactions depend on the selected reservoir diameter, a simplified linear model, based on the simplified model structure showed in **Figure 7** is considered. The inverse shuttle valve is assumed ideal (no pressure drop), the gas pressure constant, while pump shaft dynamics and leakage is neglected.

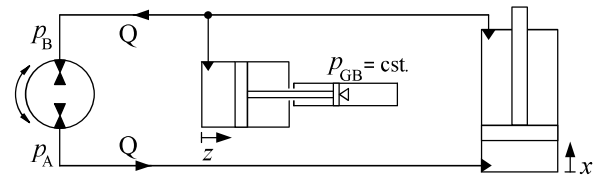


Figure 7: Simplified model used for linear analysis.

The linear model is derived in Appendix B, and based on the linearized equations, the transfer function from $Q(s)$ to $\dot{x}(s)$ may be established.

This is found to contain two complex pole pairs and one complex pair of zeros. The variation of the poles and zeros as the reservoir diameter is changed from 30 mm to 100 mm, is shown in **Figure 8**. The viscous damping coefficient is scaled linearly as a function of piston circumference, while the reservoir volume is fixed leading the reservoir stroke length to be ranging from 720 mm ($D_R = 30$ mm) to 65 mm ($D_R = 100$ mm). The remaining parameters are fixed, including the mass of the bootstrap rod and pistons of 10 kg. In **Figure 8**, the linearization point is at the centre position and a positive cylinder speed of 100 mm/s. No qualitative differences are found by varying the linearization point.

At $D_R = 30$ mm **Figure 8** shows that the cylinder motion dynamics are dominated by the complex pole pair located at $-0.75 \pm 250i$, because the dynamics from the complex zeros and the other complex pole pair are located close to each other at $-7.5 \pm 60i$, thus cancelling each other. At large reservoir diameters the complex pair of zeros accompanies the complex pole pair that started at $-0.75 \pm 250i$, while the complex pole pair starting $-7.5 \pm 60i$, moves towards the starting position of the other pole pair. Thus, for large reservoir diameters the motion dynamics are also dominated by a complex pole pair at $-0.75 \pm 250i$. However, for critical diameters the cylinder motion dynamics may not be dominated by second order dynamics only, as the complex pair of zeros is located far away from any of the complex pole pairs in the complex plane.

From a dynamical point of view, the reservoir diameter should therefore be chosen far away from the critical diameters. From a practical point of view, it may be infeasible to select a small diameter, as this yields a long stroke length, and requires low friction. Large reservoir diameters are therefore recommended. For the given system parameters a reservoir diameter of 100 mm is feasible, and thus selected for all three considered systems. Likewise an area ratio of $\alpha_B = 0.1$ is chosen.

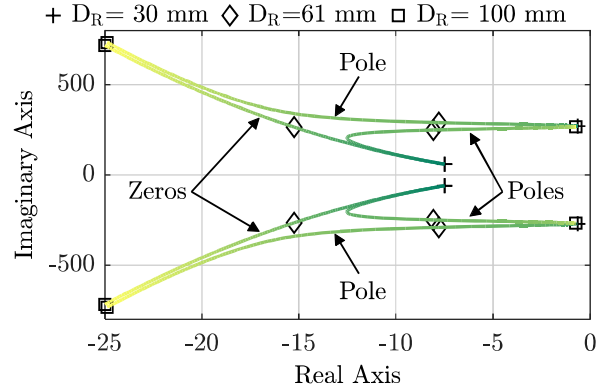


Figure 8: Variations of poles and zeros, as a function of reservoir diameter for the transfer function from $Q(s)$ to $\dot{x}(s)$.

3.2. Simulation Results

A simulation model of the system in **Figure 5 (a)** has been formulated and solved using MATLAB/Simulink. The full set of equations is found in Appendix A, while the modelling parameters are found in the Nomenclature. The load is modelled as a mass/spring/damper system as seen in **Figure 9 (a)**, where the spring pre-tensioning is such that four quadrant operation is obtained. This load system is used for the remainder of the paper.

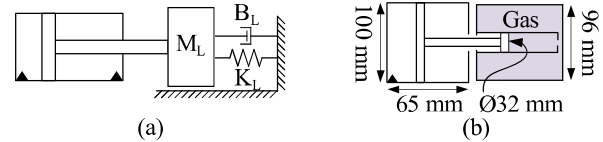


Figure 9: (a) Load system. (b) Bootstrap reservoir dimensions used in simulation study.

For the chosen cylinder dimensions (63/36-500mm), the needed ΔV is 0.51 L. The bootstrap reservoir is modelled with a maximum friction force of $A_A \cdot 0.75 \text{ bar} = 590 \text{ N}$ and $\alpha_B = 0.1$. From **Table 2** it is seen that the needed accumulator/reservoir volume is reduced from 1.66 L to 0.97 L. An example of bootstrap reservoir dimensions is given in **Figure 9 (b)**. The cylinder piston is controlled to follow a sinusoidal position reference, using a proportional position feedback controller and static/passive velocity feedforward. The simulation results for four quadrant operation is given in **Figure 10**.

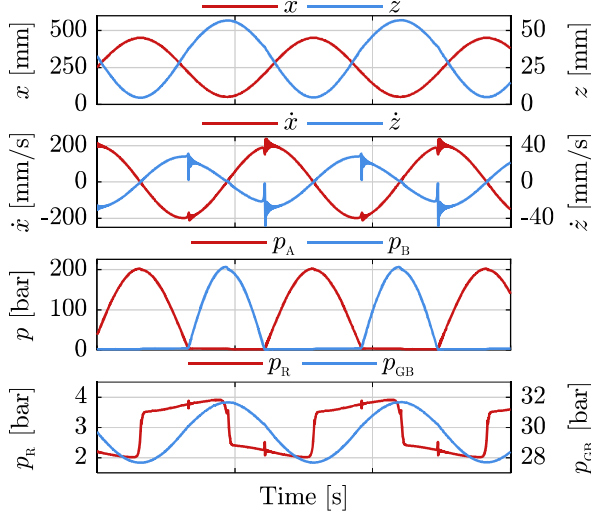


Figure 10: Four quadrant simulation results for the ECD incorporating a gas-loaded bootstrap reservoir (Figure 5 (a)).

The primary observation is that the reservoir pressure p_R is kept within the design limits from two to four bar. The gas pressure p_{GB} is only position dependent, while p_R is also motion direction dependent, due to the directional shift of the friction force. Severe velocity oscillations are observed for both \dot{x} and \dot{z} , when the direction of the external load changes. This is caused by the position change of the inverse shuttle valve, which is a general drawback of valve-compensated ECD [14], [15] and is not related to the use of the bootstrap reservoir. This is confirmed in Figure 11 where no abrupt velocity oscillations are observed. Here the pre-tensioning of the load spring is adjusted such that the load is unidirectional.

The robustness towards changed friction forces working on the bootstrap reservoir, is investigated in Figure 12. If the maximum friction force equals the design friction force, the reservoir pressure approaches the design limits. If the friction force is reduced, the reservoir pressure is kept well within limits, while it is exceeding the limits, if the friction force is larger than expected.

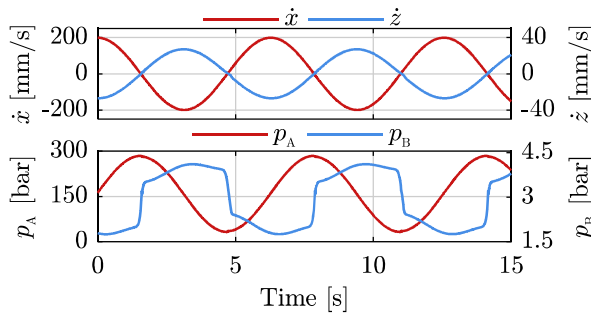


Figure 11: Simulation results for two quadrant operation.

Note that the changed friction is only observed in the reservoir pressure and not the gas pressure, as this is only position dependent.

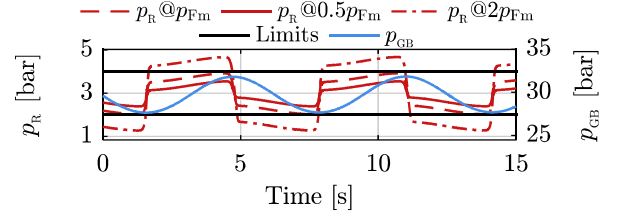


Figure 12: Simulation results in two quadrant operation, for varying bootstrap friction forces.

4. GASLESS SYSTEM ARCHITECTURE

To investigate the potential for avoiding a gas volume, additional circuitry is added to the system configuration in Figure 5 (b). The proposed system is shown in Figure 13, where conventional pressure compensator valves PC2 and PC3, are used to charge and discharge the bootstrap chamber respectively.

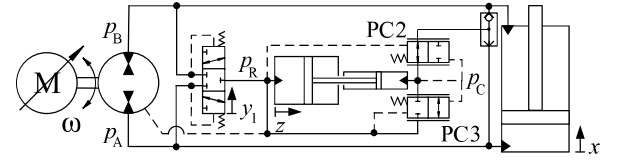


Figure 13: Proposed gasless system. A charge valve (PC2) and a discharge valve (PC3) are included.

The functionality of the added circuitry is illustrated in Figure 14. When the bootstrap reservoir retracts (positive cylinder speed), the bootstrap chamber volume increases, requiring an inlet/charge flow to maintain the charge pressure. This flow must be acquired from the cylinder chamber with the largest pressure, as the low pressure chamber is connected to the reservoir side of the bootstrap reservoir, otherwise violating $p_C > p_R$. To control the charge flow, a normally open pressure compensator PC2 is proposed. When p_C is smaller than the reservoir pressure plus some equivalent spring force, the chamber is charged, while the valve is closed if p_C exceeds the equivalent spring force plus the reservoir pressure. A shuttle valve, is used to select the largest system pressure as the charge source, rendering this approach functional for bi-directional external load directions.

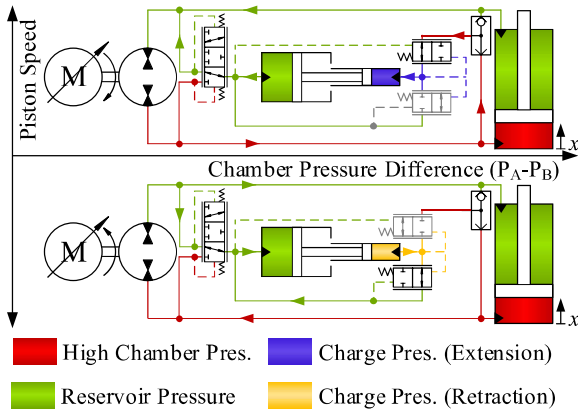


Figure 14: Two quadrant operation diagram of the proposed circuit. In the two remaining operation quadrants, the only difference is the opening direction of the inverse shuttle and the shuttle valve.

When the bootstrap reservoir extends (negative cylinder speeds), the bootstrap chamber volume decreases, requiring a flow to leave the bootstrap chamber. This is achieved by the normally closed discharge valve PC3, which directs the discharge flow to the reservoir chamber, when p_C exceeds the reservoir pressure plus some equivalent spring force.

It is pivotal for the functionality of the proposed system that the limits of p_C enable the valve springs to be selected such that at least one of the valves PC2 and PC3 are fully closed at all times. As indicated in **Figure 14**, this entails the pressure in the bootstrap chamber to be dependent on the motion direction rather than the piston

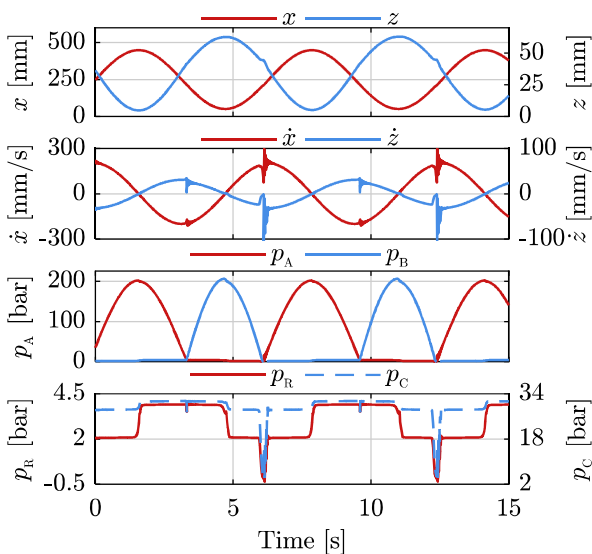


Figure 15: Simulation results for the proposed gasless system, operated in four quadrants.

position, in-turn causing p_R to be motion direction dependent.

Because the bootstrap reservoir does not need to contain any gas at the fully extended position, the volume of the reservoir can be made smaller than for the system in Sec. 3. The total active reservoir volume for the gasless system is 0.62 L compared to 0.97 L for the gas-loaded bootstrap reservoir (Sec. 3).

4.1. Simulation Results

Similarly to Sec. 3.2, the proposed system is investigated via a simulation study. The set of equations can be found in Appendix A. For the valves PC2 and PC3, it is assumed that the valve dynamics are dominated by the pressure dynamics in the pilot lines. Therefore the spool opening dynamics are simplified and modelled as first order systems ($\tau_V=10$ ms), with the input being the effective pressure difference experienced by the valve spool.

Figure 15 shows the simulation results for the gasless system for the four quadrant operation cycle. As with the system based on the gas-loaded bootstrap reservoir, severe velocity oscillations are observed as the direction of the external load force changes. When this happens, the gasless system is furthermore experiencing a more critical problem. When both chamber pressures are low (small external load), there is no charge source available to fill the bootstrap chamber at positive cylinder speeds. This causes p_C to decline, in turn lowering p_R below acceptable limits. If no friction forces were present p_R would approach atmospheric pressure. Due to friction p_R drops even further, in the given example to -0.5 bar (relative), which is non-tolerable. In the simulated example, the chamber pressures are low, while the cylinder speed is large, which make the problem more apparent, as the demand of charge flow is large under these conditions. At standstill, it is possible for the system to operate at low chamber pressures (no external load), without p_R dropping below atmospheric pressure, but p_R cannot be elevated without sufficient charge pressure. When the bootstrap reservoir extends, while the load force is low, the drop in reservoir pressure does not occur because no charge source is needed under these circumstances. The reservoir can be regarded self-charging in the retracting direction of the cylinder.

Figure 16 shows the simulated system in two

quadrant operation, where the external load ensures a sufficient charge flow to be provided when necessary. Under these restricted conditions, the system is observed to behave as desired. The reservoir pressure is controlled within the design limits from two bar to four bar.

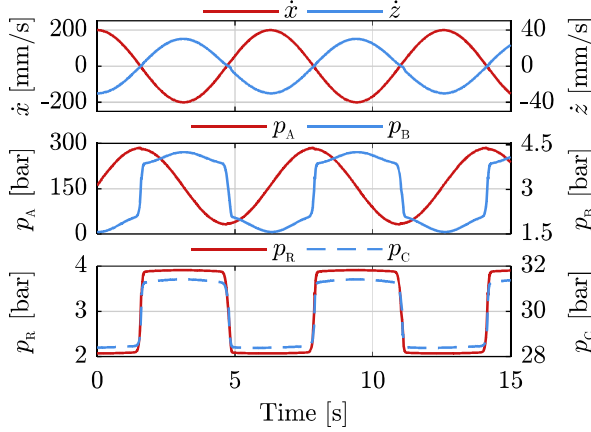


Figure 16: Simulation results for the proposed gasless system, operated in two quadrants.

Unlike the gas-loaded system, neither the pressure in the bootstrap nor reservoir chamber are position dependent, but depend on motion direction only.

The proposed gasless reservoir system should generally not be considered if there is a risk for lacking sufficient charge pressure. The proposed system may therefore be relevant for ECD architectures where it is possible to control the backpressure of the cylinder to a certain level, ensuring that a charge source is available at all times. Examples of such system architectures can be found in [16]–[20], for single variable-speed electric motor systems. Architectures with two electric machines can be found in [21], [22].

5. ARCHITECTURE FOR INCREASED DRIVE STIFFNESS

Bootstrap reservoirs may offer an opportunity to obtain the advantages that result from increased backpressure. In Sec. 2 the baseline layout for investigating this potential was selected as the double pump concept, given in **Figure 5 (c)**, and redrawn in **Figure 17 (a)**. Here the bootstrap chamber is connected to the lower line pressure via the inverse shuttle valve, allowing for elevating the backpressure, hence increasing ECD stiffness.

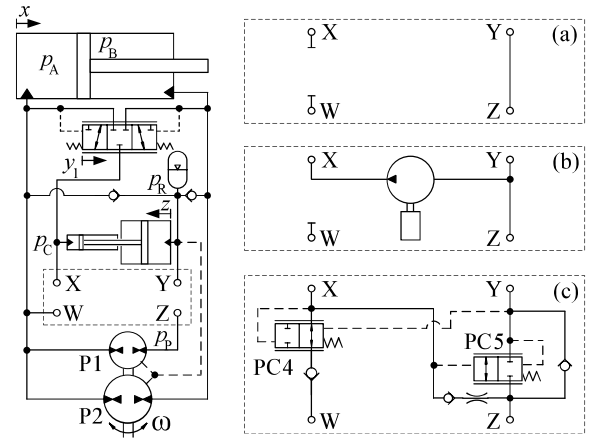


Figure 17: (a) System without leakage compensation (b) with charge-pump based leakage compensation and (c) with valve based leakage compensation.

For the conventional pump-compensated architecture in **Figure 1 (b)**, the pump displacement volumes D_{P1} and D_{P2} must match the area ratio of the cylinder ($\alpha = A_B/A_A$) in the following manner:

$$\frac{D_{P1}}{D_{P2}} = \frac{1 - \alpha}{\alpha} \quad (11)$$

The imbalance flow is compensated by the gas accumulator. When this is transferred to a system with an additional bootstrap reservoir as depicted in **Figure 17 (a)**, the gas accumulator has to be dimensioned in the same way, since it has to cover the whole volume imbalance. However, a certain mismatch of pump displacements can be applied to reduce the size of the gas accumulator. For both opening directions of the inverse shuttle valve, an optimal matching ratio of the pumps can be established (**Table 3**), such that the imbalance flow is completely covered by the reservoir chamber of the bootstrap reservoir:

Table 3: Conditions for minimal accumulator size

y_1	> 0	< 0
D_{P1}/D_{P2}	$\frac{1 - \alpha}{\alpha - \alpha_B}$	$\frac{1 - \alpha}{\alpha - \alpha \cdot \alpha_B}$

Since the state of the shuttle valve is governed by the direction of the load, a four-quadrant drive cannot be dimensioned to optimality with regard to accumulator size. As a compromise, the pump displacement ratio is chosen to be the mean value:

$$\frac{D_{P1}}{D_{P2}} = \left(\frac{1 - \alpha}{\alpha - \alpha_B} + \frac{1 - \alpha}{\alpha - \alpha \cdot \alpha_B} \right) / 2 \quad (12)$$

For low bootstrap area ratios, the deviation of Eq.

(12) compared to Eq. (11) is small, resulting in manageable changes in static speed gain when the external load changes direction.

Measures of leakage compensation in order to avoid bootstrap drifting (see Sec. 2) may include a small charge pump driven by an external motor (**Figure 17 (b)**) or pressure compensator valves (**Figure 17 (c)**). The former can be controlled using a simple on/off motor switch to keep accumulator pressure inside the working range. This will automatically ensure the bootstrap reservoir piston to be within its working range. The latter can be based purely on passive elements. Both pressure compensators PC4 and PC5 control the pressure difference $p_C - p_R$. Newton's second law for the bootstrap piston, formulated for relative pressures results in

$$p_C - p_R = (1 - \alpha_B) \cdot p_C - \frac{F_{Fz}}{A_R} + \frac{M_B \ddot{z}}{A_R} \quad (13)$$

thus p_C can be controlled via the difference $p_C - p_R$ when friction and acceleration forces are neglected.

Pressure compensator PC4 extracts a flow from cylinder chamber A to the bootstrap chamber when a positive load force is available and the pressure difference $p_C - p_R$ is below a critical pressure level. PC5 throttles the pump outflow during cylinder retraction to a pressure level just above p_C , such that a flow portion is deviated to the bootstrap chamber via an orifice, when the pressure difference is too low. Both pressure compensators have symmetric pilot areas. Note, that this valve arrangement does not allow leakage compensation under pulling loads while extending the main cylinder.

5.1. Simulation results

For a simulation study, a system with the presented valve based leakage compensation approach is parameterised according to the parameters given in the Nomenclature. The governing equations are presented in Appendix A. The simulation study performs the same load cycle as shown in Sec. 3.2, of which results are given in **Figure 18**.

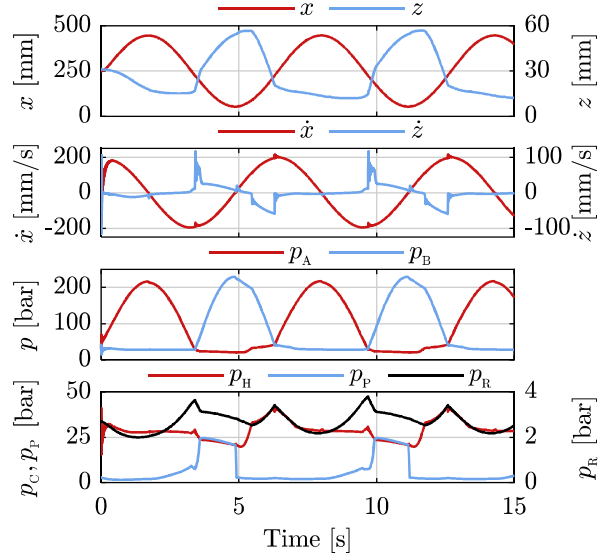


Figure 18: Simulation results of system architecture for improved drive stiffness.

The simulation results show that the leakage compensation structure is capable of keeping the bootstrap cylinder position within working range. Comparative studies without the compensation measures revealed that under the given load and pump leakage model, a bootstrap reservoir of the chosen size would hit the end stop within less than 5 seconds. The lowest cylinder pressure never drops below 20 bar while the reservoir/accumulator pressure remains within a range of two to four bar.

It is worth noting that the chosen gas accumulator volume is 1 L, compared to a minimum required volume of 2 L in the conventional system. The total volume of the bootstrap reservoir is 0.6 L, while the main cylinder takes a fluid volume of 1.6 L.

6. DISCUSSION

This paper presents a conceptional study, investigating how bootstrap reservoirs may be incorporated in the design of electro-hydraulic compact drives, to improve compactness and/or stiffness of the drive systems.

Focus has been placed on investigating the general applicability of the presented three concepts via a simulation study. Here, simplifying assumptions, such as first order valve dynamics and simple cylinder friction models have been applied. This means that the paper serves as an initial investigation of the possibilities arising when combining bootstrap reservoirs and ECD, rather

than a complete design guide. Therefore, it is emphasized that further analysis is needed prior to realization of the presented concepts. This includes an analysis of the dynamic requirements to the pressure compensators, as well as an investigation of the extent to which the required charge flow decreases the energy efficiency of the entire system.

7. CONCLUSION

Gas accumulators are conventionally used as volume compensators in electro-hydraulic compact drives (ECD's). To stay within a narrow reservoir pressure range, a considerable gas volume is required, compromising system compactness. This paper investigates how ECD compactness may be improved by incorporating a bootstrap reservoir in the design. Based on a systematic derivation of the solution space, three improvement potentials have been identified: Reservoir downsizing, avoidance of gas volume and increased drive stiffness by elevating cylinder backpressure. Three architectures, each representing one of the three improvement potentials, have been selected for a conceptual study.

It is found that the area ratio of the bootstrap reservoir piston as well as the magnitude of friction forces severely affects the downsizing potential. A linear analysis further shows that for some architectures, system dynamics is strongly influenced by incorporating the bootstrap reservoir. To reduce this influence a thorough analysis of the system dynamics is therefore encouraged. If avoidance of the gas volume is desired, a sufficient external load force is needed to define a reservoir pressure greater than the surroundings. In the case of elevated backpressure, additional circuitry needs to be implemented for compensation of pump leakage. The exact functioning of these structures may depend on the load cycle, especially when they are hydraulically piloted.

Simulation results confirm the functionality of the proposed system architectures, and shows that a potential for downsizing/avoiding the gas volume, as well as increasing the ECD stiffness is present.

ACKNOWLEDGMENTS

The research in this paper is partly funded by The Research Council of Norway, SFI Offshore Mechatronics, project number 237896/O30.

NOMENCLATURE

A_A	Piston area	31 cm ³
A_B	Rod side area	21 cm ³
A_C	Bootstrap piston area	7.9 cm ³
A_R	Reservoir piston area	79 cm ³
B_L	Load damping coefficient	2.5 Ns/mm
B_{Fx}	Damping coefficient	0.25 Ns/mm
B_{Fz}	Damping coefficient	0.50 Ns/mm
D	Pump displacement	14cm ³ /rev
D_{P1}	Pump displacement	5cm ³ /rev
D_{P2}	Pump displacement	9.03cm ³ /rev
D_A	Cylinder piston diameter	63mm
D_B	Cylinder rod diameter	36mm
D_C	Bootstrap piston diameter	32mm
D_R	Reservoir piston diameter	100mm
ECD	Electro-hydraulic compact drives	
F_{Cx}	Friction coefficient	500 N
F_{Cz}	Friction coefficient	590 N
F_{Fx}	Cylinder friction	[N]
F_{Fz}	Bootstrap reservoir friction	[N]
K_L	Load spring coefficient	261 N/mm
K	Leakage parameter	196 N/mm
K_1	Leakage parameter	3.2 $\frac{\text{mL}}{\text{min bar}}$
K_2	Leakage parameter	1.19 $\frac{\text{mL}}{\text{min bar}}$
K_{Q1}	Valve flow gain	2.15 $\frac{\text{mL}}{\text{min bar}}$
K_{Q2}	Valve flow gain	21 $\frac{\text{L}}{\text{min } \sqrt{\text{bar}}}$
K_{Q4}	Valve flow gain	2.2 $\frac{\text{L}}{\text{min } \sqrt{\text{bar}}}$
K_{Q5}	Valve flow gain	2.7 $\frac{\text{L}}{\text{min } \sqrt{\text{bar}}}$
L_s	Cylinder stroke length	7 $\frac{\text{L}}{\text{min } \sqrt{\text{bar}}}$
L_{sz}	Bootstrap stroke length	0.5 m
m	Bulk modulus pressure gradient	65 mm
M_L	Mass of load and cylinder piston	71 mm
M_B	Moveable mass, bootstrap reservoir	11.4
p_{O}	Pressure	200 kg
p_{atm}	Atmospheric pressure	10 kg
p_{G0}	Pre-charge pressure	[Pa]
p_{G1}	Minimum working gas pressure	[Pa]
p_{G2}	Maximum working gas pressure	[Pa]
p_{aGB1}	Bootstrap min gas pressure, abs	28.4 bar
p_{aGB2}	Bootstrap max gas pressure, abs	33.4 bar
p_{aR1}	Min reservoir pressure, absolute	3 bar
p_{aR2}	Max reservoir pressure, absolute	5 bar
p_{CR1}	Cracking pressure difference	0 bar
p_{OP1}	Full open pressure difference	0.25 bar
p_{CR2}	Cracking pressure difference	25.4 bar
p_{OP2}	Full open pressure difference	26.4 bar
p_{CR3}	Cracking pressure difference	27.4 bar
p_{OP3}	Full open pressure difference	28.4 bar
p_{CR4}	Cracking pressure difference	24.3 bar

p_{OP4}	Full open pressure difference	28.8 bar
p_{CR5}	Cracking pressure difference	18.0 bar
p_{OP5}	Full open pressure difference	25.2 bar
p_F	Friction force, equivalent pressure	[Pa]
p_{Fm}	Maximum p_F	0.75 bar
$Q_{\{}$	Flow	[m ³ /s]
R_{Boot}	Volume ratio, $V_{Boot}/\Delta V$	[-]
R_{Acc}	Volume ratio, $V_{G1}/\Delta V$	[-]
R	Volume ratio, V_{Boot}/V_{G1}	[-]
V_P	Constant pilot line volume	0.5 L
V_{0A}	Initial chamber volume	0.2 L
V_{0B}	Initial chamber volume	0.2 L
V_{0R}	Initial reservoir volume	0.2 L
V_{0C}	Initial charge chamber volume	0.1 L
V_{Boot}	Total bootstrap reservoir volume	[m ³]
V_{ACC}	Accumulator volume	1 L
V_{G0}	Pre-charge gas volume	[m ³]
V_{G1}	Initial gas volume	[m ³]
V_{G2}	Minimum gas volume	[m ³]
V_{GB1}	Initial gas volume, bootstrap chamber	0.47 L
x_{S0}	Load spring pretension	21mm/0mm
x	Cylinder piston position	[m]
y_j	Normalised valve opening	[-]
\bar{y}_j	Reference valve opening	[-]
z	Bootstrap piston position	[m]
α	Cylinder area ratio (A_B/A_A)	0.67 [-]
α_B	Bootstrap area ratio (A_C/A_R)	0.1 [-]
β_F	Bulk Modulus of pure fluid	11000 bar
ΔV	Compensation or active volume	0.51 L
ϵ	Volumetric air ratio	1 %
κ	Polytropic coefficient	1.4
τ_v	Time constant	10 ms
γ	Friction switching parameter	500
ω	Motor speed	[rad/s]
$\bar{\omega}$	Reference motor speed	[rad/s]
ω_n	Eigenfrequency of motor drive	50 Hz
ζ	Damping coefficient	0.707

REFERENCES

- [1] S. Ketelsen, D. Padovani, T. Andersen, M. Ebbesen, and L. Schmidt, "Classification and Review of Pump-Controlled Differential Cylinder Drives," *Energies*, vol. 12, no. 7, p. 1293, 2019, 10.3390/en12071293.
- [2] G. K. Costa, "A Critical Analysis of Valve-Compensated Hydrostatic Actuators: Qualitative Investigation," *Actuators*, vol. 8, no. 59, 2019, 10.3390/act8030059.
- [3] S. Michel and J. Weber, "Electrohydraulic Compact-drives for Low Power Applications considering Energy-efficiency and High Inertial Loads," *7th FPNI PhD Symposium on Fluid Power*, 2012, pp. 1–18.
- [4] A. Imam, M. Rafiq, E. Jalayeri, and N. Sepehri, "A Pump-Controlled Circuit for Single-Rod Cylinders that Incorporates Limited Throttling Compensating Valves," *Actuators*, vol. 7, no. 2, p. 13, 2018, 10.3390/act7020013.
- [5] D. Padovani, S. Ketelsen, D. Hagen, and L. Schmidt, "A Self-Contained Electro-Hydraulic Cylinder with Passive Load-Holding Capability," *Energies*, vol. 12, no. 2, p. 292, Jan. 2019, 10.3390/en12020292.
- [6] S. Michel and J. Weber, "Energy-efficient electrohydraulic compact drives for low power applications," *ASME/BATH 2012 Symposium on Fluid Power and Motion Control*, 2012, pp. 93–107.
- [7] K. G. Cleasby, A. R. Plummer, and T. Company, "A novel high efficiency electrohydrostatic flight simulator motion system," *ASME/BATH 2008 Symposium on Fluid Power and Motion Control*, pp. 437–449, 2008.
- [8] H. C. Pedersen, L. Schmidt, T. O. Andersen, and M. H. Brask, "Investigation of New Servo Drive Concept Utilizing Two Fixed Displacement Units," *JFPS Int. J. Fluid Power Syst.*, vol. 8, no. 1, pp. 1–9, 2014, 10.5739/jfpsij.8.1.
- [9] T. Minav, S. Panu, and P. Matti, "Direct-Driven Hydraulic Drive Without Conventional Oil Tank," *ASME/BATH 2014 Symposium on Fluid Power and Motion Control*, 2014, pp. 1–6.
- [10] B. Brahmer, "CLDP - Hybrid Drive using Servo Pump in Closed Loop," *8th International Fluid Power Conference*, 2012, pp. 93–102.
- [11] Parker Hannifin, "Bootstrap Hydraulic Reservoirs." Product Catalogue. Webpage.
- [12] J. Aaltonen, "Interaction of Bootstrap Reservoir and Hydraulic Pump in Aircraft Hydraulic Systems," Tampere University of Technology, PhD. thesis, 2016.
- [13] L. Schmidt, H. C. Pedersen, V. H. Donkov, and T. O. Andersen, "Analysis & Control of a Self-contained Hydraulic Winch Drive," *ASME/BATH 2018 Symposium on Fluid Power and Motion Control*, 2018.
- [14] H. Çalışkan, T. Balkan, and B. E. Platin, "A Complete Analysis for Pump Controlled Single Rod Actuators," *10th Int. Fluid Power Conf.*, pp. 119–132, 2016, 10.13140/RG.2.2.13163.75046.
- [15] L. Wang, W. J. Book, and J. D. Huggins, "A Hydraulic Circuit for Single Rod Cylinders," *J. Dyn. Syst. Meas. Control*, vol. 134, no. 1, p. 011019, 2012, 10.1115/1.4004777.
- [16] L. Schmidt, M. Groenkjaer, H. C. Pedersen, and

- T. O. Andersen, "Position Control of an Over-Actuated Direct Hydraulic Cylinder Drive," *Control Eng. Pract.*, vol. 64, pp. 1–14, Jul. 2017, 10.1016/J.CONENGPRAC.2017.04.003.
- [17] L. Schmidt, D. B. Roemer, H. C. Pedersen, and T. O. Andersen, "Speed-Variable Switched Differential Pump System for Direct Operation of Hydraulic Cylinders," *ASME/BATH 2015 Symposium on Fluid Power and Motion Control*, 2015.
- [18] L. Schmidt, S. Ketelsen, M. H. Brask, and K. A. Mortensen, "A Class of Energy Efficient Self-Contained Electro-Hydraulic Drives with Self-Locking Capability," *Energies*, vol. 12, no. 10, p. 1866, 2019, 10.3390/en12101866.
- [19] L. Schmidt, S. Ketelsen, D. Padovani, and K. A. Mortensen, "Improving the Efficiency and Dynamic Properties of a Flow Control Unit in a Self-Locking Compact Electro-Hydraulic Cylinder Drive," *ASME/BATH 2019 Symposium on Fluid Power and Motion Control*, 2019.
- [20] S. Ketelsen, L. Schmidt, V. H. Donkov, and T. O. Andersen, "Energy saving potential in knuckle boom cranes using a novel pump controlled cylinder drive," *Model. Identif. Control*, vol. 39, no. 2, 2018, 10.4173/mic.2018.2.3.
- [21] P. H. Gøyttil, D. Padovani, and M. R. Hansen, "On the Energy Efficiency of Dual Prime Mover Pump-Controlled Hydraulic Cylinders," *ASME/BATH 2019 Symposium on Fluid Power and Motion Control*, 2019.
- [22] S. Ketelsen, T. O. Andersen, M. K. Ebbesen, and L. Schmidt, "Mass Estimation of Self-Contained Linear Electro-Hydraulic Actuators and Evaluation of the Influence on Payload Capacity of a Knuckle Boom Crane," *ASME/BATH 2019 Symposium on Fluid Power and Motion Control*, 2019.

APPENDIX A – SIMULATION MODELS

Simulations models are presented in the following, while parameters can be found in the Nomenclature.

System architecture from Sec. 3

Considering **Figure 19 (a)**, the system incorporating a gas-loaded bootstrap reservoir is modelled using Eq. (14) to (31).

The pressure gradients of p_A , p_B , p_R , and p_{GB} are given as:

$$\dot{p}_A = \frac{\beta_A}{V_A} (Q_A - Q_{CA} - A_A \dot{x}) \quad (14)$$

$$\dot{p}_B = \frac{\beta_B}{V_B} (A_B \dot{x} - Q_B - Q_{CB}) \quad (15)$$

$$\dot{p}_R = \frac{\beta_R}{V_R} (Q_L + Q_{CA} + Q_{CB} - A_R \dot{z}) \quad (16)$$

$$\dot{p}_{GB} = \dot{p}_C = \frac{p_{aGB} \kappa}{V_G} A_C \dot{z} \quad (17)$$

The variable volumes V_A , V_B , V_R and V_G are described as:

$$V_A = V_{0A} + x A_A \quad , \quad V_B = V_{0B} + (L_s - x) A_B \quad (18)$$

$$V_R = V_{0R} + z A_R \quad , \quad V_{GB} = V_{GB1} \left(\frac{p_{aGB1}}{p_{aGB}} \right)^{\frac{1}{\kappa}} \quad (19)$$

p_{aGB1} is the initial gas pressure at volume V_{GB1} , with κ being the polytropic process constant.

The nonlinear motion dynamics is described by:

$$\ddot{x} = M_L^{-1} (p_A A_A - p_B A_B - K_L (x - x_{s0}) - B_L \dot{x} - F_{Fx}) \quad (20)$$

$$\ddot{z} = M_B^{-1} (p_R A_R - p_C A_C - F_{Fz}) \quad (21)$$

x and z are the cylinder and bootstrap piston positions, with M_L , M_B , and F_{Fx} , F_{Fz} being mass and friction forces. x_{s0} , K_L and B_L are spring pre-tension, spring and damping coefficients of the modelled load.

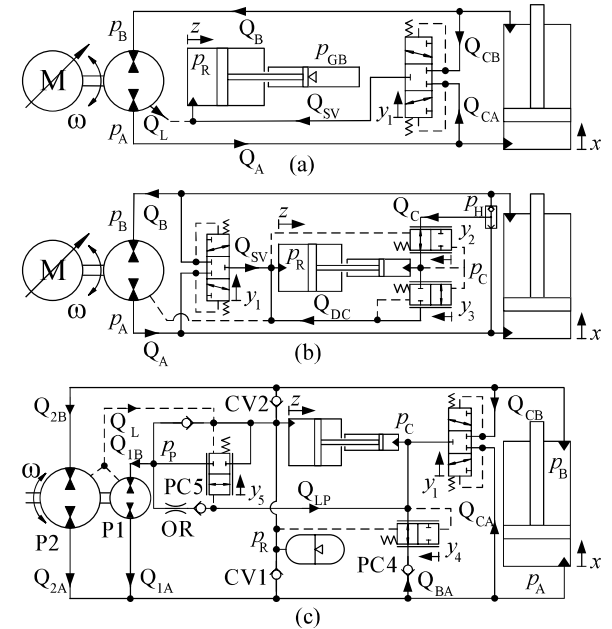


Figure 19: Circuit architectures of the three systems investigated in this paper, including quantity designations.

The friction forces F_{Fx} and F_{Fz} is found as:

$$F_{Fx} = \tanh(\gamma \dot{x}) F_{Cx} + B_{Fx} \dot{x}, F_{Fz} = \tanh(\gamma \dot{z}) F_{Cz} + B_{Fz} \dot{z} \quad (22)$$

$F_{CX}, F_{CZ}, B_{FX}, B_{FZ}$ are Coulomb and viscous friction coefficients. Q_{CA}, Q_{CB} are modelled by the orifice equation as:

$$Q_{CA} = \begin{cases} 0 & , y \geq 0 \\ K_{Q1} |y_1| \sqrt{|p_A - p_R|} \text{sign}(p_A - p_R) & , y < 0 \end{cases} \quad (23)$$

$$Q_{CB} = \begin{cases} K_{Q1} |y_1| \sqrt{|p_B - p_R|} \text{sign}(p_B - p_R) & , y > 0 \\ 0 & , y \leq 0 \end{cases} \quad (24)$$

with y_1 normalised valve opening and K_{Q1} flow gain. The valve opening y_1 , are modelled as a first order dynamic system with time constant τ_V and input \bar{y}_j , which is calculated based on valve cracking (p_{CR1}) and full open (p_{OP1}) pressure:

$$\bar{y}_1 = \begin{cases} 0 & |p_{D1}| \leq p_{CR1} \\ \text{sign}(p_{D1}) \frac{|p_{D1}| - p_{CR1}}{p_{OP1} - p_{CR1}} & p_{CR1} < |p_{D1}| < p_{OP1} \\ \text{sign}(p_{D1}) & |p_{D1}| \geq p_{OP1} \end{cases} \quad (25)$$

$$p_{D1} = p_A - p_B$$

$$\dot{y}_j = \frac{\bar{y}_j - y_j}{\tau_V} \quad (26)$$

Q_A, Q_B, Q_L are pump flows modelled by the Wilson model, using pump displacement D and laminar leakage coefficient K :

$$Q_A = \omega D - K(p_A - p_B) - K(p_A - p_R) \quad (27)$$

$$Q_B = \omega D - K(p_A - p_B) + K(p_B - p_R) \quad (28)$$

$$Q_L = K(p_A - p_R) + K(p_B - p_R) \quad (29)$$

ω is the motor shaft speed modelled as a second order dynamic system

$$\ddot{\omega} = (\bar{\omega} - \omega)\omega_n^2 - 2\zeta\omega_n\dot{\omega} \quad (30)$$

with eigenfrequency ω_n and damping ratio ζ , with $\bar{\omega}$ being the system input.

Finally β_i is the effective bulk modulus of the fluid air mixture with β_F the bulk modulus of the pure fluid, ϵ the volumetric air content at atmospheric pressure and m the pressure dependent bulk modulus parameter:

$$\beta_i = \frac{(1 - \epsilon) \left(1 + \frac{m(p_i - p_{atm})}{\beta_F} \right)^{\frac{1}{m}} + \epsilon \left(\frac{p_{atm}}{p_i} \right)^{\frac{1}{\kappa}}}{\frac{(1 - \epsilon) \left(1 + \frac{m(p_i - p_{atm})}{\beta_F} \right)^{\frac{m+1}{m}}}{\beta_F} + \frac{\epsilon}{\kappa p_{atm}} \left(\frac{p_{atm}}{p_i} \right)^{\frac{\kappa+1}{\kappa}}} \quad (31)$$

$$i = \{A, B, R, C\}$$

System architecture from Sec. 4

Considering **Figure 19 (b)** the gasless systems is modelled. The pressure dynamics, are given as:

$$\dot{p}_A = \frac{\beta_A}{V_A} (Q_A - Q_{CA} - A_A \dot{x} - Q_{CHA}) \quad (32)$$

$$\dot{p}_B = \frac{\beta_B}{V_B} (A_B \dot{x} - Q_B - Q_{CB} - Q_{CHB}) \quad (33)$$

$$\dot{p}_C = \frac{\beta_C}{V_C} (Q_C - Q_{DC} + A_C \dot{z}), \quad p_H = \max(p_A, p_B) \quad (34)$$

$$\dot{p}_R = \frac{\beta_R}{V_R} (Q_L + Q_{CA} + Q_{CB} + Q_{DC} - A_R \dot{z}) \quad (35)$$

The variable volumes of V_A, V_B and V_R are found by Eq. (18), (19). V_C are found as:

$$V_C = V_{OC} + (L_{sz} - z)A_C \quad (36)$$

The motion dynamics, friction forces, shuttle valve opening and flows are modelled as the previous system using Eq. (20) to (25). The opening of the pressure compensator valve are modelled as a first order dynamic system given in Eq. (26), with the input \bar{y}_j , and valve flows described by:

$$\bar{y}_j = \begin{cases} 0 & (p_C - p_R) \leq p_{CRj} \\ \frac{(p_C - p_R) - p_{CRj}}{p_{OPj} - p_{CRj}} & p_{CRj} < (p_C - p_R) < p_{OPj} \\ 1 & (p_C - p_R) \geq p_{OPj} \end{cases} \quad (37)$$

$$Q_C = \begin{cases} K_{Q2}(1 - y_2)\sqrt{|p_H - p_C|} & p_H \geq p_C \\ 0 & p_H < p_C \end{cases} \quad (38)$$

$$Q_{DC} = K_{Q2} y_3 \sqrt{|p_C - p_R|} \text{sign}(p_C - p_R)$$

$$Q_{CHA} = \begin{cases} Q_C, & Q_{CHB} = \begin{cases} 0, & p_A > p_B \\ Q_C, & p_A \leq p_B \end{cases} \end{cases} \quad (39)$$

Finally, the pump flows, shaft dynamics and bulk modulus are described by Eq. (26) to (31).

System architecture from Sec. 5

The modelling of the ECD depicted in **Figure 19 (c)** is carried out in line with the previously described models. Pressure gradients are given by:

$$\dot{p}_A = \frac{\beta_A}{V_A} (Q_{1A} + Q_{2A} - Q_{CA} - Q_{BA} - A_A \dot{x}) \quad (40)$$

$$\dot{p}_B = \frac{\beta_B}{V_B} (A_B \dot{x} - Q_{2B} - Q_{CB}) \quad (41)$$

$$\dot{p}_P = \frac{\beta_P}{V_P} (Q_S - Q_R - Q_{LP} - Q_{1B}) \quad (42)$$

$$\dot{p}_C = \frac{\beta_C}{V_C} (A_C \dot{z} + Q_{CA} + Q_{CB} + Q_{LP} + Q_{BA}) \quad (43)$$

$$\dot{p}_R = \frac{p_{aR} \kappa}{V_{ACC} \left(\frac{p_{aR1}}{p_{aR}} \right)^{\frac{1}{\kappa}}} (Q_R + Q_L - Q_S - A_R \dot{z}) \quad (44)$$

Pump flows $Q_{1A}, Q_{1B}, Q_{2A}, Q_{2B}$ are calculated in

analogy to Eq. (27) to (29), with leakage parameters K_1 and K_2 . Flows through the pressure compensators (Q_{BA}, Q_R) are calculated in analogy with Eq. (38), using flow gains K_{Q4} and K_{Q5} and spool opening dynamics using Eq. (26) and (37). Motion dynamics, inverse shuttle valve behaviour and bulk modulus are modelled as in previous sections, while orifice flow is modelled by:

$$Q_{LP} = \begin{cases} K_{Q2} \sqrt{p_P - p_C}, & p_P > p_C \\ 0, & p_P \leq p_C \end{cases} \quad (45)$$

APPENDIX B – LINEAR MODEL

For the system shown in **Figure 7** on page 5 a linearized model is derived considering Eq. (14) to (16) and Eq. (20), (21), by assuming the inverse shuttle valve ideal, thus combining the reservoir chamber and the B-chamber in a single continuity equation. By neglecting shaft dynamics and pump leakage, $Q_A = Q_B = Q$ is the system input. Assuming bulk modulus, chamber volumes, external load, gas pressure (p_G) and Coulomb friction constant at the linearization point, linear equations can be formulated as:

$$\dot{P}_A = \frac{\beta_{A0}}{V_{A0}} (Q - A_A \dot{X}) \quad (46)$$

$$\dot{P}_B = \frac{\beta_{B0}}{V_{B0}} (A_B \dot{X} - A_R \dot{Z} - Q) \quad (47)$$

$$\ddot{X} = M_L^{-1} (P_A A_A - P_B A_B - B_{FX} \dot{X}) \quad (48)$$

$$\ddot{Z} = M_B^{-1} (P_B A_R - B_{FZ} \dot{Z}) \quad (49)$$

Change variables are given as capital letters and variables evaluated at the linearization point with an indexed “0”. From the linearized equations the transfer function from $Q(s)$ to the selected output may be established.

EFFICIENCY THAT BORDERS ON THE IMPOSSIBLE ELECTROHYDRAULIC DRIVES

Dipl.-Ing.(FH) Walter List

Head of Product Development, WEBER-HYDRAULIK GMBH, Emil-Weber-Platz 1, A-4460 Losenstein, Österreich
Tel.: +43 7255 6237 12125; E-mail address: walter.list@weber-hydraulik.com

ABSTRACT

Hydraulic displacement systems are a technology that has been known for many years. Nevertheless, the impression is created that the large fields of application are not only being developed very tentatively, but in many cases are being completely denied. What might be the reason for this? Are the electromechanical solutions better? What is the missing element to build the bridge from the available hydraulic-mechatronic technology to broad customer application?

This paper provides an overview of how the targeted use of the latest technologies in the product and in the entire value-added chain has resulted in a complete mechatronic hydraulic system that pushes the limits of feasibility in terms of power, accuracy and efficiency and delivers a clearly calculable benefit for both the plant manufacturer and the end customer. In addition to the great accuracy and high reliability, there are also considerable savings in the total cost of ownership (TCO) due to a previously unattained level of efficiency.

The thoughts of health and environmental protection are just as much a part of the considerations as product safety and personal protection.

Finally, an outlook on possible expansions is given, and which areas of application are possible for the technologies developed within the project. The aim is not to show how the traditional fields of application of hydraulics are to be defended, but rather to use the strengths of a hydraulic-mechatronic approach in a conscious and clearly structured way to make new applications possible.

Keywords: linear actuator, servohydraulic, elektrohydraulic drive

1. INTRODUCTION

"Over 80 years of experience in hydraulics make WEBER-HYDRAULIK a competent specialist for hydraulic drive and control technology. This is our obligation".

The WEBER-HYDRAULIK Group now comprises seven locations. Together they stand for tailor-made and functionally reliable hydraulic solutions. The aim of bundling expertise is to be able to offer successful solutions in the demanding and challenging market of mobile and stationary hydraulics.

"Our investments in research, development and modern production technologies as well as the continuous qualification of our employees ensure that we have the short path to progress".

The development of high-quality cylinders, control blocks, valves and power units has a long tradition in the group of companies and is therefore our technological core competence.

Building on this, the Group also offers its customers the realisation of sophisticated application-specific system solutions as a leading international, innovative and future-oriented partner.

2. EHA-ELEKTROHYDRAULIC ACTUATOR

2.1. Initial situation

Hydraulic linear units are a technology known for many years and have significant advantages compared to electromotive drives and electric linear drives. Where large forces, precise movements and high efficiency are required, the electro-hydraulic linear actuator represents a technology with almost no alternatives. Nevertheless, sometimes the impression is given that the very large applications are only very tentatively being developed.

WEBER-HYDRAULIK has been developing customer-specific electro-hydraulic and servo-hydraulic linear axes for several years and supplies them to well-known companies in the automotive, mechanical engineering and plant construction industries.



Figure 2: compact linear actuator for mobile use (WEBER HYDRAULIK)

The specifications range from electro-hydraulic compact units for the automotive industry, through resolved systems for industrial applications, to compact linear drives in highly dynamic machine axes. The fields of application are just as broad as the customer segments.

The present work will be limited to industrial applications. These axes are manufactured in the Austrian plant of WEBER-HYDRAULIK, in Losenstein, Upper Austria. The electro-hydraulic axes for mobile applications are developed and manufactured at the sites in Güglingen (Heilbronn, Germany) and Veenendaal (Utrecht, Netherlands).

2.2. Theoretical aspects, classification

Electrohydraulics vs. electromechanics - a comparison of unequal technologies.

Electromechanics and electrohydraulics are not mutually exclusive systems.

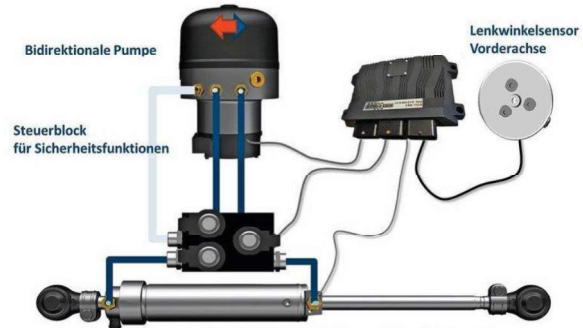


Figure 1: linear actuator (WEBER HYDRAULIK)

Many applications use these technologies in a complementary manner, whereby electrohydraulic drives fully exploit their advantages when large forces are applied. The main decision criterion for the use of an electrohydraulic actuator is therefore usually the high forces required with good efficiency. Pneumatic cylinders and electromechanical axes are advantageous for very small loads during operation. In terms of energy technology, however, pneumatics also have major deficits

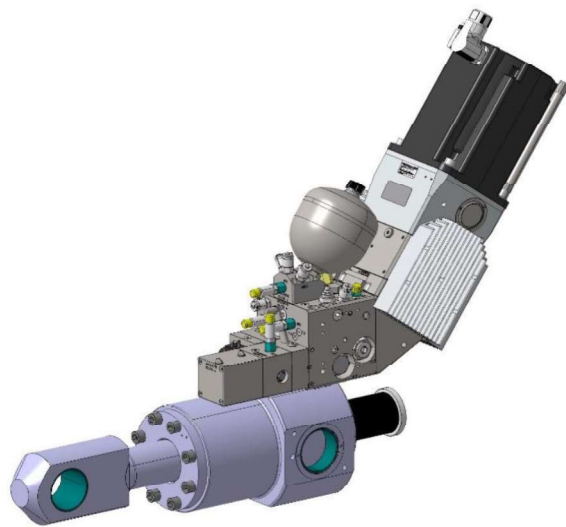


Figure 3: compact linear actuator for industrial purposes (WEBER HYDRAULIK)

here. Only about 1/3 of the primary energy used is converted into power by pneumatics. For electromechanical drives, a primary energy utilization of about 80% can be assumed. Depending on the drive solution (ball screw,

roller screw, ...) and the forces generated, the values vary greatly and can also be significantly lower.

The figure shows a summary of the system boundaries of the individual alternatives. Electric axes are a viable solution with good efficiency

components makes the whole much more than the sum of the individual components.

In order to produce an application-specific optimized EHA, it is important that all components are optimally matched to each other. Even if the performance data of a pump, a

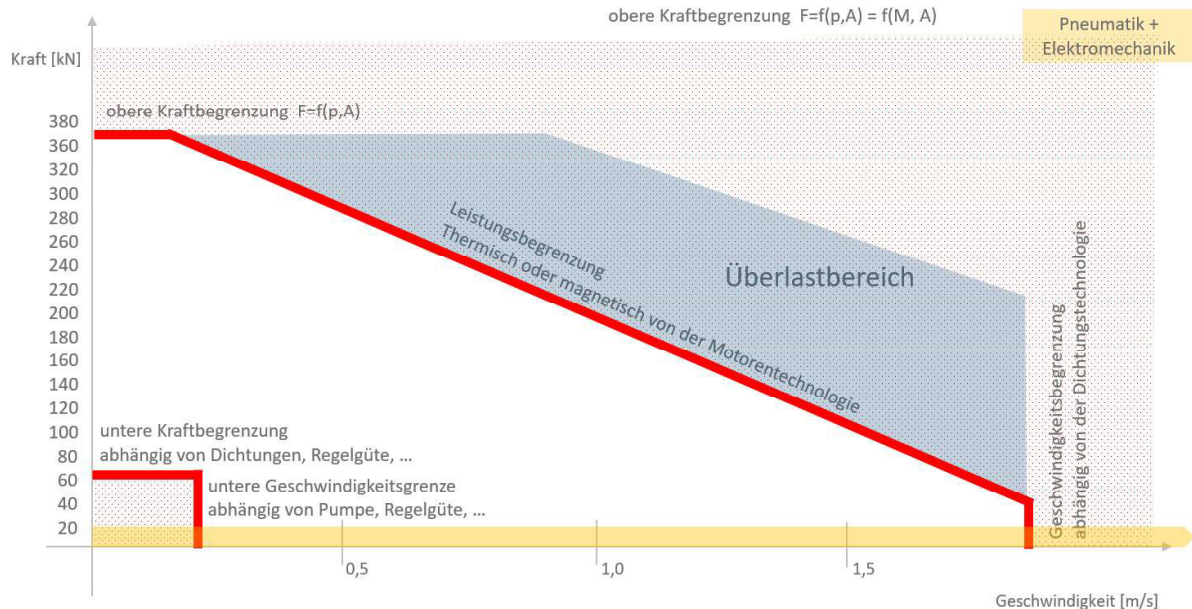


Figure 4: application area hydraulic linear actuator

values at low forces. Likewise, very high speeds and strokes can be achieved with electric axes at very low forces (e.g. toothed belt axes). At higher forces, electromechanical axes quickly reach system-related limits, and the speeds and dynamics are then relatively low due to the performance.

When high forces, high dynamics, high precision and high efficiency are combined in the specifications, the advantages of the electrohydraulic axis come into their own. The relatively low rotational masses allow very high dynamics. The robustness of the hydraulics allows high overloads in the short term. When using high-quality measuring systems, the EHA also achieves an exceptionally high, hardly expected precision that is not inferior to electromechanical axes.

3. EFFICIENCY CONSIDERATIONS EHA'S

Hydraulic linear actuators are not classic hydraulic components such as pumps, cylinders and valves, which are procured from a catalogue program. Rather, they are mechatronic systems in which the precise coordination of the individual

cylinder and a drive motor can be derived with simple mathematics, the real overall performance of the EHA is difficult to determine and calculate analytically. This calculation becomes almost impossible when working with highly fluctuating, different load and operating profiles. Currently, only insufficient numerical methods are available which are suitable, for example, for predicting the overall efficiency of the EHA's in a specific application. Here WEBER HYDRAULIK takes a pragmatic approach and typically tests EHA's together with the end customer in the final application by means of a practical test. Strictly speaking, there is no better way to prove functionality and efficiency than in the customer application. This involves measuring the total energy consumption in the application under many other parameters.

The main design issues and problems that arise in this context will be briefly discussed below.

3.1. Motors

Modern motors, especially servo motors, have quite high efficiencies. Due to the possibility of short-term multiple overloads, it is possible to

operate the motors in a range that is significantly higher than the rated power, but at which quite useful operating values are obtained for the EHA

designer of valves is also in a commercial and technical field of tension. Large valves have large actuating forces and are expensive. Small valves

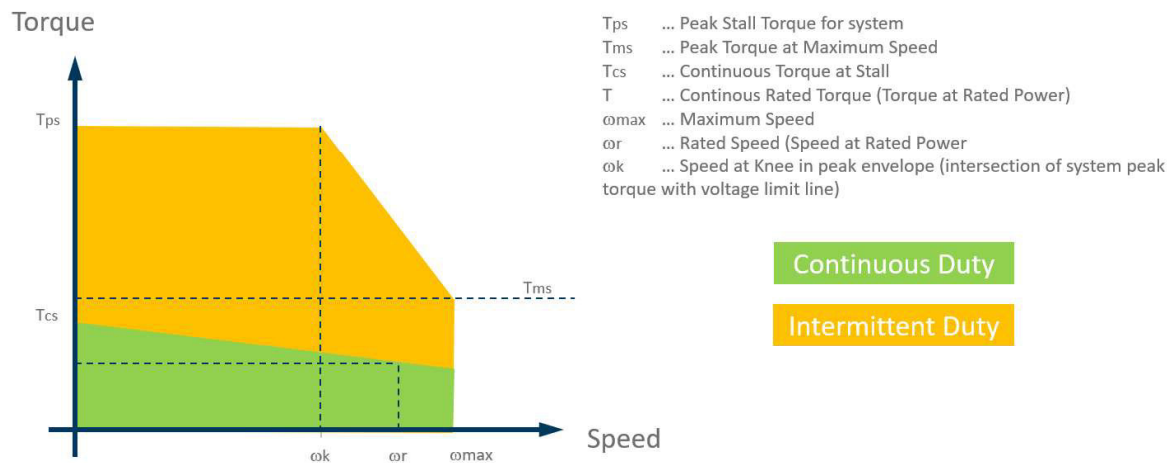


Figure 5: application map servo motor

system.

For the design of the motors themselves it is often not the last percentage point of nominal efficiency that is important. For particularly dynamic applications, it is often a question of the mass moment of inertia and the acceleration capability of the system. In spite of all these theoretical considerations, it is hardly possible to calculate the motor efficiency reasonably using a dynamic application. The same considerations regarding the load profile apply here as for the overall axis.

Overall, the designer's influence on the exact motor characteristics is very small in reality, since modern motors are usually purchased as catalogue goods. For simple applications where dynamics and efficiency are not the main focus, we also select more cost-effective motor concepts, such as speed-controlled DC motors with a control system adapted to the vehicle electrical system. The variety of variants here is almost unmanageable.

3.2. valves

The influence of valves on the overall efficiency of hydraulic equipment is undisputed. A reduction in flow losses inevitably leads to a higher efficiency of the overall system. In principle, this thesis is clearly understandable and does not need further explanation. However, the

have small actuating forces and are cheaper.

For reasons of system safety, load holding valves are also necessary in many cases. This is mainly used to enable the machine manufacturer to maintain the appropriate safety level (SIL) in order to achieve CE conformity with the machines and devices. In connection with functional safety, there are many issues that are not discussed here in detail.

If these valves, which are usually generously dimensioned in the flow, also have to switch quickly - the switching time is usually less than 50 milliseconds and directly affects the dynamics of the application - large, fast switching solenoids are required. Since there is typically little oil in the closed system EHA, the pilot control of valves can become a challenging design task. This is where it is of great advantage within the WEBER-HYDRAULIK Group to have access to



Figure 6: cartridge valve (WEBER HYDRAULIK)

the appropriate valve know-how in order to solve such tasks accurately.

3.3. cylinders

Cylinders have been part of our core business for many decades. At the Austrian location of the WEBER-HYDRAULIK Group alone, more than 160,000 cylinders are manufactured annually. Hydraulic cylinders are technologically already highly exhausted and their efficiency is difficult to improve. The tribological systems seal-cylinder wall and seal-rod surface are the main factors influencing the overall efficiency of a hydraulic cylinder. There is a large number of scientific papers on this subject (it is beyond the scope of this paper to present the overall context here). When using commercially available sealing systems, there is little room for maneuver at this point anyway due to the specifications of the seal manufacturers.

Our decades of experience have shown that the efficiency of hydraulic cylinders with a piston diameter of approx. 100 mm reaches a value of more than 98%.

An exception to this is servo cylinders with hydrostatic rod guidance and without contacting seals. However, these are used almost exclusively in extremely dynamic special applications, such as vibration testing. Here, even greater mechanical efficiencies are achieved, but there are also high leakage oil losses through the gap seals.

3.4. pumps

The best energy saved is the energy that was not generated.

The pump, as a hydraulic energy generator, is therefore one of the most critical components in terms of the overall efficiency of the EHA.

The pump efficiency is composed as follows:

$$\eta_{ges} = \eta_{vol} \cdot \eta_{hm}$$

$$\eta_{vol} = \frac{Q}{n \cdot V_{th}}$$

$$\eta_{hm} = \frac{\eta_{ges}}{\eta_{vol}} = \frac{\Delta p \cdot Q}{M \cdot 2 \cdot \pi \cdot n} \cdot \frac{n \cdot V_{th}}{Q} = \frac{\Delta p \cdot V_{th}}{2 \cdot \pi \cdot M}$$

$$P_{mech} = M \cdot 2 \cdot \pi \cdot n$$

$$P_{hydr} = \Delta p \cdot Q$$

By simply looking at the formulas, it can be seen that the pump efficiency is dependent on the pressure difference, the torque and the speed. In the literature, therefore, the representation of pump efficiency as a function of pressure difference and torque is also a common way of representation.

The picture is taken from a test series in our company and shows the typical course of the efficiency of a high-quality hydraulic pump at a certain speed. It is also easy to see that an optimum is achieved at a certain pressure. In every servo-motor hydraulic pump drive, this simple representation is overlaid by the speed. In order to be able to fully evaluate a pump, the efficiency curve must be determined for each relevant speed range.

The pump manufacturers themselves are very reluctant to provide such precise information on

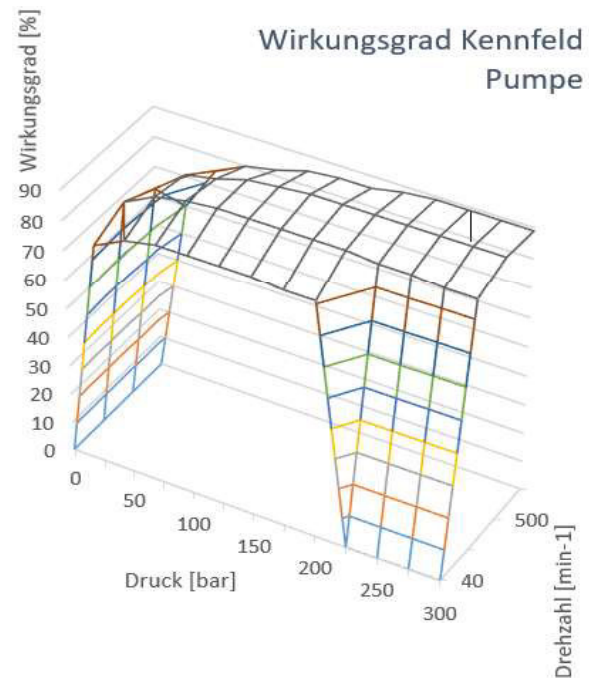


Figure 7: pump efficiency (WEBER-HYDRAULIK)

their products.

We have therefore carried out these tests on pumps from different manufacturers together with a partner close to the university and have drawn up corresponding characteristic diagrams. From the complexity of the interrelationships it can be concluded that a precise prediction of the

overall efficiency, as already described, is almost

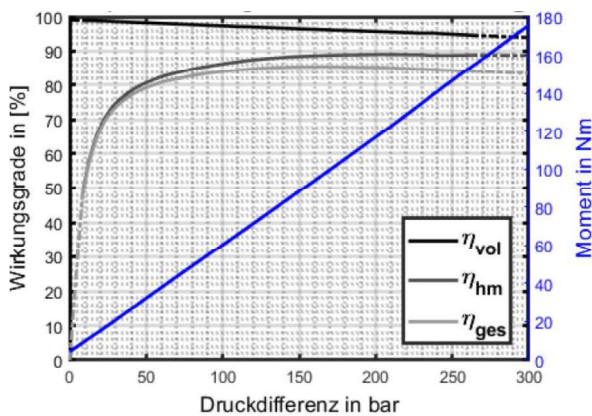


Figure 7 efficiency curve

impossible.

3.5. electronics, sensors and software

A very important topic in the interaction of mechatronic systems are sensors and data acquisition devices. In most cases 2 different goals are pursued. On the one hand, it requires sensors that are fast and adapted to the application in terms of their accuracy to record the operating parameters required for the control. On the other hand, more and more data is collected which is not directly used for control but seems to be important for topics like predictive maintenance, industry 4.0 and IoT. There is currently a lot of hype here, with data often being collected without a precisely defined purpose.

Experience has shown that electro-hydraulic axes have a very specific technology base, strongly oriented towards existing customer experience. They are usually installed in an already existing environment and very often replace conservative hydraulic cylinders in existing machine concepts as part of an evolutionary development. This is due to the fact that in the vast majority of projects an already existing situation is improved. Thus, the largest projects in mechanical engineering are found in the replacement of servo valve solutions. Current experience shows us that linear actuators are less susceptible to failures than the servo valves that were replaced by the actuator. This is most likely due to the high long-term requirements on the purity of the operating medium. Here EHA's have a clear advantage due to the much more robust and less dirt sensitive design approach.

Due to the very specific development situation, it is understandable that users want to

install their own, already known components in the devices. For the supplier of electro-hydraulic servo axes, this means that for the majority of applications there is no unconditional freedom in the selection of peripheral components. For sensors, filters, ... and many other small parts, it is necessary to implement the customer's specifications.

WEBER-HYDRAULIK also uses displacement sensors of various designs. Particularly good experience has been made with measuring systems that act directly on the piston rod. The advantage of a displacement measuring system that measures the actual position directly at the piston rod is primarily the rigidity and tolerance insensitivity of the measuring point. By eliminating manufacturing tolerances and effects based on the temperature response, very precise positioning and repeatability can be achieved.

In the high-precision drives, for example, we use linear measurement technology that directly uses electromagnetic field effects on the piston rod as a measurement signal. The measurement is made directly on the piston rod. This systematically excludes the entire tolerance chain of the EHA from the position measurement. The process for manufacturing these piston rods is complex and technologically very demanding. However, the effort is more than compensated by the positioning accuracy, which is extraordinarily precise for EHA.

4. SUMMARY, USE, PROSPECT

The technology "servo-hydraulic linear axis" has reached a very mature and industrial standard. Many systems are now in the field in various applications.

WEBER-HYDRAULIK provides its decades of experience in the design and production of high quality hydraulic components and develops sample systems in close cooperation with the customer. These sample systems are already tested in the customer's facilities and are then transferred into highly competitive series solutions within the framework of professional serialization. It goes without saying that these projects are carried out in accordance with recognised standards and development systems customary in the industry.

This ensures right from the start that the finished devices fit perfectly into the

environment defined by the customer and that all project goals are achieved.

Today, revolutionary improvements are no longer to be expected for individual components. However, a big secret still lies in the precisely coordinated technology mix. Here, of course, the use of electronics in any form is a major future topic. However, the precise mechanical and hydraulic design and tuning of the components is the key competence that continues to lead to significant improvements. Predefined kits with predefined components are inevitably at a disadvantage. The apparent cost advantage of purchasing the application by using a modular system is lost, at least for highly dynamic applications in operation, due to the loss of the last percentage points of efficiency, dynamics and precision. Therefore, we have developed a technology construction kit for us, in which all necessary technologies are available. These are selected, combined, optimized and transformed into an inseparable hydraulic system together with the customer.

In the field of digital hydraulics there have been some promising approaches for quite some time. Especially in positioning, in load holding functions and in finest control tasks, the combination of servo-hydraulic drive and digital-hydraulic control technology seems to us to be an interesting combination which we will continue to pursue. Here, the near future will show whether new ideas and solutions from this field will be applied more widely in industry.

The integration of the individual disciplines will certainly lead to further improvements in the future. The extent to which pump, engine, valve technology and cylinder are merged into a single unit also depends on our customers and the respective applications and is difficult to estimate today.

It is to be expected that the actuators will also find their way into areas of application in which nature conservation and environmental protection play a major role. Due to the small quantities of oil in circulation, EHAs in compact design represent a very low risk to nature and the environment. An application is therefore also conceivable in environments where hydraulics are today viewed very critically.

By using our actuators, we have been enabling our customers for years to reduce the primary energy consumption of their applications by up to 75%, depending on the load profile. Tons of CO₂

have already been saved through the real application of the technology. Thus WEBER-HYDRAULIK linear actuators are already making an active contribution to climate



Figure 8 EHA (without cylinder)

protection and the reduction of greenhouse gases at our customers.

5. COPYRIGHT

This lecture text, the included pictures and tables are released by WEBER-HYDRAULIK GMBH and may be copied and passed on provided the source (WEBER-HYDRAULIK GMBH 2020) is mentioned.

ELECTRO-HYDRAULIC SWOT-ANALYSIS ON ELECTRO-HYDRAULIC DRIVES IN CONSTRUCTION MACHINERY

Dr.-Ing. Martin Inderelst, Dr.-Ing. David Prust, Michael Siegmund, M.Sc.

XCMG European Research Center GmbH, Europark Fichtenhain B4, 47807 Krefeld

* Corresponding author: Tel.: +49 2151 7830 200; E-mail address: inderelst@xcmg-erc.com

ABSTRACT

This paper discusses the potential of centralized or decentralized electro-hydraulic (EH)-drives in comparison to conventional hydraulic systems. The systems are presented in diagrams covering the major electric and hydraulic components for an exemplary application, but also include specific technical data like the sizing of the components according to power, pressure, rotational speeds etc. In a second step, all systems are compared and evaluated based on criteria like design effort, energy saving potential, controllability, and servicing and maintenance of the machine. The resulting effects on fuel consumption are summarized as well. Finally, an evaluation of the potential of EH-drives in construction machinery and a derivation of the demands for future customization of electro-hydraulic linear drives is given on the basis of a SWOT-analysis from the point of view of a construction machinery OEM.

Keywords: Electro-hydraulics, sizing, fuel consumption, controllability, zonal, centralized, SWOT

1. INTRODUCTION

Today, global climate change and industry 4.0 are the main drivers for new technologies in the field of mobile hydraulic systems and components. Legislation already put pressure on the development of solutions for CO₂-free primary power technologies to replace the combustion engines widely used in today's mobile applications. Electric motors driven from battery energy are the favored alternative. The German government promotes this technology by their climate change strategy that anchors electromobility in the budget until 2029 using commitment appropriations [1]. In addition, industry 4.0 is the driver to realize automation also in the field of mobile applications and hence, to improve safety, process stability and efficiency. Final solutions to achieve new targets are not yet available, but allowed time to fulfil the requirements is already demanding for the mobile machinery sector.

Driven by electrification, some mobile applications already feature electric primary power instead of diesel engines. Beneficial boundary conditions are a direct access to electric power networks along with small machine movement ranges or batteries providing

sufficient energy for occasional tasks, thereby allowing re-charging by energy recuperation or during parking and driver breaks. Examples are mining excavators and fork lifter trucks that already feature full-electric drive trains. Mini excavators and small wheel loaders are also available with 100% battery power instead of the diesel engine.

For replacing hydraulic drives, especially for powerful linear movements, alternatives are still missing. To adapt hydraulic drives or systems to electrically powered machines, activities of the hydraulic industry and university research have focused on compact linear electro-hydraulic (EH) drives. Those are combining the electric motor, the hydraulic pump including corresponding valve functionalities, and the cylinder directly into a single compact assembly that also incorporates the idea of a plug-and-play solution. As zonal or decentralized EH drives look like a compact approach today, public discussions have not yet focused on customization for the final integration in mobile machines used in hazardous areas with moving obstacles. The conformity to standards, safety level and safety functions are demanding while keeping the high level of controllability in terms of response and fine

control, etc. to finally realize a machine design that will be accepted by the customer and therefore can be sold to the market.

2. STATE OF TECHNOLOGY

2.1. Hydraulic System Environments

Hydraulic systems are part of many machines in the industrial or the mobile sectors. Major reasons are the high power density, high forces for linear drives and high torques in rotary drives. However, the industrial sector varies a lot when being compared to the mobile sector, especially the sector of construction industry. **Table 1** gives a comparison of the different fields of applications for hydraulics:

Table 1: Sectors for hydraulic applications

Criterion	Industrial	On-Road	Off-Road
Work location	fixed	variable	variable
Automation	high	low	low
Primary power	electric	fuel	fuel
Collisions	no	low	high
On-road homologation	no	yes	no
Life-time	high	moderate	low
Risks for persons	low	high	high
Load conditions	defined	known	unclear
Weather conditions	stable	flexible	flexible
Accuracy	high	moderate	moderate
Installation restrictions	low	high	moderate

The industrial sector focuses on mass production and therefore demands automation, accuracy, and a high degree of task specialization to serve high cycle rates and high accuracy with low rejects. Therefore, huge investments, less restrictions to the machine size and mass are tolerable. The mass production processes serve known boundary conditions for load profiles and the operation range of those systems. Stationary machines, e.g. hydraulic presses, are directly connected to local or public electric power networks. Regarding safety, industrial machines can run without workers and hence, reduce the event of dangerous situations to persons by avoiding the direct access to the machine.

In comparison to the industrial sector, the

mobile sector primarily differs by the mobility of the machine that often requires a human operator and fossil fuels to provide power to the hydraulic network. The safety of mobile machines is more difficult to achieve than for stationary machines, because mobile machines often work close to bystanders. Mobile machines can be generally distinguished between on-road and off-road applications. Here, the evaluation and rating of the off-road sector considers the mining and construction machinery, but omits the maritime and aviation industry.

Mobile hydraulic on-road machinery, like cranes, concrete pumps, waste trucks, etc., often consist of a machine attached or assembled to a truck. The truck is transferring the working machine to a new location, while the working functions are often performing only while the truck is parking. Thus, the truck engine provides power to the hydraulic system and the driver can operate the working attachments for tasks like lifting, pressing, towing, tilting, etc. For on-road machinery, homologation demands special restrictions to dimensions, packaging, safety and axle loads. Hydraulic loads are often predictable as the task is very specific and sudden collisions do not occur. As on-road machinery is often used stationary and in urban areas, electric power access is generally available.

In contradiction to on-road machines, off road machinery is working in an environment without existing infrastructure like roads or electricity. The on-road homologation is not necessary when the driving speed is low and the machine is on a trailer for long-distance transfers to new working locations. Off-road machines, especially construction machinery such as wheel loaders, excavators, milling machines, dozers and graders, are frequently or permanently in direct contact to soil, stones and hidden obstacles in the ground. In consequence, collisions occurring under these circumstances result in high peak loads or even over-loading of the active or passive drives for steering, lowering, milling, digging, and other functions. It becomes obvious, that load-conditions of construction machines are less clearly definable, so that over-load protection of the drives is essential. Many off-road machines frequently and even continuously drive along limits when accomplishing their tasks, so that available diesel engine power often limits the work hydraulic systems. Off-road machines operating under cyclic conditions have in general

a high potential to recuperate potential and/or kinetic energy.

2.2. Electrification and Hybridization of Mobile Hydraulics

Hydraulics vs Electrics

In contrast to mechanical drive train solutions, e.g. gearboxes that achieve highest efficiency and lowest wear in geometric-fit configuration, hydraulics transmit power based on the force-fit principle with reduced but tolerable stiffness. Electric power transmission works likewise contact-free using magnetic fields generated by electric currents. The electric signal flow is very fast and enables an easy and flexible realization of customized features. **Table 2** introduces the differences between the domains of hydraulics and electrics that have been pointed out by e.g. [2] and [3].

Table 2: Hydraulics versus electrics

Criterion	Hydraulics	Electrics
Applicable sub-systems	drive train, controls, safety features	primary power, drive train, controls, sensors, safety functions
Power density	high	medium
Energy density	low	high
Transmission	Force-fit	Contact-free Lorenz force-fit
Linear motion	Easy / flexible	complex
Rotary motion	low to medium speeds	low to high speeds
Overload-protection	simple	complex
Position locking	good	bad
Highest precision	Force / Torque control	Positioning
Automation / controls	moderate	advanced
Dynamics	moderate	high
Stiffness	moderate	low
Inertia	low	high
Cooling and lubrication	good	bad

The different characteristics of the domains are reasons why both of them have been successfully applied in various mobile applications.

Hybridization

Due to decreasing fossil fuels and corresponding

expectation of raising energy costs in future, activities to more efficiently fuel energy in mobile machinery have started. Today, especially high-cyclic operation or peak power demands are reasons for the successful implementation of hybrid solutions in mobile applications. The challenge for OEMs is that customers tolerate additional costs for new technologies when these obtain return on invest within the first year by fuel savings or higher productivity. **Table 3** gives an overview about the differences of both hybrid technologies, hydraulic and electric hybrids.

Table 3: Hydraulic versus electric hybrids

Criteria	Hydraulic Hybrids	Electric Hybrids
Available network / system	hydraulic	electric
Operation	highly cyclic	flexible
Hybrid Energy Consumption	engine torque, auxiliary	flexible
Peak power handling	good	bad
Recuperation	complex, specific	easy, flexible
Diesel engine operation	continuous	start-stop, range extending
External charging	complex	Easy

In general, hybrid systems are today more or less add-on systems, and the selection of the hybrid domain mainly corresponds with the domain of the existing drive train. Hydraulic hybrids are compliant to high-cyclic operations with high power peaks while electric hybrids can more easily provide larger quantities of energy assisted by the diesel engine running in start-stop or range-extending operation. Furthermore, they are capable of supporting operation strategies which aim at reducing overall power consumption by buffering peak loads in batteries, then recharging them in times of low power demand. Electrics transform energy or power in a more simple and flexible way than by hydraulic transformers. In consequence, electric drive trains are more readily capable of recuperating braking energy, which is often available in mobile machines, but cannot be handled by hydraulic systems easily. The lack of transformers in these systems limit the re-use of recuperated energy, whenever accumulator pressure level is lower than the system pressure. Therefore, hydraulic systems often utilize recuperated energy to support

auxiliary functions or to generate additional torque to assist the diesel engine.

Electrification

Climate change is demanding solutions to operate mobile machinery free from carbon-dioxide emissions in the future. In consequence, several European countries enforce electrification, as there is currently no alternative and competitive technology to generate, store and transport renewable energy as efficiently and safely than electrics. In addition, smart features improving productivity and enhancing functionality and services to mobile machines, are driven by the Internet of Things. Both technologies demand re-thinking and re-configuration with respect to the following sub-systems in mobile machinery.

- Primary power and energy
- Drive train and power distribution
- Automation, assistance, controls and actuation
- Monitoring and safety features
- Auxiliary functions

Mobile hydraulic systems in construction machinery already feature sensors for condition monitoring and the support of control functions. To overcome restrictions from machine directives and standards, more stringent exhaust emissions and engine restrictions as well as higher customer expectations for comfort and ergonomics, mobile applications already feature electric controls, many sensors, and electro-hydraulic pressure-reduction valves replacing the conventional hydraulic actuation system. Some machines already feature full-electric primary power or electric-hybrid systems driving rotary power functions. In consequence, electric power is about to be established as the prior power domain in construction machinery. Nevertheless, it is still lacking suitable and effective solutions for robust linear power functions, which make it likely that hydraulics will continue to be of importance to construction machinery.

2.3. Electro-Hydraulic Linear Control

To minimize or avoid valve resistance-related losses, different solutions for controlling linear hydraulic motions directly by the pump flow have been developed, investigated, and presented already.

Open-Circuit Control (OCC)

One approach is to control the linear movement by independent metering valves in combination with an over-center open-circuit pump (or so-called mooring pump), see **Figure 1**. It was tested and investigated for example on a Volvo 220L wheel loader [4]. Similar structures using a constant pump combined with an electric high-speed motor is in the focus of investigations in a mini excavator [5].

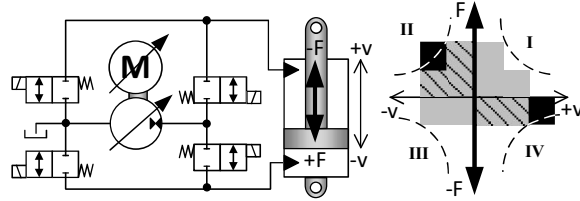


Figure 1: Open-circuit control system with independent metering edges

The diagram on the right-hand side in Figure 1 demonstrates the operation range related to speed and corresponding forces. The cylinder can recuperate energy in both directions and hence is connectable to the pump's high pressure side in each of the four quadrants. For the following observation, the cylinder ratio α is defined as the effective rod side area A_R divided by the piston area A_P .

$$\alpha = \frac{A_R}{A_P} = \frac{(D_P^2 - D_R^2)}{D_P^2} = 1 - \frac{D_R^2}{D_P^2} \quad (1)$$

The quadrants I and II describe the cylinder operation for pushing force conditions. The pump flow Q_P proportionally sets the speed v_P whenever the full piston area A_P is effectively connected to the pump, see eq. (2). Eq. (3) defines the corresponding range of forces F_P .

$$v_P = \frac{Q_P}{A_P} = \frac{4 \cdot Q_P}{\pi \cdot D_P^2} \quad (2)$$

$$F_P = p_p \cdot A_P \quad (3)$$

Furthermore, the configuration also enables differential operation realized by a short-cut connection between rod and piston side. Hence, the effective piston area A_D is the cross-sectional area of the cylinder rod. The speed v_D in the differential mode is higher as smaller effective piston area consumes the full pump flow.

$$v_D = \frac{Q_P}{A_D} = \frac{Q_P}{(1 - \alpha) \cdot A_P} = \frac{v_P}{(1 - \alpha)} \quad (4)$$

However, the available force F_D is lower under these conditions, as the effective operating area A_D is also smaller.

$$F_D = p_P \cdot A_D = F_P \cdot (1 - \alpha) \quad (5)$$

The quadrants III and IV describe cylinder operation with pulling forces. The cylinder speed v_R is faster than in quadrants I and II, as the effective cylinder area is smaller, see eq. (6). Eq. (7) describes the corresponding range of forces F_R in quadrants III and IV.

$$v_R = \frac{Q_P}{A_R} = \frac{4 \cdot Q_P}{\pi(D_P^2 - D_R^2)} = \frac{Q_P}{\alpha \cdot A_P} \quad (6)$$

$$F_R = p_P \cdot A_R = p_P \cdot \alpha \cdot A_P = \alpha \cdot F_P \quad (7)$$

The cylinder ratio α allows to adjust the force F_D in differential mode between quadrants I and II or III and IV respectively. For $\alpha=0.5$, the forces and speeds remain unchanged, while for $\alpha < 0.5$, F_D increases and v_D decreases and vice versa, see equations (8) and (9).

$$F_D > F_R \text{ for } \alpha < 0.5 \quad (8)$$

$$v_D < v_R \text{ for } \alpha < 0.5 \quad (9)$$

Besides the grey-shaped area described by the eq. (6) to (9), the cylinder can be driven by potential energy only when both the cylinder chambers are connected only to the tank and the pump is disconnected. Hence, applying the orifice equation with

$$Q_V = K \cdot A(y) \cdot \sqrt{\Delta p_T} \quad (10)$$

to such valve or resistance-controlled mode, this system setup allows a speed boost function at higher power level, as Δp_T over the tank edge can be significantly larger as the pump edge pressure difference Δp_P in normal OC operation.

Displacement-control (DC)

The idea of a closed circuit configuration serves the basis for the principle of displacement control for linear hydraulic cylinders. To balance the flow discrepancy caused by the cylinder ratio between rod and piston side while the cylinder is moving, piloted check valves are located in the short-cut between both cylinder ports, see **Figure 2**. Both of them can only open separately when the counter-port pressure is higher, so that flow compensation always takes place under low-pressure conditions.

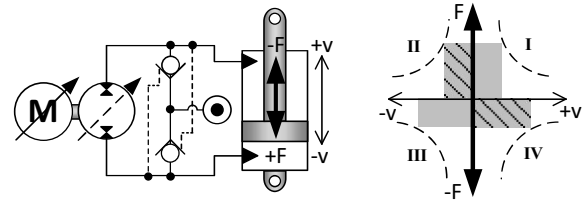


Figure 2: Displacement Control System

In comparison to the open-circuit control, the displacement control does not feature any metering valves or logic valves. The pump displacement controls the speed, and the piloted check-valve opening state only depends on the direction of the force. For functions with changing load directions during movements, this can cause undesired sudden speed changes that might disturb the machine operator. Furthermore, it is not possible to connect either cylinder side in differential mode or to the tank using this configuration. The DC principle has been investigated by [6] in a 6t excavator.

Direct Driven Hydraulics (DDH)

The zonal or direct driven hydraulics (DDH) compensates the flow discrepancy by the integration of a second pump. The approach connects the second pump's outlet directly to the cylinder's piston side as shown in **Figure 3**, whereas the second pump port is connected to the tank. The ratio of active displacements connected to cylinder ports is equal to the cylinder ratio. The realizable speed and forces are equal to the DC in the quadrants I and II.

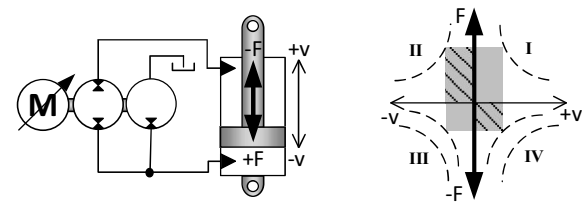


Figure 3: Zonal / Direct Driven Hydraulics (DDH)

As no bypass flows exist to relief or feed the circuit, maximum speed is the same in all quadrants, as would also be the case for electro-mechanical spindle drives. Research and investigations with the DDH have been conducted on a micro-excavator boom cylinder system [7].

EH Linear control comparison

To conclude and evaluate all EH linear drives presented above, **Table 4** compares the system

with regard to different criteria. The reference for the rating is a 70 kW cylinder with 350 bar maximum pressure. For pressures lower than 300 bar the use of gear pumps in the DDH will lead to better ratings in the criteria space and costs.

Table 4: Comparison of EH linear control systems

Criterion	Valve	OCC	DC	DDH
Space	++	-	+	+
Costs	++	-	+/-	-
Modes	+/-	++	-	--
Piston Speed	+/-	++	+/-	+/-
Rod speed	++	++	-	--
Boost	++	++	--	--
Regeneration	++	++	--	--
Recuperation	--	++	+	+
Pilot pressure	-	-	-	++
Leakage, drain oil	+	+	--	-
Flexibility	+/-	++	--	--
Complexity	-	--	+	++

The criteria chosen in the table create the impression that DC and DDH control systems cannot compete with OCC systems. Nevertheless, depending on the application and its respective requirements, both system can be suitable and even beneficial.

2.4. State of the Art of Crawler Excavators

History of hydraulic crawler excavators has started in the middle of the last century. First machines were operating fully hydraulically with constant pumps and full-hydraulic joystick control. Over years, development focused on improvements of productivity, controllability and ergonomics, but also reduction of fuel consumption. In the last decade, diesel engine restrictions like Euro Stage III-V or Tier 3a-4 final and the EU machines directive caused a shift of the focus towards advanced controls to realize hydraulic hybrid functionality, high sophisticated power matching and safety features in the machines. In consequence, sensors and electric controllers demanded the integration of electro-hydraulic pressure reduction valves as interface to high electric controls. The availability of electric controls then spawned

semi-automated driver assistance features like levelling control and other automation features or virtual walls to set emergency stops whenever the machine operates outside its allowed envelope. Middle size excavators between 20 and 30 tons have the highest demands to performance and controllability, so that hydraulic system suppliers offer tailor-made valve manifolds for these machines.

To enable functions such as turning, lifting/lowering the boom, moving the arm and load or rather unload the bucket, directional valves direct flow to hydraulic cylinders and motors. **Figure 4** shows a simplified hydraulic system for mid-size hydraulic excavators providing the above-mentioned major functionalities.

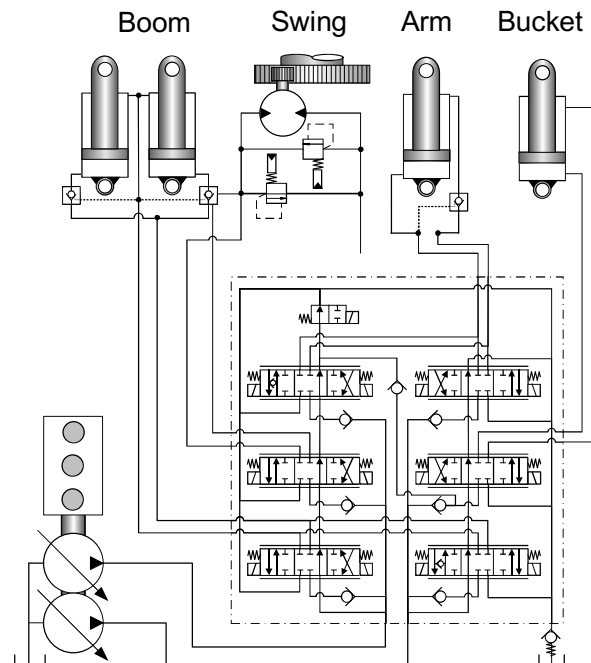


Figure 4: Simplified conventional Positive Flow Control system for hydraulic excavators

The valve spools of each function are connected to one or two pumps that are driven by the diesel engine. The allocation to different pump circuits enables a prioritization of multi-function operation and further avoids stopping of one or more functions when the pump flow is not sufficient. This phenomenon, called saturation, results from either limited diesel engine power or pump displacement. Each function therefore also has one check valve integrated in the pump line to avoid the function moving in wrong directions in case of insufficient pump pressures. All cylinders of the attachment feature individual valves for locking, anti-cavitation and pressure-

relief functions. Those features are important to avoid undesired movement for lifted attachment or to protect both the hydraulic cylinders and the steel structure from mechanic overload. In construction machinery, overloads can easily occur also in all inactive functions of the attachment along with the collision of the bucket with stones or ground material. Thus, load conditions in construction machinery are critical and unpredictable compared to other machines.

All cylinders of a 21t excavator realize full movements, end stop to end stop, within 3 seconds. Thus, the operator demands high response and low valve hysteresis to keep the machine under control at any time. As moving mass for the attachment parts is above 1 ton and more, acceleration and deceleration must be smoothed by the pilot actuation systems in either hydraulic or electric layouts to avoid uncomfortable jolts.

The main valve spools feature flow curves providing a feeling of significant flow changes over the full joystick range, but also have small tank edges in the opening range to pre-load the cylinder capacitance during braking and this way, clamp the cylinder for higher stiffness of the attachment. In addition, check valves inside the arm and boom spools regenerate flow during operation under pulling load conditions.

3. ELECTRO-HYDRAULIC DRIVE TRAIN CONFIGURATION AND SIZING

3.1. Electro-hydraulic drive train design

In contradiction to the solutions described before, Asian market construction machinery OEMs already introduced diesel-electric drive trains for excavators, similar to **Figure 5**. These consist of mostly conventional hydraulic system architecture, but an electric instead of a hydraulic motor provides power to the swing drive function. The electric motor is controlled through an inverter, consumes energy from or recuperates energy to the battery during braking.

An electric generator charges the battery to load the diesel engine or consume battery power to provide additional torque/power to the diesel engine shaft that supports the hydraulic pumps. In this constellation, the electric drive train allows both downsizing of the diesel engine and smoothed engine operation in a permanent highly energy-efficient working mode.

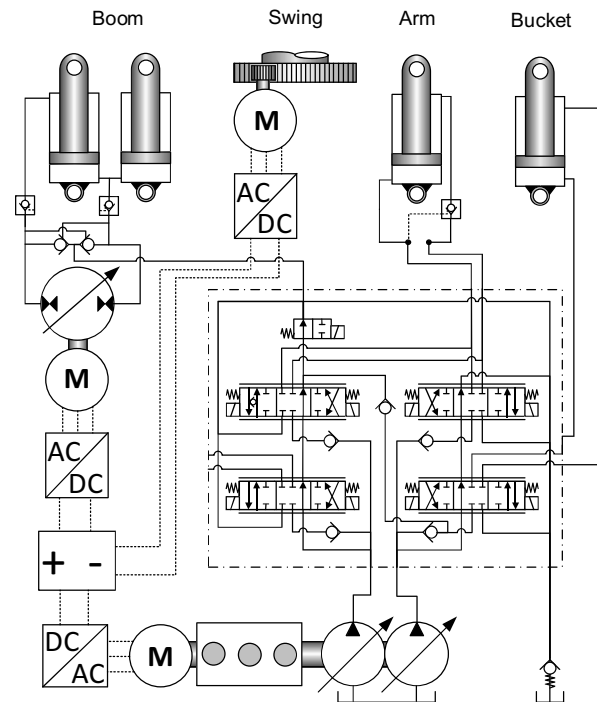


Figure 5: Hydraulic excavator with electric hybrid for swing and EH drive for boom cylinders

In addition to the system described before, the diagram in Figure 5 also replaces the main control valve spools of the boom hydraulics by an EH drive. This setup is able to recuperate potential energy from boom lowering during the digging cycle. [8] points out that the boom function has higher energy recovery potential than the swing function. Hence, it is expected to reduce fuel consumption by this approach. The boom EH linear drive is presented in DC architecture, but has not been fixed yet. The next chapter will focus on the identification and sizing of a suitable EH linear cylinder drive for a 21t hydraulic excavator.

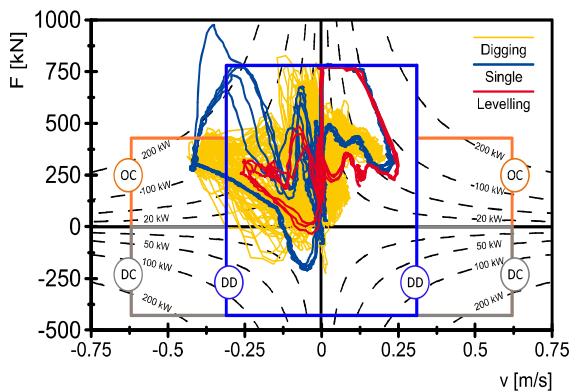
3.2. Identification of suitable EH linear drive concept

In the beginning, the focus is set to all drives. The analysis will be presented for all cylinder drives. Therefore, **Table 5** provides all necessary cylinder design parameters. These parameters are fixed to not change maximum forces or speeds of the cylinder and this way also guarantee for at least the same performance in multi-function operation like digging and levelling. The first step of finding the suitable EH linear approach is to analyze the cylinder speeds and forces for different tasks during single and multi-function operation.

Table 5: Cylinder data

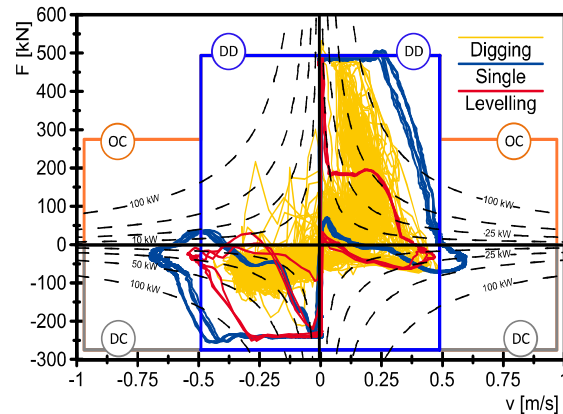
Cylinder	Boom	Arm	Bucket
Piston	120 mm	135 mm	115 mm
Rod	85 mm	95 mm	80 mm
Ratio	0.5	0.5	0.5
Stroke	1221 mm	1475 mm	1060 mm
p _{max}	345 bar	345 bar	345 bar

Figure 6 shows a power map for the boom cylinder operation. The abscissa represents the cylinder velocity, the cylinder forces are recorded on the ordinate. The diagram also introduces lines of constant power in all four quadrants of energy consumption and furthermore fixes the operating ranges of the OCC, the DC and the DDH.

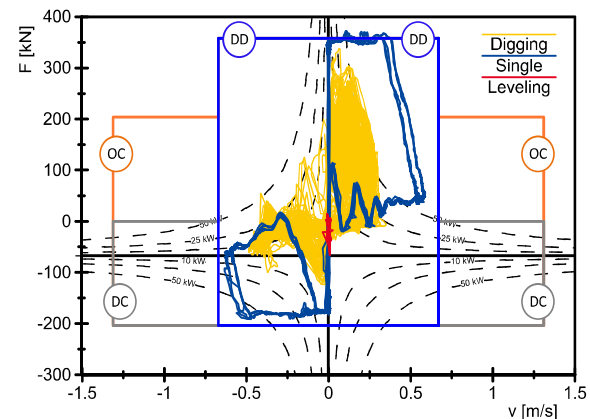
**Figure 6:** Power map for the boom cylinders

Cycle data for the boom cylinders is plotted for single function, a 30 minutes 90° digging cycle as well as for a few levelling periods. While in quadrants I and IV the boom cylinders could be operated by all three approaches for lifting tasks, the lowering demands very high speeds in differential configuration in the second quadrant. This is a strong argument to apply the OCC principle to the EH drive for boom cylinders, to later chose a small pump operating always in areas of high energy-efficiency. In general, the high speed lowering by dissipating energy through valve edges instead of recovering by the EH power pack is also possible.

Figure 7 plots the operational points for the arm cylinder in the same type of diagram for the same cycles. The results show, that the arm cylinder covers the working range of the DC approach very well.

**Figure 7:** Power map for the arm cylinder

The bucket cylinder data plotted in the diagram of **Figure 8** indicates that the DDH can be sufficiently applied. The results show that the sizing of the hydraulic cylinders lead to different configurations for the EH linear drive. Highest efforts need to be considered for the boom function using also active valves whereas bucket and arm can be operated with simpler approaches.

**Figure 8:** Power map for bucket cylinders

Due to the operation conditions, anti-cavitation and pressure relief-valves have to be installed to each of the cylinder ports with regard to the high risk of peak overloading caused by collisions. Locking valves are required at all cylinder ports in order to avoid cylinder settlement for inactive functions through internal leakage inside the pump.

3.3. Electro-hydraulic Power Pack

The electro-hydraulic power pack consists of the electric motor and the hydraulic pump. Both of them can either feature constant (C) or variable (V) operation for either the rotational speed (S) or the displacement (D). **Figure 9** introduces

different configurations of variable and constant electro-motors and pumps.

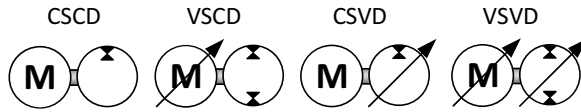


Figure 9: EH power pack configurations

Table 6 summarizes the characteristics of the different configurations. The CSCD is the simplest solution to provide constant speed operation and therefore is only suitable to operate at fixed speeds features. With the VSCD electric motor, speed becomes variable, but cannot provide permanent high-torque at low speeds, due to existing torque limits of the drive motor. The CSVD controls the speed instead by variable pump displacement. It is beneficial to use when more pumps for different drives attach to a common electric motor shaft. Highest flexibility and opportunity to balance operational points for high reliability and efficiency of both the components offers the configuration VSVD.

Table 6: Evaluation of EH power pack

	CSCD	VSCD	CSVD	VSVD
Continuous operation	yes	yes	yes	yes
Cyclic operation	no	yes	yes	yes
Pilot pressure supply	no	yes	no	yes
High torque @ low speed	no	--	+	++
Multi-drive control	--	--	++	+/-

Besides the more general thinking, the performance of available pumps and electric motor is also limiting the options. Based on their principle, hydraulic pumps significantly vary in maximum pressure range, inertia, internal leakage, noise, pulsation, low-speed behavior and costs. Floating-cup pumps feature high pressures for very low speeds, have a wide speed range, low inertias, and high efficiency values. Gear pumps cannot provide the pressure needed and variable displacement axial piston pumps are prone to wear at very low speeds. In consequence, the VSVD is chosen for the 21t excavator EH boom cylinder, as this configuration has the potential for good fine control and high reliability of all components.

4. SIZING OF EH LINEAR DRIVES FOR 21T EXCAVATOR

Based on the descriptions of all given boundary conditions, **Table 7** introduces the final selection and dimensions for all EH linear drive.

Table 7: EH linear drive data

	Arm	Boom	Bucket
Principle	DC	OCC	DDH
EH power pack	VSVD	VSVD	VSCD
E-motor speed [rpm]	3600	3600	4000
H-pump type	Variable axial piston pumps		Floating -cup
H-pump size [cm ³]	2x56	2x56	56/28

For all cylinder functions, arm, boom, and bucket, different approaches have been identified as the most suitable solution.

5. SIMULATION RESULTS AND ANALYSIS ON CONTROLABILITY

5.1. Controllability

Hydraulic mid-size excavators are one of the most dynamic, fully human controlled applications in the field of construction machinery. Controllability in this context means that the operator cannot feel any remarkable deviation from his expectation when operating the joysticks or pedals. Excavator systems feature fast response, low hysteresis in the valve as well as on system level and fulfill fluent movement without oscillations.

Regarding response of the cylinder functions, typical delay times between start signals set on the joystick and the beginning of a movement at the cylinders or rotary drives range from 90ms to 140ms. Those values are realistic to be achieved by electric controls.

Figure 10 shows raising flow curves and decreasing tank-edge pressure setups for the counter side of each cylinder. The flow curves feature progressive behavior starting with a fine control range in the beginning and higher gain in the end of the spool or joystick stroke. Skilled excavator operators can identify up to six major steps of speed changes over the full range of the joystick stroke, and thus accept full resolution of the function. If the speed ratio develops too weak, operators report dead zones during the

commissioning or debugging process. There are no functions demanding maximum single function speed for any task or multi-functions. A reasonable explanation serves the placebo that operators suggest high resolution in multi-functions when the system performed at high resolutions in the single function test.

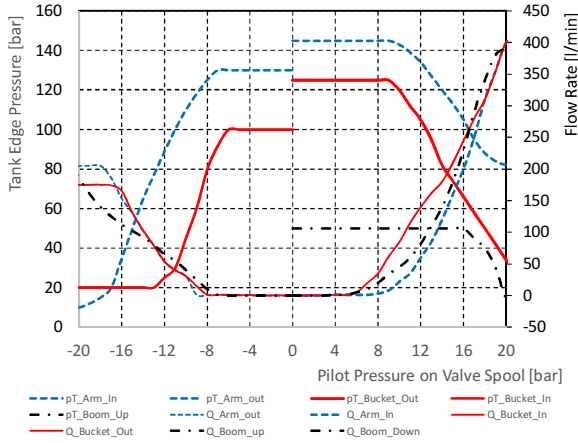


Figure 10: Flow curves and tank pressure setups

Table 8 lists the relative movement times measured for the reference system (R) and four other machines of different suppliers in the same machine size that are sold to markets and thus, can be accepted by customers.

Table 8: Times of single function movements

	Boom		Arm		Bucket	
	Up	Down	In	Out	In	Out
R	100%	100%	100%	100%	100%	100%
A	103%	100%	141%	88%	194%	113%
B	66%	76%	129%	79%	172%	108%
C	75%	81%	152%	85%	194%	100%
D	107%	93%	128%	86%	172%	93%

As higher time values in the table correspond with slower movements of the single functions, only arm and bucket permit a reasonable speed reduction to allow a smaller EH power pack configuration.

Another important aspect is the stiffness of active and non-moving cylinder drives that are building a kinematic chain whereas the bucket load affects also arm and boom forces. For valve-controlled systems, tank edge areas are small in half of the opening range to raise pressure level during movements and during braking of the functions. Finally, this measure provides higher stiffness of the cylinders. As the feed pressure

level to balance the flow discrepancy is significantly lower than the tank edge pressures in conventional valve systems, EH linear drives may differ in terms of cylinder stiffness compared to valve systems. Equation (11) derives the stroke difference dx resulting from the lack of pressure difference Δp in the cylinders.

$$\Delta x_{C,i} = \frac{\Delta V_i}{A_{C,i}} = \frac{\Delta p_i \cdot (A_{C,i} \cdot x + V_{Pipe})}{E_{Oil} \cdot A_{C,i}} \quad (11)$$

Based on the equation, **Table 9** gives the compression-based stroke for the EH cylinder linear drives and corresponding pipe data as a reference. The values for the stroke are given for the zonal ($\Delta x_{C,Z}$) and the centralized ($\Delta x_{C,C}$) configuration. These indicate a risk of oscillations downgrading/deteriorating the precise positioning of the attachment.

Table 9: EH oil compression in centralized and zonal / decentralized configuration

	V_{PIPE} [dm ³]	$\Delta p_{V,T}$ [bar]	$\Delta x_{C,C}$ [mm]	$\Delta x_{C,Z}$ [mm]
Boom up	1.28	50	2.7	2.8
Boom down	1.28	90	6.9	7.9
Arm In	5.1	130	13.6	15.9
Arm Out	3.5	145	15.5	18.8
Bucket In	5.4	100	7.0	9.4
Bucket Out	5.4	120	8.8	14.8

Since the EH linear system approach has the lowest pressure on the counter side (of those systems taken into account), the arm function has high risk of oscillation due to the reduced stiffness or clamping of the cylinder. For the bucket cylinder, this risk grows with the size of the piping capacitance. In general, this observation points out that EH linear drives feature less stiffness of the cylinder by reduced pressurizing on the pump inlet size. Especially for the centralized installation of EH power pack along with long piping or hosing to the drives, stiffness decreases whereas the risk of oscillation rises. In addition to controllability features such as response, fine control, resolution, etc. start and stop impacts are also important characteristics to consider in the matching of systems. Impacts occur whenever acceleration or deceleration ratios are too high, most likely for fast changing demands set on the joystick. To avoid impacts in excavators, electric control system already

widely apply more flexible and smooth behavior compared to hydraulic control systems based on the valve principle.

5.2. Zonal or Centralized Integration

The comparison of central versus zonal EH arrangements in **Table 10** highlights the different characteristics allowing a decision which designs to choose for the new system layout. Major arguments are given by the installations on a common shaft, the load impact by the EH drive's weight and the risk of oscillations due to force conditions along with a high hydraulic capacitance. In addition, the comparison accounts for the effort to compensate internal leakage of the pumps or the service of the mobile machine.

Table 10: Zonal versus centralized arrangement of EH linear drives

Criteria	Central	Zonal / Decentral
Installation on common shaft	++	--
Additional weight on moving parts	+	--
Leakage oil re-feed	++	--
Efficiency	-	+
Stiffness / clamping	-	+
Damping	+	-
Oscillation risk	-	+
Cavitation risk	-	+
Filtration	+	-
Cooling	+	-
Service	+	-

5.3. Energy Saving Potentials

System simulations were conducted to analyse the energetic characteristics of three different systems, similar to the system shown in Figure 5. According to this, **Table 11** shows the simulation results for the reference positive-flow control system (REF), a similar system (ES) using an electric instead of the hydraulic swing drive motor as well as the system (ES+EHB) introduced by Figure 5 using also EH boom cylinders. In addition, all system are based on the same diesel engine to show the downsizing potential by stating the effective diesel engine torque.

Table 11: Digging cycle comparison

	REF	ES	ES+ EHB
Engine Power [kW]	103	103	103
Max. Torque [Nm]	600	580	430
Battery size [kJ]	-	225	585
Generator size [kW]	-	25	70
Generator efficiency [%]	-	0.9	0.9
Battery efficiency [%]	-	0.9	0.9
Inverter efficiency [%]	-	0.95	0.95
Fuel [l/h]	22.7	18.3	17.3

The results show that even for the simpler ES system, approximately 20% fuel savings can be achieved by applying electric generator, swing motor and battery to the system and thus smoothen the diesel engine's power output as well as recuperating swing braking energy. Diesel engine downsizing is not possible by the configuration selected. In comparison to this, the system also adding EH boom cylinder drives can save additional 4.4%. As the average engine torque is significantly lower for this approach, downsizing of the diesel engine seems reasonable and can lead to further fuel savings. Further detailed simulations in future might show whether the downsizing along with further fuel savings can justify the higher system costs for implementation of the EH boom cylinder drives.

6. SWOT-ANALYSIS

Hereinafter, a SWOT-analysis is conducted to conclude the derivations and results discussed in the chapters above and to further debate the future potential of the technology in the field of construction machinery. The SWOT-analysis is outlined in **Figure 11**.

The major strengths of hydraulics in general, but also EH drives, are their high power density, the ability to provide and control force robustly, and the simple realization of overload-protection and locking of positions even without available power. These are typical demands in mobile construction machinery. Due to this, the OEM either tolerates weak spots like low energy density, worse power transformation, cavitation and a reduced flexibility to customize the controls of the machines or compensates them with high

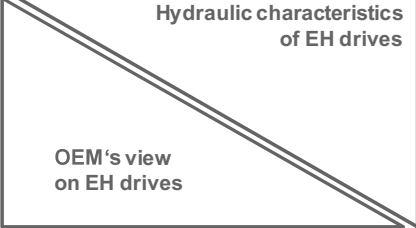
	Strengths <ul style="list-style-type: none"> ➤ High power density ➤ Good force control ➤ Robust linear drives ➤ Self-lubrication and cooling ➤ Direct solutions for wearless overload-protection and load-holding 	Weakness <ul style="list-style-type: none"> ➤ Low energy density ➤ Less position accuracy ➤ Difficult transformation ➤ Leakage, Cavitation ➤ Less control flexibility ➤ Easy to oscillate, less stiffness
Opportunities <ul style="list-style-type: none"> ➤ Automation / non-human control ➤ Easy connection to electric power and signals ➤ Downsizing of diesel engines 	<ul style="list-style-type: none"> ➤ Connect benefits of hydraulics and electrics ➤ Eliminate disadvantages by the combination 	<ul style="list-style-type: none"> ➤ Solve lacking energy density in combination with the electrics ➤ Ease power transformation ➤ Increase dynamics and control flexibility
Threats <ul style="list-style-type: none"> ➤ Engineering, Service safety efforts with regard to high voltage ➤ Additional drive weight on moving parts reduces performance ➤ Costs 	<ul style="list-style-type: none"> ➤ Less pumps available performing high-speeds or low speeds ➤ Zonal approaches as stand-alone plug-and-play components in tools or non-moving parts 	<ul style="list-style-type: none"> ➤ Higher efforts in service ➤ High risk as solutions are still not series production approved ➤ Zonal approaches add weight to kinematics

Figure 11: SWOT-analysis on EH drives in construction machinery

efforts in the development process. In general, the idea of EH drives is driven by combining both domains, hydraulics and electrics, to end-up in a stronger system covering most of the advantages and avoiding disadvantages for hydraulic drives such as lower positioning accuracy and less flexibility in settings and control features. These circumstances promise opportunities for the construction machinery OEM like energy recuperation on existing diesel-electric drive trains, downsizing of the diesel engine and higher positioning accuracy with regard to automation.

Nowadays, the biggest threats are seen in the higher efforts for development and servicing, as the relevant staff needs to be trained and skilled to identify and solve problems in the high-voltage systems. Furthermore, the electro-hydraulic components are still not tailored for this application and series products are not available. Ultimately, the potential exists to increase energy efficiency along with better controllability in mobile machines like wheel loaders, graders, and excavators, as these machines have high potential to utilize hybrid drive train structures, but also require robust linear drives. Markets are still waiting for the customization and industrialization of EH drives. Further research should focus on new pump concepts covering the whole electric motor speed range and further feasibility studies should show the correlation of EH power and fuel savings.

In general, hydraulics play an important role in the construction machinery sector as they are currently still the best drive train solutions to cope

with the often high and undefined forces caused by the very diversified the working tasks. However, further electrification of mobile machinery will pave the way for using more EH drives in the future.

7. SUMMARY AND OUTLOOK

The article discusses electro-hydraulic drives with regard to different aspects, e.g. the special demands for utilization in construction machinery, the characteristics in comparison to the electrics, and central or zonal arrangements. Furthermore, it evaluates different configurations for linear cylinder drives and the electro-hydraulic power pack and provides the sizing and customization for an exemplary application. It gets obvious that the customization of EH drives in construction machinery is complex and selection of the right configuration for linear drives must be made carefully.

Simulation results point out that diesel engine downsizing and significant fuel savings can potentially be achieved in 21t excavators, when electro-hydraulic cylinders are applied to an existing diesel-electric drive train. Conventional hydraulic systems will still play an important role in the future for high-force functions in low time share use like travelling or hammer tools.

A SWOT analysis finally shows that electro-hydraulic drives are an alternative for electric power driven construction machinery, but need further improvements in terms of customization, production, service and the reduction of costs.

NOMENCLATURE

α	Cylinder ratio
A_D	Effective area in differential mode
A_P	Cylinder piston area
A_R	Cylinder rod diameter
$A(y)$	Valve opening area depending to stroke y
CO_2	Carbon-dioxide
D_P	Cylinder piston diameter
D_R	Cylinder rod area
DC	Displacement control
DHH	Direct driven hydraulic
EH	Electro-Hydraulic
E_{Oil}	Bulk-modulus of oil
F_D	Cylinder force in differential mode
F_P	Cylinder force acting on piston area
F_R	Cylinder force acting on rod area
K	Valve factor
OCC	Open-circuit control
p_P	Pump high-pressure
p_T	Tank pressure
Q_P	Pump flow rate
Q_V	Flow rate through metering edge
v_D	Cylinder speed in differential mode
v_P	Cylinder speed for driving piston area
v_R	Cylinder speed for driving rod area
V_{pipe}	Capacitance / volume of pipes
x	Cylinder stroke

Hydraulic Systems. Ph.D. Thesis, Purdue University, USA

- [7] Minav T. (2019) The effects of control methods on energy efficiency and position tracking of an electro-hydraulic excavator equipped with zonal hydraulics. In: Automation in Construction, Journal, vol. 100, 129-144
- [8] Inderelst M. (2018) Quantification of Energy Saving Influencers in a 21t Excavator Hydraulic System - A Holistic Investigation? 11th International Fluid Power Conference (IFK), Aachen, Germany

REFERENCES

- [1] Bundeshaushaltsplan 2019, Einzelplan 60, Allgemeine Finanzverwaltung, Germany, 2019
- [2] Kempermann C., et al. (2016) More Efficient Refuse Trucks by the Application of Electrohydraulics. 4th International Commercial Vehicle Technology Symposium 2016, Kaiserslautern, Germany
- [3] Schmitz K., Murrenhoff H. (2018) Fundamentals of Fluid Power – Part 1: Hydraulics. Shaker Verlag GmbH, Aachen, Germany
- [4] Heybroek K. (2017) On Energy Efficient Mobile Hydraulic Systems, Ph.D. Thesis, Linköping University, Sweden
- [5] Pietrzyk T. (2019) Design of a high speed internal gear pump to increase the power density of electro hydraulic actuators (EHA) in mobile applications. International Mechanical Engineering Congress and Exposition, IMECE2019, Salt Lake City, USA
- [6] Zimmermann J. (2012) Toward Optimal Multi-actuator Displacement Controlled Mobile

MODULAR INDEPENDENT METERING SYSTEM FOR MOBILE APPLICATIONS PROVIDING SMOOTH MODE TRANSITION

Jan Lübbert^{1*}, Jürgen Weber¹, Christian Stauch², Peter Bruck²

Institute of Mechatronic Engineering, Technische Universität Dresden, Helmholtzstraße 7a, D-01069 Dresden, Germany

HYDAC Fluidtechnik GmbH, Justus-von-Liebig-Straße, D-66280 Sulzbach/Saar, Germany

* Corresponding author: Tel.: +49 351 463 33701; E-mail address: Jan_Frederik.Luebbert@tu-dresden.de

ABSTRACT

Independent metering valve systems open up for more flexibility because of the ability to control meter in and meter out flow individually, thus enabling many possibilities to adapt the actuator's behaviour to the user's needs without altering any hardware. Furthermore, with alternative flow modes significant energy savings are possible. In many applications like excavators smooth switching between flow modes is required, a demand the market does not provide a satisfying solution for yet. Here, an approach using a short circuit path for smooth switching has been developed. The control algorithm hands over the volume flow from one path to another continuously depending on the current actuator load. Due to the flexible software structure the developed control algorithm can be applied to a very broad variety of independent metering valve layouts. Simulation results are promising and currently the solution is undergoing test rig evaluation.

Keywords: independent metering, mobile machines, energy efficiency, control strategy

1. INTRODUCTION

Hydraulic systems for actuating human controlled mobile machines have undergone a long history regarding development and optimisation. The state of the art changed from constant flow open centre systems, which emerged in the 1950s, over negative (NFC) and positive flow control systems (PFC) to load sensing and flow sharing [1]. Nowadays, after several decades of technological progress, these conventional systems satisfy most requirements regarding controllability, but they significantly lack energy efficiency – a topic becoming more and more important. One reason for the low of energy efficiency are unnecessary throttling losses at meter-out orifices of coupled-metering-valves designed for control of altering, especially overrunning loads [2].

The common closed-centre load sensing (CC-LS) and open-centre systems (OC) behave very different and are therefore more or less suited for different tasks. For example, when grabbing a pipe with an excavator bucket or accelerating a long and heavy boom, the good force control properties of OC-systems are desirable, but for finishing a surface it might be more desirable to

have the good velocity control of an LS-flow-sharing system. These different kinds of principal behaviour cannot be changed in a conventional system. So the customer must accept a trade-off regarding his type of hydraulic system and the intended application of the machine. On the other hand side OEMs need to equip their machines with different valve systems to meet the customer expectations in different countries. Furthermore they have to put a lot of effort into the design and tuning of complex valve spools. Another aspect becoming more and more important is automation. Coping with the cross interactions and load dependency of conventional systems to perform an accurate movement under varying load autonomously is a challenging task.

Independent Metering (IM) is the ideal technology to overcome the aforementioned limitations of common valve systems in mobile machines: Decoupling of inlet and outlet into separate valves eliminates the need for complex and application-specific spool design – standard valves can be applied to any task with comparable flow requirements. With adaption of the opening ratio between inlet and outlet throttle by means of IM controllability and energy efficiency can be

improved at the same time. The energetic savings are obtained by prevention of unnecessary throttling of the outlet flow and by utilisation of regenerative flow circuits. Also automation and productivity can be facilitated by IM, since this technology enables complete load compensation.

2. MODE SHIFTING PROBLEM AND STATE OF THE ART

The major part of the energetic benefits of IM lies in the alternative flow modes. The feasibility and efficiency of these modes depends on the load. In case of an excavator, loads are not predictable in advance, so it must be possible to change the flow mode quickly during an ongoing movement without irritating the operator. To make IM suitable and attractive for mobile machines - especially excavators – the challenging task of mode switching must be solved.

The easiest way to cope with mode shifting is to prevent mode shifting during the movement. This can be accomplished by predefining suitable flow modes for typical movements and loads [3]. The mayor drawback of this approach is the fact, that loads change during the movement and without shifting into the optimal mode energy efficiency decreases, for example when a high load must be pushed in high pressure regeneration, causing an unnecessarily high pump pressure. This would explain the relatively low energetic saving of around 10% in the cited publication. The mentioned kind of situations can also lead to functional problems, for example slowdown or stop of a movement.

There are two possible ways to shift between modes; discrete or continuous:

Discrete shifting implies an instant step from one mode to another. Pressure compensators can help to suppress the impact of sudden changes in the pressure drops over the affected metering orifices. The flow path must by no means be disrupted during the mode shift, a demand that most currently available IM systems (Eaton CMA [4], Danfoss PVX [5], IM valve by Wessel Hydraulik [6]) do not fulfil. A discrete mode shift implies a sudden change in the pump flow demand on which the pump cannot react immediately because of its limited dynamics. The results are disturbances in the supply line which can negatively affect other consumers.

So the preferable way to avoid the aforementioned problems is continuous mode

switching within a certain time or load window [7]. A market solution capable of continuous mode switching is INCOVA by Husco [8], but its major drawbacks are the missing compensation of supply disturbances and its need for a pressurised tank line for energy-neutral lowering. This would be a constant source of energy losses.

A solution to enable energy-neutral lowering without pressurizing the tank line is the short-circuit-valve (SC). Such an IM valve system is not available on the market yet, even though it would reduce the number of proportional valves needed for continuous mode switching from four to three.

3. SYSTEM ARCHITECTURE AND CONTROL ALGORITHMS

This section starts with the general IM valve structure, followed by the software architecture. Afterwards the key functionalities velocity and pressure control as well as mode shifting will be explained.

3.1. General independent metering valve system

In [9] a general IM system has been proposed which consists of five flow paths (**Figure 1**), marked with arrows in the figure, together with additional paths which will be referred to later. These five flow paths are PK from pump (P) to piston side node (K), KT from piston side node to tank, PS from pump to rod side node (S), ST from rod side node to tank and KS from piston side node to rod side node. In addition to the work in [9] the two paths K and S for safety shut-off or counterbalance valves at the cylinder ports have been added. Most IM system can be classified as special cases of this system comprising all or a subset of these flow paths.

So far, according to **Figure 1**, the general IM system consists of up to seven 2/2-valves. Controlling each valve as a separate element would exclude any 3/3- or 4/3-valves. Therefore the circuit is divided into subcircuits (grey in the figure with bold names and italic ports): PATK with its ports P, A and T connects the piston side node K with pressure or tank. PATS does the same with the node S. KS is the short circuit path and the safety valves are also separate subcircuits.

The IM control software does not refer to the individual valves as actor elements but only to encapsulated control code of these subcircuits.

Hence, these subcircuits can be implemented with any hardware. The interfaces are the flows Q_i in **Figure 1** and the pressures at the ports of the subcircuits. This architecture makes the control software on axis level independent from the valve circuit layout. A change in the valve circuit layout affects only the control software of the corresponding subcircuit rather than the complete control software of the axis.

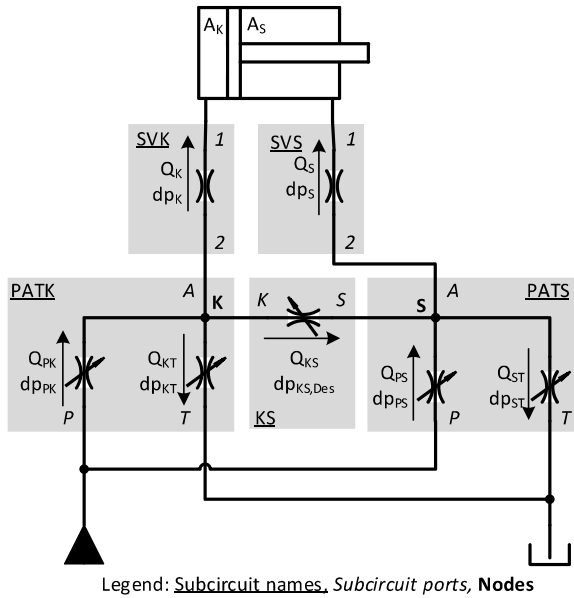


Figure 1: General independent metering valve system

3.2. Software Architecture

The architecture of the developed control software is shown in **Figure 2**. For the sake of simplicity as an example only the path from the operator input to the valve PK (see **Figure 1**) is displayed. The complete architecture comprises all axes, all subcircuits and all valves.

The top end of the control chain is the machine controller, which receives the desired velocities v_{Des} from the joysticks. The machine controller hands over the velocity commands v_{Des} to the individual axis controllers, in this case axis 1. The axis controller measures the cylinder load using pressure sensors and selects the flow mode. From the mode and velocity command it calculates the required pump flow $Q_{1,Req}$ and pressure $p_{1,Req}$ and provides these values to the machine controller. The machine controller then determines the overall pump flow $Q_{0,Req}$ and pressure $p_{0,Req}$ and sends these to the pump controller.

The axis controller also selects and executes the velocity and pressure control scheme. This

algorithm is independent from the flow mode. From the pressure and velocity controller and the current flow mode the axis controller derives the pressure, flow or conductance commands for the subcircuits (in **Figure 2** $p_{K,Des}$ and $Q_{PK,Des}$ for PATK) and hands these values over to the respective subcircuit controller, in the example PATK.

Gathering possibly required information (depending on the functionality requested by the axis controller) from assigned sensors – in the example the pump pressure $p_{P,Meas}$ the subcircuit controller calculates the set values for its valves. These are conductances K for throttling elements, pressures p for pressure control valves or volume flows Q for flow control valves.

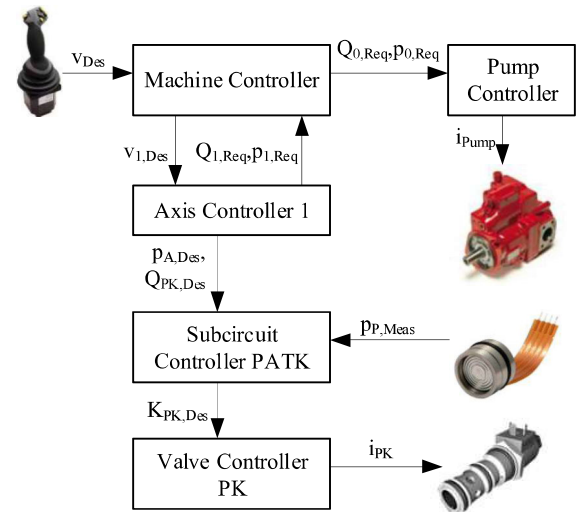


Figure 2: General software architecture

The corresponding valve controller then derives the required spool current i from the set value K , p or Q . The valve controllers can comprise calibration or learning algorithms.

With the proposed software architecture all subcircuits and their valves are completely interchangeable without affecting the axis controller as long as the overall valve circuit can be classified as a special case of the general valve layout shown in **Figure 1**.

3.3. Velocity and Pressure Control

Independent metering allows for the control of the two variables pressure level and volume flow of a hydraulic consumer independently. The IM operation strategy defines the desired inlet chamber pressure $p_{in,Des}$ and velocity v_{Des} of the actuator, while the IM control strategy calculates the required set values for the flow paths to

outlet chamber pressure $p_{Out, meas}$. With this and Q_{Out} the outlet valve's conductance K_{Out} is calculated.

Since this control scheme refers to the workports of the consumer it is independent from the flow mode – switching between flow modes only hands over the control task on the workport to another valve. Thus, disruptions of the pressure and flow control process, as encountered in [10], are circumvented.

The results of a linear MIMO coupling factor analysis in [2] showed that the velocity of resistive loads should be controlled on the inlet side and the pressure on the outlet side. With aiding loads it is advisable to swap these two functions to keep the dynamic cross-interactions between pressure and flow control minimal. To account for this, it is possible to add such a pressure and flow control swap functionality in the software if test rig results indicate the necessity to do so.

3.4. Flow modes and mode shifting algorithm

The principal approach to smooth mode shifting used here has been initially developed by Shenouda [7]. A smooth mode shift requires a continuous transition between two distinct flow modes, thus leading to a transition mode, called continuously variable mode (CVM). While Shenouda worked with a Wheatstone bridge valve circuit his approach has been adapted to a short circuit layout here. In the following the mode transition between normal extension NM+ and high pressure short circuit regeneration extension with node on piston side (hpREGscK+), both special cases of their common CVM NMhpREGscK+, will be explained as an example (Figure 4):

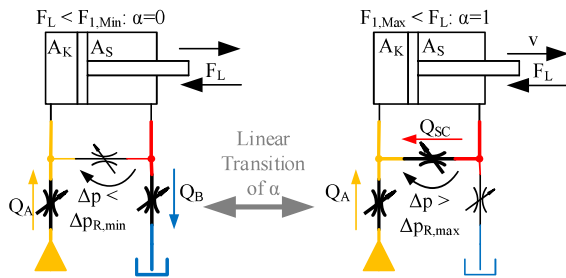


Figure 4: Flow modes during extension

The transition takes place in a load force window

$$F_{1,min} < F_L < F_{1,max} \quad (1)$$

where the force thresholds $F_{1,min}$ and $F_{1,max}$ are defined by minimum and maximum pressure drop over the short circuit path. Within this force window the mode shifting variable α transitions from 0 to 1 in a linear manner. With α between 0 and 1 three flow paths are active, since the outlet flow vA_S is divided between tank line (Q_B) and short circuit (Q_{SC}):

$$Q_A = v(A_K - \alpha A_S)$$

$$Q_B = (1 - \alpha)vA_S \quad (2)$$

$$Q_{SC} = \alpha vA_S$$

During a continuous mode transition the outlet flow is “handed over” smoothly between tank and short circuit line.

To prevent unnecessary mode switching fluctuating load forces should be filtered before comparing them to the shift level.

4. TAYLORING TO SPECIFIC APPLICATION

4.1. Sample application case and energetic potential

Sample application. As a sample application a medium sized excavator of 20 t weight has been chosen. Its hydraulic system is characterized by a relief pressure of 350 bar and peak volume flows of 200 l/min per axis. In the field of mobile machines the excavator is the most demanding machine type regarding the requirements on motion controllability: During typical excavating and handling tasks several consumers are operated in parallel under varying loads and velocities. Therefore, to exploit the full energetic potential of IM, mode shifting during movements is crucial.

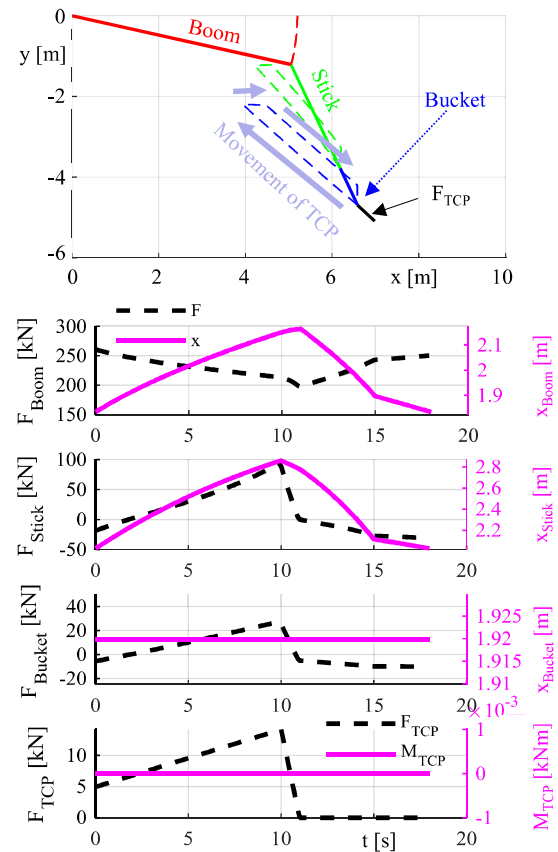
Energetic analysis. For the sake of cost and complexity reduction only the operation modes of significant energetic relevance shall be implemented. This reduces the number of required flow paths and valves and mode switching events. To identify these energetically attractive modes an energetic analysis according to [9] has been performed. Force and displacement profiles $x(t)$ and $v(t)$ serve as input for the analysis. The overall worktime of the excavator has been divided into realistic portions for different tasks. These tasks and their corresponding time shares are listed in Table 1.

Table 1: Work tasks for excavator

Work task	Time share [%]	Source of profile
Power digging	64	Experiment
Pulled levelling	10	Synthetic
Pushed levelling	10	Synthetic
Slope grading	9,5	Synthetic
Utility handling	6,5	Synthetic

The power digging task has been carried out as an experiment with the real excavator in grown soil, while the other tasks have been defined as synthetic loads and motions of the tool centre point (TCP) at the bucket tip or bucket joint respectively. These motion and load profiles of the TCP have been transformed into the corresponding cylinder profiles by means of an analytical kinematic and kinetic model of the machine. As an example for this procedure the slope grading cycle is displayed in **Figure 5**. The solid lines represent the excavator implement's position at the beginning, while the dashed lines show the movement of the links' end points over the whole cycle. The resulting cylinder forces are shown black dashed and the strokes in solid purple.

The method in [9] identifies the energetically optimal combination of flow modes and the corresponding flows and pressures for the valves according to **Figure 1** and for the pump for each time step individually, taking into account the given restrictions regarding pressure, volume flow and flow coefficient of the paths. Hence, the algorithm assumes ideal, infinitely fast switching. So far all theoretically possible modes listed in [9] are available and therefore the result is the highest theoretically possible energy saving.

**Figure 5:** Movement and cylinder loads for grading

To find an optimal combination of only a few flow modes to implement the method has been adapted: Each mode can be allowed or forbidden individually. The analysis is repeated many times automatically while systematically allowing or forbidding different modes. By doing so, an energetic ranking of different combinations of two or three flow modes in addition to the self-evident normal operation can be derived.

The low pressure short circuit regeneration (lpREGsc) and high pressure short circuit regeneration (hpREGsc) next to normal mode turns out to be a good trade-off between energy-efficiency and complexity. This way the hydraulic pump energy consumption can be reduced to 68% theoretically compared to pure normal operation.

At this point it should be kept in mind that the results of the energetic potential analysis cannot be fully achieved in reality because of the time needed for mode switching, an effect not considered in the analysis. So the result of the analysis should be interpreted as a qualitative ranking rather than quantitative numbers.

4.2. Application tailored valve system

The valve system used for the laboratory tests is depicted in **Figure 6**. For resolution purposes during slow lowering movements the meter out orifices in the subcircuits PATK and PATS as well as the short circuit flow from rod to piston side are mechanically pressure compensated. With this approach not only lowering but all movements are load compensated, as postulated in [11]. The concept described by Vucovic and Murrenhoff has been enhanced by pressure control valves in the inlet path to decouple the consumers from dynamic disturbances in the pump line. Apart from disturbance rejection the pressure control valves allow for fine pressure and force control and implement the directional switching function. Depending on the requirements on resolution and fine control and the characteristics of the used valves pressure and flow control could also be implemented electronically, like implied in **Figure 3**.

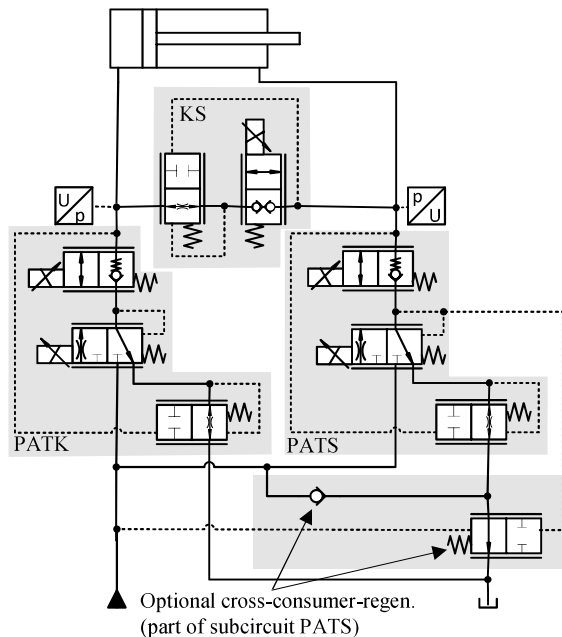


Figure 6: Test rig valve setup

The cross-consumer-regeneration subcircuit in the lower right corner of **Figure 6** is an optional element that reroutes the outflow during a lowering movement (piston retraction with aiding load) back to the pump line to supply other consumers, in case the outflow pressure is higher than the pump pressure. In this case the switch valve in the lower right corner closes and the outflow oil passes the check valve to the pump line instead of flowing into the tank. In the control

architecture the cross-consumer-regeneration-element belongs to the subcircuit PATS.

5. SIMULATIVE EVALUATION

5.1. Simulation model and method

The valve system has been modelled as a 1D-system with concentrated parameters, using the software-environment ESI SimulationX. For the simulations the circuit depicted in **Figure 6** has been implemented for the boom, stick and bucket cylinder of an excavator arm, with the cross-consumer-regeneration-element only in the boom circuit since the boom is the only consumer with reasonable energetic recovery potential.

As throttling elements internally piloted seat valves are used and modelled as physical systems. The system is supplied by a displacement-controlled pump. Its control algorithm is designed as a feed-forward flow-matching-control combined with an LS-pressure-controller, an adaption of the suggestions in [12]. The control code runs on a CoDeSys-based virtual ECU with a sampling time of 10ms. The ECU communicates with the simulation model via an OPC-server.

The cylinders move constant reduced masses of the example-excavators work implement (see section 4.1). For simulation of the work cycles of section 4.1 the velocity signals $v(t) = dx(t)/dt$ are fed to the controller while the forces $F(t)$ are acting on the cylinders at the same time. Individual PI position controllers for each axis act as a virtual operator who tries to follow the given position trajectories $x(t)$ as close as possible.

A conventional flow sharing LS-system of similar size serves as a reference for comparison purposes. It's LS pressure margin is $\Delta p_{LS} = 16$ bar.

5.2. Results

Velocity Tracking. The simulation results for a pushed levelling cycle are shown in **Figure 7**: The reference trajectory $v_{Des}(t)$ is plotted with a black dotted line.

The conventional system's input velocity command is represented as a red dashed line while the actual velocity is red solid. The ideal behavior would be a perfect fit between reference, velocity command and actual velocity.

However, especially during the lowering period of the boom between 4-8 and 12-15 s the actual velocity is much higher than the command. This is due to the load-dependent flow over the meter-out-edge of the spool valve.

The behaviour of the proposed novel IM system is represented by the green lines, dashed for command and solid for actual velocity. As can be seen the actual velocity is much closer to the command due to the compensation of both resistive and aiding loads by the meter-out pressure compensation.

Even though an experienced operator is able to control a conventional system quite well, the machine itself – for the purpose of automation – cannot. Especially in this case the IM system has clear advantages.

Mode Transition. Figure 8 shows the chamber pressures (red and green), the pump pressure p_0 (black dashed) and the volume flow from the pump to the corresponding consumer (black solid) for the IM systems on boom and stick during the pushed grading cycle from Figure 7. Furthermore, the plot is divided into several time sections, in which the IM circuits run in different flow modes (grey lines and headings).

An example for a mode shift during an ongoing movement can be seen at around 12 s:

From 8,5 to 12 s the boom lifts (see Figure 7 top) and thus raises the pump pressure p_0 to a high level of around 100 bar (Figure 8). The stick cylinder moves against a much lower load, causing the rod pressure to be much higher than the piston pressure (Figure 8 bottom). In this condition the stick operates in high pressure regeneration hpREGscK+. Once the boom stops extending at 12 s the pump pressure drops and so do the stick chamber pressures. The stick shifts back into normal operation NM+ smoothly, as can be seen at the continuous raise of its pump flow (black solid) between 12 – 12,5 s in Figure 8 bottom. The shifting event has only little impact on the cylinder velocity (green solid in Figure 7 bottom).

Energy efficiency. In the simulated pushed levelling cycle the novel IM system has saved 36% hydraulic pump output power compared to the conventional flow sharing system. This is mainly achieved by the reduction of pump flow by means of regenerative flow modes. In the whole operation cycle defined in section 4.1 approximately 30% have been saved. An exact number cannot be given because the measured digging cycle, which has been used for the potential analysis as a whole, is very long and

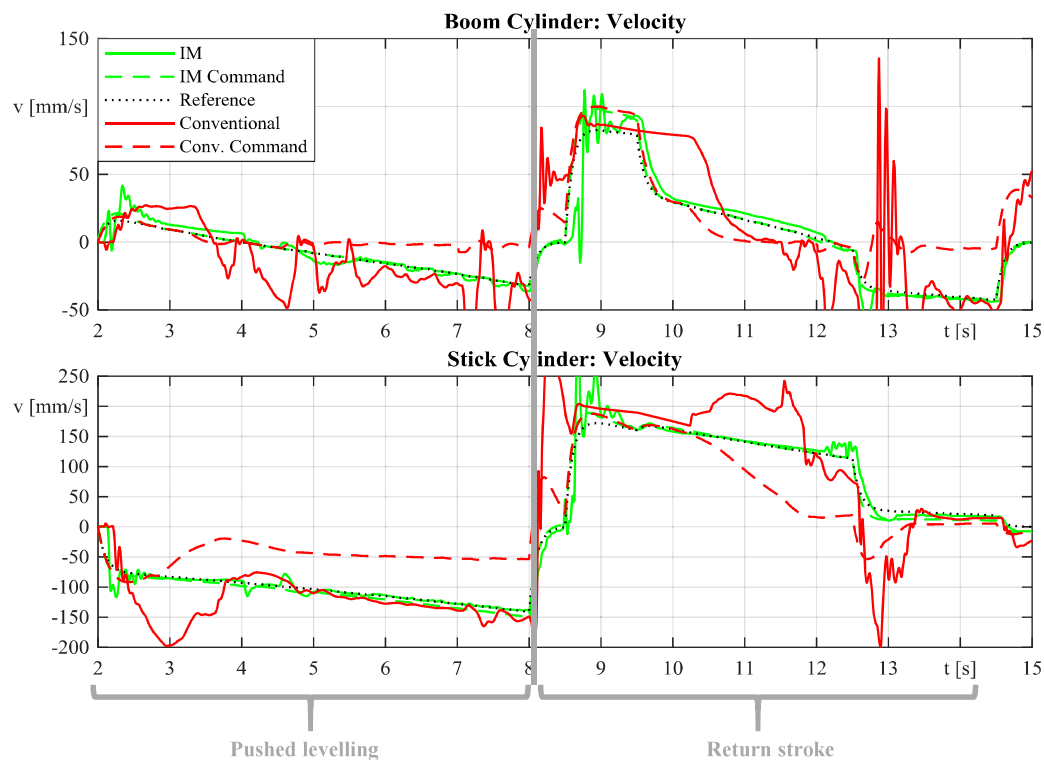


Figure 7: Velocity tracking during pushed levelling for conventional flow sharing and novel IM system

therefore has not been completely simulated with the valve system model in section 5.1.

6. SUMMARY AND OUTLOOK

Smooth mode switching plays a major key role in exploiting the benefits of independent metering, especially in mobile applications. In this project, the approach of continuously variable modes in [7] has been adapted to a valve layout with short circuit path, thus enabling smooth switching with only three proportional flow paths. A flexible software structure has been derived from a general valve structure. The software is able to control a very broad variety of IM valve circuits. According to the results of an energetic analysis for typical work cycles of a medium sized excavator the three modes normal operation and high and low pressure short circuit regeneration have been identified as a good trade-off between cost and engineering effort on the one hand side and energy efficiency on the other.

On the basis of these results and functional requirements a valve layout for excavators has been developed and set up on a test rig. While the test rig is still under commissioning, 1D-simulations with concentrated parameters already show promising results: Smooth mode switching with very low impact on the velocity and up to 36% reduction of hydraulic pump output energy. Measurements in terms of mode transition,

velocity tracking, force control and energy efficiency will be carried out soon within 2020.

NOMENCLATURE

0		Supply line
A	mm^2	Piston Area
α		CVM shift variable
CVM		Continuously Variable Mode
Des		Desired
F	N	Force
IM		Independent Metering
K		Piston side
K	$l/(min \cdot \sqrt{bar})$	Flow Coefficient
LS		Load Sensing
$meas$		Measured
OC		Open Centre
P		Pump
p	bar	Pressure
PC		Pressure Control
Q	l/min	Volume flow
Req		Required
S		Rod side
T		Tank
t	s	Time
TCP		Tool Centre Point
v	mm/s	Velocity
x	mm	Position

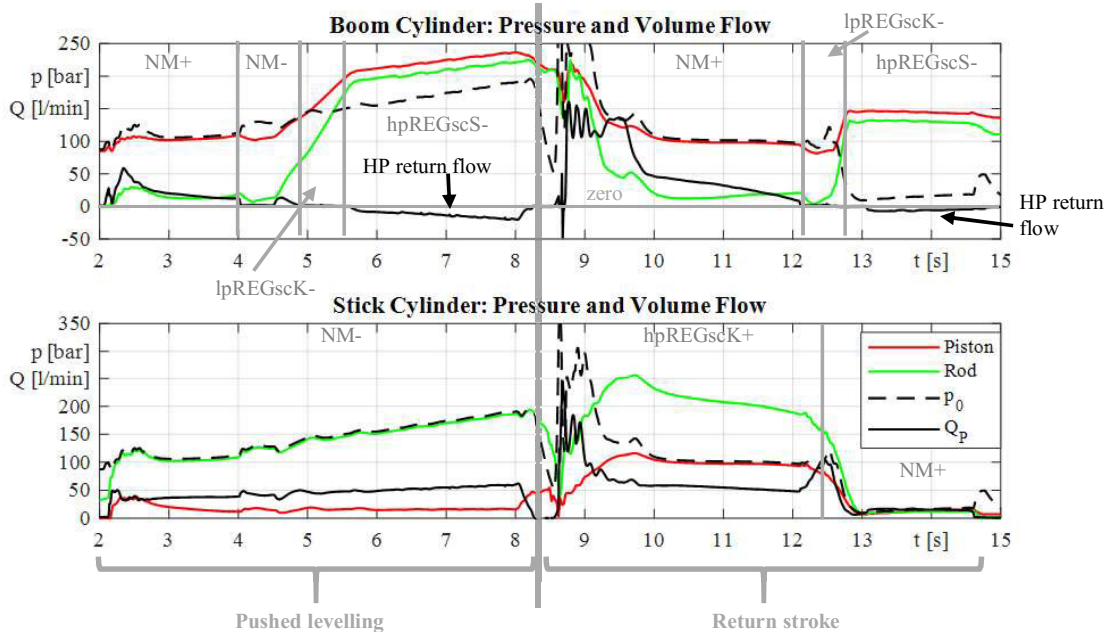


Figure 8: Chamber pressures and flow modes of IM system during pushed levelling

REFERENCES

1. Finzel R (2010) Elektrohydraulische Steuerungssysteme für mobile Arbeitsmaschinen. Dissertation, TU Dresden
2. Sitte A, Weber J (2013) Structural design of independent metering control systems. In: Proceedings of the 13th Scandinavian International Conference on Fluid Power. Linköping (S)
3. Lee J-C, Jin K-C, Kwon Y-M, et al (2016) Development of the Independent Metering Valve Control System and Analysis of its Performance for an Excavator. In: Proceedings of the BATH/ASME 2016 Symposium on Fluid Power and Motion Control. Bath, UK
4. EATON CMA200 Advanced Independent-Metering Mobile Valve. Product data sheet by EATON Company.
https://www.eaton.com/ecm/groups/public/@pub/@eaton/@hyd/documents/content/pct_1451917.pdf. Accessed 11 Feb 2019
5. Danfoss (2016) Proportional Valve PVX (product data sheet).
<https://assets.danfoss.com/documents/DOC152986483080/DOC152986483080.pdf>
6. Wessel Hydraulik GmbH (2013) Proportional valve with Autonomous Spools (Product data sheet).
http://www.hydpac.com/lib/common/download.php?fpath=/data/bbs/solution/237.pdf&fname=Informationsbrochure_PAS_20_28EN_29.pdf
7. Shenouda A (2006) Quasi-Static Hydraulic Control Systems and Energy Savings Potential Using Independent Metering Four-Valve Assembly Configuration. Dissertation, Woodruff School of Mechanical Engineering, Georgia Institute of Technology
8. Husco (2007) INCOVA® Hydraulic Control System for Excavators (Product data sheet by Husco).
<http://hydrodream.ru/upload/iblock/e56/e5619a3a7f4f1aed0b1be538c1b0e743.pdf>. Accessed 3 May 2019
9. Kolks G, Weber J (2016) Modiciency - Efficient industrial hydraulic drives through independent metering using optimal operating modes. In: Proceedings of the 10. International Fluid Power Conference. Dresden
10. Ding R, Xu B, Zhang J, Cheng M (2016) Bumpless mode switch of independent metering fluid power system for mobile machinery. *Autom Constr* 68:52–64
11. Vukovic M, Murrenhoff H (2014) Single Edge Meter Out Control for Mobile Machinery. In: Proceedings of the ASME/BATH 2014 Symposium on Fluid Power & Motion Control FPMC2014. Bath (UK)
12. Djurovic M (2007) Energiesparende Antriebssysteme für die Arbeitshydraulik mobiler Arbeitsmaschinen – „Elektrohydraulisches Flow Matching“. Dissertation, TU Dresden

DEVELOPMENT OF A HYDROSTATIC TRANSMISSION WITH INTEGRATED SUPPLY FOR WORKING HYDRAULICS

Jihao Guo*, Ludger Frerichs

Institute of Mobile Machines and Commercial Vehicles, Technische Universität Braunschweig, Langer Kamp 19a, 38106 Braunschweig

* Corresponding author: Tel.: +49 531 3917196; E-mail address: j.guo@tu-braunschweig.de

ABSTRACT

The paper presents a study of a highly integrated hydraulic powertrain for mobile working machines. The highlight of this new concept is the replacement of separated drive and working pumps in conventional systems with only one displacement pump. After a comparison of different system architectures, the appropriate operating and control strategies for the chosen topology were applied and optimized. With the help of simulations in AMESim, a proof of the function of the hydraulic circuit and the controlling has been established. In addition, the energy saving potential of the integrated hydraulic system is also considered, by comparing the energy consumption of the new and the conventional powertrain in different duty cycles.

Keywords: Mobile Hydraulics, Integrated System, Energy Efficiency

1. GENERAL INSTRUCTIONS

The reduction of fuel consumption and emissions from construction equipment is required - from a global perspective - due to the lack of fossil resources and the problems of global warming. On the other hand, the industry is making effort to build mobile working machines with lighter and more compact constructions. For the achievement of above-mentioned goals, a concept of an integrated hydraulic drivetrain has been developed.

The widely used powertrain in construction machines mainly consists of two separate subsystems - a closed circuit for traction drive and an open circuit for working functions, which are connected by a shaft between the drive and working pump [1]. A power exchange between them is only possible with significant energy losses, because of the double conversion between hydraulic and mechanical energies.

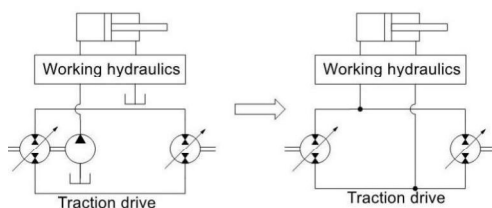


Figure 1: Schematic representation of the project idea

The aim of this research project is to develop a hydrostatic transmission with an integrated supply of working hydraulics for mobile machines. This means that both the traction drive and the hydraulics for working functions are supplied only by one hydraulic pump (as shown in **Figure 1**). Besides the benefit of component saving, a flexible flow rate and power distribution without additional hydraulic components is possible. The peak flow rate and power for driving or working functions are not restricted by the dimension of the corresponding pump as well. Furthermore, the regenerated energy from braking actions could be used directly e.g. in a wheel loader for raising the bucket or for steering.

In this paper, integrated systems with different kinds of basic circuits (closed or open) are compared and evaluated. Appropriate scales of components or sub-systems have been chosen for the selected topology. The hydraulic circuit and the control strategy of the hydraulic pump and motor are modeled in AMESim with rational simplification and parameterized with parameters given by the manufacturer. The simulations demonstrate the performance and the energy saving potential of the new hydraulic powertrain by different applications. After analyzing the dynamic properties of the system shown in the

simulation results, optimization potentials and possibilities for simplification are discussed.

2. DESIGN OF SYSTEM TOPOLOGY

The drive and working hydraulic circuit of the new drivetrain must be directly connected by hydraulic lines, as the whole system is supplied by only one variable displacement pump. Therefore, the architecture of the circuits should be adapted, thus the two subsystems could be operated independently.

2.1. Topology of the working hydraulic system

In the partial load range, a Closed Center Load Sensing System (CC-LS) has a higher efficiency comparing with an Open Center Load Sensing System (OC-LS) due to the adjustment of pump flow rate to the demands of the cylinders [2]. Therefore, the efficiency of the working hydraulics in conventional drivetrain (OC-LS) could be significantly improved, if the supply unit is replaced by a variable displacement pump (CC-LS). As a variable displacement pump is necessary for the traction drive, a working hydraulic with CC-LS system could be applied in the integrated drivetrain without additional components.

2.2. Topology of the traction drive

The hydrostatic transmissions in mobile applications are generally closed circuits, by which the driving direction could be changed with the reversible drive pump [3]. However, the suction and the discharge sides exchange by every reverse, which is an unfavourable condition for the new integrated system. A directional control valve is necessary between the traction drive and working hydraulics, otherwise the direction of the flow in working hydraulics would be influenced by reverses of the driving direction. The requirement of the directional valve is extremely high, as the pressure by switching could be higher than 400 bar [4], which is normal in hydrostatic transmissions in mobile working machines. Another difficulty for an integrated system with closed circuit is to balance the difference of flow rate in loop, which is caused by differential cylinders in the working hydraulic system.

For the reasons mentioned above, a traction drive with open circuit (shown in **Figure 2**) is considered. The challenging point of this architecture would be the reverse of the driving direction. Switching with valves in main circuit is difficult because of the high operating pressure. Additional mechanisms, for example reverse gear unit, means there are not only more cost and packaging space, but also much lower dynamic. The system performance by applications with frequently reverse or switching between acceleration and deceleration could not be guaranteed. Another possibility is by using reversible drive motor instead of pump. The direction of flow in main circuit or rather the driving direction is adjusted by the direction of swivel angle of the hydraulic motor, while the high pressure remains on the same side. Unfortunately, such reversible drive motor (in swash plate form) for mobile application is not yet in mass production because of its lower efficiency and speed range comparing to axial piston motors. Therefore, reversible motor for industry application is used in the first step of the research for the purposes of verification of functionality.

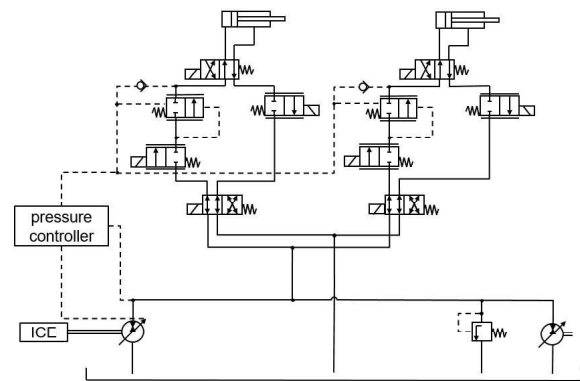


Figure 2: Simplified system topology of the new powertrain

2.3. Selection of components and determination of dimension

A secondary control shown in the **Figure 3** has been chosen as the basis of the integrated drivetrain, as the pressure controller of pump and speed/torque controller of motor the demanding requirements of response speed fulfill can. Bosch Rexroth A4VSO axial piston units with 315 bar nominal pressure are used as pump and drive motor. The accumulator, which is used to cover flow peaks [5], should be downsized in

consideration of the limited packaging space. The both axial piston units work with 16 bar pre-supply pressure, in order to cover a wider speed range.

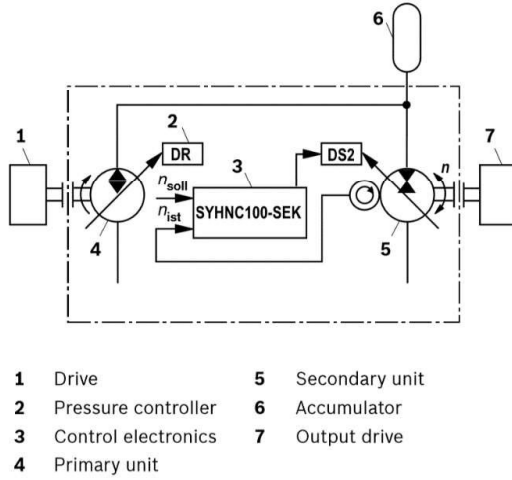


Figure 3: Schematic representation of the Bosch Rexroth secondary control [5]

The dimension of hydraulic components is determined according to the reference machine, a wheel loader in power class 40 ~ 50 kW. Comparing to conventional powertrain, the hydraulic pump in new system should have a larger dimension, to enable the supplying of traction drive and working hydraulics at the same time. Taking account of the available size of the series, axial piston units with 71 cm³ displacement have been used as both pump and drive motor.

3. DESIGN OF CONTROL STRATEGY

The design of the control strategy for the new powertrain is based on the controller in existed secondary control system. The torque/speed control for hydraulic motor can also be used in mobile applications. The drivetrain delivers torque proportional to accelerator pedal or according to the difference between actual and desired speed. On the other side, a pressure controlled pump is used for achieving the demand oriented supply in the working hydraulics. In consideration of the efficiency of both axial piston units, which is relevant to their opening degrees, the system should work with variable pressure. Therefore, the control requires not only a torque/speed but also a pressure specification as input variables. In the case of reaching the power or flow rate limitation, the priority of working hydraulics will be guaranteed by the timely swivelling back of the drive motor. To avoid the

undersupply of pump, which causes significant pressure drop in system, a control strategy for limiting the motor swivel angel should be developed.

3.1. Control strategy to determinate system pressure

The system pressure is dependent on both traction drive and working hydraulics, because of the direct connection between two subsystems. The pressure in the working hydraulics (CC-LS system) is determined by the loads on cylinders. The output torque of the traction drive is proportional to the product of displacement volume of the hydraulic motor and the system pressure. As the axial piston units have higher efficiency by larger swivel angles, the pressure in traction drive should be kept as low as possible. Furthermore, throttling losses between the two subsystems could be minimized, if they require a similar pressure. As the pressure class in traction drive is generally higher than working hydraulics, a possible lower target pressure in traction drive has the benefit of higher efficiency.

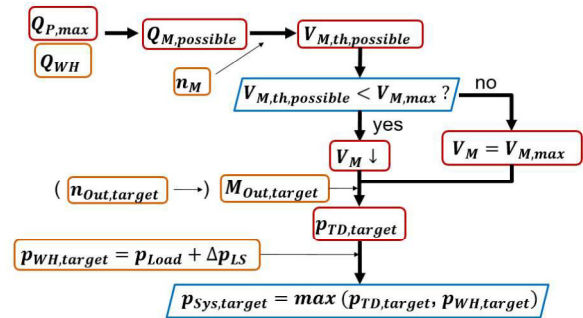


Figure 4: Schematic representation of the control strategy [6]

The control strategy shown in **Figure 4** is used for the definition of the target system pressure $p_{Sys,target}$. For safety reasons, the supply for the working hydraulics (incl. steering system) should be always be guaranteed. Therefore, the maximal available flow rate for traction drive $Q_{M,possible}$ is calculated with Equation 1:

$$Q_{M,possible} = Q_{P,max} - Q_{WH} - Q_{acc,charge} = n_P V_{P,max} - k_{WH} Q_{WH,max} - Q_{acc,charge} \quad (1)$$

In the next step, the swivel angle of the drive motor is adjusted according to the available flow rate and its current shaft speed, in order to avoid undersupply of the pump. Equation 2 represents

the maximum allowed displacement of the drive motor.

$$V_{M,th,possible} = \frac{Q_{M,possible}}{n_M} \quad (2)$$

If the motor controller is in torque control mode, the target pressure of traction drive $p_{TD,target}$ can be defined with Equation 3. The target output torque $M_{Out,target}$ depends on operations (for example acceleration pedal) of the driver. Considering the nominal pressure of the secondary control system, the value will be restricted in the range of 20 ~ 315.

$$p_{TD,target} = \frac{2\pi M_{Out,target}}{V_{M,th,possible}} \quad (3)$$

However, further equations are necessary for establishing mathematical relation between the target rotary speed of the hydraulic motor and the target torque, if the controller is in speed control mode. This part will be explained in detail in chapter 3.2.

On the other hand, the target pressure in the working hydraulics could be defined with Equation 4:

$$p_{WH,target} = p_{Load} + \Delta p_{LS} \quad (4)$$

The target system pressure should follow the higher value:

$$p_{Sys,target} = \max(p_{WH,target}, p_{TD,target}) \quad (5)$$

If $p_{TD,target} > p_{WH,target}$, the unnecessary pressure for working hydraulics would be throttled by pressure compensator valves in the CC-LS system. On the contrary, the displacement of the drive motor must be further reduced, in order to keep the output torque in its target value, as the pressure in traction drive could not be throttled.

3.2. Strategy for speed control of the drive motor

As mentioned above, the relation between target speed and target torque still needs to be established. The output torque of the drive motor actually means the accelerating ability or in other words, the ability, to compensate the difference between the current and the target speed. Therefore, the target pressure of traction drive, which is proportional to target torque, should also demand on the speed difference.

$$p_{TD,target} = fx(M_{out,target}) = fx(\Delta n) \quad (6)$$

By selecting function form and setting parameters in Equation 6, the following criterions should be considered:

1. the traction drive must deliver appropriate torque, in order to compensate the speed difference in acceptable time without overshoot
2. the target pressure should be possibly slow varied, in order to avoid extremely high dynamic demands on secondary control system

With the help of simulation, the following two functions are selected for the determination of target pressure in traction drive:

- Linear: $\{p_{TD,target}\} = 2 * \{\Delta n\}$ (7)

- Cubic: $\{p_{TD,target}\} = \frac{\{\Delta n\}^3}{5000}$ (8)

with $\{p_{TD,target}\}$ in bar, $\{\Delta n\}$ in min^{-1}

The performance of these two control strategies will be shown and compared in chapter 4.

4. VERIFICATION OF FUNCTIONALITY

The function of the system architecture and control strategies has been proofed by means of computer simulations. In the first step, a model of the hydrostatic drive with the whole control strategy is built in AMESim. Secondly, the performance of the system by various applications is tested with the help of the measuring data from example machine. Finally, the control quality of different strategies is compared and evaluated.

4.1. The Simulation Model of the integrated system

As the research focuses on the power distribution between the traction drive and the working hydraulics, it is not necessary to build the internal structure of working hydraulics in detail. Which means, the flow rates in lift, dump and steering cylinder are considered as a whole. The total flow in working hydraulics is emulated by a flow control valve. The pressure in working hydraulics, which depends on the highest pressure load, is simulated with the help of a pressure relief valve. In the integrated powertrain, the recuperated energy from the working hydraulics is available for traction drive. Therefore, a model for return flow is built and connected with the high pressure side.

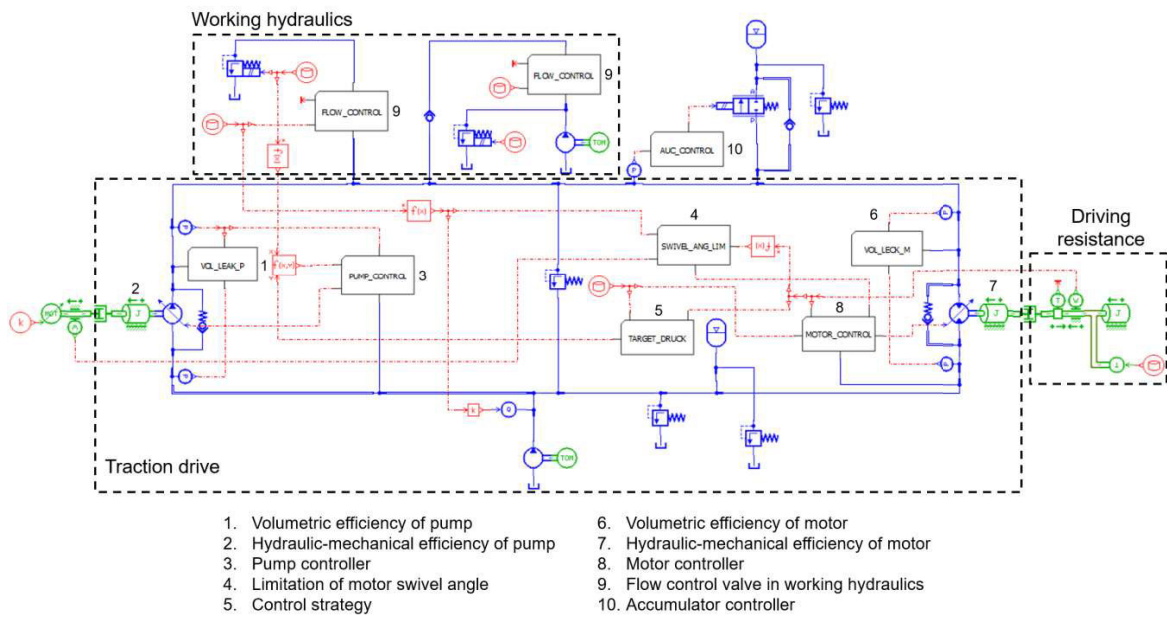


Figure 5: Simulation model of the integrated system

In order to analyse the energy saving potential of the new system, the efficiency of the axial piston units is considered in the simulation model. The flow source and the rotary load simulate respectively the volumetric and the hydrodynamic and mechanical losses. The leakages of valves, accumulators and pipelines are ignored.

After modelling the hydraulic components and circuit, simplified models of controllers of the axial piston units are built. The pressure control of the pump is realized by PID controller. The target pressure is calculated with the strategy mentioned in chapter 3.1. The controller of the motor is built on the basis of the Bosch Rexroth secondary control. Additionally, the limitation of motor swivel angle is considered according to the current displacement of pump, in order to avoid the undersupply in system.

The entire model shown in **Figure 5** consists of the hydraulic circuit, controllers for both axial piston units, the load on working hydraulics and the driving resistance. The load, driving resistance, and (target) speed profiles are generated according to the given measurement data.

4.2. Proof of functionality and discussion

The functionality of the system architecture and the speed control strategy are proven with the help of the model mentioned in chapter 4.1. For a

better simulation of the practical applications of the wheel loader, the following duty cycles (Y, Load & Carry and VDI forklift cycles [7]) are considered.

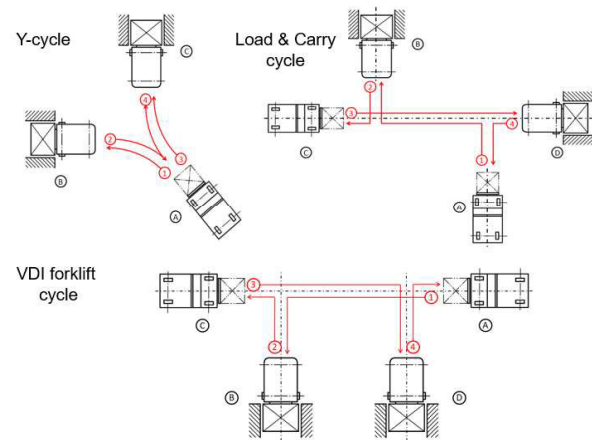


Figure 6: Duty cycles of wheel loaders

The outputs of the new powertrain – the rotary speed of the hydraulic drive motor and the flow rate in working hydraulics, have been compared with the conventional (measurement data), under the assumption of same load profile in the duty cycle. The verification of functionality of the integrated powertrain with both control strategies are shown below in **Figure 7** and **8** (red, dashed – target value; green, solid – actual value, $\{p_{TD,target}\} = 2 * \{\Delta n\}$ and black, dotted – actual value, $\{p_{TD,target}\} = \{\Delta n\}^3 / 5000$).

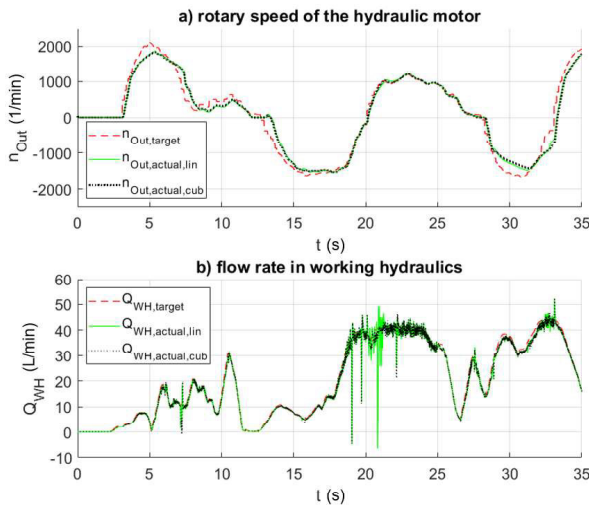


Figure 7: Verification of functionality of the new system by application of Y-cycle

As shown in **Figure 7**, the hydraulic powertrain with integrated supply provides a similar performance as the conventional powertrain in wheel loaders. The new system is implemented with both control strategies mentioned in chapter 3.2 (Equation 7 and 8). As the system pressure is proportional or cubical to speed deviation according to the chosen control strategy, the steady-state error of the rotary speed (delay) cannot be completely eliminated. The swivel angle of the hydraulic motor must be timely decreased by working in the high-speed range, in order to avoid a pressure drop in traction hydraulics, which leads to less output torque or slower acceleration shown in the diagram at the time of 5 and 30 s (**Figure 7(a)**). The rapid change of target system pressure shown in **Figure 8**, which increases the demands on pressure controller of the hydraulic pump, is caused by the varying rotary speed deviation. The delay and overshoot of the pressure control leads to the vibration of flow rate in working hydraulics at around 20 s (**Figure 7(b)**).

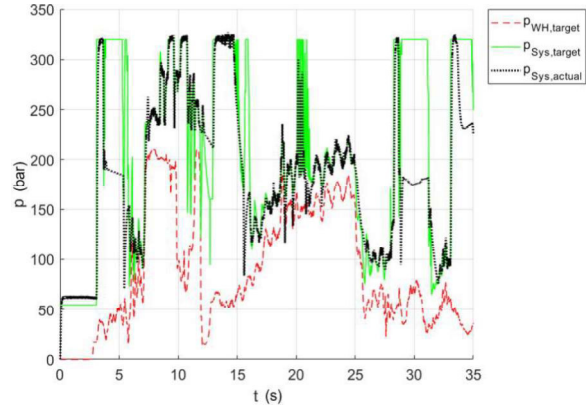


Figure 8: Target and actual pressure in system by application of Y-cycle ($\{p_{TD,target}\} = 2 * \{\Delta n\}$)

As shown in **Figure 7(a)**, both control strategies meet the requirement of the speed control. The strategy with cubic function has the advantage that, the target pressure changes rapidly only if the speed deviation is already high. Therefore, this strategy has generally lower dynamic requirements on the pump controller, which also means less vibration of flow rate in working hydraulics (**Figure 7(b)**).

4.3. Optimization potentials and possibilities for simplification

As shown in **Figure 8**, the actual pressure in system is much lower than the target value around 5 and 30 s. The possible solutions of the problem are either optimizing the motor controller for faster response, or increasing the reserved flow rate for working hydraulics (Q_{WH} in Equation 1) and accumulator ($Q_{acc,charge}$ in Equation 1) by means of introducing safety factor for an earlier beginning of the swing back of the hydraulic motor. Generally, the target pressure changes fast according to the control strategy, which means high dynamic requirements on the pump controller. In addition, the accumulator retards the pressure change in system, which makes the rapidly changing target pressure even harder to achieve. Therefore, the control strategy should be optimized, in order to avoid frequently step changes or oscillations between 20 and 22 s. On the other hand, the accumulator, which stabilizes the pressure in constant pressure secondary control, should be downsized or completely renounced. Its function of covering flow peaks should be achieved with additional swivel angle control of the pump.

5. ENERGIE SAVING POTENTIAL OF THE NEW POWERTRAIN

After proofing the functionality of system topology and control strategy, the efficiency of the new powertrain has been compared with the conventional system. In the reference machine, the working hydraulics will be supplied by a separate constant working pump.

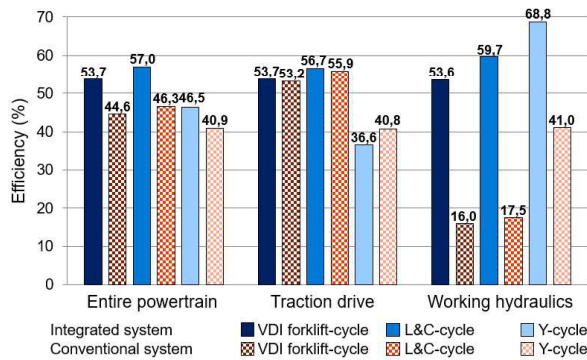


Figure 9: Efficiencies of the new and conventional powertrains by different applications

Figure 9 shows the efficiency comparison of the new and conventional systems by different applications. The efficiency of working hydraulics increases drastically, due to the appropriate and adequate supply of the variable pump. As shown in **Figure 10**, the recoverable energy by deceleration is relatively less compared to the total consumption. For this reason, the efficiency of the traction drive has not been improved apparently in spite of its direct connection with working hydraulics. In summary, the entire system has a saving potential of 6 ~ 10 %, mainly due to the enhancement of working hydraulics.

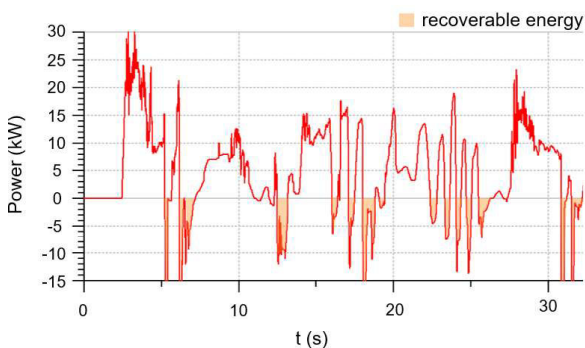


Figure 10: Recoverable energy in traction drive (Y-cycle)

The efficiency enhancement of working hydraulics is on account of the demand-oriented supply, as the variable pump is used. The

indicated orange fields in **Figure 11** are the saved flow by contrast with the working hydraulics in conventional powertrain. In the integrated system, the system pressure (both traction drive and working hydraulics) in the connected subsystems is always oriented to the higher target value. Considering the common duty cycles, the traction drive usually has a higher pressure level. Therefore, the pressure losses in working hydraulics in the integrated system are higher, comparing to a CC-LS system with separate variable pump. However, the energy losses have not increased clearly, as the required flow rate for working hydraulics is usually low, when the traction drive demands a higher pressure level (**Figure 11**). Hence, a relative high energy saving potential of the working hydraulics can be seen in **Figure 9**.

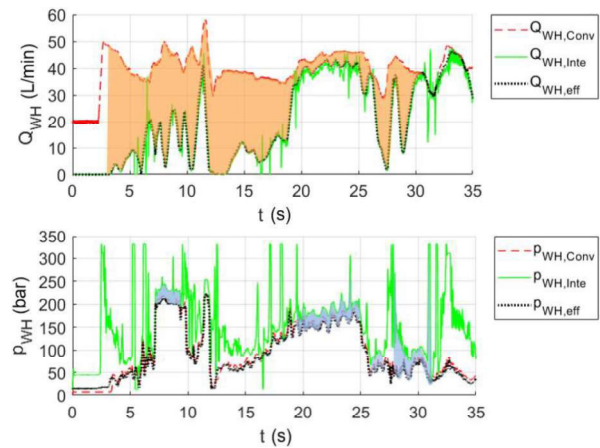


Figure 11: Pressure and flow losses in working hydraulics of the integrated and conventional powertrain (Y-cycle)

6. CONCLUSION AND OUTLOOK

The paper presents the development of a hydrostatic transmission with an integrated supply of working hydraulics for mobile machines. Considering the possible influences on the working hydraulics by reversion, the new drivetrain is developed on basis of the secondary control system with open circuit. After determination of the strategy for pressure and torque/speed control of the hydraulic pump and motor, the functionality of the whole system has been proofed with simulation. The new system can meet the requirement of common duty cycles of wheel loaders. However, the control strategy should be further optimized, in order to downsize the accumulator and reduce the dynamic requirements on the axial piston units. To

evaluate the energy saving potential, the efficiency of the new and conventional system is calculated with the help of simulation models. The integrated system provides an efficiency enhancement of 6 ~ 10 %, as the flow in working hydraulics is supplied as required.

In the following step, the functionality of system architecture and control will be validated on the test bench. The operating and control strategy will be adjusted and optimized according to the system dynamics in practice. On the other hand, the possibility of renouncement of accumulators and other methods to simplify the system topology will be examined. Finally, an integrated system with components for mobile applications will be implemented.

7. ACKNOWLEDGEMENTS

The content of this contribution is mainly based on the research project “Leistungsverzweigter Fahrtrieb mit integrierter Versorgung der Arbeitsantriebe für mobile Maschinen”, IGF-Vorhaben Nr. 18092 N/1. The authors would like to thank the research association Forschungskuratorium Maschinenbau e. V. – FKM, the Forschungsvereinigung Baumaschinen und Baustoffanlagen of the VDMA and the belonging companies for supporting the project.

NOMENCLATURE

$CC-LS$	Closed Center Load Sensing
k_{WH}	Opening degree
$M_{Out,target}$	Target output torque [Nm]
n_M	Rotary speed of drive motor [1/min]
$n_{Out,target}$	Target output rotary speed [1/min]
n_P	Rotary speed of pump [1/min]
$OC-LS$	Open Center Load Sensing
p_{Load}	Load pressure [bar]
$p_{Sys,target}$	Target system pressure [bar]
$p_{TD,target}$	Target pressure of traction drive [bar]
$p_{WH,target}$	Target pressure of working hydraulics [bar]
$Q_{acc,charge}$	Charging flow rate of the accumulator [L/min]
$Q_{M,possible}$	Maximal available flow rate for traction drive [L/min]
$Q_{P,max}$	Maximal pump flow rate [L/min]
Q_{WH}	Flow rate in working hydraulics [L/min]
$Q_{WH,max}$	Maximal flow rate in working hydraulics [L/min]
V_M	Displacement of motor [cm ³]
$V_{M,max}$	Maximal displacement of motor [cm ³]

$V_{M,th,possible}$	Maximal allowed displacement of drive motor [cm ³]
$V_{P,max}$	Maximal displacement of pump [cm ³]
Δn	Rotary speed difference [1/min]
Δp_{LS}	Load Sensing pressure [bar]

REFERENCES

- [1] N.N (2010) Shop Manual: KOMATSU VEBM550101, 2010-11. pp: 10-7.
- [2] Frerichs L (2018) Ölhydraulik - Schaltungen und Systeme. Vorlesungsskript Institut für mobile Maschinen und Nutzfahrzeuge, TU Braunschweig. pp: 74-76.
- [3] Findeisen D (2006) Ölhydraulik: Handbuch für die hydrostatische Leistungsübertragung in der Fluidtechnik. 5., neu bearbeitete Auflage. pp: 18-29.
- [4] Roos L, Untch J (2012) Traktorhydraulik. In: Frerichs, L. (Hrsg.): Jahrbuch Agrartechnik 2012, pp: 1-10.
- [5] N.N (2012) Data Sheet: Bosch Rexroth RE 92057/12.2012
- [6] Guo J, Kossen H.N, Frerichs L (2018) Aufwertung hydraulischer Antriebe am Beispiel Radlader. 10th MHK, Braunschweig.
- [7] VDI-Richtlinien 2198 (2012) Typenblätter für Flurförderzeuge.

GROUP 13 | 15

Actuators & sensors

GENERAL LECTURE:

MEMS SENSORS IN HYDRAULICS, AN OPPORTUNITY TO CREATE SMART COMPONENTS

Giorgio Massarotti¹, Cristian Ferrari¹, Esteban Codina Macia², Massimiliano Ruggeri^{1*}

¹*Institute for Agricultural and Earthmoving Machines - CNR, via Canal Bianco 28, 44124 Ferrara – Italy*

²*LABSON-UPC- Campus de Terrassa (Barcelona) - c/Colon 7-1, 08222 Terrassa - Spain*

* Corresponding author: Tel.: +39 0532 735631; E-mail address: massimiliano.ruggeri@cnr.it

ABSTRACT

Modern electronic technologies allow for the design and production of Micro Electro-Mechanical Systems, also called MEMS. These microchips are widely used as sensors in many fields of application, also in embedded systems in heavy-duty and agricultural vehicles and in automotive applications. In addition to the classic uses of these sensors, new architectures and sensor topologies exploit electromechanical principles of great interest for the field of hydraulic applications. This paper presents some examples of the application of a new MEMS architecture based on self-oscillating micro-resonators, which offer interesting capabilities in the measurement of mechanical deformation of mechanical components. MEMS are applied as non-invasive pressure and oil flow sensors, and represent an interesting option for creating smart components. All the applications described are intended to show the sensor's potential and have a qualitative and exemplary character, but they can provide a basis for in-depth studies on the potential and applicability of these sensors.

Keywords: MEMS, DETF, Sensors, Flow, Pressure, strain

1. INTRODUCTION

Sensors and sensorization are two of the most important keywords for future components and systems in hydraulic and mechatronic applications. There are several reasons to invest in sensors. One of the first reasons is that, considering functional safety standards both for earthmoving and construction machines ([1] and [2]), agricultural machines [3] and the automotive sector [4], including newly approved [5] (the ones soon to come into effect), it is clearly impossible to reach a high performance level in terms of functional safety, without a wide diagnostic Coverage (DC); DC is only possible through direct observation, then through sensors.

The second reason, which is probably the most evident to customers and users, is performance: machine manufacturers demand for hydraulic systems performing better in terms of precision, dynamics and efficiency. Precision control and the best working point can be obtained only with sensors and a high level of system observability. Finally, yet importantly, confidence in reliability

is still an open point for many products. For new products there is no historic information on lifetime and product fatigue testing under real working conditions, due to the use of accelerated tests, the only ones compatible with time-to-market requirements. Interest in sensors is growing not only in mechatronics, but also in the whole field of electronics applications. The most important industry associations in the European Community, like Ecsel, Artemis, Penta and Eposs, are promoting research on sensors through specific calls in H2020 related programs. This heterogeneous research trend represents an opportunity in the field of hydraulics, where sensors are not the primary business but they are becoming an indispensable necessity.

2. MEMS TECHNOLOGY

MEMS is the acronym for Micro-Electro-Mechanical Systems. MEMS techniques allow both electronic circuits and mechanical devices to be manufactured on a silicon chip; the process of manufacturing MEMS chips is similar but more

complex than the one used for integrated circuits.

MEMS are widely used today and there are many success stories about MEMS chips used as: Pressure sensors, Accelerometers, Inclometers, IMU and AHRS units, Gyroscopes, RF Microphones. MEMS are also used as Actuators: Inkjet Nozzles, Piezoelectric actuators and generators, RF switches.

In recent years, production technology has reached optimal component quality and reproducibility of performance and many new architectures have been invented and proposed.

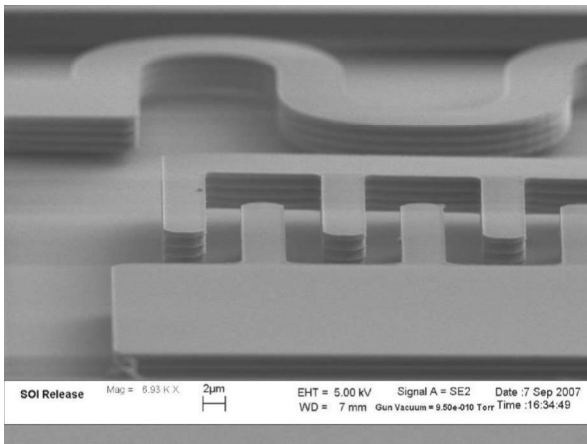


Figure 1: Example of Capacitive MEMS with moving part and anchored part

The MEMS principle is generally based on moving parts in a microchip (as shown in the example in **Figure 1**), and the small mass and the silicon-based material's characteristics allow mechanical principles and forces to be combined with electric principles and forces. This relationship leads to fast processes and high operating frequencies, thanks to the stiffness of silicon-based materials and high dynamics allowed by silicon-based junctions and components.

Thermal, electrostatic, capacitive, resistive and strain effects and mechanical levers and torques, controlled or measured using both resistive and capacitive effects are generally the physical phenomena underlying the operating principles of MEMS sensors.

3. DOUBLE-ENDED TUNING FORK TOPOLOGY

Not all MEMS are applicable for acquiring the same physical phenomena and it is very important to choose the best MEMS for each physical measurement. One of the most

promising MEMS geometries and functional principles that has been invented in recent years in the field of mechanical systems sensorization, is the Double-Ended Tuning Fork (DETF) MEMS ([7], [8]).

This sensor architecture was recently successfully tested in various systems and there are examples of promising applications. In [9] a pressure sensor with temperature compensation was developed, and this application is one of the most interesting in the field of fluidics. It must be noted that, as it is a strain sensor glued or fixed to surfaces of different materials, the thermal strain effect could be significant and should be considered; nonlinear strain characteristics of the nonlinear DETF subclass of sensors was analysed in [10]. A step ahead in the design of DETF sensors was made with linear DETF sensors based on CMOS elements, as presented for example in [11]. This evolution has also led to more accurate control of the geometry, which allows a wider linear range of measurement, as shown in [12], and higher measurement precision.

A very high-speed strain measurement allows DETF technology also to be used for different types of applications, like accelerometers [13] and tilt sensors [14], useful in the field of heavy duty and agricultural machines.

Regarding classic mechanical strain sensing applications, the ones discussed in this paper, in recent years DETF technology has been refined to increase sensitivity, like in [15], where a CMOS resonator with 33 nano-strain resolution was designed and tested, and at least one DETF has recently been developed in a production-ready configuration, as reported in [16].

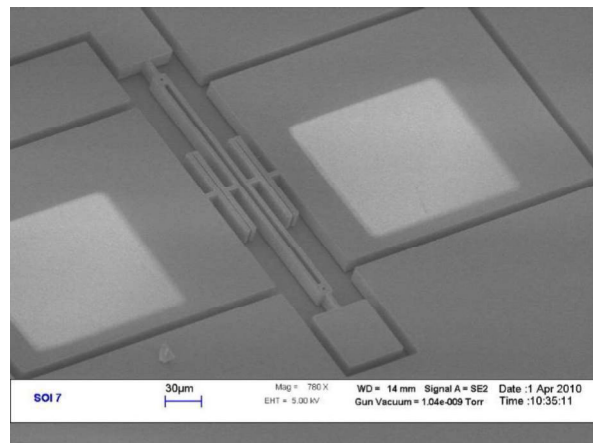


Figure 2: The CNR MEMS DETF Resonator

The DETF used for this experimental work was developed over the years by CNR. In the next paragraph, the functional principle is explained in order to clarify the benefits of its application to hydraulic components in fluid power applications.

4. THE CNR MEMS DETF

The Italian National Research Council (CNR) is the largest public research body in Italy and is organized into departments and institutes. The MEMS technology described in this paper was developed in the Institute for Microelectronics and Microsystems (IMM) of the CNR Department for Materials and Components .

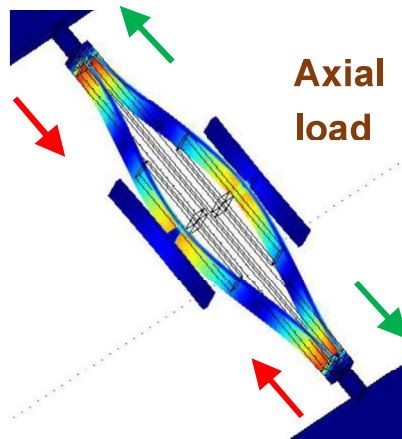


Figure 3: The DETF Resonator Asymmetrical Strain Geometry and Direction for compression (Red) and extension (Green)

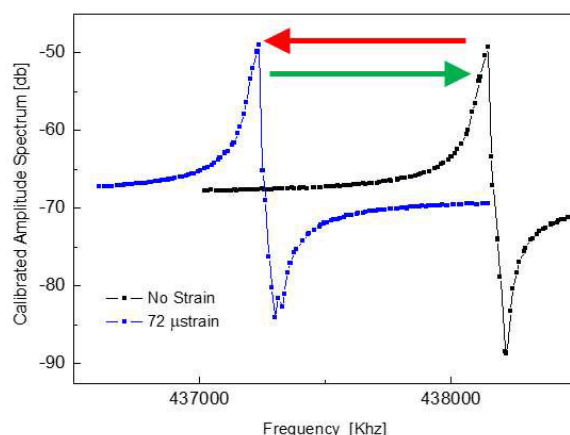


Figure 4: The DETF Resonator Frequency Shift for compression (Red) and extension (Green) strain, respectively

The Institute has a clean room, a chip factory where MEMS and other components are made.

The MEMS used to create new examples of hydraulic applications sensorization was designed, built and adapted by IMM researchers and is described in [17], [18] and [19].

The sensor in **Figure 2** is composed of a DETF on silicon substrate, which is maintained at the resonance frequency through the action on two electrodes, connected to an external electronic circuit. The external analogue electronic circuit has the dual function of supplying power and providing a stimulus at the resonance frequency, in a frequency tracker topology. The same circuit is also used to acquire the resonance frequency through the digital part of the control system, using a microcontroller. As shown in **Figure 3** and **Figure 4**, the DETF element changes its resonance frequency when it is subjected to mechanical strain, and the frequency shift is opposite in opposite strain directions: compression and extension.

The sensor structure is vacuum packed in a chip. In a $5\text{ mm} \times 5\text{ mm}$ chip, 8 sensors are assembled. Chip thickness is approximately 0.1 mm. The chip can be fixed to mechanical components with epoxy glue, like traditional strain gauges.

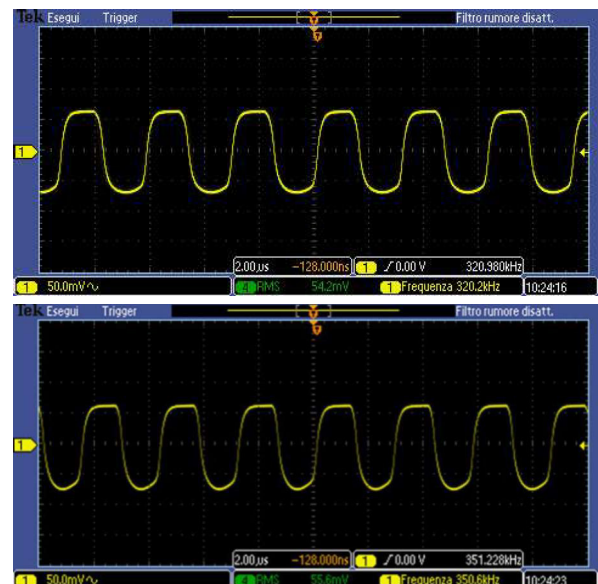


Figure 5: MEMS DETF output signal acquisition in no-strain condition (up) and in extension condition (down) at frequency of 320.280 Hz and 351.228 Hz

5. MEMS DETF CHARACTERIZATION AND GEAR PUMP APPLICATION

In [20], the sensor had already been characterized

and presented. The study was focused on sensor linearity and resolution; both characteristics were found to be considerably higher compared to other similar sensors, such as the one described in [15]. In fact, the CNR DETF sensor can reach a resolution of 190 pε (Figure 6), while the previously presented ones have a maximum resolution of 33 nε.

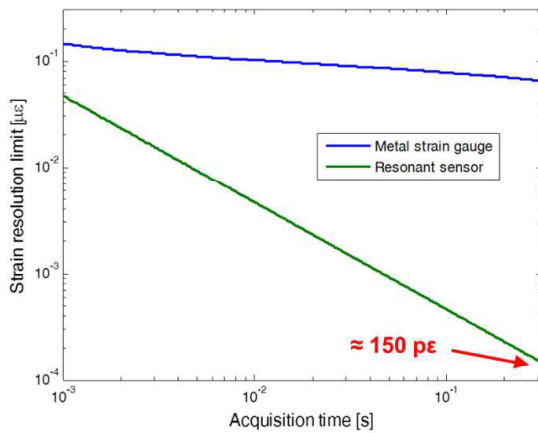


Figure 6: The DETF resonator resolution compared to traditional strain gauges function of acquisition time.

The only aspect that should be underlined is that, when acquiring a frequency-based signal, the accuracy of frequency acquisition is directly dependent, not only on sensor characteristics and on quality, but also on electronic system performance. In fact, due to the *reciprocal frequency counter* driver structure, the sensor waveform is acquired by the microcontroller at the resolution of the base counter, whose maximum frequency is a function of the main oscillator of the microcontroller itself. The limit of the base counter resolution is compensated by acquiring more than one pulse of the sensor, collecting a buffer of pulses and counting the number of pulses in the period. One immediately realizes that accuracy is proportional to the number of pulses, while the maximum dynamic of the resulting sensor is limited by the interval of time needed to collect the pulses.

In order to characterize the sensor, a first application was implemented and described in [20] where the strain model was calculated using the method described in [21].

In order to define how the adoption of a better performing microcontroller will positively affect the precision of sensor signal acquisition, a new electronic control unit was designed and prototyped using a 168 Mhz ARM Cortex M3

microcontroller, whereas in the previous electronic control unit a 40 Mhz-based microcontroller had been used. The higher oscillator frequency allows a counter resolution that is 4 times higher. The calculation can be made by comparing the performance of both microcontrollers in acquiring the resonance frequency of a DETF operating at 370.300 Hz. As the same resonant sensor is in the same condition for both microcontrollers, the time for each pulse is always the same, but the resolution of the measurement is different, due to the maximum resolution of the microcontrollers. The two examples of this calculation are shown in **Table 1** and **Table 2**; it can be noted that, using a 1000 pulse buffer, the error in Hz is 3,42 and 0,81 respectively.

If this measurement is applied in the example of a gear pump application, it corresponds to an error of 0,94 and 0,22 bar, respectively, for the two microcontrollers. It can also be noted that the signal acquisition and digital conversion of strain will take 2,7 ms and corresponds to a dynamic of more than 350 Hz in sensor signal acquisition.

Table 1: Microcontroller 40 MHz

n.of pulses	Measuring time [ms]	Max error [Hz]	error (%)	Pressure. Error (bar)
1	$2,7 \times 10^{-3}$	3.454,45	0,9336	943,84
10	27×10^{-3}	342,57	0,0926	93,60
100	0,27	34,23	0,0093	9,35
500	1,3	6,85	0,0019	1,87
1000	2,7	3,42	0,0009	0,94

Table 2: Microcontroller 168 MHz

n.of pulses	Measuring time [ms]	Max error [Hz]	error (%)	Pressure. Error (bar)
1	$2,7 \times 10^{-3}$	816,68	0,2207	223,14
10	27×10^{-3}	81,51	0,0220	22,27
100	0,27	8,15	0,0022	2,23
500	1,3	1,63	0,0004	0,45
1000	2,7	0,81	0,0002	0,22

This example demonstrates that, using a better performing microcontroller, will increase the accuracy and resolution of the strain measurement linearly, as a function of the base frequency and number of pulses considered (measurement buffer).

6. SENSITIVITY DEMONSTRATION APPLICATION: THICK PIPE

The first application was successful and the calculation executed to compare the performance of different microcontrollers in terms of measurement precision suggested setting up a new application in order to stress the limit on the sensor's measurement resolution and evaluate the limits for applicability in hydraulic applications. In fact, the measurement acquisition method is virtually capable of detecting even a very small strain on a component, using both the basic signal acquisition frequency and the length of the measurement period. Based on experience, the limited signal acquisition frequency can be compensated by using a longer measurement period (measurement buffer), as shown in the previous experiment.



Figure 7: 100 x 96 mm steel cylinder with 8 mm pipe and DETF sensor.

In order to set up the new application and new test bench, a 100 mm diameter steel cylinder was made, with an 8 mm hole simulating a thick pipe for hydraulic oil flow. A DETF sensor was externally applied on this thick pipe, and the pipe was mounted on a static pressure test bench, equipped with a certified pressure measurement digital sensor, connected through a serial line to a personal computer. One of the cylinder sides was connected to the hydraulic oil port of the static test bench, while the other side was plugged in order to prevent oil flow and allow the generation of a static pressure in the pipe, without oil leaks

through the bench actuator. The aim of this bench configuration was to perform a static pressure measurement and experimentally assess the limits of the MEMS sensor.

The steel cylinder construction data and the related theoretical deformation data, obtained from classic literature formulas, are shown in **Table 3**.

Table 3: Parameters of the Steel Cylinder

Cylinder parameter	Value
Cylinder length [mm]	96
Cylinder Diameter [mm]	100
Hole diameter [mm]	8
Tangential def. ($\mu\text{m}/\text{mm}$)	0,0004578
Tangential def. (nm/mm)	0,45
Strain [ne]	450
Young Module E (Pa)	210.000

The table shows a theoretical deformation of 450 ne, which, given the sensor resolution (190 pe), could allow an internal pressure measurement by cylinder external strain sensing under the pressure effect.

Therefore, as shown in **Figure 7**, the sensor was glued externally to the cylinder surface, halfway up to reduce edge effects, and bonded through micro-wires. Then it was connected to the hardware digital electronic unit in order to power and stimulate the sensor and acquire the feedback signal of the oscillator at resonance.

The electronic control unit is connected through a USB port to a personal computer, where an application was set up to acquire the sensor data. To demonstrate the DETF's sensitivity, a series of tests were executed, always under the same oil and ambient temperature conditions, in order to evaluate only the pressure strain effects and reduce the thermal strain effects, which are not negligible for steel.

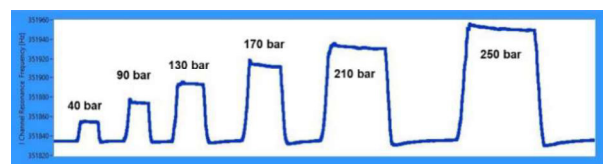


Figure 8: Static Strain/Pressure measurement in the thick cylinder

The results of some tests are reported in **Figure 8**; a complete test session is represented in the graph, where the strain values (in Hz on the vertical axis) are shown with respect to time (in s

on the horizontal axis). In the figure, it can be noted that the strain is not regular on pressure changes, but this is due to the test bench set-up, where pressure is manually adjusted. It can also be noted that the strain is constant after the transient and adjustment phases.

Considering a sensitivity of $120 \text{ Hz}/\mu\epsilon$, the strain can also be calculated. The average data of the experiment are shown in **Table 4**. Both pressure (acquired by the instrument on the bench) and the resonant frequency (acquired through the electronic control system) are shown together with some calculated data in the left columns. It is important to underline that the resolution is less than $1 \text{ Hz}/\text{bar}$, but that 1 Hz is much higher than the microprocessor resolution for frequency acquisition, so that hundredths of Hz can be easily calculated.

Table 4: Parameters of the Steel Cylinder

Oil Pressure [bar]	Resonant Frequency [Hz]	Strain($\mu\epsilon$)	$\Delta(\text{Hz})$
0	351835	0	0
40	351850	1,8	15
90	351872	4,44	37
130	351892	6,84	57
170	351912	9,24	77
210	351932	11,64	97
250	351952	14,04	117

The experiment shows that even under extreme steel thick pipe conditions, the sensor is able to sense the strain on the material. Based on this experience, we could imagine how to apply the sensor to hydraulic components like pumps and valves, because the sensor is able to acquire the internal pressure even when the metal thickness is greater than the typical pipe thickness. Indeed, the oil pressure generates a force sufficient for good strain, with respect to sensor sensitivity. In order to find other new applications, it is necessary to think differently.

As an example, it may be inferred that it is also possible to acquire small forces capable of creating minor strain in materials with a small thickness.

That idea suggests the possibility of also acquiring oil flow-related data.

7. NEW COMPONENT: FLOW SENSOR

Oil and, in general, a fluid flowing in a pipe, generates forces against any obstacle. This was the main concept for the design of the new flow sensor.

7.1. The Mechanical Design of the Flow Sensor

The principle is to create a new component where an obstacle to the oil flow, placed in a pipe, is capable of transferring to the outside part of the force applied to the obstacle by the oil itself. The aim of this experiment was to calculate the amount of force at the oil flow rates and pressure rates normally available in a mobile application. For this experiment and all related simulated mathematical models, a maximum pressure of 250 bar and maximum oil flow of 190 l/m was considered.

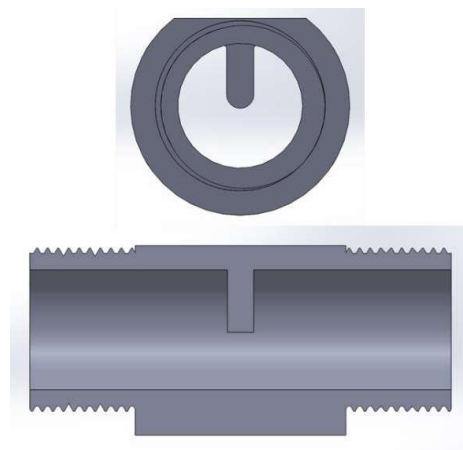


Figure 9: The Flow Sensor mechanical component

In order to set up an experimental rig, a pipe with the simplest obstacle was designed by drawing a parallelepiped shaped, obstacle with a rounded apical part. This partial obstruction was fixed orthogonally to the oil flow, so as to intercept the flow in the area of maximum speed (with reference to the laminar flow profiles). One of the design requirements was to generate a minimum reduction in the pipe cross-sectional area, in order to minimize pressure losses. The form factor of the obstacle represents a critical part of the project, because it has to be enough to generate a sufficient resistance to the fluid flow, but should not create too big a pressure drop in the section. Optimization of the form factor is the main goal of the mechanical sensor's component design.

7.2. The Design Methodology

The solid model of geometry was analysed through 3D CFD (Computational Fluid Dynamics) analysis, in order to evaluate the oil flow and calculate the pressure flow forces applied to the obstacle. In a second phase, a structural FEM (Finite Element Method) was used to calculate the resulting strain on the outer wall of the pipe, at the base of the obstacle to the hydraulic flow subject to the force of the flow itself. If the strain is of a magnitude compatible with the DETF sensor, then a new flow sensor is possible.

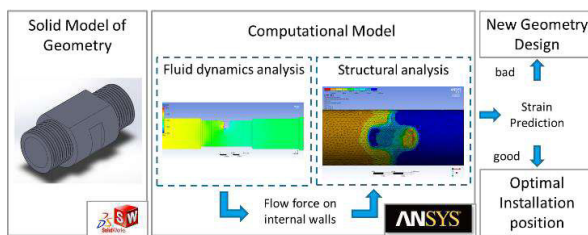


Figure 10: The Flow Sensor design recursive method

Simulations were carried out from 10 bar to 250 bar and with oil flow from 10 l/min to 150 l/min $T = 50^{\circ}\text{C}$, $\nu = 44 \text{ mm}^2/\text{s}$ for temperature and kinematic viscosity of the oil used.

One result is shown in **Figure 11**, where it is evident in which area the greatest force resistant to the oil is located; this is also the area that generates the maximum torque on the outer wall of the pipe. The resulting pressure is around 0,31 bar, which corresponds to $3,1 \text{ N/cm}^2$. The area of the obstacle is around $0,5 \text{ cm}^2$, thus the resulting force is around 1,55 N. These data were used in the structural analysis to evaluate the resulting strain on the outer wall of the pipe.

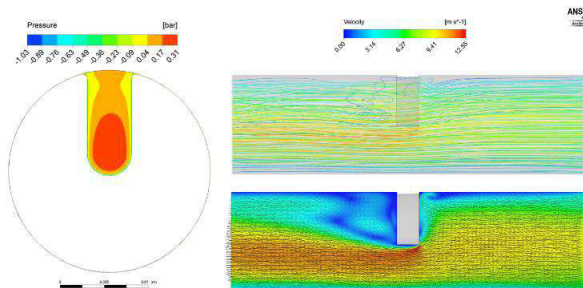


Figure 11: Fluid Dynamic Analysis at 150 l/min oil flow

Figure 12 shows the resulting solid model of the mechanical component, where the fluid force is applied in the centre of force of the obstacle, as

per fluid dynamic analysis. In the figure, the two areas of greatest strain are highlighted by two arrows oriented in opposite directions, respectively in front and behind the base of the parallelepiped, which constitutes the barrier to the hydraulic flow. In these two points the strain is respectively inward, upstream of the obstacle, and outward, downstream of the obstacle, from the oil flow point of view. This will enable a very good measurement, because the pressure strain has the same outward direction in both points, so that the difference in the resonance frequency shift will be the exact strain measurement.

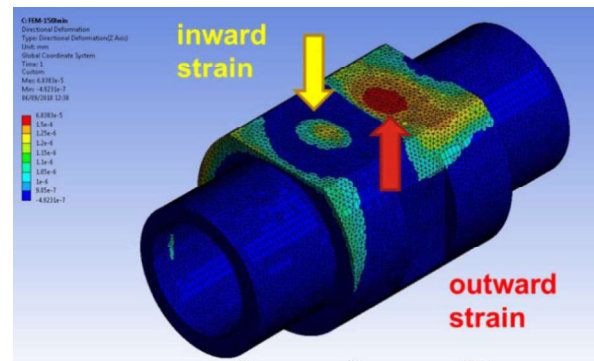


Figure 12: Structural Analysis with maximum strain points in the outer wall of the pipe for sensor placement.

The combined effects of direct pressure deformation and of indirect flow force deformation are evident in the figure, which shows the extent of deformation in upstream and downstream of the obstacle. The directional deformation on the Z axis (vertical axis in the figure), in the area in front of the obstacle is an order of magnitude higher than in the area behind it ($1,2 \times 10^{-6} \text{ mm}$ vs. $6,8 \times 10^{-5} \text{ mm}$). The deformation values are in the range of measurement of the DETF sensor; therefore the sensor is theoretically feasible. The main problem to be addressed, in order to move to a sensor prototype, is the optimal positioning of the microchip with DETF resonators.

7.3. Prototype and Testing

For a rigorous test of maximum deformation in a real prototype, two chips positioned above the areas of maximum deformation should be used. However, given the limited distance between the two areas (3 mm) and the availability of 8 DETF resonators inside each chip, it was decided to glue only one chip onto the external surface of the

sensor. The chip size is 6 mm × 6mm. Therefore, two DETF resonators placed at the two far ends of the chip were used, each very close to one of the two areas of maximum deformation.

In **Figure 13**, the DETF sensor and the bonding interfaces are shown mounted in the prototype in the sensor on the outer wall of the pipe.

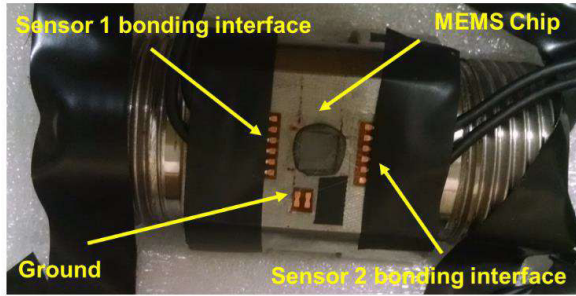


Figure 13: Sensor prototype with 1 chip and 2 DETF bonded.

One of the most critical points for the mounting phase and for testing on a real test bench are the micro-wires needed to connect the DETF stimulation terminals to the external wiring interfaces. A plastic protection was thus made with a 3D printer (in red in **Figure 14**) and the sensor assembly was installed on the bench in order to test it under real working conditions.

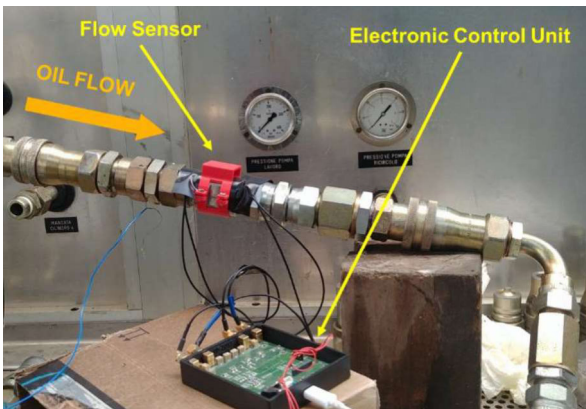


Figure 14: Oil flow sensor with DETF resonator test bench.

Some tests were carried out at a constant oil temperature of 50 °C in order to reduce the temperature effects in the strain on the component. Temperature strain is compensated using two sensors with different spatial orientations (90°) and applying the compensation formula:

$$f = f_1 - (f_2 \times 0.38) \quad (1)$$

instead of a simple difference in resonator frequencies, which could be applied if both

sensors had the same spatial orientation, but in that case temperature compensation would not be possible. Equation 1 was obtained experimentally by testing the sensor inside a climatic chamber and acquiring the difference in resonance frequency of the different DETF resonators as the temperature changes. The need for experimental determination derives from the dimensional differences of the resonators, which are still obtained by growth of silicon elements in an experimental process.

The test bench allows the initial inlet pressure and oil flow to be adjusted and tests were conducted at different pressures and oil flow rates. The data of one of the test sessions is represented graphically in **Figure 15**, where it can be noted that the sensor measures a mixed effect of pressure and flow force.

The sensor output was filtered using a low pass Butterworth filter (1st order at 50 Hz).

In the Figure it is also possible to note that the sensor shows no hysteresis error either in pressure or flow measurements.

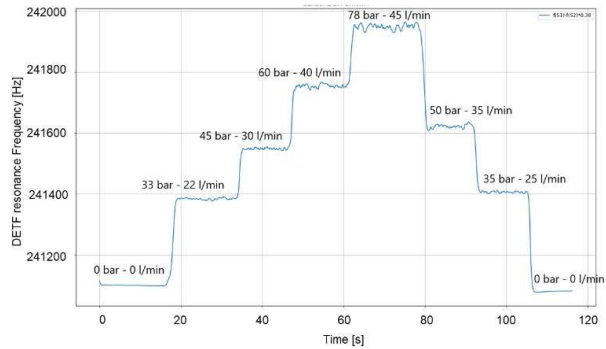


Figure 15: Oil flow sensor with DETF resonator test results.

In the awareness of the need for a pressure sensor that takes into account the contribution of pressure in the component strain, a correlation analysis was performed, using the acquired pressure and flow data from the test bench, in order to infer a mathematical equation.

A first and second set of tests were performed maintaining 20 bar and 70 bar of oil pressure, respectively. The frequency shift values for both DETF resonators were collected at different oil flow rates. The first results are presented in **Figure 16**, where a linear relationship may be noted between the two series of data (lower blue line and dots at 20 bar and upper orange line and dots at 70 bar).

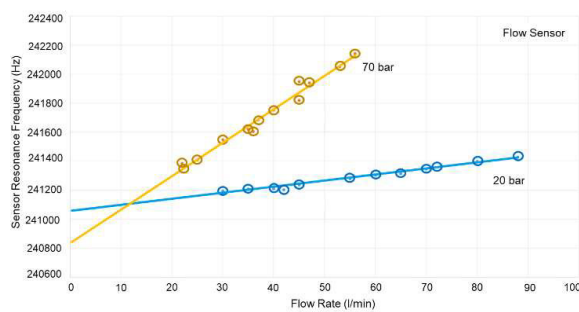


Figure 16: Oil Flow Sensor Characterization

Multiple test sessions are needed to completely characterize the sensor and a second DETF sensor must be installed in an area of the pipe not affected by deformation due to oil flow. In this way it will be possible to isolate the contribution of pressure, so as to divide the two components that contribute to deformation of the sensor's mechanical component. In any case it will be necessary to characterize the resonators and to derive the empirical relationships correlating them to temperature-induced deformation.

The first experimentation of this new component gave interesting results and further studies will be carried out both on the geometry of the element resistive to the oil flow and its position and on the sensor placement and composition, in order to arrive at an interesting component for industrial and mobile applications.

8. CONCLUSIONS

The MEMS DETF application experiments presented here in relation to the field of hydraulic components and circuits, demonstrate that DETF sensor architecture represents a very interesting MEMS technology for new hydraulic components and for new sensorization techniques in both industrial and mobile applications. The examples described demonstrate the sensor's ability to measure, from the outer wall of components and pipes, both pressure and flow without energy losses. Further research and investigations will be conducted in order to thoroughly evaluate DETF technology and arrive at a complete characterization. The CNR DETF chip will be further developed and improved, to allow a simpler and more robust application to mechanical production systems:

- metal pads will be added to the silicon chip to allow direct bonding on the sensor side,

thus avoiding the need for micro-wires and a bonding machine,

- a floating DTEF resonator will be added inside each chip, in order to obtain a temperature reference oscillator and compensate for temperature frequency shift effects.

As regards the possible applications, new mechatronic components will be tested, combining new geometries and applying more than one DETF component, in order to acquire pressure, temperature and oil flow data and completely characterize system working conditions.

Today, the high number of studies related to MEMS technologies are an incentive to evaluate more sensor architectures and create new sensorization models and technologies for hydraulic components and systems.

NOMENCLATURE

ε	Strain ($\mu\text{m/m}$)
f	Resonance Frequency (Hz)
F	Force (N)
ν	Fluid kinematic viscosity (mm^2/s)
P	Pressure (bar)
T	Temperature ($^{\circ}\text{C}$)

REFERENCES

- [1] ISO 13849 (1, 2, TR100) Safety of machinery — Safety-related parts of control systems, International Organization for Standardization ISO, 2015
- [2] IEC 62061, Safety of machinery - Functional safety of safety-related electrical, electronic and programmable electronic control systems, International Electrotechnical Commission – IEC, 2015.
- [3] ISO 25119 (1-14) Tractors and machinery for agriculture and forestry — Safety-related parts of control systems, International Organization for Standardization ISO, 2019
- [4] ISO 26262 (1-12) Road vehicles — Functional safety, International Organization for Standardization ISO, 2018
- [5] ISO 19014 (1-4), Earth-moving machinery — Functional safety, International Organization for Standardization ISO, 2018
- [6] Ali E, Weber J, Wahler M (2016) A Machine Learning Approach for Tracking the Torque

- Losses in Internal Gear Pump - AC Motor Units. 10th Int Fluid Power Conf 121–134
- [7] W. Chen, M. Li, Y. Liu, W. Fang and S. Li, "A Fully Differential CMOS–MEMS DETF Oxide Resonator With $Q > 4800$ and Positive TCF," in *IEEE Electron Device Letters*, vol. 33, no. 5, pp. 721–723, May 2012. doi: 10.1109/LED.2012.2188774.
- [8] J. Verd, A. Uranga, J. Segura and N. Barniol, "A 3V CMOS-MEMS oscillator in 0.35 μ m CMOS technology," 2013 Transducers & Eurosensors XXVII: The 17th International Conference on Solid-State Sensors, Actuators and Microsystems (TRANSDUCERS & EUROSENSORS XXVII), Barcelona, 2013, pp. 806–809. doi: 10.1109/Transducers.2013.6626889
- [9] D. Han et al., "A Mems Pressure Sensor Based on Double-Ended Tuning Fork Resonator with on-Chip Thermal Compensation," 2019 20th International Conference on Solid-State Sensors, Actuators and Microsystems & Eurosensors XXXIII (TRANSDUCERS & EUROSENSORS XXXIII), Berlin, Germany, 2019, pp. 2061–2064. doi: 10.1109/TRANSDUCERS.2019.8808719
- [10] Q. Shin, A. Qiu, Y. Su and R. Shi, "Nonlinear oscillation characteristics of MEMS resonator," 2010 IEEE International Conference on Mechatronics and Automation, Xi'an, 2010, pp. 1250–1253. doi: 10.1109/ICMA.2010.5589936.
- [11] E. Marigó et al., "Linear operation of a 11MHz CMOS-MEMS resonator," 2010 IEEE International Frequency Control Symposium, Newport Beach, CA, 2010, pp. 158–161. doi: 10.1109/FREQ.2010.5556351.
- [12] W. Chiu, C. Chou, M. Li and S. Li, "A ring-down technique implemented in CMOS-MEMS resonator circuits for wide-range pressure sensing applications," 2016 IEEE International Frequency Control Symposium (IFCS), New Orleans, LA, 2016, pp. 1–3. doi: 10.1109/FCS.2016.7563594.
- [13] E. E. Moreira, B. Kuhlmann, J. Gaspar and L. A. Rocha, "Small Size And Highly Sensitive Differential MEMS Accelerometer Based On Double-Ended Tuning Fork Resonators," 2019 20th International Conference on Solid-State Sensors, Actuators and Microsystems & Eurosensors XXXIII (TRANSDUCERS & EUROSENSORS XXXIII), Berlin, Germany, 2019, pp. 602–605. doi: 10.1109/TRANSDUCERS.2019.8808174.
- [14] S. Wang, J. Ren, T. Zhang, Y. Weng, Z. Jiang and X. Wei, "A MEMS resonant tilt sensor with high sensitivity maintained in the whole 360° measurement range," 2016 IEEE SENSORS, Orlando, FL, 2016, pp. 1–3. doi: 10.1109/ICSENS.2016.7808792.
- [15] K. E. Wojciechowski, B. E. Boser and A. P. Pisano, "A MEMS resonant strain sensor with 33 nano-strain resolution in a 10 kHz bandwidth," SENSORS, 2005 IEEE, Irvine, CA, 2005, pp. 4 pp.–.doi: 10.1109/ICSENS.2005.1597857
- [16] M. Li, C. Chen, C. Li, C. Chin, C. Chen and S. Li, "Foundry-CMOS integrated oscillator circuits based on ultra-low power ovenized CMOS-MEMS resonators," 2013 IEEE International Electron Devices Meeting, Washington, DC, 2013, pp. 18.4.1–18.4.4. doi: 10.1109/IEDM.2013.6724654
- [17] M. Ferri, F. Mancarella, L. Belsito, A. Roncaglia, J. Yan, A. A. Seshia, K. Soga, J. Zalesky, "Strain sensing on steel surfaces using vacuum packaged MEMS resonators", *Procedia Eng.*, vol. 5, pp. 1426–1429, Jan. 2010.
- [18] L. Belsito, M. Ferri, F. Mancarella, A. Roncaglia, J. Yan, A. A. Seshia, K. Soga, "High-resolution strain sensing on steel by Silicon-On-Insulator flexural resonators fabricated with chip-level vacuum packaging", in *Proc. 17th Int. Conf. Solid-State Sens. Actuators Microsyst.*, Barcelona, Spain, Jun. 2013, pp. 992–995.
- [19] L. Belsito, M. Ferri, F. Mancarella, L. Masini, J. Yan, A. A. Seshia, K. Soga, A. Roncaglia, "Fabrication of high-resolution strain sensors based on wafer-level vacuum packaged MEMS resonators", *Sens. Actuators A, Phys.*, vol. 239, pp. 90–101, Mar. 2016.
- [20] M. Ruggeri, G. P. Massarotti, L. Belsito, A. Roncaglia, Indirect Pressure Measurement on Hydraulic Components Through New MEMS Strain Sensors, ASME/BATH 2017 Symposium on Fluid Power and Motion Control, doi: 10.1115/FPMC2017-4355.
- [21] W. Koellek, U. Radziwanowska, Energetic efficiency of gear micropumps, *Archives of Civil and Mechanical Engineering*, 15 (2015) pp. 109–115, DOI: 10.1016/j.acme.2014.

SELF-SENSING POSITION DETERMINATION ON A SENSOR-DESIGNED PROPORTIONAL SOLENOID

Thomas Kramer*, Jürgen Weber

Chair of Fluid-Mechatronic Systems, Institute of Mechatronic Engineering, Technische Universität Dresden, Helmholtzstrasse 7a, 01069 Dresden

* Corresponding author: Tel.: +49 351 463 31964; E-mail address: thomas.kramer@tu-dresden.de

ABSTRACT

Proportional valves are widely used in fluid systems for controlling the volume flow rate or fluid pressure. The actuation of this valves is done by PWM-driven proportional solenoids, which enable self-sensing position determination abilities due to air gap-dependent electrical behaviour, e. g. for condition monitoring or position controlling tasks. However, the sensor properties of conventional proportional solenoids are poor due to ambiguities caused by hysteresis effects (magnetic hysteresis, eddy currents) and saturation effects. Thus, a sensor-designed actuator was developed with very low hysteresis effects and unique position determination by using electrical sheet and a particular air gap design. This paper deals with investigations of a novel self-sensing position determination approach on a demonstrator of the sensor-designed solenoid. The advantage of this method is an online consideration of transient effects such as mean current change and armature motion as well as temperature-dependent resistance. For this, a combined evaluation of the differential inductance and flux linkage during PWM periods is proposed.

Keywords: self-sensing position determination, proportional solenoid, sensor design

1. INTRODUCTION

Proportional solenoids are well-known drives for proportional valves in order to control the volume flow rate or fluid pressure in a continuous manner. The working principle is based on the reluctance principle. By exciting the solenoid's coil, a magnetic field arises and a magnetic force F_m acts on the movable armature (**Figure 1**). The magnetic force works against a spring force F_s for setting a specific position according to the equilibrium of the forces. A linear behaviour between the electrical input (coil current i) and mechanical output (armature position x) is achieved with a particular air gap design and a magnetic excitation in the saturation area. A cone shaped counterpart of the armature results in a nearly position-independent magnetic force [1]. The excitation in the saturation area leads to a current proportional magnetic force [2]. The coil is usually excited by an energy efficient PWM voltage u_{in} to avoid static friction.

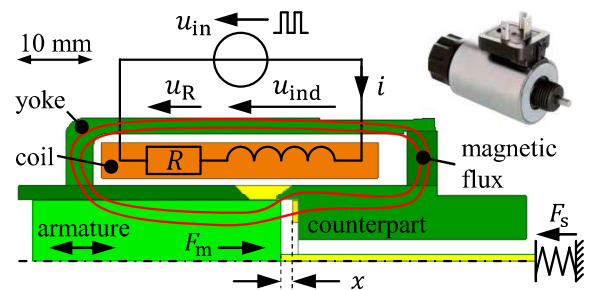


Figure 1: Design of conventional proportional solenoid (axisymmetrical magnetic circuit; without fluid stage)

It is well-known that this electro-magneto-mechanical operating chain is not reactionless. The magnetic behaviour is air gap-dependent and has an influence on the electrical side due to its inductive effect. This behaviour can be exploited to get information about the armature position only by measuring electrical values such as current and voltage. So-called self-sensing position determination methods can be used for various applications, e. g. for condition monitoring [3] or position controlling tasks [4].

However, the sensor properties of conventional proportional solenoids are poor due to ambiguities caused by hysteresis effects (magnetic hysteresis, eddy currents) and saturation effects. Reason for this is the focus on the actuator capability in nowadays development activities of conventional actuators. Thus, a sensor-designed actuator was developed with very low hysteresis effects and unique position determination by using electrical sheet and a particular air gap design.

The focus of this paper is the investigation of a novel self-sensing position determination approach on the developed sensor-designed solenoid. Firstly, some basics of the position observation and the sensor properties of conventional proportional solenoids are shown. Based on this, a demonstrator of the sensor-designed proportional solenoid and its electromagnetic behavior is presented. In the main part, a promising self-sensing position determination method is described and extended according to considering transient effects such as mean current change and armature motion. The coil resistance is an important value for position observation methods. An online capable method for calculating the resistance is presented. After that, the used test rig for investigating the methods is described. Finally, the achieved results of position observation and resistance determination applied on the demonstrator are presented.

2. SELF-SENSING POSITION DETERMINATION

As described above, the air gap-dependent magnetic behaviour can be used for self-sensing position determination. There are several methods known from literature. Richter gives an overview in [5] and [6], especially for application at typical valve's solenoids. The most promising methods for PWM-driven proportional solenoids are the evaluation of the differential inductance [7] and differential current change [8]. These methods work with the existing PWM excitation and do not need any additional test signal. Furthermore, they are not based on numerical integration such as flux linkage method [4][9], which is especially difficult in the continuous working principle of proportional solenoids. In this work, only the differential inductance method is considered, because the differential

current change is only a consequence of the position-dependent inductance.

The differential inductance L_d is derived from flux linkage Ψ according to

$$L_d = \frac{d\Psi}{di}. \quad (1)$$

The flux linkage is the magnetic flux summed over all windings. It can be calculated by integrating the induced voltage u_{ind} according to the induction law with

$$\begin{aligned} \Psi &= \int u_{ind} dt + \Psi_0 \\ &= \int (u_{in} - Ri) dt + \Psi_0. \end{aligned} \quad (2)$$

The induced voltage is calculated from measured coil current i and input voltage u_{in} (see **Figure 1**). Thus, the differential inductance is calculated according to

$$L_d = \frac{u_{in} - Ri}{\frac{di}{dt}} \quad (3)$$

without any numerical integration.

3. SENSOR PROPERTIES OF CONVENTIONAL PROPORTIONAL SOLENOIDS

Generally, existing proportional solenoids are developed considering only the actuator properties, while sensor behaviour is not included in the developing process. In order to investigate the current sensor properties, the electromagnetic behaviour has to be analysed. The evaluation of flux linkage $\Psi(i, x)$ maps all relevant effects. From this, the characteristic map of differential inductance $L_d(i, x)$ is derived, which is necessary for self-sensing position determination. The maps are generated from measurements of coil current i and input voltage u_{in} in steady state (**Figure 2**). Therefore, the armature is fixed at various positions x and the solenoid is excited by a PWM voltage with a constant duty cycle d (PWM period: T_{PWM}). The measurements are evaluated as soon as the mean current value does not change anymore. The map values are calculated from the measurements according to equations (2) and (3), here by neglecting the unknown start value Ψ_0 (remanent flux linkage) in equation (2).

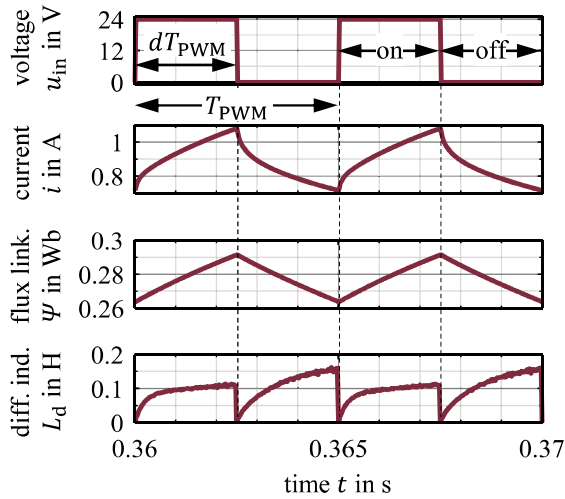


Figure 2: Time-dependent measurements of electrical values in steady state and map values calculated therefrom

Figure 3 illustrates both maps depending on coil current i at various PWM duty cycles d and armature positions x .

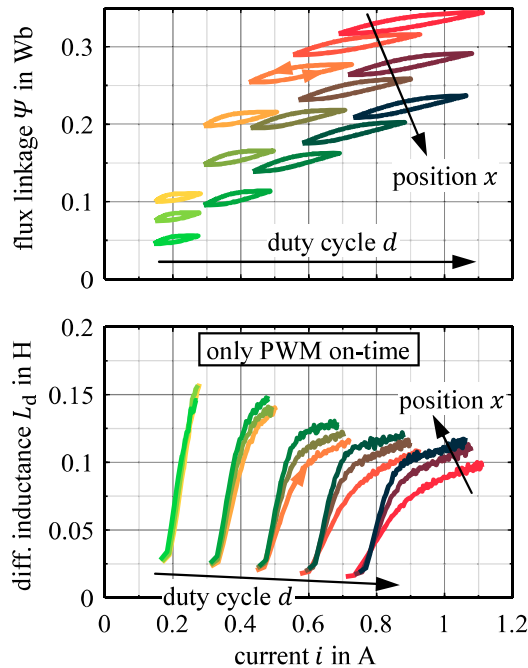


Figure 3: Map of flux linkage $\Psi(i, x)$ and differential inductance $L_d(i, x)$ of a conventional proportional solenoid calculated from measurements (in operating range)

Two main effects can be derived from the behaviour. Firstly, there are striking hysteresis loops during PWM excitation (**Figure 3**, top), which represent the inductive energy losses due to magnetic hysteresis and eddy currents. In

relation to the position observation, they lead to ambiguities in position determination (**Figure 3**, bottom), since a clear assignment of the evaluated differential inductance to exactly one position is unfeasible. This problem becomes even greater, when transient processes are considered (armature motion, change of mean current). The second effect becomes visible, when hysteresis effects are not taken into account (**Figure 4**). The so-called anhysteretic curves are derived from FE simulations. They show nearly no position dependency in the range of larger currents due to saturation effects.

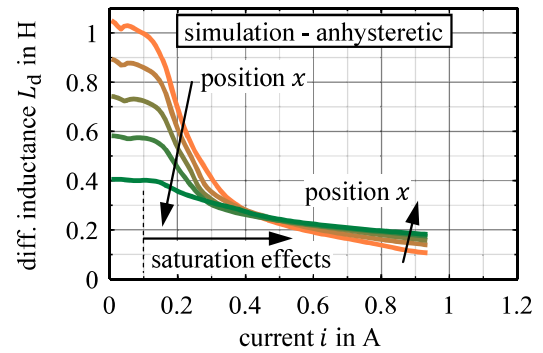


Figure 4: Map of differential inductance $L_d(i, x)$ of a conventional proportional solenoid simulated without hysteresis effects (in operating range)

For these reasons, it was investigated how a proportional solenoid can be designed regarding proper sensor behaviour by considering the actuator characteristics as well. On this basis, a promising self-sensing design was built up as demonstrator. Detailed investigations for the development of sensor-designed solenoids will be published in a further article.

4. SENSOR-DESIGNED PROPORTIONAL SOLENOID

The aim of sensor-designed actuators is an unambiguous linear behaviour between the evaluated value for position observation (differential inductance) and the armature position. This basic characteristic can be achieved by a particular air gap design and an excitation of the magnetic circuit below saturation. In addition, the hysteresis effects have to be significantly reduced. The most promising method for lower hysteresis effects is the usage of electrical sheets. This material has a reduced

magnetic hysteresis and avoids large eddy currents due to its isolated sheets. An excitation below saturation and a lamination of the magnetic circuit was already proposed in [10].

Figure 5 shows the developed demonstrator design of a sensor-designed proportional solenoid in size comparison to the conventional solenoid. The increased actuator size is necessary for achieving the same force level by considering an excitation below saturation.

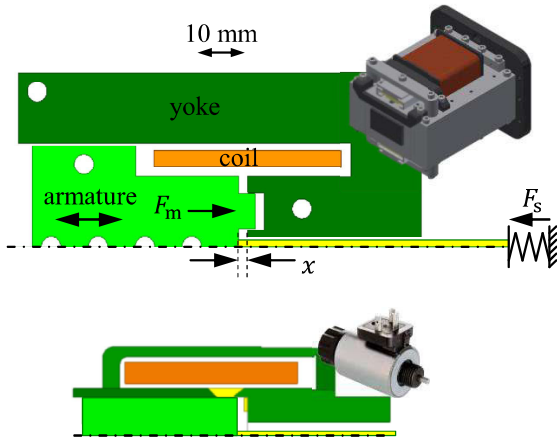


Figure 5: Design of sensor-designed proportional solenoid (planar magnetic circuit, top) in size comparison to the conventional solenoid (bottom)

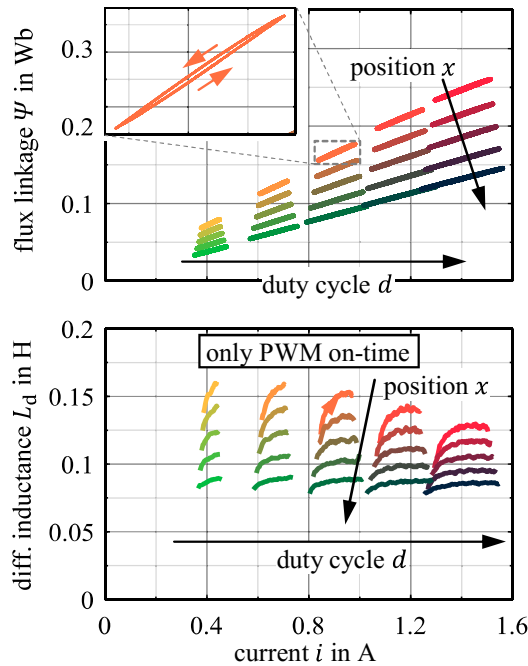


Figure 6: Map of flux linkage $\Psi(i, x)$ and differential inductance $L_d(i, x)$ of the developed sensor-designed solenoid calculated from measurements (in operating range)

The magnetic behaviour was measured and simulated in the same way as on the conventional proportional solenoid. The improved magnetic behaviour is illustrated in **Figure 6** and **Figure 7**.

Compared to the behaviour of conventional solenoids presented in **Figure 3**, a significant reduction of the hysteresis losses can be seen (**Figure 6**, top). However, small loops still occur due to remaining small magnetic hysteresis effects and eddy currents. This results in a varying differential inductance during PWM on-time respectively off-time (**Figure 6**, bottom), which requires a special handling.

Furthermore, the linear position-dependent behaviour of the differential inductance, which is derived from FE simulations, is pronounced over the entire operating range (**Figure 7**). Slight saturation effects occur at large currents. This is due to a compromise between actuator size and sensor properties.

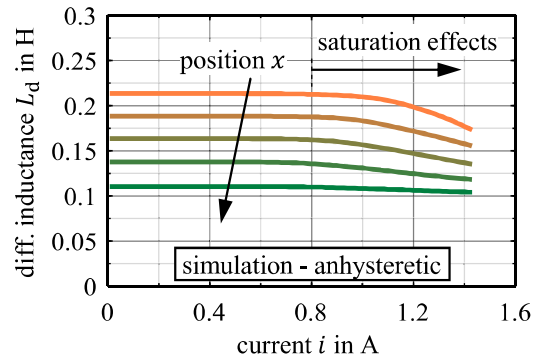


Figure 7: Map of differential inductance $L_d(i, x)$ of the developed sensor-designed solenoid simulated without hysteresis effects (in operating range)

5. POSITION OBSERVATION STRATEGY FOR SENSOR-DESIGNED SOLENOID

5.1. Position observation

The remaining hysteresis effects can be handled by a mean value strategy. This is allowable due to nearly linear curves in the map $\Psi(i, x)$ and triangular current behaviour (**Figure 8**). Therefore, the averaged differential inductance is calculated from the current and voltage values according to **Figure 8** with

$$L_{d,on} = \frac{u_{in,on} - Ri_{on}}{\frac{\Delta i_{on}}{dT_{PWM}}} \quad (4)$$

for PWM on-time and with

$$L_{d,off} = \frac{u_{in,off} - Ri_{off}}{\frac{\Delta i_{off}}{(1-d)T_{PWM}}} \quad (5)$$

for PWM off-time.

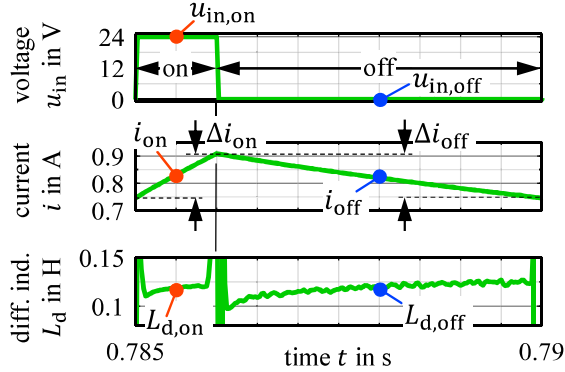


Figure 8: Measured and calculated values for mean value strategy

By using this mean value strategy, the resulting map has a clear correlation, shown in **Figure 9**. Exactly one position is assigned to a defined pair of differential inductance and current value. Due to nearly same inductance values $L_{d,on}$ and $L_{d,off}$, the averaged value $L_{d,ss}$ of both is used in the following (ss: steady state).

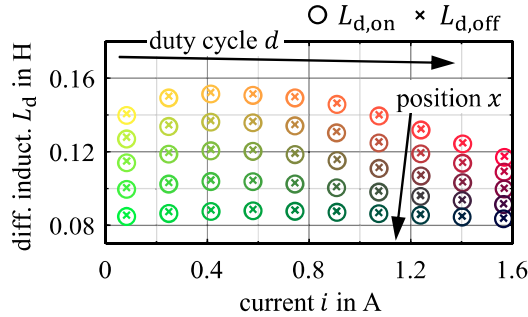


Figure 9: Map of differential inductances $L_{d,on}(i_{on}, x)$ and $L_{d,off}(i_{off}, x)$ in operating range by applying mean value strategy (unipolar PWM voltage)

For these investigations, a unipolar PWM voltage was used (on-time: 24 V, off-time: 0 V). As the duty cycle is zero ($d = 0$, zero mean current), a position determination is not possible. However, a bipolar PWM voltage can overcome this issue and will be used in the following (on-time: 24 V, off-time: -24 V). The corresponding map is illustrated in **Figure 10** and shows the feasibility at zero mean current.

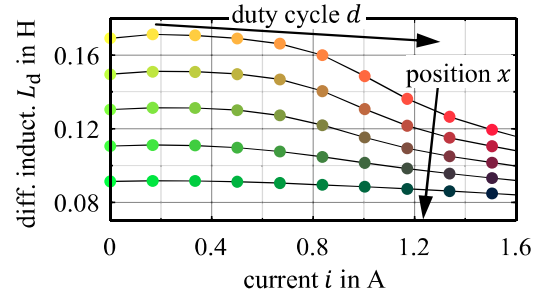


Figure 10: Map of differential inductances $L_{d,ss}(i, x)$ in operating range by applying mean value strategy (bipolar PWM voltage)

The described method works for steady state without changing the mean current value and without armature motion. If there is a change of the mean current, the hysteresis loops are not closed. This results in different inductance values $L_{d,on}$ and $L_{d,off}$ as for steady state ($L_{d,ss}$) due to transient behaviour. **Figure 11** depicts the behaviour schematically.

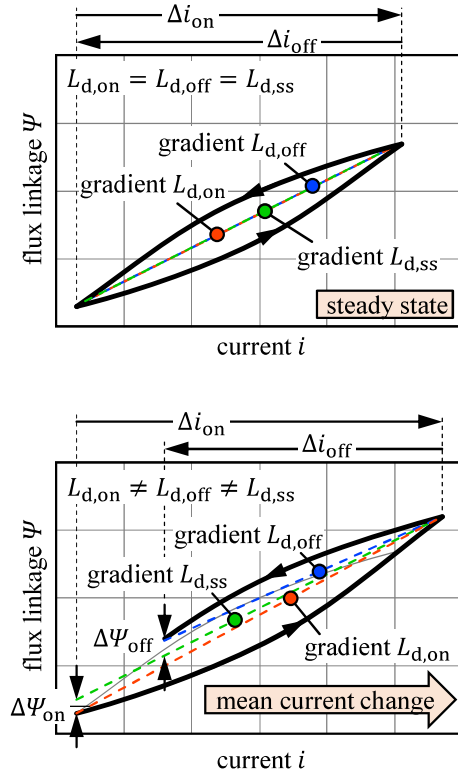


Figure 11: Schematic behaviour of flux linkage over current during a PWM period (top: at steady state, bottom: at change of mean current)

A change of the duty cycle leads to a transient phenomenon of the mean current value. If the duty cycle is increased, the mean current increases successively as well. Therefore, the

bent flux linkage curve at PWM on-time increases further than in the comparable operating point of steady state. This results in a larger gradient $L_{d,on}$ (**Figure 11**, bottom). During PWM off-time, the curve is shortened with a resulting smaller gradient $L_{d,off}$. A similar behaviour occurs during armature motion due to the position-dependent change of flux linkage (**Figure 12**). If the air gap decreases due to armature motion, the flux linkage increases and vice versa (compare also **Figure 6**, top: position-dependency of flux linkage).

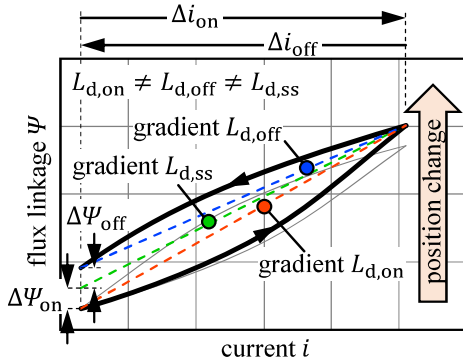


Figure 12: Schematic behaviour of flux linkage over current during a PWM period at armature motion

However, a real armature movement is initiated by a change of the mean current. Therefore, the effects from mean current change (**Figure 11**, bottom) and armature motion (**Figure 12**) are superimposed.

Both effects can be considered by a correction term. The induction law (see equation (2)) provides an appropriate approach. Therefore, the Kirchhoff's voltage law for the electrical domain can be written as

$$u_{in} = Ri + u_{ind} = Ri + \frac{d\Psi(i, x)}{dt} \quad (6)$$

with a current- and position-dependent flux linkage $\Psi(i, x)$. The partial derivation of the flux linkage results in

$$u_{in} = Ri + \frac{d\Psi(i, x)}{di} \frac{di}{dt} + \frac{d\Psi(i, x)}{dx} \frac{dx}{dt}. \quad (7)$$

The last term describes already the influence of the armature motion, but can consider a change of the mean current due to its similar behaviour as well. By using equation (1) for the second term and defining the third term as a general induced voltage correction term, equation (7) can be written as

$$u_{in} = Ri + L_d \frac{di}{dt} + \frac{d\Psi_{cor}}{dt}. \quad (8)$$

The application of equation (8) to PWM on-time and off-time by considering the mean value strategy results in

$$u_{in,on} = Ri_{on} + L_{d,on} \frac{\Delta i_{on}}{dT_{PWM}} + \frac{\Delta\Psi_{on}}{dT_{PWM}} \quad (9)$$

and

$$u_{in,off} = Ri_{off} + L_{d,off} \frac{\Delta i_{off}}{(1-d)T_{PWM}} + \frac{\Delta\Psi_{off}}{(1-d)T_{PWM}}. \quad (10)$$

The flux linkage values $\Delta\Psi_{on}$ and $\Delta\Psi_{off}$ are the deviations over PWM on-time respectively off-time compared to steady state behaviour (see also **Figure 11**, bottom and **Figure 12**). These values can be calculated by numerical integration according to equation (2). The integration is possible here, since the integration time is short (maximum: T_{PWM}) and only the difference is calculated (Ψ_0 not considered).

If the induced voltage correction is considered, the differential inductance values in equations (9) and (10) are without influences of armature motion and mean current change. It applies

$$L_{d,ss} = L_{d,on} = L_{d,off}. \quad (11)$$

The equations (9) to (11) yield the final calculation of differential inductance. By equating the coil resistance R , the differential inductance can be calculated with

$$L_{d,ss} = \frac{u_{in,off}i_{on} - u_{in,on}i_{off}}{\frac{\Delta i_{off}}{(1-d)T_{PWM}}i_{on} - \frac{\Delta i_{on}}{dT_{PWM}}i_{off}} + \frac{\frac{\Delta\Psi_{on}}{dT_{PWM}}i_{off} - \frac{\Delta\Psi_{off}}{(1-d)T_{PWM}}i_{on}}{\frac{\Delta i_{off}}{(1-d)T_{PWM}}i_{on} - \frac{\Delta i_{on}}{dT_{PWM}}i_{off}}. \quad (12)$$

The position can now be determined using this differential inductance value, the weighted mean current

$$i_{avg} = di_{on} + (1-d)i_{off} \quad (13)$$

over a PWM period and the map from **Figure 10**.

5.2. Resistance determination

The calculations of the flux linkage values $\Delta\Psi_{on}$ and $\Delta\Psi_{off}$ require the actual value of the coil

resistance according to (2). Unfortunately, the resistance value is temperature-dependent and has to be determined online for a correct calculation. There are some methods known from literature (e. g. [11][12][13]), which are mostly complex or are not accurate enough. A simple approach is an averaging over one PWM period according to

$$R_{\text{avg}} = \frac{\overline{u_{\text{in}}}}{\overline{i}} \bigg|_{T_{\text{PWM}}} \quad (14)$$

Another approach is equating the differential inductance according to equation (9) and (10) [14]. It must be taken into account that the calculation of the correction terms (similar to equation (12)) itself depends on the resistance. In order to avoid numerical loops, the correction terms are negligible, and the resistance value can be calculated with

$$R_{\text{eq}} = \frac{u_{\text{in,off}} \frac{\Delta i_{\text{on}}}{dT_{\text{PWM}}} - u_{\text{in,on}} \frac{\Delta i_{\text{off}}}{(1-d)T_{\text{PWM}}}}{\frac{\Delta i_{\text{on}}}{dT_{\text{PWM}}} i_{\text{off}} - \frac{\Delta i_{\text{off}}}{(1-d)T_{\text{PWM}}} i_{\text{on}}} \quad (15)$$

Both methods work well at steady state, but result in deviations during armature motion and change of the mean current. The results can be improved by using low pass filtering (similar to [11]). This is possible due to very different time constants between the slow thermal behavior of the resistance change and the fast-acting armature motion as well as a change of the mean current. The filtered resistance is calculated by

$$R_{f,k} = \frac{R_{\text{avg/eq}} + \frac{\tau}{T_{\text{PWM}}} R_{f,k-1}}{1 + \frac{\tau}{T_{\text{PWM}}}}, \quad (16)$$

where $R_{\text{avg/eq}}$ is the calculated resistance according to equation (14) or (15), $R_{f,k-1}$ is the previous calculated filtered value and $R_{f,k}$ the new filtered value. The time constant τ is an adjustable parameter and defines the filter characteristic.

6. TEST RIG

The above described methods were investigated by using the test rig, which is seen in **Figure 13**.

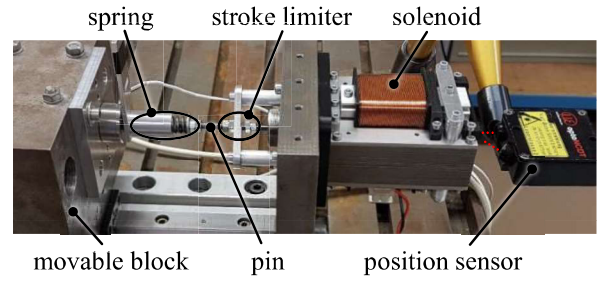


Figure 13: Test rig for investigations of the sensor-designed proportional solenoid (here: configuration for armature motion with spring)

The steady state behavior is measured at fixed armature position. Therefore, the movable block is directly connected to the pin (without spring). Pin and armature are force-fit linked. Various air gap values are set with the block position. The actual armature position is measured with a position sensor (laser triangulation).

The behavior during mean current changes is measured with the same configuration.

For measurements of armature motion, the armature respectively pin works against a spring (see **Figure 13**). In order to move the armature only in the position's operating range, a stroke limiter is used.

During all measurements, coil current, input voltage and armature position are recorded by a LabVIEW-based cRio-System. All used analogue digital converters have a resolution of 16 bit. The time resolution is 25 μs . Based on the measured values, the described methods for position observation and resistance determination are investigated.

7. RESULTS

The above developed novel method for self-sensing position determination is investigated step by step. Therefore, results are shown for steady state and transient behavior. Firstly, the accuracy at steady state is determined. Thus, the repeatability of the map operating points as well as intermediate operating points are investigated. **Figure 14** depicts the different operating points in relation to the map points.

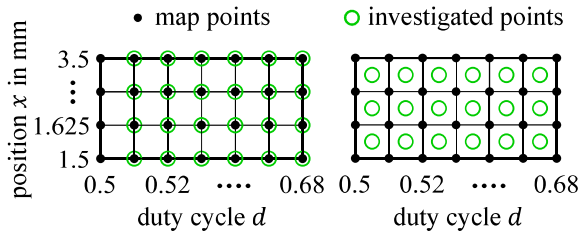


Figure 14: Operating points for investigations in steady state related to the map points (left: repeatability of map points, right: accuracy of intermediate operating points)

The results are illustrated in **Figure 15**. Therefore, the various operating points were analysed once. The relative differences between the measured position value x_m (from position sensor) and observed position value x_{ss} in relation to the operating range $\Delta x_{op} = 2$ mm are evaluated according to

$$\Delta x_r = \frac{x_m - x_{ss}}{\Delta x_{op}}. \quad (17)$$

The induced voltage correction is not considered due to steady state investigation.

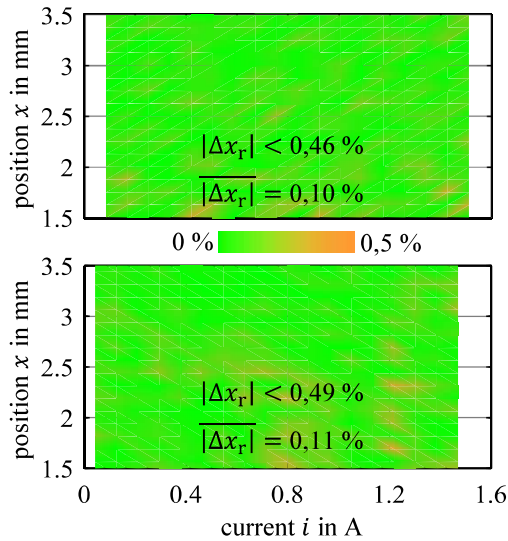


Figure 15: Accuracy of position observation at steady state (top: repeatability of map points, bottom: accuracy of intermediate points)

The plots show very good matches between position observation and position measurement over the entire operating range. Reasons for the small deviations may include interpolation during map generation and position observation as well as measurement noise.

Secondly, the position observation at a mean current change and fixed armature position is investigated. Therefore, **Figure 16** depicts the current response as well as measured and calculated position values after a duty cycle step. The mean current change at beginning can be read from the current curve. Consequently, the magnetic force arises and leads to a small movement due to the elasticity of the test rig. The position observation without considering the correction terms (x_{on} and x_{off} by using equations (4) and (5)) illustrates the deviations during the mean current change. The extended method with induced voltage correction enables an improved position determination, here with good matches as well ($\Delta x_{r,cor} < 1\%$). All calculations are based on the steady state resistance value R_{avg} according to equation (14).

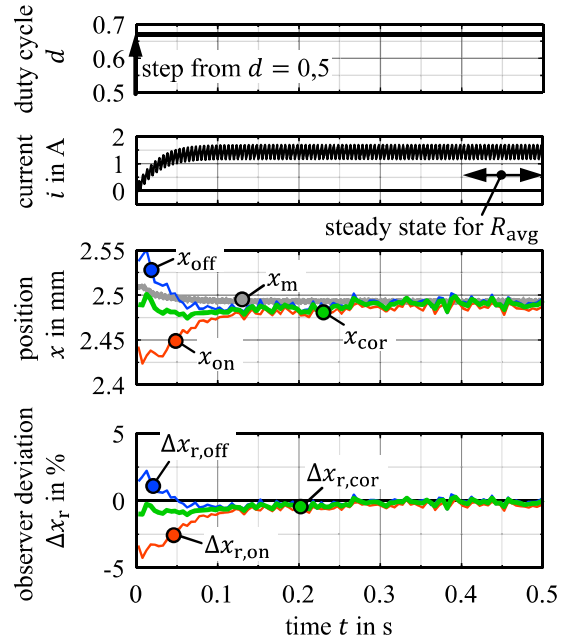


Figure 16: Position observation at change of mean current due to duty cycle step, without and with considering induced voltage correction

In the third step, the position observation method is analysed at armature motion. Therefore, a duty cycle step initiates the position change and a second step back leads to the return motion. The step's edge time t_{edge} is adjustable. The results are shown in **Figure 17**.

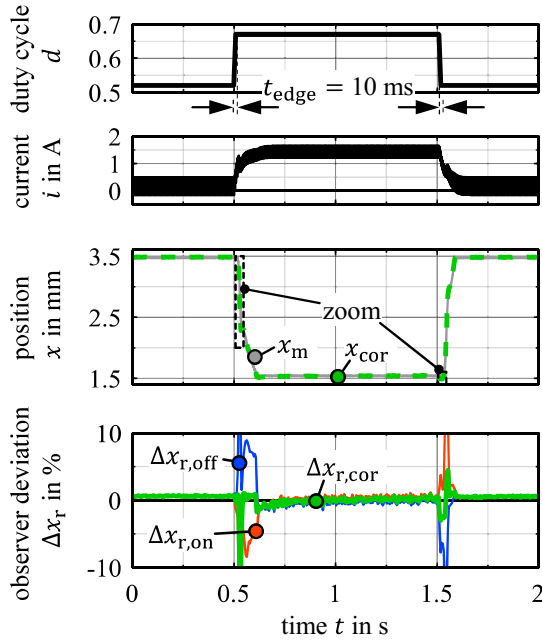


Figure 17: Position observation at fast armature motion due to duty cycle step, without and with considering induced voltage correction

Here, again, the non-consideration of the correction terms causes deviations in the self-sensing position determination. The observation is significantly improved by using the novel method. Large differences still occur at fast armature motion (**Figure 18**). These can be caused by dynamic effects at the test rig and by the mean value based observation method. However, the maximum deviation is only about half the distance the armature moves during a PWM period $T_{PWM} = 5$ ms.

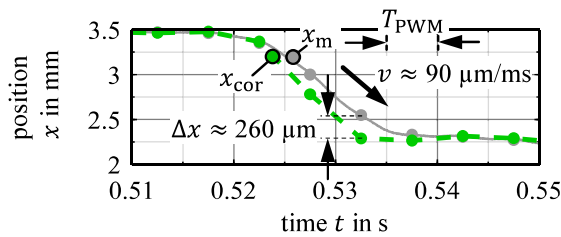


Figure 18: Zoomed behaviour of measured and observed position during armature motion

Further deviations occur at high mean current gradient, especially at high currents and small air gaps (**Figure 19**). In this area, the map of the differential inductance has a pronounced non-linear current dependency due to saturation effects (**Figure 20**). This results in deviations when using the averaging method, which is based on linear interpolation.

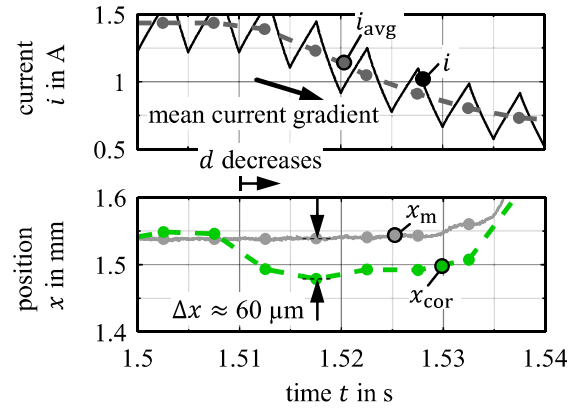


Figure 19: Zoomed behaviour of current as well as measured and observed position during mean current gradient

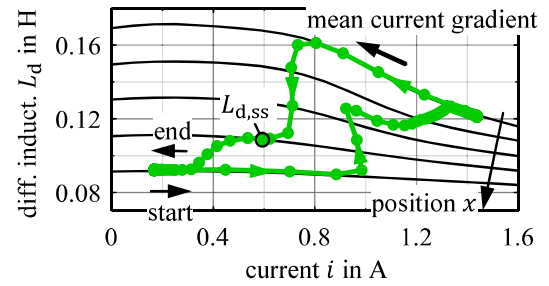


Figure 20: Behaviour of the time-dependent calculated differential inductance over the measuring time in the map

An increased PWM frequency can reduce the deviations. But it must be taken into account that the resolution of one PWM-period and of the current difference Δi decreases.

The above shown investigation uses the resistance value from steady state according to equation (14). This method is not online capable. Therefore, the proposed methods for resistance determination are analysed in the following. **Figure 21** illustrates the calculated resistance values for the same control regime as in **Figure 17**. The basis is the reference value R_{ref} , which is obtained from the averaged resistance value R_{avg} in steady state (same as used for previous investigation).

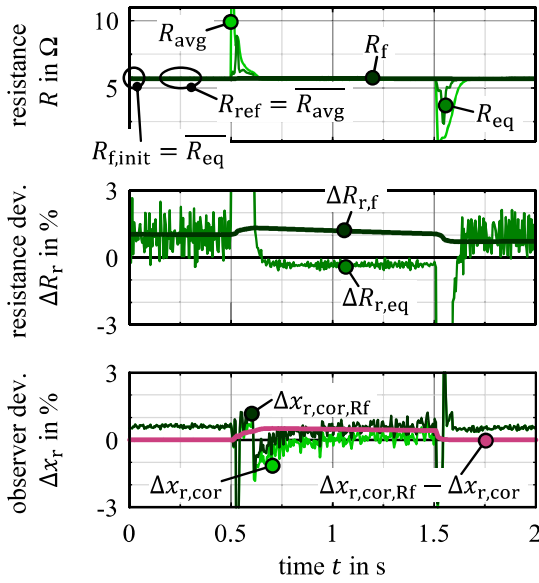


Figure 21: Resistance determination methods at armature motion and resulting observer deviation

As expected, deviations occur at armature motion respectively mean current change. By applying the described filter, the calculated resistance value can be smoothed. Therefore, the proposed equating method with R_{eq} (equation (15)) is filtered due to its smaller deviation in contrast to the averaged method with R_{avg} (equation (14), see **Figure 21**, top). The filter parameter is set to $\tau = 5$ s and the mean of the first five calculations of R_{eq} is used to initiate the filter ($R_{f,init}$). Based on the relative resistance deviation

$$\Delta R_{r,f} = \frac{R_f - R_{ref}}{R_{ref}}, \quad (18)$$

the working principle of the filter can be seen. At transient effects, the filtered resistance value changes only slightly. An armature motion in one direction results in a slight increased resistance value, while the return motion leads to a decreased resistance value. During steady state, the resistance value R_f aligns slowly to R_{eq} .

The resulting difference of the position observation between both methods ($R_{ref} \rightarrow \Delta x_{r,cor}$ and $R_f \rightarrow \Delta x_{r,cor,Rf}$) is in the order of magnitude of resistance deviation $\Delta R_{r,f}$ (ca. 1 %).

In order to analyse the real online capability of this method, further works are planned. Especially longer durations have to be

investigated, where the resistance changes significantly due to thermal effects.

The position observation works with further control regimes as well. Exemplary, **Figure 22** shows a second investigation. The armature does not move between the stroke limits, but has a smaller stroke. In addition, the step's edge time is set to $t_{edge} = 300$ ms.

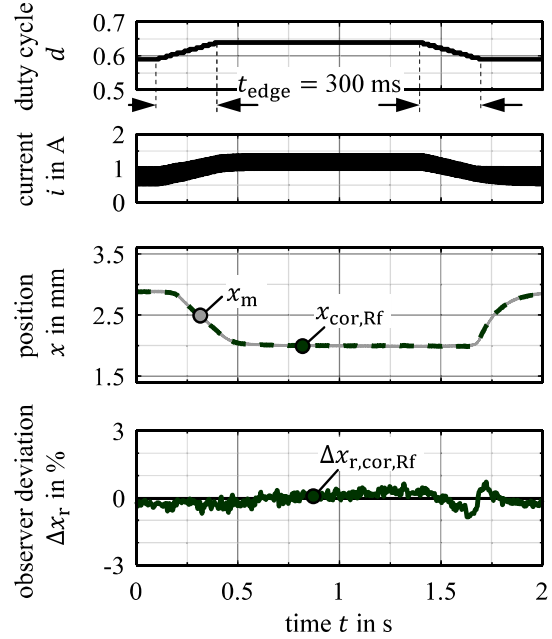


Figure 22: Position observation at slow armature motion due to duty cycle step, only with considering induced voltage correction

The results show a similar behaviour. Due to slower armature motion, a smooth behaviour without deviation peaks can be seen.

8. CONCLUSION AND OUTLOOK

In this work, a novel self-sensing position determination method for a sensor-designed proportional solenoid is proposed. This method considers in addition to steady state behaviour also transient effects such as mean current change and armature motion. It is based on a combined evaluation of differential inductance and flux linkage.

Firstly, issues of conventional proportional solenoids concerning sensor behavior are described. These are mainly hysteresis and saturation effects. On this basis, a sensor-designed proportional solenoid is proposed, which exhibits improved sensor characteristics due to a particular air gap design and a magnetic

circuit made from electrical sheets. Because of remaining small hysteresis effects, a mean value strategy is proposed for self-sensing position determination. The basic position observation uses the differential inductance method. In order to consider also transient effects, the method is extended by an induced voltage correction, which is based on the evaluation of the flux linkage. Furthermore, the position determination method requires the coil resistance value, which must be known online. Different simple methods for calculating the coil resistance are described. Finally, investigations at a demonstrator of the sensor-designed solenoid are presented. The analyses show promising results. The position observation can be significantly improved by applying the novel observation method. Remaining deviations occur especially at high armature velocities and partly at high mean current gradients.

The method is appropriate for condition monitoring the armature position and simple position control tasks, applied on similar working solenoids as well. For a more precise control, further investigations have to be done especially concerning higher resolution of time and analogue digital converter. For an application as valve drive, the design has to be adapted.

Further works will deal with investigations of the resistance determination method at longer evaluation durations, where the resistance value changes significantly due to thermal effects. Therefore, it is also planned to implement the entire observation method and the solenoid control into electronics, in order to show potential industrial usability.

9. ACKNOWLEDGEMENT

The research presented in this paper is based on the project “Sensorgerechte Konstruktion elektromagnetischer Ventilaktoren” (Ref.-No. AiF 19093 BR/1), which was financed and supervised by the Research Association Mechanical Engineering (FKM). In the scope of the Programme to promote Industrial Collective Research it was funded by the German Federation of Industrial Research Associations (AiF) with means of the

Supported by:



Federal Ministry
for Economic Affairs
and Energy

on the basis of a decision
by the German Bundestag

Federal Ministry of Economic Affairs and Energy (BMWi) on the basis of a decision by the German Bundestag.

NOMENCLATURE

d	duty cycle (-)
F	force (N)
i	current (A)
L	inductance (H)
R	resistance (Ω)
t	time (s)
T	time period (s)
u	voltage (V)
v	velocity (m/s)
x	air gap, position (m)
τ	time constant (s)
ψ	flux linkage (Wb)

REFERENCES

- [1] Kallenbach E, Eick R, Ströhla T, Feindt K, Kallenbach M, Radler O (2018): Elektromagnete - Grundlagen, Berechnung, Entwurf und Anwendung. 5th edition, Springer Vieweg, Wiesbaden, Germany, 2018
- [2] Kramer T, Weber J (2019), Sensorgerechte Konstruktion elektromagnetischer Ventilaktoren, Final report, AiF 19093 BR/1, Dresden, Germany, September 27, 2019
- [3] Kramer T, Weber J, Pflug G, Harnisch B (2018), Intelligent Condition Monitoring of Bi-stable Process Valves. 11th International Fluid Power Conference, IFK 2018, Aachen, Germany, March 19-21, 2018
- [4] Kramer T, Petzold M, Weber J, Ohligschläger O, Müller A (2016), Smart control of electromagnetically driven dosing pumps. 10th International Fluid Power Conference, IFK 2016, Dresden, Germany, March 8-10, 2016
- [5] Richter S, Weber J (2013), Sicherheitsorientierte Zustandsüberwachung an elektromagnetisch betätigten Ventilen. Informationsveranstaltung des Forschungsfonds des Fachverbandes Fluidtechnik im VDMA, Frankfurt/Main, Germany, June 26, 2013
- [6] Richter S (2016), Ein Beitrag zur Integration von Maßnahmen der Funktionalen Sicherheit in einen geregelten elektrohydraulischen Antrieb für stationäre Anwendungen. Dissertation, Technische Universität Dresden, Dresden, Germany, 2016

- [7] Rahman M F, Cheung N C, Lim K W (1995), Position Estimation in Solenoids Actuators. Conference Record of the 1995 IEEE Industry Applications Conference Thirtieth IAS Annual Meeting, IAS 1995, Orlando, Florida, USA, October 8-12, 1995
- [8] Renn J C, Chou Y S (2004), Sensorless Plunger Position Control for a Switching Solenoid. JSME International Journal Series C47, June, 2004
- [9] Kallenbach M (2005), Entwurf von magnetischen Mini- und Mikroaktoren mit stark nichtlinearem Magnetkreis. Dissertation, Technische Universität Ilmenau, Ilmenau, Germany, 2005
- [10] Maridor J (2011), Design, Optimization, and Sensorless Control of a Linear Actuator. Dissertation, École Polytechnique Fédérale de Lausanne, Lausanne, Switzerland, 2011
- [11] Glück T, Kemmetmüller W, Tump C, A Kugi (2010), Resistance estimation algorithm for self-sensing magnetic levitation systems. 5th IFAC Symposium on Mechatronic Systems, Cambridge, Massachusetts, USA, September 13-15, 2010
- [12] Jung H G, Hwang J Y, Yoon P J, Kim J H (2007), Resistance Estimation of a PWM-driven solenoid. International Journal of Automotive Technology, Vol. 8, No. 2, pp. 249–258, 2007
- [13] Dülk I, Kovács házy T (2015), Parameter Estimation in Linear Electromagnetic Devices. IEEE Transaction on Industrial Electronics, Vol. 62, No. 6, June, 2015
- [14] Kramer T, Weber J, Pflug G, Harnisch B (2018), Smart Realisation of Energy Savings during Switching Operation at Bi-stable Process Valves. Actuator 2018 - 16th International Conference on New Actuators, Bremen, Germany, June 25-27, 2018

ON/OFF SOLENOID WITH SENSORLESS POSITION DETECTION

Peter Tappe*, Jürgen Heinzmann, Ralf Raupold

Magnet-Schultz GmbH, Allgäuer Str. 30, 87700 Memmingen

* Corresponding author: Tel.: +49 8331 104 392; E-mail address: peter.tappe@magnet-schultz.de

ABSTRACT

As is generally known, pressure-resistant solenoids for valves are used in hydraulics and pneumatics. These solenoids, for example, consist of a so-called pole tube with an integrated armature and a separate solenoid coil. Suitable displacement measuring systems are used in order to measure the armature's as well as valve spool's position constantly; these are directly mounted to the solenoid. Examples here are Hall Effect sensors or LVDT transducers. In case of lesser requirements, it is also possible to measure the valve spool's position directly and in simplified manner. Here, partially standard proximity sensors are employed, which use the valve spool directly as measuring object. In these cases, however, only discrete position measurement is possible. A constant displacement measurement is not necessary. By means of the sensorless position-control developed by MSM, the armature's position can be executed directly by analyzing the solenoid coil, partly replacing the usual sensors, under adapted basic conditions.

Keywords: Sensor, LVDT, Hall-Effekt, sensorless

1. INTRODUCTION

The on/off solenoids usually used in hydraulic valves have a comparably thick-wall pole tube, with a non-magnetic zone integrated. The armature inside such pole tube creates the necessary linear force in order to achieve the valve's full function. Such constructions are also used for sophisticated pneumatic valves.

In many valve applications, the valve spool's position needs to be measured. This is usually achieved by separate sensors, whose measuring elements are connected to the valve spool or, at least, to the solenoid armature. The functionality principle of such sensors is, for example, based on the LVDT principle or uses Hall Effect sensors.

Future developments may promote using sensor information. As application areas, the keywords Industry 4.0 or Predictive Maintenance can be mentioned.

However, regarding such applications, there is a lesser requirement for the position detection. For example, it might be sufficient to sense the currentless solenoid armature's final position only. The valve spool's position determined here displays the valve's cut-off state and so the unpressurized working port.

If, in such cases, sensing the armature's final position is sufficient, the procedure developed by MSM for sensorless position detection may be used.

The basics of the solenoid coil's direct usage to determine the armature's position are described in this article.

2. CONSTANT PATH SENSORS

Principally, sensing of final position is also possible with constantly operating transducers and has been frequently applied in practice. The LVDT principle is widespread. As is generally known, a non-permanent core is moved within a 3 chamber coil system. The position has an impact on the current induced into the secondary coils by a primary coil, so that position detection is possible.

For an exemplary measuring range of ± 4 mm, a linearity of $\pm 1\%$ within a temperature range of -25 to $+75^\circ\text{C}$ can be achieved.

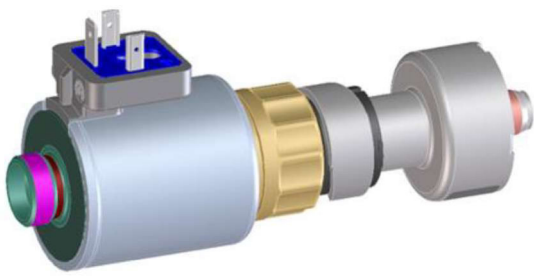


Figure 1: Solenoid with path sensor (LVDT measuring principle)

Even in hydraulics and pneumatics, transducers that use Hall Effect sensors are widespread. These sensors measure the magnetic field of a permanent magnet fastened with a measuring object. Such sensors may also be used as autonomous sensors, independent of actuators.



Figure 2: Solenoid with position sensor (hall sensor)

With this method of action, for example, a linearity of $\pm 1,5\%$ within a temperature range of -25 to $+105^\circ\text{C}$ and a measuring range of $\pm 6\text{mm}$ can be achieved.

2.1. Position control

Due to cost advantages, the hall sensor principle is increasingly important for position control. Position control is also based on a constantly measurable physical principle, however, only final positions are issued.



Figure 3: Solenoid with position control (hall sensor)

When a position control detects 2 positions, for example, the following data is achieved: measuring range $\pm 8.5\text{ mm}$, output voltage $>7\text{ V}$ and/or $<1.5\text{ V}$ within a temperature range of -40 to 100°C

3. SENSORLESS POSITION CONTROL

3.1. Inductance of a solenoid coil

On contemplating such an air coil, its inductance is ideal and constant. However, a coil within the solenoid's iron circle is not constant when taking into account the progression versus the armature's position.

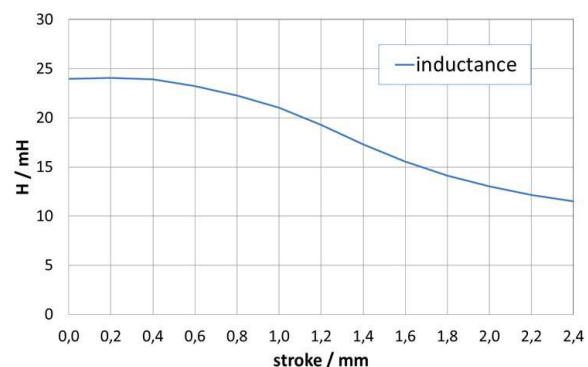


Figure 4: Inductance of a copper coil within an iron circle

The diagram of the typical inductance progression points out that it is apparently attractive to make use of these characteristics in order to detect the armature's position.

It must be emphasized, however, that such a progression can only be achieved under quasi-static basic conditions. In order to measure such an inductance progression, the solenoid's armature is analyzed in discrete measuring positions, for example. In case of energized solenoids in real applications, induced voltages are created within the magnetic field by the armature's movement. So the impact on coil current due to inductance is not only changed solely by position but also by the armature's dynamic movement itself, making it very difficult or even impossible to analyze constantly when considering usual requirements for the optimal functioning of solenoids in valves. Such requirements include, for example, the accuracy of a constant path signal or the optimal design of the solenoid's circle with regard to efficiency.

This is the reason why the method presented here concentrates on the analysis of the currentless solenoid coil's idle state.

3.2. Analysis principle

When taking power off an energized copper coil, a typical voltage peak is created. The voltage's height is usually limited by TVS diodes. Principally, the transient progression of the voltage is influenced by the coil's inductance.

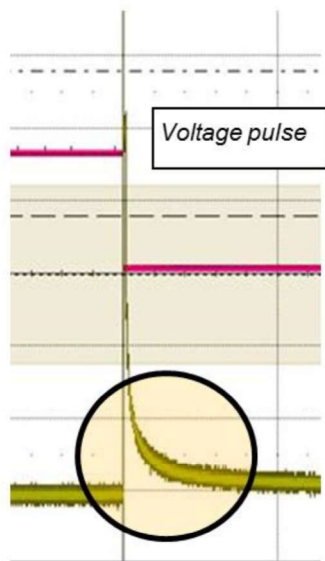


Figure 5: voltage pulse during switch-off

Since now, in turn, the inductance is dependent on the armature's position, an analyzable criteria regarding the armature's position is available. Our MSM patented procedure includes analysis of the duration from switch-off to a defined voltage level's underrun. Duration is measured by evaluating a timer.

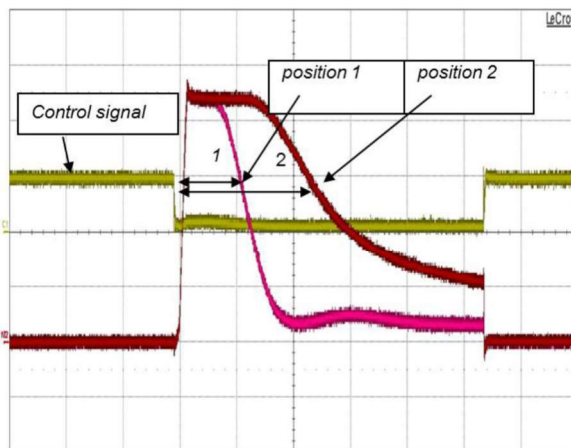


Figure 6: voltage pulse of 2 armature positions

For an application's usage, the solenoid coil is energized by regular measuring pulses so that enough position information is created. The respective pulse during energizing does not lead to the armature's movement when suitably dimensioning the overall function.

In order to complete the description of the measuring principle, the following situation explains when a solenoid is energized. In case a solenoid coil is regulated by the usual PWM operation, particularly in shift valves, cyclical switch-offs are created. These may be analyzed as well. An elaborate harmonization is needed for such switch-off practicability without negative impact on the valve's function, so this operation situation is not part of this report.

4. FUNCTIONAL EXAMPLE

The following Picture demonstrates the integration of a sensorless position detection in a bi-stable shift valve. This solenoid is a pulling version which may be operated in bi-stable manner by using a permanent solenoid. Due to the bi-stable active principle, position may be ideally analyzed in currentless state.

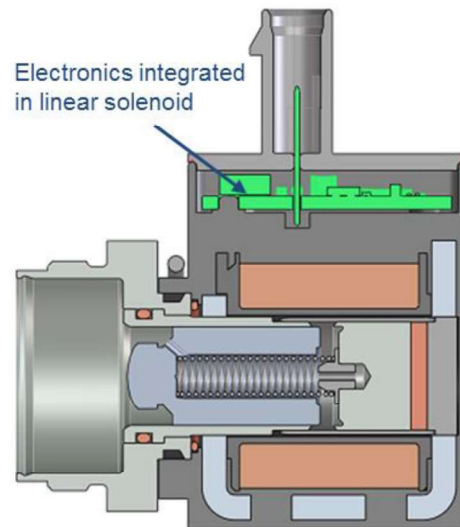


Figure 7: integration of sensorless position detection in a bi-stable shift valve

The solenoid is completed as a shift valve by the customer. The electronic systems include the following functions:

- Energizing by H bridge
- Controlled by LIN/CAN bus
- Supply voltage 9-18 V DC
- Peak current 5 A

- - Temperature range $-40 \dots 125^{\circ}\text{C}$
- - Dimension of printed board $31 \times 31 \text{ mm}^2$

The magnetic stroke of the shift valve used here is 0 to 3.0 mm. Within this range, the sensorless position detection can issue a range of $0.1 \dots 0.7 \text{ mm}$ (typically 0.45 mm) for the energized state. Regarding the off-peak state, an armature position of 1.3 mm and larger (typically 1.41 mm) can be detected.

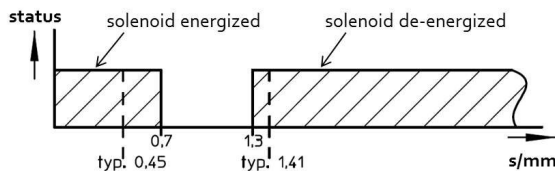


Figure 8: position detection

The switch point precision was achieved under the following basic conditions:

- Ambient temperature $-40 \dots 125^{\circ}\text{C}$
- Supply voltage $9 \dots 16 \text{ V}$
- Use of an averaged temperature compensation

Under the above-mentioned basic conditions, the measurement precision as indicated is achieved. At the same time, the disadvantages of the analysis of the inductance caused by physical conditions are visible. In case of a large stroke, the typical inductance progression flattens increasingly, with the measuring principle's resolution deteriorating due to physical conditions in case of large strokes.

By means of an individual programming of temperature compensation, the measuring quality, however, can be improved considerably.

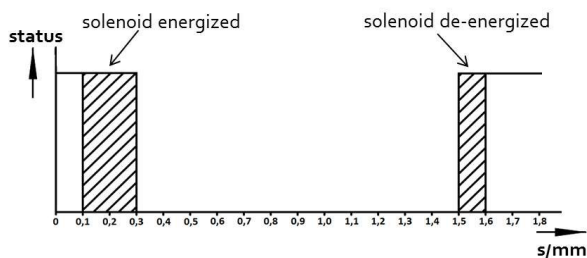


Figure 9: Optimized position detection

4.1. Application

The next picture shows the usage of two on/off solenoids for a hydraulic valve. In order to achieve the valve spool's position detection, the use of ordinary sensors is possible. If the sensors mounted on solenoids are replaced by sensorless

position control, a subsequent functional detection might be possible.

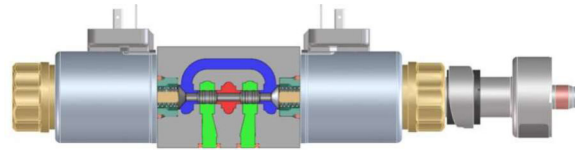


Figure 10: Valve with 2 on/off solenoids including sensor

The uncritical operation state is the valve spool's centered middle position. In this state, working ports are without pressure. The valve spool's deficient eccentric position inevitably moves one of the solenoid's armature from its operation position towards idle stroke. If the armature position is now being monitored, a hydraulic malfunction of such type can be detected.

For a typical solenoid, the principle signal quality's progression (number of metering pulses) of the sensorless position detection can be recognized in the next picture. It can be seen that due to the physical characteristics of the inductance, partial areas are created – these may be analyzed as well.



Figure 11: signal quality above stroke area

If both solenoid coils are differentially analyzed, the signal's resolution can, under ideal basic conditions, be improved.



Figure 12: Signal quality above stroke area in case 2 solenoid coils are used

5. BASIC CONDITIONS

A solenoid's inductance progression is the basis for the position determination by means of sensorless position detection. This progression can certainly not be optimized independent of force/stroke behavior. The arrangement of magnetizable areas of the iron circle and the operation of the iron components in saturation usually aim at an ideal force/stroke behavior for the application in valves.

For a reasonable usage of the sensorless position detection, an optimal configuration of the inductance at the expense of the force/stroke behaviour is necessary. This is the reason why the application of a sensorless position detection is actually not possible without amending the valve's dimensioning and potentially limiting the hydraulic parameters.

6. CONCLUSION

In this report, the inductance characteristics of a solenoid are used to create a sensorless position detection. When the armature of an energized solenoid moves, the current progression is influenced by self-induced voltages due to the armature's movement. So the usage of a sensor principle only makes sense in a case where the armature is in idle state, for example, after a switching procedure's completion.

The sensor principle measures the progression of the switch-off excess voltage which is typically created during switch-offs. So, if measuring pulses are applied onto the solenoid coil, measurements are possible in sufficient chronology.

In the report, valves which are, amongst others, operated by two solenoids, have been examined. In this configuration, one of the solenoids is used as sensor element while the opposite solenoid is energized in order to operate the valve.

Usually, the force/stroke behavior is adjusted ideally to the valve's function. The inductance's characteristic diagram that is created here depends thereon and can certainly not be optimized independently. So it is necessary to optimize the whole valve comprehensively in order to be able to make reasonable use of the inductance progression. The valve, together with the solenoid, must be configured virtually in "sensor conforming" manner.

With such valves and the respective solenoids, replacing traditional sensors is possible under fixed basic conditions.

REFERENCES

- 1) Jürgen Heinzmann: Sensorless Position Detection for Electromagnetic Actuators, IFK-Proceedings 8. IFK 2012

ROTOR SWIVEL MOTOR AS ACTUATOR OF AN INNOVATIVE CONTROL VALVE

M. Sc. Ingo Dietrich*, M. Sc. Lukas Zinßer, M. Sc. Tim Müller, Dr.-Ing. Gerhard Ludwig, Prof. Dr.-Ing. Peter F. Pelz

Chair of Fluid Systems, Technische Universität Darmstadt, Otto-Berndt-Straße 2, 64287 Darmstadt

* Corresponding author: Tel.: +49 6151 16-27110; E-mail address: ingo.dietrich@fst.tu-darmstadt.de

ABSTRACT

To minimize the complexity of existing process control valves, the authors derived a new control valve design by functional separation and functional integration of functions. One key element of this new valve design is the functional integration of the actuator into the valve's throttle. A hydraulic swivel motor is operated with the process fluid, in this case water. The pressure difference to operate the motor comes from the valve itself. Within this paper we present the control valve design and show in detail how we used the Fail-Early design method to develop the hydraulic swivel motor. The construction is discussed using the experience from manufacturing the prototype and the first experimental results are shown. The experiments yield, that the swivel motor principle is promising. Finally, the next development issues are discussed.

Keywords: Swivel Motor, Displacement Actuator, Process Control Valve

1. INTRODUCTION

125 different process control valves are listed in the product selector on Samson AG's Homepage [1]. This number is symbolic for the capital goods industry. For customers, a high product individualization with low application complexity (external complexity from product's view) is of steadily increasing, high importance. For manufacturers of fluid components, this results in an enormous number of variants (internal complexity).

The complexity can be attributed to two main characteristics: (i) existing control valves tend to have a dependency between physical and functional structure and (ii) the actuator is sold separately to the valve, requiring knowledge on the customer side to choose the right valve-actuator combination.

To reduce the mentioned complexity, we used the methods functional separation and functional integration to derive a new process control valve design with less complexity. A presentation of the new valve design and an evaluation regarding the complexity was published by Dietrich et al. [2]

Of particular interest for the 12th International Fluid Power Conference (IFK) is the functional integration of a hydraulic swivel motor into the

valve's throttle. There are two main reasons why the actuator for state-of-the-art globe valves is sold separately from the control valve: (i) the dependency of the needed actuating force on the process pressure and (ii) the available energy source at the valve's installation site, which might be pneumatic or electric. This leads to a complex system from which the customer needs to choose the best fitting product for his requirements.

To overcome the dependency of the needed actuating force (i) on the process pressure we design the seals self-enhancing. To be independent from the available energy source (ii), we use the process fluid itself to operate the swivel motor. Only small pilot valves are necessary to use the existing pressure difference across the valve. Moreover, no high requirements for leakage in the swivel motor are required due to the use of the process fluid.

Within this paper we will give a general presentation of the new valve design, and a more detailed one of the hydraulic swivel motor. During product development we used the Fail-Early method to derive a prototype as fast as possible [3]. By testing this prototype, we are able to identify potentials and errors in an early design stage. Thus, closing this paper, we are able to show first experimental data from our prototype

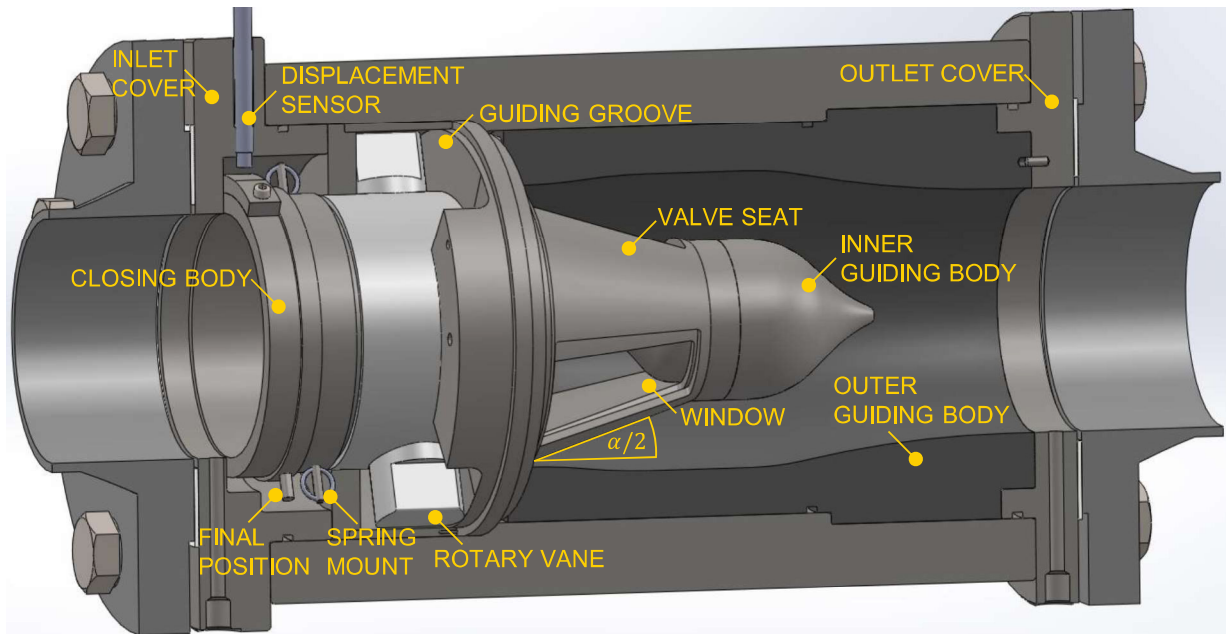


Figure 1: The first prototype of the new process control valve.

and evaluate estimates made during the product development.

2. NEW VALVE DESIGN

The first prototype of the developed control valve is shown in Figure 1. It fits the dimensions of a standard DN80 control valve, giving it a length of 310 mm [4]. An integrated swivel motor is used to change the passed through area of two cone-shaped throttle inserts. These throttle inserts are variable, thus allowing different valve characteristics. All components are mounted in a standard housing.

Process fluid enters the valve through a standard flange and gets into the inner movable throttle insert – the closing body. It is located inside of the fixed outer throttle insert – the valve seat. Both, the closing body and the valve seat, contain at least one or more windows, which are passed by the process fluid. The superimposed windows determine the passed through area. This area can be changed by rotation of the closing body. Additionally, the closing body carries out a slight axial movement to achieve an enhanced inner sealing in the valve's closed position.

The cone angle α of both throttle inserts has to be restricted to avoid self-locking while pressing the closing body into the valve seat. Otherwise, a high breakaway force is needed to release the junction between the throttle inserts. Generally, the static friction coefficient μ_0 , which is crucial

for self-locking, has to be determined by doing experiments. Since we decided to exert agile product development, we rely on standard values from literature. To have a conservative estimation we looked for static frictional coefficients in dry environment of the used material combination steel/steel. Found values vary between 0.25 [7] and 0.45 [8], therefore we used $\mu_0 = 0.30$ for our estimation. In case of changing one of the inserts' material to plastic to achieve a better sealing in closed position, the frictional coefficient tends to stay equal or get better. We conclude the cone angle to be

$$\frac{\alpha}{2} \geq \arctan(\mu_0) = 16.7^\circ. \quad (1)$$

In order to reduce additional forces on the closing body we choose the cone angle close to the restriction from equation (1) to $\alpha/2 = 18^\circ$.

The closing body is driven by a swivel motor with rotary vanes in guiding grooves to perform the rotational and axial movement. Process fluid is the operating medium for the rotary vanes. The process fluid is taken from holes in the inlet and outlet cover of the valve. It is guided through a pilot valve and subsequently back into the process control valve. Thus, the differential pressure across the valve is used for the displacement of the rotary vanes and therefore the actuation of itself.

Based on the new valve design we expect lower pressure losses than in conventional globe

valves across the valve in fully open position because of fewer deflections (see Figure 1). Together with the shape of the windows in the throttle inserts, the inner and especially the outer guiding body have a strong impact on the deflection of the flow. CFD studies have been conducted and found the loss factor of the new throttle valve to be reduced by a factor of approximately seven, in comparison with a globe valve [2]. The pressure losses of the first prototype will be examined at our test rig in Darmstadt in the future.

An inductive displacement sensor is used in combination with an eccentric component to measure the current angle of rotation. The high spatial and temporal resolution of the sensor also allows us to detect vibrations of moving parts. This is a benefit especially for the prototype status. Later on, the expensive inductive displacement sensor could be replaced by a low-cost Hall effect sensor.

The final position for the fully closed and fully open valve is marked by touching dowel pins. Threaded pins in different threaded holes can be used for mounting spring loops of a tension spring. In this way, it is possible to apply a restoring torque on the moving parts in case of blackout.

The first prototype of the throttle valve was designed for operation with water and pressures up to 16 bar.

As already mentioned, a modular design is sought to reduce the internal complexity for the manufacturer as well as the developer and the external complexity for the customer. The modularized structure consists of four different modules: (i) the casing module, (ii) the drive module, (iii) the throttle & closing module and finally (iv) the guiding module.

3. HYDRAULIC SWIVEL MOTOR

The newly developed swivel motor is part of the drive module and can be further divided into the moving rotor and the fixed guiding grooves. It is driven hydraulically by the pilot operated process fluid.

3.1. Requirements

Some definite advantages and disadvantages arise, when using process fluid and the differential pressure across the valve to operate

the swivel motor. The fact to use process fluid as operating medium for the rotary vanes decreases the necessity for leakage free dynamic sealing as leakage flow does not contaminate the process fluid. On the other hand, the functionality of the swivel motor depends on the available differential pressure. Thus, it is required to achieve low friction in the system to guarantee the possibility to actuate the motor when there is only a small differential pressure available. For high differential pressures, the pilot flow has to be throttled in the pilot valve to reduce the actuating speed.

The rotational and axial movement shall be executed simultaneously and continuous to avoid discontinuities and therefore increase robustness of the drive module. The result is a screw movement of the rotor along the centerline of the throttle valve, which has to be mapped by the guiding grooves.

The requirements in terms of dynamics are relatively small, considering minimal actuating times of 18 to 90 s [5] for a full opening or closing cycle of a conventional globe valve in ordinary operation. Possible actuating times for emergency operation may reach 4 s [6].

3.2. Concept

For the first prototype, a window design of three quadrangular openings in the closing body and the valve seat is chosen. This results in 120° action area at the circumference for each window. The expansion of one opening must not exceed 60° to secure a complete superimposition of the windows in fully open position of the valve and additionally a complete coverage of the windows in fully closed position. Furthermore, the actual expansion of one opening is chosen to be 55° to establish a 5°-sealing surface for each window in order to enhance the inner sealing in the closed position. The required entire rotational movement is $\gamma = 60^\circ$ and independent of the sealing surface.

The material combination steel/PTFE is used for every area that is moved and in steady contact to its counterpart to decrease the mentioned friction in the system. The static and kinetic frictional coefficient of this combination are equal, but can vary between $\mu = 0.04$ and 0.25 [8]. Due to the equality of those two parameters for this material combination, the stick-slip effect will be prevented. The areas that are moved to

their counterpart represent the bearing of the closing body and the sealing of the guiding grooves. We omitted separate bearing and sealing, since we want to reduce friction and complexity. In addition, PTFE is traditionally used for both functions.

The movement of the rotor, together with the guiding grooves represent a screw drive, which can be self-locking. The occurrence of self-locking depends on the lead angle β of the drive as well as the material of the rotary vanes and the guiding grooves. In this case, self-locking is desirable to prevent the valve from being actuated by the process flow that acts on the pressure effective area of the closing body. The corresponding material combination is steel/PTFE, therefore both, the static and kinetic, frictional coefficient is assumed to be $\mu = 0.08$. To achieve self-locking the lead angle has to be

$$\beta \leq \arctan(\mu) = 4.6^\circ \quad (2)$$

and is chosen to $\beta = 3^\circ$.

With the length between the centerline of the rotor and the pressure center of a rotary vane of $l_{rv} = 55$ mm the screw pitch h is calculated to

$$h = 2\pi l_{rv} \tan(\beta) = 18.1 \text{ mm}. \quad (3)$$

The resulting axial movement l_{ax} of the rotor during an opening or closing cycle is derived to

$$l_{ax} = \frac{\gamma}{360^\circ} h = 3 \text{ mm}. \quad (4)$$

An estimation for the number of rotary vanes is carried out by calculating the needed drive torque. The performed estimation is uncertain because the friction in the final parts is difficult to predict. According to our development method, the accuracy of the prediction will be determined in the first tests. The most critical case is opening the throttle valve while there is only a small pressure difference Δp_v across the valve, because the same pressure difference is used for actuation. The needed torque T_{stat} for overcoming the static pressure force on the closing body F_{stat} is calculated and will be compared with the drive torque T_d for a different number of rotary vanes.

The needed torque T_{stat} depending on the pressure difference Δp_v

$$T_{stat}(\Delta p_v) = \frac{F_{stat}(\Delta p_v)h}{2\pi\eta} \quad (5)$$

is calculated with the static pressure force on the closing body F_{stat} , the screw pitch h and the efficiency of the screw drive η . Furthermore F_{stat} is derived to

$$F_{stat}(\Delta p_v) = \Delta p_v A_{proj} \quad (6)$$

with the pressure difference Δp_v across the valve and the pressure effective area A_{proj} of the closing body. A_{proj} corresponds to the area of the nominal diameter minus the three windows of the closing body and a hole for the inner guiding body. The efficiency of the screw drive is calculated to

$$\eta = \frac{\tan(\beta)}{\tan(\beta + \arctan(\mu))} = 39.4 \% [8] \quad (7)$$

with the lead angle β and the frictional coefficient of steel/PTFE. By inserting equation (6) and (7) in equation (5) we receive T_{stat} .

The drive torque T_d is built with the number of rotary vanes n , the pressure difference Δp_v , the pressure effective area of one rotary vane A_{rv} , and the lever between the centerline of the rotor and one rotary vane l_{rv}

$$T_d = n\Delta p_v A_{rv} l_{rv}. \quad (8)$$

The resulting torques are shown in Figure 2. It is visible that for one as well as two rotary vanes the drive torque is always higher than the torque needed to overcome the static pressure difference. Since partially constant friction in the

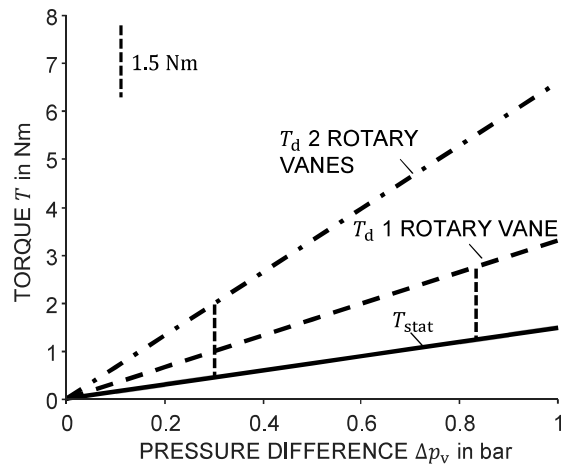


Figure 2: Drive Torque T_d and torque for overcoming the static pressure difference on the closing body T_{stat} in dependence of Δp_v .

system and pressure losses in the pilot control as well as in the swivel motor are not considered in this estimation, the absolute and not the relative difference is crucial. If constant friction and pressure losses resulting in about 1.5 Nm are assumed (as shown in Figure 2), a certain pressure difference across the valve is needed. For one rotary vane, we need at least 0.3 bar and for two rotary vanes at least 0.82 bar. Because we want to have a robust design, we choose $n = 2$ rotary vanes for the first prototype to secure the actuation also at low available pressure differences. Moreover, two symmetrical arranged rotary vanes, cancel out the radial forces on the closing body. Another possibility to strengthen the robustness is, for example, a larger pressure effective area of the rotary vanes.

A 4/3-way proportional valve has to be used as pilot valve for operating the throttle valve (see Figure 3). The three pilot valve positions are for opening and closing the throttle valve as well as remaining in position. As already mentioned, the pressure difference Δp_v is taken from the inlet and outlet cover of the throttle valve. A calculation of the flow coefficient for the pilot valve $K_{VS,pv}$ is carried out to ensure proper operation of the throttle valve. The volume flow going through the pilot valve Q_{pv} is derived with the number of rotary vanes n , the pressure effective area of one rotary vane A_{rv} , the travelled path of the rotary vanes along the circumference l_{tp} and the target actuating time t_a (emergency operation (ref. sec. 3.1) to

$$Q_{pv} = \frac{nA_{rv}l_{tp}}{t_a} = 0.06 \frac{\text{m}^3}{\text{h}}. \quad (9)$$

If a relatively small pressure loss over the pilot valve of $\Delta p_{pv} = 0.25$ bar is aspired, the flow coefficient is calculated to

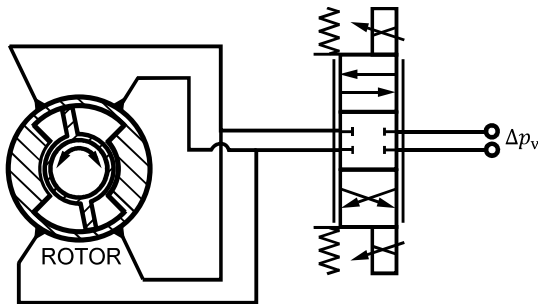


Figure 3: 4/3-way proportional valve as pilot to control the throttle valve.

$$K_{VS,pv} \geq Q_{pv} \sqrt{\left(\frac{\Delta p_{1 \text{ bar}}}{\Delta p_{pv}}\right)} = 0.12 \frac{\text{m}^3}{\text{h}}. \quad (10)$$

The density correction factor in equation (10) is neglected since we are using water as process fluid.

For high available pressures of up to $\Delta p_v = 16$ bar it has to be granted, that the 4/3-way proportional valve is still in its designated control range, depending on the chosen type of the pilot valve.

3.3. Design

Figure 4 shows a halve cut of the guiding groove. It consists of three main parts, the front part, the rear part and the groove base. It is made out of stainless steel and machined by turning and milling. Two pressure line connect to the inlet cover (see Fig. 1), the orientation is ensured by pins. On the right side the valve seat is mounted.

Figure 5 shows the rotor in an exploded view. The two rotary vanes are mounted to the closing body with a pin and a screw. They hold the sliding bushing in its position. The sliding bushing ensures the rotational and axial movement of the closing body. Rotary vane and sliding bushing are made out of PTFE by turning and milling. On the closing body we further mount the excentre, that transforms the angle of

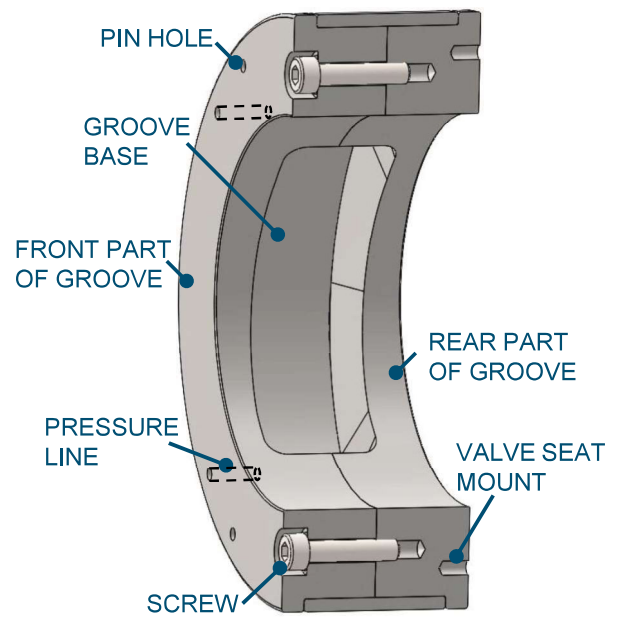


Figure 4: Half cut of the guiding groove.

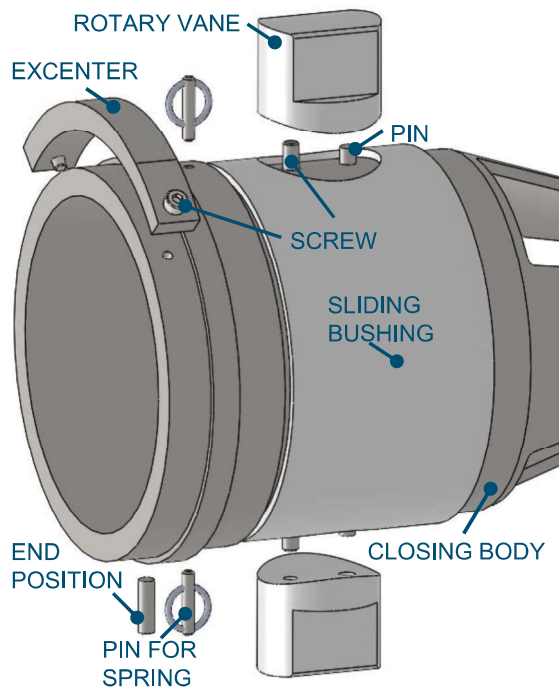


Figure 6: Rotor in exploded view.

rotation into a displacement for our displacement sensor.

Figure 6 shows the working principle of the throttle insert. The rotational and axial movement is visible. In the center position the center line and the edge of the closing body's window are not parallel, due to the necessary 5° sealing area, that needs to be maintained in the fully closed position. In our design, the rotational angle at which the closing body and the valve seat have solid state contact is determined by the axial manufacturing tolerances. To be able to set it for the first prototype we included a peel plate between the guiding groove and the valve seat. It consists of 10 slices, each being 0.05 mm thick.

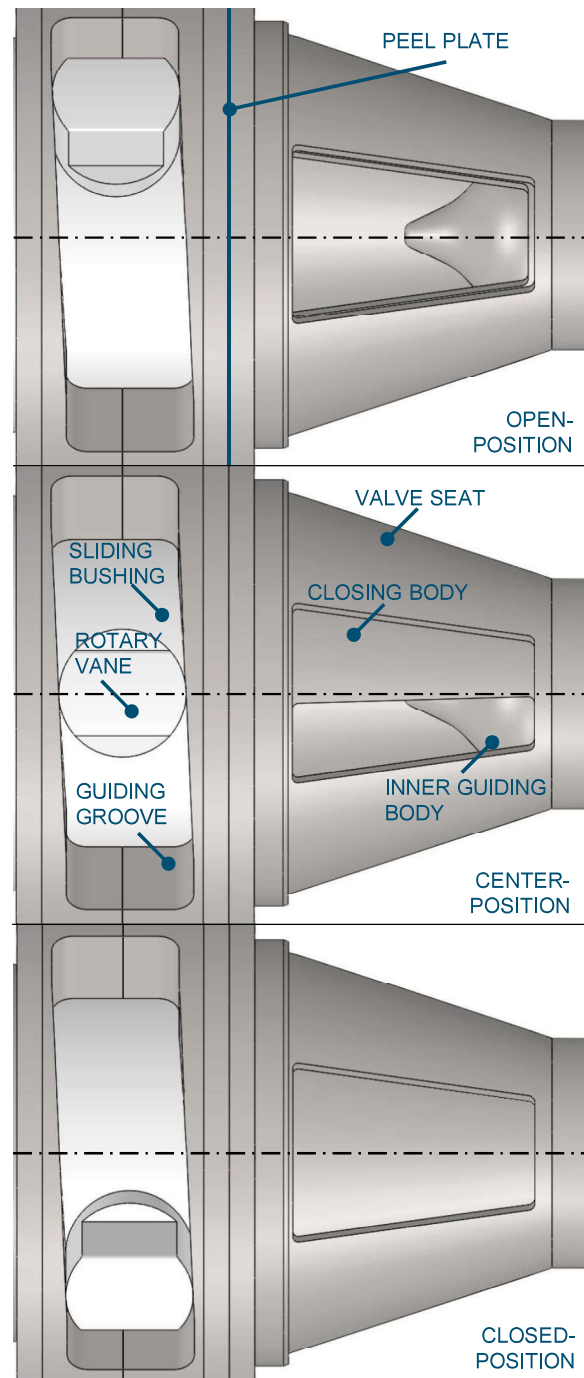


Figure 5: Three positions of the throttle insert.

4. EVALUATION

From the manufacturing of the prototype we derived potential improvements for the next development step.

PTFE has a tendency for cold flow/creep which might disqualify it for a long-term operation. Secondly, the sliding bushing is thin walled, with a big diameter. The residual stresses in our PTFE-material made it difficult to stick to

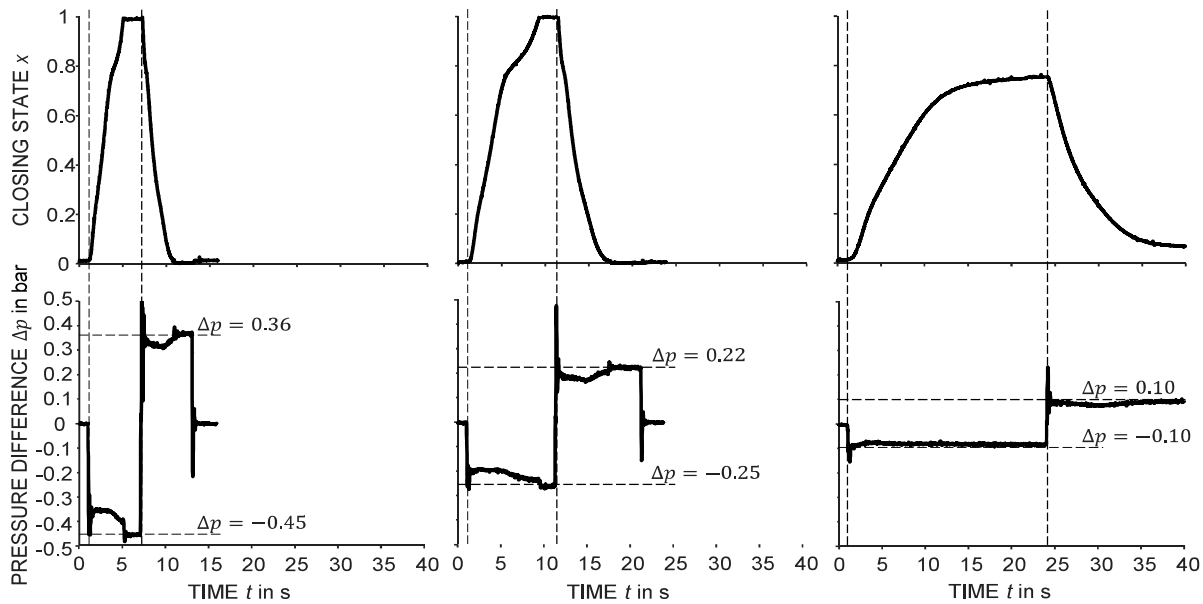


Figure 7: Closing state and pressure difference applied on the swivel motor over time for three different pressure ranges.

the necessary tolerances. Both problems might be tackled by using PTFE with suitable fillers in the next prototype. Finally, the machining of the closing body was challenging, because of the thin walls and the length of the part. Cutting out the windows, alters the tolerances as residual stress deforms the machined parts. A further functional separation of the actuator (consistent of the sliding bushing and the rotary vanes) and the part with the windows might be beneficial.

Another aspect for further improvement is the necessary turndown ratio of the pilot control valve. As it should provide good controllability for high- and low-pressure differences. For our first prototype a suitable 4/3-way proportional valve could not be found. We build the same functionality with one proportional valve and four switching valves.

For the first experimental tests we assembled the prototype as shown in Figure 1. We applied an external, controllable pressure difference Δp to our pilot control. To have better insight, we did not mount the process control valve into a piping, but rather placed it in a bucket. This way we could visually inspect the leakage and the movement of the closing body. Proceeding this way, we can ensure, that the kinematic is working, we can evaluate our estimates about the needed torque for actuation and the opening/closing time.

Figure 7 shows the closing state and pressure difference over time for three different pressure

ranges. The closing state x equals 0 for the fully open position and 1 for the fully closed position. Since the change of volume for a given change of rotational angle inside the swivel motor is constant and the volume flow rate Q_{pv} is constant for a constant pressure, one would expect a linear characteristic for the closing state. As Figure 7 shows this is true for the closing state up until ≈ 0.7 , when the slope changes. Since this occurs independent from the pressure difference, we derived that the reason is probably the manufacturing quality of the groove. For the pressure difference $\Delta p = 0.1$ bar we can see, that the valve is not able to open and close to the full working range anymore.

Figure 8 shows the time t necessary to close or open the valve for a given pressure difference. The difference for opening and closing most likely comes from our pilot control set up, and different loss coefficients for the piping/hosing for the different states opening and closing. For our design point $\Delta p_v = 0.25$ bar we wanted to achieve an operational time of 4 s (sec. 3.2). In our experiments we were able to open the valve in 5 s for that pressure difference. Since we neglected any losses in the piping, this is a rather good result.

Figure 9 shows the working range of the swivel motor over the applied pressure difference for an opening of the valve. We can see, that for a pressure difference Δp between 0.2 and 0.4 bar a full range operation is possible. For 0.15 bar it

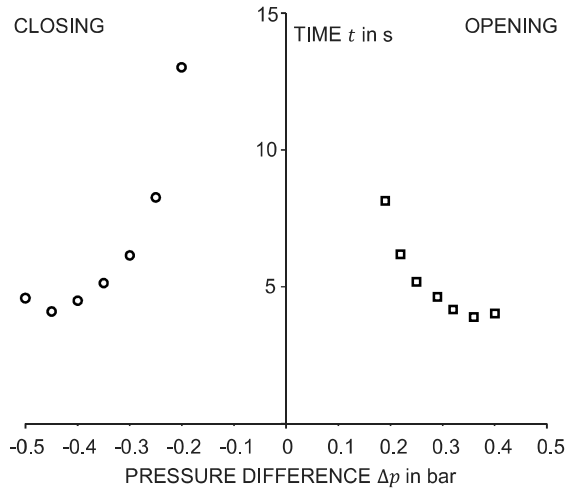


Figure 8: Actuating time of the swivel motor over applied pressure difference.

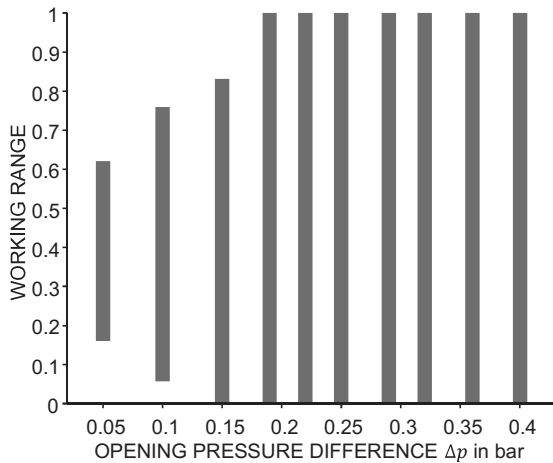


Figure 9: Working range of the swivel motor over applied opening pressure difference.

is not possible to fully close the valve, and below 0.1 bar it is not possible to fully close and open the valve. Using Figure 2, we can derive the friction torque for a given pressure difference Δp . However, this represents an upper boundary, since there is also a, yet, unknown amount of leakage across the rotary vane driven by this pressure difference. For the minimum working difference $\Delta p = 0.2$ bar we read a friction momentum of 1.32 Nm.

5. CONCLUSION AND OUTLOOK

In this paper we presented a new process control valve design, which we derived through functional separation and functional integration.

Of special interest for the 12th International Fluid Power Conference (IFK) is the functional integration of a hydraulic swivel motor into the

valve's throttle. The swivel motor is operated with the process fluid, in this case water, and is made of the material combination PTFE/stainless steel.

We explained our construction in detail and presented the necessary assumptions and calculations during the design phase.

Using the Fail-Early design method, we were able to derive the first prototype within six months from the project's start. First experiments show, that the swivel motor is working almost as designed. We achieve our desired opening/closing time, and the friction within the system is very low. However, we see issues with the manufacturing quality and a different behaviour for opening and closing the valve, which most likely comes from our pilot control set up. With the first prototype we will continue experimental testing. We are especially interested in the valves characteristic and behaviour when it is operating in a flow circuit.

Taking our lessons learned we will improve our design and start building the second prototype. We see three main challenges: i) long term operation of the swivel motor with water or other process fluids in terms of erosion and sedimentation, ii) the necessary turn down ratio of the pilot valve and iii) the long-term behaviour of the PTFE parts.

NOMENCLATURE

A_{proj}	pressurized projected area of the closing body
A_{rv}	pressurized projected area of one rotary vane
F_{stat}	force to overcome static pressure on the closing body
h	screw pitch of the drive
$K_{VS,pv}$	flow coefficient of the pilot valve
l_{ax}	axial movement of the rotor
l_{rv}	length between the centreline and the rotary vane
l_{tp}	travelled path of the rotary vanes
T_d	drive torque of the rotary vanes
T_{stat}	torque to overcome static pressure on the closing body
t_a	time
Δp	externally applied pressure difference
$\Delta p_{1\text{ bar}}$	pressure for normalization
Δp_v	pressure difference across the throttle valve
α	cone angle of closing body and valve seat
β	lead angle of the screw drive
η	efficiency of the screw drive
μ_0	static frictional coefficient
μ	(kinetic) frictional coefficient

REFERENCES

- [1] Samson, „Ventile Produktselektor,“ 14 05 2019. [Online]. Available: https://www.samson.de/de/produkte-anwendungen/produkte/ventile/?tx_solr%5Bfilter%5D%5B0%5D=usage%3A1.
- [2] Dietrich I, Müller T, Meck M, Zinßer L, Nakhjiri M, Ludwig G, Pelz P (2019) One valve for many purposes – reduced complexity by separation of functions. 4th International Rotating Equipment Conference - Pumps and Compressors. Sep 24-25, 2019, Düsseldorf, Germany.
- [3] Moogk D R (2012) Minimum Viable Product and the Importance of Experimentation in Technology Startups. Technology Innovation Management Review, vol. 2, no. 3, pp. 23-26.
- [4] DIN EN 60534-3-1:2000-12 Stellventile für die Prozessregelung – Teil 3-1: Abmessungen – Einbaulängen von geflanschten Durchgangsventilen und geflanschten Eckventilen (IEC 60534-3-1:2000).
- [5] SAMSON Aktiengesellschaft (2019) Typenblatt T 5824. Frankfurt, March 2019.
- [6] SAMSON Aktiengesellschaft (2019) Antriebe für elektrische Stellventile. Frankfurt, 2019.
- [7] Gomeringer R, Kilgus R, Menges V, Oesterle S, Rapp T, Scholer C, Stenzel A, Stephan A, Wieneke F (2019) Tabellenbuch Metall, 48. Auflage, Europa, 2019.
- [8] Grote K.-H., Feldhusen J Dubbel (2005) – Taschenbuch für den Maschinenbau mit Tabellen, 22., neubearb. und erw. Aufl. ed. Berlin u.a., Springer, 2005.

EXPERIMENTAL AND NUMERICAL STUDY OF A NOVEL PIEZO-ELECTRIC PILOT STAGE FOR SERVOVALVES

Paolo Tamburrano^{1*}, Andrew R. Plummer², Pietro De Palma¹, Elia Distaso¹ and Riccardo Amirante¹

¹*Department of Mechanics, Mathematics and Management (DMMM), Polytechnic University of Bari, Bari, Italy;*

²*Centre for Power Transmission and Motion control (PTMC), University of Bath, Bath, UK.*

**Corresponding author; e-mail address: paolo.tamburrano@poliba.it*

ABSTRACT

Two - stage servovalves, despite being widely used in aircraft and industry because of their reliability and high performance, have a few disadvantages that are still unsolved at the state of the art, such as the power consumption caused by the quiescent flow (internal leakage) in the pilot stage, and the complexity and high number of parts of the torque motor assembly of the pilot stage. The solution to these problems can help to reduce costs, weight, power consumption, and to enhance the reliability and producibility as well as the performance of these valves. This paper presents a novel configuration of servovalve, which has the potential to overcome the above-mentioned issues. The proposed servo-valve includes a novel architecture for the pilot stage by using two piezo-electric actuators (ring benders). In this paper, the performance of this novel pilot stage is assessed. To this end, a valve prototype has been constructed and tested; the experimental results are also used to validate a numerical model obtained with the software Simscape Fluids. The results show that, acting on specific parameters, the performance of the piezo-valve can be very competitive, while ensuring very low internal leakage and complexity.

Keywords: servovalves, internal leakage, piezoelectric actuators, ring bender

1. INTRODUCTION

The architectures of commercially available two-stage servovalves, which have not substantially changed for many years, can provide high reliability and excellent dynamics [1, 2]. Regardless of the pilot stage, which can be a double flapper-nozzle pilot stage or a deflector jet pilot stage, the main stage is usually a spool valve in which the main spool is actuated by a differential pressure generated at its extremities by the pilot stage. In this way, very high actuation forces are generated, which results in a much faster response and higher shear forces than proportional valves using proportional solenoids to directly drive the spool [3-6]. These characteristics have led to widespread use of these servovalve designs, which are fundamental components in closed-loop electro-hydraulic motion control systems demanding high performance levels. However they present some weak points that are still unsolved, such as: the quiescent flow in pilot stage (to be referred to as the internal leakage of the pilot stage), which is continuous and constant regardless of the

opening degree of the main stage, thus causing unwanted power consumption during operation [1, 2], and the electromagnetic torque motor assembly which is composed of many sensitive mechanical and electrical parts that penalise simplicity, set-up, duration of manufacture and manufacturing costs [1, 2].

To date, research studies in the scientific literature have mainly been focused on the reduction of the complexity of servovalves. In particular, a promising research field aims to replace the electromagnetic torque motor assembly with piezoelectric actuators, thus reducing complexity and manufacturing costs [2]. Different types of piezoelectric actuators have been used to directly drive the main stage spool or to drive the flapper, jet pipe, or deflector jet in the pilot stage [7-16], showing that the idea of using a piezo-electric actuator to drive a servovalve is feasible and promising. Both piezo-stack actuators, in which several piezo elements are joined together to form a multi-layer actuator [7-9], and amplified piezo-stack actuators, which can provide higher displacement but lower forces [10-12], have been proposed to be used.

However, both types seem to be too heavy and large to be employed in servovalves, which must be compact and light, especially for applications in aircraft. As an alternative to stack actuators, lighter piezo-actuators, such as rectangular benders, have been employed in novel designs to drive the pilot stage of servovalves in place of the torque motor [13-15]; in this case, the main deficit is the very low actuation forces obtained with these actuators.

Instead, the most promising solution for these applications seems to be “the ring bender”, which is a flat annular piezo-disc deforming in a concave or convex fashion depending on the polarity of the applied voltage, providing a very good compromise between actuation force and displacement, while being sufficiently compact for this type of applications. In this regard, in [16, 17] two ring benders, mounted in tandem to provide redundancy, were used in place of the torque motor to drive the flapper in a double flapper-nozzle pilot stage. The preliminary results obtained in [16, 17] prove the feasibility, in terms of actuation forces, displacement and dimensions, of using ring benders as actuators for the pilot stages of servovalves.

All the above-mentioned research studies have had the objective of reducing the complexity of servovalves. However, to date the problem concerning the quiescent flow (internal leakage) in the pilot stage has not been addressed in the scientific literature, apart from the work presented in [18], in which a small spool actuated by a ring bender was employed for the pilot stage in order to minimise the internal leakage of the pilot stage.

In this scenario, the present research project aims at developing a novel configuration of piezo-valve capable of reducing both the complexity and the internal leakage of two stage servovalves. The novel valve concept is described in the following section.

2. NOVEL SERVOVALVE CONCEPT

Fig. 1 shows the proposed valve design. In place of the torque motor, flapper and flexure tube of typical servovalves [2], the proposed architecture includes two small piezo-valves actuated by ring benders. Each piezo-valve is a very simple two-way two-position (2/2) valve that has the advantage of being normally closed, which means that the ring bender stops the oil flow

when the spool is at null. This can represent a huge improvement in terms of power consumption compared to the typical configurations, since the quiescent flow (internal leakage in the pilot stage) is ideally null when the spool is at null. In addition, the torque motor with all its drawbacks (complexity and noise sensitiveness) is removed. The only drawback resulting from the proposed solution is that the mechanical feedback is no more possible, and only an electrical feedback can be used, like a linear variable differential transformer (LVDT).

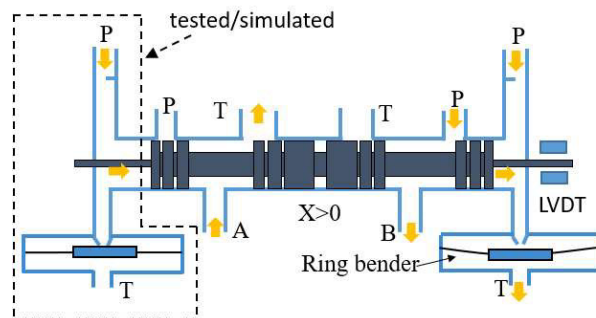


Figure 1: Operating principle of the novel servovalve pilot stage actuated by a ring bender

The feasibility of the proposed solution was already demonstrated in [19], in which a full simulation model of the full valve concept was used. The simulations showed that this valve architecture has a high potential in terms of response speed, in addition to minimising the internal leakage.

The feasibility study provided in [19] prompted the authors of this paper to construct a prototype of one of the two 2/2 piezo-valves representing the novel pilot stage concept. The prototype was tested in a hydraulic test rig located at the Fluid Power Laboratory of the Centre of Power Transmission and Motion Control (PTMC) of the University of Bath. The prototype and the test rig are described in the next section.

3. VALVE PROTOTYPE AND HYDRAULIC TEST RIG

A prototype and a test rig were constructed and assembled in order to test one of the two piezo-valves modulating the pressure at the main spool extremities. The test rig reproduces a part of the valve concept shown in Fig. 1 (see dashed box), being composed of the following components: supply line (P), fixed restriction, piezo-valve, and chamber comprised between the fixed restriction,

the spool end and the piezo-valve. A schematic representation and a photograph of the test rig are shown in Fig. 2 and Fig. 3, respectively. The supply line is composed of a volumetric pump (1), a non-return valve (2), a pressure relief valve (3) and an accumulator (4). A pressure transducer (5) is positioned upstream of the restriction (6), whose area can be changed manually. This restriction represents the fixed restriction shown in Fig. 1, with the difference that, in the test rig, its flow area can be adjusted. The pressure drop across the restriction is measured by a second pressure transducer (7). After the restriction (6), the oil can enter the piezo-valve, whose components are positioned inside a case (8). An adjuster (9) was mounted inside the valve body through a nut so that the position of the nozzle (10) can be adjusted against the closure member (11). In this way, it is possible to provide the ring bender with a pre-compression to close the valve effectively. The closure member (11) was inserted through the hole of the ring bender (12), and the latter was fixed to the valve body using elastomers o-rings (13). This choice results from the fact that, in this way, the mechanical integrity of the ring bender is ensured while deforming inside the valve. The position of the closure member (therefore, the displacement of the ring bender) is measured through an eddy current sensor (14). Another adjustable mechanical stop (15) is also present in order to allow the maximum displacement of the ring bender (i.e., the maximum opening of the valve) to be adjusted. The pressure of the oil discharged from the piezo-valve is measured by a pressure transducer (16).

Note that the volume comprised between the restriction (6) and the nozzle (10) represents the volume of Fig. 1 comprised between the fixed restriction, the spool end and the nozzle of the piezo-valve.

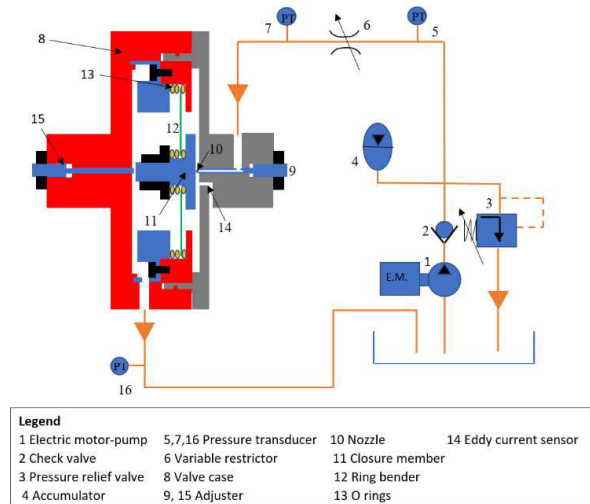


Fig. 2. Schematic representation of the test rig

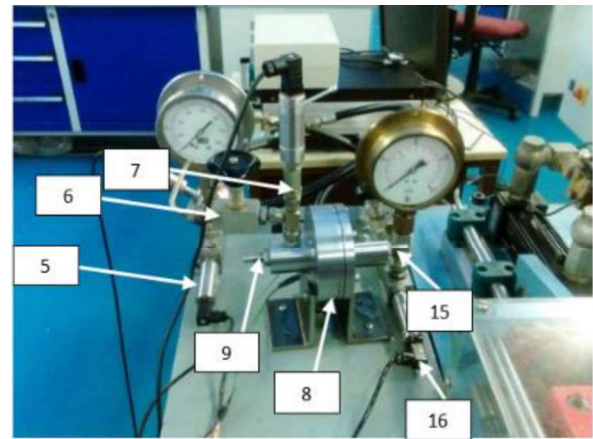


Fig. 3. Photograph of the test rig (see legend in Fig. 2 for comparison)

An external PC and a LabVIEW code were used to control the test rig and to acquire the signals from the transducers with a sample frequency of 10 kHz. The control signal was a control voltage (from -5 V to +5 V) sent to the amplifier, which transformed this signal into a high voltage signal (from -100 V to +100 V) applied to the ring bender. The pressure transducers are strain gages with a measurement error lower than 1% of the full scale (100 bar). Both the amplifier and the ring bender (model CMBR07) were purchased from the manufacturer Noliac [20]. The outer diameter and height of the ring bender are 40 mm 8 mm, respectively. The ideal maximum displacement and force of the ring bender are $\pm 185 \mu\text{m}$ and $\pm 13 \text{ N}$, respectively (+ denotes opening direction; - denotes closing direction). The tests were performed using ISO VG 32 hydraulic oil at a temperature of approx. 50 °C (oil density=851 kg/m³ and viscosity=22.0 cSt).

In the following, the same symbolism as that shown in Fig. 2 and Fig. 3 will be used to describe the numerical model and the experimental tests.

4. NUMERICAL MODEL OF THE PIEZO-VALVE

A numerical model simulating the test rig shown in Fig. 2 and Fig. 3, and hence the right part (or, equivalently, the left part) of the valve concept shown in Fig. 2, has been developed. The equations of the numerical model, which have been implemented into the Simscape Fluids environment [21], are described in the following.

The pump, pressure relief valve and accumulator are simulated through a “Hydraulic pressure source”, which is an ideal source of hydraulic energy able to maintain a specific pressure at its outlet regardless of the flow rate consumed by the system. The value of the supply pressure is set equal to the value of the experimental tests, namely 71 bar.

The pressure drop from the supply line (4) to the pressure transducer (5), and across the variable restrictor (6), is simulated using the orifice equation:

$$q = C_D A_r \sqrt{\frac{2\Delta p}{\rho}} \quad (1)$$

where q is the flow rate, Δp is the pressure drop and ρ is the oil density ($\rho=851 \text{ kg/m}^3$). The values of the equivalent restriction areas are tuned to match the experimental pressure drops, namely, $A_{r,4-5} = 4 \text{ mm}^2$ and $A_{r,6} = 0.42 \text{ mm}^2$ (with $C_{D,4-5} = C_{D,6} = 0.7$, under the hypothesis of turbulent flow).

The volume of oil comprised between the restriction (6) and the nozzle (10) is simulated using a block named “Constant Volume Hydraulic Chamber”. With this block, a fixed-volume chamber with rigid walls is simulated and the fluid compressibility is taken into account. The following equations are applied:

$$V_{cham} = V_0 + \frac{V_0 p}{E} \quad (2)$$

$$q_c = \frac{dV_{cham}}{dt} = \frac{V_0}{E} \frac{dp}{dt} \quad (3)$$

where V_0 is the geometrical volume of the chamber (equal to the product of an internal diameter $D_0 = 20 \text{ mm}$ and an overall internal length $L_0=60 \text{ mm}$), V_{cham} is the oil volume in the

chamber at the pressure p , with q_c denoting the flow rate through the chamber. The actual bulk modulus E is corrected according to the relative gas content ε , which has been assumed equal to $\varepsilon=0.01$.

The hydraulic part of the piezo-valve is simulated using the orifice equation (1), in which the orifice area is calculated as $A_{r,v} = \pi d x$, where $d=1 \text{ mm}$ is the diameter of the nozzle (10) and x is the displacement of the ring bender (calculated with reference to the nozzle tip). The discharge coefficient of the piezo-valve is assumed equal to $C_{D,v}=0.65$ under the hypothesis of turbulent flow. The displacement x of the ring bender is determined according to the equilibrium of the actuation force and the resistant forces acting on the ring bender, as follows:

$$F_{rb} + F_{flow} - m_0 \ddot{x} - C_{rb} \dot{x} - k_{rb}(x + x_0) = 0 \quad (4)$$

where F_{rb} denotes the force exerted by the ring bender having a stiffness $k_{rb}=70000 \text{ N/m}$ (data provided by the manufacturer); C_{rb} is the damping coefficient of the moving parts (ring bender, o-rings and closure member) having equivalent mass $m_0 = 90 \text{ kg}$; $x_0 = 50 \text{ }\mu\text{m}$ is the pre-compression obtained through the adjuster (9), and F_{flow} is the flow force acting on the ring bender. The damping coefficient was tuned to match the transient behaviour of the experimental displacement, thus obtaining $C_{rb} = 26 \text{ Ns/m}$.

Considering that the flow exiting the piezo valve can be assumed radial, the flow forces acting on the ring bender is calculated using equation (5):

$$F_{flow} = p_7 \frac{\pi d^2}{4} \quad (5)$$

The ring bender stroke is limited by a lower bound, which simulates the mechanical stop due to the presence of the nozzle (10). This stop is simulated as a spring and a damper having a spring stiffness $K_{stop}=10^7 \text{ N/m}$ and a damping $C_{stop} = 500 \text{ Ns/m}$. These two parameters were tuned to obtain the same bouncing behaviour obtained experimentally when the closure member hits the mechanical stop.

Piezoelectric hysteresis is considered by implementing the Bouc-Wen hysteresis model, described and used in [19]. The Bouc-Wen model is represented by an equation [19] which allows the calculation of the hysteresis nonlinear term n . The hysteresis non-linear term allows the force of

the ring bender F_{rb} to be expressed as a function of the output voltage from the amplifier, as follows:

$$F_{rb} = K_{d,v}(V_{amp} - n) \quad (6)$$

where $K_{d,v}=0.13$ N/V (data provided by the manufacturer) is the ring bender maximum force divided by the maximum operating voltage, which represents the ring bender conversion factor (namely, from amplified voltage to force).

The amplifier is simulated by using a second order transfer function:

$$V_{amp} = \frac{K_a \omega_n^2}{s^2 + 2\xi\omega_n s + \omega_n^2} V_c \quad (7)$$

where V_c is the control voltage that is supplied to the amplifier (from -5 V to +5 V), and K_a is the gain of the amplifier ($K_a = 20$). In addition, to model the current limit ($I_{max} = 1$ A), the rate of change of the amplified voltage is limited according to the following equation:

$$\frac{dV_{amp}}{dt} = \frac{I_{max}}{C} \quad (8)$$

where $C=3480$ nF is the capacitance.

The unknown parameters of the amplifier (natural frequency $\omega_n = 1400$ rad/s and damping factor $\xi=1.5$) have been set to obtain the same transient as that of the measured amplified voltage.

5. RESULTS

5.1. Experimental results and comparison with the numerical model

Step tests were performed on the test rig shown in **Fig. 2** and **Fig. 3**. The supply (absolute) pressure was kept equal to 71 bar (namely, 70 bar relative), and the absolute pressure at the outlet of the valve was around 1 bar, with the oil temperature being kept around 50 °C. These tests consisted in sending a step voltage to the amplifier, which, in turn, sent a corresponding amplified step voltage to the ring bender. The resulting displacement of the ring bender was measured along with the pressure at points 5 and 7 (see **Fig. 2**). The experimental results of these step tests are here presented and compared with the corresponding simulated step tests obtained with the numerical model described in Section 4.

In these step tests, the ring bender was pre-compressed with $x_0=50$ μm by acting on the adjuster (9); instead, the other adjuster (15) was

kept far from the closure member, so that no mechanical stop was imposed to the maximum opening of the ring bender (11).

In the first test considered in this analysis, the control voltage (input voltage from the PC to the amplifier) was changed from -5 V to +5 V, which produced an amplified voltage step from -100 V to +100 V. **Figure 4 (a)** shows the control signal, and the amplified voltage measured and simulated during this test.

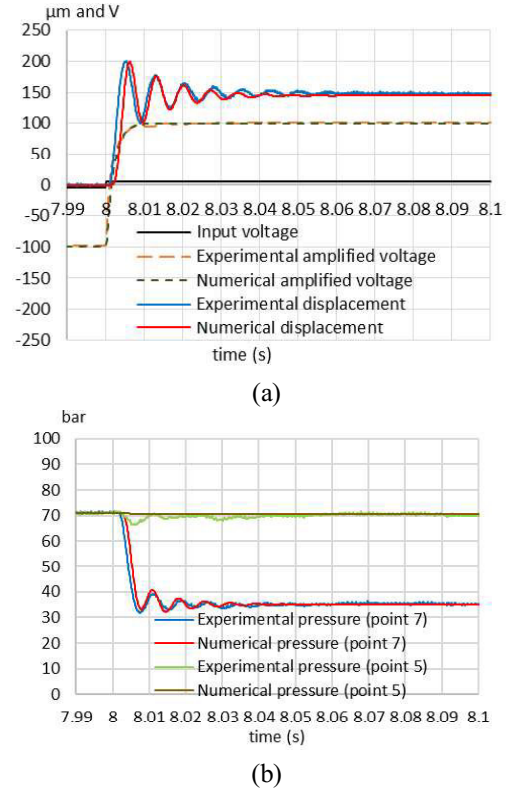


Fig. 4. Comparison between measured amplified voltage and simulated one and between measured displacement and simulated one for a positive step control voltage from -5 V to +5 V: (a); comparison between measured pressures and simulated ones: (b).

The good correspondence between the experimental amplified voltage and the numerical one demonstrates the good accuracy achieved with the numerical model and the good choice of the parameters used for the simulation of the amplifier.

Fig. 4 (a) also shows the displacement of the ring bender experimentally measured and simulated during the same step test. When -100 V was applied to the ring bender, the latter applied a blocking force of about -13 N to the nozzle (10) without moving (because it was pre-compressed). In contrast, when +100 V was applied, the ring

bender moved from the nozzle, thus opening the valve with a force of about +13 N. It can be noted that the simulated displacement matches the experimental one; this very good superimposition confirms the reliability of the numerical model. It is also revealed from the graph of **Fig. 4 (a)** that, because there is not a mechanical stop in the opening direction, the ring bender oscillates producing overshoots and undershoots until reaching a stable position. A further consideration that can be done is that the risetime is very fast, with less than 5 ms being needed to reach 90% of the maximum opening.

With reference to the same test, **Fig. 4 (b)** shows the comparison among the experimental pressures at points (5) and (7) and the corresponding numerical predictions. Also in this case, the comparison between the experimental data and numerical predictions is very good, especially regarding the pressure at point (7). With regard to the pressure at point (5), the numerical model is not able to reproduce the oscillations present in the experimental signal, which might be due to inertia effects of the oil comprised between the supply line and point (5). However, what is important in this analysis is the good prediction of the pressure at port (7), because this pressure signal is the one to be used for the control of a main spool.

As shown by the graph of **Fig. 4 (b)**, the initial pressures measured at point (5) and point (7) were the same, namely, 71 bar, because the valve was initially closed by the ring bender. When the ring bender opened the valve, the pressure at port (7) decreased down very quickly to about a half of the supply pressure (this pressure drop was achieved by adjusting the variable restrictor (6)), reaching 90% of the minimum value within 5 ms.

A second step test is now described; this test is the continuation of the previous one, in that, after reaching the maximum opening shown in **Fig. 4**, the valve was closed by changing the input signal to the amplifier from +5 V to -5 V. The amplified voltages are reported in **Fig 5 (a)**. Also in this case, there is a good correspondence between the experimental measurement and the numerical prediction, even though a slight delay is noticed in the experimental signal when the amplified voltage is approaching the minimum value (-100 V). However, this effect can be considered negligible since the experimental voltage and the numerical one reach a very high level of amplification (i.e., about -90 V) at the same time,

which corresponds to a very high level of force (namely, about -12 N).

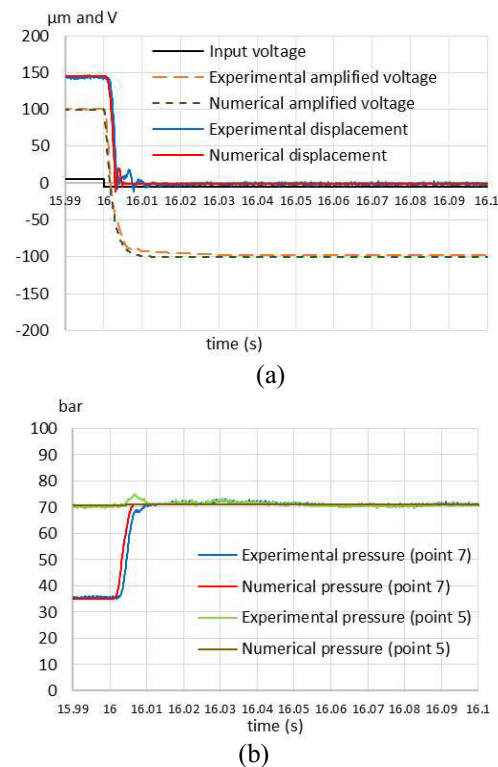


Fig. 5. Comparison between measured amplified voltage and simulated one and between measured displacement and simulated one for a negative step control voltage from +5 V to -5 V: (a); comparison between measured pressures and simulated ones: (b).

With reference to this second test, **Fig. 5 (a)** also shows the comparison between the experimental displacement and the numerical one: this graph again confirms the reliability of the numerical model, given the very good superimposition between the two curves. Moreover, the very good performance of the valve is highlighted by the very short time taken by the ring bender to close the valve (less than 5 ms). In this case, no oscillations are present, because the nozzle (10) acts as a mechanical stop for the ring bender.

Fig. 5 (b) shows the pressure trends measured and predicted at points (5) and (7) in this second test. In addition to noticing, once again, the good accuracy of the numerical model, one could notice that the ring bender perfectly achieves its task, namely, it fully closes the valve, and the pressure at point (7) is brought back to its initial value of 71 bar very quickly.

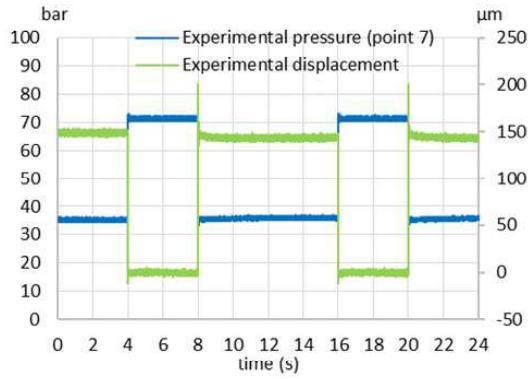


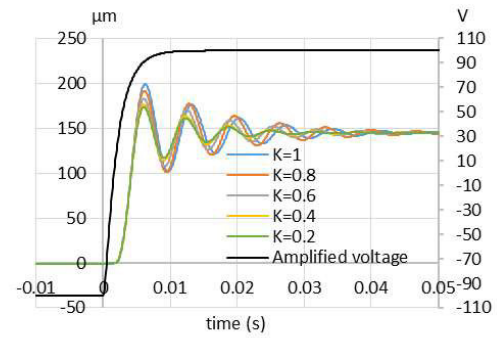
Figure 6. Pressure at point (7) and displacement measured during repeated opening and closing procedures of the piezo-valve.

Finally, **Figure 6** shows, on the same graph, the displacement and the pressure at point (7) measured during repeated opening and closing procedures of the valve. This graph is instrumental in pointing out that, when the valve is closed, the pressure at point (7) is maintained constant over time and is equal to the supply pressure (71 bar). This means that the leakage through the valve is very low (almost null), thus achieving the main goal of this project, which is the drastic reduction of the internal leakage.

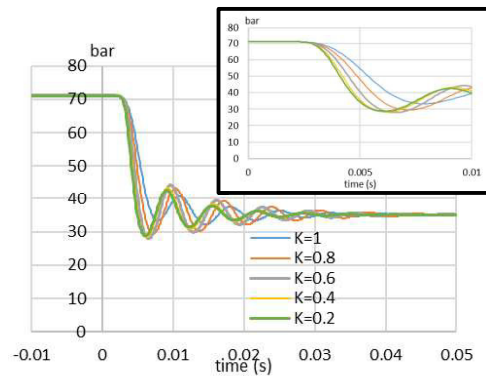
5.2. Numerical analysis of the piezo-valve

After having validated the numerical model, a numerical analysis is provided in this section to prove that, by properly acting on some geometrical parameters, the valve concept can be profitably applied for the control of a main stage spool valve.

At first, the effects of the volume of the chamber comprised between the restrictor (6) and the nozzle (10) are assessed. To assess the effects of reducing this geometrical volume, this analysis considers five volumes, having diameters $D=K D_0$ and lengths $L=K L_0$ ($D_0 = 20$ mm $L_0 = 60$ mm) with $K=1, 0.8, 0.6, 0.4, 0.2$. The five cases are here compared in terms of simulated displacement of the ring bender and pressure at point (7), since these parameters are representative of the valve performance. In this regard, **Fig. 7 (a)** shows the ring bender displacement simulated for an amplified step voltage from -100 V to +100 V and supply pressure=71 bar. It is noteworthy that the reduction of the volume causes a reduction of the oscillations.



(a)



(b)

Fig. 7. Ring bender displacement (a) and pressure at point 7 (b), simulated for an amplified voltage from -100 V to +100 V and for $D=K D_0$ and $L=K L_0$, with $K=1, 0.8, 0.6, 0.4, 0.2$

The effects of the volume reduction are also important in terms of the pressure drop at point (7); as shown in **Fig. 7 (b)**, smaller oil volumes cause the pressure to drop more quickly, as a consequence of the fact that a smaller oil volume can be discharged from the nozzle (10). This is particularly important for the actuation of a main spool: by reducing the oil volume in the system, the pressure at the spool ends will change more quickly, and the performance of the valve will be enhanced.

Similarly, **Fig. 8** shows the ring bender displacement simulated for the five volumes, but, in this case, for an amplified voltage step from +100 V to -100 V. In contrast to the previous case (voltage from -100 V to +100 V), in this case the simulated trends of the displacement are almost identical, which means that the change in the volume does not affect the displacement.

However, as shown in **Fig. 8 (b)**, the volume has a remarkable effect on the pressure rise at point (7), because lower volumes cause the compressibility effects to be less important. For this reason, it is important to reduce the volume of the chamber comprised between point (6) and

the valve nozzle (10) to improve the performance of the valve. However, for $K=0.2$ and $K=0.4$, the simulated trends of the pressures are very similar, which means that a further reduction of the volume will not much change the results.

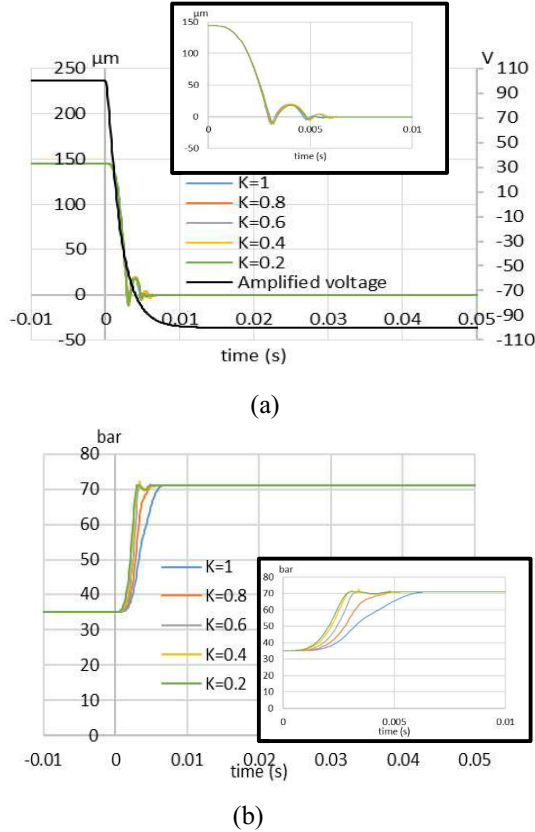


Fig. 8. Ring bender displacement (a) and pressure at point 7 (b), simulated for an amplified voltage from +100 V to -100 V and for $D=K D_0$ and $L=K L_0$, with $K=1, 0.8, 0.6, 0.4, 0.2$

Another parameter that can be optimised to further improve the performance of the piezo-valve is the mass of the moving parts. To assess the effects of this parameter, this analysis considers five values for the mass, namely, $m=K m_0$, with $K=1, 0.8, 0.6, 0.4, 0.2$ (with m_0 denoting the mass of the prototype). The diameter and length of the volume comprised between the restriction (6) and the nozzle (10) are taken equal to $D=0.6 D_0$ and $L=0.6 L_0$. The five cases are again compared in terms of simulated displacement of the ring bender and pressure at point (7). **Fig. 9 (a)** shows the different trends of the displacement for an amplified step voltage from -100 V to +100 V. It is notable that the oscillations around the set point are remarkably reduced by reducing the mass of the moving

parts; as a result, a lower mass allows the maximum displacement to be stably reached in shorter times.

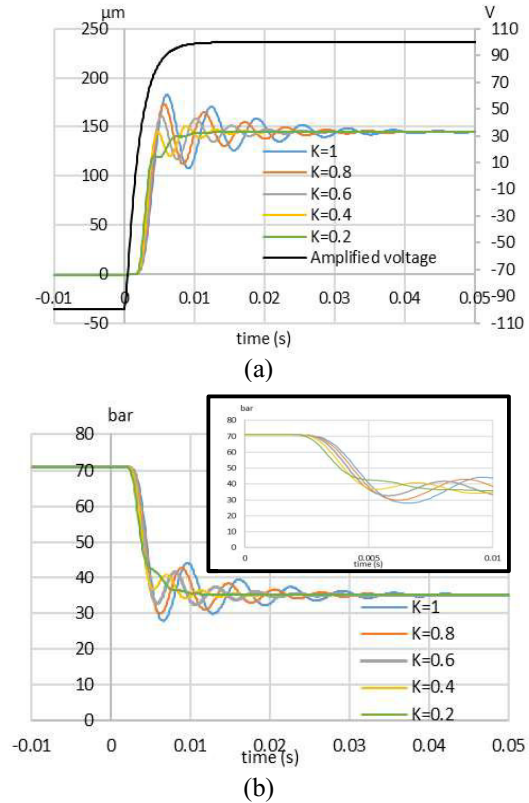
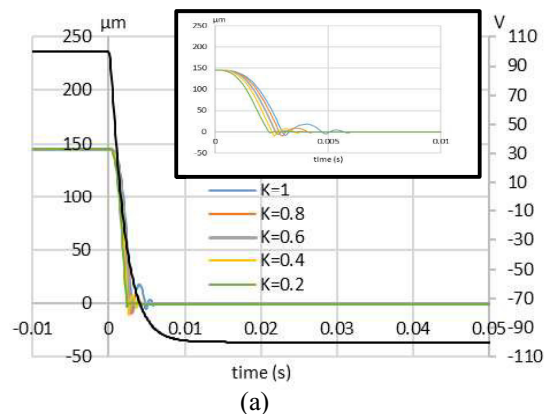


Fig. 9. Ring bender displacement (a) and pressure at point 7 (b), simulated for an amplified voltage from -100 V to +100 V and for different values of the mass of the moving parts: $m=K m_0$, with $K=1, 0.8, 0.6, 0.4, 0.2$ (supply pressure=71 bar, $D=0.6 D_0$ and $L=0.6 L_0$)

The beneficial effect of reducing the mass of the moving parts is also evident by analysing the simulated pressure drop at point 7, as shown in **Fig. 9 (b)**. It can be noticed that the lower values of the mass make the pressure reach a stable value more quickly than higher values of the mass, in addition to providing a slightly faster response due to the lower inertia.



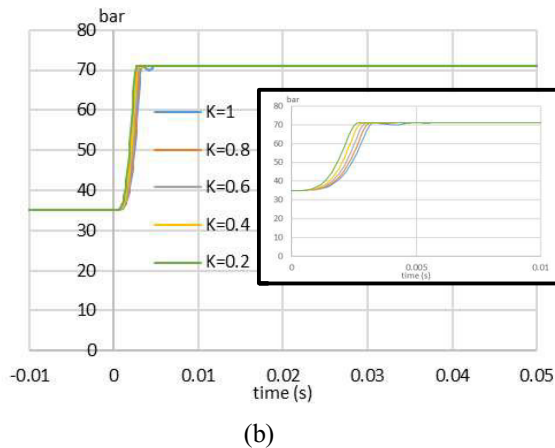


Fig. 10. Ring bender displacement (a) and pressure at point 7 (b), simulated for an amplified voltage from +100 V to -100 V and for different values of the mass of the moving parts: $m=K m_0$, with $K=1, 0.8, 0.6, 0.4, 0.2$ (supply pressure=71 bar, $D=0.6 D_0$ and $L=0.6 L_0$).

Similarly, **Fig. 10** shows the ring bender displacement simulated for $m=K m_0$, with $K=1, 0.8, 0.6, 0.4, 0.2$, but, in this case, for an amplified voltage step from +100 V to -100 V. A difference is noticed in the final part of these curves. In fact, a lower mass causes the ring bender to bounce back with lower intensity after hitting the nozzle, in addition to providing a slightly faster response due to the lower inertia. Also in terms of pressure rise at point (7), as shown in **Figure 10 (b)**, lower values of the mass cause the pressure at point (7) to increase slightly faster.

Overall, this numerical analysis has shown that the valve performance can be enhanced by reducing the volume of oil in the system and by reducing the mass of the moving parts. In these conditions, the response time of the valve is very fast, with the response time to reach 90% of the final value being lower than 5 ms. This response time is comparable with commercially available pilot stages, but with the advantage of having eliminated the quiescent flow, which can be as high as 1 l/min for commercially available units [17].

6. CONCLUSION AND OUTLOOK

This paper has proposed a novel architecture for the pilot stage of two stage servovalves, composed of two 2/2 piezo-valves actuated by ring benders, which are compact elements providing good displacement and actuation forces. This novel configuration has the potential

to overcome two main issues occurring in servovalves, namely, the complexity and the internal leakage of the pilot stage. To assess the validity of the proposed solution, an experimental prototype of the 2/2 piezo-valve was constructed and experimentally tested in a hydraulic test rig. The step tests performed on the test rig show that the piezo-valve has a high potential in terms of response speed in addition to drastically reducing the internal leakage. The experimental data have been used to validate a numerical model obtained with Simscape Fluids. This model has been used to show that, by acting on some crucial parameters, such as the volume of oil in the system and the mass of the moving parts, the performance of the valve can be further improved.

REFERENCES

- [1]. A. Plummer, "Electrohydraulic servovalves – past, present, and future," 10th Int. Fluid Power Conf., pp. 405–424, 2016.
- [2]. Tamburrano, P., Plummer, A. R., Distaso, E., & Amirante, R. (2019). A review of electrohydraulic servovalve research and development. *International Journal of Fluid Power*, Volume 20, Issue 1, 2019, Pages 53-98.
- [3]. Tamburrano, P., Plummer, A. R., Distaso, E., & Amirante, R. (2019). A review of direct drive proportional electrohydraulic spool valves: industrial state-of-the-art and research advancements. *Journal of Dynamic Systems, Measurement, and Control*, 141(2), 020801.
- [4]. Amirante, R., Distaso, E., & Tamburrano, P. (2016). Sliding spool design for reducing the actuation forces in direct operated proportional directional valves: Experimental validation. *Energy Conversion and Management*, 119, pp. 399-410
- [5]. Amirante, R., Distaso, E., & Tamburrano, P. (2014). Experimental and numerical analysis of cavitation in hydraulic proportional directional valves. *Energy Conversion and Management*, 87, pp. 208-219
- [6]. Amirante, R., Catalano, L. A., Poloni, C., & Tamburrano, P. (2014). Fluid-dynamic design optimization of hydraulic proportional directional valves. *Engineering Optimization*, 46(10), pp. 1295-1314.
- [7]. Bang, Y.B., et al. (2003). Development of a two-stage high speed electrohydraulic servovalve systems using stacktype piezoelectric elements.

- In IEEE/ASME international conference on advanced intelligent mechatronics, AIM (Vol.1, pp. 131–136). Kobe, Japan: IEEE. doi:10.1109/AIM.2003.1225084J.
- [8]. Branson, D.T., et al., 2011. Piezoelectrically actuated hydraulic valve design for high bandwidth and flow performance. Proceedings of the Institution of Mechanical Engineers. Part I: Journal of Systems and Control Engineering, 225 (3), 345–359. doi:10.1177/09596518JSCE1037
 - [9]. Reichert, M., 2006. High response hydraulic servovalve with piezo-actuators in the pilot stage. *Olhydraulik und Pneumatik*, 12, 1–17.
 - [10]. Lindler, J.E. and Anderson, E.H. (2002). Piezoelectric direct drive servovalve. In SPIE's 9th annual international symposium on smart structures and materials, 2002, San Diego, California, United States. doi:10.1044/1059-0889(2002/er01)
 - [11]. Jeon, C. Han, Y. M. Han, and S. B. Choi, "A new type of a direct-drive valve system driven by a piezostack actuator and sliding spool," *Smart Mater. Struct.*, vol. 23, no. 7, 2014.
 - [12]. S. Karunanidhi and M. Singaperumal, "Mathematical modelling and experimental characterization of a high dynamic servo valve integrated with piezoelectric actuator," *Proc. Inst. Mech. Eng. Part I J. Syst. Control Eng.*, vol. 224, no. 4, pp. 419–435, 2010.
 - [13]. Milecki A. Modelling and investigation of electrohydraulic servovalve with piezo element. *Proc Inst Mech Technol* 2006; 26: 181–188.
 - [14]. Zhu, L., et al. (2010). Development of hydroelectric servovalve based on piezoelectric elements. In 2010 Int. conf. mech. autom. control eng. MACE2010 (pp. 3330–3333).
 - [15]. Cheng, G.M., et al., 2005. Double-nozzle piezoelectric servovalve. *Guangxue Jingmi Gongcheng/Optics and Precision Engineering*, 13 (3), 276–282.
 - [16]. Bertin, M. J. F., Plummer, A. R., Bowen, C. R., Johnston, D. N., & City, S. (2014, September). An investigation of piezoelectric ring benders and their potential for actuating servo valves. In Proceedings of the Bath/ASME symposium on fluid power and motion control (Vol. 6).
 - [17]. Tamburrano, P., Amirante, R., Distaso, E., & Plummer, A. R. (2018). Full simulation of a piezoelectric double nozzle flapper pilot valve coupled with a main stage spool valve. *Energy Procedia*, 148, pp. 487-494
 - [18]. J Persson, L. J., Plummer, A. R., Bowen, C. R., & Brooks, I. (2015, October). Design and modelling of a novel servovalve actuated by a piezoelectric ring bender. In ASME/BATH 2015 Symposium on fluid power and motion control.
 - [19]. Tamburrano, P., Amirante, R., Distaso, E., and Plummer, A.R. (2018). A Novel Piezoelectric Double-Flapper Servovalve Pilot Stage: Operating Principle and Performance Prediction. In Bath/ASME Symposium on Fluid Power and Motion Control FPMC 2018, 12 - 14 September 2018, University of Bath, Bath (UK).
 - [20]. Noliac, http://www.noliac.com/products/actuators/plates_tacks/. Accessed September 2017
 - [21]. Matlab & Simulink. Simscape™ user's guide R2018a. Mathworks.

ACKNOWLEDGMENT

This research has been supported by the European Commission under the Marie Curie Intra-European fellowship Programme. EC Grant Agreement n. 701336, H2020 MSCA Individual Fellowship: Development of a novel servovalve concept for aircraft (DNSVCFA). Start date: 01/09/2017, End date: 19/10/2019, Location of the project: University of Bath.

DEVELOPMENT AND CONTROL OF SMART PNEUMATIC MCKIBBEN MUSCLES FOR SOFT ROBOTS

Min Pan*, Zhe Hao, Chenggang Yuan, Andrew Plummer

Centre for Power Transmission and Motion Control, Department of Mechanical Engineering, University of Bath, BA2 7AY, Bath, UK

* Corresponding author: Tel.: +44 1225 383023; E-mail address: m.pan@bath.ac.uk

ABSTRACT

Animals exploit soft structures to move smoothly and effectively in complex natural environments. These capabilities have inspired robotic engineers to incorporate soft actuating technologies into their designs. Developing soft muscle-like actuation technology is one of the grand challenges in the creation of soft-body robots that can move, deform their body, and modulate body stiffness. This paper presents the development of smart pneumatic McKibben muscles woven and reinforced by using conductive insulated wires to equip the muscles with an inherent sensing capability, in which the deformation of the muscles can be effectively measured by calculating the change of wire inductance. Sensing performance of a variety of weaving angles is investigated. The ideal McKibben muscle models are used for analysing muscle performance and sensing accuracy. The experimental results show that the contraction of the muscles is proportional to the measured change of inductance. This relationship is applied to a PID control system to control the contraction of smart muscles in simulation, and good control performance is achieved. The creation of smart muscles with an inherent sensing capability and a good controllability is promising for operation of future soft robots.

Keywords: McKibben muscle; Pneumatic artificial muscle; Self-sensing muscle; PID feedback control; Soft robots.

1. INTRODUCTION

The pneumatic McKibben artificial muscle was developed for artificial limb research in the 1960s [1-2]. They have been commercialized by the Bridgestone Rubber Company of Japan for robotic applications in the 1980s under the name of Rubbertuators [3]. In the 1990s, the Shadow Robot Group [4] developed the 'Digit Muscle' and in 2001 the Festo developed the 'Fluidic Muscle' [5]. The McKibben muscle is an efficient and widely used fluidic artificial muscle which consists of an elastomer inner tube and a double-helix-reinforcing-braid and can be pressurised to contract or extend. They show great advantages of flexibility, adaptability and compliant actuation compared to the conventional rigid linear cylinders. They are also remarkable for lightweight property and high energy density. The McKibben muscles have been used for many applications such as bionic arm [6] and soft manipulators [7-9]. Ideal McKibben muscle kinematic models have been developed for the

field. A comprehensive survey presented the details of kinematic and static McKibben muscle models can be found in [2]. Recently, the McKibben artificial muscle started to gain more attentions as one of typical soft actuators in an emerging area of soft robotics. However, researchers are facing a variety of technical challenges in developing and understanding McKibben artificial muscles. Firstly, derived from limited strength of external fiber sleeve, McKibben actuators are still not able to survive very high operating pressure, which limits their potential applications. Secondly, the deformation of the McKibben muscle is difficult to accurately model due to its continuous and irregular shape and complex distribution of stress and friction. Thirdly, the state-of-the-art sensing technologies (e.g. conventional rigid displacement and pressure sensors) used onto McKibben muscles still have significant dimensional restrictions. This paper presents the development of smart self-sensing McKibben muscle and the design of PID control system based on the real-time self-

sensing measurement. The muscle was woven and reinforced by using conductive insulated wires, in which the deformation of the muscle can be effectively measured by calculating the change of wire inductance [10-11]. The weaving angles 20° , 30° and 40° were investigated regarding sensing and control performance. The ideal McKibben muscle models were also introduced and used for analysing muscle performance and validating sensing accuracy. The simulated results show very good control performance which is promising for operation of future soft robots.

2. PREVIOUS WORK

2.1. Smart Sensing Braid

The smart sensing braid concept was proposed and introduced by Felt *et al* [10-11]. They made the reinforcing braid of a pneumatic artificial muscle (PAM) by weaving it from conductive insulated wires in order to measure the deformation of the muscle. When the muscle is pressurized and contracted, the wire inductance increases; when the muscle is extended, the wire inductance decreases. From simulated and experimental results, the muscle deformation can be effectively predicted by using a linear function of the measured inductance. This technique can be implemented without using additional embedded flexible sensors or elastomers into the muscle, which offers the advantages of easy-manufacturing and cost-efficiency.

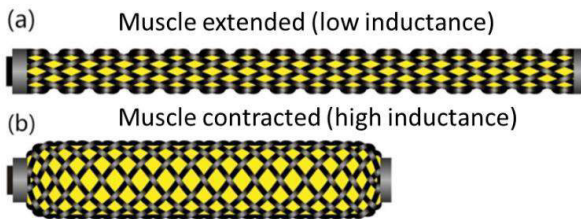


Figure 1: Smart sensing braid for measuring the deformation of a PAM

The team has also conducted some dynamic tests of the PAM for deformation measurement, which showed no phase lag and change in magnitude response for the driven frequencies up to 4 Hz. This shows that the smart braid can provide accurate measurements over a very good dynamic range for a pneumatic actuator.

2.2. Ideal McKibben Muscle Braid Model

Considering a planar network of sensing braid in a rectangular shape as shown in Figure 2, where the initial braid and contracted braid are compared in (a) and (b):

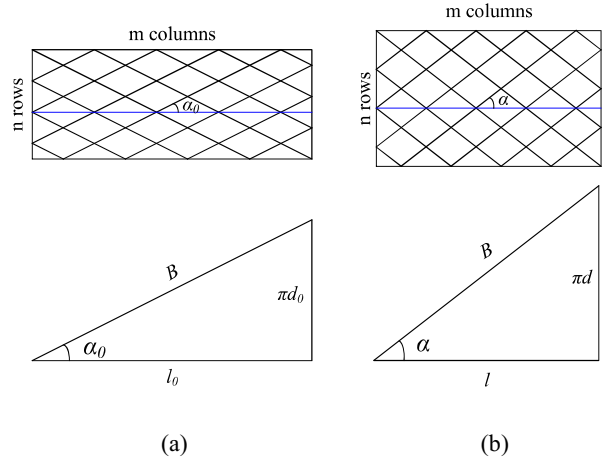


Figure 2: Geometrical characterization of the McKibben muscle braid (a) normal resting (2) pressurized

With the assumptions,

- The braid fibers are inextensible;
- The effects of the tapering at the ends of the muscle is neglected;

The initial muscle length l_0 and diameter d_0 of the braid can be written as:

$$l_0 = B \cos \alpha_0 \quad (1)$$

$$d_0 = \frac{B \sin \alpha_0}{\pi} \quad (2)$$

where B is the length of the cord and α_0 is the initial fiber angle.

The contraction ratio of the artificial muscle is:

$$\varepsilon = \frac{l_0 - l}{l_0} \quad (3)$$

where l is the contracted muscle length.

Normalized diameter and length are given by:

$$\frac{d}{d_0} = \frac{\sin \alpha}{\sin \alpha_0} \quad \text{and} \quad \frac{l}{l_0} = \frac{\cos \alpha}{\cos \alpha_0} \quad (4)$$

Assuming an ideal McKibben artificial muscle is an ideal cylindrical fluidic actuator, the ideal muscle force is [2]:

$$F_{ideal}(\varepsilon) = \pi r_0^2 P [a(1 - \varepsilon)^2 - b], \quad 0 \leq \varepsilon \leq \varepsilon_{max} \quad (5)$$

where $a = \frac{3}{\tan^2 \alpha_0}$ and $b = \frac{1}{\sin^2 \alpha_0}$.

The maximum force is achieved when $\varepsilon = 0$; while the maximum contraction is realized when

$F_{ideal} = 0$. Therefore, we can derive the ideal muscle

$$F_{ideal\ max} = \frac{1}{4} \pi d_0^2 P(a-b) \quad (6)$$

$$\varepsilon_{ideal\ max} = 1 - (1 / \sqrt{3} \cos \alpha_0) \quad (7)$$

$$d_{ideal\ max} = \sqrt{2/3} (d_0 / \sin \alpha_0) \quad (8)$$

$$\alpha_{ideal\ max} = \arctan(\sqrt{2}) \quad (9)$$

2.3. Ideal Inductance Model

The smart braid can be seen as a long solenoid and the inductance can be modelled as [10, 12]:

$$L = \mu \frac{N^2 A}{l} \quad (10)$$

where μ is the magnetic permeability of the core and N is the number of turns. A and l are the cross-sectional area and the length of the muscle.

Researchers have also used the Neumann formula for modelling the braid inductance [10], which provides better accuracy but requires more computation.

In this work, the ideal McKibben muscle braid model (6)-(9) and the inductance model (10) are used for analysing muscle performance and sensing accuracy.

3. SMART MUSCLE CONTROL

Unlike rigid actuators and robots, which are generally designed to function in well-defined environments, soft actuators and robots, are developed to adapt to more unpredictable environments with insufficient information of precise location. The open-loop control approach is effective for a variety of applications when the estimated models of the actuators are sufficiently sophisticated. For PAMs, open-loop control has been tried but is not very effective [13-15] as the current numerical muscle models are not sufficiently accurate. Closed loop control requires an accurate real-time contraction measurement, which is hard to achieve without compromising the multi-degree of freedom compliance of the muscles.

3.1. Smart Muscle Prototyping

The smart braid was used as the displacement sensor and the protective shell of the muscle to reinforce the inside muscle flexible tube. To prototype the muscles and ensure the consistence

of weaving, three 3D-printed Smart Braid templates were manufactured using an Ultimaker 2+ 3D printer with weaving angles of 20°, 30°, and 40°, as shown in Figure 3. The shape of the templates was designed in CATIA and the TPU 95A printing material was used to fabricate the weaving templates. The TPU 95A provides softer and more flexible properties, compared to PLA material. The completed weaving braids can be easily removed from the TPU templates, in which has significantly improved the fabrication efficiency. The braided wire sleeve was built by weaving a single strand of flexible electrical wire over two TPU 95A soft templates. The 22 AWG ultra-flexible wire manufactured by Daburn was used to weave the templates as smart braids. The inner the wire is made up of 168 strands of soft tinned copper thread. The large number of strands makes the inductance measurement more stable and easier to measure.



Figure 3: 3D-printed weaving templates

Three smart muscle prototypes using weaving angles of 20°, 30°, and 40° and rubber latex tubes were constructed, as shown in Figure 4. The muscle length is 250mm.



Figure 4: Smart muscle prototypes with different weaving angles

3.2. Inductance Measurement

The inductance of the smart braid was measured using a Newtons4th PSM3750 Phase Sensitive Multimeter, which provides high accuracy and superior stability. The measured real-time data

was acquired and sent to the Simulink Real-Time System, as shown in **Figure 5**.

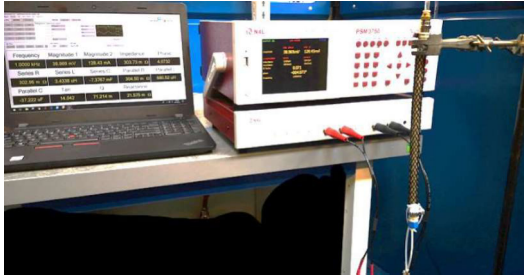


Figure 5: Inductance measurement using Newtons4th PSM3750 Phase Sensitive Multimeter

Figure 6 shows clear linear relationships of the muscle length and the measured inductance for three different weaving braids. The results show that the inductance-measurement approach is versatile and can be used for a variety of muscles with different reinforcing arrangements.

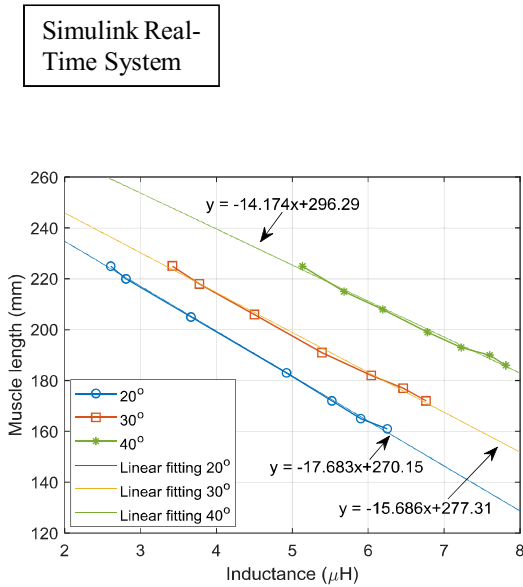


Figure 6: Relationships of the muscle length and the measured inductance for three different weaving braids

Three fitting curves were achieved based on the experimental results:

$$l(L) = \begin{cases} -17.683L + 270.15 & \alpha_0 = 20^\circ \\ -15.686L + 277.31 & \alpha_0 = 30^\circ \\ -14.174L + 296.29 & \alpha_0 = 40^\circ \end{cases} \quad (11)$$

where α_0 is the weaving angle, l is length in mm, and L is the inductance in μH.

3.3. PID Controller Design

Muscle dynamic response and identification

In order to design a feedback controller for the smart muscle, the muscle dynamic response was investigated firstly using the frequency analyser. Figure 7 shows the experimental setting-up of the muscle dynamic response test. A Festo proportional directional control valve MPYE-5-M5-010-B was used to control the air flow and one high-precision Festo pressure transmitter SPTW-P25R-G14-VD-M12 was used to measure the system pressure. The smart muscle with a weaving angle of 30° was tested without load. A sinusoidal pressure with a frequency of 1-4 Hz with a step of 0.25 Hz and a maximum amplitude of 2.5 bar was used to drive the smart muscle to determine the dynamic response. Figure 7 shows the schematic of the testing bench.

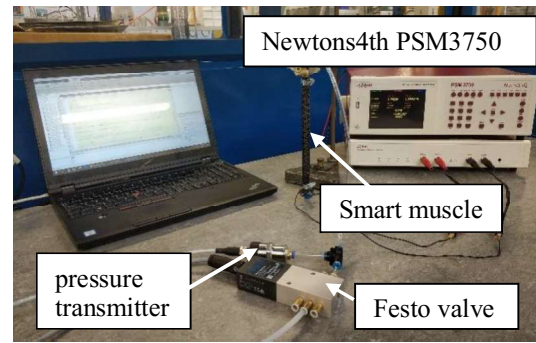


Figure 7: Schematic of muscle dynamic test

The dynamic inductance response is shown in Figure 8, where the inductance measurement responded well to 4 Hz.

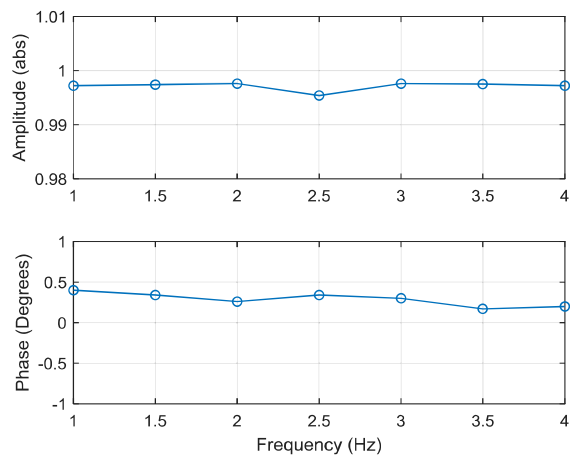


Figure 8: Dynamic inductance response of a smart muscle with a weaving angle of 30°

Simulated results

The proposed control system is shown in Figure 9, where the PID algorithm is applied to the system. The flow control valve is modelled as a second-order transfer function with a natural frequency of 115Hz [16] and a damping ratio of 0.8, given as:

$$H(s) = \frac{5.221 \times 10^5}{s^2 + 1156.1s + 5.221 \times 10^5} \quad (12)$$

The sensing braid is used to measure the muscle length (displacement), which is feedback to the PID controller.

The muscle is modelled by using a second-order function with a natural frequency of 2Hz and a damping ratio of 0.8.

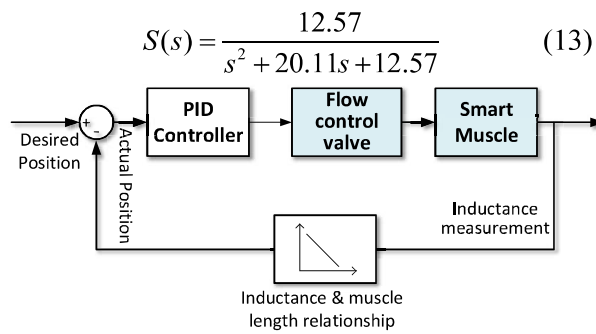
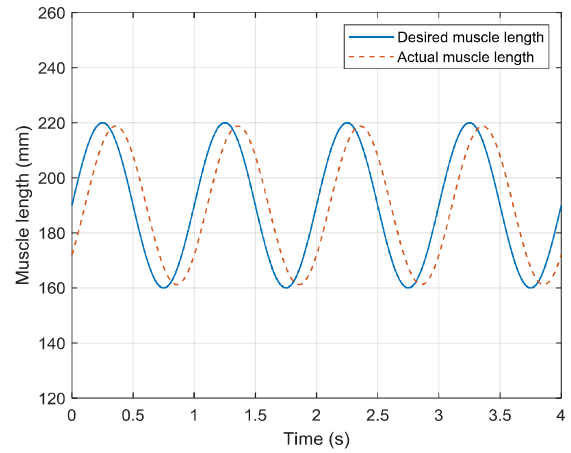
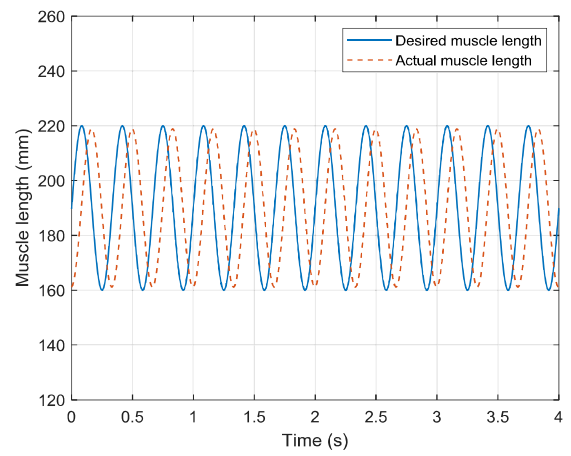


Figure 9: PID controller for smart muscles

The flow control valve was driven by the desired voltage from the PID controller. Figure 10 shows the simulated results from the feedback control system with a desired sinusoidal muscle displacement. The frequencies of the driven signal were 1 Hz and 3 Hz. The PID controller is tuned with the proportional gain of 14, the integral gain of 12.32 and the derivative gain of 0.369 to control the smart muscle operating at 1 Hz. For 3Hz, the controller is tuned with the proportional gain of 25, the integral gain of 24.55 and the derivative gain of 0.475. The results showed that the actual displacement agrees well with the desired signal. The inductance measurement of muscle deformation provides an effective means to the control of muscle.



(a) 1 Hz



(b) 3 Hz

Figure 10: Simulated muscle lengths with a sinusoidal driven signal of frequencies of (a) 1 Hz (b) 3 Hz

Figure 11 shows the simulated results of the muscle length with a step driven signal of 1 Hz. The results showed that the smart muscle has a settling time within 0.5 s. When pressurized, the muscle is contracted, and its length decreased to 160 mm from 220 mm. The designed PID controller (P: 35, I: 39.24, D: 0.66) is robust and can effectively control the muscle length with the inductance sensing approach.

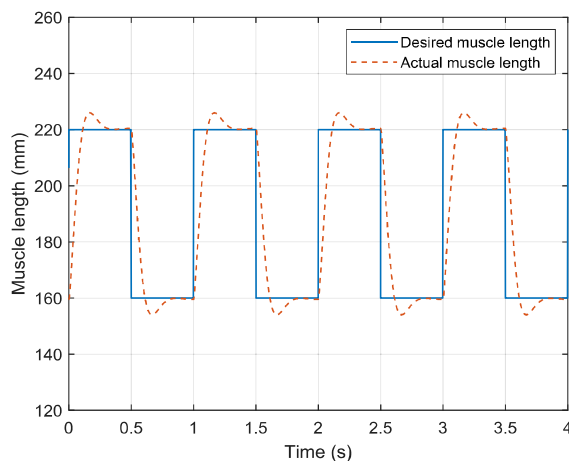


Figure 11: Simulated muscle lengths with a step driven signal of a frequency of 1 Hz

4. DISCUSSION AND CONCLUSIONS

In this work, the smart sensing braid approach proposed in [10-11] was investigated and validated through a PID feedback control system. Well-calibrated smart braid can provide rapid and precise measurements of actuator length. Different to the work in [15], the muscle prototypes used were reinforced by the smart braid directly, and a PID control system is designed with a targeted bandwidth up to 3 Hz. A second-order transfer function is used to represent muscle dynamics. The simulated results showed good control performance when the muscle was driven by the sinusoidal and step inputs. However, we believe the nonlinearity of the muscle in practice could affect control performance and the muscle dynamics could be more complicated. A simple transfer function could be insufficient to representing varying muscle deformation and dynamics. We are developing an adaptive control system to accommodate this aspect. A nonlinear PID control system can be also developed for improved control performance in practice. The smart braid has offered a very good approach to map the muscle motion. Currently the calibration curves are based on the steady-state measurement. Dynamic measurements and accurate inductance models could benefit the accuracy and performance of the control system and the understanding of muscle motion in multiple degree-of-freedom.

ACKNOWLEDGEMENT

The authors would like to thank the research group at the University of Michigan sharing the ideas on <https://softroboticstoolkit.com/smart-braids>.

REFERENCES

- [1] Artificial muscle, Life, pp. 87-88, March, 1960.
- [2] Tondu, B. (2012) Modelling of the McKibben artificial muscle: A review. *Journal of Intelligent Material Systems and Structures*, 23(3), pp.225-253.
- [3] Bridgestone Corporation (1987) Rubbertuators and applications for robots, Technical Information.
- [4] Greenhill, S., (1993) The digit muscle. *Industrial Robot: An International Journal*, 20(5), pp.29-30.
- [5] Festo AG (2001) Fluidic muscle MAS. Technical document trend 11, IS 1101 www.festo.com.
- [6] Tondu, B., Ippolito, S., Guiochet, J. and Daidie, A., 2005. A seven-degrees-of-freedom robot-arm driven by pneumatic artificial muscles for humanoid robots. *The International Journal of Robotics Research*, 24(4), pp.257-274.
- [7] Thanh, T.D.C. and Ahn, K.K., 2006. Nonlinear PID control to improve the control performance of 2 axes pneumatic artificial muscle manipulator using neural network. *Mechatronics*, 16(9), pp.577-587.
- [8] Andrikopoulos, G., Nikolakopoulos, G. and Manesis, S., 2011, June. A survey on applications of pneumatic artificial muscles. In *2011 19th IEEE Mediterranean Conference on Control & Automation (MED)* (pp. 1439-1446).
- [9] Li, H., Kawashima, K., Tadano, K., Ganguly, S. and Nakano, S., 2011. Achieving haptic perception in forceps' manipulator using pneumatic artificial muscle. *IEEE/ASME Transactions on Mechatronics*, 18(1), pp.74-85.
- [10] Felt, W., Chin, K.Y. and Remy, C.D., 2015. Contraction sensing with smart braid McKibben muscles. *IEEE/ASME Transactions on Mechatronics*, 21(3), pp.1201-1209.

- [11] Felt, W. and Remy, C.D., 2014, September. Smart braid: Air muscles that measure force and displacement. In *2014 IEEE/RSJ International Conference on Intelligent Robots and Systems* (pp. 2821-2826). IEEE.
- [12] Felt, W., Lu, S. and Remy, C.D., 2018. Modeling and design of "Smart Braid" inductance sensors for fiber-reinforced elastomeric enclosures. *IEEE Sensors Journal*, 18(7), pp.2827-2835.
- [13] Nakamura, T. and Shinohara, H., 2007, April. Position and force control based on mathematical models of pneumatic artificial muscles reinforced by straight glass fibers. In *Proceedings 2007 IEEE International Conference on Robotics and Automation* (pp. 4361-4366).
- [14] Hao, L., Yang, H., Sun, Z., Xiang, C. and Xue, B., 2017. Modeling and compensation control of asymmetric hysteresis in a pneumatic artificial muscle. *Journal of Intelligent Material Systems and Structures*, 28(19), pp.2769-2780.
- [15] Felt, W., Chin, K.Y. and Remy, C.D., 2017. Smart braid feedback for the closed-loop control of soft robotic systems. *Soft robotics*, 4(3), pp.261-273.
- [16] FESTO Proportional Directional Control Valves MPYE

MULTISTABLE VALVE TECHNOLOGY WITH MAGNETIC SHAPE MEMORY ALLOY AS PASSIVE ELEMENT ACTIVATED BY A BIDIRECTIONAL SOLENOID ACTUATOR

Julius Happel*, René Schnetzler, Markus Laufenberg

ETO MAGNETIC GmbH, Hardtring 8, 78333 Stockach

* Corresponding author: E-Mail: j.happel@etogruppe.com

ABSTRACT

Magnetic Shape Memory (MSM) alloys show a superelastic behaviour with possible deformation rates up to 6% until 12% and a sufficient lifetime performance [1, 2]. In this paper, a passive application for a superelastic Ni-Mn-Ga-alloy is presented by using the MSM element as an accurately defined inner friction in a system of a multistable actuator, in particular a multistable proportional valve. The multistable valve is characterized by a currentless holding of the valve displacement in any position of the stroke. This circumstance makes the concept a very low energy consumption valve, compared to conventional proportional valves with solenoid actuators. The new aspect of a rigid connection of MSM Materials enables an absorption of tension as well as compressive forces. To realize an applicable controlling valve, a simple and effective controlling strategy has been implemented. Due to the stabilizing effect of the MSM element, an accurate controlling of the valve stroke and the usage for example as a pressure-, mass-flow or temperature-controlling valve was made possible. Furthermore, some potential applications in pneumatics as well as in hydraulics are presented.

Keywords: Shape Memory Alloy, MSM, Ni-Mn-Ga, multistability, energy efficient proportional valve

1. INTRODUCTION

Multistable actuators, especially multistable valves, based on magnetic shape memory (MSM) materials have been investigated in several publications [3, 4]. These concepts are using the actuation of MSM and the multistability due to the inner friction of the material. Different control strategies have been implemented to this active MSM principle in a proportional valve to reach a sufficient repetitive accuracy and low energy consumption. For MSM based actuators, often relatively high currents are necessary, which is generally in contrast to the energy efficient target of the multistable valve principle. In this paper a new actuation concept of multistable valves with MSM is presented, a simple and efficient control strategy is shown and aspects relevant for valve applications are discussed.

2. STRESS-STRAIN BEHAVIOUR OF MAGNETIC SHAPE MEMORY ALLOYS

MSM elements are produced from single crystal Ni-Mn-Ga alloys, which show a magnetic anisotropy along two defined crystallographic axes. This anisotropy leads to an elongation of the element in one axis, if the other axis is in the direction of a moderate magnetic field > 0.8 T.

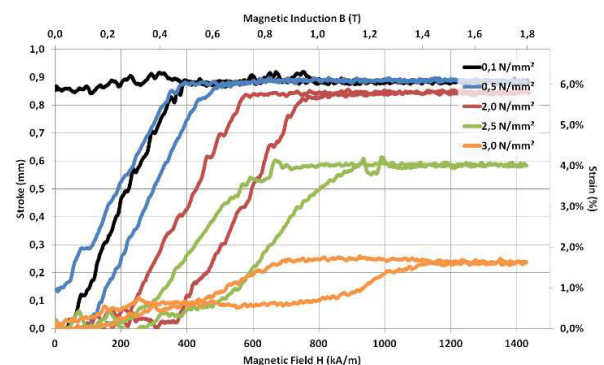


Figure 1: Stroke over field measurement of magnetic shape memory alloys.

The elongation depending on the magnetic field is shown in **Figure 1** for different pre-stresses from 0.1 MPa to 3 MPa. Taking a look at the purely mechanical stress-strain characteristics of MSM materials, one can also observe a hysteretic behaviour. In **Figure 2**, the force-over-stroke curve for a mechanical tension (positive force) and a subsequent compression (negative force) of a $3 \times 5 \times 25 \text{ mm}^3$ sized MSM element is shown, demonstrating the hysteretic and superelastic behaviour.

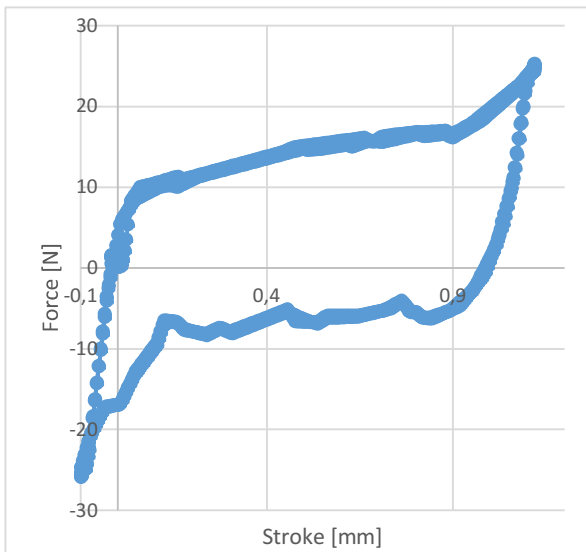


Figure 2: Passive force-stroke behaviour of a MSM tension and compression cycle.

If the element is deformed mechanically up to 6% in length, it remains in this position. The necessary force to mechanically deform the element is the so-called twinning stress, which can be understood as an inner friction of the material. This force-stroke characteristics is not velocity-dependent and the force rises with increasing stroke, because the twins with the highest mobility (or lowest twinning stress) move first. The twinning stress is between 0.2 MPa and 1 MPa for MSM-elements, which is between 3 N and 15 N for a sample with a cross-section of $3 \times 5 \text{ mm}^2$, which corresponds with a type I twinning stress [5]. Important for the controllability of the passive MSM valve is the fact, that each stroke value is disambiguously linked to a defined force value, i.e. that the force-stroke behaviour is strictly monotonous. If the element is not entirely elongated, the force required for initializing the antagonistic motion is similar like the force for initializing the initial motion, allowing hysteretic minor loops to be performed easily.

For the design of actuator and control system the twinning stress has to be properly modelled. This is done with a piecewise linear fit of the force-stroke curves, which represents most measured curves in a suitable way.

3. DESIGN OF MULTISTABLE MSM-ACTUATORS

Compared to previous multistable MSM actuators [3, 4] a modified design has been developed with the aim to increase control quality and to minimize current consumption. The design is based on a superelastic or passive use of the MSM element, which has been introduced in chapter 2 and has been also discussed in other publications yet [6, 7, 8]. To transfer both compression and tension forces between the MSM element and the actuator, it requires a rigid connection with the housing on one side and with the plunger or armature at the other side. This connection is made by laser welding, which has been proven a robust solution.

The actuation is then realized by a bidirectional solenoid actuator, which has a very accurate horizontal force-stroke behavior at every current level. This is advantageous for the controlling behavior of the actuator. Different solenoid systems have been tested, one of them is schematically illustrated in **Figure 3**. Two coils are used, to induce a force in both directions, deforming the MSM element and opening or closing the valve in a proportional way. On the left side of the plunger in **Figure 3**, the valve can be attached, which is presented in the following chapter.

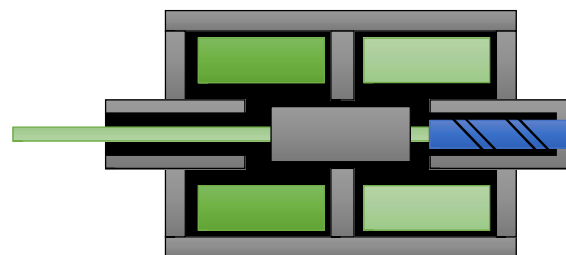


Figure 3: Schematic design of multistable valves with magnetic shape memory alloy as passive element.

In this study, two different valve designs are considered. Both designs are 2/2 proportional seat valves with a nominal stroke of 1 mm. The first design is completely pressure balanced, which makes it suitable for pneumatic as well as

hydraulic applications at higher pressure rates on both sides. The second one has the same design but is not pressure balanced at the outlet, and is, thus, primarily suitable for pneumatic applications with low outlet pressures. The pressure balanced system is tested with a nominal diameter of 10 mm, the other one with a nominal diameter of 3 mm.

The valve stroke of 1 mm requires a MSM element length of 25 mm at a strain of 6%, which takes into account that around 0.2 mm of the potential stroke are lost by the pinning of the twin boundaries at material zone influenced by the laser welding process. The cross-sectional area of the element depends on the twinning stress and, furthermore, determines the level of absorbed force. If we assume fluid forces up to 10 N, the required element area is about 15 mm² for an initial twinning stress value of 0.7 MPa. Experiments with the non-balanced design demonstrated, that lower twinning stresses with an initial force of 5 N also compensate the fluid forces sufficiently at an inlet pressure of 5 bar and a flow up to 100 l/min. This can be explained by additional friction forces of the sealing.

4. ENERGY EFFICIENCY

The current consumption of this type of multistable valves is considered in this chapter. Generally, the valve only consumes current during changing the position of the valve piston. The huge benefit is a current-free holding of any valve stroke under stationary force conditions. The average power consumption P_{mean} is the quotient of the required duty cycle time t_{DC} and the time between consecutive adjustments t_{period} multiplied with the nominal current and voltage of the actuator as follows:

$$P_{mean} = U_N * I_N * \frac{t_{DC}}{t_{period}} \quad (1)$$

While the nominal voltage and the control dynamics, represented by t_{period} in Equation 1, are mainly determined by the application of the valve, the current consumption and the switching time are design parameters. To analyze the influence of these parameters, the boundary values and the average power consumption at different time periods are compared in **Table 1** and **Table 2** for two different actuator concepts.

Table 1: Parameters actuator type II @ $U_N = 24$ V.

Nominal current I_N	1.2 A
Duty cycle time t_{DC}	250 ms
Power consumption P_{mean} @ $t_{period} = 1$ s	6 W
Power consumption P_{mean} @ $t_{period} = 5$ s	1.2 W
Power consumption P_{mean} @ $t_{period} = 20$ s	0.3 W

Table 2: Parameters actuator type II @ $U_N = 24$ V.

Nominal current I_N	8 A
Duty cycle time t_{DC}	10 ms
Power consumption P_{mean} @ $t_{period} = 1$ s	1.9 W
Power consumption P_{mean} @ $t_{period} = 5$ s	0.38 W
Power consumption P_{mean} @ $t_{period} = 20$ s	0.1 W

The valve type II (**Table 2**) exhibits a significantly lower average power consumption compared to valve type I (**Table 1**) due to a lower duty cycle time and smaller dimensions even though it requires a nearly seven times higher nominal current.

The differences between these two valve concepts are dominated by the reduced inductance of the magnetic circuit and the reduced mass of the armature and valve piston. Therefore, an optimization problem between switching time and nominal current results. In the above case, the reduction of the switching time by more than 10 times has a larger influence than the higher nominal current.

In order to find the optimized actuator design for very low energy consumption a holistic optimization study would be required, while the design focus in the present study has been on the horizontal force-stroke characteristics of the actuator to allow a good control behavior.

5. CONTROL STRATEGY

Conventional valves with a mechanical spring typically have a perfect proportional behaviour due to the linearity of the spring which leads to a linear dependency of valve stroke on current. This characteristic is compatible with familiar controllers, like a PID-controller.

However, the output of the multistable valve depends on the current of two coils. Furthermore, the hysteresis and the tolerances of force-stroke behaviour of the MSM elements lead to a dependence on temperature and cycle number. These circumstances make it very difficult to control the valve with model based controlling

methods, which are often applied to conventional proportional valves.

In order to guarantee a stable system, a new simple and effective control strategy has been developed which is based on the stable behaviour of an alternately compressed and strained MSM element as discussed in chapter 2. A monotonously increasing twinning stress is required.

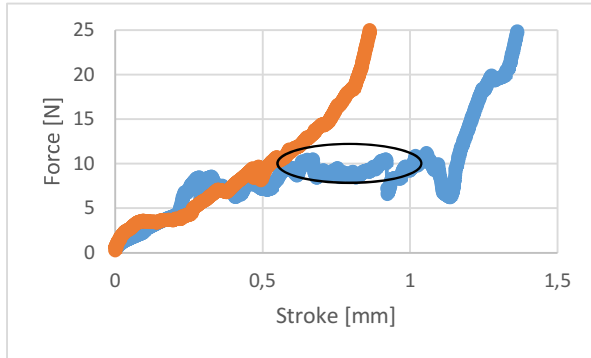


Figure 4: Passive force-stroke curve with a noisy plateau in the marked section.

This is given for the majority of the MSM elements measured with few exceptions such as presented by the blue curve in **Figure 4**. A noisy plateau between stroke of $\sim 0,65$ mm until $\sim 0,85$ mm leads to an undefined position at a force level of 10 N, illustrated by the circle in **Figure 4**. This may cause an overshoot of the valve stroke and can be a problem which must be accounted for by the controller. In contrast to the noisy blue characteristic, a well monotonously increasing twinning stress is figured by the red curve, which corresponds to a $3 \times 5 \times 20$ mm³ sized MSM element.

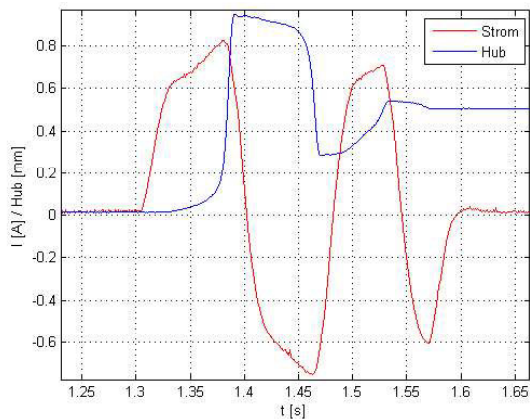


Figure 5: Control behaviour with a target position of 0.5 mm and a flat force-stroke curve.

The control strategy is a simple ramp profile of the current as long as the actual position is deviating from the target position. In our experimental setup, a laser triangulation sensor measures the position as control input. In case of an overshoot, e.g. due to a non-monotonous force-stroke behaviour of the MSM material, the antagonistic coil has to be activated with the same control strategy until the overshoot is within the tolerance. The influence of the different force-stroke characteristics of the MSM material twinning stresses in **Figure 4** is compared in **Figure 5** and **Figure 6**.

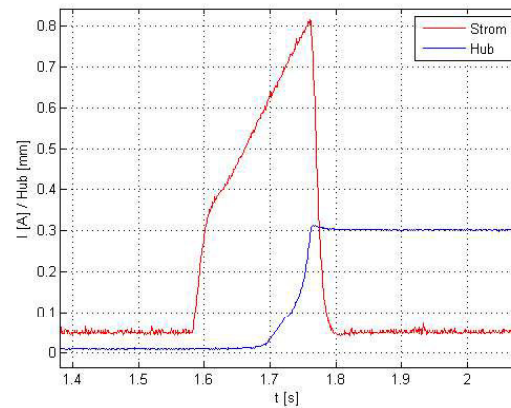


Figure 6: Control behaviour with a target position of 0.3 mm and a steep force-stroke curve.

The force-stroke curve of the MSM element used in **Figure 5** has large slope for low strains and a subsequent plateau with a weak force increase (blue curve in **Figure 4**). This causes the tendency of frequent overshoots until reaching the target position of 0.5 mm. In contrast, the force-stroke curve of the element used in **Figure 6** has a constantly increasing force (red curve in **Figure 4**), which reduces the probability of an overshoot to a minimum.

In both measurements an error $< \pm 1\%$, hence $< \pm 10$ μm , can be achieved by using the laser triangulation sensor. The measurement quantity in an industrial fluidic system typically is a fluidic parameter such as pressure or flow rate, thus the control accuracy is significantly influenced by the measurement accuracy.

6. SENSITIVITY ANALYSIS OF INFLUENCE PARAMETERS FOR CONTROL DESIGN

In order to analyze the stabilizing influences of various parameters in this control strategy a 1D transient model of the valve has been developed. A sensitivity study of the overshoot depending on

different parameters has been performed using the software optiSLang®. The model describes the inertia of the plunger, a friction term and the modelled nonlinear force-stroke curve and the modelled actuator force. The resulting differential equation

$$m\ddot{x} + d\dot{x} + F_{TW}(x) = F_{act}(x, t) \quad (2)$$

is solved numerically. The twinning force of the material is modelled by two linearized sections as introduced in chapter 2. The force-stroke-dependence of the actuator is taken into account and the time dependent ramping profile is implemented. The considered parameters including their boundary values are listed in **Table 3**. The output value is the error between the target value and the overshoot after a current pulse excitation.

Table 3: Model parameters and their boundaries

Time to switch on	$t_{ein} = 1 \dots 50 \text{ ms}$
Slope of force-stroke curve of actuator	$s = -10 \dots 10 \text{ N/mm}$
Deviation from target value	$x_{Ziel} = 0.05 \dots 0.9 \text{ mm}$
Plunger and armature total mass	$m = 0.005 \dots 0.2 \text{ kg}$
Duration of current ramp	$t_{Rampe} = 5 \dots 500 \text{ ms}$
Maximum twinning force of MSM material	$F_2 = 6 \dots 25 \text{ N}$

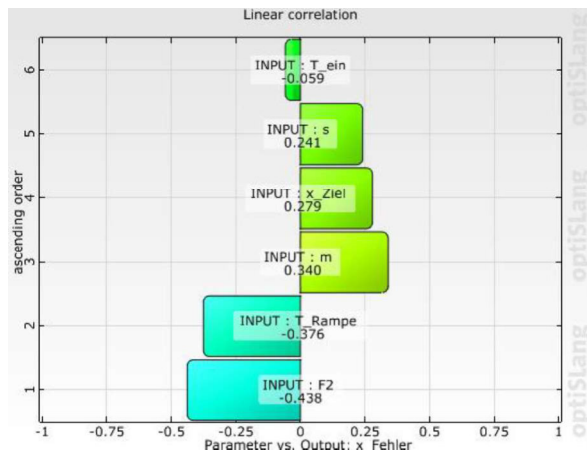


Figure 7: Influence of the model parameters on the displacement error

A sensitivity analysis based on 100 different designs within the parameter range of **Table 3** is performed and the resulting dependence of the overshoot on the parameters is compared in **Figure 7**. A positive dependence value means

that an increase of the respective parameter causes an increase of the overshoot and vice versa.

The maximum twinning stress F_2 and thus the slope of the force-stroke behavior has the largest influence on the overshoot with a high value being beneficial for a reduced overshoot. This corresponds with the analysis of the stability for two different characteristics a in **Figure 5** and **Figure 6**. The second and third important parameters are the ramping time and the mass of the plunger, which affect the dynamic behaviour. A higher mass and a lower switching time increase the inertia forces and cause a higher probability of an overshoot error.

The forth relevant parameter is the deviation of the stroke from the target value. The distribution in **Figure 8** shows that deviations from target $x_{Target} < 0.2 \text{ mm}$ cause only small contributions to the overshoot probability which can be expected.

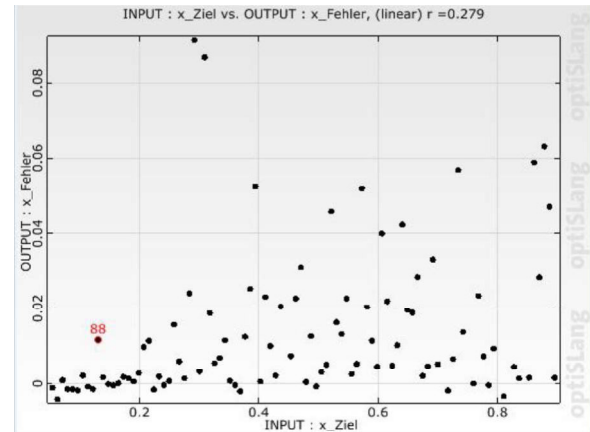


Figure 8: Error distribution depending on the target displacement.

7. APPLICATIONS

As mentioned in chapter 3, pneumatic as well as hydraulic applications can be realized with the proposed type of multistable valves. Such valves are designed for applications, in which a constant mass or volume flow is preserved for longer periods and which require a very low power consumption. If the application requires high control dynamics, the valve can be used due to its fast switching.

The restricting parameter is the time between consecutive adjustments of the fluid flow. If this time becomes too small, the advantage of the multistability is lost. The minimum useful time

depends on the size of the valve and the flow parameters and thus from the application.

The most common controlled quantities in fluidics are a mass or volume flow or a pressure. In contrast to the plunger position used as control input in this study, this requires a measurement signal with the necessary accuracy. The pressure can be controlled at the inlet or outlet and the measurement signal should have a low noise level, to avoid that the controller and the fast actuator start oscillating. An analog problem may occur, if a mass-flow controlled valve has a fluctuating inlet pressure, which leads to frequent control adjustments if the error range for is too narrow. Further potential control quantities are a fluid temperature or fill level.

Different fields of application can be considered. Power plants like fuel cells or combined heat and power generation systems, whose efficiencies are diminished by the power consumption of any system component, are often driven in stationary conditions which makes them attractive candidates for energy efficient multistable valves. The same argument holds for air-conditioning systems with various coolant fluids. For mobile medical care devices, a multistable valve can be suitable, too. Such systems are often electrically supplied from a battery, so that an energy efficient and compact system contributes to their maximum independent operation time without recharging the battery.

8. CONCLUSION AND OUTLOOK

In this paper, recent progresses in the development of multistable valves with MSM have been presented. Therefor an optimization of the entire design concept has been done compared to previous designs and two different actuator types have been investigated. The focus of research was on the controllability and the energy efficiency of the valve. A new control strategy has been implemented, which leads to a stable behaviour, due to the combination of an aligned bidirectional solenoid actuator and the typical characteristic of a passive deformed MSM element. The energy efficiency of two different actuator types is regarded. A comparison has shown, that a reduction of the switching time has a greater influence on the energy consumption reduction than lower nominal current rates. To optimize the energy consumption, the actuator

design has to be investigated holistically. Furthermore, the average power consumption of the multistable valve with passive MSM utilization will always depend on the application and its control requirements.

Future investigations will be done on the improvement of the control strategy with respect to the measurement and control of a fluidic value. Another topic of investigation is the usage of high temperature alloys, which could make applications with temperatures higher than 80°C possible.

REFERENCES

- [1] Aaltio I, Söderberg O, Ge Y, Hannula S, *Long-term cyclic loading of 10M Ni-Mn-Ga alloys*, Materials Science Forum Vol. 684 (2011) pp 201-212
- [2] Schiepp T, Detkov V, Maier M, Pagounis E, Laufenberg M, *Failure mechanisms and high-cycle fatigue of MSM actuators*, Proc. 4th Int. Conf. on Ferromagnetic Shape Memory Alloys (ICFSMA), Boise, Idaho, 2013.
- [3] Schiepp T, Schnetzler R, Riccardi L, Laufenberg M, *Energy-efficient multistable valve driven by magnetic shape memory alloys*, 10th International Fluid Power Conference (IFK), March 8-10, 2016, Dresden, Germany.
- [4] Schiepp T, Riccardi L, Schnetzler R, Laufenberg M, *Multistable pneumatic valve based on magnetic shape memory alloys*, ACTUATOR 2016
- [5] Muellner P, *Twinning stress of type I and II deformation twins*, Acta Materialia 176, 2019, p 211 - 2019
- [6] Pagounis E, Müllner P, *Materials and actuator solutions for advanced magnetic shape memory devices*, International Conference on New Actuators (ACTUATOR), June 25-27, 2018, Bremen, Germany.
- [7] T. Schiepp, M. Laufenberg, *Patent DE 102016107461 A1*.
- [8] Schropp M, Riccardi L, Schnetzler R, Nägele R, *An innovative electromagnetic actuator based on magnetic shape memory alloys*, 16th International Conference on New Actuators (ACTUATOR), June 25-27, 2018, Bremen, Germany.



GROUP 14

**Safety &
reliability**

LIFETIME IMPACT PREDICTION OF COMPONENT MODIFICATIONS IN AXIAL PISTON UNITS BY THE FAILURE LIKELIHOOD ASSESSMENT

Ivan Baus^{1*}, Robert Rahmfeld¹, Andreas Schumacher¹, Henrik C. Pedersen²

¹*Danfoss Power Solutions, Krokamp 35, 24539 Neumünster, Germany*

²*Aalborg University, Department of Energy Technology, Pontoppidanstraede 111, 9220 Aalborg*

* Corresponding author: Tel.: +49 4321 871 731, E-mail: ibaus@danfoss.com, ivb@et.aau.dk

ABSTRACT

In this paper, a new methodology is presented to estimate the lifetime impact of design changes, called Failure Likelihood Assessment (FLA). The discussion in this paper is on the fatigue lifetime prediction of axial piston units, especially after a design change. The demonstration object is an axial piston pump due to extreme environmental conditions and high specification demands, where the FLA is applied to a manufacturing change in an existing product and delivers an effect on the unit reliability. The resulted reliability improvement, if combined with typical calculation methods like Weibull analysis, delivers an increase in predicted lifetime considering the intended modification. As demonstration subject, a change of the manufacturing process of the cylinder block hub in an axial piston pump is used. The effect to the lifetime is predicted via the FLA-method and the results are calculated with test data and compared to theoretical results. The paper shows that the methodology delivers highly accurate results providing that the FLA is a powerful tool to analyze design changes as well as new designs in regard to reliability and lifetime. The benefit for the user of this methodology will hence be more reliable products with optimized designs to best fulfil customer's performance requirements.

Keywords: Axial Piston Units, Reliability Assessment, Lifetime Prediction, Drivetrain, Design

1. INTRODUCTION

Appropriate functioning of an axial piston unit is fundamental to every operation of a drivetrain system in an off-road application. To ensure the proper function and/or to observe the reliability of a system, the market trend is growing in case of condition monitoring. The current trend in many different research fields shows a big focus on condition monitoring and real-time prediction of service life [1, 2]. This trend is generally forced by the uptime-efficiency requirements of today's products. The uptime-efficiency is in this regard defined as the optimal use of the service life before a relevant failure occurs and is depended on the accurate knowledge of the risk versus reliability mechanisms, which aids/ results in lifetime prediction values. A proper risk assessment methodology leads to an accurate prediction of a failure and downtime reduction of a system, whereby the reliability of lifetime-relevant system components is playing the main role [3]. The prediction research may be divided

mainly in two different groups: offline and online concepts. The online prediction includes a.o. real-time condition monitoring, fault detection and diagnostics concepts like e.g. fault detection by learning algorithms or threshold diagnostics. These methods are typically used on board of a vehicle [4, 5]. An actual research in field of online lifetime analysis is the work of Mr. Brinkschulte, where the development of the damage reduction strategy for mobile machines is connected to the intelligent identification of the machine operator is in focus [6]. On the other side are the offline methods, which include theoretical calculation tools like the prediction of the fatigue-relevant lifetime or product reliability analysis during the development or redesign phases. These offline methods and the FLA methodology are in focus of this work sequel, where this paper covers the impact analysis of a manufacturing change. Especially in case of fatigue-relevant analysis of the lifetime, different theoretical methods are in use. This long-term phase of a product lifecycle is described in the last stage of

the bathtub curve and represents an increasing failure rate, where the reliability tends toward zero [7]. Beside the fatigue-focused analysis the friction-relevant research is playing an important role in lifetime analysis, where a.o. an actual work was published by L. Brinkschulte [8].

Performing a system analysis with theoretical methods and the related evaluation of occurred results is often difficult due to the complexity of axial piston units. The complexity further increases from the system requirements, not least due to the integration into off-road applications which are subject to a high combination of variable load factors in the field [9, 10].

Additionally, when developing new products, field data rarely exist (e.g. load spectrum or environment conditions), why the methods require proper experience with previous product loads. Here an improper approximation or a wrong estimation of relevant factors/loads may lead to a deviation in the lifetime prediction. Thus, precise theoretical methods with high accuracy in prediction avoid negative impact on the uptime. The state-of-the-art theoretical methods, which are typically used, are a.o.:

- Weibull Analysis [7]
- SN / Wöhler curve [11]
- Palmgren-Miners Rule [12, 13]
- Mean Time to Failure (MTTF) [14]
- System State Enumeration [15]
- WeiBayes / Zero Failure Test [16, 17]

A typical result of these lifetime calculation methods is defined as L_{10} (theoretical nominal lifetime), where the first 10 % of a product lot would theoretically fail. These methods, which have existed for decades, normally deliver conservative results, like seen in field and test lab data. Therefore, in previous work a new methodology so-called FLA was developed and evaluated by field data to improve the accuracy of the lifetime prediction [18]. Hence, this work is a sequel of the lifetime research and the purpose of the current work is a demonstration of the Failure Likelihood Assessment methodology (FLA) as a means in impact analysis of a design change in case of lifetime prediction. A typical procedure for lifetime evaluation includes the definition of the product characteristic and the applied load. These factors are used as a basis for calculating the lifetime. Afterwards, the values may be verified in a test lab by using the Weibull analysis [17]. Hence, the practical analysis of

lifetime relevant values/coefficients covers test lab evaluation by endurance or other qualification tests [19-22].

The current work here focuses on the Weibull or more specifically the fatigue-related SN-curve analysis in combination with FLA feasibility. This is especially in connection to the lifetime prediction and reliability analysis after a design change. Thus, the proceeding of the FLA results in a change of the reliability curve after a specific design change, which can be applied to the lifetime calculation. The impact of a design change is directly linked to the lifetime calculation based on the Weibull-analysis.

A demonstration of the experimental data acquisition and the FLA analysis is presented, which is based on an exemplarily applied change of the manufacturing process of the cylinder block hub used in an axial piston pump. Here the issues of the experimental testing are discussed as well. Hence, an analysis based on experimental acquisition of the failure rate has been performed, where B_{10} is defined as experimental nominal lifetime and is typically used in the market as the reference value for different purposes, like e.g. maintenance management. In this case, a test lab setup was developed, and the results from the experiments were analyzed. Here, an application-specific load equivalent is playing an important role as the boundary condition. Due to the practical and economical limitations of the experimental analysis, the FLA analysis follows as a statistical approach. The extended analysis combines the experimentally-determined failure probability with the reliability change of the previously mentioned manufacturing change of a cylinder block hub. The FLA-extended Weibull calculation with the failure probability allows a highly accurate lifetime prediction. Finally, the FLA validation concludes the work by using process data of the part manufacturer.

2. STATE-OF-THE-ART CALCULATION OF THE LIFETIME

The general goal of each engineer is a reliable product with optimal design margin according to the state-of-the-art requirements, which at the same time has a high economic efficiency. Not least, the focus of the engineer should be at a proper design of fatigue-relevant components so that the lifecycle of the affected product is fulfilling the requirements. In case of dynamic

loads, a load equivalent is connected to the fatigue strength of a component. The equations typically used for lifetime analysis and failure rate evaluating in mechanical systems and parts are the following:

Weibull reliability:
$$R(x) = e^{-\left(\frac{x}{\eta}\right)^\beta} \quad (1)$$

Miner's Rule:
$$X = \sum_{i=1}^l \frac{n_i}{N_i} \leq 1 \quad (2)$$

SN curve:
$$L_{10} = \left(\frac{C}{P}\right)^k \quad (3)$$

The mathematical correlation of stress (typically called duty cycle, load spectrum or load equivalent) with fatigue strength build the essential part of the SN-curve analysis. Thus, degradation of the component strength against dynamic loads or rather the damage accumulation is analyzed. In particular, it is desirable that under different types of loads, e.g. axial tensile-compression or bending and torsional stress, the calculation accuracy of the lifetime prediction can be achieved by high statistical certainty. The accuracy of the lifetime calculation thus depends strongly on knowledge about the damage accumulation, load spectrum and fatigue strength of a component.

These mathematical hypotheses, the so-called linear damage accumulation hypotheses, are used to calculate the lifetime of components, where k is defined as the lifetime exponent of the SN-curve and may be drawn as a straight line in a double logarithmic plot, like it can be seen in **Figure 1**. The scientific significance of the predicted results is on the evaluation by experimental and theoretical analysis and depends crucially on the nature of the mathematical accumulation rule. Normally, the objective of lifetime research is to provide

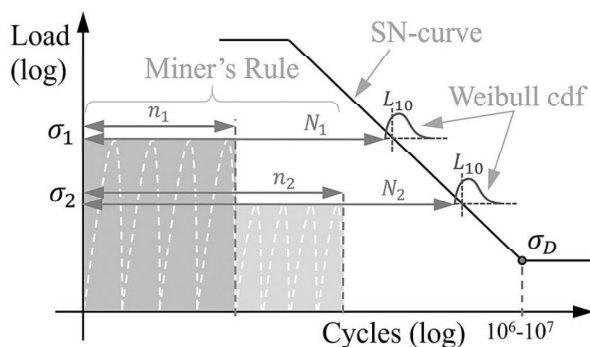


Figure 1: Lifetime calculation according to linear damage accumulation

customers and engineers with an improved approach for predicting lifetime. Thus, the comprehensive load spectrum determination is playing a very important role and should be taken into account. Significant improvements have been made to the well-known linear Palmgren-Miner hypothesis (Miner's Rule) by the use of exponential damage approaches [12, 13]. In general, new theoretical approaches must be analyzed with regard to accuracy and parameters, where the influencing factors or rather the impact must be determined twice: quantitatively and qualitatively.

However, the theoretical results deliver shorter lifetime values compared to what is experienced in the field or test lab: different endurance tests like "steady-state"- and "flywheel"-tests show that the state-of-the-art prediction methods deliver conservative results. Therefore, more reliable and precise prediction methods are required. Thus, the FLA method was developed and validated in a previous work of the current authors. The validation of the method was done by using field data and did show successful and accurate results in different cases of reliability research [18].

3. SN-CURVE ANALYSIS OF COMPLEX SYSTEMS IN PRACTICE

An axial piston unit consists of many different components, which are affected by different load factors like temperature, rotation speed, pressure, friction, vibration and others. This very complex environment makes it difficult to analyze a specific sub-component separately. Therefore, an axial piston unit is typically tested as a complete system in case of endurance or evaluation testing, even if only one single component has changed.

The problem is that Miner's Rule or rather the SN-curve analysis only considers one dynamic load applied to one component only. Otherwise, the combination of many dynamic factors in an evaluation approach may create an infinite value of unknown conditions. This fact leads to a need for endurance testing concepts, where the testing conditions can be taken into account as a constant load of the whole system, where the components in rotation e.g. kit-subsystem are affected by alternating load, as shown in **Figure 1**.

An additional issue in case of the lifetime analysis is the experimental acquisition of the failure probability by low loads. Normally, the

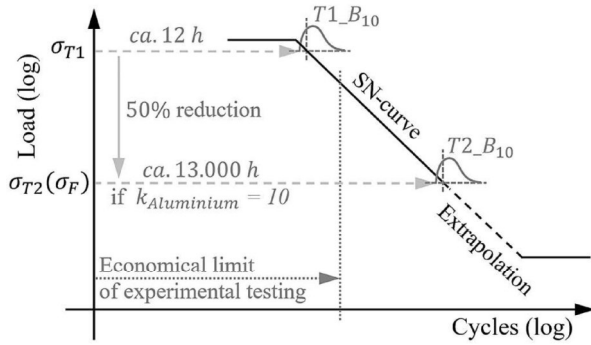


Figure 2: Experimental data acquisition vs. theoretical extrapolation of the SN-curve

financial aspect of the testing is very sensitive due to the proportional connection of testing costs to the lifetime exponent k , as shown in **Figure 2**, where the lifetime exponent k can be seen as the SN-curve gradient in a log-log chart. Therefore, from an economic point of view, an experimental approach could take too much time in some cases. If an application in the field does require an experimental evaluation at the existing load equivalent, this could lead to high testing costs, which can be calculated with (4).

$$\left(\frac{\sigma_{T2}}{\sigma_{T1}}\right)^k \frac{\text{Price}[h]}{\text{rpm} \cdot 60} = \text{Price}[\text{run}] \quad (4)$$

To demonstrate an economical issue more detailed an illustrative load spectrum is shown in **Table 1**, where a load example of a drivetrain application is illustrated as pressure ratio. This example covers a typical loading cycle of a wheel loader, also known as the standardized Y-cycle [23]. Here, the load equivalent in field is seldom higher than 50% of max. strength (if σ_F covers

the system pressure) like shown in **Figure 2**. Here the σ_F is the calculated load equivalent defined as the **Root Mean Effective Pressure (RMEP)**, while the economical limit in this picture is an illustrative assumption only.

Table 1: Load ratio of a wheel loader

ratio	35%	18%	12%	12%	11%	6%	3%	2%	1%
Δp [bar]	0-40	<80	<120	<160	<200	<240	<280	<320	<360
σ_F	ca. $p_{\text{max}} \cdot 0,5$								

The endurance testing in such conditions ($\sigma_{T2} = \sigma_F$) would require ca. 13.000 hours per failure if the testing object is made of aluminum. Considering that more than one failure event is required for a sufficient confidence in statistical methods, the costs are also connected to the number of required failure events as well. The environmental conditions and the cost factors represent a big challenge, which requires a high level in accuracy of theoretical analysis methods.

4. EXPERIMENTAL ACQUISITION OF B_{10}

In this chapter, an experimental setup is described, which includes the determination of B_{10} . Industry-used B_{10} value is defined as the experimentally-investigated lifetime point, where the first 10 % of a product lot would fail by the applied load. This value is also used as the reference for the reliability calculation of the FLA, see next chapter. The aim of this test setup is the analysis of the product-specific failure rate. Hereby, the focus is on the Weibull slope and SN-curve gradient.

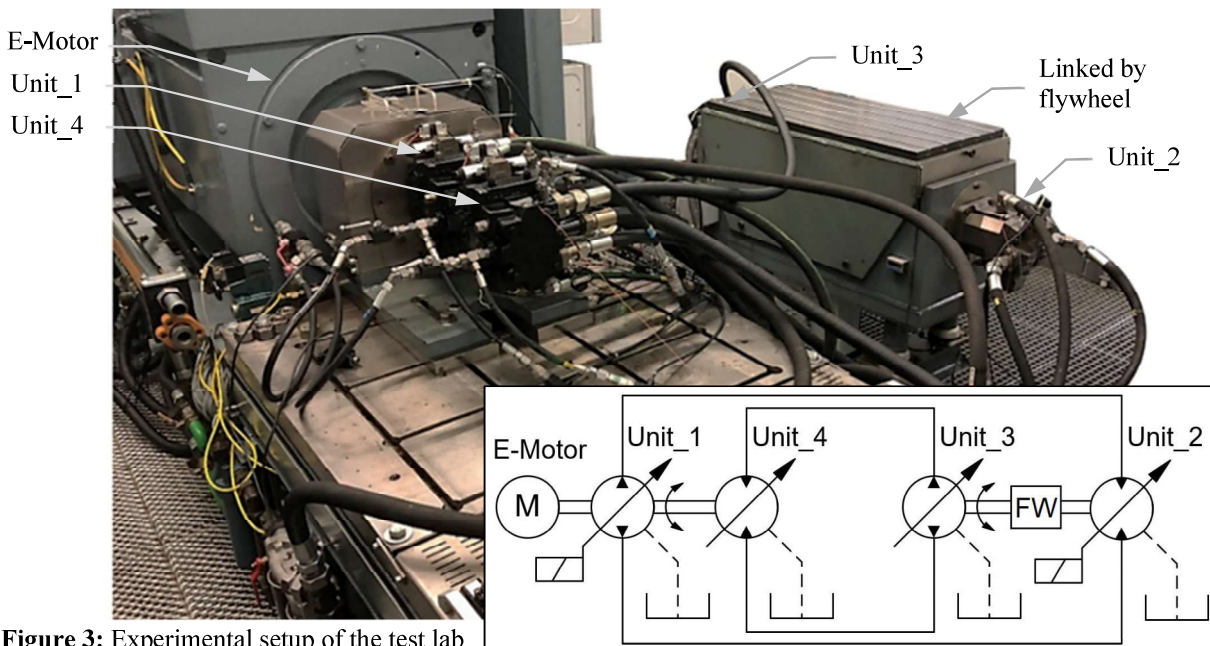


Figure 3: Experimental setup of the test lab

The steady-state conditions were defined for two constant load levels as shown in **Figure 2** as σ_{T1} and σ_{T2} . Both conditions were set before the economical limit. The difference between both conditions was only the system pressure which describes the load factor. All other factors like temperature, speed etc. were constant. The setup between the units did realize the following hardware situation as shown in **Figure 3**.

- Unit_1 in pumping mode
- Unit_2 in motor mode
- Unit_3 in pumping mode
- Unit_4 in motor mode

These different modes are typically present in the field as well, where different load scenarios for the components do exist and also have to be addressed by the lifetime investigation in general. In this paper, only results of the Unit_1 are shown for illustration purposes.

The results of the endurance testing can be seen in **Figure 4**, where the X-axis represents the cycles (x) before a failure occurs and the Y-axis represents the unreliability ($F(x)$) of the tested component. Subsequent results of the Weibull analysis deliver specific values like η or β . Eta (η) is defined as the characteristic lifetime at 63,2 % of the unreliability, while Beta (β) is defined as the Weibull slope and shown as gradient of the 50% confidence line in **Figure 4**. Both values do characterize the lifetime behavior of the tested

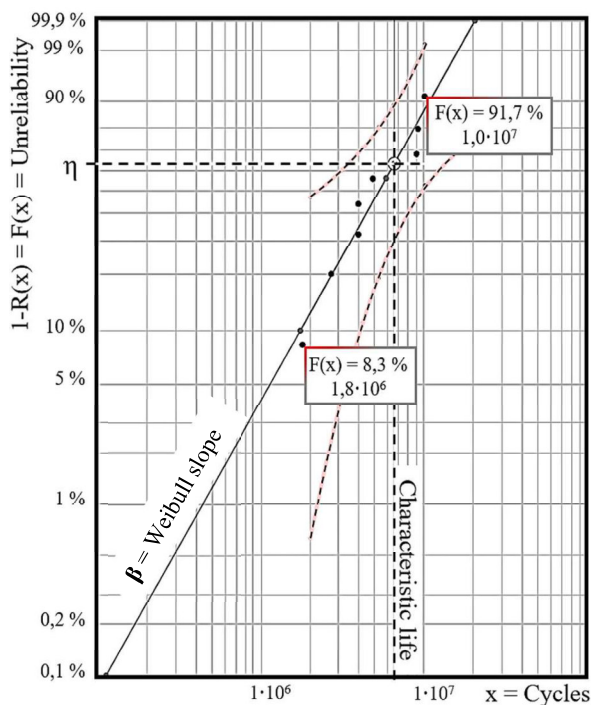


Figure 4: Weibull probability plot (90% confidence)

component. The characterization covers a.o. the reliability curve, which is used as the reference curve for the next step of the FLA connecting calculation.

5. ANALYSIS BY USING OF THE FAILURE LIKELIHOOD ASSESSMENT

The FLA method combines two (industrial-used) standard methods, Fault Tree Analysis (FTA) and Failure Mode and Effect Analysis (FMEA). Thus, the analysis of the risk assessment is based on a failure propagation (FTA) and a quantitative assessment (FMEA), where the main advantages are: identification of all possible failure causes, failure propagation in the present/defined system, identification of its reliability and detection of the weak link ranking [18].

The core steps of the methodology are shown in **Figure 5**. Here the **first step** is the “System definition” of the investigated system. Standard documents/sheets like exploded views or circuit diagram makes it easy to apply this methodology to many different sub-systems. In this paper, a change in the manufacturing process is used as calculation and evaluation example.



Figure 5: FLA Analysis proceeding phases/steps

An exploded-view as shown in **Figure 6** allows selecting an appropriate detail level, according to the focus of the requested investigation topic. The FTA tree allows covering the whole system, starting by the top-level through sub-assemblies and components down till material and environmental conditions.

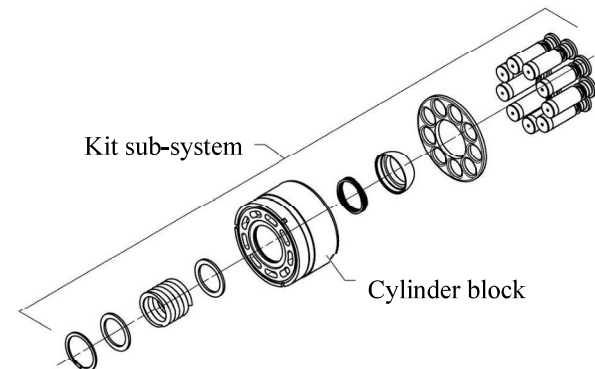


Figure 6: Exploded view of a kit sub-assembly

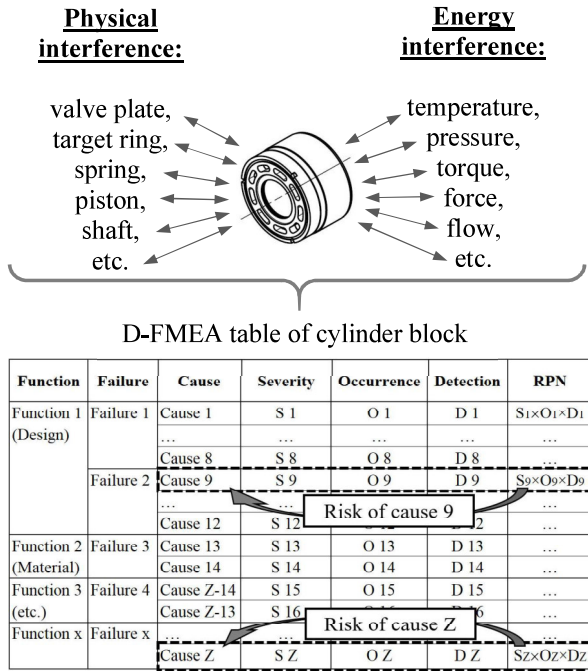


Figure 8: Risk analysis (conventional D-FMEA)

The **second step** is the definition of the functions and potential failures. Thus, the recommendation is to use both FTA and Design-FMEA in alternating sequence to avoid gaps in the investigation, which leads to corruption of the reliability assessment. As soon as the system is defined, the sub-levels (function, failure and cause) are drawn, the completeness of the fault tree is verified by the FMEA structure/tables, and the risk analysis can move to the third step.

The result of the **third step** consists of a propagation overview as a fault tree structure with quantitative nodes or rather occurrence nodes as seen in **Figure 7**. The previous methods/tools like FTA or D-FMEA would deliver only an incomplete picture of the intended change. In case of the FTA, only a fault tree without a possibility of quantitative assessment would exist, while the D-FMEA would deliver the Risk Priority Number (RPN) of each single cause without a relation to the relative lifetime impact of the change, like shown in **Figure 8**, where the RPN is typically calculated by using severity (S), occurrence (O) and detection (D) [24]:

$$RPN_{cause} = S \times O \times D \quad (5)$$

In case of the cylinder block demonstration example, the change covers a surface treatment process, where the manufacturer predicted a significant improvement ($\Delta L_{10M} = 30\%$) of the fatigue strength. Hence, the FLA was calculated

at a single component only and deliver the reliability values of the applied change, like shown in **Figure 7**. Here the number of causes and the corresponding occurrence values were determined from the occurrence-table and propagation-tree, especially related to sub-tree of the cylinder block.

The results of the **fourth step** conclude in weighted occurrence values of the manufacturing change, which can be seen in Equations (7) and (8). The weighting of the occurrence is related to the number of applied causes, where a high number of causes or rather a high failure amount has a high impact on the investigated system. In case of the FLA, only the occurrence of the causes is taken into account due to the previous evaluation of the FLA method related to the relevance and best-fit impact of the occurrence [18]. The derivation of the weighted occurrence as an appropriate value for the FLA analysis is based on the definition and the cross-connection

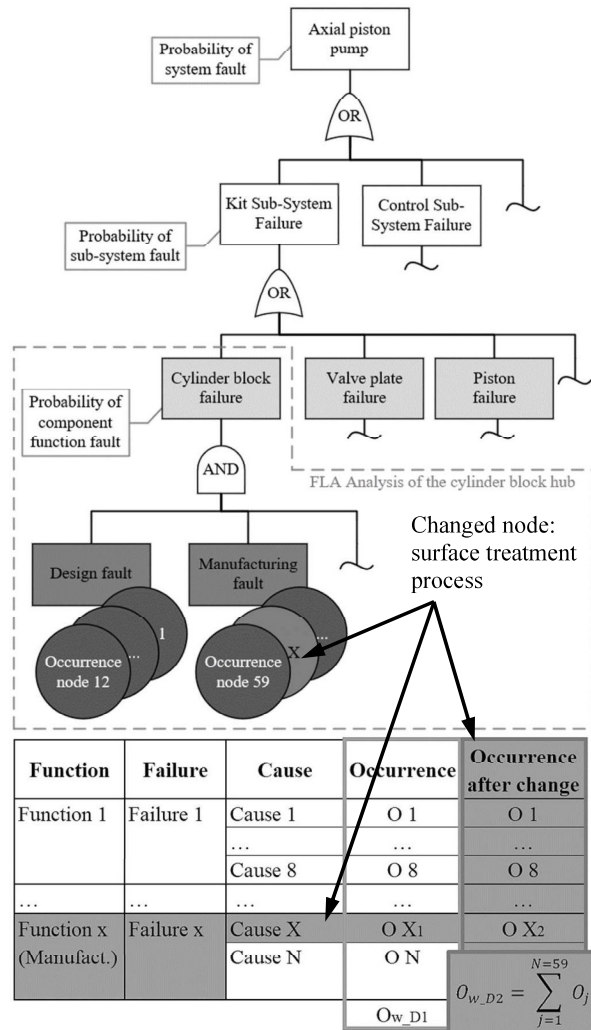


Figure 7: Failure Likelihood Assessment (FLA)

of the failure probability in all FLA-relevant methods:

D-FMEA

Occurrence = failure probability (level) of a specific cause.

FTA

Failure propagation = failure probability in a system (relative)

Weibull analysis

Unreliability = failure probability related to the number of cycles

Therefore, the FLA allows calculating the failure probability or rather the reliability for the given sub-structure. The results can be seen below, where $N_{D1/2} = 59$ is the number of causes and the $O_{w_D1/2}$ is the weighted occurrence of a specific change. The reference part is marked with $D1$ while the changed part is marked with $D2$. After the manufacturing modification N is unchanged as the number of causes stay the same. Only the occurrence has changed due to the engineering assessment.

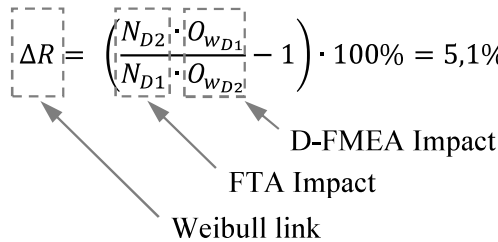
$$N_{D1} = N_{D2} = 59 \quad (6)$$

$$O_{w_{D1}} = \sum_{j=1}^{N=59} O_j = 145 \quad (7)$$

$$O_{w_{D2}} = \sum_{j=1}^{N=59} O_j = 138 \quad (8)$$

The design improvement is calculated below in (9) and is used as a positive reliability change of the product if the outcome is positive:

$$\Delta R = \left(\frac{\left(\frac{N_{D2}}{N_{D1}} \cdot \frac{O_{w_{D1}}}{O_{w_{D2}}} \right) - 1}{1} \right) \cdot 100\% = 5,1\% \quad (9)$$



This reliability improvement was added to the experimentally-derived results, where the failure rate of the experimental data was used as the reference curve. The reliability improvement ΔR was applied to the B_{10_D1} -characteristic point, which is defined as experimentally-determined nominal lifetime, where 10% of units may fail, as it can be seen in **Figure 9**. Here the reliability $R(x)$ of the product is equal to 90,4%. The calculated nominal life after change is therefore defined as

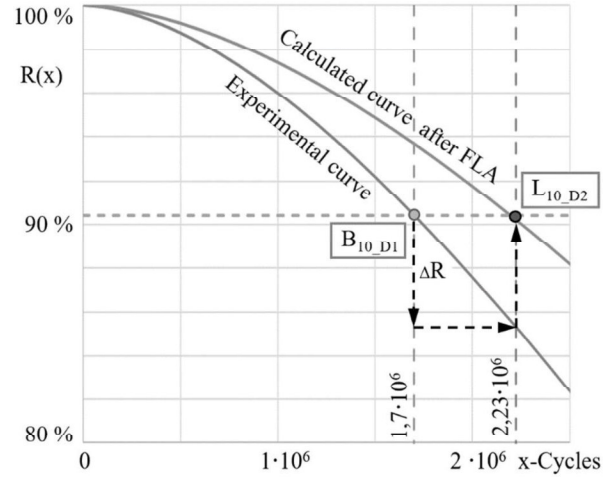


Figure 9: Experimental and calculated reliability

L_{10_D2} and deliver a new reference for the lifetime, where 10% of units may fail according the Weibull density function. The comparison of the B_{10_D1} (before change) and L_{10_D2} shows that the change gives a significant improvement in lifetime. The potential of the improvement can be calculated with the following:

$$\Delta L_{10FLA} = \left(\frac{L_{10D2}}{B_{10D1}} - 1 \right) \cdot 100\% = 31\% \quad (10)$$

Hence, this specific engineering change in the manufacturing process may improve the fatigue strength or rather the lifetime of the component by 31% (ΔL_{10FLA}). The difference between the specification value of the manufacturer and the FLA-calculated results ($\Delta L_{10FLA} - \Delta L_{10M}$) is remarkably small. This result can be applied to the whole SN-curve, so that the effect for different load spectra or equivalents (application characteristics) can be precisely predicted. Thus, each D-FMEA change can be precisely analyzed related to the change in lifetime and allows a better impact understanding of manufacturing, design and/or other changes.

6. CONCLUSION

In this work, the failure rate of a cylinder block under certain conditions was experimentally determined, with the focus on the fatigue strength analysis. Thus, the experimental feasibility and its issues like the economic aspects were discussed as well. It is obvious that a new or improved theoretical approach is required. The accuracy of the theoretical prediction was in focus, where a new methodology the so-called **Failure Likelihood Assessment (FLA)**, was

applied. This failure assessment method is based on the FTA and D-FMEA as standards tools. Thus, the FLA is a systematical method which combines the failure propagation in a system with the quantitative characteristics and therefore allows a calculation of the failure probability or rather the reliability of a system. The FLA method was applied to a manufacturing change of the cylinder block. The relation between FLA and change evaluation was taken in account, where the advantages of the connection to the load equivalent in the field were shown. The results showed that the FLA methodology delivers accurate results so that it becomes a powerful tool to analyze design changes as well as new designs in regard to reliability and lifetime prediction already in the early design phase. The accuracy increase in calculation improves the lifetime prediction and thereby supports the fulfillment of customer requirements. More reliable product with an optimized design is here the benefit for the user of this methodology.

7. OUTLOOK

An experimental evaluation of both, the FLA-calculated and manufacturer-specified values are the next steps. Moreover, the FLA feasibility to different change types in a multi-component system will follow in the succeeding researches. The focus will be on analysis of the system and component reliability related to the lifetime. Especially, the connection between a design change and lifetime impact in a system will be addressed here.

NOMENCLATURE

$F(x)$	Unreliability (in cycles)
$R(x)$	Reliability (in cycles)
ΔR	Reliability improvement
L_{10}	Calculated Nominal Lifetime
ΔL_{10FLA}	FLA-Calculated Lifetime Improvement
ΔL_{10M}	Manufacturer-Predicted Lifetime Improv.
B_{10}	Experimental Nominal Lifetime
x	Cycles Before Failure
β	Weibull Slope
η	Characteristic Lifetime
n	Occurred Number of Cycles
N	Maximum Number of Cycles (Miner's Rule)
X	Linear Damage Accumulation
N_{D1}	Number of Root Causes (First Design)
N_{D2}	Number of Root Causes (Second Design)

k	Gradient of the Lifetime Curve
C	Dynamic Load
P	Equivalent Dynamic Load
σ_X	Load at Level X
σ_{TX}	Load of Testing Number X
σ_F	Load equivalent in Field
O_{wD1}	Weighted Occurrence (First Design)
O_{wD2}	Weighted Occurrence (Second Design)
Δp	System Pressure
p_{max}	Maximum Pressure

ABBREVIATIONS

<i>RMEP</i>	Root Mean Effective Pressure
<i>FLA</i>	Failure Likelihood Assessment
<i>cdf</i>	Comulative Density Function
<i>T1_{B10}</i>	Test with condition 1
<i>T2_{B10}</i>	Test with condition 2
<i>SN</i>	Stress related to Number of cycles
<i>FTA</i>	Fault Tree Analysis
<i>D-FMEA</i>	Design-Failure Mode and Effect Analysis
<i>RPN</i>	Risk Priority Number
<i>S</i>	Severity
<i>O</i>	Occurrence
<i>D</i>	Detection
<i>D1</i>	Design 1 (before change)
<i>D2</i>	Design 2 (after change)

REFERENCES

- [1] Bauer J. A., Wang M., Yaun Q., Gust M. "Automation, Connectivity and Big Data in Fluid Power Systems and Off-Road Vehicles." Symposium of Fluid Power and Motion Control (GFPS), Sarasota, USA, October 9th, 2019
- [2] Boog, M., "Steigerung der Verfügbarkeit mobiler Arbeitsmaschinen durch Betriebslast-erfassung und Fehleridentifikation an hydro-statischen Verdrängereinheiten". Karlsruhe Institute of Technology, PhD thesis, 2010.
- [3] Martin K. F., "A review by Discussion of Condition Monitoring and Fault Diagnosis in Machine Tools", Int. J. Mach. Tools Manufact. Vol. 34, No. 4, 1994
- [4] Fusko M., Rakyta M., Krajcovic M., Dulina L., Gaso M., Grznar P., "Basics of Designing Maintenance Processes in Industry 4.0", University of Zilina, Faculty of Mechanical Engineering, Department of Industrial Engineering, Zilina, Slovak Republic, DOI: 10.17973/MMSJ.2018_03_2017104, ISSN 1805-0476, 2018
- [5] Liu X., Cui D., Wang L., Zhang L., "Reliability Evaluation of Hydraulic Pump Based on

- Performance Degradation", 11th International Fluid Power Conference (IFK 2018), Aachen, Germany, 2018.03.19-21
- [6] Brinkschult, L., Mattes J., Geimer, M. "An approach to wear simulation of hydrostatic drives to improve the availability of mobile machines." 11th International Fluid Power Conference (IFK), Aachen, 19.-21. März 2018. Vol. 1. Ed.: H. Murrenhoff, 392–407, RWTH Aachen University, Aachen. doi:10.18154/RWTH-2018-224523, 2018
- [7] Weibull, W., "A statistical distribution function of wide applicability", *Journal of Applied Mechanics*, pp. 293-297., 1951
- [8] Brinkschulte L., Geimer M., "Intelligent Machine Operator Identification to Develop Damage Reducing Operating Strategies for Mobile Machines", Symposium of Fluid Power and Motion Control (GFPS), Sarasota, USA, October 9th, 2019
- [9] Lorösch, H.-K., "Die Gebrauchsdauer von Wälzlagern hängt nicht nur von der Tragzahl ab", *Wälzlagertechnik - Industrietechnik (FAG)*, S15-21, 1992
- [10] Kunze, G., "Methode zur Bestimmung von Normlastkollektiven für Bau- und Fördermaschinen - Lebensdauerabschätzung an Baugruppen von Bau- und Fördermaschinen." Wissensportal: www.baumaschine.de/Portal/Archive/1_2005/Wissenschaft/lastkollektive/laskollektive.pdf, 2005.
- [11] Siemon A., "Qualitative und quantitative Analysen der linearen und nichtlinearen Schadensakkumulationshypothesen unter Einbeziehung der statistischen Versuchsplanung", Diss., Universität Kassel, Kassel, Germany, 2006-12-21
- [12] Palmgren A., "Die Lebensdauer von Kugellagern. " *Zeitschrift des Vereins Deutscher Ingenieure* 68 H. 14, S. 339-341, 1924
- [13] Miner M.A., "Cumulative Damage in Fatigue. ", *Journal of Applied Mechanics* 12 (1945) Bd. 3, Pages. 159-164, 1945.
- [14] Schuster U., "Reliability of hydraulic valves - determining the MTTFd value of hydraulic directional control valves.", Customer Benefits of Fluid Power, Internationales Fluidtechnisches Kolloquium, 5, Customer Benefits of Fluid Power, International Fluid Power Conference (IFK), 5 in Fluidtechnik: T; 6; 71-81, 2006
- [15] Bobbio A., Trivedi, K. S., Muppala J., "State Enumeration", *Reliability and Availability Engineering / 2017*, ISBN-10: 1107099501, s. 271–285, Cambridge University Press; Edition 1, 19. Sep. 2017
- [16] Nicholls D., Lein P., "Weibayes testing: What is the impact if assumed beta is incorrect?", 2009 Annual Reliability and Maintainability Symposium, Fort Worth, TX, 2009, pp. 37-42.
- [17] Abernethy R.B., *The New Weibull Handbook*, 4th ed., in: R.B. Abernethy (ed.), Florida, USA, 2000.
- [18] Baus I., Rahmfeld R., Schumacher A., Pedersen H.C. "Systematic Methodology for Reliability Analysis of Components in Axial Piston Units" Symposium of Fluid Power and Motion Control (GFPS), Sarasota, USA, October 9th, 2019
- [19] Zhang, J., Li, H., Fu, J., "Research of Sequential Accelerated Life Test Method for Aviation Gear Pump", *Chinese Hydraulics & Pneumatics*, No. 05, pp. 101-104, 2012
- [20] Guo, R., Shi, Y., Zhao, J., "Short-time Test Method of Reliability for Hydraulic Pumps", *Transactions of the Chinese Society of Agricultural Machinery*, No. 03, pp. 405-412, 2016.
- [21] Ma, J., Ruan, L., Fu, Y., "A Review on Method of Accelerated Lifetime Test for Aircraft Hydraulic Pump", *Chinese Hydraulics & Pneumatics*, No. 6, pp. 6-12, 2015.
- [22] ISO 281 "Rolling bearings - Dynamic load ratings and rating life" (ISO 281:2010-10)
- [23] Deiters H., "Standardisierung von Lastzyklen zur Beurteilung der Effizienz mobiler Arbeitsmaschinen", Copyright Shaker Verlag 2009, Aachen, ISBN 978-3-8322-8111-3, 2009
- [24] Xiao N., Huang H.-Z., Li Y., He L., Jin T., "Multiple failure modes analysis and weighted risk priority number evaluation in FMEA", *Engineering Failure Analysis*, Volume 18, Issue 4, Pages 1162-1170, ISSN 1350-6307, <https://doi.org/10.1016/j.engfailanal.2011.02.004>, 2011

SIMULATION-BASED SYSTEM RELIABILITY ANALYSIS OF ELECTROHYDRAULIC ACTUATOR WITH DUAL MODULAR REDUNDANCY

Maxim Andreev*, Artem Kolesnikov, Uwe Grätz, Julia Gundermann

ESI ITI GmbH, Schweriner Str. 1, 01067 Dresden, Germany

* Corresponding author: Tel.: +49 351 260 50 249; E-mail address: maxim.andreev@esi-group.com

ABSTRACT

This paper describes the failure detection system of an electro-hydraulic actuator with dual modular redundancy based on a *hybrid twin*TM concept. *Hybrid twin*TM is a combination of *virtual twin* that operates in parallel with the actuator and represents its ideal behaviour, and a *digital twin* that identifies possible failures using the sensor readings residuals. *Simulation-based system reliability analysis* helps to generate a dataset for training the digital twin using *machine learning* algorithms. A *systematic failure detection approach* based on decision trees and the process of analysing the quality of the result is described.

Keywords: failure detection system, reliability, digital twin, machine learning

1. INTRODUCTION

The objective of *reliability engineering* is to provide the ability of the device to function within the specified period of time. The problem is that at the design phase it is very difficult to predict all the possible factors that could lead to failure, so unplanned failures are almost impossible to be completely eliminated from the device life cycle.

The consequences of failures can be significantly reduced by, for example, developing *fault-tolerant systems*, providing *predictive maintenance* and *system diagnostics* design. This makes possible to correct the inaccuracy of design-stage reliability estimations by adjusting to the real operating conditions. But reliability engineers often face at this point a conflict of increasing device complexity to improve reliability (e.g. by *redundancy*), which in turn makes maintenance and diagnostics more difficult.

However, *digital transformation* brings new opportunities in these challenges. As an example, model-based development is becoming more and more important. Device simulation models can be used both in designing and predicting the reliability of devices, as well as during operation

of a real device [1].

The aim of this paper is to demonstrate the workflow of a simulation-based system reliability improvement by providing an accurate *failure detection system*. We use *machine learning* methods that allow us to move from virtual prototype simulation models, already widely used in product development by many manufacturers, to a system that accurately identifies failure at the earliest stages of its occurrence with minimal use of physical experiment.

2. RELIABILITY OF AN ELECTROHYDRAULIC ACTUATOR

The object of this study is an electrohydraulic aileron actuator with *dual modular redundancy*. The typical structure of such actuators used in civil aviation, as described in [2], is taken as an example.

We assume that the optimal actuator structure was obtained at the previous development stage (for example, with the help of *fault tree analysis*) and thus it consists of two electro-hydraulic actuators with independent energy sources connected in parallel to the load (aileron). In normal mode, both actuators work in parallel, so

that failure of one of them does not lead to a loss of control and implements the *fault-tolerant system* concept.

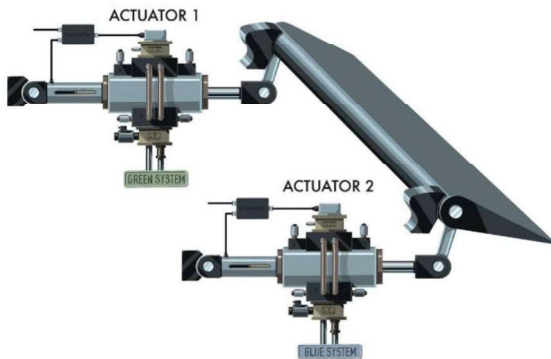


Figure 1: Electrohydraulic aileron actuator with dual modular redundancy

As with any system with *modular redundancy*, it must be equipped with an automatic diagnostic and control system that automatically switches off the failed actuator. A specific problem for *dual modular redundancy* systems is the difficulty of detecting which of the two actuators failed. One failed actuator causes disturbances in the system, both at the mechanical system level and via the control system, which leads to abnormal behaviour of the other actuator (which can be monitored by sensors).

The next challenge is to accurately localize the failure. Not all failures require the same response from the control system. For example, a leakage

in an actuator requires its immediate shutdown to provide the availability of the remaining hydraulic system; while a pressure sensor failure allows the actuator to remain functional by switching the control mode. Thus, the failure detection system must be able to differentiate between such cases and prevent false actuator shutdowns.

On the other hand, failure must be detected and localized at the earliest stage with minimum intensity. This would avoid the emergency consequences of gradual failures and eliminate them through *predictive maintenance*.

These problems can be solved by a failure detection system based on a system simulation model in combination with machine learning.

3. HYBRID TWIN™ BASED FAILURE DETECTION SYSTEM

The failure detection system is shown in **Figure 2**. The *electro-hydraulic actuator 2* (for simplicity, only one actuator is shown) receives from the *flight control computer 1* an electrical signal proportional to which the aileron 4 must be turned. Various sensors (position, pressure, temperature) are also available in the actuator, which can be used for control and diagnostics, and whose data from both actuators is collected in the receiver 5.

The same input signal is received by the actuator's *virtual twin 3*. The *virtual twin* is a real-

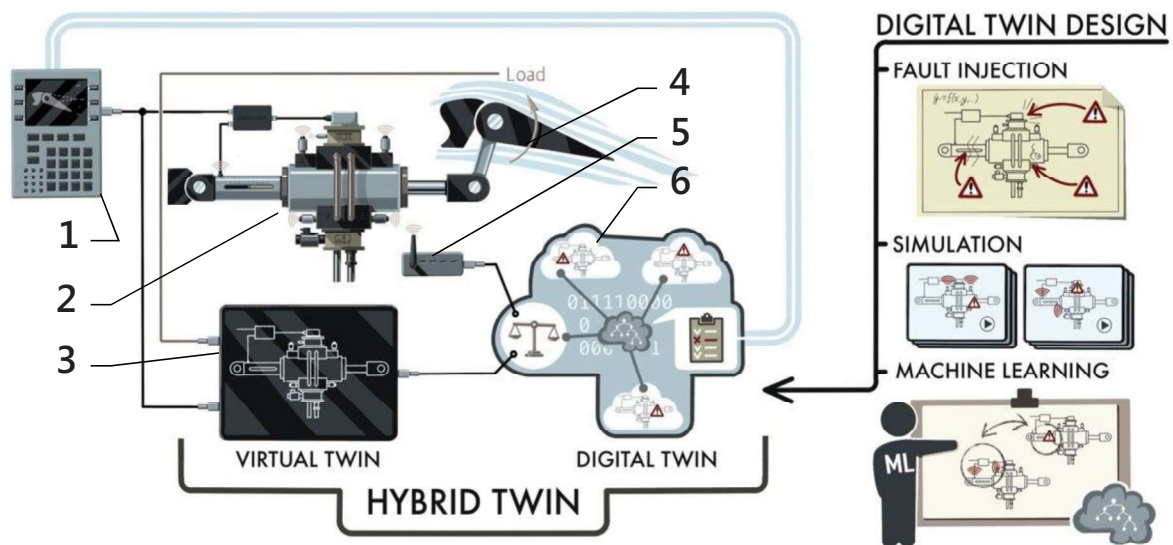


Figure 2: Hybrid Twin™ based failure detection system

time (or semi-real-time) simulation model based on an ODE describing the *nominal behaviour* of the actuator. To perform the twin function, the model must receive data from the sensors on the current values of the boundary conditions (supply and drain pressure, fluid temperature at the inlet, etc.) as well as load values. The output variables of the *virtual twin* are the calculated sensor data, which essentially represent their required values. Deviation of the real sensor readings from the virtual sensors readings of the *virtual twin* (assuming that the load sensors and boundary conditions are correct) will indicate that there are faults in the system. To extract more detailed information on failure, a *digital twin* is required.

The *digital twin* is a real-time capable decision algorithm whose input receives all sensor values and whose output provides information about a possible failure. To train a *digital twin*, we use thousands of variations of the *virtual twin*, containing models of different failures. The result of the digital twin prediction can be used to update the virtual twin by fitting parameters and to trigger a flight control computer for correction (e.g. to generate a control signal to shut down one of the actuators).

This combination of physically-based models and data-science is called a "*hybrid twin*" and represents the next generation of twins by ESI Group [3].

3.1. Simulation model as a virtual twin

The first step to the actuator's *hybrid twin* is to create its *virtual twin*. The *virtual twin* design starts at the product prototype stage, when simulation models are created to check the requirements. In the process of product design, models are corrected, modified, validated in laboratory conditions and by the certification stage, as a rule, there is a set of models with a given accuracy simulating the device behaviour.

In the next step, based on this model set, a compromise simulation model should be created, that can be used for real-time (or semi-real-time) applications. For our research we developed a detailed simulation model of the electro-hydraulic actuator in *SimulationX*, the general structure of which is shown in **Figure 3**.

The virtual twin of each actuator is placed in a *virtual environment*, that is a model of the environment of the real device with the same behaviour. This means that the *virtual twin* must receive not only control signals, but also environment information, such as the supply and tank pressure and temperature at the input of the output hydraulic line of each actuator, inertial and aerodynamic load on aileron.

These data can be obtained either simply from sensors (as in the case of fluid pressure and temperature that can be measured by the sensors) or a combination of sensor data and a simulation model (as in the case of aerodynamic aileron load

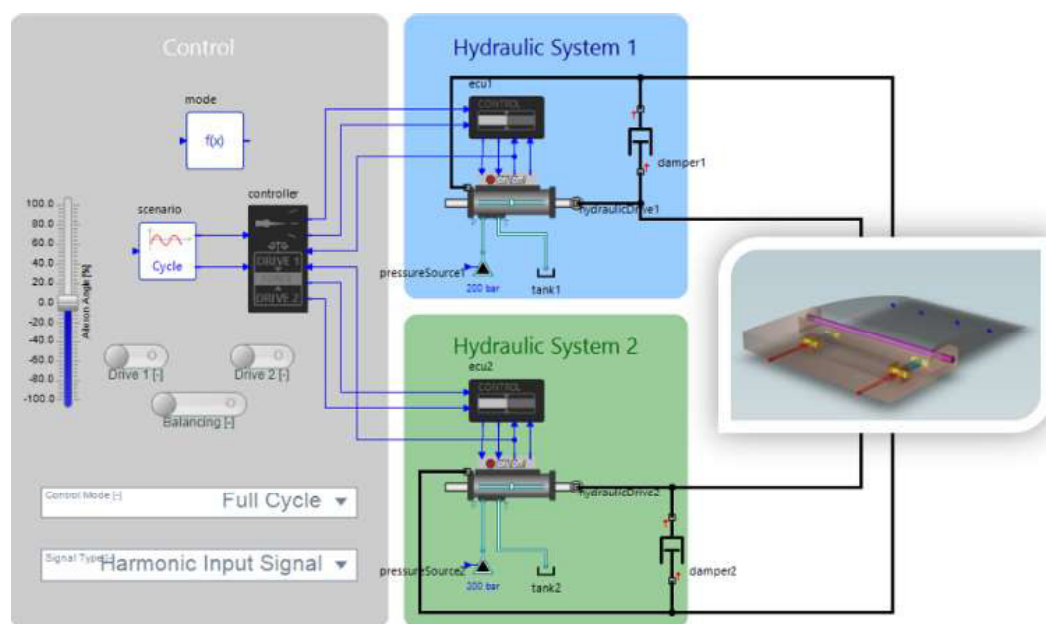


Figure 3: Diagram view of the aileron control system model in *SimulationX*

that can be simulated based on altimeter data, the spatial orientation of the aircraft and its air speed). For further steps, it is important to note that for reliable use of the *virtual environment* data, all sensors and simulation models must be equipped with their own failure diagnostic system. Data on the state of the object can be obtained only based on the assumption that the *virtual environment* is working properly.

Another important requirement for the *virtual twin* model is the degree of detail of its physical content. The model assumptions should not be limited to the calculation of system state variables in which sensors are installed but should also be able to simulate the behaviour in case of possible failures. **Figure 4** shows the detailed structure of the model of the electrohydraulic actuator developed in *SimulationX*.

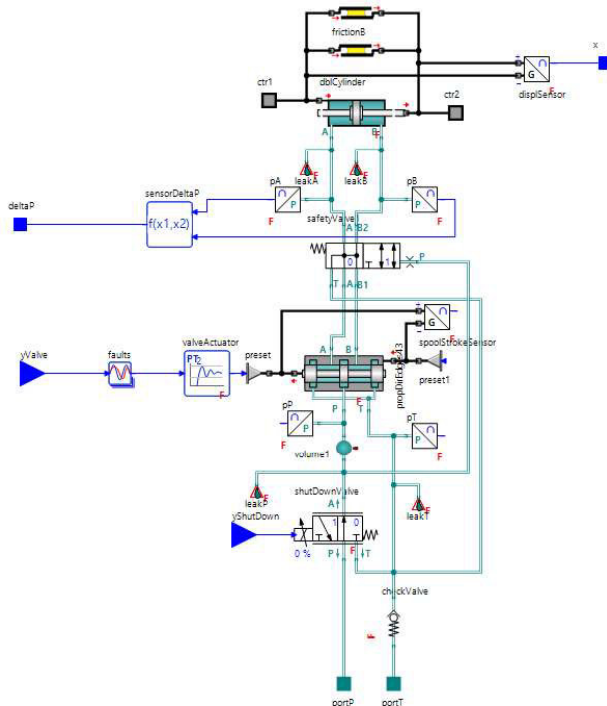


Figure 4: Diagram view of the electro-hydraulic actuator model in *SimulationX*

The following requirements should be considered in the hydraulic drive simulation model used as *virtual twin*:

- The model of the *hydraulic control servo valve* contains a spool model based on edge geometry. This is important for further modelling of the clogging of one of the control edges.
- All sensor models not only transmit state

variables, but also consider the process of converting a physical value into an electrical or a dimensionless value. At conversion points, fault models will be built in later.

The final stage of *virtual twin* design is the validation of the model with the real actuator. The result of the validation is a field of *confidence intervals* of the model depending on the input variables. These confidence intervals are a basis of the failure diagnostics system, as we will show later.

3.2. Fault-augmented virtual twin

A *digital twin* training requires a large amount of data where the sensor data are clearly related to the detected failures. Collecting enough data in real-world conditions seems to be a big challenge that is difficult to realize in practice because of the need to create crashable prototypes and a large number of experiments. However, the same simulation model that was used to create the *virtual twin* can be used to generate this data. For this purpose, the model has been augmented with fault models that can occur in real operation. Manual *fault augmentation* requires a deep understanding of the system and analysis of device operation history data. At the same time, a precise physical description of all possible failures is hardly possible due to their difficult predictability. Paper [4] describes a way to simplify and partially automate this process. The main idea is that faults are semi-automatically injected in the simulation model. The faults are similar for different physical domains (leakage, increased friction, signal noise, etc.), simulated as simple as possible, but can be parametrically changed with different intensity. This allows to generate a large dataset containing many theoretically possible failures without requiring manual modelling of each failure individually.

The following types of failures were simulated in our study:

- Fluid internal and external leakage
- Valve edge clogging
- Servo valve actuator fault
 - Natural frequency reduction
 - Damping loss
- Signal faults
 - Bias
 - Calibration error

A detailed description of the simulation of these failures is given in [5].

We presume that failures should be detected at an early stage. As a result, we can assume that the occurrence of failure combinations is unlikely and thus significantly reduce the required number of models. Nevertheless, even in this case we are talking about hundreds and thousands of possible failures with different intensities. All failures should be classified into a limited number of categories to be used in a failure detection system. **Table 1** shows the classification we propose.

Table 1: Failure Categories

Failed Actuator	Command	Failure Information	Components	Faults
Actuator 1 (2) Failed	Shut Down!	External Leakage	4	40
		Control Valve Failure	1	100
		Supply Valve Failure	1	10
		Tank Valve Failure	1	10
		Cylinder Pressure Sensor Failure	2	80
	Change Control Mode!	Displacement Sensor Failure	1	40
		Cylinder Internal Leakage	1	10
	Warning!	Valve Displacement Sensor Failure	1	40
		Supply/Tank Pressure Sensor Failure	2	80
		Sum (x2 Actuators):		28

First of all, failures differ by the actuator in which they occur. After that, failures should be classified according to the required control system actions. Three categories have been defined:

- “*Shut Down!*” includes failures that require the immediate disconnection of the failed actuator from the hydraulic system and its switch to passive damping mode.
- “*Change Control Mode!*” refers to failures that require a change in the operating mode of the ECU.
- “*Warning!*” faults do not require an

immediate response but must be fixed by technical staff during maintenance.

To fix a failure during maintenance, it is necessary to accurately localize it by the component in which it occurred. However, within the same component, failures may have different nature. For example, category “*Control Valve Failure*” includes both control edge clogging and actuator fault or accuracy loss.

3.3. Failure detectability and sensor readings

Any failures that occur in the actuator during the operation lead to deviations of variables, that defining the system state $\mathbf{X}(t)$ at time t from the *nominal* behaviour $\mathbf{X}^{Nom}(t)$, called *errors* $\mathbf{E}(t)$.

$$\mathbf{E}(t) = \mathbf{X}(t) - \mathbf{X}^{Nom}(t) \quad (1)$$

A failure can be *detected* if one of the components of $\mathbf{E}(t)$ at the time point t_F exceeds a certain threshold ε :

$$|e_i| > \varepsilon \quad (2)$$

In the failure detection system, the *unobservable* nominal behavior is replaced by the behavior of a *virtual twin* $\mathbf{X}^{VT}(t)$ with output discrete virtual sensor variables $\mathbf{S}^{VT}(s_1^{VT}, s_2^{VT}, \dots, s_n^{VT})$. The state variables of the real actuator are estimated using the sensor readings $\mathbf{S}(s_1, s_2, \dots, s_n)$. Thus, the theoretical error value $\mathbf{E}(e_1, e_2, \dots, e_n)$ is replaced by the observable *residual* value $\mathbf{R}(r_1, r_2, \dots, r_n)$:

$$r_i = s_i - s_i^{VT} \quad (3)$$

It is necessary to note that in this case only those failures can be detected and classified which lead to *errors* of state variables $x_i = x(t_i)$ measured by available sensors. The first problem is that the *errors* in sensors themselves lead to *deviations* of their readings s_i .

The next problem is that the results of the *virtual twin* are *calculated* virtual sensor readings s_i^{VT} , which we assume to be distributed around the real $\mathbf{X}^{Nom}(t)$.

This leads to a distribution of the residual value r_i . Thus, not any deviation of r_i from zero indicates an error but could be only a result of sensor error and/or virtual twin model error. A condition must be defined for when the value(s) of r_i significantly deviate(s) from zero. This

condition and with it the accuracy of failure detection both depend on the accuracy of the sensors used, the accuracy of the virtual twin, as well as the size of the dataset sample.

In this demonstrator is assumed, that failure is detectable if one of the residuals to be out of $\pm 3\%$ band for each scaled residual value $r'_i = \frac{r_i}{x_{Scale}}$:

$$r'_i \notin (-0.03, +0.03) \quad (4)$$

The random nature of the model inaccuracy requires statistical processing of the *residuals*. **Figure 5** and **Figure 6** show histograms of scaled sensor residual probability distribution for two types of failures (external leakage and pressure sensor bias). The histograms were recorded with sampling rate 100 Hz during 90 s of simulation of the actuator's operation.

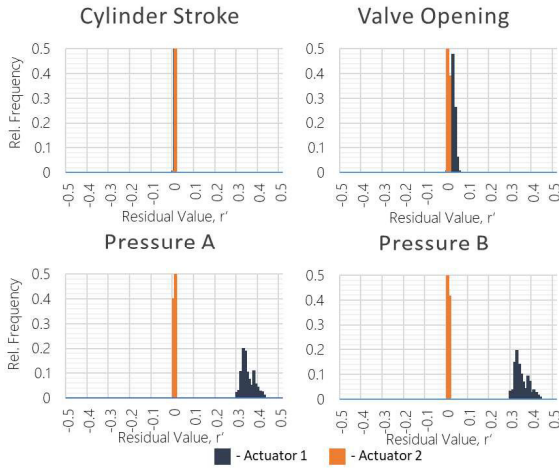


Figure 5: Residuals relative frequency distribution. External leakage in the hydraulic cylinder.

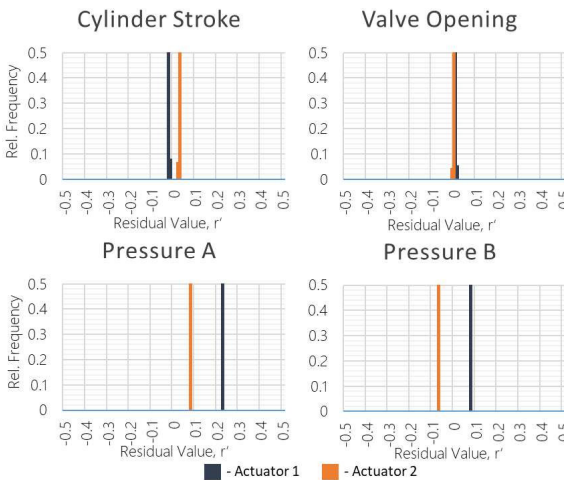


Figure 6: Residuals relative frequency distribution. Cylinder pressure sensor bias.

A residual in one part of the system leads to the spread of residuals into other parts of the system, including the faultless actuator. This is also observed in the residual distribution: leakage in one of the cylinder chambers leads to an increase in the pressure residual of the other chamber, and a variation in the control valve behaviour. If the pressure sensor fails, this affects the pressure behaviour in the chambers of all actuators and the cylinder stroke sensor residual.

To detect and localize failures, it is important to *extract features* from the residuals sample. Regardless of the type of residual distribution, the main features that can be used to identify faults are:

- Residual sample mean value:

$$\bar{r}' = \frac{\sum(s'_i - s_i^{VT'})}{N} \quad (5)$$

- Residual variance of sample mean:

$$Var(r') = E[(r'_i - \bar{r}')^2] \quad (6)$$

In addition, a discrete indicator is required to show whether the residual is inside the confidence interval or not.

The indicator is defined by the following equation:

$$r_{noDev} = \begin{cases} 1 & |\bar{r}'| < 0.03 \wedge Var(r') < 0.01^2 \\ 0 & \text{otherwise} \end{cases} \quad (7)$$

Thus, each *residual* has three *features* that will be used to identify faults.

3.4. Dataset generating

Machine learning algorithms require a training dataset as input data. The dataset is based on simulation results and should be as close as possible to the conditions of the real device operation. Within the framework of this demonstrator it was generated three white noise-based control signals with different amplitudes and spectrum and simulated each of them for two load levels (50% and 100%).

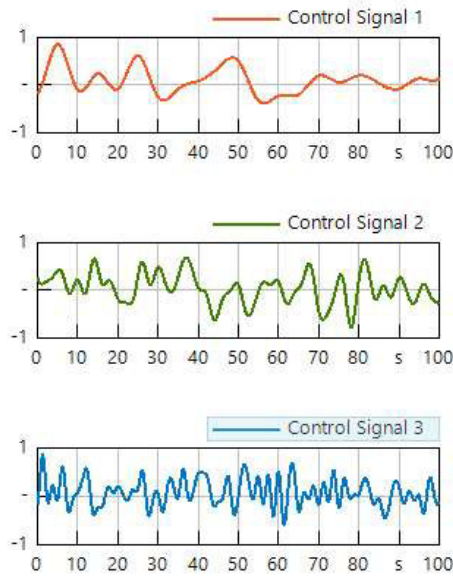


Figure 7: White noise-based control signals for dataset generating

Thus, the dataset will consist of six sets of possible failures (each of 820 variants), in total 4920 variants. It would take a lot of work to create so many model modifications and collect results manually. To solve this problem more effectively, the *System Reliability Analysis (SRA) AddIn* of *SimulationX* was used. The *SRA-AddIn* has the following functions: automatically create a specified number of models with different failures and fault intensities, simulate all variants using all allocated processor cores and collect the results on the dataset [4].

After generation, the dataset must be prepared for machine learning algorithms. Namely, simulated failures must be classified and the variants whose residuals do not exceed the confidence interval have to be filtered out. The structure of the dataset is shown in **Figure 8**.

Variant No	Faults Intensities			Fault Classifier			Residuals Features			
	fault1.intensity	fault2.intensity	...	faultF.intensity	Failed Actuator	Command	Detailed Info	Residual 1, Mean	Residual 1, Var	...
1	0.1	0	...	0	Actuator 1	Shut Down!	Valve Failure	0.112	0.0012	...
2	0.2	0	...	0	Actuator 1	Warning!	Sensor Failed	0.453	0.0354	...
...
n	0	0	...	1	Actuator 2	Warning!	Sensor Failed	0.112	0.0012	...

Figure 8: Dataset structure after processing

3.5. Machine learning based failure analysis

Recently methods of machine learning in tasks for error detection and forecasting of failures in technical systems have become widespread [6, 7]. Currently, a large number of machine learning algorithms are available for fault diagnosis and predictive maintenance [8, 9]. We analysed various available classifiers such as:

- Linear Support Vector
- Decision tree
- Multi-layer Perceptron
- Gaussian Naïve Bayes
- Random forest
- Linear Discriminant Analysis
- AdaBoost classifier
- Logistic Regression

All classification methods have strengths and weaknesses depending on the available data size, needed accuracy and interpretability as well as selected features [10]. In the applied tasks for multiclass classification, it is recommended to compare the main metrics of the algorithms to each other and select the most exact and reliable one. According to the sufficient accuracy and interpretability the decision tree classifier using the *CART* algorithm with the *Gini* impurity metrics were chosen for the data set with faults [11]. The data set was investigated by the

decision three in the data analytics tool *ESI Mineset*.

The objective of the classification algorithm in the context of *failure detection* is to find a rule based on the sensor residuals (column *Residuals Features*), which will uniformly group the failures of one type (column *Fault Classifier* in **Figure 8**). Using the resulting rules for the real sensor residuals analysis, it is theoretically possible to obtain in real time a decision about the occurrence of a certain failure class in the system.

In reality, if all available sensor residual features are used to identify detailed failure information, the following problems may occur:

- the algorithm will be very sensitive to changes in training data
- the resulting rules will be very complex and contain many conditions caused by the randomness contained in the dataset

An illustration of the last point can be the result we have obtained with a direct approach to learning: some key decisions depend on a value lying within a range of tank pressure sensor residual which is less than 0,001% of the whole residual range. This effect is called *overfitting* and such algorithms cannot be used in practice.

To avoid these problems, we used a *systematic*

failure detection approach. First, the detection of the failed actuator is trained on the complete dataset. Then, on a dataset containing only the failures of one actuator, the classifier of the control command is defined. Third, on the corresponding samples detailed failure detection is trained. This allows us to reduce the complexity of each classifier by limiting the height of the tree to 5-7 levels and avoid possible *overfitting* due to *early stopping*.

As mentioned above, to identify the failed actuator, a *decision tree algorithm* is used. All residual features of all sensors are included in the training set, but the maximum height of the tree is limited to 7. The result is shown in **Figure 9**.

The resulting tree uses mostly the discrete features *rNoDev*, and final splitting criteria do not have extremely small ranges. 1/3 of the dataset was used to estimate the accuracy of the algorithm. As result the model quality was 91,49% (error rate $-0,085 \pm 0,005$). The analysis of the most problematic terminal nodes (with the lowest *purity value*) shows that the most difficult case for the algorithm is to recognize and differ the failure of the cylinder piston stroke sensor of one actuator from another. This shows that possible actuator design changes (that would, for

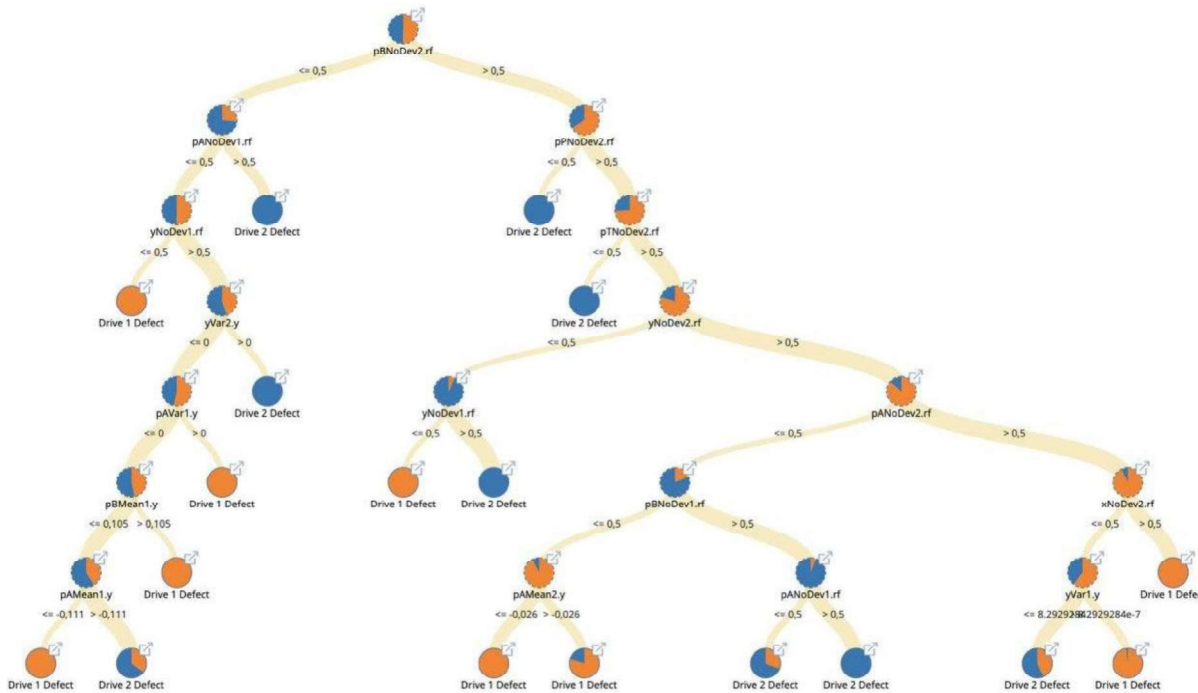


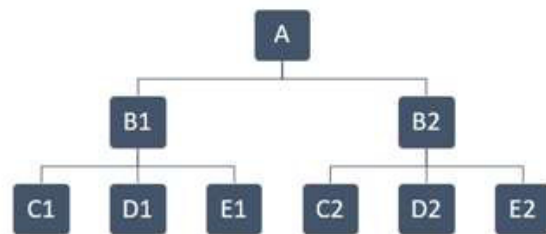
Figure 9: Structure of the decision tree that detects failure of one of the actuators.

example, identify a piston stroke sensor failure on a majority vote basis) would increase the accuracy of the failure detection system.

Further, based on a data sample containing only *Actuator 1* failures, the algorithm for recognition of failures classified by the command of the control system is similarly trained. The result obtained using the features of all the sensors (incl. *Actuator 2*) by very good model quality showed clear *overfitting* symptoms: many secondary features were involved in the decision process (such as drain pressure sensor variance), as was the focus on small changes in the cylinder piston stroke sensor readings. Using only *Actuator 1* sensors for training improved the quality of the algorithm but did not solve the drain sensor problem. The best result was obtained after excluding the drain sensor readings: model quality – 98,44% (error rate – $0,016 \pm 0,006$).

The training approach for *detailed failure detection* algorithms is similar to that described above, so this paper does not cover it.

As a result of a systematic approach, a complex symmetrical structure of 9 decision trees is developed (see **Figure 10**), on the basis of which an algorithm for device diagnostics can be implemented into the flight control computer.



A – Failed actuator classification,

B – Control system trigger classification,

C, D, E – Classification of detailed failure information

Figure 10: Macrostructure of failure classification algorithm

4. CONCLUSION

1. The implementation of the *hybrid twin*TM approach shown in this paper allows to significantly increase the reliability of the electro-hydraulic actuator with dual modular redundancy through a failure detection system.

2. Successful detection of the failure categories (with very small deviations from the nominal behaviour) depends on the accuracy of the *virtual twin* representing the real actuator.
3. Generation of the failure detection algorithm for the *digital twin* requires the calculation of many fault augmented variations of the simulation model of the device, that can be significantly accelerated through parallel computing.
4. The developed *systematic failure detection approach* using the *decision tree* algorithm is sensitive to the overfitting problem which can be resolved by training gradually from a more general category of failures to more detailed.

NOMENCLATURE

ODE Ordinary Differential Equations

ECU Electronic Control Unit

SRA System Reliability Analysis

CART Classification and Regression Trees

REFERENCES

- [1] Negretti D (2019) Modeling and simulation for predictive maintenance: a survey, Master's thesis, Polytechnic University of Milan, Italy, <http://hdl.handle.net/10589/148668>
- [2] Shumilov I.S (2009) *Sistemy Upravleniya Rulyami Samolyotov* (Aircraft rudder control systems), Moscow.
- [3] Chinesta F, Abisset-Chavanne E, Cueto E (2018) Virtual, Digital and Hybrid Twins: A New Paradigm in Data-Based Engineering and Engineered Data – Archives of Computational Methods in Engineering
- [4] Kolesnikov A, Tretsiak D, and Cameron M (2019) Systematic Simulation of Fault Behavior by Analysis of Vehicle Dynamics, Proceedings of the 13th International Modelica Conference, March 4-6, 2019, Regensburg, Germany, doi: 10.3384/ecp19157451
- [5] Kolesnikov A, Andreev M, and Abel A (2018) The Fault-Augmented Approach for the Systematic Simulation of Fault Behavior in Multi-Domain Systems in Aerospace, SAE Technical Paper 2018-01-1917, doi:10.4271/2018-01-1917.
- [6] Liu W.Y, Tang B.P, Han J.G, at all (2015) The Structure Healthy Condition Monitoring and

- Fault Diagnosis Methods in Wind Turbines: A Review - Renewable and Sustainable Energy Reviews. Volume 44, 466–472
- [7] Ali, E (2016) A Machine Learning Approach for Tracking the Torque Losses in Internal Gear Pump - AC Motor Units, 10th International Fluid Power Conference. Dresden, March 8-10, 2016, Dresden, Germany
- [8] Choi S, Haque M. Sh, Tarek M. T. B (2018) Fault Diagnosis Techniques for Permanent Magnet AC Machine and Drives—A Review of Current State of the Art, IEEE Transactions on Transportation Electrification. Volume 4, Issue 2, doi: 10.1109/TTE.2018.2819627
- [9] Miller S, (2019) Predictive Maintenance Using a Digital Twin, MathWorks Technical Articles, <https://www.mathworks.com/company/newsletters/articles/predictive-maintenance-using-a-digital-twin.html> Accessed 23 Jan 2020
- [10] Jegadeeshwaran R, Sugumaran V (2013) Comparative Study of Decision Tree Classifier and Best First Tree classifier for fault diagnosis of automobile hydraulic brake system using statistical features - Measurement. Volume 46, Issue 9, 3247–3260
- [11] Loh Wei-Yin (2011) Classification and Regression Trees - WIREs Data Mining and Knowledge Discovery. Volume 1, 14–23

ENABLING SIL2 SAFETY CERTIFIED APPLICATIONS FOR MOBILE MACHINE OEMS

Dr. Peter Lauer

Eaton Cooperation, Industrial Sector COE, Hydraulics, 7945 Wallace Road, Eden Prairie, MN 55344 USA

Tel.: +1 952 937 7119; E-mail address: petermlauer@eaton.com

ABSTRACT

Eaton created a new safety controller architecture to allow our customers to design implement, verify and maintain a SIL-2 safety certified application for compliance with IEC 61508:2010 and ISO 13849 Functional Safety Standards.

The new architecture has been implemented in a line of safety controllers SFX12 and SFX20 that extend the line of existing mobile controllers HFX12 to HFX48. The new controllers are targeted for controlling mobile and stationary machine applications with focus on steer by wire and propel by wire.

Keywords: functional safety, IEC 61508, Safety Integrity Level

1. INTRODUCTION

Functional Safety for mobile machinery is a new challenge for machine OEMs that are integrating hydraulics with electronic control systems. Several standards have emerged that can be used to prove compliance to the machinery directive by the European Union.

In this document we will outline a path to certify a mobile machine for functional safety using one of Eaton's safety controllers.

2. THE PROCESS TO A CERTIFIED SIL2 SAFETY APPLICATION

2.1. Overview over safety standards

By signing the Machinery Directive into law, the European union mandated that products must be assessed for safety. The overarching standard for functional safety is IEC 61508 for electric, electronic and programmable electronic systems.

It defines in detail how to design verify and validate an E/E/EP system and defines four SIL, safety integrity levels. ISO 13849 focuses on machinery safety and includes guidance for the

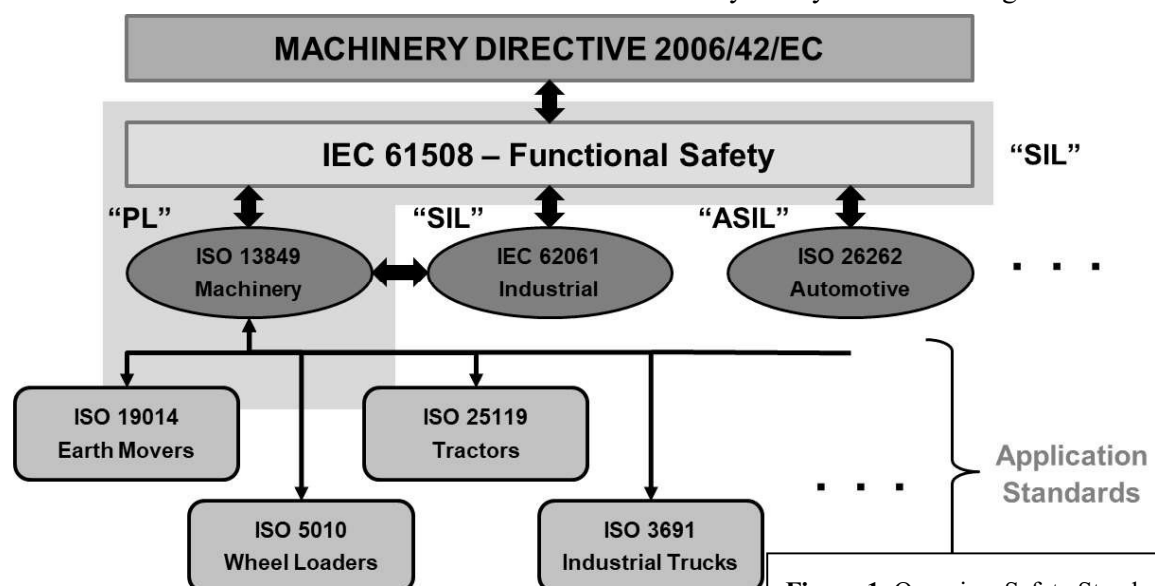


Figure 1: Overview Safety Standards

mechanical part of the machinery in addition to the electronic control. IEC 62061 and ISO 26262 apply the safety aspects to industrial application and automotive applications (Figure 1).

ISO 19014 Earth moving machines, ISO 5010 Wheel loaders, ISO 25119 Tractors, ISO 3691 Industrial trucks and others are application standards for specific groups of machines. If you are creating a safety application for a machine where an application standard exists, that standard will contain the most detailed information, since the operating conditions of the machines are known.

2.2. Steps to functional safety compliance

Select a safety standard

The machine builder/ OEM is responsible for selecting the safety standard to apply. Each standard has named their safety levels differently and associates different requirements to these levels. Once selected, the Hazard and Risk analysis will determine which safety level needs to be achieved in that standard.

Create a Hazard and Risk analysis (HARA)

The HARA is a formal process to list, classify, assess and rank the risks and hazard in the system. The standard ISO 12100 gives guidance and a basic framework to conduct the HARA.

define the safety function AND SAFE STATE

The risk in the safety related part of the control system that needs to be reduced according to the HARA will be supervised by the Safety Function. Creating a FMEA (failure mode and effect analysis) will create the necessary input for the requirements and creates data for the diagnostic coverage. The safety function will be able to detect a hazardous state and put the system into the safe state.

The standards have design criteria that specify safety functions and safe states that must be met. An important part of the verification and validation process is to prove the correct execution of these functions.

Define and verify safety requirements

Safety standards require a formalized process to manage requirements through out the life cycle of the product.

The V model (Figure 2) is always referenced when higher level system requirements are decomposed in to lower level software and hardware requirements. Part of the planning process is to create test procedures that will be executed during the verification and validation phase.

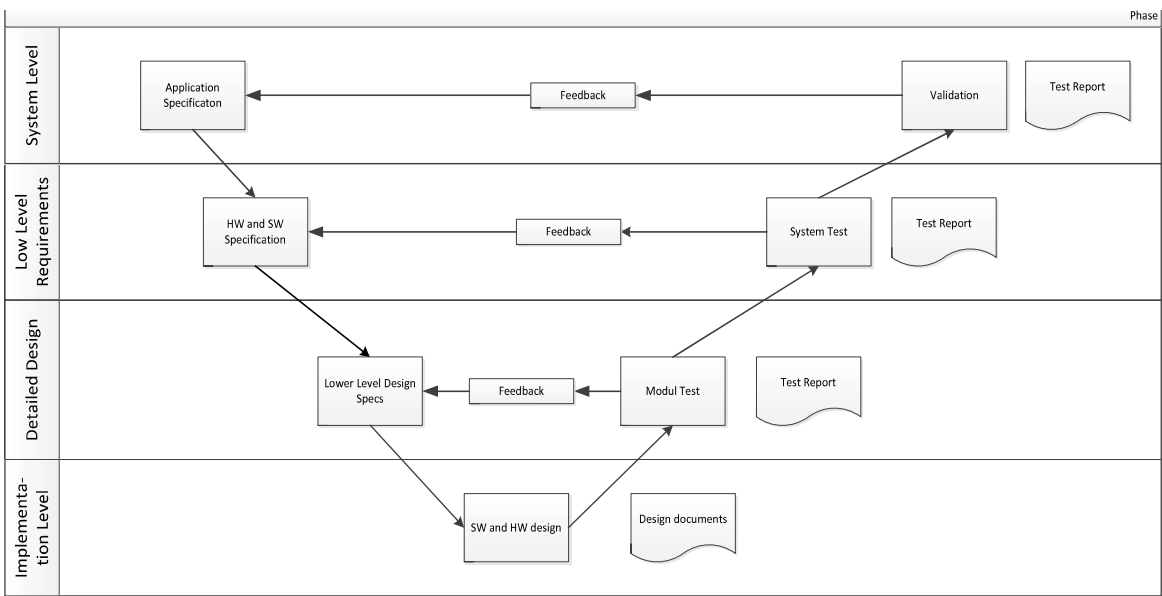


Figure 2: V Model for System Verification and Validation

Design and implement functional safety

In the development process, the individual requirement elements will be realized. Hardware will be designed or purchased, software will be written, and the system will be built.

Verify and Validate functional safety

Verification and validation will prove that the system requirements are implemented and perform as expected. It is important that each requirement is covered with an appropriate test case, and no requirements will be missed. Testing needs to be well documented and serves as proof to the certification agency.

Operation and Support

The functional safety standard requires the machine builder to have processes in place for operation, production and long-term support. The product needs to have a complete life cycle support.

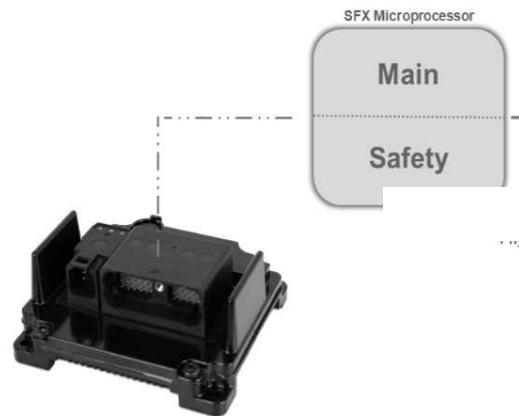


Figure 3: SFX Controller

3. THE EATON SFX CONTROLLER

The SFX product is certified for functional safety and is a version of the Eaton HFX mobile controller family. The HFX product line is a mobile controller with typical inputs and outputs that are needed in mobile machinery. They are designed to drive hydraulic proportional valves and interface with a variety of sensors, digital and analog.

Connectivity is provided via CANbus ports using the SAE J1939 or CANopen standards.

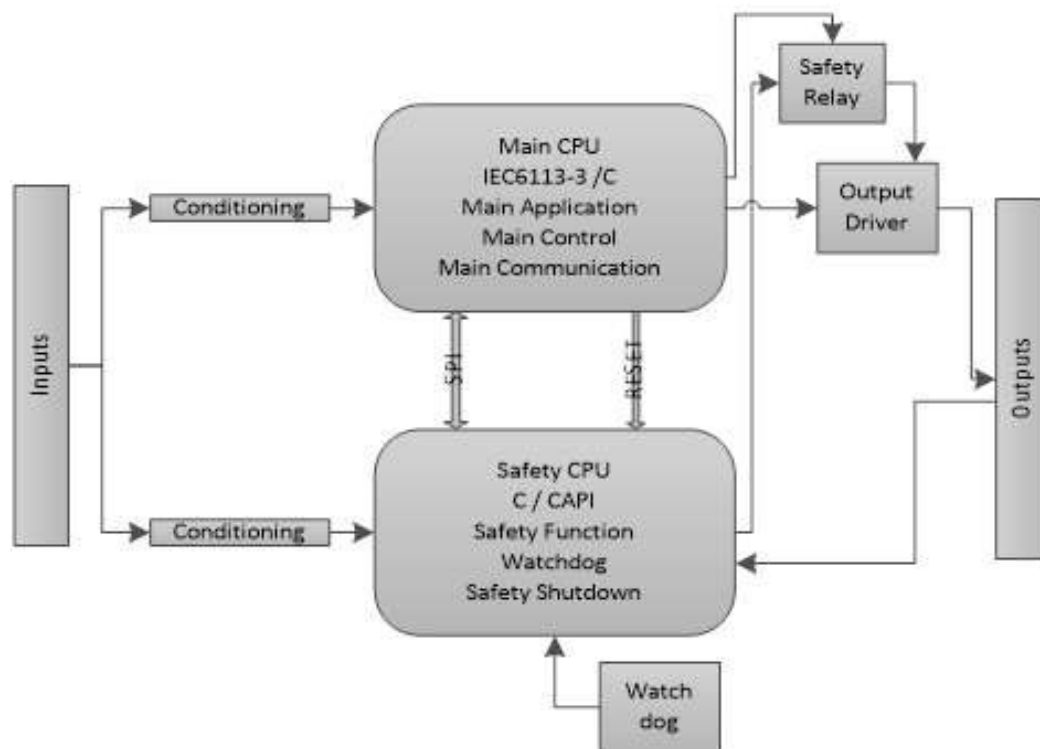


Figure 4: Safety Controller Architecture

Two sizes with four versions of programmable IO configurations, from 6 inputs and 6 outputs to 24 inputs and 24 outputs allow fitting the controller perfectly to the machine application.

Software programming in the application domain can be done in C with an extensive C-API library, MATLAB / Simulink or any of the IEC 61131-3 languages.

In addition to the standard HFX application controller with the I/O functions, the SFX version contains a separate safety CPU (Figure 3). The safety CPU monitors all inputs and outputs independent of the application CPU to allow for the implementation of application-specific safety functions that are physically isolated in the safety domain (Figure 3). The safety domain provides greater than 90% fault detection coverage.

This includes supervision of all internal voltages and servicing a hardware watchdog timer. The lockstep core ensures very low FIT numbers for the processor chip.

3.1. Channel Structure

The safety CPU is connected to the sensor input. (Figure 5). It will read the voltage directly from the pin and has its own sensor conditioning. If

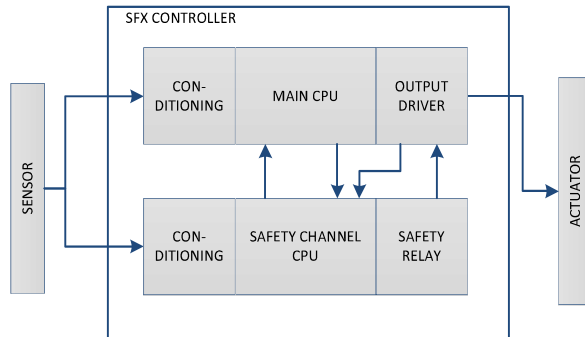


Figure 5: 1001 Channel architecture according to IEC61508

there is a fault in the sensor input conditioning of the Main CPU in the application channel, it does not affect the reading of the safety CPU. With the knowledge of the connected sensor in the application it can decide if the application is safe. The safety CPU queries the application CPU about the type of sensor connected, to interpret

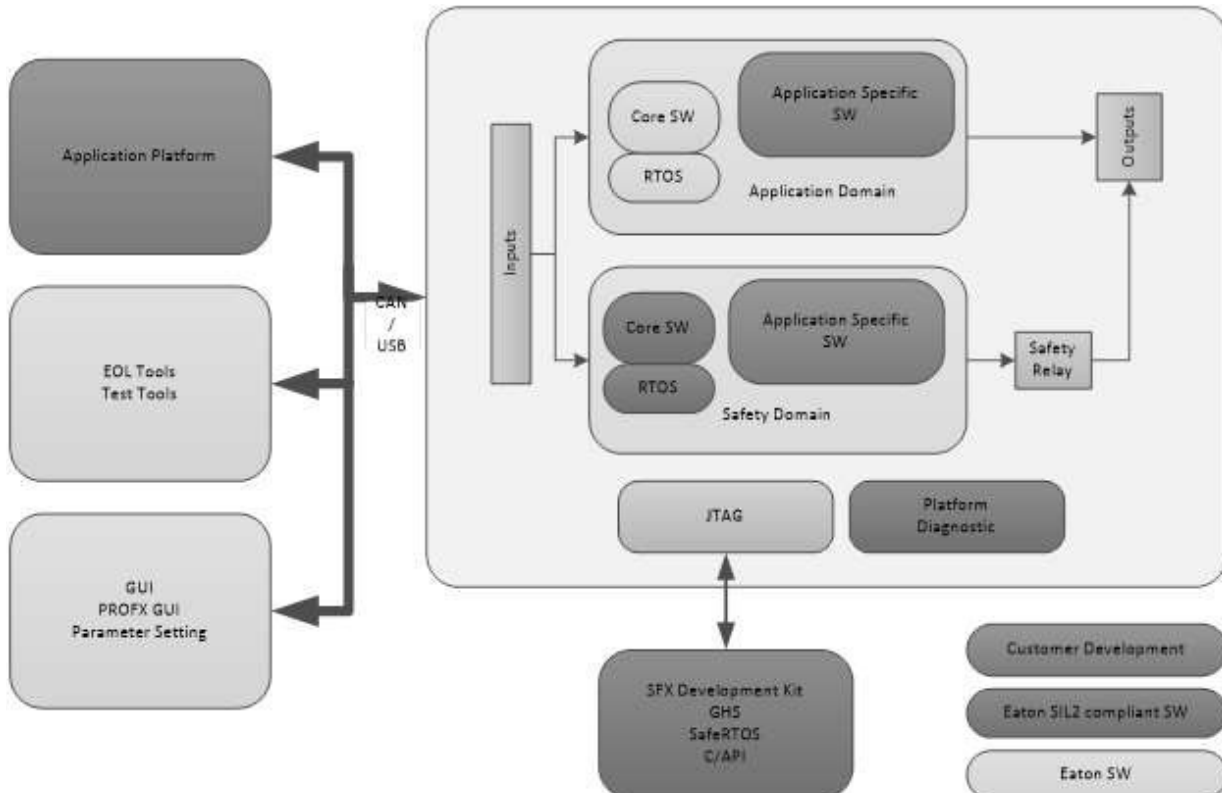


Figure 6: SFX software architecture block diagram

the pin voltage correctly. In case the safety CPU detects a faulty sensor, it can open the safety relay that will then disable the output driver of the main CPU. That way it can prevent the application to operate with a faulty sensor and put the system into a dangerous state.

3.2. Safety function

The safety CPU will execute the user written application specific safety functions that will supervise the machine operation. In a fault condition the safety function will deactivate a safety relay that will remove power to all outputs. This will remove power from all actuators and valves that will then move into their fail-safe position.

3.3. Software architecture

The software architecture block diagram is shown in Figure 6, illustrating the software modules.

In the application domain, the core software contains all low-level drivers to service the hardware, general real time operating system functions (RTOS) and the communication interfaces. These elements are provided by Eaton. The main domain application software is created by the machine builder / OEM and contains the functions that the machine will execute. Since the main domain application is separated from the safety domain, this software does not have to meet the requirements from the safety standard. For example, once the product is released and the safety software is certified, changes in the application software will not affect the safety certificate.

In the safety domain, the core software provided by Eaton is SIL 2 compliant. The RTOS is a commercial of the shelf operating system (SAFERTOS) that is pre-certified by the vendor. All the code development is done with a SIL certified compiler (Greenhills C). A verification and validation model is executed (Figure 2), and the code quality was assessed with static and dynamic verification tools such as MISRA, Polyspace bug finder and other code analysis methods for timing, complexity and memory utilisation.

4. THE PRODUCT DESIGN PROCESS

This chapter will layout the process to design a system that requires functional safety. From the overall functionality of the machine, the safety critical functions need to be isolated. ISO 18349 calls them SRP/CS, Safety Related Part of the Control System. The hazard analysis of the system will guide through that process and identify if a SIL2 system is necessary.

For example, if the system is a truck mounted crane with a hydraulic actuator and an electronic control, then the SRP/CS is the cylinder actuation of the boom of the crane.

The next step is to identify the safe state the system needs go into in case of a failure. On a hydraulic system the safe state can be zero output flow from the hydraulic valve and no movement of the boom cylinder. In the example the hazard analysis determined a SIL2 system to be necessary. The function is a type B, high demand. Since the system has no fault tolerance, the safety failure fraction of the system needs to be 90% to 99%, the PFD below $10e-6$ hours.

The safety function will be able to ensure that the SRP/CS executes correctly, that there are no faults and the actuator response is in accordance with the command input. The safety controller supervises the hydraulic system and will detect unintended cylinder motion. The safety controller will shut down the hydraulic valve via a mechanism (electronic power off or external hydraulic shut down) within a specified time, for example 0.2 seconds. It is verified by the user of the machine that when the safety function brings the system into the safe state within that specified time that the hazard has been avoided. In the verification and validation process test cases will be created that verify that the specified time can be achieved by the functionally safe system.

Creating of safety software

Application-specific safety functions monitor commands, cylinder motion and decide if unintended motion is occurring and activates the safety function. Since the main application and safety software on the SFX controller run in different domains on different processors, the safety software does not need to include application code. This simplifies the creation and verification of the software and reduces the design cycle time and effort. The safety software

will be more robust and will require no changes when the application software is modified.

verify the metrics

With the system completed, the actual SFF (safe failure fraction), MTBFd (mean time to dangerous failure), DC (diagnostic coverage) for the system can be calculated. The results for the SFX controller are provided by Eaton.

Verification and validation tools shall be applied to the safety software to satisfy the requirements of IEC61508. Test cases on the complete system that verify safety function, shall be executed.

Document results

An important part of safety system design is to create good and detailed documentation from requirements to test results. Good requirements management tools ensure valid documentation through the product life cycle. The documentation is critical for the approval process from the certification agency.

Creating safety manual

The documentation created during the design process are internal documents. Customer facing documents are catalogs, operation and instruction manual and most importantly the safety manual.

The safety manual gives the OEM detailed instructions under what conditions the safety integrity level is achieved.

5. CONCLUSION AND OUTLOOK

The newly designed SFX controllers will help more easily to introduce functional safety compliant machinery into the market with their unique safety architecture. This architecture is important because it allows changes to the application to be made later without having to re-certify the entire system.

NOMENCLATURE

SIL Safety Integrity Level
 SFF Safe Failure Fraction
 MTBFd Mean Time to dangerous Failure
 DC Diagnostic Coverage
 SRP/CS Safety Related Part of the Control System
 PFD Probability of dangerous failure per hour
 RTOS Real Time Operating System

OEM Original Equipment Manufacturer
 HARA Hazard and Risk Analysis
 FMEA Failure Mode and Effect Analysis
 HFX Eaton Hydraulics Controller
 SFX Eaton Safety Controller

REFERENCES

- [1] IEC 61508:2010 Standard functional Safety
- [2] ISO 13849 Standard Machine Safety
- [3] ISO 26262 Automotive Safety Standard
- [4] IEC 61133-3 PLC languages
- [5] ISO 12100:2010 Safety of machinery – General principals

SUPPLEMENTARY FAILURE MODE AND EFFECT ANALYSIS (FMEA) FOR SAFETY APPLICATION STANDARDS DIN EN ISO 13849 SAFETY FUNCTION-FMEA

Dipl.-Ing. Christa Düsing*, Dr.-Ing. David Prust

XCMG, European Research Center GmbH, Europark Fichtenhain B4, 47807 Krefeld,

* Corresponding author: Tel.: +49 2151 7830380; E-mail address: duesing@xcmg-erc.com

ABSTRACT

In the automotive industry, the Safety Function-FMEA according to ISO 26262 and its application to functional safety relevant systems is a well-established process in the form of Automotive Safety Integrity Levels (ASILs). These represent the failure mitigation that must be applied to ensure an acceptable residual risk of malfunctioning behaviour. The DIN EN ISO 13849 (ISO 13849) already describes a process to reduce risks for machines which starts with a Hazard And Risk Analysis (HARA) as described in DIN EN ISO 12100 and concludes with the Safety Requirements Specification (SRS). The SRS is a functional and technical safety concept defining requirements and guidelines to make sure the design conforms to defined safety goals. ISO 13849 lists important faults and failures for various technologies. The defined Safety Functions (SFs) can be classified in corresponding categories that lead to the particular hardware/system structure. This applies to mechatronic systems consisting of at least one sensor, one control unit and one actuator to monitor the system and effect a response in case of failure. Compared to the methods described in ISO 13849, the Safety Function-FMEA allows systematic identification of additional failures resulting from combinations of effects, rather than only listing the main failure causes. Based on the complexity of the machines it is highly recommended to perform a Safety Function-FMEA as a complementary method to assess and improve the overall safety of machinery.

Keywords: Mobile hydraulic machine, DIN EN ISO 13849, Failure Mode and Effects Analysis, FMEA, Safety Function-FMEA

1. INTRODUCTION

The standard ISO 13849 [1] [2] provides safety requirements of machinery for the design and integration of Safety-Related Parts of Control Systems (SRP/CS), e.g. in the hydraulic boom system for a loader crane. Amongst other issues, it provides general principles of design and validation. One of the main topics is to generate safety standards for machinery.

According to ISO 13849, a separate FMEA is proposed or recommended for quantification purposes for each of these described four steps:

- Risk assessment according to DIN EN ISO 12100 [3]
- Identification of preventive measures that are converted in the form of SFs
- Determine the required Performance Level (PL_r)
- Selection of the categories

The first step in the FMEA process is the risk assessment according to DIN EN ISO 12100 (ISO 12100), followed by the identification of the Performance Level (PL) according to ISO 13849 [1] [2]. Once completed, the first step outlines the hazards involved in the design, the process of risk analysis and risk evaluation and the strategy for risk reduction.

The second step details the identification of preventive measures that are converted in the form of SFs, according to ISO 13849. The SF is defined in this standard as “function of the machine whose failure can result in an immediate increase of the risk(s)” [4]. As an example, types of SFs for a hydraulic loader crane are:

- Avoiding unexpected start-up movements
- Emergency Stop function
- Safety-related stop function – initiated by a safeguard, e.g. *Overturing Protection*

Relationship between categories and PL

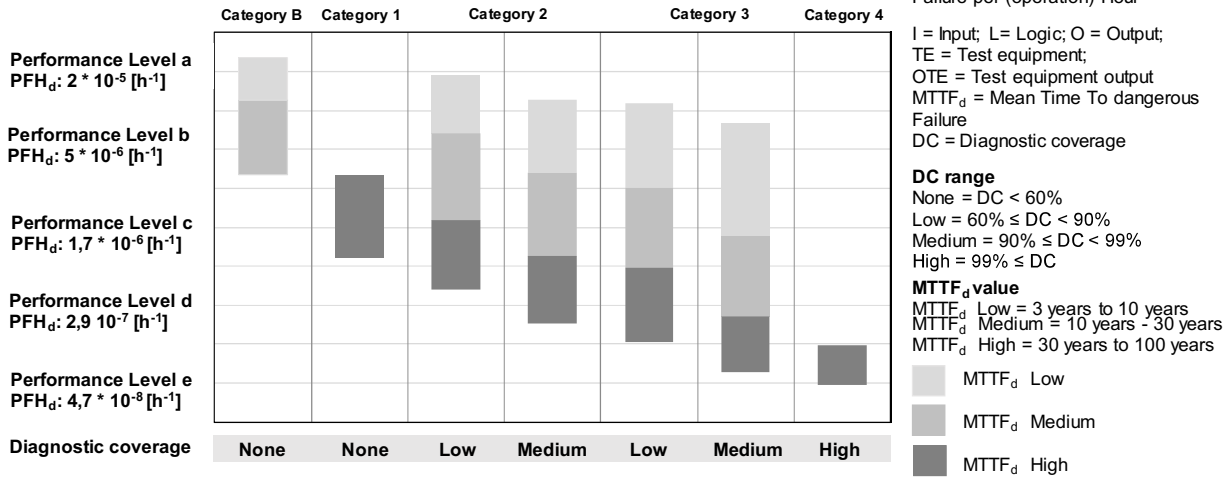


Figure 2: Relationship between categories and PL according to ISO 13849 [1] [2]

Figure 1 shows the *Overturning Protection* as an example. To avoid the loader crane from tipping over, the overturning torque (T) must be less than the counter torque for stability realized through the stabilizers, shown in equation (1):

$$T_{Overturning} < T_{Stability} \quad (1)$$

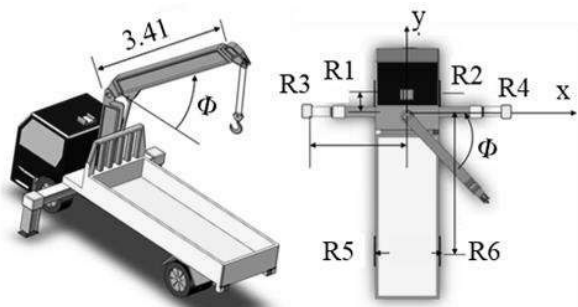


Figure 1: Detailed example for the calculation – *Overturning Protection* [5]

The third step is to determine the PLr by selecting the level of requirements for each SF. ISO 13849 [1] provides a risk graph for the elementary determination of the appropriate PLr, which includes:

- Severity of injury (S),
- Frequency and/or exposure to hazard (F)
- Possibility of avoiding hazard or limiting harm (P)

The defined risk parameters lead directly to the PLr and represent the level of risk. The higher the PLr, the higher the fault resistance of the control system has to be designed.

Next, the categories are selected. Depending on the category selection, the influence on the design of the SRP/CS becomes apparent; for the

relationship between the categories and the PL, see **Figure 2**. Each category shows typical hardware architectures of the SRP/CS and a corresponding assignment is required for each defined SF. The quantification is using the Mean Time to Dangerous Failure ($MTTF_d$) values, the Diagnostic Coverage (DC) values, and the Probability of dangerous Failure per Hour (PFH_d) values for the PL. These are integrated into the Category table according to ISO 13849 [1] see **Figure 2**, to realize the classification of the categories. The $MTTF_d$ values give a statistical probability of the failure of a specific component, e.g. a main control valve section, thus rating the reliability of the SFs. The DC defines the effectiveness of diagnostics, being the ratio between the rate of dangerous failures or total dangerous failures. All these parameters in total define the PL. The design architecture for each SF of the SRP/CS, for each Category is shown in **Figure 3**, **Figure 4** and **Figure 5**.

The structure of the architecture for Category B and Category 1 corresponds to a single-channel system (not redundant), as shown in **Figure 3**, with input, logic – processing and output. With Category B PL b is the maximum achievable performance level, see **Figure 2**. In Category B the minimum standard shall be designed, constructed, selected, assembled, and combined in accordance to fulfil the basic safety principles for the specific application. Category 1 shall be designed and built to use well-tried components and well-tried safety principles, according to ISO 13849 [1].

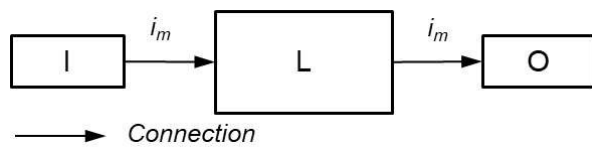


Figure 3: Designated architecture for Category B and Category 1 according to ISO 13849 [1]

Therefore, Category 1 requires that the customer can request a component which is well-tries and state of the art. Applying the standards guides manufacturers on how to confirm the achievement of well-tries components. The Category 1, supports PL b to c. In Category 2, the occurrence of a failure can result in the loss of the SFs, see **Figure 4**. As well as in Category B and Category 1, the architecture corresponds to a single-channel and continuously monitored system. The test allows detecting a dangerous failure of a component. Thereby, the choice of the frequency of the test rate decreases the occurrence of dangerous failures. With the output of the test equipment, the hardware structure includes a supplementary shutdown path.

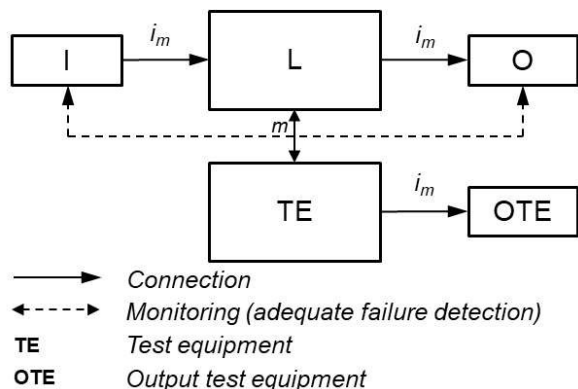


Figure 4: Designated architecture for Category 2 according to ISO 13849 [1]

As shown in **Figure 5**, the architecture for Category 3 illustrates that the performance of the SF detects some single failures with a two-channel structure (redundant), but not all failures. However, a loss of the SF can result from the accumulation of undetected failures. Category 4 additionally uses extensive monitoring to limit undetected failures and hence the accumulation thereof. Here, the SFs always come into action when switching the machine on or during the working cycles, regardless of the accumulation of failures.

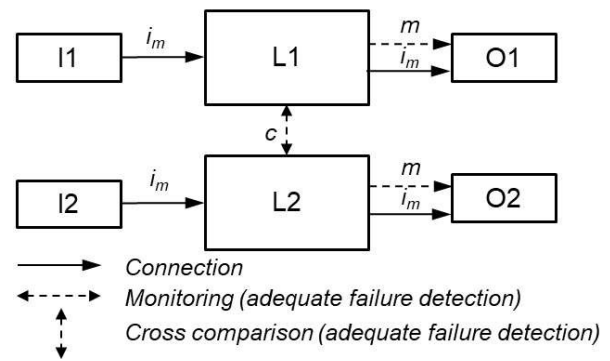


Figure 5: Designated architecture for Category 3 and Category 4 according to ISO 13849 [1]

2. FMEA GENERAL STRUCTURE

The Automotive Industry Action Group (AIAG) and the German Association of the Automotive Industry (VDA) released the latest publication on FMEA in 2019 [6]. FMEA structures have been completely revised and expanded by adding a new method, the “FMEA Supplement for Monitoring and System Responses” (FMEA - MSR) according to ISO 26262 [7]. The AIAG & VDA FMEA [6] standards are tailored to the automotive industry and thus, do not include a process of ISO 13849 [1] [2] for the required SFs in hydraulic control systems.

This circumstance serves the following fundamental question:

“How to integrate the defined SFs and the corresponding categories within the structure of the FMEA process?”

As guidance, this paper proposes several approaches how to perform an FMEA process for SFs in hydraulic control systems in practice. A function - as a non-safety-related function - usually describes the intended purpose of an object or a system element. One or more functions can be assigned to each other respectively AIAG & VDA [6]. Unlike this definition, safety-related functions of a mobile machine, e.g. for a hydraulic loader crane, are higher-level functions, supplemented as an add-on. These usually monitor the state of a functional system consisting of one to multiple inputs, one logic and several outputs. In the event of safety-relevant failures, the system will switch off or fall back to a safe state to maintain required safety levels.

3. INTEGRATION OF SFS INTO THE FMEA PROCESS FOR HYDRAULIC CONTROL SYSTEMS

When preparing a system or sub-system FMEA, it is recommended to implement a P - Diagram. The P - Diagram is a graphical representation of the system structure and shows the relationship between systems parameters, system elements and their functions in form of a block diagram. They are determined and elementarily visualized. For the standard FMEA process, the P - Diagram is built around the object under consideration of the product, system, sub-system and single component according to the scope of the analysis. It shows the input signals, the output signals, the unintended outputs, the control factors and the confounders [8]. **Figure 6** shows an example of a modified P - Diagram supplement including Failure Modes and the SFs.

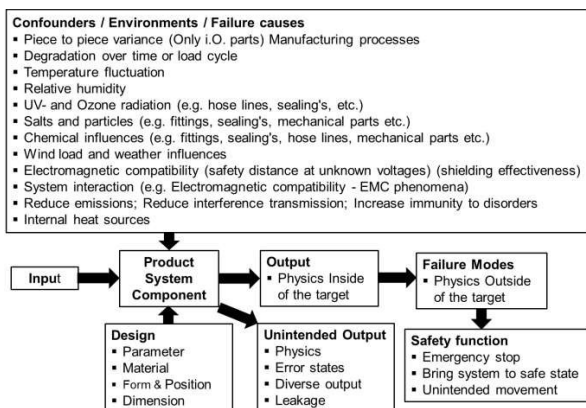


Figure 6: Proposed P – Diagram example, Quality in product development [8], with modified structure

The P - Diagram is advantageous when analysing complex systems with various system interactions, operating conditions, design parameters and complex relationships of functions. The focus in the P - Diagram may be on the input and output variables or the respective functions for the system, the sub-system or the single-components.

3.1. Theoretical models of a failure sequence chain

The analysis of each FMEA generally consists of three various failure aspects:

- Failure Effects
- Failure Modes
- Failure Causes

These three different aspects are linked together and show a failure sequence chain depending on the focus element. For connecting Failure Causes with Failure Modes, the question is: “Why does the failure occur?” [6] and for linking Failure Effects with Failure Modes, the question is: “What happens when the Failure Mode occurs?” [6]. The standard failure sequence chain according to AIAG & VDA [6], as shown in **Figure 7**, does not comprise the SFs. The following four models of failure sequence chains represent different solutions including the integration of SFs.

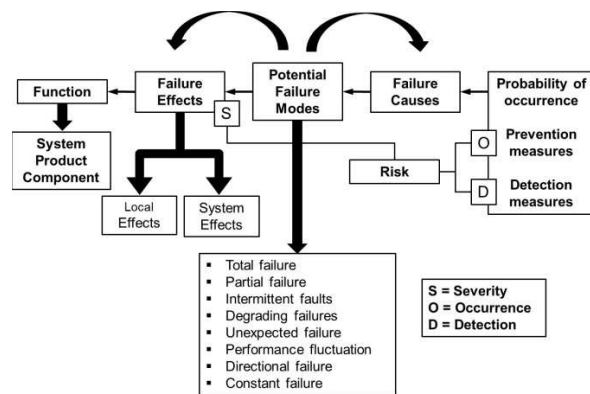


Figure 7: Standard model of a failure sequence chain according AIAG & VDA [6]

For better clarification, the following solutions show practical examples, using the sub-system first boom of a loader crane, as shown in **Figure 8** and shown as a hydraulic circuit diagram in **Figure 9**. According to the described process and the defined SFs, Category 2 PL d and Category 3 PL d are determined for the sub-system ‘first boom of a loader crane’.

In the case of the loader crane, the hydraulic pump is included in the scope of the truck hydraulics. The truck provides the required pressure supply and the corresponding flow rate via a specified hydraulic pump powered by the power take off (PTO) of the engine.

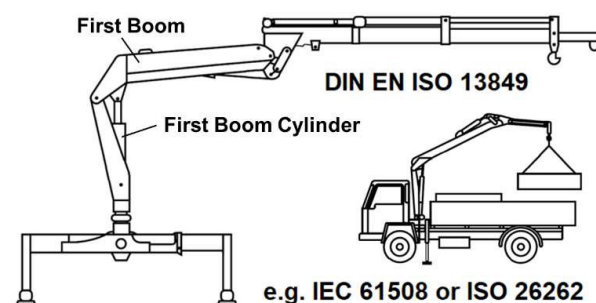


Figure 8: Loader Crane, First Boom, DIN EN 12999:2013-02+A2:2012 [9]

Thus, the hydraulics of the loader crane are directly connected to those of the truck.

The analysis of the hydraulic circuit diagram, **Figure 9**, shows all components that are essential for compliance with the SFs for the sub-system first boom.

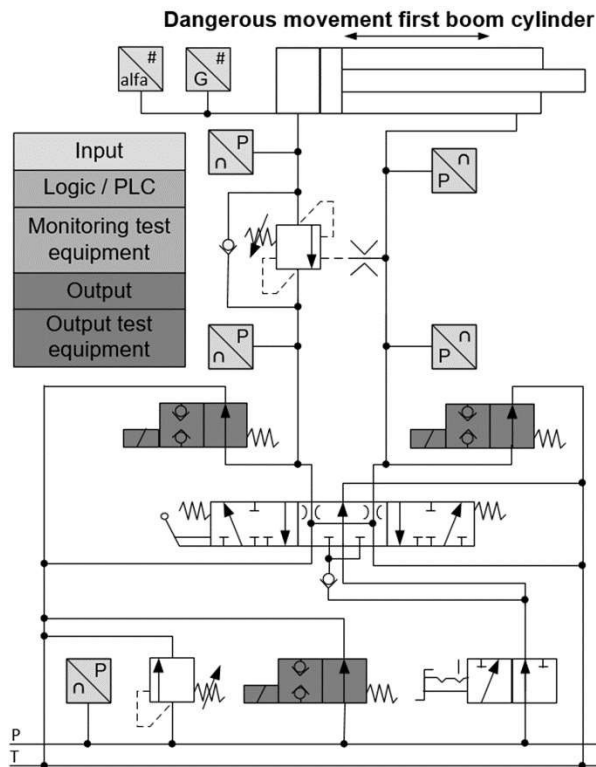


Figure 9: Hydraulic circuit diagram, First Boom, according to the IFA Report [10]

The sensors pointed out in light grey trigger the SFs. The switching valves, shown in dark grey, act as actuator of the logic and monitor values marked in mid-grey to prevent the dangerous movement of the first boom cylinder. This depends on the failure modes of the sensors and their interfaces. In compliance with basic and proven safety principles, safety valves (pressure relief valve and counterbalance valve) support the cylinder function. All electrical components are monitored by the Logic/PLC. According to the defined SFs and the corresponding Category 2 PL d the circuit implements two shutdown paths. Depending on the defined SFs, the first boom hydraulic also implements the Category 3 PL d with a two-channel structure.

First method of safety-related solution:

The first method of the safety-related solution of a failure sequence chain divides the Failure Modes into a safety-related part and non-safety related part. For all non-safety-related Failure Modes, the standard procedure of the FMEA process is applied according to AIAG & VDA [6]. If the Failure Modes are safety-related, further steps supplement the standard process see **Figure 10**. To achieve a better identification, a further column „How Failure Modes can disrupt safety goals/requirements“, supplements the failure sequence chain. Furthermore, the SFs are defined as preventive measures for the respective failures. The corresponding Categories defined in ISO 13849 [1] for the individual SF specify the detection structures for the relevant SFs, see **Chapter 1** Introduction. With the example of the respective SFs and their corresponding Category 2 PL d see **Figure 10**, the SFs will be defined as preventive measures to protect the system from damages. Additionally, the output of the test equipment is triggered by the safety detection measures; this reflects the two shutdown paths.

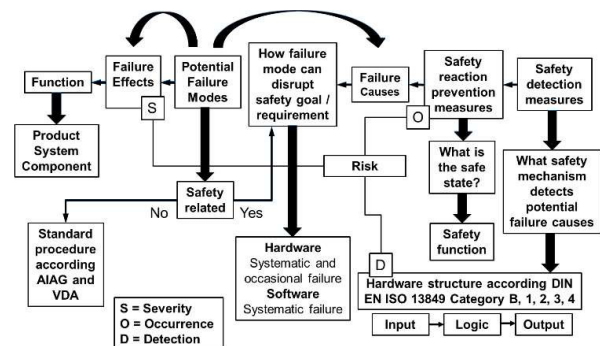


Figure 10: Proposed safety-related solution I, according ISO 26262 [7], kVA by UL [11], with modified structure to ISO 13849 [1]

The following example shows the conversion of the failure sequence chain into an FMEA structure, considering the SFs. This method of preliminary evaluation simplifies the system analysis and serves as a basis for the interface definition, and to generate the function and failure identification, see **Figure 10**.

XCMG				FMEA				Number:
System				First Boom Hydraulic of Loader Crane				Page: 1
Effect	S	C	Failure mode	How failure mode can disrupt safety goal / requirement	Cause INPUTS	Prevention action OUTPUTS	Detection action TE and OTE	RP AP N
Loader Crane, First Boom Hydraulic								
System element: Main Control Block Q38 - Hydraulic supply for cylinder system								
Function: Crane Mode on (change from pressure free circulation to closed state)								
[Loader Crane] Doesn't transfer pressure supply from main pump determines the load (bar)	8	C	Crane Mode on not possible (Doesn't change from pressure free circulation to closed state)	Reasons, e.g.: - The cable is cut - Wires are cut - Loose cable connection - Wire inside cable are twisted - Short circuit to supply - Short circuit to ground - Input / output values are stucked	Initial state: 04/12/2019 [Logic / PLC] Doesn't read Sensor Signals	Safety communication: > CANopen safety BUS-System	Test equipment: Separate Processor -> Evaluation of status information, functional target ranges, time delays, and maintenance information in the context of built-in functions	4 96 L
Loss of main function								
[Loader Crane] Doesn't transfer volume power from main pump determines the flow rate (l/min.)	8	C		Reasons, e.g.: - Output value is stucked - Input value is stucked - Measured value is outside the defined range - Transferred values are corrupted	Initial state: 04/12/2019 [Position Sensor B3 Digital] Doesn't generate a Digital Signal that the 1st Boom is in Transport position	SF: Inclination monitoring -> The SF is used to block the boom movements if the inclination angle exceed the max. allowed value	Output of Test equipment: -> Monitoring the SF	4 96 L
Loss of main function								
[Loader Crane] Doesn't guide the power supply to actuate the magnetic of Main Control Valve and Cylinder Valves	8	C		Reasons, e.g.: - Output value is stucked - Input value is stucked - Measured value is outside the defined range - Transferred values are changed	Initial state: 04/12/2019 [Position Sensor B3 Digital] Generate an incorrect Digital Signal that the 1st Boom is in Transport position	SF: Inclination monitoring -> The SF is used to block the boom movements if the inclination angle exceed the max. allowed value	Output of Test equipment: -> Monitoring the SF	4 96 L
Loss of main function								

Figure 12: Proposed FMEA Form Sheet, First Boom Hydraulic, Loader Crane

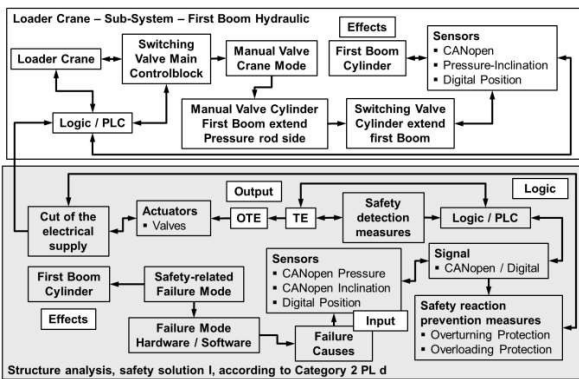


Figure 11: Proposed structure analysis, safety-related solution I

Figure 11 and Figure 12 show that the SFs are defined as safety reaction prevention measures. The task of these prevention measures is to bring the system to a safe state. The sensor signals of the respective components are monitored at start-up and/or during cyclical operation with the defined parameters for faulty signals outside the tolerance for value and time. The structure analysis also shows the two shutdown paths according to Category 2 PL d see Figure 11. Compared to the standard FMEA and their possibilities on how to integrate defined absolute characteristics into the FMEA structure, the SFs are implemented into the prevention action column of the form sheet, as shown in Figure 12. With this solution, it is not mandatory to build up the SFs with the corresponding Category 2 PL d in the function and failure networks. There is a possibility to integrate both FMEA processes (safety-related and non-safety-related) into one

structure. Accordingly, the disadvantage is that the structure gets very complex.

Second method of safety-related solution:

The second method of the safety-related solution of a failure sequence chain, see Figure 13, implements only SFs. Separately, a non-safety-related solution can be designed.

The standard model of a failure sequence chain was used as the basis. The difference to the standard model is that the Failure Causes are subdivided into three sections:

- Technical Failure Causes - Within the system
- Technical Failure Causes - Outside the system
- Failure Causes – Non-technical leads to Hazards

Additionally, there are safety-related causes triggered by the user, which influence the SFs. The implementation of the Category 2 PL d and Category 3 PL d, according to ISO 13849 [1], shall be realized in this solution through the function and failure networks.

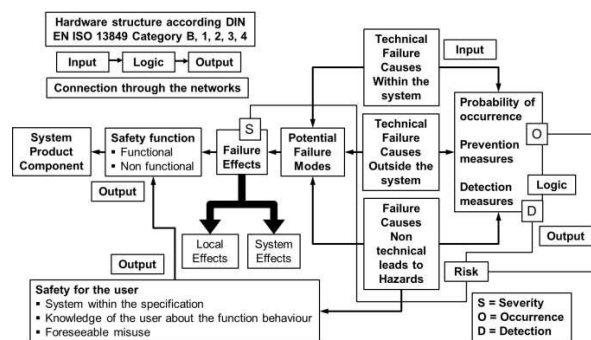


Figure 13: Safety-related solution II, Schellbach [12]

The structure analysis for the second solution into an FMEA structure, as shown in Figure 14

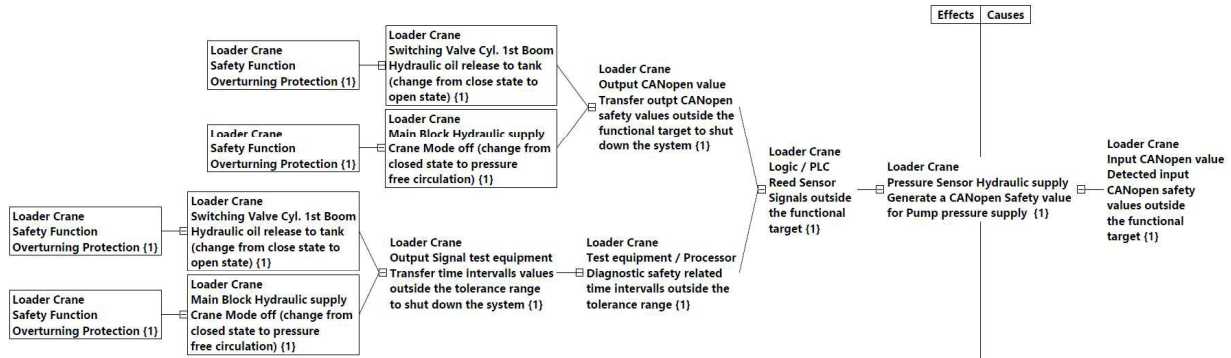


Figure 17: Proposed function network - Pressure sensor hydraulic supply - SF “Overturning Protection Category 2 PL d”

Fourth method of safety-related solution:

The fourth safety-related solution also divides the Failure Modes into non-safety related and safety-related Failure Modes. The difference to the other solutions is that all SFs and their corresponding categories are integrated into the failure sequence chain see **Figure 18**. The clear structure of the failure sequence chain thus simplifies the structure analysis and provides a good overview.

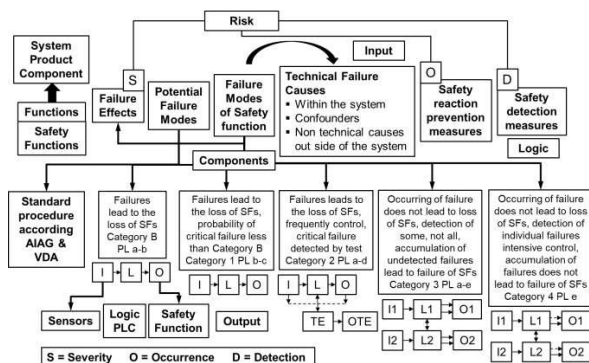


Figure 18: Proposed safety-related solution IV, according ISO 26262 [7], with modified structure to ISO 13849 [1] [2]

With this solution, the SFs are displayed directly with their associated category in the structure. The following example of a structure analysis see **Figure 19** shows the Category 3 PL d for the SF *Emergency Stop*. For this SF and depending on the focus of the failure causes, all involved components which are responsible for the subsystem ‘first boom hydraulics’ trigger the individual input. The SF as an add-on switches off the system depending on the output signals from the Logic/PLC. The structure analysis **Figure 19** illustrates the redundant functionality of the Category 3 PL d. The specified parameters and requirements for the Category 3 PL d controlled by the Logic/PLC cut off the electrical

supply if failures occur in channel 1 and channel 2 at the same time or when affecting the same function.

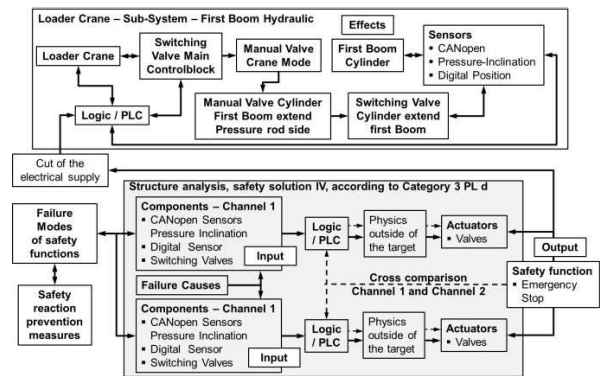


Figure 19: Proposed structure analysis, safety-related solution IV

When combined in one FMEA structure, the number of subsystems and the number of the defined SFs with different categories can easily make it very complex to build up a function and failure network including the non-safety-related functions, and the safety-related functions.

Figure 20 shows the proposed function network as a simplified example for the SF *Emergency Stop*, for the pressure sensor ‘hydraulic supply’ and the pressure sensor of the switching valve ‘cylinder bottom side’ of the sub-system ‘first boom hydraulics’ the proposed function network. Because all involved components on each sub-system influence the SF *Emergency Stop*, it is necessary to generate the function network for each component and for each sub-system, which triggers the SF.

For clear structuring, it is recommended to first create the individual function and failure networks of the responsible components for the SF *Emergency Stop* and then to combine these individual networks accordingly.

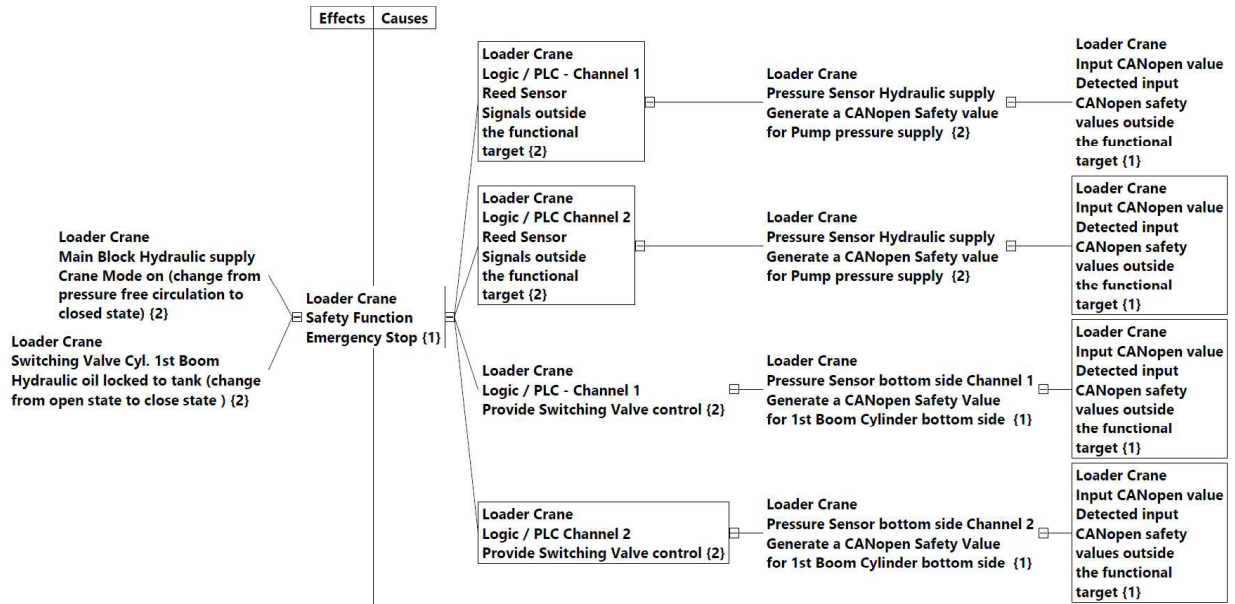


Figure 20: Proposed function network - Pressure sensor hydraulic supply - SF “Emergency Stop Category 3 PL d”

4. EVALUATION AND RESULTS

Four possible methods answer the question:

“How to integrate the defined SFs and the corresponding categories within the structure of the FMEA process?”

Figure 21 compares the four different methods, starting with a combination of a safety-related solution and a non-safety-related solution with the emphasis on the safety-related perspective, but with a complex FMEA structure when combined. The first and the fourth solution illustrate that the SFs are realized as preventive and detection measures. The second solution only looks at the safety-related parts and the SFs are realized as detection measures. Therefore, it has a clear structure in the function and failure networks. In the third and the fourth method, the SFs are supplemented as an add-on. Systematic four shows a fully integrated approach with a clear overview of the defined categories for all involved SFs, see **Figure 18**, but also includes a complex FMEA structure.

Comparison of possible safety-related solutions	First solution	Second solution	Third solution	Fourth solution
Various solutions				
Safety-related solution	x	x	x	x
Non-safety-related solution (Standard System FMEA)	x	possible	x	x
Combination of safety-related and non-safety-related solution (Standard System FMEA)	possible		possible	possible
Safety Functions				
Safety function as an add-on			x	x
Safety function as Prevention Measures	x			x
Test equipment with Outputs as Detection Measures	x	x	x	x
Category B, 1, 2, 3, 4 with corresponding hardware structure				
Integrated into the function and failure network		x	x	x
Failure Modes				
Divided the Failure Modes into safety-related and non-safety-related solution	x	x		x
Failure Causes				
Failure causes divide in different variants		x		
Structure of the function and failure networks				
Complicated structural design	x		x	x
Clear structural design		x		

Figure 21: Comparison of the methods

Figure 22 compares the advantages of the possible solutions based on the evaluation criteria. The practical implementation of the favoured third method can then be carried out as shown in for the example of the loader crane.

Evaluation criteria for the possible solutions Comparing the benefits	First solution	Second solution	Third solution	Fourth solution
Presentation of the categories into the FMEA process basically to be realized	-	+	++	++
Implementation into the structure feasible	+	+	+	+
Can be used as a starting point for functional analysis	+	+	+	+
Graphical representation of the scope of observation depended on a combination of safety-related and non-safety-related functions	+ -	+	++	- -
Adaption of evaluation criteria out of the FMEA-MSR possible	+	+	+	+
Can be used for various mobile machine systems	+	+ -	++	++

Figure 22: Evaluation criteria for possible solutions

5. CONCLUSION AND OUTLOOK

These methods not only apply to the one particular hydraulic mobile machine presented. Generally, they apply to all hydraulic mobile machines, which are a combination of a vehicle with a separate machine, such as loader cranes, fire trucks, truck-mounted concrete pumps or mobile cranes. The research using the loader crane example shows that separating the mobile machine and vehicle allows implementing the safety function and the corresponding categories into the FMEA structure.

For other mobile working machines, e.g. graders, wheel loaders or wheeled excavators where separation is not possible and where street approval must also be taken into account, the entire process must be re-examined to show whether the proposed approach can be applied as well. Therefore, the following question arises again:

“How to integrate SFs, corresponding categories and street approval with their risks within the structure of the FMEA process?”

NOMENCLATURE

<i>AIAG</i>	Automotive Industry Action Group
<i>ASILs</i>	Automotive Safety Integrity Levels
<i>DC</i>	Diagnostic Coverage
<i>DIN</i>	German institute for standardization
<i>EN</i>	European Standard
<i>F</i>	Frequency
<i>FMEA</i>	Failure Mode and Effects Analysis
<i>MSR</i>	Monitoring and System Response
<i>HARA</i>	Hazard And Risk Analysis
<i>ISO</i>	International Organisation for Standardization
<i>MTTF_d</i>	Mean Time To dangerous Failure
<i>P</i>	Possibility
<i>PFH_d</i>	Probability of dangerous Failure per Hour
<i>PL</i>	Performance Level
<i>PL_r</i>	Performance Level required
<i>PLC</i>	Programmable Logic Controller
<i>PTO</i>	Power take off
<i>S</i>	Severity
<i>SRP/CS</i>	Safety-Related Parts of Control System
<i>SRS</i>	Safety Requirements Specification
<i>T</i>	Torque
<i>VDA</i>	German Association of the Automotive Industry

REFERENCES

- [1] DIN EN ISO 13849-1, Safety of machinery – Safety related parts of control systems – Part 1: General principles of design (ISO 13849-1:2015)
- [2] DIN EN ISO 13849-2, Safety of machinery – Safety related parts of control systems – Part 2: Validation (ISO 13849-2:2012)
- [3] DIN EN ISO 12100, Safety of machinery – General principles for design – Risk assessment and risk reduction (ISO 1200:2010)
- [4] Barg J, Eisenhut-Fuchsberger F, Orth A, Ost J, Springhorn C (2012) 10 steps to performance level, Bosch Rexroth Group
- [5] Yang, Chia-Feng, (2010) Mechanics Based Design of Structures and Machines
- [6] AIAG & VDA, FMEA Handbook (2019), Failure Mode and Effect Analysis, AIAG
- [7] ISO 26262, Road vehicles – Functional Safety – (ISO 26262:2011-11-15)
- [8] von Regius B (2006) Qualität in der Produktentwicklung – Vom Kundenwunsch bis zum Fehlerfreien Produkt, Carl Hanser
- [9] DIN EN 12999, Cranes – Loader cranes; (DIN EN 12999:2013-02+A2:2012)
- [10] DGUV IFA Report (2/2017) Functional Safety of machine controls
- [11] kVA by UL, technical and management consulting group focused on functional safety and ISO 26262 standards
- [12] Schellbach A, Dörfel L (2019) Gesamtheitliche Betrachtung mittels der FMEA

